Jorge Rodas, PhD

Editor

Power Electronic Converters and Induction Motor Drives

Renewable Energy: Research, Development and Policies

nova
science publishers

www.novapublishers.com

Renewable Energy: Research, Development and Policies

The Future of Wind Energy
M. Dhurgadevi, PhD**,** P. Sakthivel, PhD and Gunasekaran, PhD (Editors)
2022. ISBN: 979-8-88697-232-0 (Softcover)
2022. ISBN: 979-8-88697-344-0 (eBook)

Microbial Fuel Cell: Electricity Generation and Environmental Remediation
Arpita Roy, PhD **and** Amit Kumar Roy, PhD (Editors)
2022. ISBN: 979-8-88697-190-3 (Hardcover)
2022. ISBN: 979-8-88697-238-2 (eBook)

Technical Challenges in the Commercialization of Transformers for Solar Photovoltaic Technology Applications
Bonginkosi Allen Thango (Author)
2021. ISBN: 978-1-68507-214-8 (Softcover)
2021. ISBN: 978-1-68507-249-0 (eBook)

Biofuel Production from Microalgae, Macroalgae and Larvae: Processes and Conversion Technologies
Man-Kee Lam, PhD, AMIChemE (Editor)
Jun-Wei Lim, PhD, ChM, MRSC (Editor)
Yoke-Wang Cheng, PhD (Editor)
Inn-Shi Tan, PhD, FHEA, Grad I.E.M (Editor)
2021. ISBN: 978-1-68507-116-5 (Hardcover)
2021. ISBN: 978-1-68507-159-2 (eBook)

Applied Soft Computing Techniques for Renewable Energy
Amit Kumar Thakur (Editor)
Rajesh Singh (Editor)
Ajay Kumar Kaviti (Editor)
Anita Gehlot (Editor)
J.V Muruga Lal Jeyan (Editor)
2020. ISBN: 978-1-53618-180-7 (Hardcover)
2020. ISBN: 978-1-53618-209-5 (eBook)

More information about this series can be found at
https://novapublishers.com/product-category/series/renewable-energy-research-development-and-policies/

Jorge Rodas

Editor

Power Electronic Converters and Induction Motor Drives

Additional color graphics may be available in the e-book version of this book.

Contents

Preface

With the increased emphasis on climate change and reducing harmful emissions in the atmosphere, interest in power electronics converters and electric motor drives has led to significant new developments in renewable energy systems or electric propulsion. By and large, an electric machine and a power converter are required as a means of propulsion in transportation-related applications, and an electric generator and a power converter are indispensable parts of many wind-energy-based generation systems.

This book entitled "Power Electronic Converters and Induction Motor Drives" resulted in five chapters covering some of the following topics:

- Linear and nonlinear control of three-phase and multiphase motor drive systems;

- Linear and nonlinear control of power electronics converters;

- Winding types of multiphase machines;

- Fault-tolerant control of multiphase machines;

I believe that the chapters published in this book, written by the world's leading researchers in the field, will provide a further impetus to the developments in the field, stimulating new research endeavours in an area that will likely increase in importance in the forthcoming years.

Acknowledgments

Chapter 1

Current and Voltage Control of AC Power Electronic Converters in Microgrids

Diego Pérez-Estévez and Jesús Doval-Gandoy[*]
CINTECX, Universidade de Vigo,
Applied Power Electronics Technology Research Group (APET),
Vigo, Spain

Abstract

Electrical grids are becoming more complex due to an increasing penetration of distributed power generation systems (DPGSs). Examples of DPGSs include renewable energy sources such as small water turbines, solar photovoltaic, wind turbines, and small non-renewable sources like engine generators, gas turbines and, fuel cells.

DPGSs provide some advantages compared to a traditional system with a centralized generation of electric power. These technologies place generation close to demand. This improves power quality, reduces feeder losses, and improves the regulation of local voltages. Moreover, it also enhances local reliability due to a decentralized generation structure combined with an effective integration of renewable sources.

Nonetheless, DPGSs also pose some challenges that should be addressed for a safe and efficient operation of the power grid. As the number of DPGSs that are connected increases, the grid becomes more difficult to control. Such problem is caused by the interaction between parallel energy sources with variable dispatch times and intermittent production. Therefore, new algorithms should be developed to control the power balance and to protect the distributed sources. In order to address this problem, the concept of microgrid (MG) arises.

A MG is a collection of local loads and generators that are coordinated in a decentralized way. The utility sees the MG as a single cell of the power system that behaves as a single producer or load; therefore, it reduces the control burden on the grid.

In order to effectively integrate the different types of sources and energy storage systems in a MG, power-electronic equipment is typically used. In particular, VSCs are commonly employed in the interface between the different elements that conform the MG due to their flexibility. They permit to regulate the output voltage and balance the power sharing by controlling both the magnitude and phase of their output voltage. Depending on the electrical variables regulated by the voltage

[*]Corresponding Author's Email: jdoval@uvigo.es.

source converters (VSCs), two different modes of operations are possible, namely, grid-following converter (GFLC) and grid-forming converter (GFMC). On the one hand, GFLCs usually behave as ideal current sources and they do not provide significant grid support in terms of grid voltage and grid frequency regulation. On the other hand, GFMCs can provide grid support when connected to a weak grid by regulating the voltage at the point of common coupling (PCC). These chapters focus on the design of high-performance current and voltage regulators for the control of power converters in a MG. The contents presented in these chapters have been published in seven articles in JCR-indexed journals [2, 1, 8, 4, 5, 6, 7] and have also been presented in six communications to the IEEE Energy Conversion Congress and Exposition (ECCE) [10, 9, 11, 12, 3, 13].

Keywords: power converters, current controller, voltage controller, finite control set (FCS), L filter, LC filter, LCL filter, harmonics, disturbance observers, resonant frequency, Bode's sensitivity integral, robustness

1.   Introduction

1.1.   Motivation and Objectives

Electrical grids are becoming more complex due to the increasing penetration of distributed power generation systems (DPGSs). Examples of DPGSs include renewable energy sources such as small water turbines, solar photovoltaic (PV), wind turbines (WTs), and small non-renewable sources like engine generators, gas turbines and, fuel cells.

DPGSs provide some advantages compared to a traditional system with a centralized generation of electric power. These technologies place generation close to demand. This improves power quality, reduces feeder losses, and improves the regulation of local voltages. Moreover, it also enhances local reliability due to a decentralized generation structure combined with an effective integration of renewable sources. Nonetheless, DPGSs also introduce some challenges that should be addressed for a safe and efficient operation of the power grid. As the number of DPGSs that are connected increases, the grid becomes more difficult to control. Such problem is caused by the interaction between parallel energy sources with variable dispatch times and intermittent production. Therefore, new algorithms should be developed to control the power balance and to protect the distributed sources. In order to address this problem, the concept of microgrid (MG) arises.

A MG is a collection of local loads and generators that are coordinated in a decentralized way. The utility sees the MG as a single cell of the power system that behaves as a single producer or load; therefore, it reduces the control burden on the grid.

The MG can operate in two different modes, namely, connected to the distribution network or in islanded mode. Examples of islanded MGs can be found in avionics, automotive, marine, and rural areas. During islanded mode, the MG should be able to track the time-varying demand of local loads. Since the local generators usually have a slow response and they are inertia-less, MGs that operate in islanded mode frequently contain additional energy storage systems in order to alleviate variations in demand and supply.

In order to effectively integrate the different types of sources and energy storage systems in a MG, power-electronic equipment is typically used. In particular, VSCs are commonly employed in the interface between the different elements that conform the MG due to their

flexibility. They permit to regulate the output voltage and balance the power sharing by controlling both the magnitude and phase of their output voltage. Depending on the electrical variables regulated by the voltage source converters (VSCs), two different modes of operations are possible, namely, grid-following converter (GFLC) and grid-forming converter (GFMC). On the one hand, GFLCs usually behave as ideal current sources and they do not provide significant grid support in terms of grid voltage and grid frequency regulation. On the other hand, GFMCs can provide grid support when connected to a weak grid by regulating the voltage at the PCC.

Nevertheless, as the number of distributed sources increases, it becomes more difficult to achieve a reliable voltage regulation and an adequate power sharing. Systems with conventional droop control loops can undergo voltage and power oscillations. In order to mitigate these problems, the control of a MG is organized into three levels [14], namely, the primary, secondary, and tertiary control.

The primary control contains the lowest level algorithms, which comprise the local voltage and current loops. This level determines the stability and the bandwidth of the whole system. The objective of this chapter is to improve the performance of the primary control in a MG by developing new voltage and current controllers that enhance the robustness and speed of the system. These controllers provide a solid foundation upon which the higher levels are being built.

The secondary control generates electrical references in the MG and ensures that they are within the required values. This level generates the voltage and current references that command the primary control. It is also responsible for synchronizing the MG with the distribution system during the transition from islanded to grid-connected mode. Finally, the tertiary control regulates the energy-production level and the power flow between the MG and the grid.

1.2.   State of the Art

A wide variety of methods have been used in the primary control of a voltage source converters (VSCs). The aim of this introduction is to present a review of the most commonly adopted current and voltage control methods and to explain their advantages and limitations when they are implemented in a microgrid (MG).

The most common approaches use techniques from classical linear control, modern linear control, nonlinear control, adaptive control, robust control, and model predictive control. Among the different methods, linear controllers are the most commonly adopted solutions for the primary control of a voltage source converters (VSCs) because, in a MG, both the physical plant and the most common types of disturbances are usually effectively represented by linear models. Moreover, compared to non-linear control structures, linear methods offer a wider range of mathematical tools for analysis, which allow to determine the stability, the performance, and the robustness under different conditions. Due to this advantages, linear controllers are particularly suited for this type of application. This chapter focuses on the design of linear controllers for the primary control of power converters in a MG.

Before presenting the different types of controllers used in the primary control of a power converter, a brief description of the most commonly installed filters is detailed in

the next section. The three types of coupling filters that are commonly used in a MG are presented, namely, the L, LC, and LCL filter. A special emphasis is placed in the case of the LCL filter, which is used in most of the current controllers presented in this chapter. Next, the previously proposed current and voltage controllers are described and their limitations are indicated. In particular, proportional-resonant (PR) and proportional-integral (PI) controllers are studied in detail because they are the most commonly adopted type of controller in these applications.
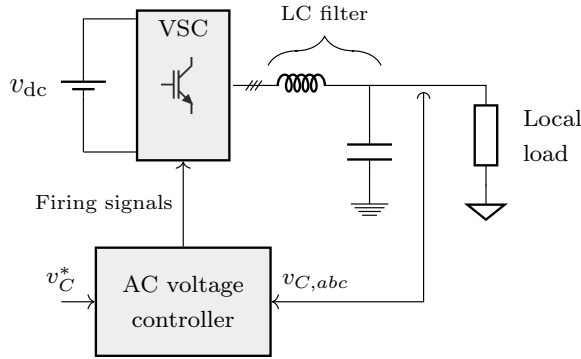
Figure 1. A voltage source converters (VSCs) that operates in stand alone mode feeding some local loads through an LC filter.

1.2.1.   Coupling Filters Used in Microgrids

A voltage source converters (VSCs) that operates in stand-alone mode or as a grid-tied inverter requires a coupling filter in order to be connected to the grid or to feed some local loads. This filter attenuates the high-frequency switching noise that the voltage source converters (VSCs) generates and provides a voltage with a low distortion at the PCC. Nonetheless, the type of coupling filter installed in a power converter also influences the performance of the converter itself and can cause instability or accentuate undesirable interactions, such as resonances, between the different elements that conform the MG. Therefore, a thorough understanding of the characteristics of the coupling filter installed is key to understand the performance of any primary control in a voltage source converters (VSCs).

Different filter topologies can be used. Commonly, during stand-alone operation, an LC filter is installed, cf. Figure 1, whereas a grid-tied inverter typically uses an L or an LCL filter. Figure 2 shows an a grid-tied voltage source converters (VSCs) that is coupled to the grid using an LCL filter. The parameters L_1, L_2, and C represent the reactive elements of the LCL filter; R_1, R_2, and R_c model the equivalent series resistances of the filter (R_2 also includes the equivalent loss resistance of the voltage source converters (VSCs) [15]); $u'_{d,abc}$ is the voltage source converters (VSCs) output voltage; $i_{1,abc}$, $i_{2,abc}$, and v_{abc} are the LCL-filter state variables (the grid-side current, the converter-side current, and the capacitor voltage, respectively); $v_{g,abc}$ is the grid voltage at the PCC; and $i^*_{1,dq}$ denotes the grid-side current reference in the direct quadrature (dq) frame.

Compared to an L filter, an LCL filter can offer a higher attenuation slope with a smaller size because LCL filters attenuate the grid-side current with a slope of 60 dB per decade

above its resonant frequency, cf. Figure 3. Nonetheless, a voltage source converters (VSCs) with an LCL filter is more difficult to control because it has higher-order dynamics compared to a system with an L filter. Moreover, such dynamics contain lightly damped poles placed at the resonant frequency of the LCL filter, which can cause instability and degrade the robustness to plant parameter variations and disturbances such as low-order grid voltage harmonics.

In order to mitigate these problems, a current controller is required to control the operation of a grid-tied inverter with an LCL filter. Different current control strategies have been published in the literature. In the following, a review of the different current controller types is presented.
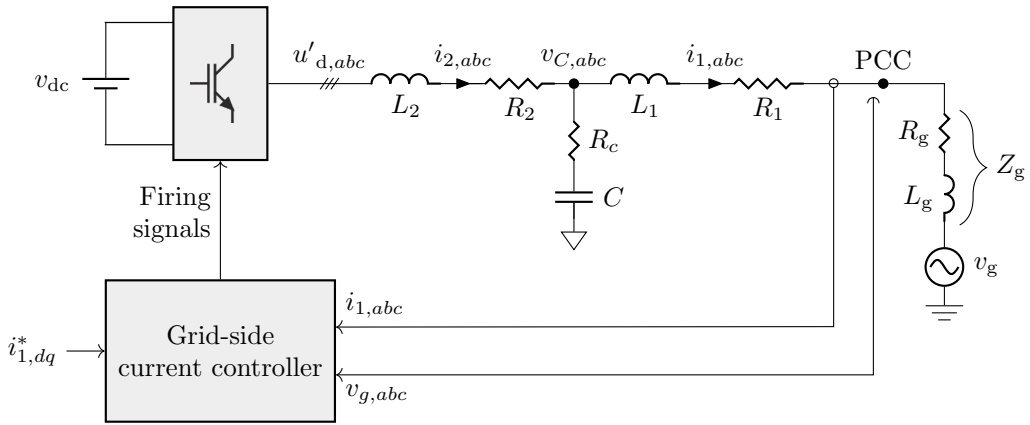
Figure 2. A grid-tied voltage source converters (VSCs) with an LCL filter and grid-side current controller.

1.2.2. Current-Control Techniques in Microgrids

The primary control in a power converter regulates the current and voltage at the output of the power converter according to a reference. In the case of a grid-tied VSCs with an LCL filter, two different variables are commonly controlled, namely, the converter-side current $i_{2,abc}$ and the grid-side current $i_{1,abc}$, cf. Figure 2. In this chapter, the grid-side current is always the variable that is controlled. This choice allows to control more accurately the power delivered to the grid compared to a converter-current controller.

Various current controllers for grid-tied VSCs with LCL filter capable of eliminating low-order harmonics in the grid-side current have been proposed in the literature. According to the modulation strategy employed, the current controllers can be classified as direct controllers [16, 17, 18, 19, 20, 21, 22, 23, 24, 25, 6, 26, 27, 28, 7] or pulse width modulator (PWM)-based controllers [29, 30, 31, 32, 33, 34, 35, 36, 37, 38, 39, 40, 41, 43, 44, 45]. Direct controllers use a finite control set (FCS) operation, i.e., they directly generate the firing signals that command the voltage source converters (VSCs), whereas PWM-based controllers require an additional modulation stage that converts the continuous controller reference voltage to a suitable sequence of voltage source converters (VSCs) switching states.

Among, the PWM-based designs, some of the proposed solutions use techniques from modern control theory [29, 44] or sophisticated feedforward schemes [30, 31]; however, conventional proportional-integral (PI) [32, 33, 34, 35] and proportional-resonant (PR) [36, 38, 37, 39, 40, 41, 43] controllers placed in different frames (so as to selectively target the desired harmonics) are the most commonly adopted solutions in the literature.
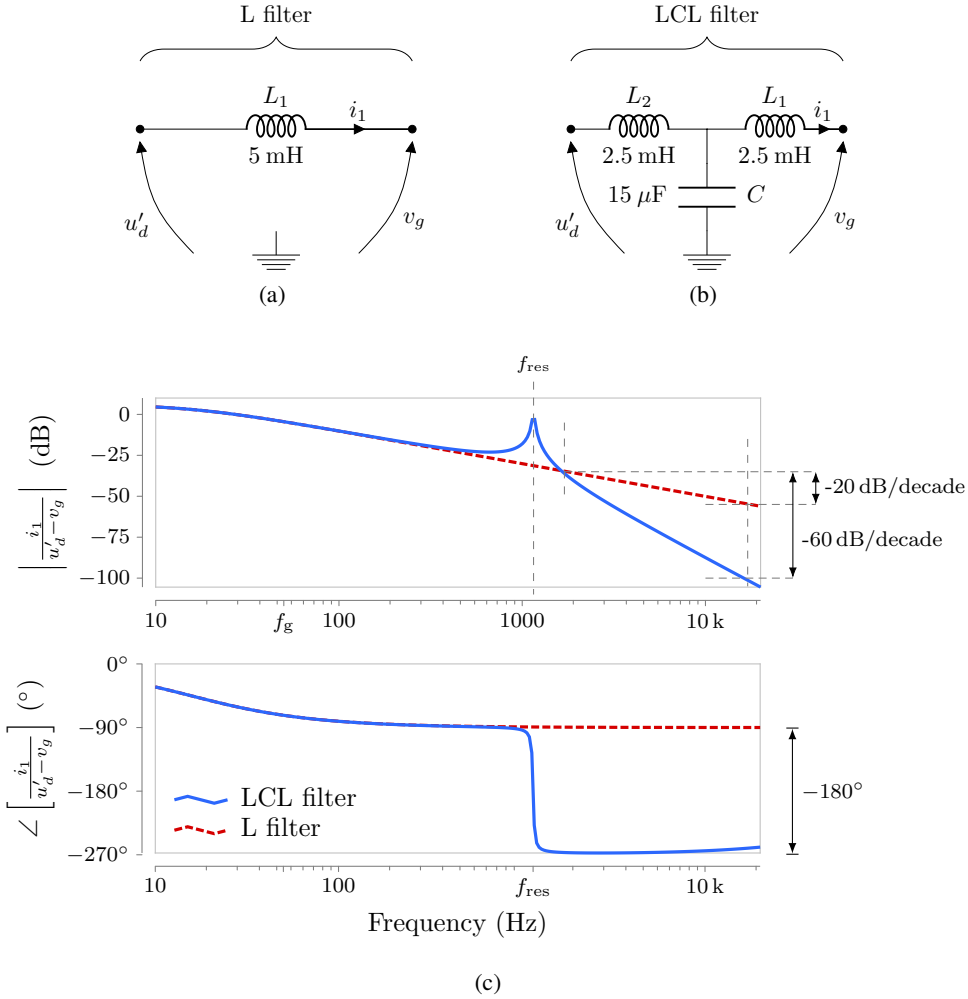
Figure 3. Examples of coupling filters. (a) L filter. (b) LCL filter. (c) Grid current i_1 attenuation provided by an L and an LCL filter.

A common problem of any linear feedback controller is the existence of a tradeoff between the the disturbance-rejection capability and the robustness to plant parameter variations. An example of such limitation is a repetitive controller [45]. This type of controller completely eliminates any periodic disturbance because it contains a resonant action (infinite gain) at the fundamental frequency of the disturbance and at all its harmonics. Nonetheless, such design results in a low robustness to plant parameter variations; therefore, practical implementations often have to limit the gain of the resonant action and consequently reduce the disturbance rejection capability.

Another common problem of some linear controllers, such as PI and proportional-resonant (PR), is the existence of a tradeoff between the reference-tracking and the disturbance-rejection capability during transients [40]: if the reference tracking is improved by a change in the controller gains, then the disturbance rejection worsens (and vice versa). A clear example of such limitation is a dead-beat controller [46]. This type of controller places the closed loop poles of the system at the origin of the z plane. Therefore, the response from its reference input to its output is equivalent to a delay of $T_s n$, where T_s is the sampling period and n is the number of poles of the system. Nevertheless, this extremely fast response to commands gives a low robustness to voltage disturbances and plant model variations, which limits its application to low-order plant models such as a voltage source converters (VSCs) with an L filter and an embedded controller with negligible computation delay [46].

Practical designs usually reach a compromise between these trade-offs. PI and proportional-resonant (PR) controllers, which are the most popular solutions, eliminate a disturbance at a certain frequency by tuning their resonant (or integral) action at such frequency. In this manner, the designer adjusts the balance between robustness and disturbance-rejection capability by changing the number of PI and proportional-resonant (PR) controllers in the feedback loop. Nonetheless, these type of controllers do not have enough degrees of freedom to completely control the dynamics of high-order plant that includes an LCL filter and computation and modulation delays. The work in [47] studies the stability of conventional PI controllers when they control the grid-side current in a grid-tied inverter with an LCL filter. Three regions of controller operation have been identified, namely, a low resonant frequency region where a conventional controller is unstable, a high resonant frequency region where stable operation is achieved, and a critical resonant frequency (one-sixth of the sampling frequency f_s) at which the system will be unstable irrespective of the tuning of the controller, cf. Figure 4. Thus, these controllers usually include ad hoc changes in their structure to improve the reference-tracking response, the robustness to plant parameter variations, or simply to become stable with a particular set of LCL filter parameter values and sampling frequency. This bespoke changes are usually referred as delay compensation schemes [48], active damping methods [49, 50, 51], or virtual impedance terms [52, 53].

In the following some of the previously described limitations are explained in detail by studying the output impedance of a grid-tied inverter that uses a classical proportional-resonant (PR) controller.

1.2.3. Limitations of Current-Control Techniques in Microgrids

An ideal current source generates a current that is independent of the voltage changes across it, i.e., the output impedance of an ideal current source is infinite. Although, no physical current source is ideal, A designer can assess the quality of a real current source, such as a grid-tied inverter, by comparing its output impedance with that of an ideal source.

The output impedance of a grid-tied inverter is determined by two factors, namely, a hardware and a software factor. The hardware factor is the type of output filter installed. Figure 5a shows a diagram of a grid-tied inverter with an LCL filter in an open-loop configuration, e.g., when no feedback control is implemented. In such condition, the voltage
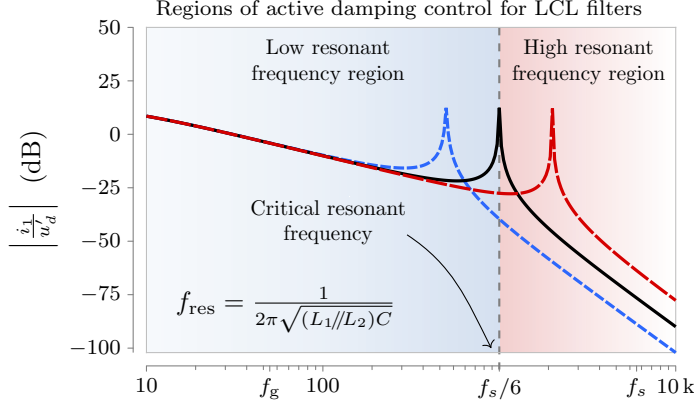
Figure 4. Regions of active damping control for LCL filters [47].

source converters (VSCs) behaves like a voltage source and the output impedance of the inverter is only determined by the reactive values of the LCL filter. Therefore, the resultant output impedance value is

$$Z_{out}^{ol} \quad = \quad -\frac{v_{PCC}}{i_1} = (Z_{L_2}//Z_C) + Z_{L_1}, \tag{1}$$

where Z_1, Z_2, and Z_c are the impedances of the reactive elements, including losses:

$$Z_1 \quad = \quad sL_1 + R_1, \;\; Z_2 = sL_2 + R_2, \;\; Z_c = 1/(sC) + R_c. \tag{2}$$

Figure 5b illustrates the magnitude of the output impedance as a function of frequency. As shown, the output impedance is low at the main low-order grid-harmonic frequencies. Moreover, at the resonant frequency of the LCL filter, the output frequency is close to zero. Hence, a small disturbance in such frequency regions causes a large grid-side current error. In order to change this undesirable response, grid-tied inverters commonly implement one of the previously presented closed-loop current-control strategies. Current-controlled VSCs present important advantages over open-loop VSCs. A current feedback loop permits to attenuate or remove the effect of disturbances on the system. Examples of disturbances that affect a voltage source converters (VSCs) that operates in a MG are low-order harmonics or voltage transients, such as sags, in the grid voltage. This characteristic is frequently denominated in the literature as virtual impedance or output impedance shaping [53].

In this manner, the second factor that determines the output impedance of a grid-tied inverter is the type of current controller installed. An important advantage of closed-loop controllers is that they can improve the dynamics of the grid-tied inverter by accurately controlling the current waveforms. Furthermore, they provides overload rejection and peak-current protection. In the case of a voltage source converters (VSCs) with an LCL filter, all these characteristics are commonly referred as the active damping capability of the controller.

Nonetheless, closed-loop controllers also impose some challenges to the designers of electrical power systems. A feedback loop can reduce the system stability, induce oscillations, or affect the robustness against electrical parameter variations in the MG, such as the

(a)

(b)
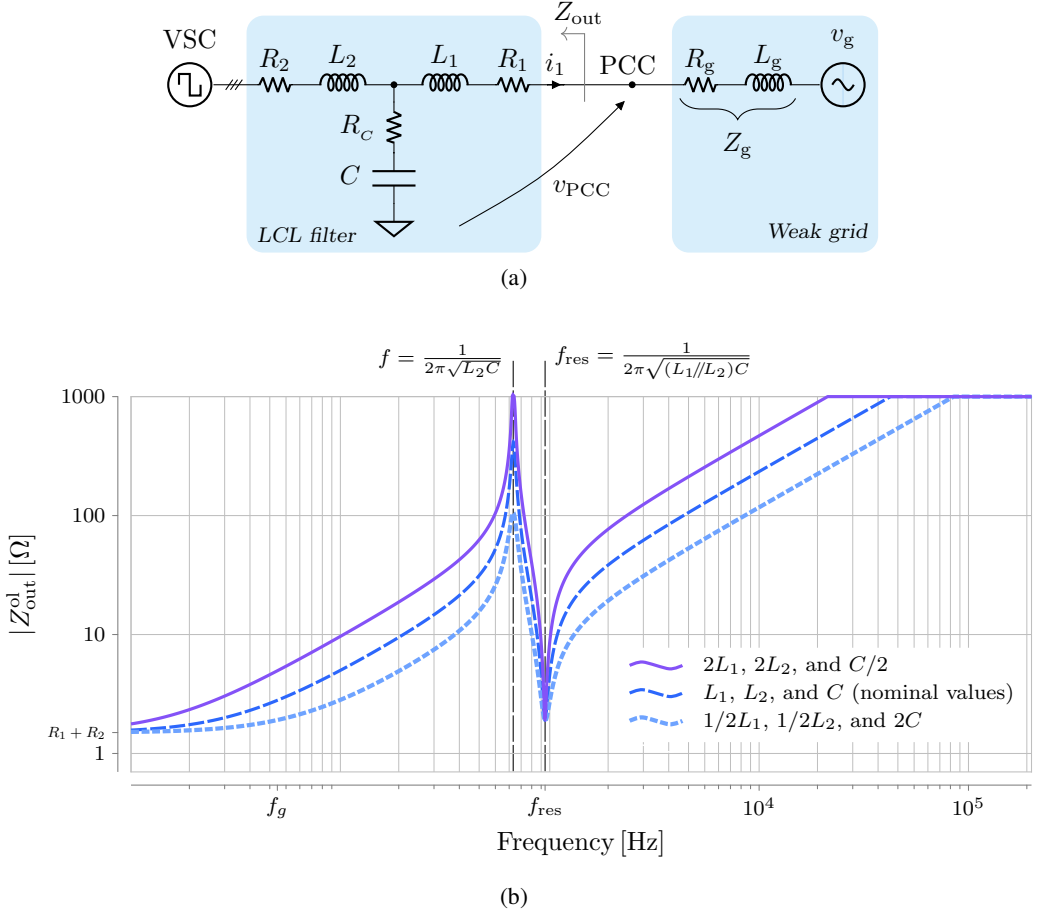
Figure 5. Output impedance of a voltage source converters (VSCs) with an LCL filter in an open-loop configuration. a Circuit diagram. b Change in the output impedance when the filter inductance is doubled and the filter capacitance is halved and vice versa.

grid impedance. In order to avoid these problems, closed-loop controllers are often tuned for a particular condition in which they operate. This typically includes the type of filter or coupling impedance and the impedance seen at the PCC.

The active damping capability, the output impedance shaping or virtual impedance, and the robustness to parameter variations: all these properties of a controller can be quickly assessed by analyzing its sensitivity function. The sensitivity function $S(f)$ of the system is a transfer function that shows how the controller responds to disturbances [54]. It indicates how much the controller modifies (amplifies or attenuates) the effect of disturbances on the grid-side current with respect to the open-loop response:

$$S(f) \;=\; \frac{i_1}{d_o}, \tag{3}$$

where d_o is a disturbance in the grid-side current. Examples of disturbances are low-order grid voltage harmonics v_g^h, voltage source converters (VSCs) nonlinearities, and plant model mismatches.
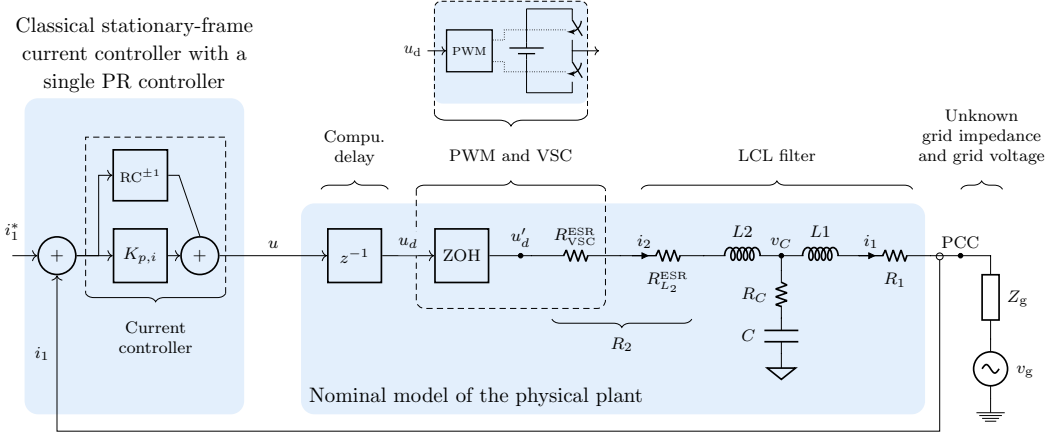
Figure 6. Clasical current controller structure and nominal model of the physical plant in the $\alpha\beta$ frame.

Such attenuation or amplification of disturbances in the grid-side current correspond to a change in the output impedance of the grid-tied inverter caused by the current-controller. The new output impedance when a closed-loop controller is installed is

$$Z_{out,cc}^{cl} \quad = \quad \frac{Z_{out}^{ol}}{S}, \tag{4}$$

Although it may seem that a designer can arbitrarily shape the output impedance of a grid-tied inverter by choosing the appropriate sensitivity function, in reality there are some constraints that limit this choice if a stable and robust system should be obtained. This constraints are presented in detail in later sections. Now, in order to illustrate this fact, an analysis of a grid-tied inverter is presented in the following.

Figure 6 shows a block diagram that depicts a system composed of a conventional proportional-resonant (PR) controller and a model of the physical plant. The physical plant model represents a voltage source converters (VSCs), an LCL filter, and it includes the effect of the PWM and computational delays. The selected current controller is a classical proportional-resonant (PR) controller with a delay compensation term ϕ'. The resonant part $RC^{\pm 1}$ is tuned at the grid frequency $\pm f_g$: It operates in the $\alpha\beta$ frame and it is discretized with an impulse invariant method and a sampling period of value T_s:

$$G_{RC} \quad = \quad k_{p,i} + \underbrace{k_{r,i}T_s \frac{cos\left(\phi'\right) - z^{-1}cos\left(\phi' - \omega_g T_s\right)}{1 - 2z^{-1}cos\left(\omega_g T_s\right) + z^{-2}}}_{RC^{\pm 1}} . \tag{5}$$

The tuning of the controller gains $k_{p,i}$ and $k_{r,i}$ and the parameter ϕ' was performed according to [37].

Although different tuning options are possible, classical resonant controllers (RCs) do not have enough order (they are second-order transfer functions) to completely control the dynamics of such a relatively high-order plant model that comprises an LCL filter model plus the computation and modulation delays (one and a half samples, respectively [15]). In

other words, this type of controller cannot arbitrarily establish the position of the closed-loop poles of the system, because their locations depend on the LCL filter installed.

The stability of classical controllers was analyzed in [47], where a threshold was found for the resonant frequency of the LCL filter: $f_s/6$ (with f_s being the sampling frequency). Such critical frequency value determines the region where an additional damping mechanism is necessary just to achieve stability. When the grid-side current is controlled, the frequency region where conventional resonant controllers are unstable is below $f_s/6$ [47]. Since the resonant frequency of the LCL filter in this setup is below one sixth of the sampling frequency ($f_{res} < 1/6 f_s$), the system is stable.

Figure 7 shows the sensitivity function S of the system illustrated in Figure 6 with the setup parameters indicated in Tables 1 and 2 and without considering the effect of the grid impedance (Z_g is assumed to be zero). It should be noticed that this transfer function determines the performance of the system because it shapes the output impedance of the current controller according to (4). As expected, at the fundamental grid frequency S tends to zero, hence Z_{out}^{cl} becomes infinity, e.g., the grid-tied inverter completely eliminates steady-state errors at such frequency. Furthermore, this controller successfully damps the resonance of the LCL filter ($S < 1$); nevertheless, it creates a new resonance at a lower frequency ($S = 8.1$). This problem occurs because a low-order controller, such as a proportional-resonant (PR) controller, does not have enough degrees of freedom to completely control the high-order dynamics of a physical plant composed of an LCL filter plus a computation and a modulation delay.

If the number of resonant controllers is increased so as to also obtain zero steady-state error at a set of grid frequency harmonics, this problem is augmented due to the additional dynamics introduced in the system by the resonant poles of the proportional-resonant (PR) controllers. Figure 8 shows the sensitivity function S of the previous system when three proportional-resonant (PR) controller are used. One controller operates in a stationary reference frame and is tuned at the fundamental grid frequency $\pm f_g$. The other two controllers operate in a synchronous frame that tracks the positive sequence of the fundamental grid frequency and they are tuned at the sixth and twelfth harmonics. As illustrated, new resonant peaks appear in the sensitivity function of the system, which introduce new low-damping (or resonant) frequencies in the system. Moreover, the designer cannot effectively modify the bandwidth of the low-sensitivity regions (blue areas), which determine the disturbance-rejection bandwidth of the controller.

Since this problems are caused by the high-order dynamics in a system composed by a grid-tied inverter with an LCL filter, other types of commonly used current controllers that were presented in Section 1.2.4 also present these limitations.

1.2.4. Voltage-Control Techniques in Microgrids

microgrid (MG) that operates in islanded mode or connected to a weak grid require a voltage controller to regulate the ac voltages within the MG. In order to regulate the ac voltage, a power converters with an LC filter can be used. This converter topology commonly implements a double-loop [55, 56] or a single-loop control structure [52] in their primary control.

On the one hand, double-loop structures provide a stable system using simple (low-
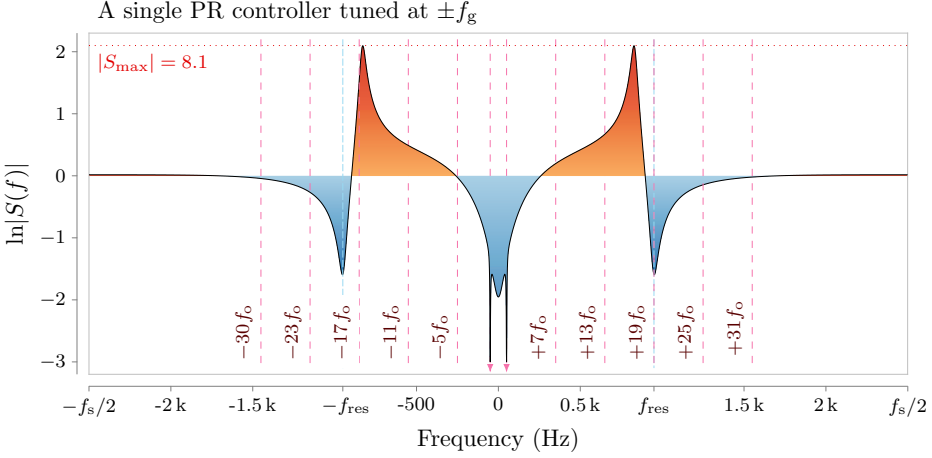
Figure 7. Graphical interpretation of the Bode integral for a voltage source converters (VSCs) with an LCL filter and a single proportional-resonant (PR) controller tuned at the fundamental grid frequency f_g.
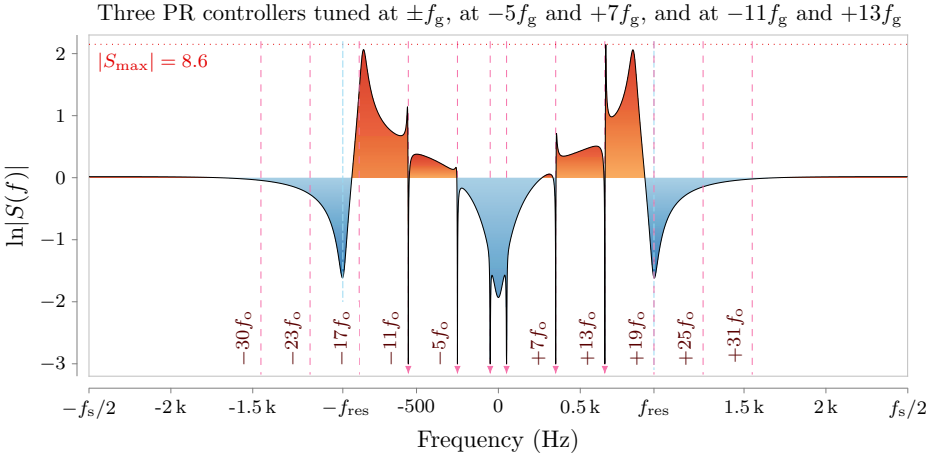
Figure 8. Graphical interpretation of the Bode integral for a voltage source converters (VSCs) with an LCL filter and three proportional-resonant (PR) controller. One controller operates in a stationary reference frame and is tuned at the fundamental grid frequency $\pm f_g$. The other two controllers operate in a synchronous frame that tracks the positive sequence of the fundamental grid frequency and they are tuned at the sixth and twelfth harmonics.

order) proportional-integral (PI) or proportional-resonant (PR) controllers because they divide the plant model into two parts. An inner current controller assumes the plant consists of an L filter and a computation and modulation delay, whereas the outer voltage loop mainly sees a capacitive plant in the low-frequency range where it operates. Nevertheless, double loop controllers have stability problems when controlling frequency components close or above the critical frequency ($f_s/6$), where f_s denotes the sampling frequency [57].

Table 1. Setup Parameters, cf. Fig 6

Base values		
Nominal power	P_{base}	10 kW
Phase voltage	V_{base}	230 V
Nominal current	I_{base}	14.5 A
Grid frequency	f_{g}	50 Hz
LCL filter		
Grid-side inductance	L_1	3.75 mH (7.4 %)
Converter-side inductance	L_2	3.75 mH (7.4 %)
Filter capacitance	C	15μ F (7.4 %)
Filter resonance	f_{res}	950 Hz
ESRs		
Grid-side ESR	R_1	0.5Ω (3.0 %)
Converter-side ESR	R_2	1.0Ω (6.0 %)
Capacitor ESR	R_C	0.1Ω (0.6 %)

Table 2. Controller Parameters

Classical Current Controller, cf. Fig 6		
Sampling frequency	f_{s}	5 kHz
Proportional gain	$k_{p,i}$	9.2
Resonant gain	$k_{r,i}$	1154.7
Delay compensation	ϕ'	0.57

On the other hand, single loop structures with classical transfer-function-based controllers [58] offer a simple design process. Nevertheless, they lack the flexibility, modularity and robustness to parameter variations of double-loop controllers [59]. Moreover, they usually need to measure additional variables, such as the converter current for protection against a short circuit or the capacitor current to achieve stability [52]. In particular, a single-loop controller cannot stabilize the system when the resonant frequency of the LC filter is less than one-fourth of the sampling frequency [60]. For these reasons, a multiloop structure is typically adopted.

Concerning the type of controller, transfer-function-based (classical) solutions are popular within the literature. The voltage loop typically contains proportional-resonant (PR) or synchronous reference frame (SRF)-PI controllers so as to remove the error in the output voltage at the fundamental frequency and at the main low-order harmonics under different loads [52]. The current loop usually contains a simple P controller [56] in order to reach a

high bandwidth and obtain a good decoupling between the two loops. Nevertheless, these solutions do not optimize the performance of the voltage controller in terms of the achievable bandwidth or the robustness against a large variation in the load impedance.

Alternatively to these classical solutions, state-space controllers from modern control theory have proven to be an interesting option that offers a high robustness [61, 62, 63]. Such robustness is convenient during grid-connected mode or during parallel operation because, in this conditions, the power converter experiences large variations in the impedance seen at its output. This impedance [64], which is the parallel equivalent of the load impedance and the grid coupling impedance, can achieve very low values and cause instability in the power converter if the controller cannot cope with such large plant model change.

Although a stable operation is always a mandatory requirement, practical implementations often need additional performance improvements, such as low steady-state error and fast disturbance rejection. The voltage controller presented in [62] incorporates an integral action to remove steady-state error at the fundamental output frequency. In [61], a voltage controller is designed using a pole-placement technique which results in fast dynamics. Such design [61] provides a stable operation in parallel configurations with a grid impedance down to short circuits and intermodule coupling impedances as low as 1%. The solution presented in [63] uses a pole-placement strategy and improves the speed of the reference tracking performance compared to transfer-function-based controllers.

1.2.5. Limitations of Voltage-Control Techniques in Microgrids

Voltage controllers in a MG can operate in two different modes of operation, namely, in stand-alone or in grid-connected mode. During stand-alone operation, the voltage controller regulates the ac voltage applied to local loads within the MG whereas, during grid-connected mode, the voltage controller adjusts the output voltage according to a reference provided by a droop control.

In order to achieve a good regulation, a voltage controller tries to reduce the output impedance of the power converter. Although this objective is the opposite of that of a current controller, the same study based on the sensitivity function of the system can be carried out in order to assess the performance and limitations of previous proposals.

In this application, the sensitivity function $S(f)$, which is the transfer function that shows how the controller responds to disturbances [54], indicates how much the voltage controller modifies (amplifies or attenuates) the effect of disturbances on the capacitor voltage d_{v_C} with respect to the open-loop response:

$$S(f) \;=\; \frac{v_C}{d_{v_C}}, \tag{6}$$

Examples of disturbances that cause a voltage disturbance in the capacitor voltage d_{v_C} are low-order load current harmonics i_o^h, voltage source converters (VSCs) nonlinearities, and plant model mismatches.

Such attenuation or amplification of disturbances corresponds to a change in the output impedance of the power converter caused by the voltage-controller. The new output impedance when the closed-loop controller is installed is

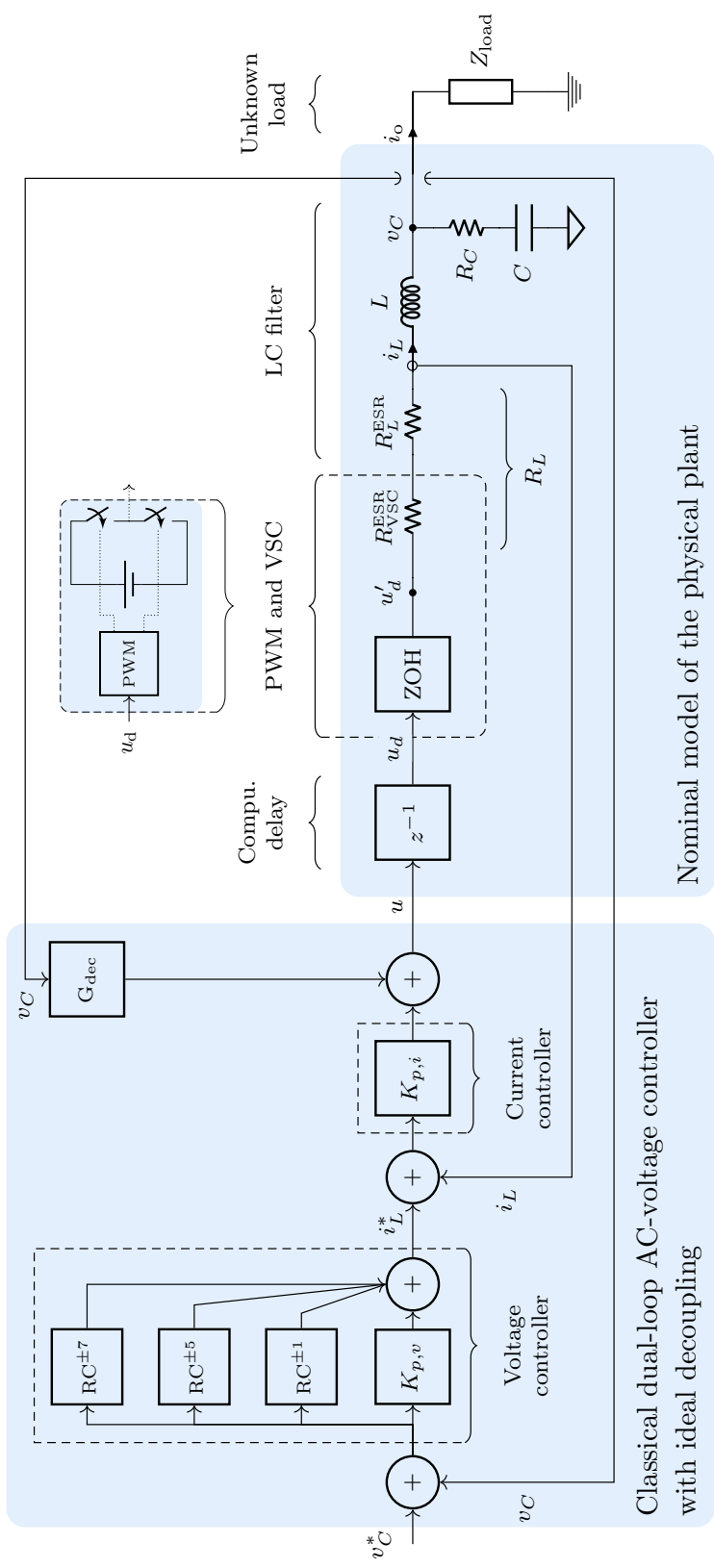$$Z_{out,vc}^{cl} \;=\; S Z_{out}^{ol}. \tag{7}$$

Figure 9. Classical double-loop voltage controller structure, nominal model of the physical plant in the $\alpha\beta$ frame, and local load.

Ideally, the voltage controller should provide a zero sensitivity (zero output impedance) at all frequencies. This would cancel any disturbances and ensure a zero steady-state error in the output voltage. Nonetheless, classical control structures, such as Figure 9, do not have enough degrees of freedom to completely control the shape of the sensitivity function $S(f)$ and change the output impedance according to a design specification. Figure 10 shows the magnitude of $S(f)$ in a logarithmic scale (the reason for such representation will become clear in Section 6). For the moment, it suffices to realize that the blue sections indicate frequency regions where the controller improves the open-loop response of the system ($S < 1$) and the red portions correspond to frequency ranges where the controller worsens the response of the system ($S > 1$) with respect to the open-loop response.

As expected from the three resonant controllers, the sensitivity (and the output impedance), cf. (7), are zero at the nominal output frequency $\pm f_o$ and at its main low-order harmonics, ± 5 and ± 7. Nevertheless, around these frequencies, S quickly increases. This yields a low disturbance rejection bandwidth and introduces new resonances in the system.

Classical transfer-function-based designs, such as [56], vary their performance depending on the particular plant parameters. If the resonant frequency of the LC filter or the sampling frequency are changed, $S(f)$ varies in an uncontrolled manner. Figure 11 shows the sensitivity of the classical controller shown in Figure 9 when the sampling frequency f_s is increased or reduced by a factor of two.

On the one hand, if the sampling frequency is changed from a single-update ($f_s = 10$ kHz) to a double-update strategy ($f_s = 20$ kHz), the performance of the power converter is significantly degraded, cf. Figure 11. This degradation is not originated by a physical limitation and it exposes a limitation of conventional PI and proportional-resonant (PR) controllers when they regulate a high order-plant. On the other hand, if the sampling frequency is reduced to 5 kHz, then the system becomes unstable. Due to these limitations, it becomes clear that an improved controller is required for this application.

1.3. Contents of This Chapter

The work in this chapter is divided into seven main sections. The first five sections present current and voltage controllers for voltage source converters (VSCs) with a pulse width modulator (PWM). In particular, the first four sections propose current controllers for grid-tied inverters with an LCL filter and the fifth section presents a voltage controller that can operate both in stand-alone and grid-connected mode. The last two main sections present two direct current controllers. The first one uses a noise-shaping design and the second is based on model predictive controller (MPC) theory. A final section summarizes the conclusions of this chapter.

1.3.1. Enhanced Resonant Current Controller for Grid-Connected Converters with LCL Filter

This section presents an enhanced current resonant controller (RC) for grid-connected converters with LCL filter. The proposed controller is designed in a systematic way and gives a consistent (in agreement with the design) and fast transient response (using all the available bandwidth), with low controller effort, no overshoot, and a good robustness to disturbances
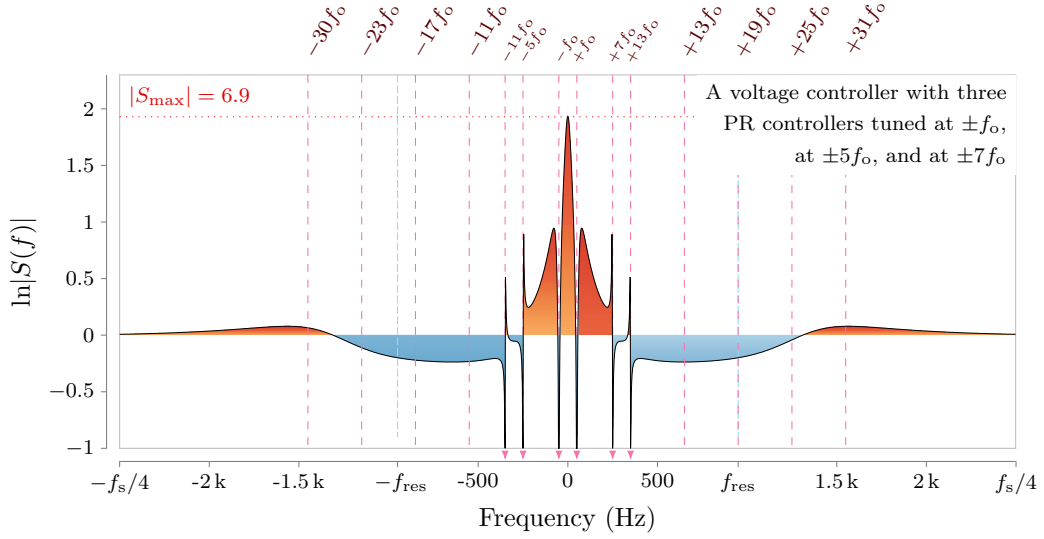
Figure 10. Magnitude of the sensitivity function $|S(f)|$ in a logarithmic scale of a voltage source converters (VSCs) with an LC filter and a double-loop voltage controller, cf. Figure 9.
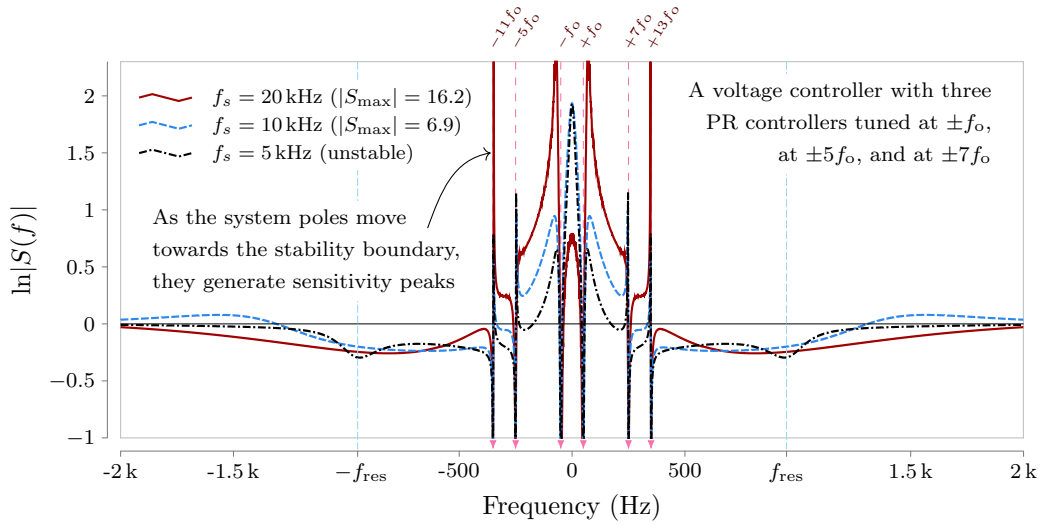
Figure 11. Effect of the sampling frequency in the magnitude of the sensitivity function $|S(f)|$ of a voltage source converters (VSCs) with an LC filter and a double-loop voltage controller, cf. Figure 9.

and variations in the grid impedance, which makes it particularly suitable for operation in a weak grid. Contrarily to classical PI or proportional-resonant (PR) controllers, the proposal provides a stable operation irrespectively of the ratio of LCL-filter resonant frequency to

sampling frequency used, without adding an extra active damping method.

The mathematical background of the presented current controller is based on a direct pole-placement strategy from the classical control theory (using transfer functions). Compared to state-space controllers that use modern control theory [1], this traditional control structure results in a simpler design process and a lower computational load. Since transfer function control theory is typically used in the field of current controllers in power applications, this solution is particularly valuable for practicing power-electronic engineers or researchers.

1.3.2.   Positive- and Negative-Sequence Current Controller with Direct Discrete-Time Pole Placement for Grid-Tied Converters with LCL Filter

This section presents a grid-side current controller for grid-tied converters with LCL filter that is able to control both positive and negative sequences of the fundamental grid frequency. Compared to a classical controller, the control structure used in this section (state-command structure) provides a better response to reference tracking than the structure typically used with transfer function design (output-error-command structure), where the controller is placed in the direct path between the reference and the plant input. Moreover, a state-command structure automatically eliminates wind-up problems in the current controller when the voltage source converters (VSCs) is commanded with a reference that cannot be achieved; hence an antiwind-up mechanism need not be implemented.

The presented current controller uses a direct pole-placement strategy from the state-space theory. Placing the poles in the specified locations results in a predictable and fast transient response, with low controller effort and no overshoot, and a good robustness to disturbances. In this manner, the reference-tracking and the disturbance-rejection capabilities, as well as the controller effort, do not depend on the LCL-filter resonance and sampling frequency used, when the design is performed according to the real values.

The state-space structure employed in this section constitutes the foundation of the mathematical background used in the following sections. In later sections, this control structure from modern control theory is further elaborated using different types of observers and plant models. This systematic design process simplifies the presentation and improves the continuity and interconnection between sections.

1.3.3.   Generalized Multi-Frequency Current Controller for Grid-Connected Converters with LCL Filter

The contribution of this section is a grid-side current controller for grid-tied inverters with LCL filter that includes harmonic current elimination. Similarly to the previously presented current controllers, the proposal only measures the grid current and voltage and it combines excellent dynamic characteristics with good robustness. The response to reference commands is completely damped and fast. The reference tracking bandwidth is set in accordance with the low-pass characteristic of the LCL filter so as to limit the control effort. Contrarily to previously proposed harmonic-current controllers, the controller offers an infinite impedance to any disturbances (such as grid voltage harmonics) at a set of arbitrarily specified frequencies. This allows the designer to eliminate all the undesired current harmonics with a simple design process.

The presented solution offers a generalized method that gives a consistent (with minimal variation in the reference-tracking dynamics) and stable performance irrespectively of the number of current harmonics to be canceled and of the resonant frequency of the LCL filter (provided that it is lower than the Nyquist frequency). In addition, the performance of the presented controller is evaluated in terms of a fundamental tradeoff that exists between robustness to variations in the grid impedance and the number of frequency components rejected. This is a fundamental constraint that all linear current controllers must meet and it can be used to assess the performance of any current controller.

1.3.4.   Grid-Tied Inverter with AC-Voltage Sensorless Synchronization and Soft-Start

This section presents a novel grid synchronization method which requires minimal computational load and provides a fast and accurate estimation of the grid voltage when connected to a weak grid. The presented synchronization method selectively tracks the positive sequence of the grid voltage in an unbalanced and distorted three-phase grid.

Contrarily to a phase-locked loop (PLL), the presented scheme does not require to measure the grid voltage, which could affect the performance when connected to a weak grid because the voltage at the point of common coupling (PCC) can be different from the grid voltage depending on the grid-side current value. The proposed structure avoids this interaction between the current controller and the synchronization mechanism, resulting in a more robust system. Furthermore, it also removes the grid voltage feedforward. This improves the stability and robustness of the current controller because it eliminates an additional path for disturbances and noise to enter the system, a common problem of feedforward schemes. The transient response is also improved compared to a controller that measures the voltage at the PCC because there is no interaction between the current controller and the synchronization scheme.

1.3.5.   AC-Voltage Harmonic Control for Stand-Alone and Weak-Grid-Tied Converter

This section proposes an ac voltage controller with a high robustness to changes in the plant model. Plant model changes can occur due to LC filter parameter variations or when the voltage source converters (VSCs) switches the mode of operation. The proposed controller can operate with small load impedances and output power factors smaller than that of previously proposed controllers without significantly degrading the transient performance. This ensures a robust operation when providing voltage support in a microgrid with distorted and unbalanced voltage.

The indicated properties are maintained irrespectively of the LC filter installed or the sampling frequency used, provided that overmodulation of the voltage source converters (VSCs) is avoided and the resonant frequency of the LC filter is lower than the Nyquist frequency of the digital controller. The design process offers a simple tuning and only requires, as input parameters, the values of the LC filter elements, the sampling frequency, and a set of frequencies where load-current circulation is expected.

Concerning the implementation, the presented controller only measures the output voltage; hence, it uses a single-loop structure with all the available bandwidth. An independent

converter-current monitor provides short-circuit protection using the saturated PWM voltage reference and the measured output voltage.

1.3.6. A Finite-Control-Set Linear Current Controller with Fast Transient Response and Low Switching Frequency for Grid-Tied Inverters

This section presents a linear current controller for a grid-tied inverter with L or LCL filter that uses a FCS operation. Thanks to the FCS operation, the proposed controller provides a very fast transient response, similarly to an FCS model predictive controller (MPC), while needing a low switching frequency and a low computational load. Contrarily to MPC solutions, the proposal uses a linear control structure. Such linear structure offers a straightforward implementation and stability assessment compared to an MPC, which usually requires complex optimization algorithms and Lyapunov functions that are a field of study in its own right. The proposal does not generate any switching or low-order harmonics. By design, the switching noise is evenly spread at all frequencies instead of it being concentrated at some harmonic frequencies like in the case of PWM-based controllers. This reduces the risk of exciting resonances in the utility grid and facilitates the operation of multiple inverters in parallel. In particular, the proposal is shown to achieve compliance with stringent grid harmonic codes using an L filter in a multimegawatt application where previous proposals required an LCL filter with the same total inductance.

1.3.7. A Model Predictive Current Controller with Improved Robustness Against Measurement Noise and Plant Model Variations

This section improves the robustness of a finite control set (FCS)-model predictive controller (MPC) for grid-tied inverters and motor drives applications to plant parameter variations and noise, without reducing its bandwidth or affecting its excellent transient response to disturbances and reference commands. The proposed modification adds an observer to the MPC controller structure, which does not significantly increase the computational burden on the embedded controller. Traditionally, observers are employed to estimate unmeasured variables and cancel the effect of disturbances, but this section employs the observer to estimate a measured variable, the converter output current. This solution leverages the benefits of observers from linear controller theory in order to remove undesired components in the measured current and improve the robustness of the controller; hence it is a valuable solution for practicing power-electronic engineers and researchers in the field of grid-tied inverters and motor drives due to its simplicity compared to some advanced techniques often required in more complex MPC designs.

1.4.   Nomenclature

Subscripts and Superscripts

abc Phase components in a three-phase reference frame.

$\alpha\beta$ Alpha and beta components in a stationary reference frame. If the subscript in a variable does not specify a reference frame, the ab frame is assumed.

dq+ Direct and quadrature components in the synchronous reference frame (SRF) which tracks the positive sequence of the grid voltage.

dq− Direct and quadrature components in the SRF which tracks the negative sequence of the grid voltage.

s^{sim} Simulated signal s.

x^{T} Transpose of x.

r^{*} Reference signal r.

$\hat{x}$ Estimation of signal x.

Base Values

I_{base} Nominal current.

f_g Nominal grid frequency.

f_o Nominal VSC output frequency.

P_{base} Nominal power.

p.u. per unit.

V_{base} Nominal voltage.

Z_{base} Base impedance.

ω_g $= 2\pi f_g$. Nominal grid frequency in radians.

Plant Model Variables

i_1 Grid-side current.

i_2 Converter-side current.

u_d' PWM output voltage.

u_d PWM reference voltage.

v_C Capacitor voltage.

$v_{\mathbf{dc}}$ DC-bus voltage.

v_g Grid voltage.

v_g^{+} Positive sequence of the grid voltage.

$v_{\mathbf{PCC}}$ Voltage at the PCC.

w $= w^{+} + w^{-5} + \ldots + w^{+13}$. Input-equivalent voltage disturbance.

w^h Symmetrical component of w that is tuned the h-th harmonic of the grid fundamental frequency.

$\boldsymbol{x}^{dis}(t)$ Continuous-time state vector of a disturbance model.

$\boldsymbol{x}^{L}(t) = [i_1]^T$ Continuous-time state vector of an L filter.

$\boldsymbol{x}^{LC}(t) = [v_c \ \ i_2]^T$ Continuous-time state vector of an LC filter.

$\boldsymbol{x}^{LCL}(t) = [i_1 \ \ i_2 \ \ v_C]^T$ Continuous-time state vector of an LCL filter.

$\boldsymbol{x}^{LC}_{cl}(k) = [v_c \ \ i_2]^T$ Discrete-time state vector of a closed-loop system with an LC filter.

$\boldsymbol{x}^{LCL}_{cl}(t) = [i_1 \ \ i_2 \ \ v_C]^T$ Discrete-time state vector of a closed-loop system with an LCL filter.

$\mathbf{x}^{dis}_{d}(k)$ Discrete-time state vector of a disturbance model.

$\mathbf{x}^{L}_{d}(k) = [i_1]^T$ Discrete-time state vector of an L filter.

$\mathbf{x}^{LC}_{d}(k) = [v_C \ \ i_2]^T$ Discrete-time state vector of an LC filter.

$\mathbf{x}^{LCL}_{d}(k) = [i_1 \ \ i_2 \ \ v_c]^T$ Discrete-time state vector of an LCL filter.

$\mathbf{x}^{L}_{dd}(k) = [i_1 \ \ u_d]^T$ Discrete-time state vector of an L filter and a one-sample computational delay.

$\mathbf{x}^{LC}_{dd}(k) = [v_C \ \ i_2 \ \ u_d]^T$ Discrete-time state vector of an LC filter and a one-sample computational delay.

$\mathbf{x}^{LCL}_{dd}(k) = [i_1 \ \ i_2 \ \ v_c \ \ u_d]^T$ Discrete-time state vector of an LCL filter and a one-sample computational delay.

$\mathbf{x}^{LC}_{add}(k) = [\mathbf{x}^{LC}_{dd}(k) \ \ \ \ \mathbf{r}]^T$ Discrete-time state vector of an LC filter and a one-sample computational delay augmented with a resonant disturbance model $\mathbf{r}$.

$\mathbf{x}^{LCL}_{add}(k) = [\mathbf{x}^{LCL}_{dd}(k) \ \ \ \ \mathbf{r}]^T$ Discrete-time state vector of an LCL filter and a one-sample computational delay augmented with a resonant disturbance model $\mathbf{r}$.

Plant Parameters

f_{res} Resonant frequency in an LCL filter.

f_{sw} Switching frequency of a VSC.

L_1 Nominal inductance in an LC filter.

L_1 Nominal grid-side inductance in an LCL filter.

L^r_1 Real grid-side inductance in an LCL filter.

L_2 Nominal converter-side inductance in an LCL filter.

L^r_2 Real converter-side inductance in an LCL filter.

L_g Grid inductance.

C Nominal capacitance in an LC or an LCL filter.

C^r Real capacitance in an LCL filter.

R_1 Nominal grid-side equivalent series resistance (ESR) in an LCL filter.

R_1^r Real grid-side ESR in an LCL filter.

R_2 Nominal converter-side ESR in an LCL filter.

R_2^r Real converter-side ESR in an LCL filter.

R_c Nominal capacitor ESR in an LCL filter.

R_c^r Real capacitor ESR in an LCL filter.

R_g Grid resistance.

Z_g Grid impedance.

State-Space Model Parameters

$\mathbf{A}^L$ State (or system) matrix of a continuous-time state-space model of an L filter.

$\mathbf{A}^{LC}$ State (or system) matrix of a continuous-time state-space model of an LC filter.

$\mathbf{A}^{LCL}$ State (or system) matrix of a continuous-time state-space model of an LCL filter.

$\mathbf{A}^{dis}$ State (or system) matrix of a continuous-time state-space model of a disturbance.

$\mathbf{A}_{cl}^{LC}$ State (or system) matrix of a discrete-time state-space model of a closed-loop system with an LC filter.

$\mathbf{A}_{cl}^{LCL}$ State (or system) matrix of a discrete-time state-space model of a closed-loop system with an LCL filter.

$\mathbf{A}_d^L$ State (or system) matrix of a discrete-time state-space model of an L filter.

$\mathbf{A}_d^{LC}$ State (or system) matrix of a discrete-time state-space model of an LC filter.

$\mathbf{A}_d^{LCL}$ State (or system) matrix of a discrete-time state-space model of an LCL filter.

$\mathbf{A}_d^{dis}$ State (or system) matrix of a discrete-time state-space model of a disturbance.

$\mathbf{A}_{dd}^L$ State (or system) matrix of a discrete-time state-space model of an L filter and a one-sample computational delay.

$\mathbf{A}_{dd}^{LC}$ State (or system) matrix of a discrete-time state-space model of an LC filter and a one-sample computational delay.

$\mathbf{A}_{dd}^{LCL}$ State (or system) matrix of a discrete-time state-space model of an LCL filter and a one-sample computational delay.

$\mathbf{A}_{add}^{LC}$ State (or system) matrix of a discrete-time state-space model of an LC filter and a one-sample computational delay augmented with a disturbance model $\mathbf{r}$.

$\mathbf{A}_{add}^{LCL}$ State (or system) matrix of a discrete-time state-space model of an LCL filter and a one-sample computational delay augmented with a disturbance model $\mathbf{r}$.

$\mathbf{B}^{L}$ Input matrix of a continuous-time state-space model of an L filter.

$\mathbf{B}^{LC}$ Input matrix of a continuous-time state-space model of an LC filter.

$\mathbf{B}^{LCL}$ Input matrix of a continuous-time state-space model of an LCL filter.

$\mathbf{B}_{cl}^{LC}$ Input matrix of a discrete-time state-space model of a closed-loop system with an LC filter.

$\mathbf{B}_{cl}^{LCL}$ Input matrix of a discrete-time state-space model of a closed-loop system with an LCL filter.

$\mathbf{B}_{d}^{dis}$ Input matrix of a discrete-time state-space disturbance model.

$\mathbf{B}_{d}^{L}$ Input matrix of a discrete-time state-space model of an L filter.

$\mathbf{B}_{d}^{LC}$ Input matrix of a discrete-time state-space model of an LC filter.

$\mathbf{B}_{d}^{LCL}$ Input matrix of a discrete-time state-space model of an LCL filter.

$\mathbf{B}_{dd}^{L}$ Input matrix of a discrete-time state-space model of an L filter and a one-sample computational delay.

$\mathbf{B}_{dd}^{LC}$ Input matrix of a discrete-time state-space model of an LC filter and a one-sample computational delay.

$\mathbf{B}_{dd}^{LCL}$ Input matrix of a discrete-time state-space model of an LCL filter and a one-sample computational delay.

$\mathbf{B}_{add}^{LC}$ Input matrix of a discrete-time state-space model of an LC filter and a one-sample computational delay augmented with a disturbance model $\mathbf{r}$.

$\mathbf{B}_{add}^{LCL}$ Input matrix of a discrete-time state-space model of an LCL filter and a one-sample computational delay augmented with a disturbance model $\mathbf{r}$.

$\mathbf{C}^{L}$ Output matrix of a continuous-time state-space model of an L filter.

$\mathbf{C}^{LC}$ Output matrix of a continuous-time state-space model of an LC filter.

$\mathbf{C}^{LCL}$ Output matrix of a continuous-time state-space model of an LCL filter.

$\mathbf{C}^{dis}$ Output matrix of a continuous-time state-space model of a disturbance.

$\mathbf{C}_{cl}^{LC}$ Output matrix of a discrete-time state-space model of a closed-loop system with an LC filter.

$\mathbf{C}_{cl}^{LCL}$ Output matrix of a discrete-time state-space model of a closed-loop system with an LCL filter.

$\mathbf{C}_d^L$ Output matrix of a discrete-time state-space model of an L filter.

$\mathbf{C}_d^{LC}$ Output matrix of a discrete-time state-space model of an LC filter.

$\mathbf{C}_d^{LCL}$ Output matrix of a discrete-time state-space model of an LCL filter.

$\mathbf{C}_d^{dis}$ Output matrix of a discrete-time state-space model of a disturbance.

$\mathbf{C}_{dd}^L$ Output matrix of a discrete-time state-space model of an L filter and a one-sample computational delay.

$\mathbf{C}_{dd}^{LC}$ Output matrix of a discrete-time state-space model of an LC filter and a one-sample computational delay.

$\mathbf{C}_{dd}^{LCL}$ Output matrix of a discrete-time state-space model of an LCL filter and a one-sample computational delay.

$\mathbf{C}_{add}^{LC}$ Output matrix of a discrete-time state-space model of an LC filter and a one-sample computational delay augmented with a disturbance model $\mathbf{r}$.

$\mathbf{C}_{add}^{LCL}$ Output matrix of a discrete-time state-space model of an LCL filter and a one-sample computational delay augmented with a disturbance model $\mathbf{r}$.

$\mathbf{I}_n$ The identity matrix of size n.

Controller Variables

i_1^* Grid-side current reference.

$\boldsymbol{\theta}$ Phase of the positive sequence of the grid voltage.

$\boldsymbol{\theta}_{\mathbf{err}}$ $\widehat{\theta} - \theta_{\boldsymbol{actual}}$. Estimated phase error.

$\boldsymbol{\theta}_{\mathbf{PLL}}$ Phase calculated by a moving average filter (MAF)-based PLL.

$\widehat{\theta}$ Estimated phase provided by a sensorless synchronization scheme.

u Controller output voltage.

u_{sat} Saturated controller output voltage.

v Nominal controller output voltage.

$\widehat{w}$ Estimated input-equivalent voltage disturbance.

$\hat{\mathbf{x}}^{LC}$ $= [i_1(t) \quad i_2(t) \quad v_c(t)]^T$ Continuous-time state vector of an LC filter.

$\hat{\mathbf{x}}_d^{LC}$ $= [i_1(k) \quad i_2(k) \quad v_c(k) \quad u_d(k)]^T$ Discrete-time state vector of an LC filter.

$\hat{\mathbf{x}}_{dd}^{LC} = [i_1 \quad i_2 \quad v_c \quad u_d]^T$ Discrete-time state vector of an LC filter and a one-sample computational delay.

$\hat{\mathbf{x}}_{add}^{LC} = [\mathbf{x}_{dd}^{LC}(k) \quad \mathbf{r}]^T$ Discrete-time state vector of an LC filter and a one-sample computational delay augmented with a disturbance model $\mathbf{r}$.

$\hat{\mathbf{x}}^{LCL} = [i_1(t) \quad i_2(t) \quad v_c(t)]^T$ Continuous-time state vector of an LCL filter.

$\hat{\mathbf{x}}_d^{LCL} = [i_1 \quad i_2 \quad v_C]^T$ Discrete-time state vector of an LCL filter.

$\hat{\mathbf{x}}_{dd}^{LCL} = [i_1 \quad i_2 \quad v_c \quad u_d]^T$ Discrete-time state vector of an LCL filter and a one-sample computational delay.

$\hat{\mathbf{x}}_{add}^{LCL} = [\mathbf{x}_{dd}^{LCL}(k) \quad \mathbf{r}]^T$ Discrete-time state vector of an LCL filter and a one-sample computational delay augmented with a disturbance model $\mathbf{r}$.

Controller Parameters

$f_{\mathbf{dom}} = \omega_{dom}/(2\pi)$. Reference-tracking bandwidth of the digital controller.

$f_{\mathbf{s}} = 1/T_s$. Sampling frequency of the digital controller.

$f_{\mathbf{sz}}$ Frequency of the slow zeros in a grid-tied inverter with an enhanced resonant current controller.

ζ Damping value of the resonant plant poles.

$\mathbf{K}_+, \mathbf{K}_-$ Reference feedforward gains in an enhanced resonant current controller.

$\mathbf{K_c}$ Compensator gain.

K_f Reference feedforward gain.

K_{ff} Grid feedforward gain.

$\mathbf{K_o}$ Observer gain.

N Measurement noise.

$(pi_i^{\mathbf{cl}})$ Set of system closed-loop poles.

$(pi_i^{\mathbf{ol}})$ Set of system open-loop poles.

$\mathbf{Q}$ Process noise.

$T_s = 1/f_s$. Sampling period of the digital controller.

(z_i) Set of system zeros.

Transfer Functions

$C(z)$ Transfer function of a pole-placement controller.

$C_{\mathbf{RC}}(z)$ Transfer function of a lossless resonant controller with unity gain tuned at the fundamental grid frequency.

$G^{LC}(s) = v_C/u_d'$.   Continuous-time transfer function that gives the ratio of the capacitor voltage v_C to the PWM output voltage u_d' in a converter with an LC filter when no other disturbances are considered.

$G^{LCL}(s) = i_1/u_d'$.   Continuous-time transfer function that gives the ratio of the grid-side current i_1 to the PWM output voltage u_d' in a grid-tied inverter with an LCL filter when no other disturbances are considered.

$G_d^{LC}(z) = v_C/u_d$.   Discrete-time transfer function that gives the ratio of the capacitor voltage v_C to the PWM reference voltage u_d in a converter with an LC filter when no other disturbances are considered.

$G_d^{LCL}(z) = i_1/u_d$.   Discrete-time transfer function that gives the ratio of the grid-side current i_1 to the PWM reference voltage u_d in a grid-tied inverter with an LCL filter when no other disturbances are considered.

$G_{dd}^{LC}(z) = v_C/u_{sat}$.   Discrete-time transfer function that gives the ratio of the capacitor voltage v_C to the controller output voltage u_{sat}, i.e., it includes the effect of the computational delay in a converter with an LC filter.

$G_{dd}^{LCL}(z) = i_1/u_{sat}$.   Discrete-time transfer function that gives the ratio of the grid-side current i_1 to the controller output voltage u_{sat}, i.e., it includes the effect of the computational delay in a grid-tied inverter with an LCL filter.

$G_{add}^{LC}(z) = G_{RC}(z)G_{dd}^{LC}(z)$.   Transfer function of a discrete-time LC-filter model augmented with a disturbance model.

$G_{add}^{LCL}(z) = G_{RC}(z)G_{dd}^{LCL}(z)$.   Transfer function of a discrete-time LCL-filter model augmented with a disturbance model.

$G_{\mathbf{cl}}(z) = i_1/i_1^*$.   Transfer function that gives the ratio of the grid-side current i_1 to the grid-side current reference i_1^* in a grid-tied inverter with an LCL filter when no other disturbances are considered.

$H(z)$ Transfer function of a prefilter.

$S(z)$ Sensitivity function.

$T(z)$ Complementary sensitivity function.

$T_{LC}^*(z) = v_C/v_C^*$.   Discrete-time transfer function that gives the ratio of the capacitor voltage v_C to the capacitor voltage reference v_C^* in a grid-tied inverter with an LC filter.

$T^*_{LCL}(z) = i_1/i_1^*$. Discrete-time transfer function that gives the ratio of the grid-side current i_1 to the grid-side current reference i_1^* in a grid-tied inverter with an LCL filter.

OLTF$(z) = C(z)G_{RC}(z)G_{dd}^{LCL}(z)$. Open-loop transfer function of a grid-tied inverter with an LCL filter and an enhanced resonant current controller.

2.   Enhanced Resonant Current Controller for Grid-Connected Converters with LCL Filter

Conventional resonant controllers (RCs) are commonly used in the current control of grid-tied converters with LCL filter due to their advantages, such as zero steady-state error at both fundamental sequences, easy design process, and straightforward implementation. Nevertheless, these traditional solutions do not permit to place the closed-loop poles of the system in convenient locations when dealing with a fourth-order plant model like the LCL filter plus the computation delay. Therefore, the reference tracking and the disturbance rejection are deficient in terms of transient behavior and depend on the LCL filter. Furthermore, an additional active damping method usually has to be designed to ensure stability. This section presents an enhanced current RC with stable and fast response, negligible overshoot, good disturbance rejection, and low controller effort for grid-tied converters with LCL filter. The developed solution uses a direct discrete-time pole-placement strategy from the classical control theory (using transfer functions), involving two extra filters, to enhance the performance of the RC. In this manner, the complexity of state-space methods from modern control theory is avoided. Simulation and experimental results are provided to verify the effectiveness of the proposed control scheme.

The increasing popularity of renewable energy sources and distributed power generation systems [65] is imposing higher requirements on the grid-connected converters. Fast regulation is required to compensate for time-varying events (e.g., voltage sags or fluctuating output power of wind generation systems) [66, 67]. Among the different converter types, the voltage source converters (VSCs) is commonly used in this type of application due to its controllability, compact design, and ease of interface with power systems [68].

However, VSCs need a filter to attenuate the high-frequency switching currents. The LCL filter is the recommended option because of its compact size and good performance [69]. Contrarily to the attenuation of $20dB$ per decade that a conventional L filter provides above its cutoff frequency, LCL filters attenuate the grid-side current with a slope of $60dB$ per decade above their resonant frequency. This increased performance

of the LCL filter is caused by its higher order [70]. A fundamental element that affects the performance of a grid-tied converter is the current controller. Among the several control structures that can be adopted, resonant controllers (RCs) are commonly used [71, 72, 70, 37, 47, 73, 74, 75, 39, 76, 50, 51, 67, 36]. They permit to control with zero steady-state error both the positive and the negative sequences of the current [71]. In addition, they offer an easy design process and straightforward implementation. The previously proposed RCs (tuned at the fundamental frequency of the grid) can be classified into three main categories: proportional-resonant [72, 70, 37, 47, 73, 74, 75, 39, 76, 50, 51]; vector proportional-integral [67]; and variations of these RCs, which improve the stability margins for certain LCL filters and for high ratios of fundamental-to-sampling frequency (e.g., by adding a phase compensation scheme [36, 71]). These references propose tuning methods for the controller gains, but they do not guarantee a closed-loop pole position independent of the LCL filter used.

Traditional RCs do not have enough order (they are second-order transfer functions) to completely control the dynamics of such a relatively high-order plant model that comprises the LCL filter model plus the computation and modulation delays (one and a half samples, respectively [15]). In other words, this type of controller cannot arbitrarily establish the position of the closed-loop poles of the system because their locations depend on the LCL filter installed. This degrades the system's reference-tracking and disturbance-rejection responses and sometimes even the stability. Recently, the authors of [77] have proposed a transfer-function-based current controller for grid-tied inverters with an L filter that uses a direct pole-placement technique resulting in an enhanced transient response when compared to the classic design. However, to the authors' knowledge, a transfer-function-based pole-placement strategy has not yet been applied to a voltage source converters (VSCs) with an LCL filter. When an LCL filter is considered, the strategy proposed in [77] is not suitable. In addition, it should be noticed that a pole-placement approach is especially convenient in this case because of the reduced stability that results when an LCL filter is used with a classic design. This stability problem was analyzed in [47], where a threshold was found for the resonant frequency of the LCL filter: $f_s/6$ (with f_s being the sampling frequency). Such a critical frequency value determines the region where an additional damping mechanism is necessary to achieve stability. When the grid-side current is controlled, the frequency region where conventional RCs are unstable is below $f_s/6$ [47].

Although the damping of the LCL filter can be implemented passively or actively, the latter is usually preferred because passive damping causes extra losses and reduces the efficiency of the system [78]. The different active damping schemes can be classified according to the signal that is fed back. Commonly, the capacitor current [74, 76, 79], the capacitor voltage [37, 72, 75], or the grid-side current [50, 80, 51] are the variables involved in the damping scheme. However, these solutions need extra sensors or mechanisms to estimate the additional signals. This increases the complexity of the control, and some algorithms also have sensitivity problems and reduce the overall robustness of the system (e.g., derivative filtering of a signal usually increases the noise [37]). In addition, the active damping techniques only provide a stable system [74, 76, 79, 72, 75, 50, 80, 51], but they do not optimize the transient response in terms of controller effort, overshoot, axis decoupling, or speed. In order to avoid these problems, new solutions often resort to state-space controllers from modern control theory that have a more complex design process compared to

conventional RCs [1].

Some of the proposed current RCs for VSCs with LCL filter control the converter-side current rather than the grid-side current [51]. However, to have precise control of the power and distortion factors of the current injected into the grid, the grid-side current should be measured or estimated accurately [29]. A good estimation requires a precise model of the plant, which sometimes (especially in the case of VSCs connected to weak grids) is not available to the designer.

In addition, there is an increasing trend in the field of control of power converters that strives to achieve designs with faster dynamics (higher bandwidth) [67]; but sometimes such work comes from abstract mathematical proposals [75] where it is difficult to assess their practical and physical consequences in terms of controller effort and robustness to plant parameter variations and disturbances.

This section presents an enhanced current resonant controller (RC) for grid-connected converters with LCL filter. The proposed controller includes two filters that enhance the behavior of the system: a loop filter, which contains an resonant controller (RC) and a prefilter. It is designed in a systematic way and gives a consistent (in agreement with the design) and fast transient response (using all the available bandwidth), with low controller effort, no overshoot, and good robustness to disturbances and variations in the grid impedance, which makes it particularly suitable for operation in a weak grid. These improvements are achieved independently of the LCL-filter resonant frequency (above and below $f_s/6$) and sampling frequency used, and without adding an extra active damping method. The mathematical background of the presented current controller is based on a direct pole-placement strategy from the classical control theory (using transfer functions). The proposed design process overcomes the problems mentioned above of previously proposed RCs (i.e., the closed-loop poles are placed in convenient locations) and give performance comparable to state-space controllers that use modern control theory [1], but based on a traditional control structure with a simpler design process and a lower computational load. Since transfer function control theory is typically used in the field of current controllers in power applications, this solution is more valuable for practicing power-electronic engineers or researchers. In addition, the assessment of robustness is commonly studied using a transfer function analysis [47, 77]. Another advantage of the proposal, compared to [1], is the huge reduction in the computational load, which makes the proposal particularly suited for implementation in an embedded controller.

The rest of the section is organized as follows. Section 2.1 introduces the model of the plant, the resonant controller (RC), and a feedforward. Then, in Section 2.2, the loop filter and the prefilter are designed and the performance of the proposed current controller concerning its time response is analyzed. Next, in Section 2.3, its robustness to grid-impedance variations is assessed. In Section 2.4, the theory is validated by simulation and experimental results. Finally, Section 2.8 summarizes the work.

2.1.   Transfer-Function Modeling of the Plant and the Resonant Controller

This section presents the model of the augmented plant (i.e., including the resonant controller (RC)) and the expression of a disturbance feedforward gain for the grid-side current controller shown in Figure 12, where L_1, L_2, and C represent the reactive elements of the
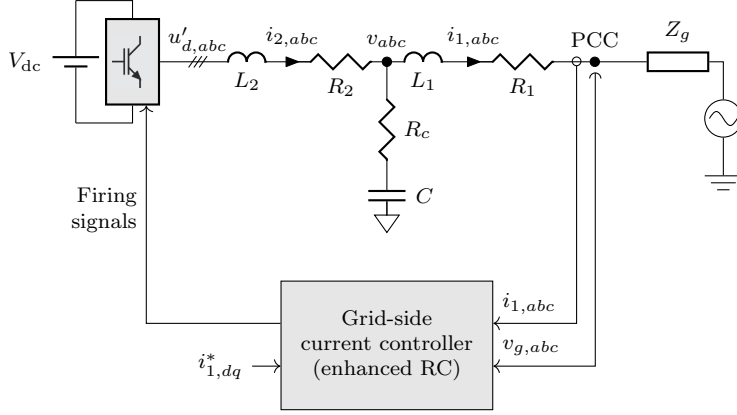
Figure 12. Grid-connected voltage source converters (VSCs) with an LCL filter and a grid-side current controller.

LCL filter; R_1, R_2, and R_c model the equivalent series resistances of the filter (R_2 also includes the equivalent loss resistance of the voltage source converters (VSCs) [15]); $u'_{d,abc}$ is the voltage source converters (VSCs) output voltage; $i_{1,abc}$, $i_{2,abc}$, and v_{abc} are the LCL-filter state variables (the grid-side current, the converter-side current, and the capacitor voltage, respectively); $v_{g,abc}$ is the grid voltage; and $i^*_{1,dq}$ denotes the grid-side current reference in the dq frame. The following modeling process successively calculates transfer functions that relate the variables of interest; each new transfer-function model is constructed from the model obtained in the previous stage. The resultant transfer function, denoted as augmented plant model, consists in an resonant controller (RC) and the discrete model of the LCL filter plus the computation and modulation delays, and is calculated in Section 2.1.1. This transfer function is used later, in Section 2.2, where the pole-placement is applied to design the remaining two filters of the controller. Finally, a feedforward gain to improve the disturbance rejection is calculated in Section 2.1.2.

2.1.1.   Model of the Augmented Plant

First, a continuous model that relates the grid-side current $i_1(t)$ to the voltage source converters (VSCs) output voltage $u'_d(t)$ for the LCL filter shown in Figure 13 is defined (when no reference frame in a subscript of a variable is detailed, the $\alpha\beta$ frame with an amplitude-invariant transformation is assumed). The grid impedance seen at the PCC Z_g is assumed to be zero in the model for the design of the controller because its value is unknown at the design stage (and often even variable); its effect is analyzed in Section 2.3. The resulting transfer function in continuous time that relates the converter output voltage u'_d with the grid-side current i_1 when the effect of the grid voltage v_g is not considered is

$$G^{LCL}(s) = \left.\frac{i_1}{u'_d}\right|_{[Z_g=0]v_g=0} = \frac{Z_c}{Z_2(Z_1 + Z_c) + Z_1 Z_c}, \tag{8}$$

where Z_1, Z_2, and Z_c are the impedances of the reactive elements including losses:

$$Z_1 = sL_1 + R_1, \ \ Z_2 = sL_2 + R_2, \ \ Z_c = 1/(sC) + R_c. \tag{9}$$
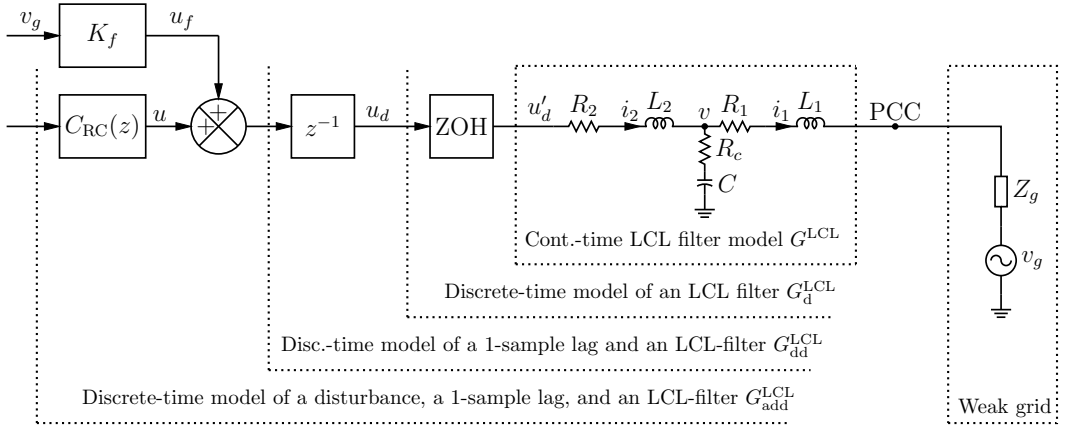
Figure 13. Stationary-frame resonant controller (RC), grid-voltage feedforward, and plant diagram: LCL filter, PWM (modeled as a ZOH), and one-sample computation delay.

Next, (8) is discretized by using a zero-order hold (ZOH) equivalent [81]. The effect of the ZOH is mainly to introduce a phase shift that corresponds to a time delay of $T_s/2$ [81]. This discretization method takes into account the half a sample delay added by the PWM [15]. This effect is illustrated in Figure 14. The expression of a half-a-sample delay is

$$G_{\text{PWM delay}}(s) = e^{-s\frac{T_s}{2}}. \tag{10}$$

This term adds an extra $90°$ phase lag to the plant model at the Nyquist frequency:

$$\angle G_{\text{PWM delay}}(s)\bigg|_{s=j\pi f_s} = \angle e^{-\pi/2}. \tag{11}$$

The resulting model relates the PWM voltage reference (before the ZOH) $u_d(k)$ with the sampled grid-side current $i_1(k)$:

$$G_d^{LCL} = \frac{i_1}{u_d}\bigg|_{Z_g=0]v_g=0} = (1-z^{-1})\mathcal{Z}\left\{\mathcal{L}^{-1}\left[\frac{G^{LCL}(s)}{s}\right]\right\} \tag{12}$$

where $\mathcal{Z}[x(k)]$ and $\mathcal{L}[x(t)]$ denote the Laplace and Z transforms of the signal x, respectively. Then, a one-sample input (computation) delay is added to (12):

$$G_{dd}^{LCL} = z^{-1}G_d^{LCL}. \tag{13}$$

Furthermore, the resonant controller (RC) $C_{RC}(z)$, which eliminates any steady-state error in the grid-side current at the fundamental grid frequency ω_g, is

$$C_{RC}(z) = \frac{1}{z^{-2} - 2\cos(\omega_g T_s)z^{-1} + 1}. \tag{14}$$

This transfer function places two conjugated open-loop poles at the fundamental grid frequency ω_g (i.e., at positions $z = e^{\pm j\omega_g T_s}$, where $T_s = 1/f_s$ is the sampling period) so as
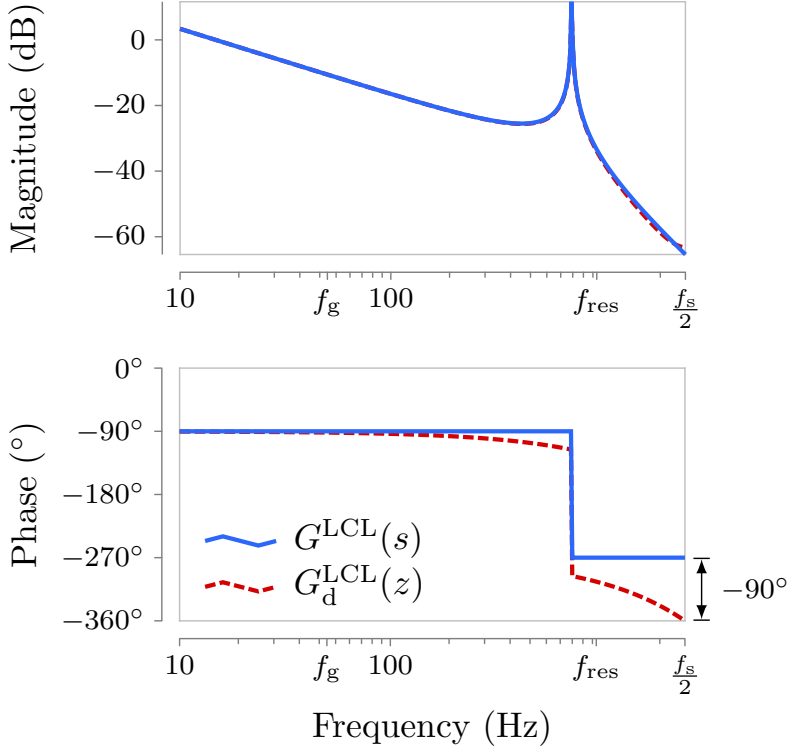
Figure 14. Bode diagrams showing that when the continuous LCL-filter model $\mathbf{G}^{LCL}(s)$ is discretized by using a ZOH equivalent, a half-a-sample delay, which models the PWM delay, is added to the resultant discrete model $\mathbf{G}_d^{LCL}$.

to control both positive and negative sequences. No other poles or zeros are added to (14). Instead, the proposed controller defers to $C(z)$ and $H(z)$ the task of adding extra degrees of freedom. In this manner, the design process is simplified and a consistent performance is obtained independently of the LCL filter used.

Hence, the model of the augmented plant (i.e., including the resonant controller (RC)), depicted in Figure 13, is

$$G_{add}^{LCL}(z) \;=\; C_{RC}(z)G_{dd}^{LCL}. \tag{15}$$

2.1.2. Disturbance Feedforward

A feedforward of the grid voltage v_g is implemented (cf. Figure 13) to improve the disturbance rejection and provide a smooth start of the converter. Nevertheless, when a weak grid is considered, the voltage feedforward can be reduced to improve the robustness, as explained in Section 2.3. Therefore, in this case, the authors recommend removing the voltage feedforward by setting K_f to zero. When the controller output u is zero, the capacitor voltage v should be equal to the grid-side voltage v_g in order for the grid-side current to be zero $i_1 = 0$. Consequently, the necessary feedforward voltage that should be generated at
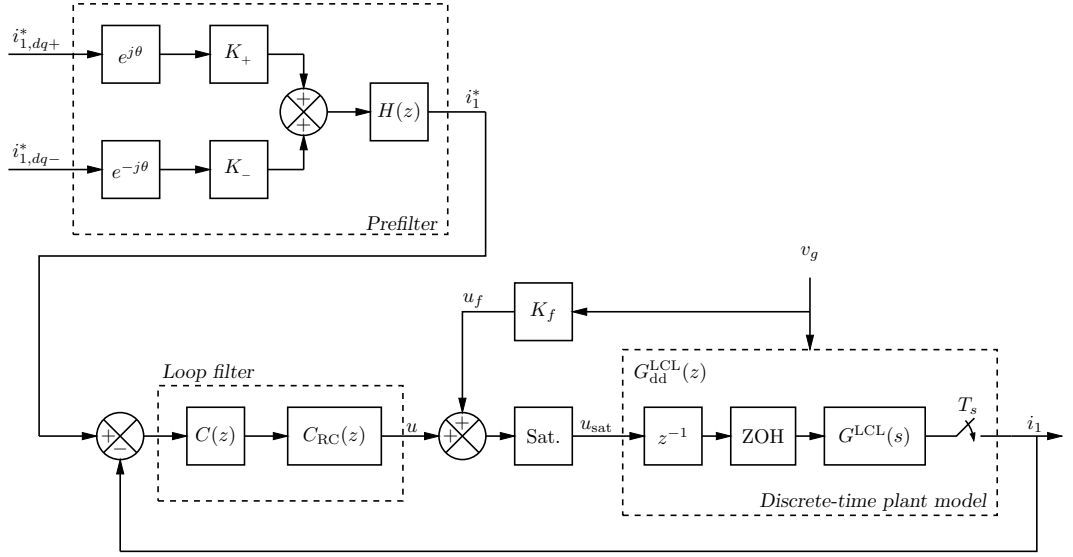
Figure 15. Scheme of the model of the plant and the proposed controller structure.

the converter output u'_d is

$$u'_d = \frac{(Z_2 + Z_c)v_g}{Z_c}. \tag{16}$$

If the effect of computation and modulation delay is compensated at the fundamental grid frequency component in the feedforward voltage u_f, then the resultant feedforward gain is

$$K_f = \frac{u_f}{v_g} = \frac{(Z_2 + Z_c)e^{j1.5\omega_g T_s}}{Z_c}. \tag{17}$$

2.2. Design of Loop Filter and the Prefilter

The proposed controller (shown in Figure 15) uses an output error feedback structure involving a loop filter and a prefilter [81]. The loop filter consists in two transfer functions, namely, $C(z)$ and $C_{RC}(z)$; and the prefilter is H(z).

$C(z)$ and $H(z)$ are described throughout this section. With the developed scheme, only the grid-side current[1] $i_{1,abc}$ and the grid voltage $v_{g,abc}$ are measured. These variables are transformed to the $\alpha\beta$ frame, resulting in i_1 and v_g. The grid-side current references of the current controller in the positive- and negative-sequence dq frames[2] are $i^*_{1,dq+}$ and $i^*_{1,dq-}$, respectively. They are transformed to the $\alpha\beta$ frame before they are applied to the prefilter. The phase of the positive-sequence fundamental grid voltage θ is estimated by a PLL. The feedforward u_f of the grid voltage v_g is added at the controller output u. Finally, the resulting sum is saturated (to take such effect of the modulator into account), obtaining the saturated PWM voltage reference u_{sat}. In the following, the two filters $C(z)$ and $H(z)$

---

[1]Since zero-sequence current cannot flow, two current sensors are enough.

[2]The synchronous frames permit an independent control of the active and reactive power.

that are included in the controller (in addition to the resonant controller (RC)) are designed. However, in order to obtain a good design, a previous knowledge of the bandwidth of the plant is required to define the dominant frequency of the system.

2.2.1. Assessment of the Dominant Frequency of the System According to the Available Bandwidth

As mentioned in the Introduction, the physical and practical implications of the design decisions, such as the bandwidth of the controller, should not be hidden behind the mathematical formulation. The response to broadband signals like sags or reference current changes is determined by the bandwidth of the controller. If a high bandwidth is set in the controller, fast references (high frequencies) can be followed. Regarding disturbances, a fast compensation is obtained. However, a fundamental fact about power-system models is that they do not exhibit good frequency response fidelity with the real power system beyond a certain frequency. This is due to plant parameter variations, unmodeled dynamics, power limits, or nonlinearities, to name a few. Here, the focus is placed on the voltage limits of the voltage source converters (VSCs) (represented by the saturator in Figure 15) in relation with the low-pass characteristics of the LCL filter. In the following, an analysis of the current slew-rate limitation and its implications on the current controller is presented. Since the LCL filter heavily blocks the grid-side current above the resonant frequency ω_{res}, the voltage source converters (VSCs) needs to generate a high actuation (possibly entering into over-modulation) when high frequencies (fast signals) are commanded [1]. This limitation does not depend on the type of control scheme adopted, but on the LCL filter and dc-bus voltage of the voltage source converters (VSCs).

The voltage source converters (VSCs) output voltage is bounded and depends on the dc-bus voltage v_{dc}. The maximum amplitude of the voltage step that the voltage source converters (VSCs) can apply per phase to the LCL filter (in the linear region of the PWM) is $u'_{d,\mathrm{max}} - v_g = (2/3)v_{\mathrm{dc}} - v_g$. The slew rate S_r (defined as the rate of change of current per unit of time, i.e., the time differentiation of i_1) that this step generates in the grid-side current is

$$S_r = \frac{z-1}{T_{\mathrm{s}}} I_1(z) = \underbrace{\frac{z-1}{T_{\mathrm{s}}}}_{\text{Time diff.}} \underbrace{\left(\frac{2v_{\mathrm{dc}}}{3} - v_g\right) \frac{z}{z-1}}_{\text{Voltage step}} \underbrace{G_d^{LCL}}_{\text{LCL filter}}. \qquad (18)$$

On the other hand, a sinusoid of frequency f_{dom} and amplitude A_p has a maximum slew rate of $S_r^{\mathrm{sin}} = 2\pi f_{\mathrm{dom}} A_p$. In this manner, the bandwidth of the current controller should be set according to the amplitude A_p and slope S_r^{sin} of the maximum expected current references and never exceed the bandwidth in the real open-loop system, which is limited by the slew rate (18). Therefore, the available bandwidth is

$$\mathrm{BW_A} = \frac{S_r}{2\pi A_p}. \qquad (19)$$

This value yields an upper limit for the dominant frequency of the system f_{dom}. In order to ensure a negligible effect of the damped resonant poles of the LCL filter on the system response (as demonstrated later in Section 2.4), the following condition should also be met:

$f_{\mathrm{dom}} \leq f_{\mathrm{res}}/2$ [1]. Therefore, the proposed controller has a dominant pole at a natural frequency

$$f_{\mathrm{dom}} \quad \leq \quad \min \left\{ \frac{S_r}{2\pi A_p}, \frac{f_{\mathrm{res}}}{2} \right\}. \tag{20}$$
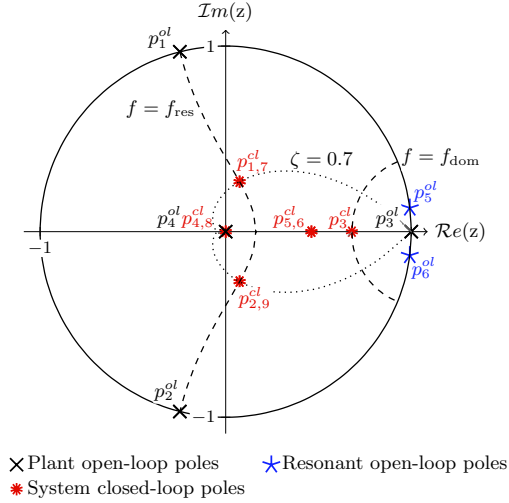
(a)
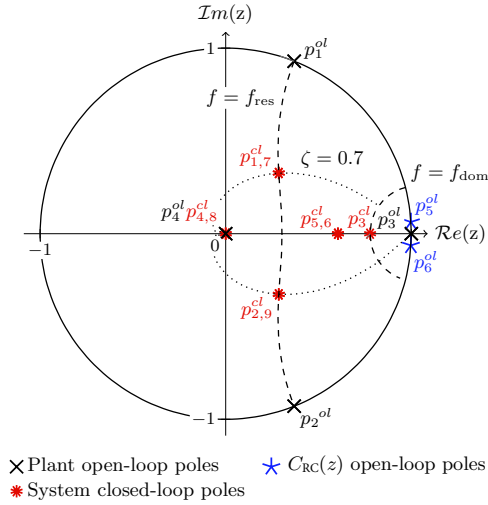
(b)

Figure 16. Continued on next page.

Plant zeros   ○ Controller zeros

(a)

● Plant zeros   ○ Controller zeros
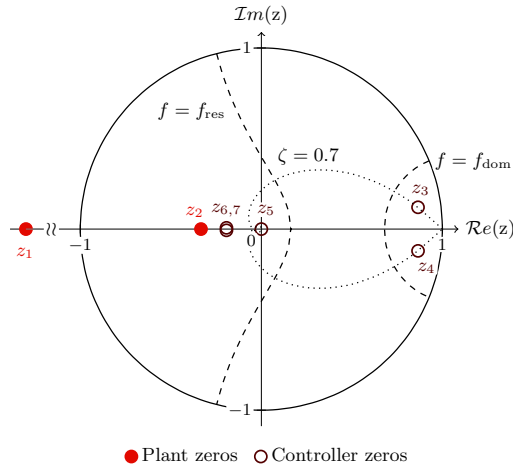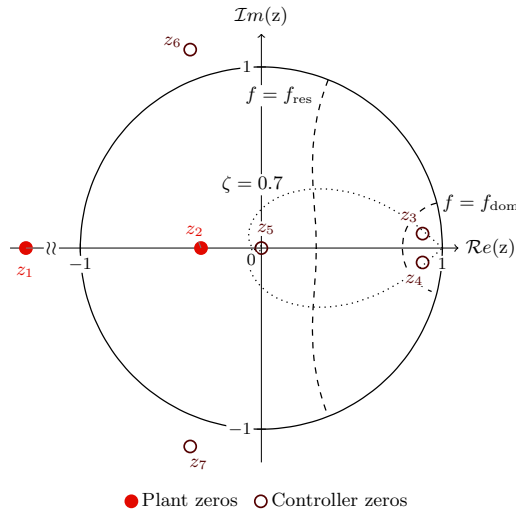
(b)

Figure 16. Roots of the complete closed-loop system (without the prefilter). a Pole map (includes the open-loop poles of the plant and of the resonant controller (RC)) for a single-update scheme. b Pole map (includes the open-loop poles of the plant and of the resonant controller (RC)) for a double-update scheme. a Zero map for a single-update scheme. b Zero map for a double-update scheme.

2.2.2.   Radial Projection and Closed-Loop Pole Placement by Means of $C(z)$

Radial projection (applied here to the resonant poles of the LCL filter) is a technique that minimizes control usage by simply adding damping to lightly-damped open-loop poles without changing their frequency [81]. Thus, the proposed closed-loop location of the

resonant poles is made dependent on the resonant frequency of the LCL filter so as to ensure uniform performance concerning the control effort regardless of the LCL filter used. Hence, a good response in combination with low controller effort are attained.

The proposed pole location aims to give a constant and predictable system performance, in combination with low controller effort, irrespectively of the LCL filter used. $C(z)$ is the part of the controller transfer function that is used to place the closed-loop poles of the system in the desired locations, and it is calculated according to the proposed pole-placement strategy.

The desired closed-loop pole locations are defined in the following. The number of closed-loop poles of the complete system is nine: four poles from the plant G_{dd}^{LCL}, two poles from the resonant controller (RC) $C_{RC}(z)$, and three poles from the controller $C(z)$. Therefore, nine closed-loop pole positions should be defined.

On the one hand, the transfer function of the plant model (13) has four (open-loop) poles, which have a direct relation with the physical system. Three of these poles model the LCL filter, which has two complex conjugate poles $p_{1,2}^{ol}$ (its resonant poles) at the resonant frequency and a real pole p_3^{ol} at zero frequency. The fourth pole p_4^{ol} models the computation delay and it is placed at the origin of the z-plane. These four poles are shown in Figure 16b, which depicts the pole map of the system. To maintain the required controller effort low, the closed-loop poles related to a physical system (as in this case) should be kept close to the corresponding open-loop poles whenever the response is not significantly degraded [81, 1].

The two resonant poles of the LCL filter impose serious limitations on the transient response. In order to provide a good response and keep the control effort low, a radial projection [81] of the resonant poles of the plant is used. As previously explained, this technique minimizes control usage by simply adding damping (a damping factor ζ of 0.7 is used) to lightly-damped open-loop poles without changing their natural frequency [81] [cf. $p_{1,2}^{cl}$ in Figure 16b].

The third pole of the LCL filter p_3^{ol} is displaced to a higher natural frequency [see p_3^{cl}, in Figure 16b] and is set to be the dominant pole of the system. A natural frequency f_{dom} [cf. (20)] is recommended for the dominant pole p_3^{cl}, as obtained from the available-bandwidth analysis.

The delay pole p_4^{ol} is not moved because it is already in an optimum location (at the origin of the z-plane).

On the other hand, the rest of the poles do not correspond to any physical system: $p_{5,6}^{ol}$, the two resonant poles of $C_{RC}(z)$; and $p_{7,8,9}^{ol}$, the three poles of $C(z)$. Hence, the locations of these poles are not restricted to yield a low control effort. Therefore, a larger bandwidth (faster poles) can be set. In this manner, it is advisable to place the corresponding closed-loop poles ($p_{5,6,7,8,9}^{cl}$) at natural frequencies higher (and sufficiently damped) than that of the dominant pole p_3^{cl} so as to ensure that the system dynamics are similar to those of this pole alone [81]. The locations already defined for $p_{1,2,4}^{cl}$ are also assigned to these closed-loop poles (cf. Table 3). An analogous reasoning was applied in [1] to place the poles of the observer in a state-feedback controller.

Table 3 summarizes the proposed locations for the closed-loop poles of the plant and the controller. Section 2.5 presents the mathematical details of the pole-placement design method applied to the system, so that the poles are effectively placed in such desired loca-

tions. In addition, the computational load of the proposed controller is given in Section 2.6.

As mentioned in Section I, the design process is straightforward compared with other techniques, because of the use of a direct discrete-time pole-placement strategy. The poles are in the desired locations [cf. Table 3] provided that the grid impedance is zero, because the design process takes into account the resonant frequency of the LCL filter.

Table 3. Pole Placement

Poles	Position in the z-plane	
	Open-loop	**Closed-loop**
G_d^{LCL} **LCL filter**	Radial projection of resonant poles to $\zeta = 0.7$.	
	$p_{1,2}^{ol} = e^{\pm j\omega_{\mathrm{res}}T_{\mathrm{s}}}$	$p_{1,2}^{cl} = e^{-(\zeta\omega_{\mathrm{res}}\pm j\omega_{\mathrm{res}}\sqrt{1-\zeta^2})T_{\mathrm{s}}}$
	Moved to make it the dominant pole, with a high bandwidth.	
	$p_3^{ol} = 1$	$p_3^{cl} = e^{-\omega_{\mathrm{dom}}T_{\mathrm{s}}}$
Comp. delay	Not moved; already in a fast and damped location.	
	$p_4^{ol} = 0$	$p_4^{cl} = 0$
$C_{\mathrm{RC}}(z)$ **Resonant controller**	Moved to twice the frequency of the dominant pole.	
	$p_{5,6}^{ol} = e^{\pm j\omega_g T_{\mathrm{s}}}$	$p_{5,6}^{cl} = e^{-2\omega_{\mathrm{dom}}T_{\mathrm{s}}}$
$C(z)$ **controller**	Placed at natural frequencies higher (and sufficiently damped) than that of the dominant pole p_3^{cl}. The open-loop pole positions of $C(z)$ (the roots of its denominator) are obtained from its denominator coefficients n_0, n_1, n_2, and n_3, which are given in Section 2.5.	
	$p_{7,8,9}^{ol} = \mathtt{roots}([n_3, n_2, n_1, n_0])$	$p_{7,9}^{cl} = p_{1,2}^{cl} \quad p_8^{cl} = p_4^{cl}$

2.2.3.   Prefilter for Eliminating the Slow Zeros

Although the location of the poles determines the system modes[3], it is the location of the zeros which determines the proportion in which these modes are combined in order to produce the system response [81].

On the one hand, the LCL filter model (8) does not have any zeros. However, all discrete-time models obtained by discretization of continuous ones turn out to have relative degree one, irrespective of the relative degree of the original continuous system [54]. The relative degree of a transfer function is the difference between the degree of the denominator (number of poles) and that of the numerator (number of zeros). Therefore, when the third-order LCL filter model is discretized, two fast (placed at much higher natural frequencies than the dominant pole) zeros $z_{1,2}$ appear. These sampling zeros (introduced by the discretization process [82]) should never be canceled or compensated [54], in order to avoid high-frequency oscillations. Figure 16b shows the zero map of the closed-loop system, where these zeros can be seen.

On the other hand, the controller $C(z)$ has five zeros [cf. Figure 16b]: two slow zeros (much closer to the stability boundary than the system dominant pole) $z_{3,4}$, one fast zero

---

[3]The system modes of a linear system determine the system behavior. Any zero-input response of a linear system is a linear combination of its system modes [81].
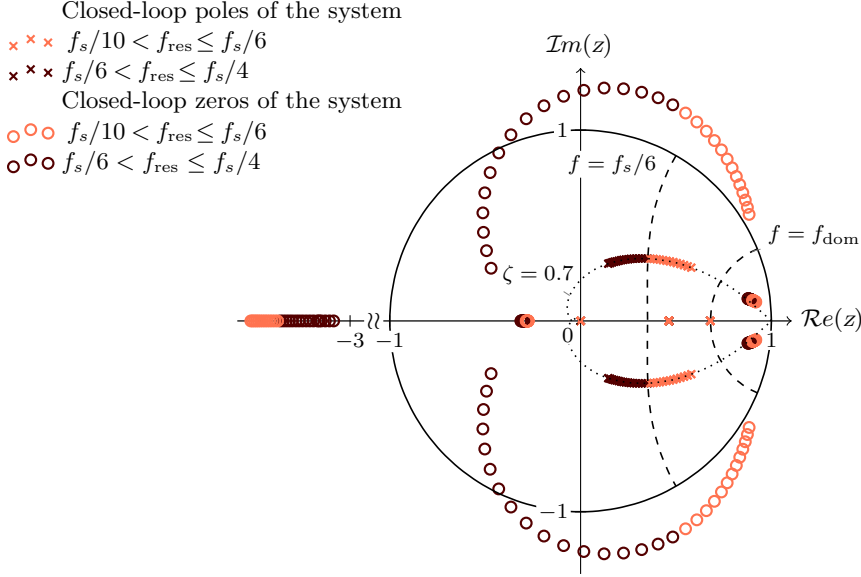
Figure 17. Root locus of the closed-loop system (without the prefilter) for a sweep in the resonant frequency of the LCL filter.

z_5, and two non-minimum-phase zeros $z_{6,7}$ whose location varies significantly with the resonant frequency of the LCL filter. This variation in the location of the zeros is shown in Figure 17, which depicts the root locus of the closed-loop system for a sweep in the resonant frequency of the LCL filter.

In order to obtain a good transient response, it should be ensured that there are no zeros with natural frequencies below that of the dominant pole [54]. The effect of the zeros $z_{1,2,5,6,7}$ on the response is negligible because they are placed in regions of natural frequencies above that of the dominant pole. However, there are two slow zeros, $z_{3,4}$ [cf. Figures 4(b) and 5], which should be removed. Hence, the following prefilter $H(z)$ is added, as depicted in Figure 15, in order to cancel the two slow zeros $z_{3,4}$ with two additional poles:

$$H(z) \quad = \quad \frac{z}{(z - z_3)(z - z_4)}. \tag{21}$$

The added zero at the origin cancels p_4^{cl}; hence, the system response is one sample faster. This prefilter also modifies the gain and phase of the closed-loop system at the grid frequency; therefore, a pair of complex gains K_+ and K_- are added (cf. Figure 15) to restore the unity gain:

$$K_+ \quad = \quad \frac{1}{H(e^{j\omega_g T_s})} \;\text{ and }\; K_- = \frac{1}{H(e^{-j\omega_g T_s})}. \tag{22}$$

In summary, the controller changes the dynamics of the open-loop plant to the desired closed-loop dynamics. The open-loop plant model G_{dd}^{LCL} does not have a flat frequency
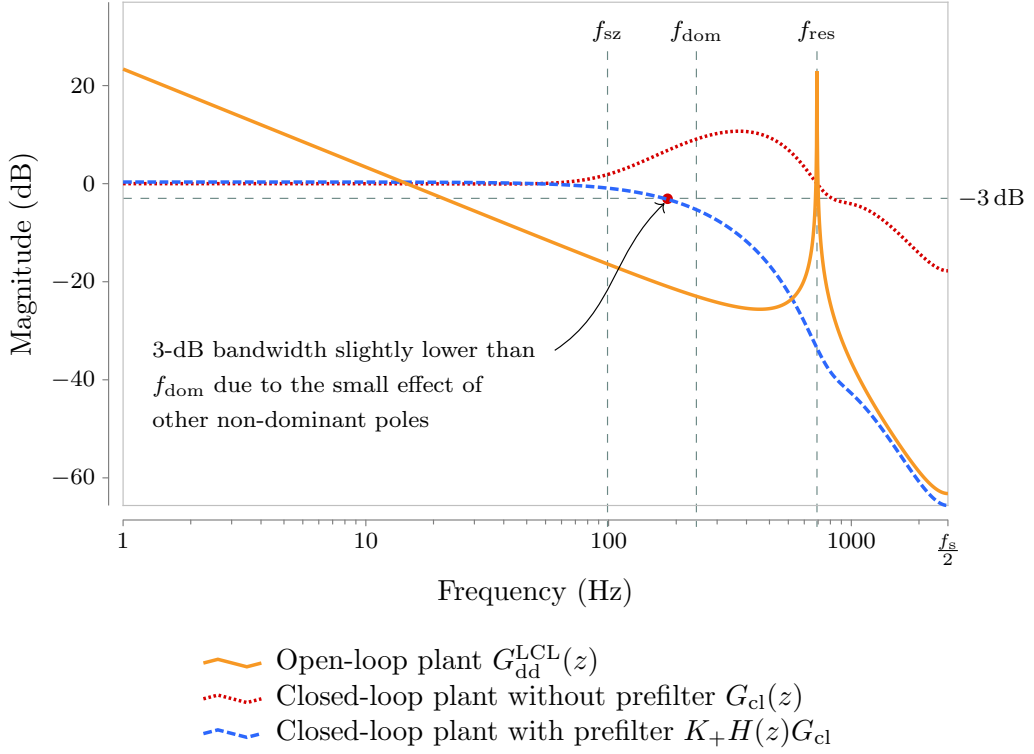
Figure 18. Effect of the proposed controller on the LCL-filter resonance frequency is analyzed through Bode magnitude plots.

response. It has a pole at dc and two complex-conjugate poles at the resonant frequency of the LCL filter, cf. Figure 18. When the loop filter is installed, the closed-loop transfer function of the system is

$$G_{cl}(z) = \left. \frac{i_1}{i_1^*} \right|_{v_g=0} = \frac{C(z)C_{RC}(z)G_{dd}^{LCL}}{1 + C(z)C_{RC}(z)G_{dd}^{LCL}}. \tag{23}$$

This transfer function has a damped response, as expected from the proposed closed-loop poles locations, cf. Figure 18. Nevertheless, the obtained response still does not have the desired flat low-pass response. $C(z)$ introduces two slow zeros at a frequency f_{sz} that is lower than the frequency of the dominant pole of the system f_{dom}. These zeros are the cause of the swell in the frequency response of the system. By adding the prefilter, the desired closed-loop response is obtained, cf. Figure 18. The final bandwidth of the current controller is slightly less than the specified f_{dom} because of the extra non-dominant poles of the system; however, the response approximates accurately that of a first order of system.

2.3.   Sensitivity to Grid-Impedance Variations

The robustness analysis to the grid impedance is structured into three parts. In the first place, the parameters involved in the analysis are discussed. This permits to generalize

the conclusions obtained to any LCL filter and sampling frequency. In the second place, a robustness analysis is carried out using a Nyquist diagram to obtain the phase and gain margins of the system for all combinations of LCL filter values and sampling frequencies. A frequency region $1/10 \leq f_{\text{res}}/f_{\text{s}} \leq 1/4$, which includes the different regions established in [47], is chosen. In the third place, the effect of the grid impedance on the gain and phase margins of the system is analyzed. Such analysis gives an insight to the previous mathematical results and helps to understand the practical implications of increasing the grid impedance.

In order to analyze the robustness of the proposed controller to variations in the grid impedance, first, the parameters involved in the analysis need to be presented. The open-loop transfer function (OLTF) is the transfer function that determines the stability of the system. It is the transfer function where the gain and phase margins of the system are calculated, and also where the Nyquist stability criterion is applied. The OLTF of the proposal is the product of the loop filter times the discrete-time plant model (cf. Figure 15):

$$\text{OLTF} = \underbrace{C(z)C_{RC}(z)}_{\text{Loop filter}} G_{dd}^{LCL}. \tag{24}$$

The plant model depends on seven parameters: the filter reactive values L_1, L_2, and C; the ESRs R_1, R_2, and R_c; and the sampling frequency f_{s}. In addition, the designer also specifies an extra parameter f_{dom}, which sets the desired bandwidth of the current controller. In order to reduce the number of parameters in the robustness analysis, the ESRs of the LCL filter are considered to be zero. This simplification assumes a high-quality-factor resonant LCL filter, which is a worst-case scenario in terms of stability. The ESRs damp the resonant poles and the dc pole of the LCL filter and yield a more stable filter. Therefore the results and conclusions derived in this analysis can also be applied to lower-quality-factor LCL filters. The parameter f_{dom} is defined as one third of the resonant frequency of the LCL filter for the analysis.

Although the physical nature of the problem can be best understood in terms of the physical parameters (L_1, L_2, C_f), it is the frequency-domain parameters (poles and zeros) that best serve the purpose of this first part of the robustness analysis. If the ESRs are assumed to be zero, then the discrete-time plant model [cf. (4)] can also be expressed in the zero-pole-gain form as

$$G_{dd}^{LCL} = \overbrace{K}^{\text{Gain}} \frac{\overbrace{(z - z_1)(z - z_2)}^{\text{Sampling zeros}}}{\underbrace{z}_{\text{Comp. delay}} \underbrace{(z - 1)}_{\text{DC pole}} \underbrace{(z - p_1^{\text{ol}})(z - p_2^{\text{ol}})}_{\text{Resonant poles}}}. \tag{25}$$

This model has one pole at dc, $z = 1$; one pole at the origin, which models the computational delay; two resonant poles $p_{1,2}^{\text{ol}}$ [cf. Figure 4(a)]; two sampling zeros $z_{1,2}$ [cf. Figure 4(b)]; and a constant gain K to complete the zero-pole-gain form of the model. The location of both $p_{1,2}^{\text{ol}}$ and $z_{1,2}$ depends on the ratio of the LCL-filter resonant frequency to sampling frequency $f_{\text{res}}/f_{\text{s}}$.

The proposed controller design gives a loop filter that yields the same closed-loop poles (cf. Table I) irrespectively of the particular value of K, due to the pole-placement strategy. In this manner, the OLTF does not depend on the value of the gain K neither. This important characteristic of the proposed controller is illustrated in Figure 19. As a consequence, both controllers $C^{\mathrm{LCL_a}}(z)$ and $C^{\mathrm{LCL_b}}(z)$, which correspond to plants with filters LCL_a and LCL_b [cf. Figure 19a and 19b], yield identical robustness in terms of phase and gain margins in spite of controlling plants with different LCL filters but the same ratio $f_{\mathrm{res}}/f_{\mathrm{s}}$. Therefore, although the OLTF seems to depend on many parameters, it is the ratio of the LCL-filter resonant frequency to sampling frequency $f_{\mathrm{res}}/f_{\mathrm{s}}$ the one that should be varied in the robustness analysis.

The developed robustness analysis is conducted for a wide sweep of such parameter: $1/10 \leq f_{\mathrm{res}}/f_{\mathrm{s}} \leq 1/4$, which includes the value $1/6$, where conventional resonant controllers become unstable [47]. Figure 20 shows the Nyquist diagram and the associated phase and gain margins of the system for a $f_{\mathrm{res}}/f_{\mathrm{s}}$ sweep. The Nyquist diagram goes several times to infinity because of the infinite gain of the OLTF at the grid frequency, at dc, and at the resonant frequency of the LCL filter. Therefore, in order not to clutter the diagram, only the part of the plot that corresponds to positive frequencies and is closest to the point -1 is depicted (the part that corresponds to the negative frequencies is a mirror image). The results show that the encirclement of the point -1 is performed with an approximately constant radius. Therefore, there are no sensitivity peaks [71] in the response. Furthermore, the results are consistent in spite of the large variation in the ratio $f_{\mathrm{res}}/f_{\mathrm{s}}$, as expected from the design process.

This analysis also gives a mathematical assessment of the well-known fact that the design of the current controller becomes more difficult as the resonant frequency of the LCL filter approaches the Nyquist frequency ($f_{\mathrm{s}}/2$), because the robustness of the system is degraded. Nevertheless, such mathematical results do not convey a good understanding of the robustness to a variation in a physical parameter such as the grid impedance. In order to tackle this problem, a careful study of the effect of such parameter, in terms of gain and phase margins, is presented next.

The previous stability margins correspond to a system where the grid impedance is zero, i.e., with nominal plant parameters. When a nonzero grid impedance is considered and the voltage feedforward is removed, the continuous plant model becomes

$$G^{\mathrm{LCL}}(s, R_g, L_g) \quad = \quad \left. \frac{i_1}{u_d'} \right|_{[K_f=0]v_g=0} = \frac{Z_c}{Z_2(Z_1 + Z_g + Z_c) + (Z_1 + Z_g)Z_c}, \tag{26}$$

where

$$Z_g = R_g + sL_g, \ Z_1 = R_1 + sL_1, \ Z_2 \quad = \quad R_2 + sL_2, \ Z_c = 1/(sC). \tag{27}$$

The feedforward of the grid voltage is implemented to improve the disturbance rejection during transient events, e.g., a sag fault and provide a smooth start of the converter. However, the voltage feedforward changes the closed-loop poles of the system when a grid impedance is considered. Therefore, in the case of a weak grid, the authors recommend removing the voltage feedforward by setting K_f to zero. On the one hand, the steady-state
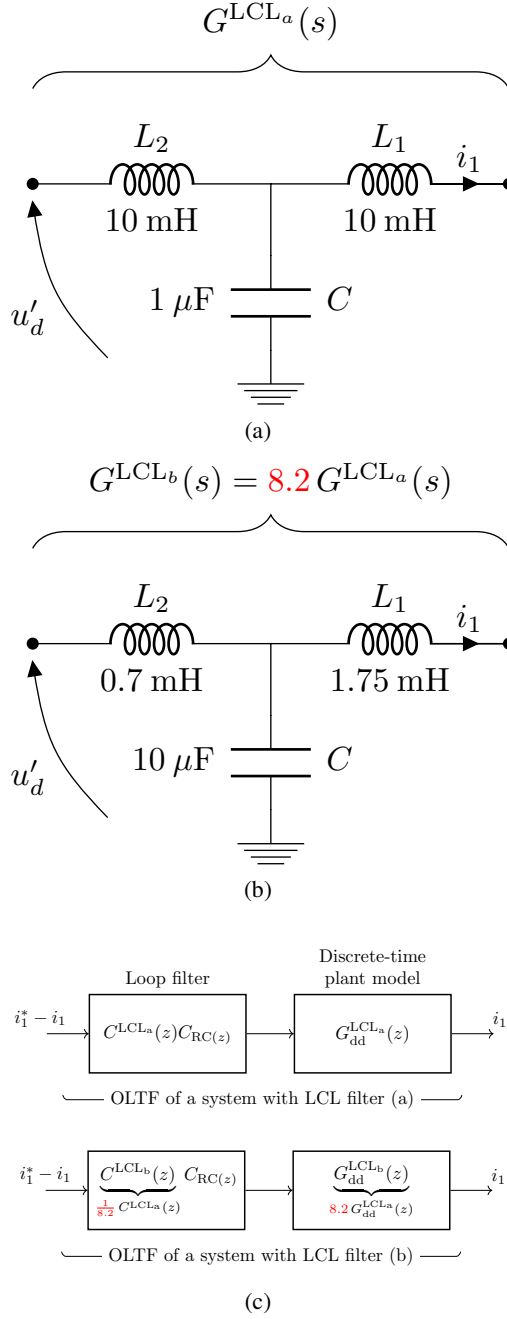
$$G^{\mathrm{LCL}_a}(s)$$

L_2

L_1 i_1

10 mH   10 mH

u'_d

1 μF $=$ C

(a)

$$G^{\mathrm{LCL}_b}(s) = 8.2\, G^{\mathrm{LCL}_a}(s)$$

L_2

L_1 i_1

0.7 mH   1.75 mH

u'_d

10 μF $=$ C

(b)

Discrete-time
Loop filter   plant model

$i_1^* - i_1$ → $C^{\mathrm{LCL_a}}(z)C_{\mathrm{RC}(z)}$ → $G_{\mathrm{dd}}^{\mathrm{LCL_a}}(z)$ → i_1

⸻ OLTF of a system with LCL filter (a) ⸺

$i_1^* - i_1$ → $\underbrace{C^{\mathrm{LCL_b}}(z)}_{\frac{1}{8.2}C^{\mathrm{LCL_a}}(z)}\, C_{\mathrm{RC}(z)}$ → $\underbrace{G_{\mathrm{dd}}^{\mathrm{LCL_b}}(z)}_{8.2\,G_{\mathrm{dd}}^{\mathrm{LCL_a}}(z)}$ → i_1

⸻ OLTF of a system with LCL filter (b) ⸺

(c)

Figure 19. Illustration of the fact that the open-loop transfer function (OLTF) does not depend on the gain of the plant model. a-b Example of two LCL filters with the same resonant frequency and with different values in their reactive elements. c The resulting OLTFs are identical.

response of the system is not affected because the resonant controller ensures zero-steady error at both fundamental sequences of the grid voltage. Furthermore, the transient response
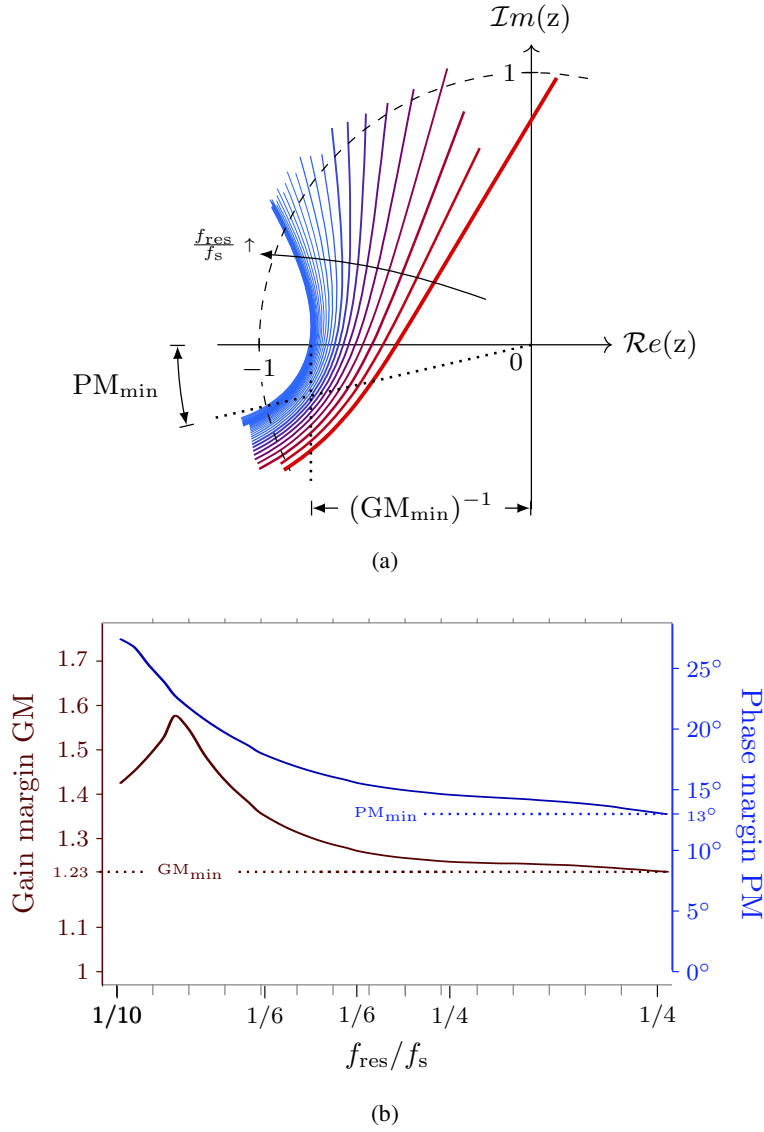
(a)

(b)

Figure 20. Robustness analysis for a sweep in the ratio f_{res}/f_s from $1/10$ to $1/4$. a Nyquist diagrams. b Stability margins.

to reference commands continues to be fast and damped.

This last part of the robustness study resorts to a numerical evaluation of the discrete plant model G_{dd}^{LCL} obtained from the modified continuous plant model (26) for a set of representative grid-impedance values and the parameters of LCL filter I from Table 4. Such study permits to obtain an insight into the problem and avoid the complexity of an analytical analysis.

Figure 21 and Figure 22 show the frequency response of the discrete-time plant model G_{dd}^{LCL} when the reactive and ohmic components of the grid impedance are independently increased. For a clearer evaluation of their effect, the ohmic and reactive components of the
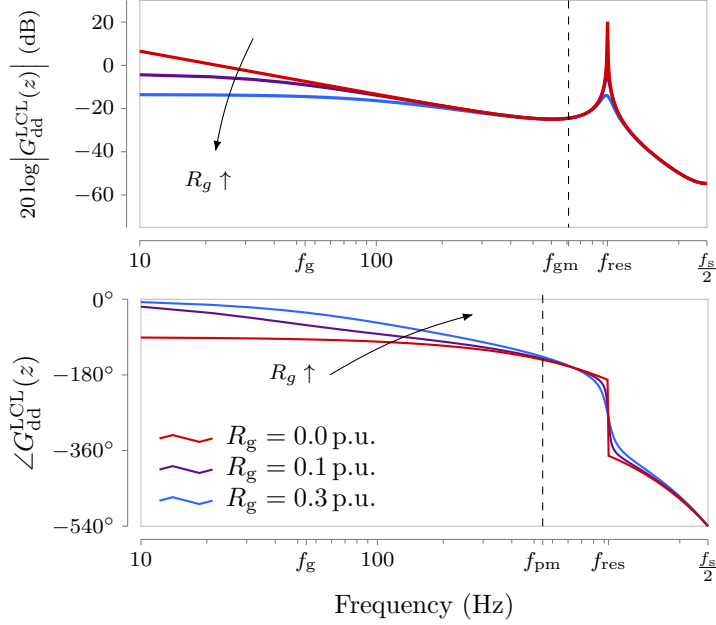
Figure 21. Effect of the resistive component of the grid impedance R_g ($L_g = 0$) on the plant model.

grid impedance are discussed separately. First, the effect of R_g is discussed assuming that L_g is zero. Then, L_g is modified while R_g is zero.

On the one hand, Figure 21 shows that if R_g is increased, then the magnitude of the plant model is reduced, especially at the highest-gain frequency ranges, namely at dc and at the resonant frequency. At the phase crossover frequency f_{gm}, the frequency where the gain margin is measured, the magnitude change is minimum; hence, robustness is maintained. In order to assess the effect of R_g on the phase of the OLTF, it is important to recall that, in an inductor, current lags voltage by $90°$, whereas in a resistor, both magnitudes are in phase. Therefore, increasing R_g while L_g is kept constant also reduces the phase lag of the system at a wide range of frequencies, including the gain crossover frequency f_{pm}, the frequency where the phase margin is measured. This improves the stability, as expected from the higher damping of the system.

On the other hand, Figure 22 shows that increasing L_g has a similar effect to rising R_g because it also boosts the overall impedance of the filter. Therefore, a lower magnitude in the plant model (and in the OLTF) is obtained. However, increasing the grid inductance also lowers the resonant frequency of the system. When the resonant frequency is lowered, the gain of the OLTF dramatically increases at the frequency of the new resonant frequency. If this change in the resonant frequency is big enough to reach the phase crossover frequency, then the system becomes unstable, because there is no gain margin large enough to compensate for the infinite gain of an LCL filter at the resonant frequency.

In order to complete the analysis, Figure 23 shows the resultant Nyquist diagram when both the reactive and ohmic components are modified simultaneously. On the one hand,
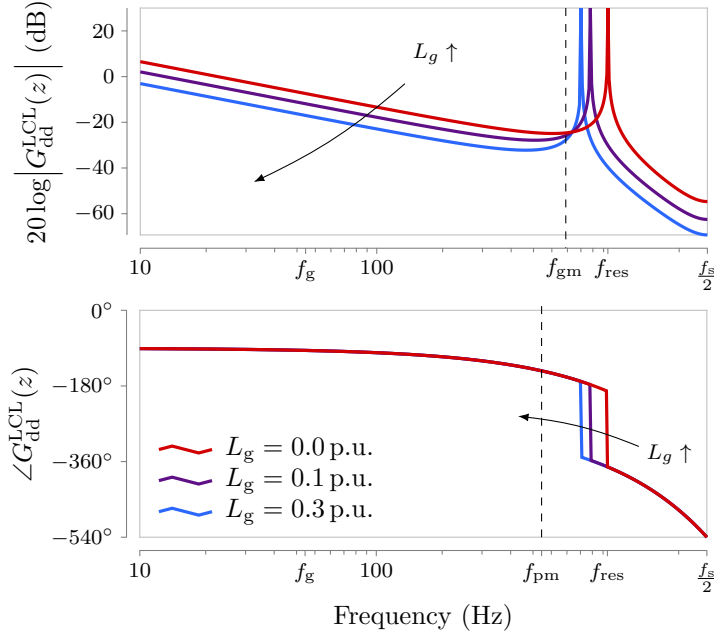
Figure 22. Effect of the reactive component of the grid impedance L_g ($R_g=0$) on the plant model.

Figures 23(a)-(c) display the effect of increasing the grid inductance from zero to a value of 0.3 p.u. for three values of grid resistance ($0, 0.1,$ and 0.3 p.u.). On the other other hand, Figures 23(d)-(f) present the effect of increasing the grid resistance from zero to a value of 0.3 p.u. for three values of grid inductance ($0, 0.1,$ and 0.3 p.u.). As indicated above, increasing R_g results in greater system stability whereas rising L_g improves the gain margin but reduces the phase margin because of the change in the resonant frequency. When L_g is 0.3 p.u. and R_g is zero, the system reaches the stability boundary.

As a conclusion from the numerical results, a brief qualitative analysis is presented here. For a given modulator reference voltage u, the grid-side current is usually reduced as the grid impedance is increased (Ohm's law). Therefore, increasing the grid impedance has a similar effect to reducing the controller gain, which typically increases the stability of a system. There are some subtleties which are neglected in this simple reasoning; hence, a complete and careful study of the numerical results is recommended for a comprehensive understanding of the problem. In order to drive the system into instability, a value of L_g equal to 0.3p.u. is required, which is higher than the inductance of a properly designed LCL filter. Since during normal operation the grid impedance is much lower than such value, it can be concluded that the proposed controller is robust to changes in the grid impedance. When the grid impedance becomes greater than such a large value, e.g. during islanded operation, a voltage controller should be used in place of a current controller.
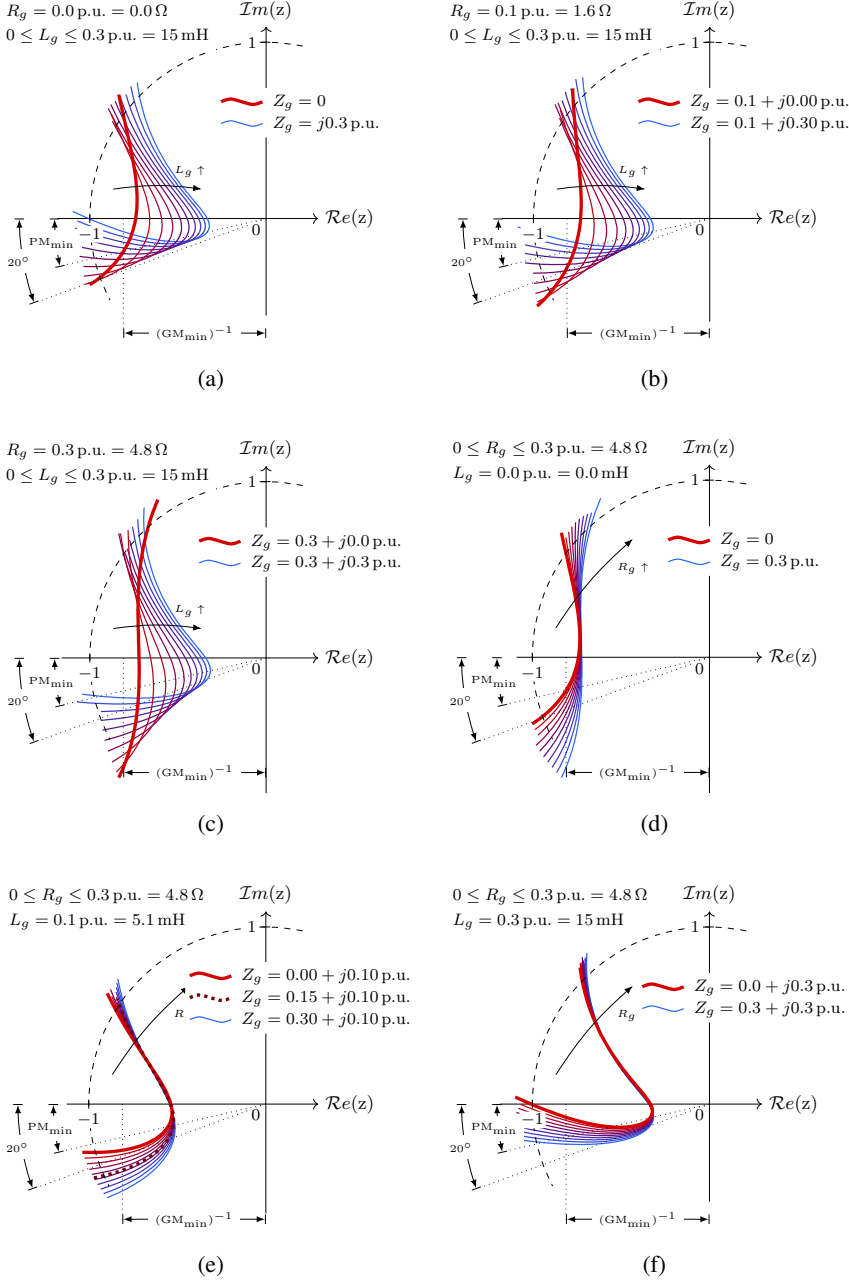
Figure 23. Nyquist diagram of the system that shows the effect of the grid impedance on the open-loop transfer function (OLTF). a-c Sweep in L_g while R_g is kept constant. d-f Sweep in R_g while L_g is kept constant.

2.4. Simulation and Experimental Results

The experimental results are carried out in a 10-kW voltage source converters (VSCs) working as an inverter with a dc-bus voltage of $v_{dc} = 730$V and connected to a 400-V line-to-line

three-phase grid of 50 Hz. The switching frequency is $f_{\text{sw}} = 2.5\,\text{kHz}$, and the dead-time is $3\,\mu\text{s}$. A low switching frequency reduces switching losses in the voltage source converters (VSCs) and it represents a worst-case scenario in terms of the effect of the computation and modulation delays. A double-update sampling strategy is used, resulting in a sampling frequency f_{s} of 5 kHz. Two LCL filters with different resonant frequencies f_{res} (above and below the threshold $f_{\text{s}}/6$ [47]) are used to connect the voltage source converters (VSCs) to the grid. The filter parameters are presented in Table 4. Filter I was designed according to [83] in order to obtain a high filter performance in combination with low reactive values. The available bandwidth [cf. (19)] with filter I and filter II is 230 Hz and 200 Hz, respectively, according to Section 2.2.1 ($A_p = 10\text{A}$ and $S_r = 14500\,\text{A/s}$ for filter I, and $S_r = 12500\,\text{A/s}$ for filter II). The implemented controllers are designed using the proposed method with a dominant frequency equal to the available bandwidth. Figures 24a and 24b show a diagram and a photograph of the experimental setup, respectively. In addition, a video demonstration that the authors feel it would enhance the reader's understanding of the research contribution has also been included.

The reference tracking (of both sequences) and the disturbance rejection (of both sequences) are tested for each of the LCL filters. The last test assesses the robustness of the controller to an increase in the grid inductance (filter I is used). The proposed scheme includes a resonant controller (14), which gives an infinite open-loop gain at both the positive and negative sequences of the grid frequency; therefore, zero steady-state error is achieved at the frequencies f_{g} and $-f_{\text{g}}$ of the $\alpha\beta$ frame.

In order to test the controller under unbalanced conditions, five tests are carried out. The frequency spectrum of the current reference for each of the five tests is shown in Figure 25. During tests 1, 2, 3, and 5, the current reference only contains one sequence at a time. This allows to visualize the results in a synchronous frame to measure the transient parameters without having a 100-Hz signal interfering with the dc signal of interest, cf. Figure 25b.

It should be remembered that the subscript in a variable name denotes the reference frame of the variable. In this manner, dq+ (dq-) denotes a positive (negative) sequence reference frame, i.e., a synchronous frame that spins at the same (opposite) frequency as the grid fundamental frequency. When no reference frame in a subscript of a variable is detailed, the $\alpha\beta$ frame is assumed, which is the reference frame where the proposed controller operates.

- Test 1 (cf. Figure 26) commands a balanced current reference ($i^*_{1,dq+} = 8\text{A}$ and $i^*_{1,dq-} = 0\text{A}$).

- Test 2 (cf. Figure 27) commands a negative-sequence current reference ($i^*_{1,dq+} = 0\text{A}$ and $i^*_{1,dq-} = 8\text{A}$).

- Test 3 (cf. Figure 28) keeps the current reference constant and balanced ($i^*_{1,dq+} = 4.5\text{A}$ and $i^*_{1,dq-} = 0\text{A}$) while a sag fault occurs. The grid voltage is unbalanced ($v_{\text{g},dq-} \neq 0$) during the sag fault.

- Test 4 (cf. Figure 29) generates a current reference according to a positive-negative-sequence compensation strategy during the sag fault [84]. Therefore, the commanded current reference contains both sequences simultaneously ($i^*_{1,dq+} = 7\text{A}$ and $i^*_{1,dq-} =$
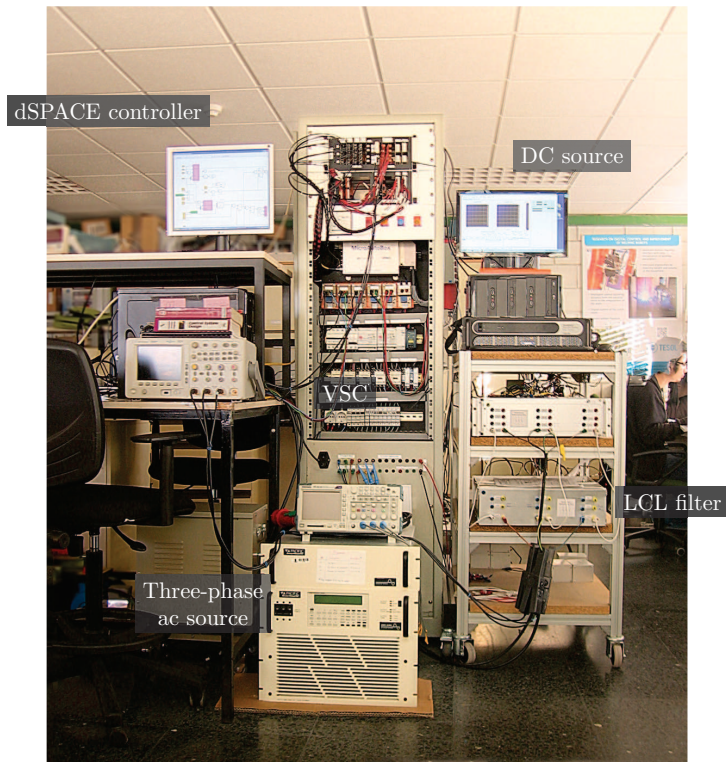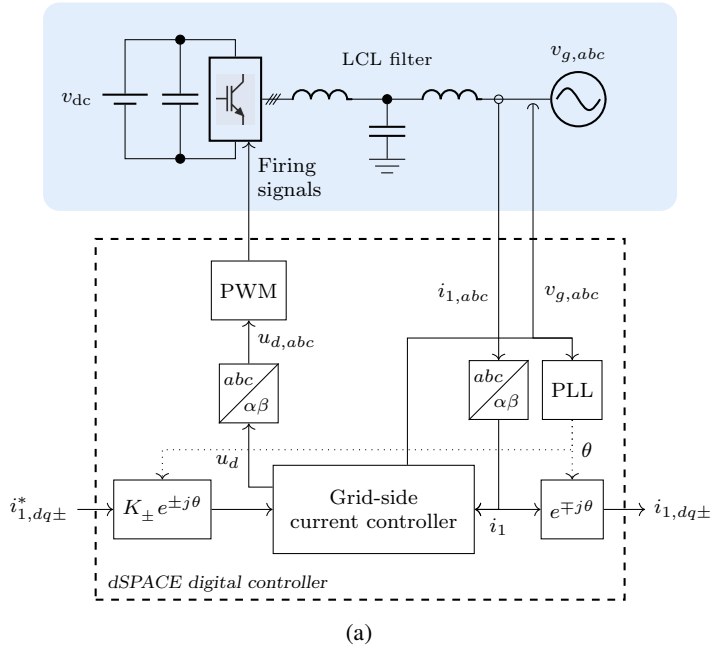
(a)

(b)

Figure 24. Experimental setup of the grid-tied inverter. a Diagram. b Photograph.
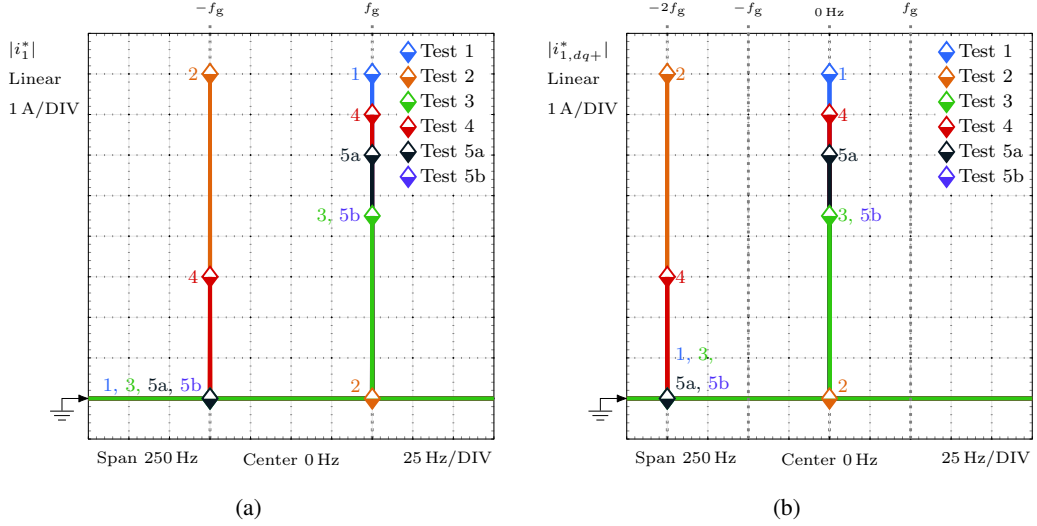
Figure 25. Frequency spectrum of the current reference for each of the five tests that are carried out in Section V. a Current reference expressed in the $\alpha\beta$ frame i_1^*. b Current reference expressed in the dq+ frame $i_{1,dq+}^*$.

3A). The results are presented in the $\alpha\beta$ frame to avoid displaying a dc component combined with a double-frequency component (cf. Figure 25b).

- Test 5 (cf. Figure 30) contains two subtests.

  - Test 5a evaluates the reference-tracking performance by commanding a balanced current reference ($i_{1,dq+}^* = 6$A and $i_{1,dq-}^* = 0$A).
  - Test 5b appraises the disturbance-rejection capability under the same conditions as Test 3, namely, an unbalanced grid voltage caused by a sag fault.

Discrete-time linear simulations obtained with Matlab are shown superimposed to the experimental results. The oscilloscope captures show the reference signal i_1^*, the simulated response i_1^{sim}, and the measured response i_1. The experimental response accurately matches that predicted by the simulation, as shown in Figures 26–29, in spite of it using a simple linear averaged model. The minor differences that appear between the simulated and the measured grid-side current are caused by nonidealities not taken into account in the system model, such as the nonlinear nature of the voltage source converters (VSCs).

First, the reference-tracking capability of the system is shown in Figures 26 and 27. In order to test the transient response of the current controller, a reference step in the d axis is generated. Figure 26 shows this reference step for the positive-sequence dq frame (dq+). The measured currents $i_{1,abc}$ are also transformed to a synchronous frame rotating at the same frequency. This transformation permits to measure the transient-response parameters (rise time, settling time and overshoot) in the variable $i_{1,dq}$. The 10%–90% rise time of the experimental response i_1 in Figure 26 is approximately $1.5ms$ for filter I and $1.75ms$ for filter II. These values are in accordance with those of a first-order system of the same

**Table 4. LCL Filter, ESRs, and Grid Impedance Parameters**

	Param.	Filter I	Filter II
	L_1	3.75 mH, 0.07 p.u.	5.4 mH, 0.11 p.u.
	L_2	3.75 mH, 0.07 p.u.	5.4 mH, 0.11 p.u.
	C	$15\mu F$, 0.07 p.u.	$18\mu F$, 0.09 p.u.
	$f_{\rm res}$	950 Hz	722 Hz
ESRs	R_1	0.5Ω, 0.03 p.u.	0.5Ω, 0.03 p.u.
	R_2	1.0Ω, 0.06 p.u.	1.0Ω, 0.06 p.u.
	R_c	0.1Ω, 0.01 p.u.	0.1Ω, 0.01 p.u.
Z_g	R_g	2.5Ω, 0.15 p.u.	
	L_g	5.4 mH, 0.10 p.u.	

bandwidth, $T_{10\%-90\%} = 2.2/(2\pi f_{\rm dom})$. Negligible overshoot and good axis decoupling are attained because the response is mainly determined by the well-damped dominant closed-loop pole p_3^{cl} (see Figure 16) placed at the natural frequency $f_{\rm dom}$. Next, Figure 27 shows a reference step of the same amplitude, but now in the negative-sequence dq frame (dq−). The obtained response has roughly the same transient-response parameters as in Figure 26, because the proposed enhanced resonant controller (RC) manages to treat both sequences in the same manner.

Next, the disturbance-rejection capability of the controller to sags in the grid voltage is assessed. Sags usually cause unbalanced voltage grid conditions. In particular, a 40%-depth type-C sag [85], which contains both voltage sequences, is generated with a three-phase ac voltage source for the remaining tests. In the first disturbance test (see Figure 28), the current reference $i_{1,dq+}^*$ is kept constant. The settling time to within 2% makes it possible to evaluate the time required by the current controller to recover from a sag disturbance. A value of settling time $t_{\rm st} = 4ms$ is obtained, which is slightly greater (but still short) than the $t_{\rm st} = 4/(2\pi f_{\rm dom})$ of a first-order system; this is due to the effect of the extra non-dominant closed-loop poles. The next test (Figure 29) evaluates the reference-tracking capability under the same sag. A reference step i_1^* is generated according to the positive-negative-sequence compensation strategy [84]. Since the currents now have a positive and a negative sequence, they are shown in stationary frame. A fast and well damped response is also obtained when both effects are combined.

In the previous tests, it can be seen that the transient-response parameters (rise time, overshoot, and settling time) are determined by the selected dominant natural frequency $f_{\rm dom}$, defined during the design process. They do not depend on the LCL filter resonant frequency. The oscilloscope captures obtained with filter I ($f_{\rm res} < f_{\rm s}/6$), shown in Figures 26a–29a display similar transient characteristics to those made with filter II ($f_{\rm res} > f_{\rm s}/6$), shown in Figures 26b–29b.

Finally, an experimental test was carried out to assess the robustness of the controller when connected to a weak grid. The weak grid has an impedance of value
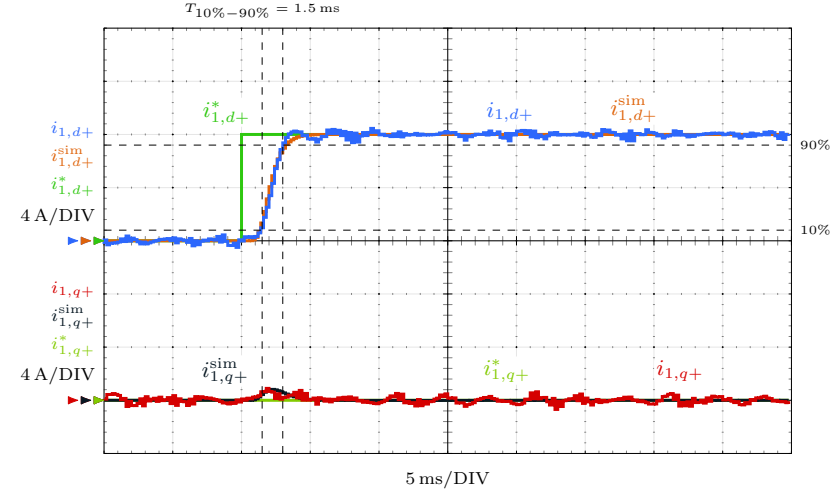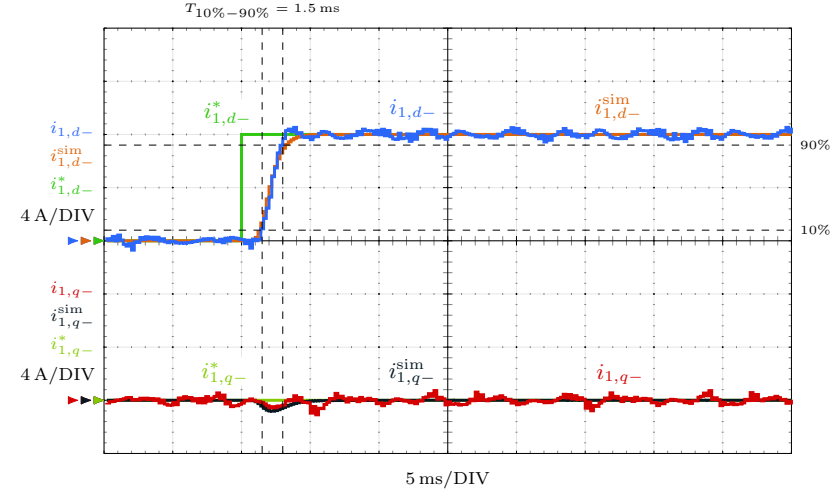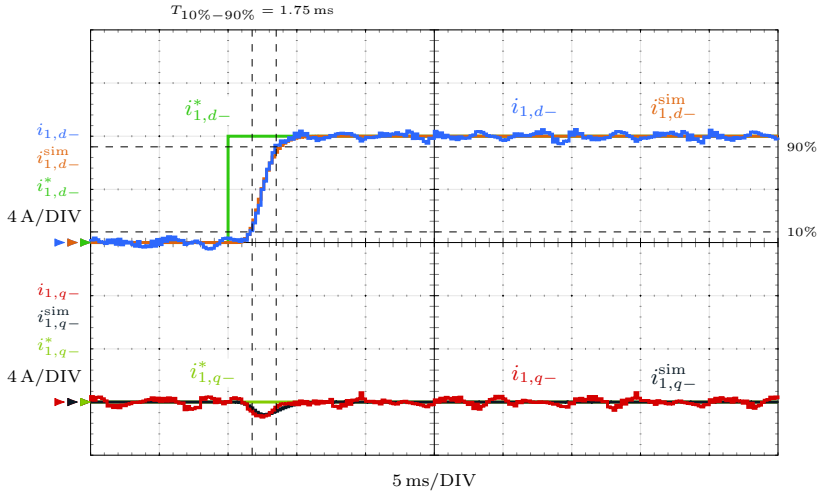
(a)
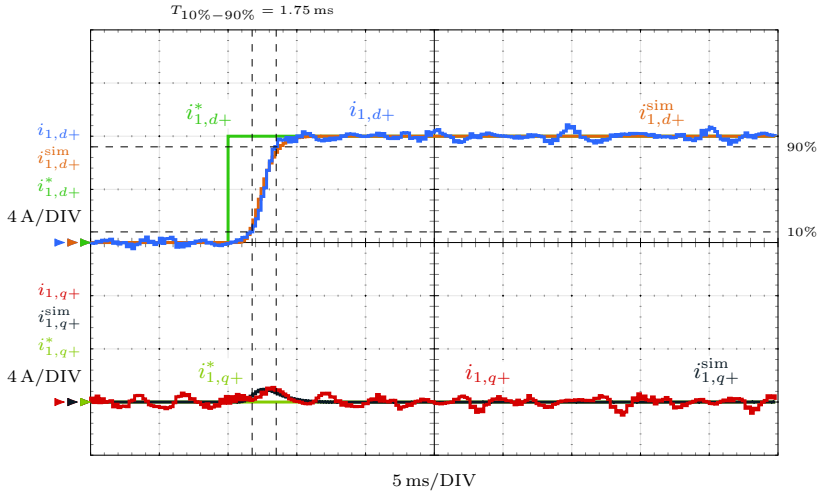
(b)

Figure 26. Experimental and simulation waveforms ($i_{1,dq}$ and $i_{1,dq}^{\mathrm{sim}}$, respectively) for a reference step $i_{1,q+}^{*}$ in the positive synchronous frame dq+ rotating at the fundamental grid frequency ω_g. a LCL filter I b LCL filter II.

$Z_g = 0.15 + j0.10$ p.u., which is one of the values analyzed in Section 2.3, cf. Figure 23e. The test is composed of two parts. In Figure 30a, a reference step is commanded to test the reference-tracking response and, in Figure 30a, the disturbance rejection is tested under the same voltage sag as in Figure 28. The responses are not significantly modified compared to Figures 26 and 28. In conclusion, the stability of the system is preserved even with substantial deviations in the plant parameters. This behavior is in accordance with the theoretical analysis presented in Section 2.3.
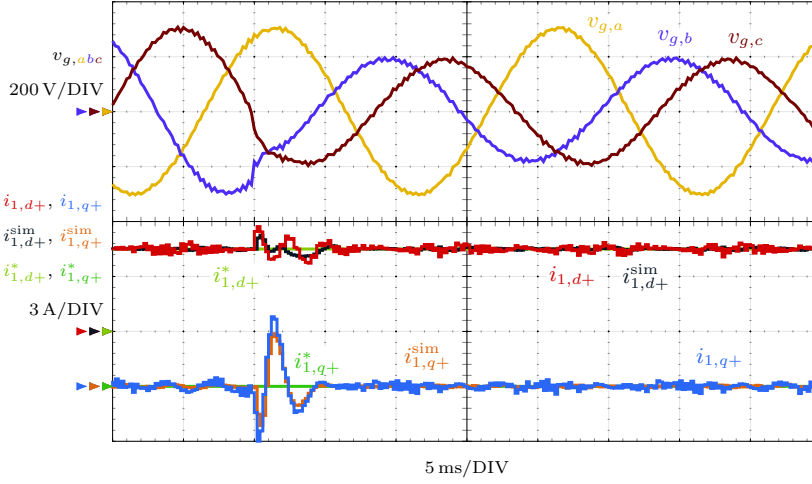
(a)

(b)

Figure 27. Experimental and simulation waveforms ($i_{1,dq}$ and $i_{1,dq}^{sim}$, respectively) for a reference step $i_{1,q-}^{*}$ in the negative synchronous frame dq− rotating at the fundamental grid frequency ω_g. a LCL filter I b LCL filter II.
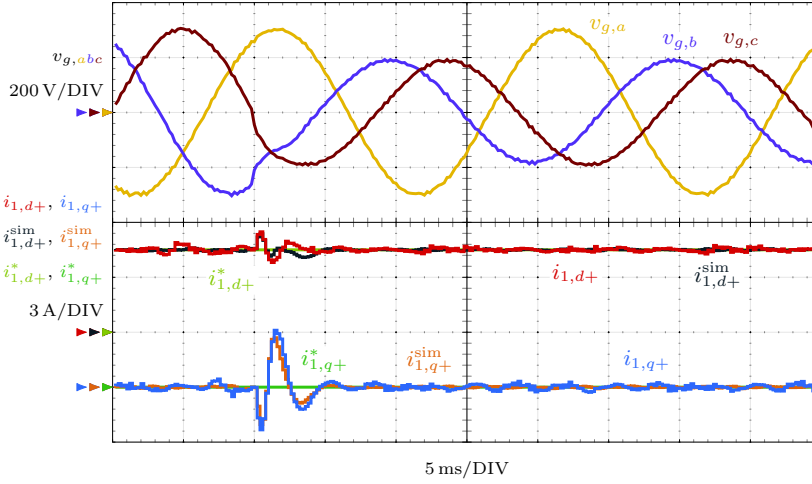
2.5. Pole-Placement Equations to Locate the Poles at the Desired Locations from Table 1

The augmented plant model (i.e., including the resonant controller (RC)) in (15) has order six and a relative degree of four:

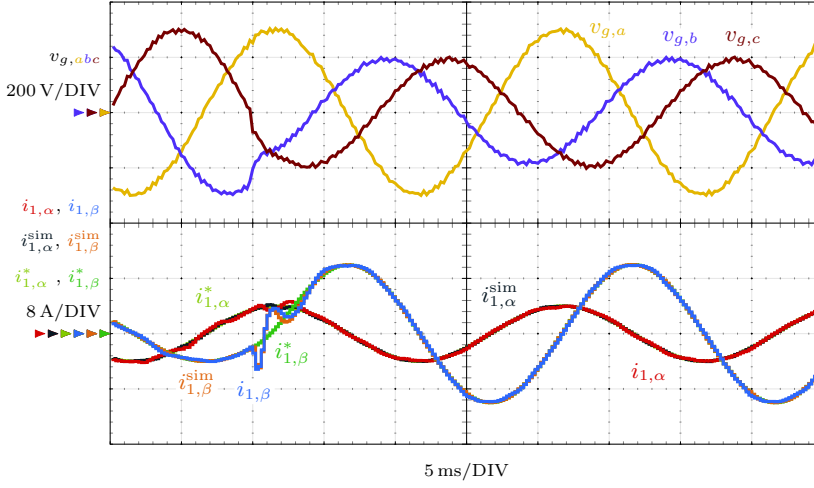$$G_{add}^{LCL}(z) \;\; = \;\; \frac{B(z)}{A(z)} \tag{28}$$

(a)

(b)

Figure 28. Experimental and simulation waveforms ($i_{1,dq}$ and $i_{1,dq}^{\text{sim}}$, respectively) for a 40%-depth type-C sag in $v_{g,abc}$ while keeping the reference $i_{1,dq}^{*}$ constant. a LCL filter I. b LCL filter II.
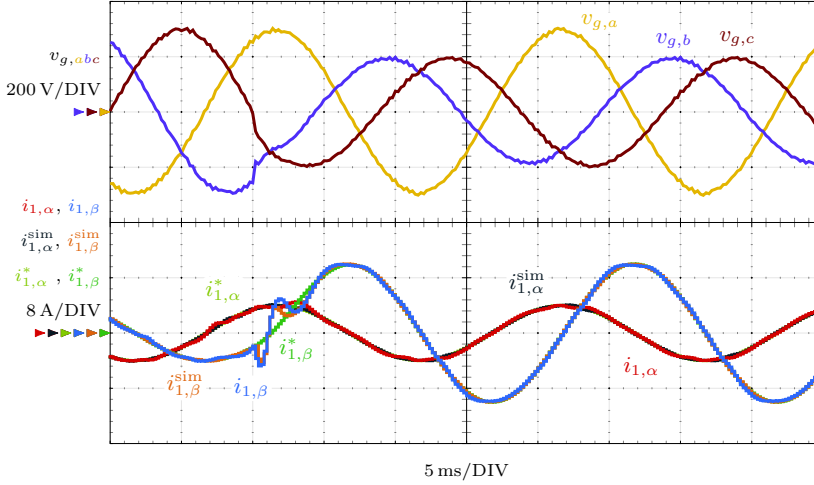
where

$$
\begin{aligned}
A(z) &= a_6 z^6 + a_5 z^5 + a_4 z^4 + a_3 z^3 + a_2 z^2 + a_1 z + 0 \\
B(z) &= b_2 z^2 + b_1 z + b_0.
\end{aligned}
\tag{29}
$$

The controller transfer function C(z) is

$$
C(z) = \frac{M(z)}{N(z)}.
\tag{30}
$$

(a)

(b)

Figure 29. Experimental and simulation waveforms ($i_{1,\alpha\beta}$ and $i_{1,\alpha\beta}^{\text{sim}}$, respectively) for a 40%-depth type-C sag in $v_{g,abc}$. The reference step i_1^* is calculated according to the so-called positive-negative-sequence compensation strategy [84]. a LCL filter I. b LCL filter II.
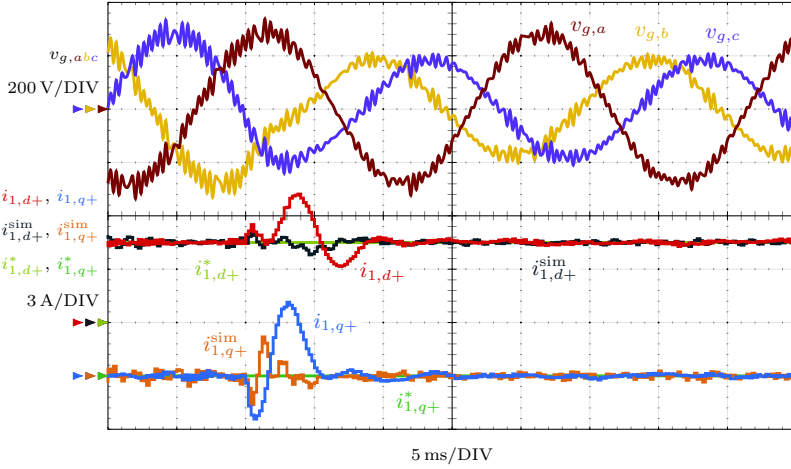
This controller permits to obtain the ten coefficients of the desired system characteristic polynomial A_{cl} according to the closed-loop pole locations defined in Section 2.2:

$$
\begin{aligned}
A_{cl} &= A(z)N(z) + B(z)M(z) \\
&= d_9 z^9 + d_8 z^8 + d_7 z^7 + d_6 z^6 + d_5 z^5 \\
&\quad + d_4 z^4 + d_3 z^3 + d_2 z^2 + d_1 z + d_0
\end{aligned}
\tag{31}
$$

where the roots of the characteristic polynomial are the desired closed-loop poles of the
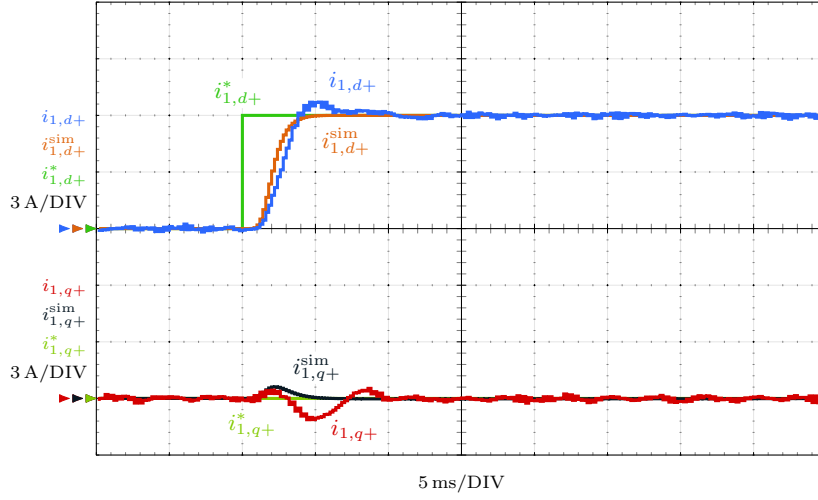
(a)

(b)

Figure 30. Experimental, simulation, and reference waveforms ($i_{1,dq}$, $i_{1,dq}^{\text{sim}}$, and $i_{1,q+}^{*}$, respectively) in the positive synchronous frame dq+ when the converter is connected to a weak grid and the LCL filter I is installed. a A reference step. b A 40%-depth type-C voltage sag in $v_{g,abc}$.

system from Table 3:

$$A_{cl} = (z - p_1^{cl})(z - p_2^{cl}) \cdots (z - p_9^{cl}).$$

To reduce the order of the complete system, the controller C(z) is designed to have the lowest order possible. C(z) can have a negative relative degree of two (which gives the minimum order achievable for the system) because the complete controller $C(z)C_{RC}(z)$ is still proper[4].

---

[4]A proper transfer function is that in which the degree of the numerator does not exceed the degree of the

Hence, since the controller C(z) has ten parameters and a negative relative degree of two, the following two polynomials [which give a third-order transfer function for C(z)] are obtained:

$$
\begin{aligned}
M(z) &= m_5 z^5 + m_4 z^4 + m_3 z^3 + m_2 z^2 + m_1 z + m_0 \\
N(z) &= n_3 z^3 + n_2 z^2 + n_1 z + n_0.
\end{aligned}
\tag{32}
$$

The polynomial Diophantine equation in (31) can be expressed in matrix notation as

$$
Sc = d \tag{33}
$$

where

$$
S = \begin{bmatrix}
a_6 & 0 & 0 & 0 & 0 & 0 & 0 & 0 & 0 & 0 \\
a_5 & a_6 & 0 & 0 & 0 & 0 & 0 & 0 & 0 & 0 \\
a_4 & a_5 & a_6 & 0 & b_2 & 0 & 0 & 0 & 0 & 0 \\
a_3 & a_4 & a_5 & a_6 & b_1 & b_2 & 0 & 0 & 0 & 0 \\
a_2 & a_3 & a_4 & a_5 & b_0 & b_1 & b_2 & 0 & 0 & 0 \\
a_1 & a_2 & a_3 & a_4 & 0 & b_0 & b_1 & b_2 & 0 & 0 \\
0 & a_1 & a_2 & a_3 & 0 & 0 & b_0 & b_1 & b_2 & 0 \\
0 & 0 & a_1 & a_2 & 0 & 0 & 0 & b_0 & b_1 & b_2 \\
0 & 0 & 0 & a_1 & 0 & 0 & 0 & 0 & b_0 & b_1 \\
0 & 0 & 0 & 0 & 0 & 0 & 0 & 0 & 0 & b_0
\end{bmatrix}
$$

$$
c = \begin{bmatrix} n_3 & n_2 & n_1 & n_0 & m_5 & m_4 & m_3 & m_2 & m_1 & m_0 \end{bmatrix}^{\mathrm{T}}
$$

$$
d = \begin{bmatrix} d_9 & d_8 & d_7 & d_6 & d_5 & d_4 & d_3 & d_2 & d_1 & d_0 \end{bmatrix}^{\mathrm{T}}.
\tag{34}
$$

Therefore, the coefficients of the controller C(z) that place the closed-loop poles at the desired locations are obtained by solving[5] this system of linear equations:

$$
c = S^{-1} d. \tag{35}
$$

2.6.   Computational Load

The computational load of the proposed transfer function controller is analyzed in number of operations and compared with an equivalent state-space controller. This is commonly regarded as valid for assessing the computational burden without further experimental verification [86].

The proposed controller implements two transfer functions, which are the prefilter and the loop filter. The prefilter (21) is a second-order transfer function with a relative degree of one (the difference between the number of poles and the number of zeros). The loop filter is the product of $C_{RC}(z)$ [cf. (14)] times $C(z)$ [cf. (30) and (32)]. This yields a strictly-proper (the same number of poles and zeros) fifth-order transfer function. The computational load required by a discrete transfer function is proportional to the number of coefficients. Each coefficient requires a multiplication of a complex variable by a real

denominator [81]. This ensures that the system is causal and can be implemented in a real control device.

[5]Sylvester's theorem [54] ensures that S is invertible.

coefficient and a complex addition to be performed. At most, the number of coefficients in a transfer function is equal to the number of poles and zeros plus two. A multiplication requires two two floating-point operations (flops) and a complex addition is performed in two two flops. Therefore, this controller has a constant complexity of 34 two floating-point operations (flops). The total number of two flops per second that the proposed current controller executes is $34f_\mathrm{s}$. In the presented implementation ($f_\mathrm{s} = 5\,\mathrm{kHz}$), a figure of 170 kilo flops per second is obtained.

On the other hand, the state space controller in [1] requires the implementation of an observer and a control law. The observer equation is

$$\hat{\mathbf{x}}_\mathbf{b}(k) = \underbrace{(\mathbf{F_{bb}} - \mathbf{K_o}\mathbf{F_{ab}})}_{5\times 5} \underbrace{\hat{\mathbf{x}}_\mathbf{b}(k-1)}_{5\times 1}$$
$$+ \underbrace{\mathbf{K_o}}_{5\times 1} \underbrace{i_1(k)}_{1\times 1} + \underbrace{(\mathbf{F_{ba}} - \mathbf{K_o}F_{aa})}_{5\times 1} \underbrace{i_1(k-1)}_{1\times 1}$$
$$+ \underbrace{(\mathbf{G_b} - \mathbf{K_o}G_a)}_{5\times 1} \underbrace{u(k-1)}_{1\times 1}. \tag{36}$$

The control law equation is

$$u(k) = \underbrace{K_f}_{1\times 1} \underbrace{i_1^*}_{1\times 1} - \underbrace{\begin{bmatrix} \mathbf{K_c} & 1 & 0 \end{bmatrix}}_{1\times 6} \underbrace{\begin{bmatrix} i_1 \\ \hat{\mathbf{x}}_\mathbf{b} \end{bmatrix}}_{6\times 1}. \tag{37}$$

Therefore, the number of operations that this controller requires is 47 multiplications of complex variables by real coefficients and 47 complex additions. This results in a constant complexity of 188 two flops ($188f_\mathrm{s}$ flops per second.

As a consequence, the computational load of the proposed controller is less than five times that of [1], which makes the former particularly suited for an implementation in a embedded controller when a high switching frequency is required.

2.7.   Example of Design Code

A reference script that summarizes the computations presented through the section for the design of the proposed controller is shown in Figure 31. The inputs of the script are the LCL filter parameters L_1, L_2, and C; the estimated equivalent loss resistances R_1, R_2 and R_c; the fundamental grid frequency ω_g; and the sampling period T_s. The outputs are the controller C(z), the resonant controller (RC) $C_{RC}(z)$, the feedforward gain K_f, the prefilter H(z) and the reference gains $K_\pm$. These transfer functions and gains are needed to implement the proposed control structure (cf. Figure 15).

2.8.   Summary

This section has presented an enhanced current RC for grid-tied converters with LCL filter. The developed method is based on direct discrete-time pole placement from the classical control theory, involving two extra filters. It provides a simple design process of the controller for a wide range of LCL filter values and it ensures stable operation without

```
% MODELING OF THE PLANT
% LCL filter in continuous time
s = tf('s'); Zc = 1/(s*C)+Rc;
Z1 = s*L1+R1; Z2 = s*L2+R2;
G_s = Zc/((Z1+Zc)*Z2+Z1*Zc);
% LCL filter in discrete time
G_d = c2d(G_s,Ts,'zoh');
% LCL filter plus 1 sample compu. delay
G_dd = tf([1],[1 0],Ts)*G_d;
% Resonant controller in discrete time
Crc = tf([1],[1 -2*cos(wg*Ts) 1],Ts);
% LCL filter, 1 sample delay and res. model
G_add = Crc*G_dd;

% CONTROLLER DESIGN USING POLE PLACEMENT
fdom = 200; damp = 0.7;
wres = sqrt((L1+L2)/(L1*L2*C));
% Controller C(z):
p1 = exp(-2*pi*fdom*Ts);
p2 = exp((-damp*wres+1i*wres*sqrt(1-damp^2))*Ts);
p3 = exp(-2*pi*2*fdom*Ts);
poles = [0 ; 0 ; p1 ; p2 ; p2 ; ...
        conj(p2) ; conj(p2) ; p3 ; p3];
Acl = poly(poles);
C = poleplacement(G_add,Acl);
% Feedforward gain, Kf
lcl_gain = evalfr((Zl1+Zc)/Zc,exp(1i*wg*Ts));
delay = exp(1i*1.5*wg*Ts);
Kf = lcl_gain*delay;
% Prefilter: H(z)
zeros_sys = roots(C.num{1});
slow_ceros = [zeros_sys(3) ; zeros_sys(4)];
F = tf([1 0],poly(slow_ceros),Ts);
% Reference gain, Kpn
Kp = 1/evalfr(F,exp(1i*wg*Ts));
Kn = 1/evalfr(F,exp(-1i*wg*Ts));
```

Figure 31. Example script that summarizes the computations that are necessary to design the proposed controller.

additional damping methods. The available bandwidth is examined in order to define the frequency of the dominant pole in the system. As a result, a fast reference-tracking capability with negligible overshoot and low controller effort are attained in combination with a fast disturbance rejection. The sensitivity to variations in the grid inductance is low due to the proposed pole-placement strategy. The proposed controller also has the well-known characteristics of the conventional resonant controllers (RCs), e.g., zero steady-state error at both fundamental sequences, and a simple implementation with a low computational load compared to state-space controllers from modern control theory. The design was validated with both simulations and experiments.

3. Positive- and Negative-Sequence Current Controller with Direct Discrete-Time Pole Placement for Grid-Tied Converters with LCL Filter

Traditionally, the current control of grid-tied converters with LCL filter is based on proportional-resonant or proportional-integral controllers, which often need an additional active damping method to achieve stability. These solutions do not permit to place the closed-loop poles in convenient locations when dealing with such high-order plants. This constraint results in degraded reference-tracking and disturbance-rejection responses. On the other hand, the existing methods based on direct pole placement or other modern control strategies, do not control with zero steady-state error both positive and negative sequences of the grid current, but only the positive one. This limitation is undesirable under unbalanced grid conditions. This section presents a current controller for grid-tied converters with LCL filters based on direct discrete-time pole placement. The proposed controller makes it possible to control both positive and negative sequences of the grid-side current with zero steady-state error. Contrarily to the classical resonant controllers, the closed-loop poles can be placed in convenient locations, yielding a fast response with negligible overshoot and low controller effort. Moreover, no additional damping methods of the resonance are necessary to achieve stable operation, regardless of the switching frequency and LCL filter used. Simulation and experimental results that validate the contents of this section are presented.

Grid-connected converters are becoming more popular nowadays due to the increasing role of renewable energy sources and distributed power generation systems [65]. The voltage source converters (VSCs) is one of the most common converter topologies used in this type of applications. In order to connect the two low-impedance voltage sources (the grid and the voltage source converters (VSCs)), this solution needs a filter to attenuate the high-frequency currents generated by the voltage source converters (VSCs). Although different filter topologies can be considered, the LCL filter is the preferred option as a consequence of its reduced size and good performance [69] (it attenuates the grid-side current with a slope of $60dB$ per decade above the resonant frequency). Nevertheless, the LCL filter presents a challenging problem to the designer of the current controller, because of its relatively high order and the small damping of its resonant poles [70].

A crucial part in a grid-tied converter is the current controller. Several current control strategies can be adopted. On the one hand, there are classical techniques such as proportional-integral control in one frame [83], in a double synchronous frame [87] and proportional-resonant [39] controllers. Some of the classical methods, such as [87, 83], are able to control both the positive and negative sequences. Nonetheless, they offer limited performance, because they do not permit to arbitrarily place the poles of the closed-loop system when dealing with a high-order plant such as that corresponding to the LCL filter

plus the computational and modulation delay (one and a half samples, respectively [15]). This results in degraded reference-tracking and disturbance-rejection responses or even instability. Parker *et al.* [47] have analyzed the stability problem that arises when poles fall outside the unit circle, and determined that there is a threshold in the resonant frequency of the LCL filter: $f_s/6$. This critical frequency value determines the region where an additional damping strategy is necessary to make the system stable when controlling the grid-side current. The damping of the LCL filter can be implemented passively or actively. Although passive damping is the most commonly used method [29], it causes extra losses and reduces the efficiency of the system [78]. Active damping strategies overcome this problem. They usually rely on feeding back a signal obtained by filtering the capacitor current [74, 76, 79, 49], the capacitor voltage [37, 72, 88, 75], or the grid-side current [50, 80, 51]. Therefore, additional sensors or estimation mechanisms (e.g., deriving the capacitor voltage to obtain the capacitor current [37]) are needed. Furthermore, estimation mechanisms such as the derivative filtering usually present sensitivity problems to noise [37]. In addition, although active damping techniques move the closed-loop poles to stable regions [74, 76, 79, 49, 72, 88, 75, 50, 80, 51, 37], they still do not offer the freedom of placing the poles in a good location in terms of transient response, controller effort, and robustness to disturbances and parameter variations.

On the other hand, modern control theory offers different methods such as linear quadratic (LQ) control [89], optimal control [90], model predictive control [91, 92], including dead-beat control [93, 94], adaptive control [95], and direct pole placement (i.e., state-feedback, which utilizes a compensator and an observer) [96, 97, 98, 99, 100, 101, 102]. These techniques already account for the damping of the open-loop poles of the plant, making it unnecessary to add more degrees of freedom or extra feedback branches to the controller to achieve a stable response.

Nevertheless, the solutions based on linear quadratic (LQ) or optimal control require a laborious selection of parameters that depend on the particular LCL filter and switching frequency used. Furthermore, in [89, 90], there is not a direct relation between the design process and the performance obtained in the real system, in terms of controller effort and transient response. The ones based on pole placement are able to avoid these inconvenients. However, the previously proposed methods based on state-space control (including both the direct-pole-placement and linear quadratic (LQ) ones) [89, 97, 98, 99, 100, 101] do not model the plant losses of the VSC, the filter, and the grid impedance. This simplification represents the least damped scenario for the resonance of the LCL filter [99]. However, if the state-feedback controller is designed with a plant model different from the real plant, the response of the real system worsens. Therefore, estimated losses should be taken into account in the design of the controller in order to avoid a detriment of the performance. In addition, the designs in [89, 97, 98, 99, 100, 101] only control with zero steady-state error the positive sequence of the current, which makes the controller unsuitable for unbalanced grid conditions. In [96], a state-feedback controller is combined with an internal model controller to overcome this problem. Nevertheless, a detailed analysis for each particular LCL filter is needed, in order to evaluate the interactions that appear between both controllers. In [102, 94, 96, 93, 76] robust controllers to grid impedance uncertainties are proposed; however, they are not tested under voltage sag faults. In case of sudden voltage dips, the dynamics of common grid-side current controllers, such as [102, 94, 96, 93, 76], are nor-
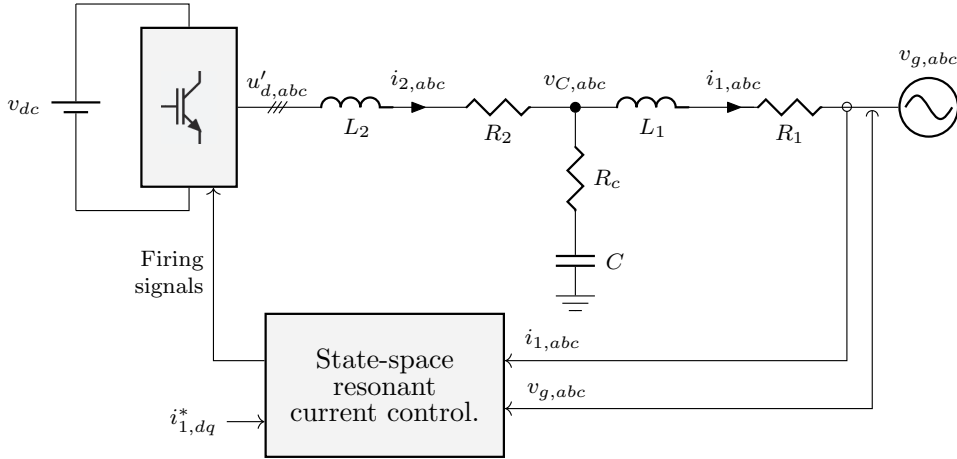
Figure 32. Grid-tied voltage source converters (VSCs) with LCL filter and grid-side current controller.

mally too slow to prevent large current transients. Finally, the model predictive controllers in [91, 92] offer a fast transient response; however the switching frequency of the converter is variable because the switching states are directly selected by the control. This generates interharmonics in the grid-side current, which are hard to filter [91].

This section presents a grid-side current controller for grid-tied converters with LCL filter that is able to control both positive and negative sequences of the fundamental grid frequency. The presented current controller uses the direct pole-placement strategy from the state-space theory. Contrarily to the classical controllers, the closed-loop poles are placed in convenient locations regardless of the LCL-filter resonant frequency and sampling frequency, and without adding an extra active damping method. Placing the poles in the specified locations results in a predictable and fast transient response, with low controller effort and no overshoot, and a good robustness to disturbances. Thus, a direct relation exists between the design process and the performance of the real system. Moreover, the reference-tracking and the disturbance-rejection capabilities, as well as the controller effort, do not depend on the LCL-filter resonance and sampling frequency used, when the design is performed according to the real values.

In addition, the controller structure used in this section (state-command structure) provides a better response to reference tracking than the structure typically used with transfer function design (output-error-command structure), where the controller is placed in the direct path between the reference and the plant input. Furthermore, the controller also takes estimated plant losses into account, in order to avoid the detriment of the robustness and performance. The robustness of the control to parameter variations, including those of the grid impedance, is also evaluated, obtaining a low sensitivity.

After this introduction, Section 3.1 presents the models of the plant and the grid voltage disturbance. Next, in Section 3.2, the compensator and the observer are designed, and the performance of the proposed current controller concerning its time response is analyzed. Then, in Section 3.3, its robustness is assessed by evaluating the sensitivity to model pa-

rameter variations and the disturbance-rejection capability. In Section 3.4, simulation and experimental results that validate the theory are presented. Summary in Section 3.7 close the work.

3.1.   Modeling of the Plant and the Disturbance

This section presents the models of the system dynamics (plant and disturbances) for the grid-side current controller shown in Figure 32, where L_1, L_2, and C represent the reactive elements of the LCL filter; R_1, R_2, and R_c model the ESRs of the filter and the voltage source converters (VSCs) [15]; $u_{d,abc}$ is the voltage source converters (VSCs) output voltage; $i_{1,abc}$, $i_{2,abc}$, and v_{abc} are the LCL-filter state variables (the converter-side current, the grid-side current, and the capacitor voltage, respectively); $v_{g,abc}$ is the grid voltage; and $i^*_{1,dq}$ denotes the grid-side current reference in the dq frame. Since the grid-side current is controlled, the impedance that the voltage source converters (VSCs) presents at the PCC can be arbitrarily specified. This permits working at unity power factor (generating a current reference with $i^*_q = 0$). In this manner, no reactive power exchange between the grid and the voltage source converters (VSCs) is drawn during operation. The modeling process takes place in several steps throughout the section; each step adds features to the model obtained in the previous stage.

3.1.1.   The Model of the Plant for the Compensator

In the first place, a continuous model, including losses, of the LCL filter in stationary frame is presented. This model relates the grid-side current $i_1(t)$ to the voltage source converters (VSCs) output voltage $u'_d(t)$ for the LCL filter of the plant shown in Figure 33a (the absence of reference frame in a subscript of a variable means $\alpha\beta$ frame). The first-order differential equations in the continuous domain (written in state-space form) are

$$\frac{d\,\mathbf{x}^{LCL}(t)}{dt} = \underbrace{\begin{bmatrix} \frac{-R_1}{L_1} & 0 & \frac{1}{L_1} \\ 0 & \frac{-R_2}{L_2} & \frac{-1}{L_2} \\ \frac{CR_cR_1-L_1}{CL_1} & \frac{L_2-CR_cR_2}{CL_2} & \frac{-(R_cL_1+R_cL_2)}{L_1L_2} \end{bmatrix}}_{\mathbf{A}^{LCL}} \mathbf{x}^{LCL}(t)$$

$$+ \underbrace{\begin{bmatrix} 0 & \frac{1}{L_2} & \frac{R_c}{L_2} \end{bmatrix}^{\mathrm{T}}}_{\mathbf{B}^{LCL}} u'_d(t)$$

$$i_1(t) = \underbrace{\begin{bmatrix} 1 & 0 & 0 \end{bmatrix}}_{\mathbf{C}^{LCL}} \mathbf{x}^{LCL}(t)$$

$$\mathbf{x}^{LCL}(t) = \begin{bmatrix} i_1 & i_2 & v \end{bmatrix}^{\mathrm{T}}. \tag{38}$$

Boldface denotes a vector or a matrix. Equation (38) does not include the effect of the grid voltage v_g applied at the PCC in the state variables. This voltage disturbance is handled in a special way, using a disturbance estimation method [81], as explained later.
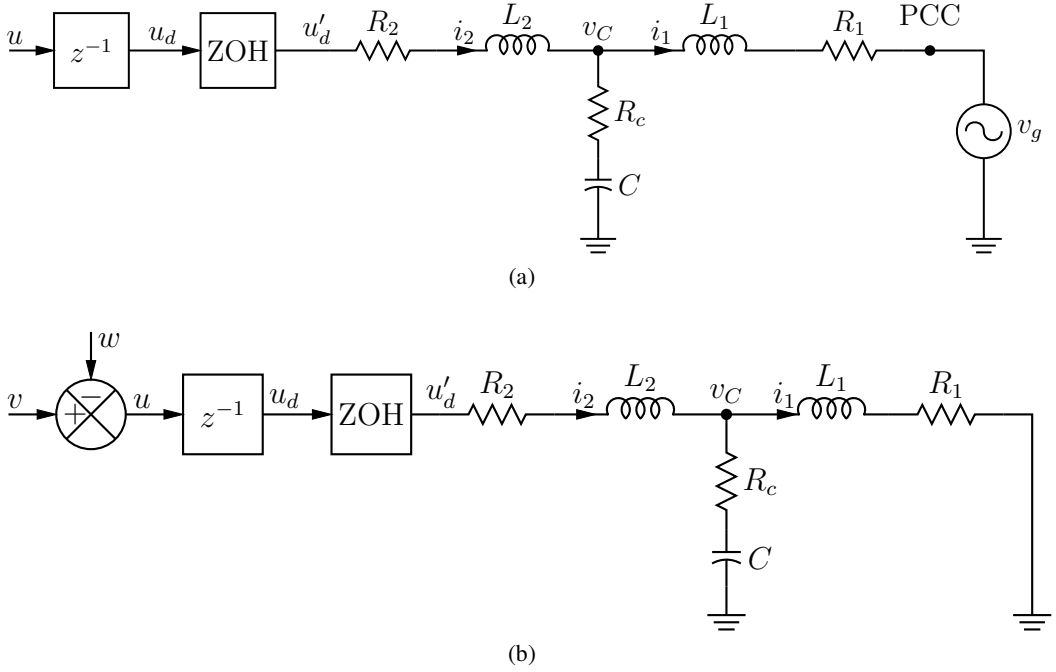
(a)

(b)

Figure 33. Stationary-frame plant diagrams: LCL filter, PWM (modeled as a ZOH), and one-sample computational delay. a Real plant model: the grid voltage v_g is applied at the PCC. b Equivalent plant model: the grid voltage v_g is eliminated and an input equivalent disturbance w is defined.

Next, (38) is discretized by using a ZOH equivalent [81]:

$$
\begin{aligned}
\mathbf{A}_d^{LCL} &= e^{\mathbf{A}^{LCL} T_s} \\
\mathbf{B}_d^{LCL} &= \mathbf{A}^{LCL-1}(e^{\mathbf{A}^{LCL} T_s} - \mathbf{I_4})\mathbf{B}^{LCL} \\
\mathbf{C}_d^{LCL} &= \mathbf{C}^{LCL},
\end{aligned}
\tag{39}
$$

where $\mathbf{I_4}$ is the 4×4 identity matrix. The sampling period T_s is equal to a switching period if a single-update strategy is used, and half the switching period in the case of a double-update strategy [59]. The PWM with triangular carrier, when approximated as a ZOH, takes into account the half a sample delay added by the voltage source converters (VSCs) PWM [15] (more accurate converter discretization methods for different carrier signals can be found in [103, 104, 105]). The resulting model relates the modulator voltage reference $u_d(k)$ with the sampled grid-side current $i_1(k)$:

$$
\begin{aligned}
\mathbf{x}_d^{LCL}(k+1) &= \mathbf{A}_d^{LCL} \mathbf{x}_d^{LCL}(k) + \mathbf{B}_d^{LCL} u_d(k) \\
i_1(k) &= \mathbf{C}_d^{LCL} \mathbf{x}_d^{LCL}(k).
\end{aligned}
\tag{40}
$$

Then, a one-sample input (computational) delay is added. The model of this delay on the modulator voltage $u(k)$ is [81]

$$
u_d(k+1) = u(k).
\tag{41}
$$

In this manner, combining (40) and (41), the system model that takes the computational delay into account is

$$
\underbrace{\begin{bmatrix} \mathbf{x}_d^{LCL}(k+1) \\ u_d(k+1) \end{bmatrix}}_{\mathbf{x}_{dd}^{LCL}(k+1)} = \underbrace{\begin{bmatrix} A_d^{LCL} & B_d^{LCL} \\ \mathbf{0} & 0 \end{bmatrix}}_{\mathbf{A}_{dd}^{LCL}} \underbrace{\begin{bmatrix} \mathbf{x}_d^{LCL}(k) \\ u_d(k) \end{bmatrix}}_{\mathbf{x}_{dd}^{LCL}(k)} + \underbrace{\begin{bmatrix} \mathbf{0} \\ 1 \end{bmatrix}}_{\mathbf{B}_{dd}^{LCL}} u(k)
$$

$$
i_1 = \underbrace{\begin{bmatrix} C_d^{LCL} & 0 \end{bmatrix}}_{\mathbf{C}_{dd}^{LCL}} \underbrace{\begin{bmatrix} \mathbf{x}_d^{LCL}(k) \\ u_d(k) \end{bmatrix}}_{\mathbf{x}_{dd}^{LCL}(k)}
$$

$$
\mathbf{x}_{dd}^{LCL}(k) = \begin{bmatrix} i_1 & i_2 & v & u_d \end{bmatrix}^{\mathrm{T}}. \tag{42}
$$

The resultant model relates the grid-side current $i_1(k)$ to the modulator voltage $u(k)$ in the plant shown in Figure 33a. Equation (42) is the plant model to be controlled by the compensator.

3.1.2. The Model of the Plant and the Disturbance for the Observer

In order to eliminate the steady-state error due to the grid voltage v_g (no feedforward of v_g is implemented) and plant modeling mismatches, the proposed controller includes a resonant action in the observer. The resonant action is obtained by placing two conjugated open-loop poles in the observer at the fundamental grid-voltage frequency ω_g (i.e., at position $z = e^{\pm j\omega_g T_s}$) so as to control both positive and negative sequences. There are two different possibilities for implementing the disturbance model in the control (in this case, the resonant action) by means of state-space methods: state augmentation and disturbance estimation [81]. The latter is chosen here for the reasons explained in the next section, and determines the way in which the plant and the disturbance should be modeled for the observer.

In the following, the model of the plant and the disturbance for the observer is developed. First, the grid voltage v_g is eliminated from the PCC and an input equivalent disturbance w is defined [81], as shown in Figure 33b. Next, a model of the disturbance w should be specified. A sinusoidal disturbance $w(t)$ of frequency $\omega(g)$, which contains both sequences (two complex conjugate poles in its model), is a solution of

$$
\frac{\mathrm{d}^2\, w(t)}{\mathrm{d}t^2} = -\omega_g^2\, w(t) \tag{43}
$$

which, in matrix notation, corresponds to

$$
\frac{\mathrm{d}\mathbf{r}(t)}{\mathrm{d}t} = \underbrace{\begin{bmatrix} 0 & 1 \\ -\omega_g^2 & 0 \end{bmatrix}}_{\mathbf{A}^{dis}} \mathbf{r}(t)
$$

$$
w(t) = \underbrace{\begin{bmatrix} 1 & 0 \end{bmatrix}}_{\mathbf{C}^{dis}} \mathbf{r}(t) \tag{44}
$$

where

$$\mathbf{r}(t) = \begin{bmatrix} r_1 & r_2 \end{bmatrix}^{\mathrm{T}} = \begin{bmatrix} w & \mathrm{d}w/\mathrm{d}t \end{bmatrix}^{\mathrm{T}}. \tag{45}$$

Then, (44) is discretized by using a ZOH equivalent (again, to model the PWM effect):

$$\begin{aligned} \mathbf{A}_d^{dis} &= e^{\mathbf{A}^{dis}\,T_s} \\ \mathbf{C}_d^{dis} &= \mathbf{C}^{dis}, \end{aligned} \tag{46}$$

where $\mathbf{I_2}$ is the 2×2 identity matrix. The resultant discrete-time disturbance model is

$$\begin{aligned} \mathbf{r}(k+1) &= \mathbf{A}_d^{dis}\,\mathbf{r}(k) \\ w(k) &= \mathbf{C}_d^{dis}\,\mathbf{r}(k). \end{aligned} \tag{47}$$

In order to design an observer that estimates the input-equivalent disturbance w [see Figure 33b] at frequencies $\pm\omega(g)$, the previous plant model (42) is augmented with the disturbance model (47) in order to include the resonant action:

$$\underbrace{\begin{bmatrix} \mathbf{x}_{dd}^{LCL}(k+1) \\ \mathbf{r}(k+1) \end{bmatrix}}_{\mathbf{x}_{add}^{LCL}(K+1)} = \underbrace{\begin{bmatrix} \mathbf{A}_{dd}^{LCL} & \mathbf{B}_{dd}^{LCL}\,\mathbf{C}_d^{dis} \\ \mathbf{0} & \mathbf{A}_d^{dis} \end{bmatrix}}_{\mathbf{A}_{add}^{LCL}} \underbrace{\begin{bmatrix} \mathbf{x}_{dd}^{LCL}(k) \\ \mathbf{r}(k) \end{bmatrix}}_{\mathbf{x}_{add}^{LCL}(k)} + \underbrace{\begin{bmatrix} \mathbf{B}_{dd}^{LCL} \\ \mathbf{0} \end{bmatrix}}_{\mathbf{B}_{add}^{LCL}} u(k)$$

$$i_1(k) = \underbrace{\begin{bmatrix} \mathbf{C}_{dd}^{LCL} & \mathbf{0} \end{bmatrix}}_{\mathbf{C}_{add}^{LCL}} \underbrace{\begin{bmatrix} \mathbf{x}_{dd}^{LCL}(k) \\ \mathbf{r}(k) \end{bmatrix}}_{\mathbf{x}_{add}^{LCL}(k)}$$

$$\mathbf{x}_{add}^{LCL}(k) = \begin{bmatrix} i_1 & i_2 & v & u_d & r_1 & r_2 \end{bmatrix}^{\mathrm{T}}. \tag{48}$$

This is the model of the plant and disturbance that the observer uses to estimate the LCL state $\mathbf{x}_{dd}^{LCL}(k)$ and the input-equivalent grid-voltage disturbance w.

Notice that the sinusoidal disturbance w cannot be controlled; hence, it is not included in the model used by the compensator. Nevertheless, it does need to be known to be compensated; thus, it is included in the observer model [81].

3.2. Compensator and Observer Design Using Pole Placement

Figure 34 shows the proposed controller architecture. The caret on a variable name indicates that the variable is an estimate calculated by the observer, also named estimator [81]. The developed scheme only measures one state variable, the grid-side current[6] $i_{1,abc}$. This state variable is transformed to the $\alpha\beta$ frame, the one where the controller is implemented, resulting in i_1. The inputs of the observer are the reference voltage after passing through the saturator u_{sat} and the measured grid-side current i_1. The input of the controller is the grid-side current reference i_1^*. The equation that the reduced-order observer implements is

$$\begin{aligned} \hat{\mathbf{x}}_{\mathrm{add_b}}^{\mathrm{LCL}}(k) &= \left(\mathbf{A}_{\mathrm{add_{bb}}}^{\mathrm{LCL}} - \mathbf{K_o}\,\mathbf{A}_{\mathrm{add_{ab}}}^{\mathrm{LCL}} \right) \hat{\mathbf{x}}_{\mathrm{add_b}}^{\mathrm{LCL}}(k-1) + \\ &\quad + \mathbf{K_o} i_1(k) + \left(\mathbf{A}_{\mathrm{add_{ba}}}^{\mathrm{LCL}} - \mathbf{K_o}\,A_{\mathrm{add_{aa}}}^{\mathrm{LCL}} \right) i_1(k-1) + \\ &\quad + \left(\mathbf{B}_{\mathrm{add_b}}^{\mathrm{LCL}} - \mathbf{K_o}\,B_{\mathrm{add_a}}^{\mathrm{LCL}} \right) u(k-1). \end{aligned} \tag{49}$$

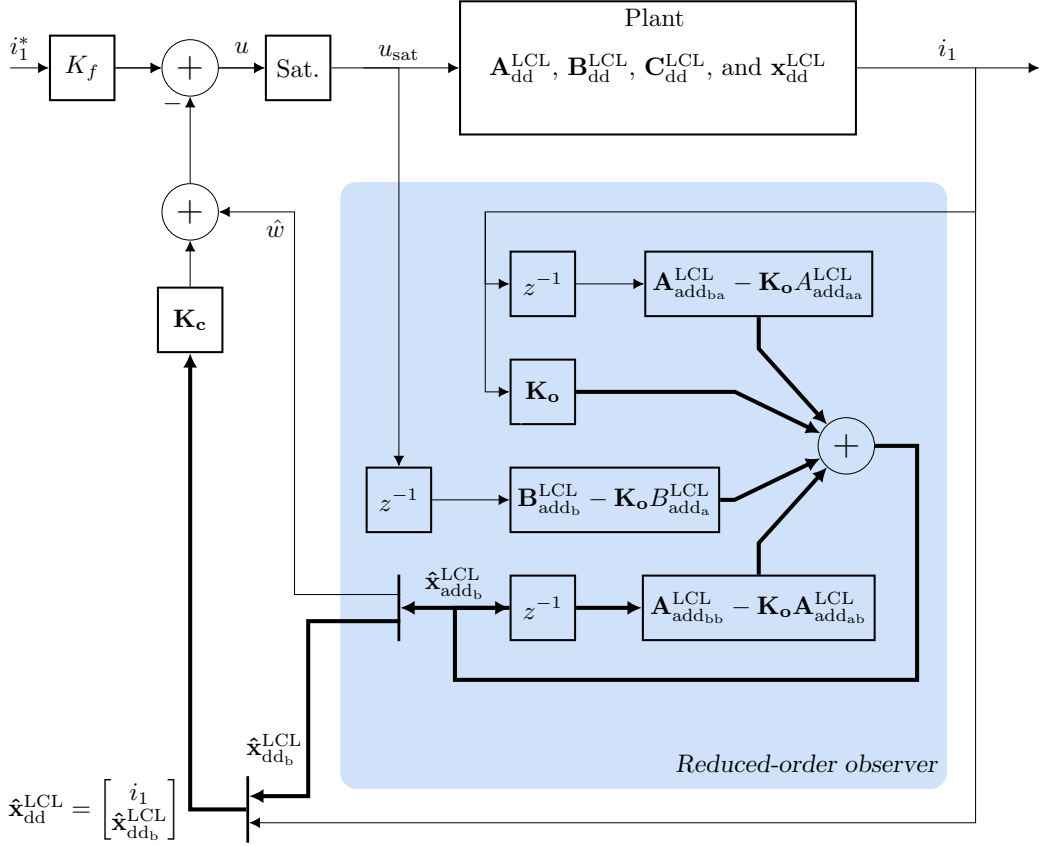[6]This can be accomplished with two current sensors, assuming no zero-sequence current is present.

Figure 34. Proposed controller architecture.

The constants $A_{\mathrm{add}_{aa}}^{\mathrm{LCL}}$, $\mathbf{A}_{\mathrm{add}_{bb}}^{\mathrm{LCL}}$, $\mathbf{A}_{\mathrm{add}_{ab}}^{\mathrm{LCL}}$, $\mathbf{A}_{\mathrm{add}_{ba}}^{\mathrm{LCL}}$, $B_{\mathrm{add}_a}^{\mathrm{LCL}}$, $\mathbf{B}_{\mathrm{add}_b}^{\mathrm{LCL}}$, $\mathbf{K_o}$ used in (49) are given in the Section 3.5 Using the estimated state $\hat{\mathbf{x}}_{\mathrm{add}_b}^{\mathrm{LCL}}(k)$ from (49), the modulator voltage in (34) is

$$u(k) \;\; = \;\; K_f i_1^* - \begin{bmatrix} \mathbf{K_c} & 1 & 0 \end{bmatrix} \begin{bmatrix} i_1 \\ \hat{\mathbf{x}}_{\mathrm{add}_b}^{\mathrm{LCL}} \end{bmatrix}. \tag{50}$$

It should be noticed that $\left(\hat{\mathbf{x}}_{\mathrm{add}_b}^{\mathrm{LCL}}\right)^{\mathrm{T}} = \left[\left(\hat{\mathbf{x}}_{\mathrm{dd}_b}^{\mathrm{LCL}}\right)^{\mathrm{T}} \;\; r_1 \;\; r_2 \right]$ includes the unmeasured states of the plant $\left(\hat{\mathbf{x}}_{\mathrm{dd}_b}^{\mathrm{LCL}}\right)^{\mathrm{T}} = [i_2 \;\; v \;\; u_d]$ and the disturbance estimation r_1 and r_2. In the implementation of the current controller from Figure 34, the observer (49) uses $u_{\mathrm{sat}}(k-1)$ instead of $u(k-1)$. This gives a particularly simple anti-windup mechanism for this controller structure [54].

In order to obtain a fast response, the following two design choices are adopted: a state-command structure for the reference-input structure, and a disturbance-estimation structure for the resonant control. These two selections are explained in the following:

1. The state-command structure [81] is chosen because it presents a better response to situations related to reference tracking than that typically obtained with transfer-function design (output error command structure). The latter places the controller in the direct path between the reference and the plant input. On the other hand, the state-command structure, provides a direct path to the plant (through the feedforward gain K_f and the saturator) for references to pass (see Figure 34) and avoids exciting the controller modes. Thus, a faster response is obtained. This advantage is particularly worthy of note when high-order controllers, such as the proposed one, are used.

2. Among the two possibilities to implement the resonant action, state augmentation and disturbance estimation, the latter is adopted here. The first, state augmentation, adds the resonant action in the direct path from reference to plant input resulting in a slower response to reference changes because of the excited extra modes. In the case of the integral control, it is possible to place an additional zero that cancels the extra closed-loop pole introduced by the integrator [99]. However, this cancellation is never perfect due to plant uncertainties. The second possibility, disturbance estimation, implements the resonant action as part of the observer. Therefore, only disturbance rejection is affected by the extra two poles introduced by the resonant action.

The response to broad-band signals like sags or reference current changes is determined by the bandwidth of the controller. High-bandwidth controllers allow fast signals (high frequencies) to pass in the case of references, or to be compensated in the case of disturbances. However, the speed at which the output can be controlled is limited to the available controller effort. The LCL filter attenuates signals above the resonant frequency w_{res} with a slope of $60dB$ per decade. Therefore, this low-pass behavior demands a huge effort from the controller when a high bandwidth is tried to be set. This fact results in the voltage source converters (VSCs) entering into overmodulation. All types of current controllers have to cope with this fundamental limitation. The pole-placement strategy is designed in this section according to a radial projection [81] of the resonant poles of the plant so as to provide a good response while keeping the control effort low.

The compensator gain $\mathbf{K_c}$ and observer gain $\mathbf{K_o}$ (cf. Figure 34), which determine the closed-loop poles of the system, are calculated according to the pole-placement strategy. Matlab has two functions, `acker` and `place`, that can be used to calculate these two gains. (a design script is given in Section 3.6). Using direct discrete-time pole placement makes the design process straightforward compared with other state-space techniques such as linear quadratic (LQ), where weighting matrices that are weakly connected to the performance specifications need to be specified [81]. In any case, it is necessary to define the position of the closed-loop poles. This is a crucial task that determines the performance of the control algorithm. In the following, the criteria developed to assign the closed-loop poles of the compensator and the observer are explained in detail. Note that the closed-loop poles of the complete system are the union of the compensator closed-loop poles and the observer closed-loop poles.

The plant model in (42) has four poles. The LCL filter has two complex conjugate poles $p_{1,2}^{ol}$ (the resonant poles) at the resonant frequency and a real pole p_3^{ol} at zero frequency. In

Table 5. Compensator Pole Placement

Poles	Position in the z-plane	
	Open-loop	**Closed-loop**
	Radial projection of LCL resonant poles, $\zeta = 0.7$.	
LCL filter	$p^{ol}_{1,2} = e^{\pm j\,\omega_{res}\,T_s}$	$p^{cl}_{1,2} =$ $e^{(-\zeta\,\omega_{res}\,\pm j\,\omega_{res}\,\sqrt{1-\zeta^2})\,T_s}$ $=$
	Moved to obtain higher bandwidth and to make it the dominant pole.	
	$p^{ol}_3 = 1$	$p^{cl}_3 = e^{-\omega_{dom}\,T_s}$
Comp. delay	Not moved; already in an optimum location.	
	$p^{ol}_4 = 0$	$p^{cl}_4 = 0$

addition, the computational delay adds a fourth pole p^{ol}_4 to the model, at the origin of the z-plane. These four poles are shown in Figure 35, which depicts the pole map of the system.

In order not to unnecessarily increase the controller effort, the closed-loop poles should be kept close to the open-loop poles whenever the response is not significantly degraded [81]. Table 5 summarizes the proposed locations for the closed-loop poles of the compensator. The proposed current controller only reallocates three poles of the LCL filter ($p^{ol}_{1,2,3}$). One of them is displaced to a higher frequency (see p^{cl}_3, in Figure 35); on the other hand, the other two are reallocated in a more damped region ($p^{cl}_{1,2}$) to obtain a fast and damped response by means of radial projection (a damping factor ζ of 0.7 is used). The delay pole p^{ol}_4 is already in an optimum location, so it is not moved. A frequency $f_{dom} = \omega_{dom}/2\pi = 150\,\text{Hz}$ is recommended for the dominant pole p^{cl}_3, because it ensures a negligible effect of the damped resonant poles $p^{cl}_{1,2}$ on the system response (resonant frequencies above twice the dominant frequency, $f_{res} > 300\,\text{Hz}$, are expected). In this manner, contrarily to other current controllers, the response is not affected by the LCL filter choice. It should be noticed that the parameter f_{dom} can be modified to a value different from the recommended $150\,\text{Hz}$.

3.2.1. Compensator Design

However, further increasing the frequency of the dominant pole would demand more control effort to the voltage source converters (VSCs), because the magnitude of the transfer function that relates the grid-side current with the voltage source converters (VSCs) output $G^{LCL}(s) = i_1/u'_d$ rolls off at $20dB$ per decade at frequencies below the resonant frequency [47].

Despite the fact that different LCL filters may have resonant poles in a wide frequency range (see $p^{ol}_{1,2}$ in Table 5), all LCL filters have a pole at zero frequency (see p^{ol}_3 in Table 5). Since this pole is moved and set to be the dominant pole of the system (see p^{cl}_3 in Table 5), the system bandwidth does not depend on the LCL filter used, but on this dominant closed-loop pole, and a consistent performance is obtained irrespectively of the filter installed.

3.2.2. Design of the Reduced-Order Observer

After the compensator closed-loop poles have been defined, the placement criteria of the observer closed-loop poles should be established. Table 6 summarizes the proposed location for the closed-loop poles of the observer. They are also shown in the pole map of the complete system in Figure 35. Now the pole assignment is not restricted to yield a low control effort, because the observer does not drive any actuator, but simply calculates the state of the system. Therefore, a larger bandwidth can be set, and it is advisable to place the observer closed-loop poles ($p^{cl}_{5,6,7,9}$) at frequencies higher (and damped) than that of the dominant pole of the compensator p^{cl}_3 so as to provide similar dynamics to those of the compensator alone [81]. The computational delay pole p^{cl}_8 is not moved because it is already in an optimum location.
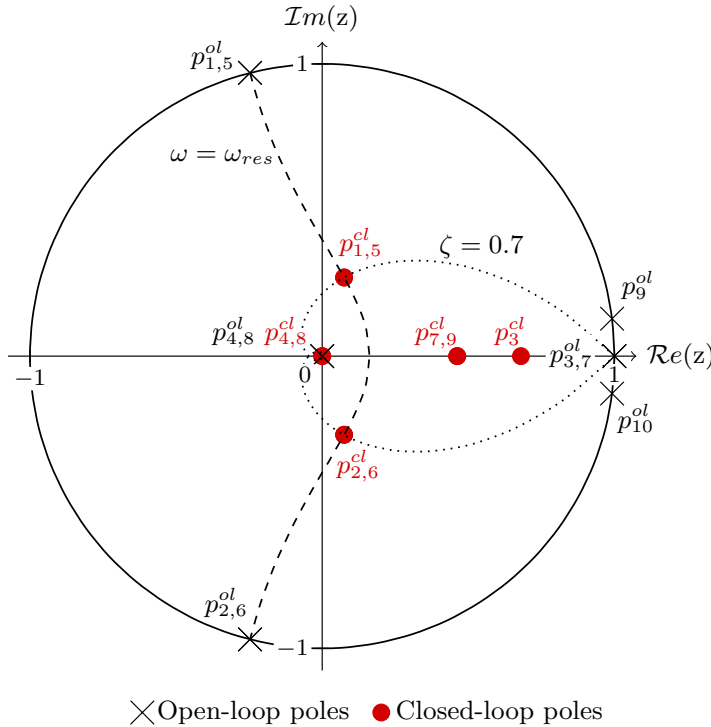
Figure 35. Open- and closed-loop pole map of the complete system.

Regarding the selection of the type of observer, there are three alternatives [81]: the predictor estimator, the current estimator and the reduced-order estimator. Here, the reduced-order estimator is recommended because of the following reasons. The predictor estimator uses the next-to-last current measurement $i_1(k-1)$, instead of the last measurement $i_1(k)$, which gives a more recent state of the plant. The current estimator cannot be implemented in plants where there are pure delays, as the z^{-1} term of the computational delay. The reduced-order estimator eliminates one pole[7] (p^{ol}_{10}), making the response faster. This reduc-

---

[7]The reduced-order estimator reduces its number of poles according to the number of state variables that are

Table 6. Observer Pole Placement

Poles	Position in the z-plane	
	Open-loop	**Closed-loop**
LCL filter	Radial projection of resonant poles to $\zeta = 0.7$.	
	$p_{5,6}^{ol} = e^{\pm j\,\omega_{res}\,T_s}$	$p_{5,6}^{cl} = e^{\left(-\zeta\,\omega_{res}\,\pm j\,\omega_{res}\sqrt{1-\zeta^2}\right)T_s}$
	Moved to twice the frequency of the dominant pole.	
	$p_7^{ol} = 1$	$p_7^{cl} = e^{-2\,\omega_{dom}\,T_s}$
Comp. delay	Not moved; already in an optimum location.	
	$p_8^{ol} = 0$	$p_8^{cl} = 0$
Resonant action	Moved to twice the frequency of the dominant pole.	
	$p_{9,10}^{ol} = e^{\pm j\,\omega(g)\,T_s}$	$p_9^{cl} = e^{-2\,\omega_{dom}\,T_s}$

tion in the order of the observer is of special convenience in order to obtain a fast disturbance rejection.

3.3. Parameter Sensitivity

A system that keeps a good regulation in the face of variations in the plant parameters is said to have low sensitivity to those parameters. In the case of a grid-tied inverter, there are several variables whose variation from the nominal value should be considered. Namely, the grid impedance Z_g (which has an inductive part L_g and a resistive part R_g), the real (or actual) LCL filter parameters (L_1^r, L_2^r and C^r) [99], and the real ESR of the voltage source converters (VSCs) [15] and of the LCL filter (R_1^r, R_2^r, and R_c^r).

3.3.1. Stability Regions

Since there are several degrees of freedom in the plant variation, a set of representative worst-case scenario parameter values should be selected. This idea was also used in [99], where different stability regions were calculated for various real LCL filter parameters values that differ by a certain amount from the nominal value. In addition, an inductive grid, as in [99], is considered. The stability of the closed-loop system is analyzed by calculating the damping factor of the most unstable closed-loop pole (i.e., the smallest one) for each of the combinations of parameters considered. Now the plant is modified from the ideal values (L_1, L_2 and C) of Figure 33a, used to design the controller, to the real (or actual) values (L_1^r, $L_2^r + L_g$ and C^r), as shown in Figure 36. The following three different cases are studied: 1) the filter inductances are the nominal ones: $L_1^r = L_1$ and $L_2^r = L_2$; 2) the filter inductances are 10% larger than the nominal values: $L_1^r = 1.1L_1$ and $L_2^r = 1.1L_2$; 3) the filter inductances are 10% smaller than the nominal ones: $L_1^r = 0.9L_1$ and $L_2^r = 0.9L_2$. In all the cases, the real filter capacitance C^r is varied from $0.2C$ to $2C$ and the grid induc-

---

directly measured [81]. The proposed implementation only measures one state variable: the grid-side current i_1.
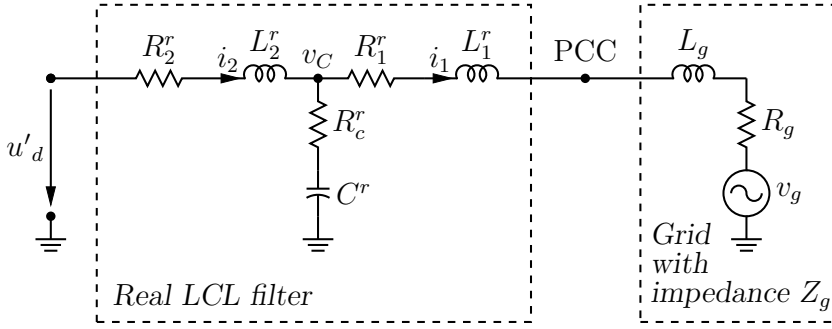
Figure 36. Space-vector circuit model in $\alpha\beta$ coordinates of the real LCL filter, with values different from the nominal LCL filter of Figure 33a, connected to a grid with impedance $Z_g = R_g + j\omega L_g$.
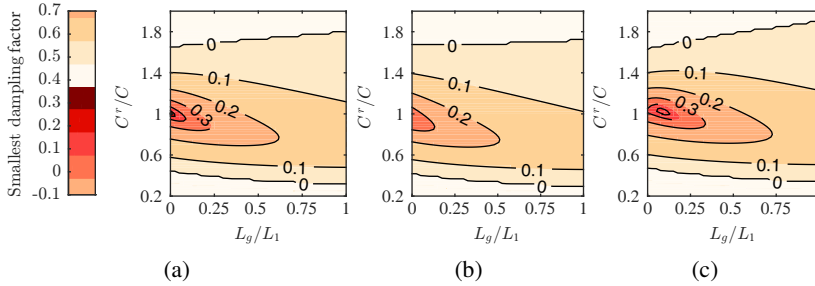

Figure 37. Stability regions for variations in grid inductance L_g and the real LCL filter capacitance C^r. a LCL filter inductances with nominal values. b LCL filter inductances with values 10% bigger than nominal. c LCL filter inductances with values 10% smaller than nominal.

tance L_g, from zero to L_1. Figure 37 shows the resulting stability regions. It can be seen that the bigger the changes in the inductance or capacitance are, the smaller the damping factor of the least damped pole is. When the damping factor reaches zero, the system becomes unstable. For a 10% tolerance in the filter components, the analysis predicts a stable operation ($\zeta > 0$) in a wide range of situations. The system is specially robust to variations in the grid inductance L_g. Comparable results were obtained for the controller proposed in [99].

Selecting $L_1 = L_2$ a minimum cost of the total inductor $L_1 + L_2$ is obtained [69] (as done, e.g., in [69, 70, 79, 97, 101, 105]. Unmatched filter inductances could be considered [83] (e.g., $L_2 > L_1$ to reduce the rating of the switches for a required f_{res}) but a higher total inductor value would be obtained. From the control point of view, these changes do not have significant impact on the performance of the system because the position of the open-loop poles of the plant depends on the resultant resonant frequency, independently of the particular LCL filter values (L_1, C, and L_2) which give this resonant frequency.

3.3.2. Root Locus for L_g and ESRs Sweeps and Pole Map for a Weak Grid

Any variation from the plant parameters used to design the controller will result in the closed-loop poles moving away from the desired location. The following analysis calculates the root locus of the closed-loop poles when certain parameters (L_g and the ESRs) are modified so as to evaluate the effect, as a whole, on all the closed-loop poles of the controller. Figure 38 shows the root locus of the transfer function from the current reference i_1^* to the grid-side current i_1 in two cases: when the grid inductance is increased, and when the ESRs are not negligible but they are ignored in the controller design. It also shows the pole map of the system when the voltage source converters (VSCs) is connected to a weak grid and the grid impedance is not included in the model used for the control design (the ESRs, for $r = 1$, are taken into account).

The parameters of filter II from Table 7 are used for the analysis.

Figure 38a shows a sweep in the grid inductance L_g from zero to a value equal to the LCL filter grid-side inductance L_1. There are four poles that exhibit a greater sensitivity. As shown in the root locus, the sensitivity is not constant with parameter variation. Small initial variations cause big displacement in these four poles, whereas large additional parameter changes do not significantly worsen the response. However, the least damped poles are still the two complex conjugate poles associated with the resonance of the LCL filter; hence, they are still the ones that determine the stability.

Figure 38b shows the effect of adding the ESRs of the filter components and the voltage source converters (VSCs) ($R_1^r = rR_1$; $R_2^r = rR_2$; $R_c^r = rR_c$ with $r \in [0, 1]$) for a controller designed without taking them into account, i.e., assuming $r = 0$, as in [99], and connected to an ideal grid ($Z_g = 0$). As it happens, any deviation from the nominal model moves the closed-loop poles from their desired location, degrading the control performance. Therefore, if estimated ESR values are available to the designer, it is recommended to take them into account. In any case, the variations in the ESRs only have a small effect on the transient response; thus, the proposed controller can be considered to be robust to them. Figure 38b also shows the closed-loop poles when the voltage source converters (VSCs) is connected to a weak grid. Now the grid impedance is the parameter that is not accounted for in the model, instead of the ESRs of the filter and the converter. The considered grid impedance $Z_g = 0.11$ p.u. has a resistive part of 1.2ω, $R_g = 0.11$ p.u., and a reactive part of 330μH, $L_g = 0.01$ p.u. (weak grids typically have a mainly resistive character [106]). This weak grid causes the closed-loop poles to move from the desired locations (worsening to a certain extent the response) when its impedance is not included in the plant model used to design the controller. Nevertheless, its effect (the pole movement) is small due to the robustness of the proposed controller.

3.4. Experimental Results

The proposed current controller is tested in a 20-kW voltage source converters (VSCs) working as an inverter and connected to a 400-V line-to-line 50-Hz three-phase grid. A three-phase ac voltage source was used to generate voltage sags as shown in Figure 39. The switching and sampling frequency is $f_s = 2.5$ kHz, with 3-μs dead-time. A low switching frequency reduces switching losses in the voltage source converters (VSCs) and it represents a worst-case scenario in terms of the effect of the computation and modulation delays.
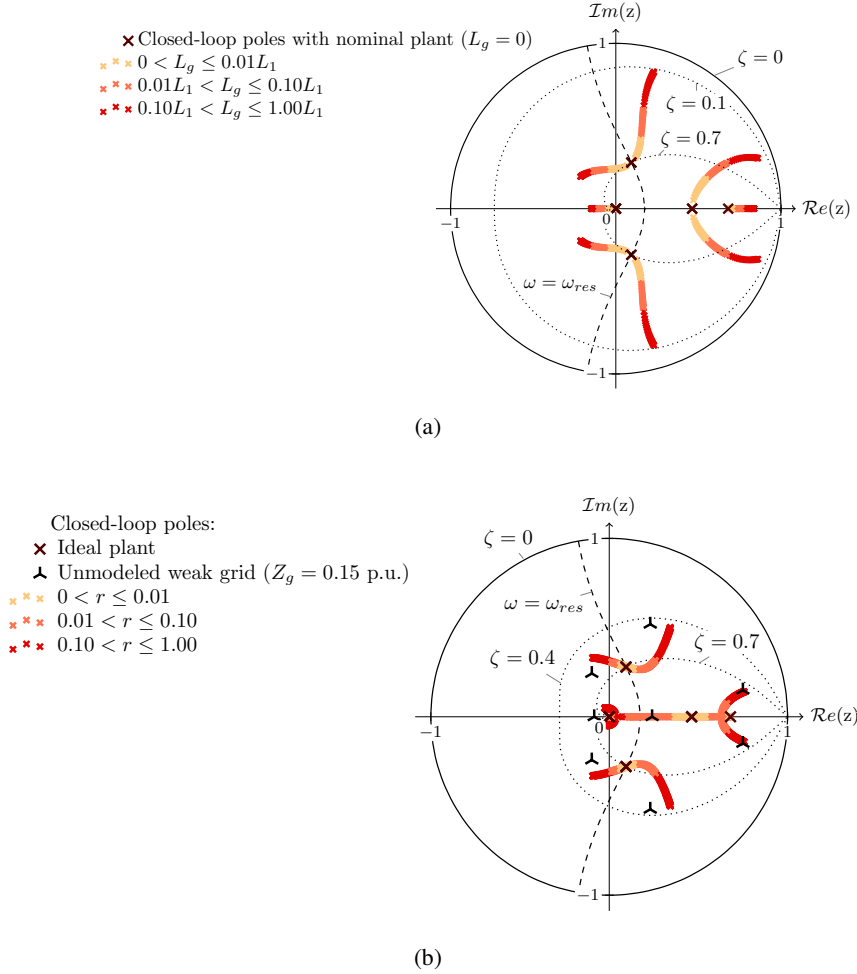
(a)

(b)

Figure 38. Root locus of the complete system under different parameter variations. a The grid inductance L_g is increased from zero to a value equal to the LCL-filter grid-side inductance L_1. b Effect of adding the ESR of the filter components and the voltage source converters (VSCs) for a controller designed with ideal plant parameters and operated with a plant with parameters $R_1^r = rR_1$, $R_2^r = rR_2$, and $R_c^r = rR_c$; and closed-loop poles when the voltage source converters (VSCs) is connected to a weak grid of impedance $Z_g = 0.11$ p.u. (the ESRs, for $r = 1$, are included in the model used to design the controller and the grid impedance Z_g is not included).

Moreover, since the single-update strategy represents the worst-case control scenario, this one was chosen for the implementation. A double-update strategy executes the control algorithm at twice the speed of a single-update strategy [59]. Therefore, the computational delay is reduced. The dc-bus voltage is $v_{dc} = 750$V. The two filters with different resonant frequencies f_{res} presented in Table 7 are used to connect the voltage source converters (VSCs) to the grid. The design of filter I was carried out according to [83], obtaining a 1.4% of grid-side current ripple. Filter II was designed to validate the proposed current
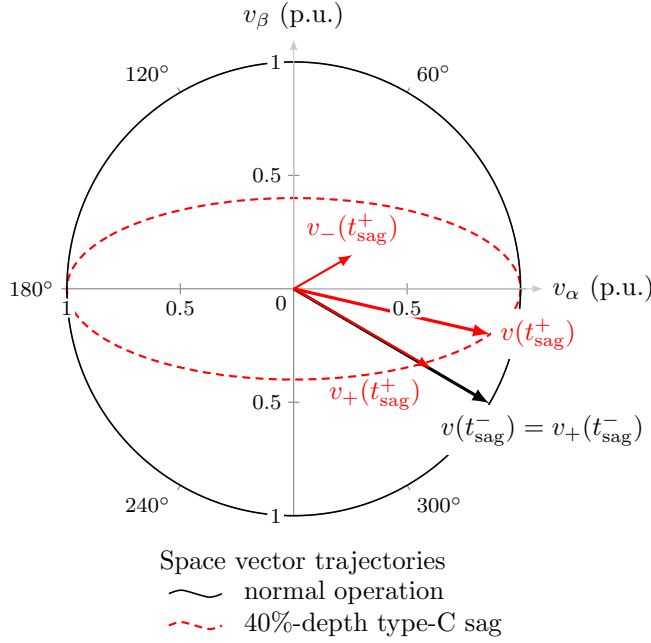
Figure 39. Space vector at the instant t_{sag} when the type-C sag happens (including its decomposition into symmetrical components), and its steady-state trajectory (during normal operation and in the fault condition).

controller in a wide range of resonant frequencies of the LCL filter. Therefore, two different resonant frequencies for the LCL filter ($f_{\mathrm{res},1} = 791\,\mathrm{Hz}$ and $f_{\mathrm{res},2} = 367\,\mathrm{Hz}$) are chosen (above and below $f_s/6 = 417\,\mathrm{Hz}$) in order to assess the stability and performance of the proposed controller in both stability regions established in [47]. If a higher sample rate were used, a resonant frequency below $f_s/6$ could also be obtained without increasing the value of the reactive elements. This would reduce the problems associated with high reactive values, such as higher losses, high voltage drop on the filter, and considerable reactive power drawing from the voltage source converters (VSCs). Unless otherwise stated, the LCL filter installed in each case corresponds to the filter parameters adopted for the design of the controller. Figures 40a and 40b show a diagram and a photograph of the experimental setup, respectively.

The following characteristics are tested with the controller being designed for each of the LCL filters: reference tracking of both sequences [Figures 41a–44a for LCL filter I, and Figures 41b–44b for LCL filter II], disturbance rejection of both sequences [Figures 45a–48a for LCL filter I, and Figures 45b–48b for LCL filter II], disturbance rejection to voltage harmonics (Figure 49), and parameter sensitivity (Figure 50 and Figure 51). Each test shows the reference signal i_1^*, the simulated response i_1^{sim}, and the measured response i_1. The simulated response accurately matches the experimental response in all the tests. The nonlinear effects of the voltage source converters (VSCs) and the interaction between the current controller and the PLL causes the negligible differences that can be observed between i_1 and i_1^{sim}. Although no phase jump is caused in the positive sequence of the grid

(a)

(b)

Figure 40. Experimental setup. a Diagram. b Photograph.

voltage [85] and the PLL bandwidth is small, disturbances in the form of harmonics, noise, or transients present in the grid voltage can be introduced in the phase generated by the PLL [107].

Figure 41 and Figure 42 show a reference step in the q axis of the positive-sequence dq

Table 7. LCL Filter Parameters

Parameter	Filter I	Filter II*	Filter III*	Filter IV*
L_1	2.7 mH	7.5 mH	15 mH	6.75 mH
L_2	2.7 mH	7.5 mH	15 mH	6.75 mH
C	30 μF	50 μF	30 μF	15 μF
R_1	0.25 Ω	0.5 Ω	0.5 Ω	0.5 Ω
R_2	0.5 Ω	0.75 Ω	1 Ω	0.5 Ω
R_c	0.1 Ω	0.1 Ω	0.1 Ω	0.1 Ω
f_{res}	791 Hz	367 Hz	330 Hz	707 Hz

* Filter II, III, and IV are not intended to be a high-performance filter design like filter I, but to validate the proposed current controller in a wide range of resonant frequencies of the LCL filter (below and above $f_s/6$).

frame (dq+ frame). The currents are also expressed in a synchronous frame rotating at the same frequency, so as to obtain a representation of characteristic parameters of dc signals (rise time, settling time, overshoot, and steady-state error) and the absence of cross coupling. The 10%–90% rise time of the measured response i_1 in Figure 41 is approximately $2.5ms$. This value is slightly greater than the rise time of a first-order system of the same bandwidth, $T_{10\%-90\%} = \ln|9|/(2\pi f_{dom}) = 2.33ms$, due to the effect of the extra poles. Negligible overshoot is attained, as expected from the well-damped dominant closed-loop pole p_3^{cl} (see Figure 35) placed at the frequency f_{dom}. The low-order harmonics (mainly sixth-order harmonic in the dq-frame) correspond to the fifth and seventh harmonics caused by nonlinearities of the voltage source converters (VSCs). Figure 43 and Figure 44 shows an identical reference step, but now in the negative-sequence dq frame (dq- frame). The resulting response is of similar form to that obtained for the step in the other sequence (cf. Figure 41), as intended, because the resonant action treats both sequences equally.

Figures 45–51 display the robustness of the controller to both disturbances (e.g., sags and harmonics in the grid voltage) and parameter variations. Figure 45 and Figure 46 shows the capability of the current controller to reject disturbances in the form of voltage sags (the sag contains both voltage sequences). A 40%-depth type-C sag [85] is generated with the three-phase ac-voltage source, while keeping the references constant. The settling time to within 2% is $6ms$, which is slightly greater than the $T_{st} = -\ln|0.02|/(2\pi f_{dom}) = 4.15ms$ associated to a first-order system; again due to the effect of the extra poles. The grid voltage at the instant when the voltage sag occurs has some high frequency oscillations [cf. Figure 45a - 48a] when the filter with lower impedance (filter I) is used. This is due to the limitation of the three-phase voltage source (model Pacific 360-AMX) to generate the defined voltage sag accurately at the PCC when connected to such a low impedance load (the voltage source converters (VSCs) with filter I). This undesirable effect increases

the settling time of the system. In order to see the response of the controller to reference changes during a sag condition, Figures 47 and 48 show the reference-tracking capability under the same sag as in Figure 45. The reference step i_1^* is calculated according the so-called positive-negative-sequence compensation strategy [84]. In this case, both currents, the grid-side current i_1 and its reference i_1^*, are shown in stationary frame because they both have a positive and a negative sequence simultaneously. The response is also fast and well damped when these effects (reference tracking and disturbance rejection of both sequences) are combined, as expected from the lineal model the system. The response may vary slightly depending on the initial phase of the sag, without altering the validity of such conclusion.

As anticipated, the rise time, the overshoot, and the settling time: all do not depend on
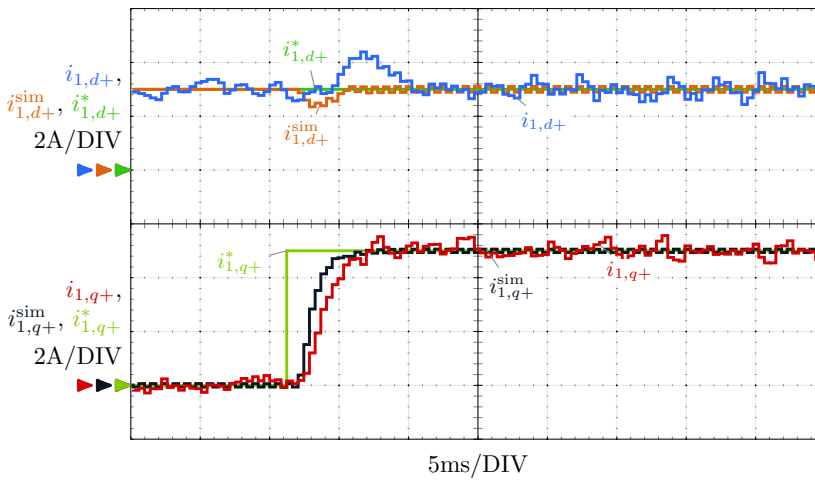
(a)
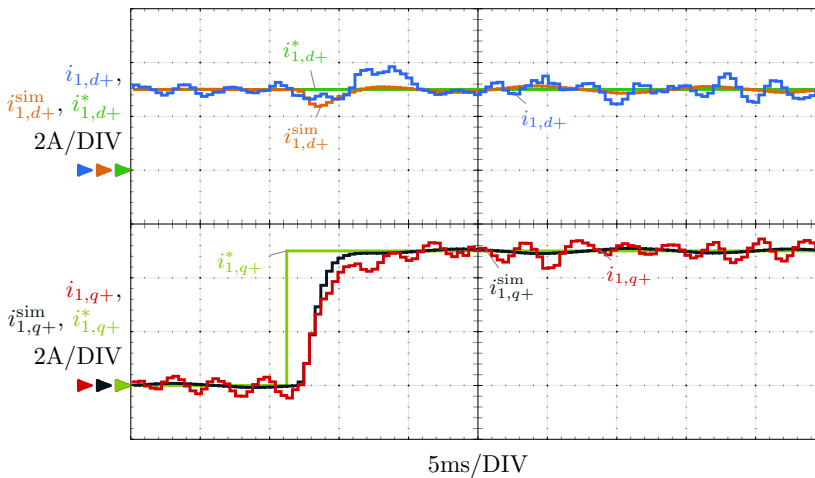
(b)

Figure 41. Continued on next page.
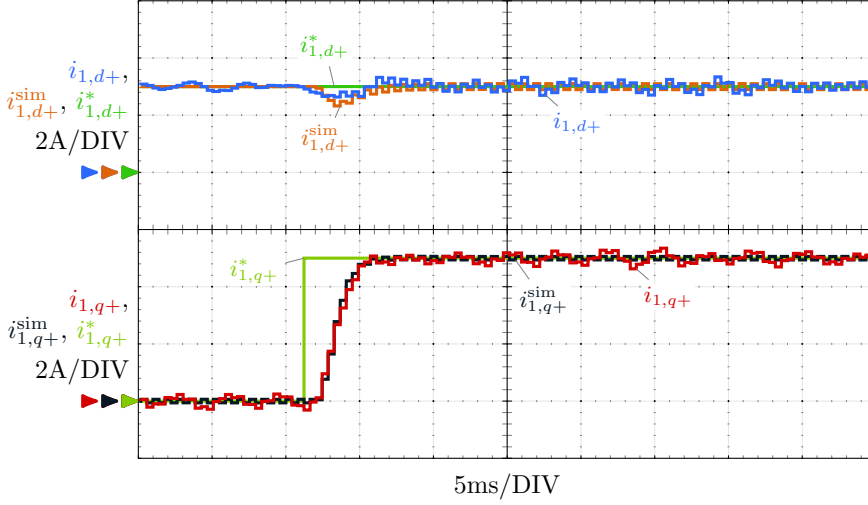
(c)
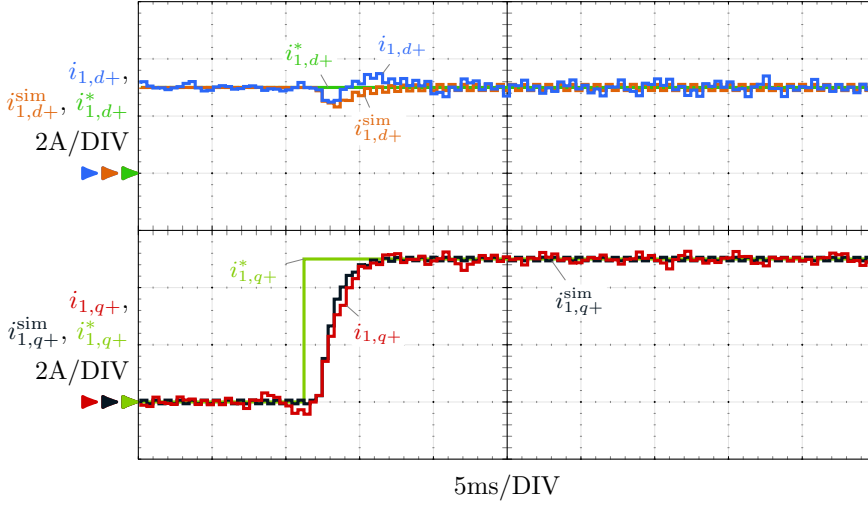
(d)

Figure 41. Experimental and simulation waveforms ($i_{1,dq}$ and $i_{1,dq}^{\text{sim}}$, respectively) for a reference step $i_{1,q+}^*$ in the positive synchronous frame dq+ rotating at the fundamental grid frequency ω_g. a LCL filter I, b LCL filter II, c LCL filter III, and d LCL filter IV.

the LCL filter resonant frequency. This can be seen by comparing the oscilloscope captures obtained with filter I ($f_{res} < f_s/6$), shown in Figures 41a–48a, with those made with filter II ($f_{res} > f_s/6$), shown in Figures 41b–48b. This behavior results from the pole-placement criteria used in the design of the controller.

Figure 49 shows the response to a reference step in the positive-sequence dq frame under the following conditions. The grid voltage has the following low-order voltage harmonics: $V_3 = 0.5\%$, $V_5 = 0.3\%$, $V_7 = 2.1\%$ and $V_9 = 0.7\%$, where the subscript denotes
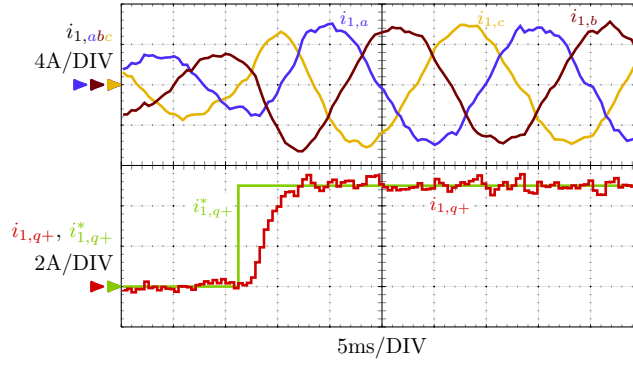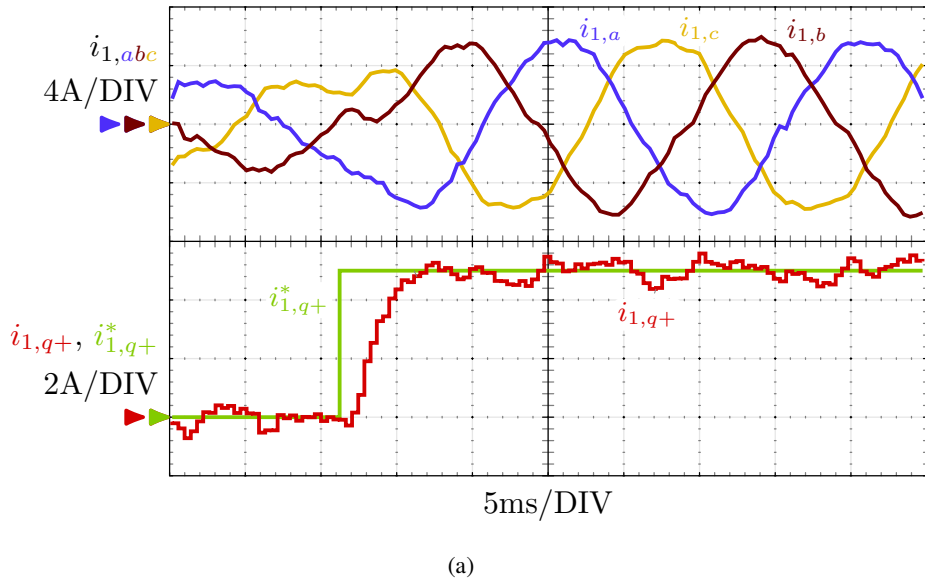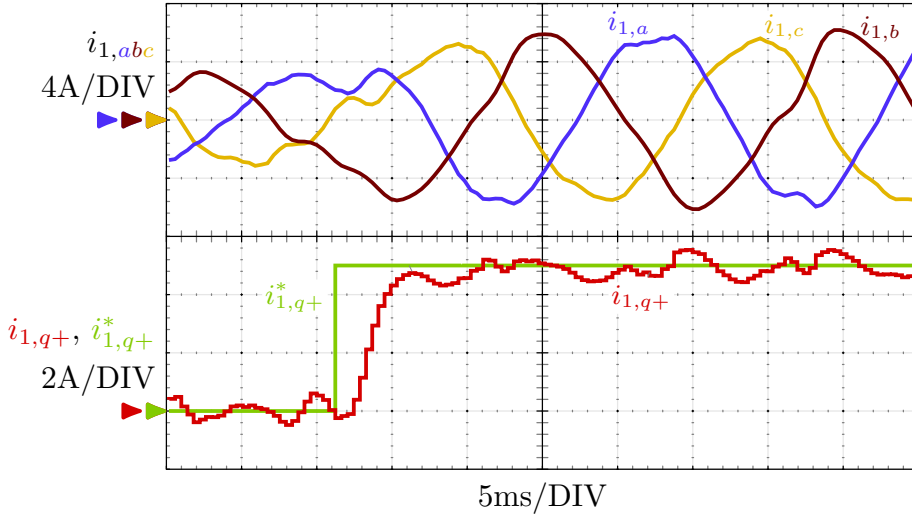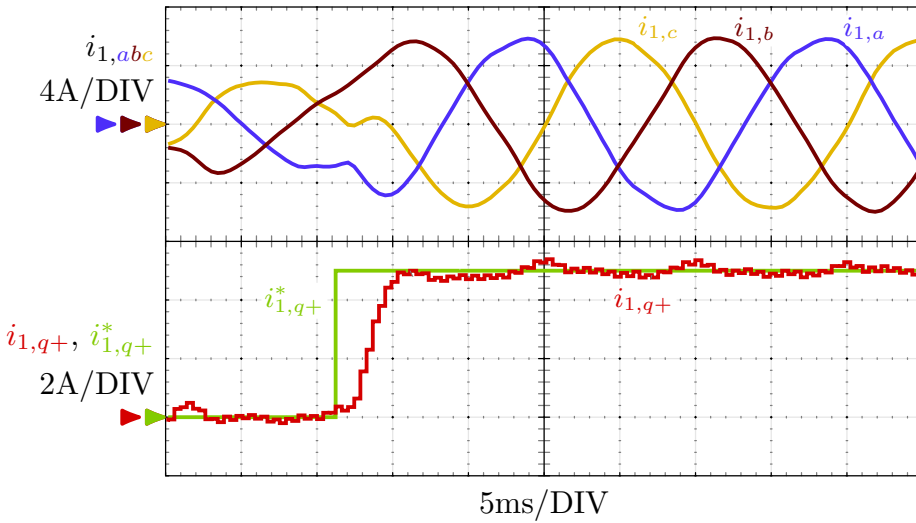
(a)
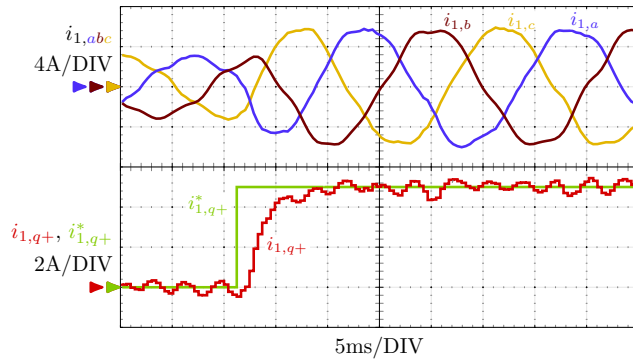
(b)
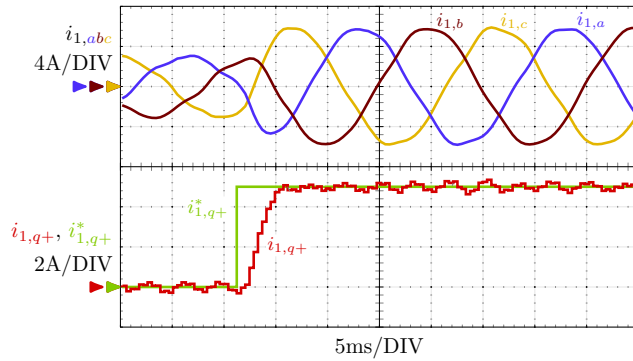
(c)

Figure 42. Experimental phase currents ($i_{1,abc}$) for a reference step $i_{1,q+}^*$ in the imaginary component ($i_{1,q+}$) of the positive synchronous frame dq+ rotating at the fundamental grid frequency ω_g. a LCL filter I and b LCL filter II. c LCL filter III.

the harmonic order. The PLL [107] includes a moving average filter, which eliminates their effect on the phase estimation. The fifth and seventh voltage harmonics cause the 500-mA sixth-harmonic current that can be seen in the dq frame. The harmonic current is low because of the good robustness of the controller to the grid voltage harmonics. Figure 50
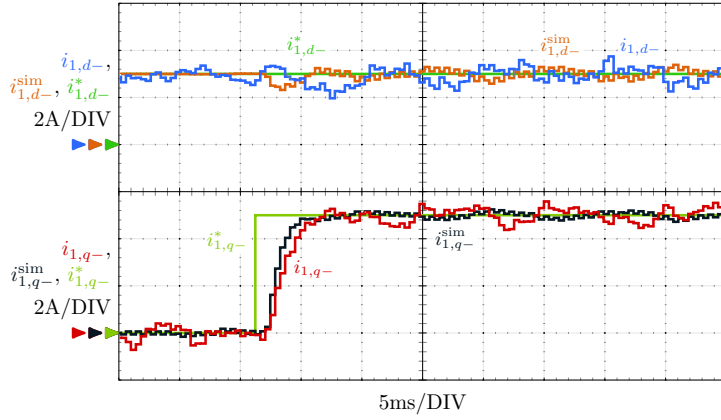
(a)
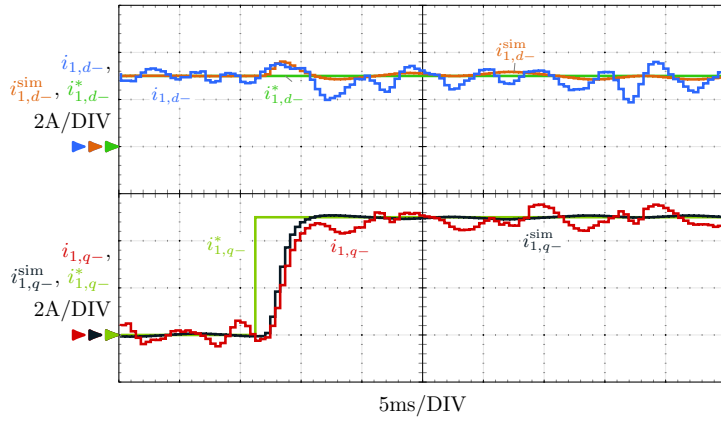
(b)
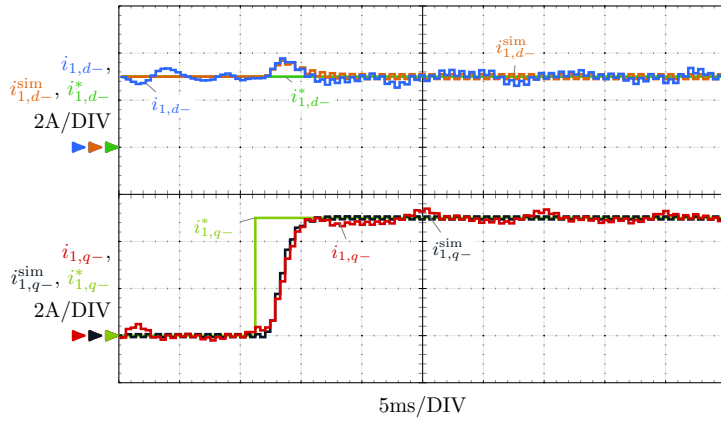
(c)

Figure 43. Continued on next page.

(d)
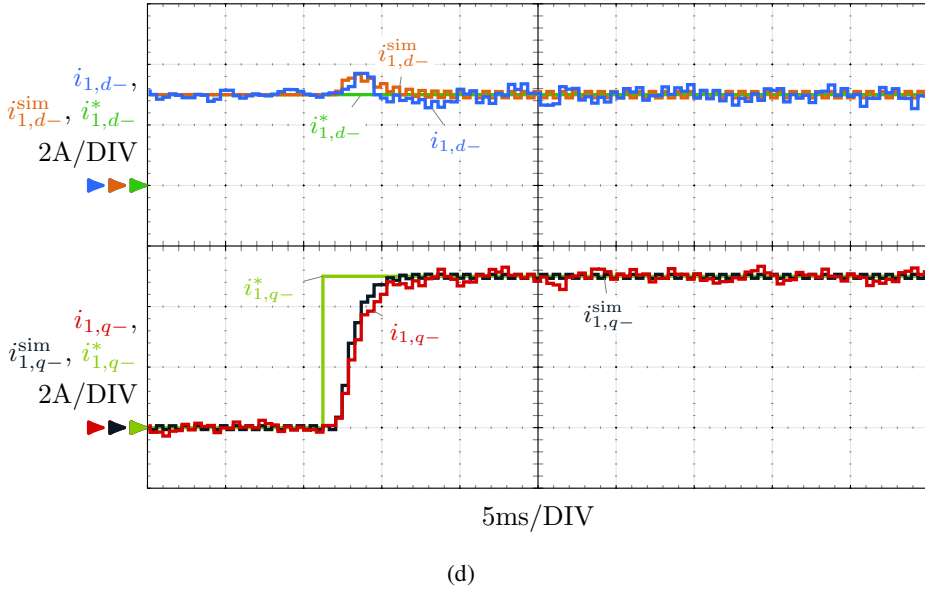
Figure 43. Experimental and simulation waveforms ($i_{1,dq}$ and $i_{1,dq}^{\text{sim}}$, respectively) for a reference step $i_{1,q-}^*$ in the negative synchronous frame dq- rotating at the fundamental grid frequency ω_g. a LCL filter I and b LCL filter II. c LCL filter III. d LCL filter IV.

shows the robustness of the control to variations in the plant parameters. In order to do this, a design is made according to the filter I parameters, but the real plant in the setup has the inductances of filter II (L_1 and L_2 are 2.8 times bigger than their nominal values). The

(a)

Figure 44. Continued on next page.

(b)

(c)

Figure 44. Experimental phase currents ($i_{1,abc}$) for a reference step $i^*_{1,q-}$ in the imaginary component ($i_{1,q-}$) of the negative synchronous frame dq- rotating at the fundamental grid frequency ω_g. a LCL filter I and b LCL filter II. c LCL filter III.

response exhibits a certain overshoot and axis cross-coupling because of the closed-loop poles displaced due to this discrepancy. Nevertheless, the system is stable despite the large parameter variations.

In Figure 51, the voltage source converters (VSCs) is connected to the weak grid presented in Section 3.3. The weak grid is emulated by an impedance in series with the grid voltage. In this case, the dynamics of the PLL are coupled to the dynamics of the cur-

rent controller [108, 109]. Nevertheless, no significant variations in the transient response parameters are observed.

3.5.   Observer Formulas

A state-feedback control needs to reconstruct the system state variables. This Section derives the equation that the reduced-order estimator implements to calculate the unmeasured state variables. The estimator uses the model of the observed system (48). To obtain an estimator for only the unmeasured part of the state vector, a partition of the state vector $\mathbf{x}_{add}^{LCL}(k)$ is defined: $x_{add_a}^{LCL}(k) = i_1(k)$ is the measured part, which is the grid-side current; and $\mathbf{x}_{add_b}^{LCL}(k) = [i_2\ v\ u_d\ r_1\ r_2]^T$ includes the rest of the state variables to be estimated. Therefore, the resultant system description, from (48), becomes

$$\underbrace{\begin{bmatrix} x_{add_a}^{LCL}(k+1) \\ \mathbf{x}_{add_b}^{LCL}(k+1) \end{bmatrix}}_{\mathbf{x}_{add}^{LCL}(K+1)} = \underbrace{\begin{bmatrix} A_{add_{aa}}^{LCL} & \mathbf{A}_{add_{ab}}^{LCL} \\ \mathbf{A}_{add_{ba}}^{LCL} & \mathbf{A}_{add_{bb}}^{LCL} \end{bmatrix}}_{\mathbf{A}_{add}^{LCL}} \underbrace{\begin{bmatrix} x_{add_a}^{LCL}(k) \\ \mathbf{x}_{add_b}^{LCL}(k) \end{bmatrix}}_{\mathbf{x}_{add}^{LCL}(k)} + \underbrace{\begin{bmatrix} B_{add_a}^{LCL} \\ \mathbf{B}_{add_b}^{LCL} \end{bmatrix}}_{\mathbf{B}_{add}^{LCL}} u(k)$$

$$i_1(k) = \begin{bmatrix} 1 & \mathbf{0} \end{bmatrix} \underbrace{\begin{bmatrix} x_{add_a}^{LCL}(k) \\ \mathbf{x}_{add_b}^{LCL}(k) \end{bmatrix}}_{\mathbf{x}_{add}^{LCL}(k)}. \tag{51}$$

Then, the observer gain $\mathbf{K_o}$ for the reduced-order estimator is calculated so as to have the observer closed-loop poles at the desired positions. This can be done by solving Ackermann's estimator formula [81] by executing one of the following two Matlab commands: $\mathbf{K_o} = \texttt{place}\left[\left(\mathbf{A}_{add_{bb}}^{LCL}\right)^T, \left(\mathbf{A}_{add_{ab}}^{LCL}\right)^T, \mathbf{p}\right]$ or $\mathbf{K_o} = \texttt{acker}\left[\left(\mathbf{A}_{add_{bb}}^{LCL}\right)^T, \left(\mathbf{A}_{add_{ab}}^{LCL}\right)^T, \mathbf{p}\right]$, where $\mathbf{p}$ is a vector with the desired poles.

Notice that the current state estimation $\hat{\mathbf{x}}_{add_b}^{LCL}(k)$ of (49) depends on the last measurement available $i_1(k)$. Moreover, the dynamics of the observer are determined by $\mathbf{A}_{add_{bb}}^{LCL} - \mathbf{K_o}\,\mathbf{A}_{add_{ab}}^{LCL}$, which has one eigenvalue (pole) less than the system matrix $\mathbf{A}_{add}^{LCL}$.

Finally, the feedforward gain K_f is computed. When the feedback path is closed using the previously calculated feedback gain $\mathbf{K_c}$, cf. Figure 34, the resultant closed-loop system is

$$\mathbf{x}_{dd}^{LCL}(k+1) = \overbrace{\left(\mathbf{A}_{dd}^{LCL} - \mathbf{B}_{dd}^{LCL}\,\mathbf{K_c}\right)}^{\mathbf{A}_{cl}^{LCL}} \mathbf{x}_{dd}^{LCL}(k) + K_f\,\mathbf{B}_{dd}^{LCL}\,i_1^*(k)$$

$$i_1(k) = \mathbf{C}_{dd}^{LCL}\,\mathbf{x}_{dd}^{LCL}(k). \tag{52}$$

Such system has the following closed-loop transfer function from its reference $i_1^*(k)$ to its output $i_1(k)$:

$$T(f) = K_f\,\mathbf{C}_{dd}^{LCL}\left(e^{j2\pi f T_s}\mathbf{I_4} - \mathbf{A}_{cl}^{LCL}\right)^{-1}\mathbf{B}_{dd}^{LCL}. \tag{53}$$
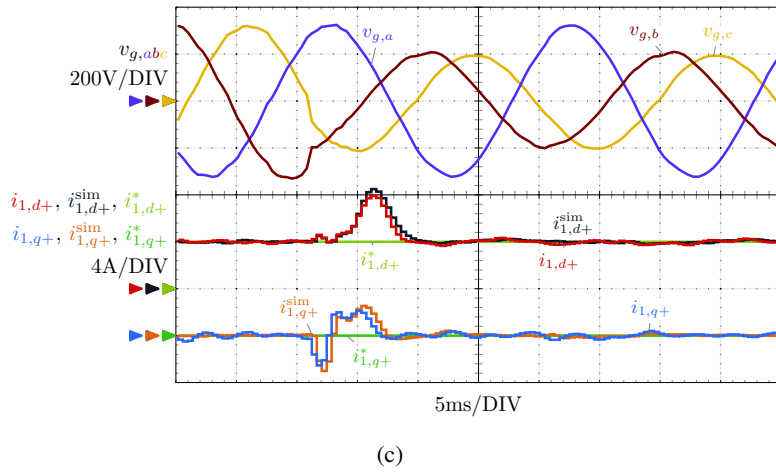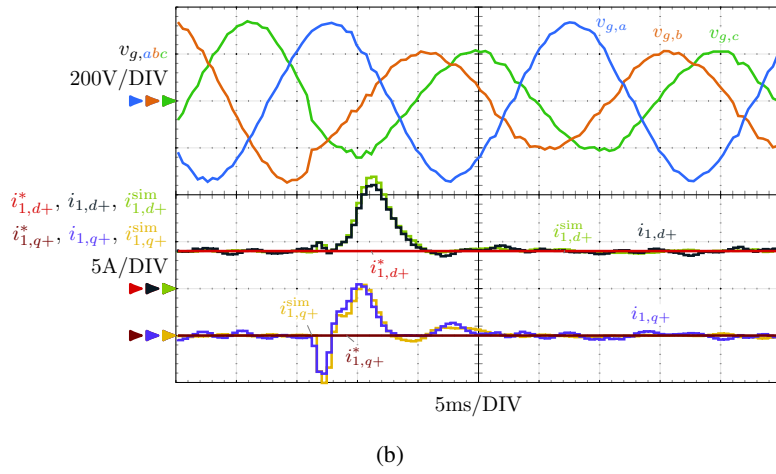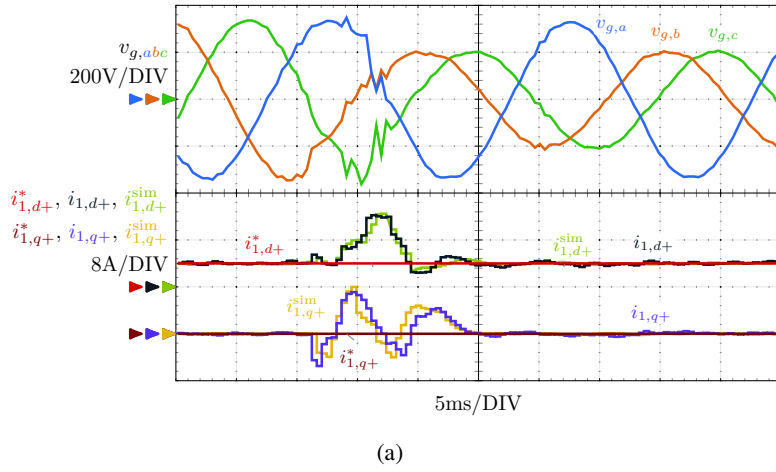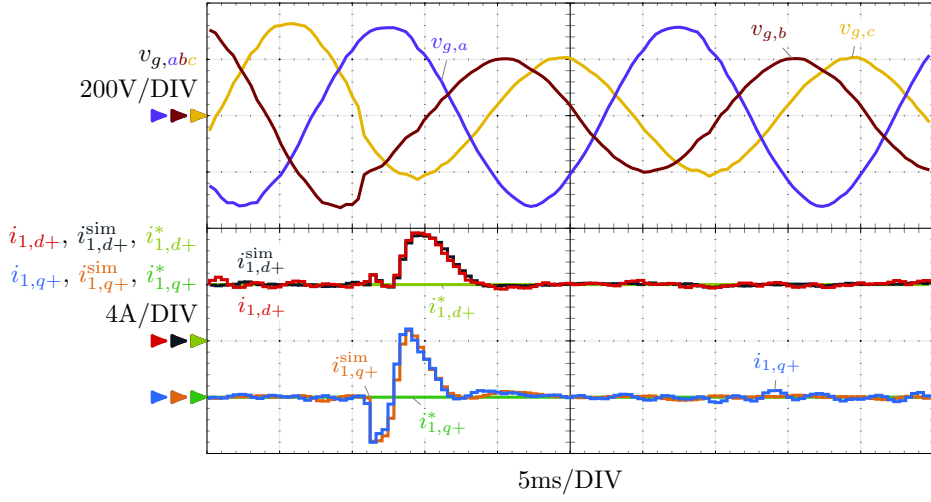
(a)

(b)

(c)

Figure 45. Continued on next page.

(d)

Figure 45. Experimental and simulation waveforms ($i_{1,dq}$ and $i_{1,dq}^{\text{sim}}$, respectively) for a 40%-depth type-C sag $v_{g,abc}$ [85] while keeping the reference $i_{1,dq}^*$ constant. a LCL filter I and b LCL filter II. c LCL filter III. d LCL filter IV.
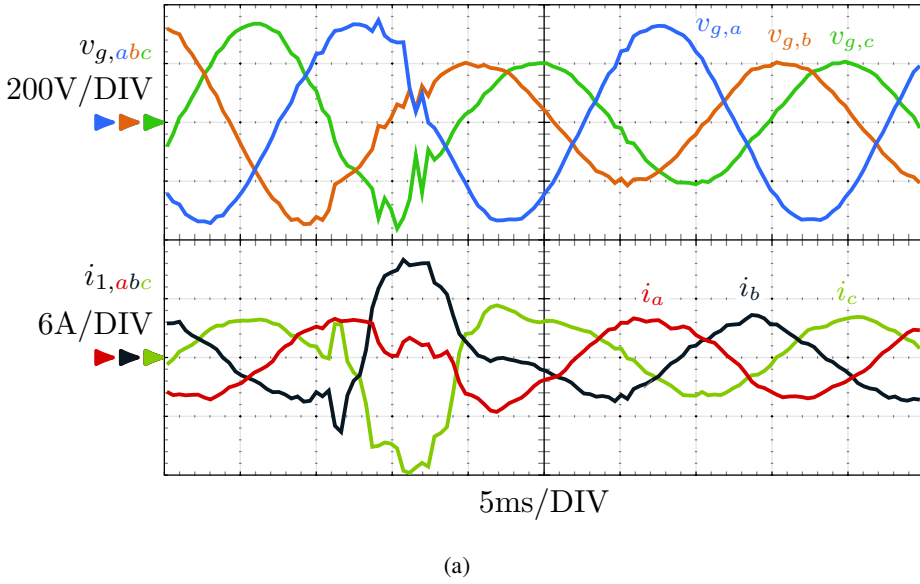

(a)

Figure 46. Continued on next page.

In order to achieve unity gain at the nominal grid frequency, e.g., $T_{\text{LCL}}^*(f_g)$, the feedforward gain K_f is

$$K_f = \frac{1}{\mathbf{C}_{dd}^{LCL}\left(e^{j2\pi f_g T_s}\mathbf{I_4} - \mathbf{A}_{cl}^{LCL}\right)^{-1}\mathbf{B}_{dd}^{LCL}}. \tag{54}$$
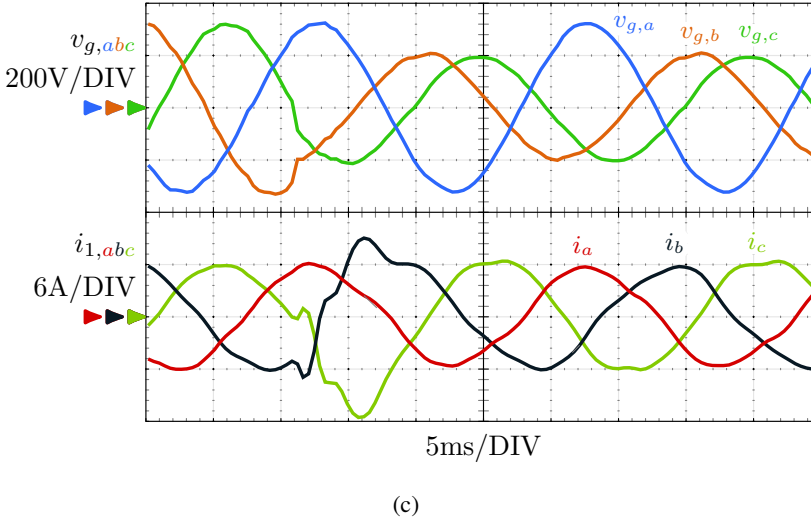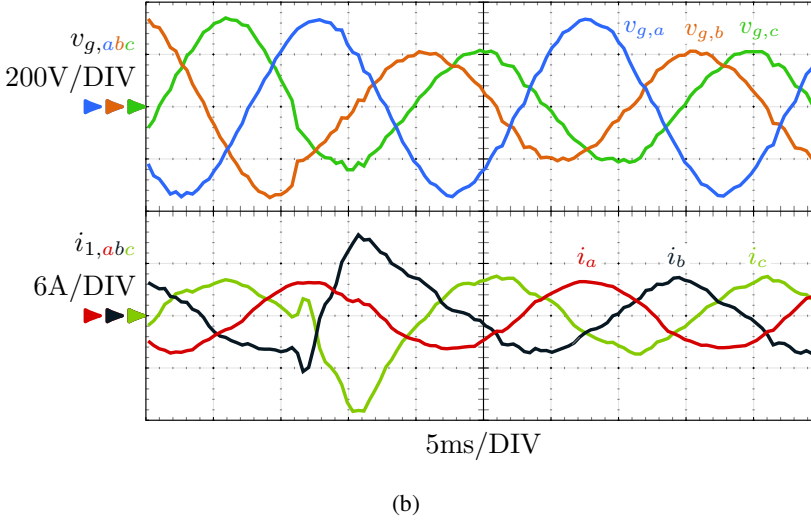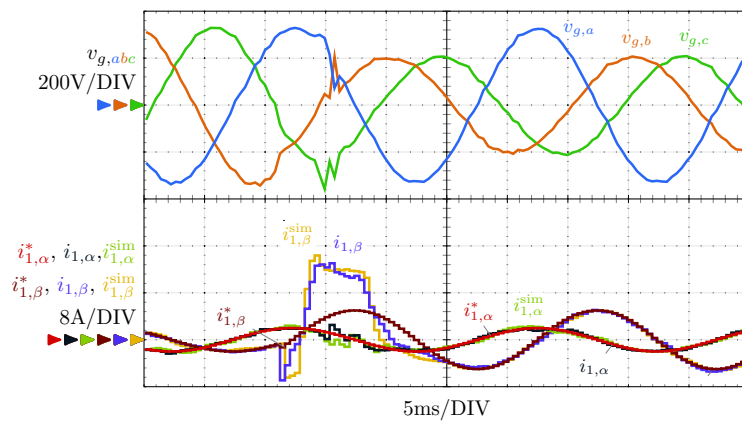
(b)

(c)

Figure 46. Experimental phase currents ($i_{1,abc}$) for a 40%-depth type-C sag $v_{g,abc}$ [85] while keeping the reference constant. a LCL filter I. b LCL filter II. c LCL filter III.

This concludes the design of the compensator.

3.6.   Example of Design Code

Figure 52 shows an example script that condenses all the computations that are necessary to design the controller presented in this section. The inputs of the script are the system matrices of the continuous LCL filter $\mathbf{A}$, $\mathbf{B}$ and $\mathbf{C}$, defined in (38), the resonant frequency of the filter f_{res}, and the fundamental grid frequency ω_g. The outputs are the compensator gain $\mathbf{K_c}$, the reduced-order observer gain $\mathbf{K_o}$, and the feedforward gain K_f. These three gains are needed to implement the proposed control structure (cf. Figure 34).

(a)
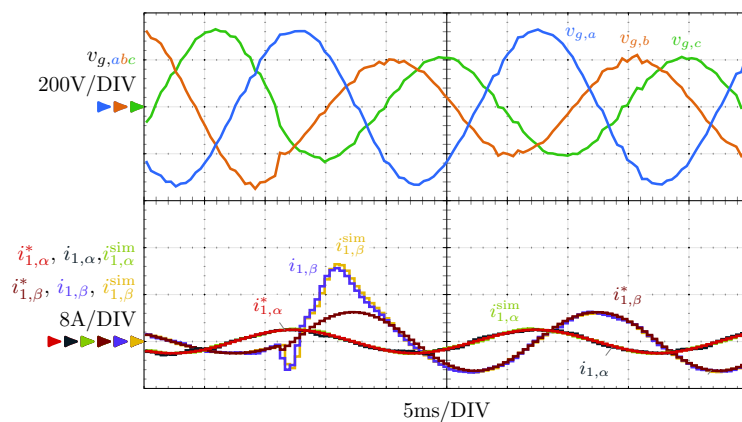
(b)
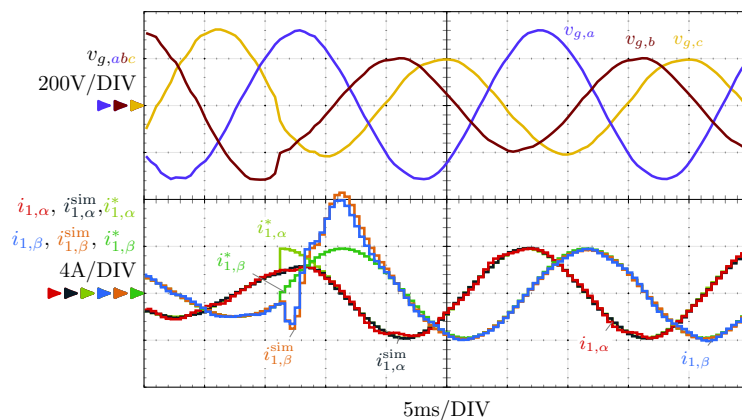
(c)

Figure 47. Continued on next page.

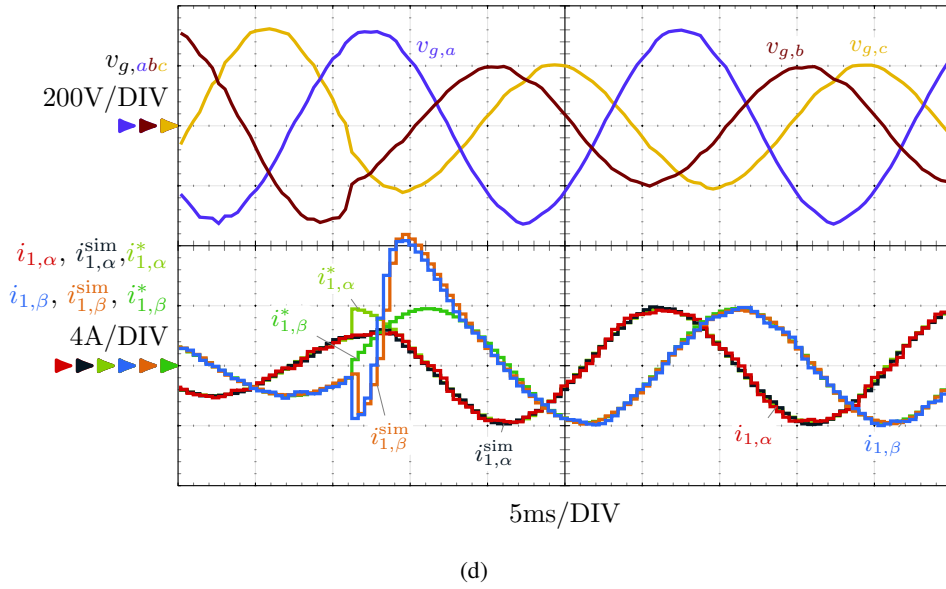Figure 47. Experimental and simulation waveforms (i_1 and i_1^{sim}, respectively) for a 40%-depth type-C sag $v_{g,abc}$ [85]. The reference step i_1^* is calculated according to the so-called positive-negative-sequence compensation strategy [84]. a LCL filter I and b LCL filter II. c LCL filter III. d LCL filter IV.
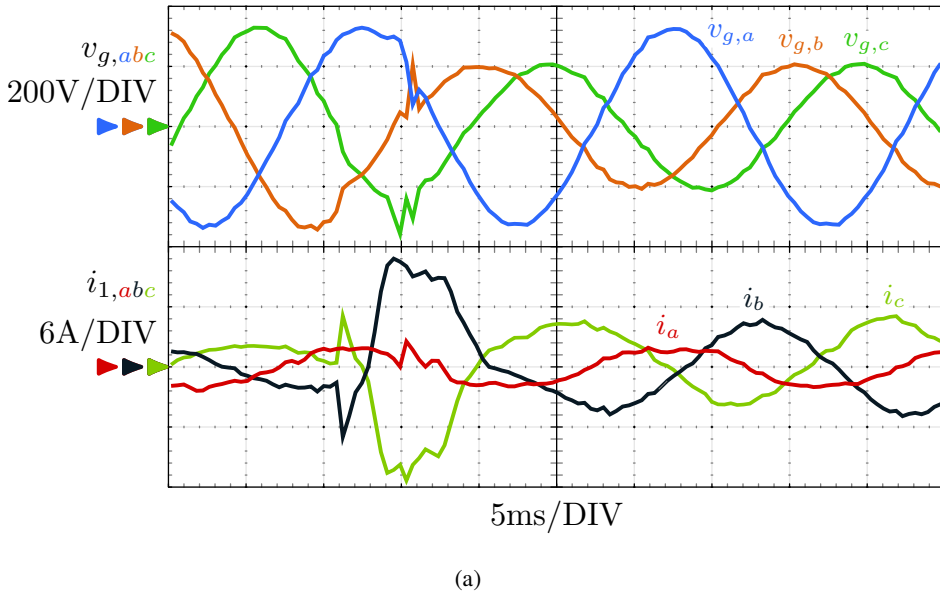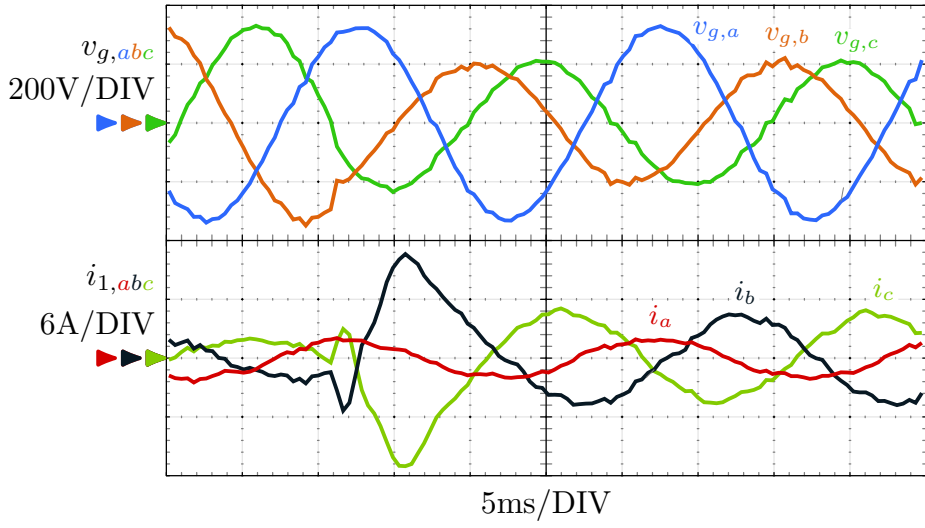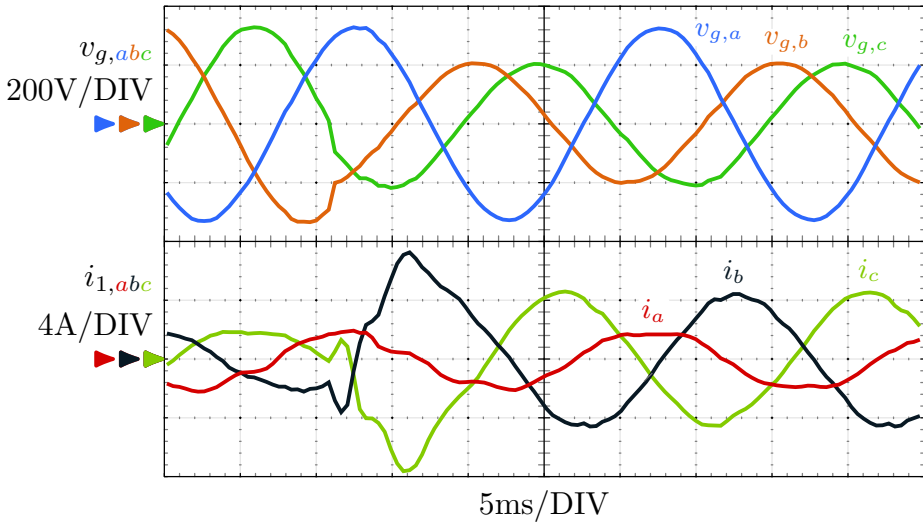
Figure 48. Continued on next page.

(b)

(c)

Figure 48. Experimental phase currents ($i_{1,abc}$) for a 40%-depth type-C sag $v_{g,abc}$ [85]. The reference step i_1^* is calculated according to the so-called positive-negative-sequence compensation strategy [84]. a LCL filter I and b LCL filter II. c LCL filter III.
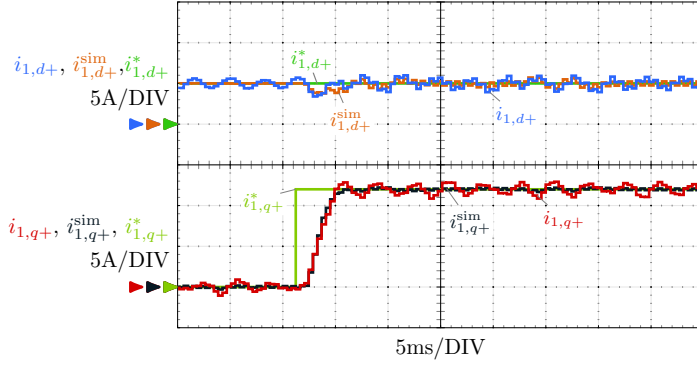
(a)
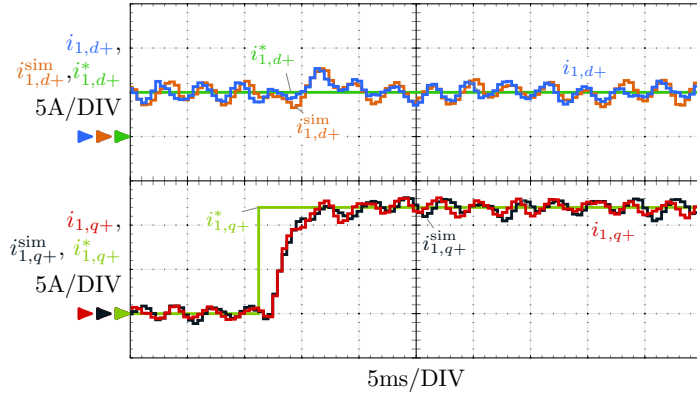
(b)
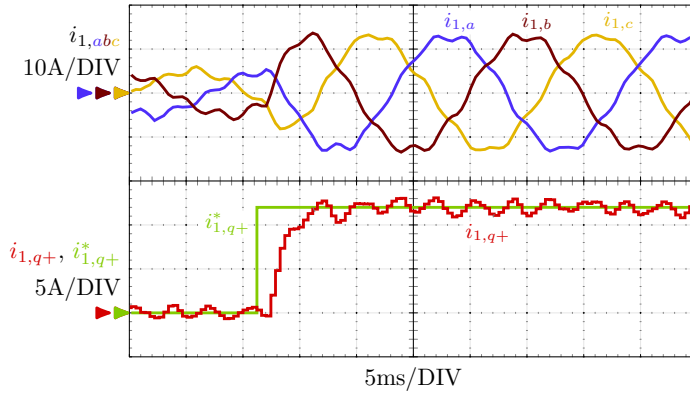
(c)

Figure 49. Waveforms for a reference step $i_{1,q+}^*$ in the positive synchronous frame dq+. The grid voltage has the following low-order voltage harmonics: $V_3 = 1.2$V, $V_5 = 0.7$V, $V_7 = 4.8$V and $V_9 = 1.6$V. a Experimental and simulation synchronous-frame waveforms ($i_{1,dq+}$ and $i_{1,dq+}^{sim}$, respectively). LCL filter I is used for the test. a Experimental and simulation synchronous-frame waveforms ($i_{1,dq+}$ and $i_{1,dq+}^{sim}$, respectively). LCL filter III is used for the test. c Experimental phase currents $i_{1,abc}$. LCL filter I is used for the test.
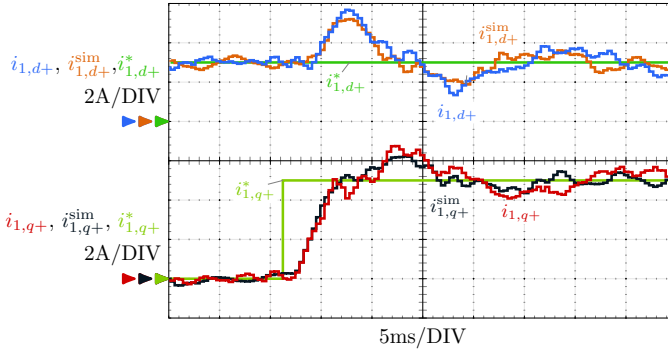
(a)
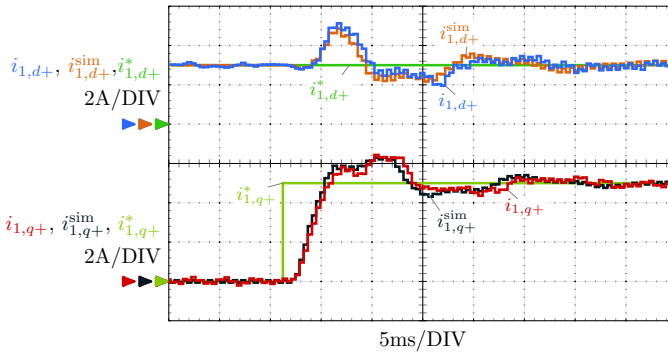
(b)
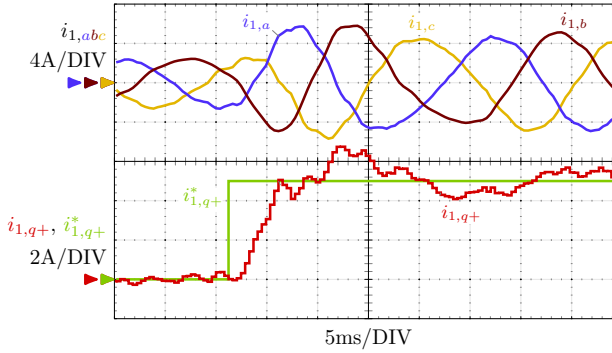
(c)

Figure 50. Waveforms for a reference step $i_{1,q+}^*$ in the positive synchronous frame dq+. The filter inductances, L_1 and L_2, are 2.8 times bigger than their nominal values. a Experimental and simulation synchronous-frame waveforms ($i_{1,dq+}$ and $i_{1,dq+}^{sim}$, respectively), using filter I nominal values. a Experimental and simulation synchronous-frame waveforms ($i_{1,dq+}$ and $i_{1,dq+}^{sim}$, respectively), using filter II nominal values. c Experimental phase currents $i_{1,abc}$, using filter I nominal values.
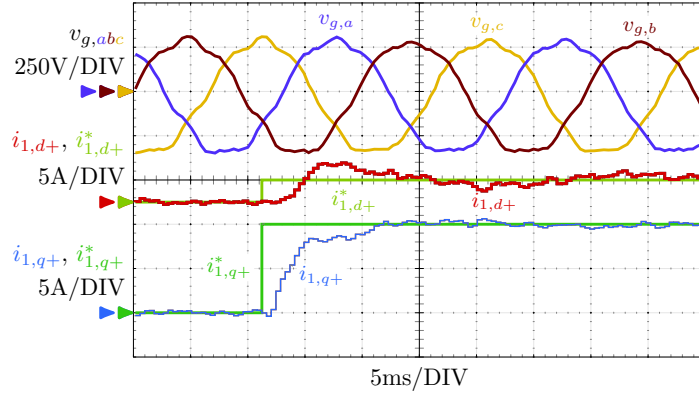
(a)
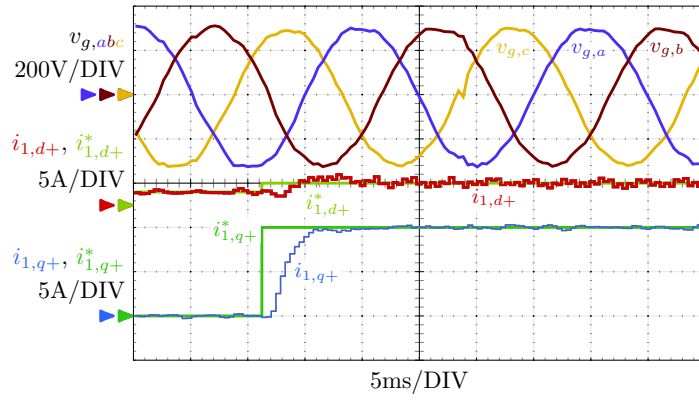
(b)
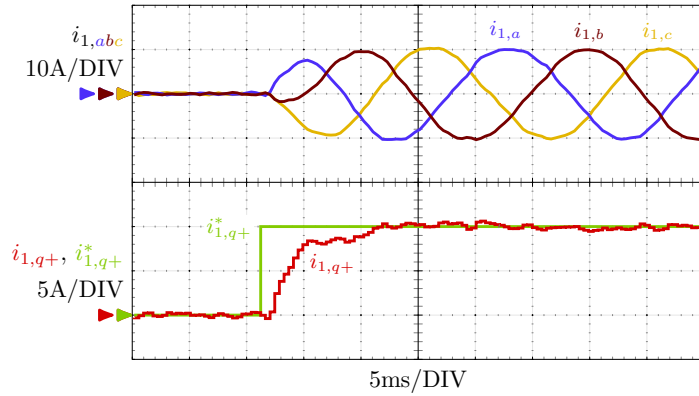
(c)

Figure 51. Waveforms for a reference step $i_{1,dq+}^*$ in the positive synchronous frame dq+ rotating at the fundamental grid frequency and connected to a weak grid $v_{g,abc}$ with a grid impedance $Z_g = 0.11$ p.u. a Experimental synchronous-frame currents $i_{1,dq+}$ using the LCL filter I. b Experimental synchronous-frame currents $i_{1,dq+}$ using the LCL filter III. c Experimental phase currents $i_{1,abc}$ using the LCL filter I.

```
% MODELING OF THE PLANT AND THE DISTURBANCE
% LCL filter in continuous time
sys = ss(A,B,C,0);
% LCL filter in discrete time
sys_d = c2d(sys,Ts,'zoh');
[A_d,B_d,C_d,H_d] = ssdata(sys_d);
% LCL filter plus 1 sample compu. delay
A_dd = [A_d B_d(:,1) ; 0 0 0 0];
B_dd = [0;0;0;1] ;
C_dd = [C_d 0];
sys_dd = ss(A_dd,B_dd,C_dd,0,Ts);
% Sinusoidal disturbance in continuous time
Adist = [0 1 ; -wg^2 0];
% Sinusoidal disturbance in discrete time
[Adist_d,Bdist_d] = c2d(Adist,[0;0],Ts);
Cdist_d = [1 0];
% LCL filt., 1 sample delay and dist. model
A_add = [A_dd B_dd*Hd ; zeros(2,4) Adist_d ];
B_add = [B_dd ; Bdist_d];
C_add = [C_dd 0 0];
sys_add = ss(A_add,B_add,C_add,[],Ts);

% COMPENSATOR AND OBSERVER DESIGN
% USING POLE PLACEMENT
fdom = 150; damp = 0.7;
wres = sqrt((L1+L2)/(L1*L2*Cf));
% Compensator gain, Kc
p1 = exp(-2*pi*fdom*Ts);
p2 = exp(-damp*wres+1i*wres*sqrt(1-damp^2)*Ts);
poles_comp = [0 ; p2 ; conj(p2) ; p1];
Kc = acker(A_dd,B_dd(:,1),poles_comp);
% Observer gain, Ko
p3 = exp(-2*pi*2*fdom*Ts);
poles_obs = [ 0 ; p2 ; conj(p2) ; p3 ; p3];
Faa = A_add(1,1);
Fbb = A_add(2:end,2:end);
Fab = A_add(1,2:end);
Fba = A_add(2:end,1);
Ga = B_add(1);
Gb = B_add(2:end);
Ko = acker(Fbb',Fab',poles_obs)';
% Feedforward gain, Kf
[Nx,Nu,Kf] = refi(A_dd,B_dd(:,1),C_dd,K);
```

Figure 52. Example script that condenses all the computations that are necessary to design the proposed controller.

3.7. Summary

This section has presented a current controller of both positive and negative grid-side current sequences for grid-tied converters with LCL filter. The proposed controller offers fast reference-tracking capability with negligible overshoot and low controller effort, regardless of the switching frequency and LCL filter used: f_{res} above or below $f_s/6$. The controller has also been proved to be robust to disturbances such as voltage sags and low-order voltage harmonics, even when combined with reference changes in both sequences. The sensitivity to parameter variations was analyzed obtaining a low sensitivity. The developed method (based on direct discrete-time pole placement) provides a simple process for the design of the controller, and includes estimated losses of the plant in the model. This method makes it possible to design a controller for any plant based on an LCL filter so that a stable operation is ensured, without additional damping methods. The design was verified using simulations and experiments.

4. Generalized Multi-Frequency Current Controller for Grid-Connected Converters With LCL Filter

This section presents a grid-side current controller for grid-tied inverters with LCL filter, including harmonic current elimination. The proposed controller only measures the grid current and voltage and it combines excellent dynamic characteristics with good robustness. Contrarily to previously proposed harmonic-current controllers, the presented solution offers a generalized method that gives a consistent (with minimal variation in the reference-tracking dynamics) and stable performance irrespectively of the number of current harmonics to be canceled and of the resonant frequency of the LCL filter (provided that it is lower than the Nyquist frequency). The response to reference commands is completely damped and fast. The response speed is set in accordance with the low-pass characteristic of the LCL filter so as to limit the control effort. Concerning the disturbance rejection, the controller offers an infinite impedance to any disturbances (such as grid voltage harmonics) at a set of arbitrarily specified frequencies. This allows the designer to eliminate all the undesired current harmonics with a simple design process. In addition, the performance of the presented controller is evaluated in terms of a fundamental tradeoff that exists between robustness to variations in the grid impedance and the number of frequency components rejected. Finally, simulation and experimental results that validate the proposal are presented.

Distributed power generation systems (DPGSs) and microgrids are gaining popularity due to the increasing use of renewable energy sources [65]. In this context, the voltage source converters (VSCs) plays a crucial role in the effective integration of the different

elements that conform a microgrid. The electronic power conditioning and control of the energy production are central aspects that should be addressed for a successful integration of DPGSs. However, the large penetration of these systems demands more stringent interconnection requirements [110]. In order to meet these requisites under different grid conditions [111], a current controller with harmonic control becomes necessary to eliminate harmonics caused by grid voltage harmonics and voltage source converters (VSCs) nonlinearities.

Current harmonics produce increased losses, operational problems, and equipment deterioration [110]. LCL filters are commonly used in place of traditional L filters because they attenuate current harmonics generated by the switching voltage of the voltage source converters (VSCs) with a slope of 60 dB per decade [69]. This high attenuation allows the designer to reduce the reactive elements while maintaining a low switching ripple in the grid-side current. Nonetheless, this improved performance of the LCL filter also augments the complexity of the system to be controlled due to the appearance of a high-quality-factor resonant circuit [69].

Different controllers for grid-tied VSCs with LCL filter capable of eliminating low-order harmonics in the grid-side current have been proposed [29, 30, 31, 32, 33, 34, 35, 36, 37, 38, 39, 40, 41, 43, 44]. Some of the proposed solutions use techniques from modern control theory [29, 44] or sophisticated feedforward schemes [30, 31]; however, conventional PI [32, 33, 34, 35] and proportional-resonant (PR) [36, 38, 37, 39, 40, 41, 43] controllers placed in different frames (so as to selectively target the desired harmonics) are the most commonly adopted solutions in the literature.

A common problem of these solutions [29, 99, 1, 30, 31, 32, 33, 34, 35, 36, 37, 38, 39, 40, 41, 44] is the existence of a tradeoff between the reference-tracking and the disturbance-rejection capability during transients [40]: if the reference tracking is improved by a change in the controller gains, then the disturbance rejection worsens (and viceversa). In addition, the transient response (to both disturbance and reference changes) is degraded as the number of controlled harmonics (or the number of paralleled regulators) increases, because of the additional poles in the system [40].

Another common problem of these harmonic-current controllers is the reduced stability margin when an LCL filter is used [37], due to the aforementioned resonance. In [50, 48, 51], such problem has been studied for the case of a single-frequency controller using PI or PR controllers. The solution presented in [50] can provide a stable system for a wide range of resonant frequencies of the LCL filter measuring only the grid-side current. The method proposed in [48] introduces a time delay to achieve stability when the grid-side current is fed back. In [51], an active damping technique for the resonance of the LCL is presented. However, such results cannot be directly applied to a system with a multi-frequency controller because adding more integral or resonant parts to the system changes its robustness. To the authors' knowledge, a transfer-function-based controller that meets a multi-frequency control requirement and can provide a stable operation for a wide range of resonant-to-sampling-frequency ratios using only the grid-side current measurements has not been published yet. Consequently, additional damping mechanisms [41, 30, 31, 37, 43] are often needed to achieve stability under certain ratios of sampling-to-resonant frequency [47]. Finally, direct pole-placement schemes such as [99, 1, 44] give good robustness and good dynamics with a simple structure, but they do not completely

eliminate the grid-induced current harmonics: only the fundamental frequency of the grid voltage is controlled with zero steady-state error.

This section is an extension of the conference presentation [8] and proposes a current controller for grid-tied inverters that offers an infinite impedance to voltage disturbances at an arbitrarily specified set of frequencies. This work has the following advantages compared to previous multi-frequency proposals:

- A stable operation, irrespectively of the resonant frequency of the LCL filter f_{res}, provided that it is lower than the Nyquist frequency of the digital controller $f_s/2$. In particular, the presented method has been experimentally verified when f_{res} is equal to the critical resonant frequency where a conventional controller cannot stabilize the system ($f_{res} = f_s/6$) [47].

- A better robustness to variations in the grid impedance compared to recently published PR- or PI-based controllers due to the absence of a critical resonant frequency where the system becomes unstable. An analysis of the robustness depending on the number of current harmonics controlled with zero steady-state error is also included.

- An improved reference-tracking performance without affecting the disturbance-rejection capabilities. The response to reference commands is equivalent to that of a first-order system (without overshoot, nor axis crosscoupling) and the speed can be set at the design stage in accordance with the low-pass characteristic of the LCL filter so as to limit the controller effort and avoid overmodulation.

As regards the computational load, the controller proposed in this section requires a higher computational load, as given in Section 4.7, in comparison to transfer-function-based methods. Nonetheless, modern microcontrollers can successfully execute the required operations without problems even when a large number of frequencies are controlled with zero steady-state error.

After this introduction, Section 4.1 presents the model of the plant (the voltage source converters (VSCs) and the LCL filter) and the disturbances. Next, in Section 4.2 such model is used to design the observer included in the controller. Section 4.3 demonstrates and justifies the characteristics and performance of the proposed controller. Section 4.4 assesses the robustness of the proposal to variations in the grid impedance. Section 4.5 presents simulation and experimental results that validate the theory. Summary in Section 4.9 close the section.

4.1. Modeling of the Plant and the Disturbance

This section presents the state-space model of the plant and the disturbance used to design the controller. Figure 53 depicts the physical plant, which consists of a voltage source converters (VSCs) connected to the grid using an LCL filter. L_1, L_2, and C are the values of the reactive elements of the LCL filter. R_1, R_2, and R_c model the equivalent series resistances of the filter and the voltage source converters (VSCs) [15]. $v_{g,abc}$ is the grid voltage at the PCC. R_g and L_g are the values of the resistive and inductive components of the grid impedance Z_g. Since these values are usually unknown, they are assumed to be zero to design the controller. $i_{1,abc}$ and $i_{1,dq}^*$ denote the measured grid-side current in the

abc frame and the grid-side current reference in the dq frame, respectively. If the subscript in a variable does not specify a reference frame, the $\alpha\beta$ frame is assumed.
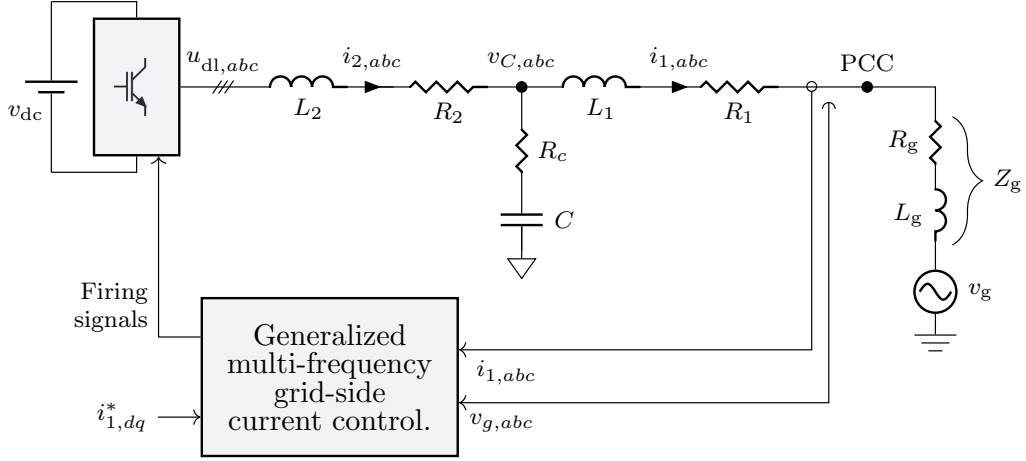

Figure 53. Grid-tied voltage source converters (VSCs) with LCL filter and grid-side multi-frequency current controller.

A block diagram representation of the plant model in the $\alpha\beta$ frame is shown in Figure 54, where u_{sat} is the saturated controller output voltage; u_{d} is the PWM voltage reference, e.g., it is the one-sample-delayed saturated controller output voltage; and u_{d}' is the voltage source converters (VSCs) output voltage.

The discrete-time modeling process that describes the LCL filter, the PWM, and the computational delay of this system was presented in section 3. Such modeling process takes place in several steps; each step adds features to the model obtained in the previous stage, cf. Figure 54. In the first place, a continuous model of the LCL filter in stationary frame is presented. Next, the continuous model is discretized by using a ZOH equivalent [81]. Then, a one-sample input (computational) delay is added. The final model relates the grid-side current $i_1(k)$ to the modulator voltage $u(k)$ in the plant shown in Figure 54:

$$\begin{aligned}
\mathbf{x}_{dd}^{LCL}(k+1) &= \mathbf{A}_{dd}^{LCL}\mathbf{x}_{dd}^{LCL}(k) + \mathbf{B}_{dd}^{LCL}u(k) \\
i_1(k) &= \mathbf{C}_{dd}^{LCL}\mathbf{x}_{dd}^{LCL}(k). \\
\mathbf{x}_{dd}^{LCL}(k) &= \begin{bmatrix} i_1 & i_2 & v_C & u_{\text{d}} \end{bmatrix}^{\text{T}}.
\end{aligned} \tag{55}$$

In order to obtain zero steady-state error in the grid-side current at a set of desired frequencies, the model of the plant in (55) is augmented with a complex disturbance model that includes the selected frequencies.

An h-order harmonic voltage disturbance as a function of time $w^h(t)$ in the $\alpha\beta$ frame has the following expression:

$$w^h(t) = A_h e^{j(\omega(g)ht+\phi_h)} \tag{56}$$

where A_h and ϕ_h are the amplitude and initial phase, respectively. The grid fundamental frequency is $\omega_g = 2\pi f_g$. The sign of h defines the sequence (positive or negative) of
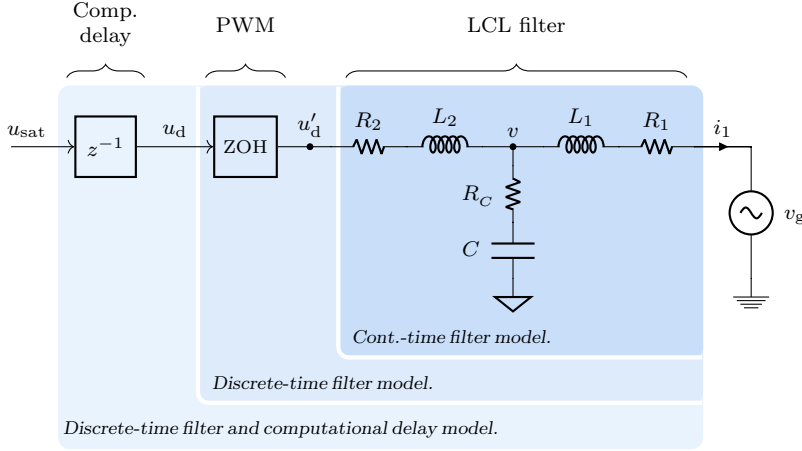
Figure 54. Stationary-frame plant diagrams: LCL filter, PWM (modeled as a ZOH), and one-sample computational delay.

the harmonic [36]. Zero-sequence voltage harmonics are not included in the disturbance model because they do not produce any current circulation in a three-wire system. A multi-frequency disturbance $w(t)$ that is composed of n harmonics $(h_1, h_2, \ldots, h_n)$ is modeled using (56) as

$$w(t) \quad = \quad w^{h_1}(t) + w^{h_2}(t) + \cdots + w^{h_n}(t). \tag{57}$$

This disturbance equation models all the harmonics (and the fundamental components, for $h = \pm 1$) that are to be rejected with zero steady-state error.

The single-frequency disturbance $w^h(t)$ in (56) is a solution of the following differential equation:

$$\frac{\mathrm{d}w^h(t)}{\mathrm{d}t} \quad = \quad j\omega_g h w^h(t). \tag{58}$$

Hence, the multi-frequency disturbance in (57) can be expressed in matrix notation as a solution of

$$\frac{\mathrm{d}\mathbf{r}(t)}{\mathrm{d}t} \quad = \quad \underbrace{\begin{bmatrix} j\omega_g h_1 & 0 & \cdots & 0 \\ 0 & j\omega_g h_2 & \cdots & 0 \\ \vdots & \vdots & \ddots & \vdots \\ 0 & 0 & \cdots & j\omega_g h_n \end{bmatrix}}_{\mathbf{A}^{dis}} \mathbf{r}(t)$$

$$w(t) \quad = \quad \underbrace{\begin{bmatrix} 1 & 1 & \cdots & 1 \end{bmatrix}}_{\mathbf{C}^{dis}} \mathbf{r}(t) \tag{59}$$

where

$$\mathbf{r}(t) \quad = \quad \begin{bmatrix} w^{h_1} & w^{h_2} & \cdots & w^{h_n} \end{bmatrix}^{\mathrm{T}}. \tag{60}$$

Then, the model in (59) is discretized by using a ZOH equivalent [81] (to model the PWM effect) [1]:

$$\begin{aligned}
\mathbf{A}_d^{dis} &= e^{\mathbf{A}^{dis} T_s} \\
\mathbf{C}_d^{dis} &= \mathbf{C}^{dis}.
\end{aligned} \tag{61}$$

The resultant discrete multi-frequency disturbance model is

$$\begin{aligned}
\mathbf{r}(k+1) &= \mathbf{A}_d^{dis}\mathbf{r}(k) \\
w(t) &= \mathbf{C}_d^{dis}\mathbf{r}(k).
\end{aligned} \tag{62}$$

Finally, the complete system model is obtained by augmenting the plant model (55) with the input disturbance model (62):

$$\underbrace{\begin{bmatrix} \mathbf{x}_{dd}^{LCL}(k+1) \\ \mathbf{r}(k+1) \end{bmatrix}}_{\mathbf{x}_{add}^{LCL}(K+1)} = \underbrace{\begin{bmatrix} \mathbf{A}_{dd}^{LCL} & \mathbf{B}_{dd}^{LCL}\,\mathbf{C}^{dis} \\ \mathbf{0} & \mathbf{A}^{dis} \end{bmatrix}}_{\mathbf{A}_{add}^{LCL}} \underbrace{\begin{bmatrix} \mathbf{x}_{dd}^{LCL}(k) \\ \mathbf{r}(k) \end{bmatrix}}_{\mathbf{x}_{add}^{LCL}(k)} + \underbrace{\begin{bmatrix} \mathbf{B}_{dd}^{LCL} \\ \mathbf{0} \end{bmatrix}}_{\mathbf{B}_{add}^{LCL}} u(k)$$

$$i_1(k) = \underbrace{\begin{bmatrix} \mathbf{C}_{dd}^{LCL} & \mathbf{0} \end{bmatrix}}_{\mathbf{C}_{add}^{LCL}} \underbrace{\begin{bmatrix} \mathbf{x}_{dd}^{LCL}(k) \\ \mathbf{r}(k) \end{bmatrix}}_{\mathbf{x}_{add}^{LCL}(k)}$$

$$\mathbf{x}_{add}^{LCL}(k) = \begin{bmatrix} \left(\mathbf{x}_{dd}^{LCL}(k)\right)^{\mathrm{T}} & w^{h_1} & w^{h_2} & \cdots & w^{h_n} \end{bmatrix}^{\mathrm{T}}. \tag{63}$$

This augmented model adds to the plant model a resonant action $\mathbf{r}$, which is applied at the plant input. This model is used in the next section to develop the proposed observer, which estimates the plant state $\mathbf{x}_{dd}^{LCL}(k)$ and the required input-equivalent voltage disturbance w that results in zero steady-state error in the grid-side current at the design-selected frequencies.

4.2.   Structure and Design of the Controller

The proposed controller (cf. Figure 55) aims to control the positive and negative sequences of the fundamental and the typical low-order harmonics of the grid current. The proposed controller structure, cf. Figure 55, contains two main parts: a compensator and a multifrequency observer. Additionally, a saturator and a grid voltage feedforward is also included. The grid voltage feedforward ensures a bumpless start and improves the response to voltage sags. The saturator provides to the observer a more accurate value of the voltage source converters (VSCs) output voltage when overmodulation occurs. With such controller structure, the wind-up problem is avoided by feeding back the saturated control signal u_{sat} to the observer rather than the control output u because the estimated states are correct and the consistency between the observer and the real plant states is maintained. This eliminates wind-up problems in the observer when the voltage source converters (VSCs) is commanded with a reference that cannot be achieved [1, 54].

In order to carry out the design of the compensator and the observer, the principle of separation of estimation and control is applied. In this manner, the design of the observer
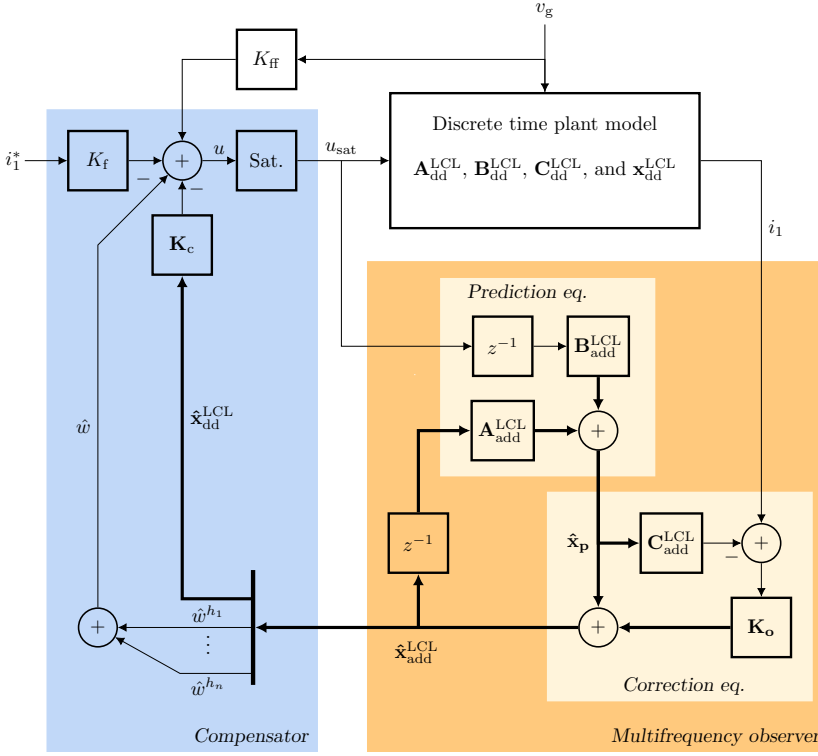
Figure 55. Proposed multi-frequency grid-side current controller in the $\alpha\beta$ frame.

and the design of the compensator are performed independently and, when combined, they keep their properties [54].

In view of this, on the one hand, the compensator is designed to provide a good transient response to reference changes. A damped response to reference commands equivalent to a first-order system is obtained due to the adopted direct discrete-time pole-placement strategy. The bandwidth that can be achieved is only limited by the sampling rate and the available bandwidth in the physical system (where overmodulation does not occur, cf. [2, Sec. III-A]).

On the other hand, the observer calculates the estimated plant state vector $\hat{\mathbf{x}}_{\mathbf{3}}$ using the measured grid-side current i_1 and the saturated controller output voltage u_{sat}. The proposed design provides a good robustness against changes in the grid impedance, as explained in Section 4.3, and removes the effect of grid voltage disturbances by providing zero steady-state error in the grid-side current at a set of design-selected frequencies.

The compensator contains two gains, namely, a feedback gain $\mathbf{K_c}$ and a reference feed-forward gain K_{f}. The proposed design method to obtain these two gains uses a direct discrete-time pole-placement strategy which only depends on the resonant frequency of the LCL filter f_{res}, the sampling period of the digital controller T_{s}, and the desired reference-tracking bandwidth f_{dom}. In the following, the required steps to obtain both gains are detailed.

First, the proposed closed-loop poles of the plant are computed according to [1, Table I].

Then, Ackermann's formula is applied to compute the gain $\mathbf{K_c}$ that yields a closed-loop system with the specified closed-loop poles:

$$\mathbf{K_c} \;\; = \;\; \begin{bmatrix} 0 & 0 & 0 & 1 \end{bmatrix} \begin{bmatrix} \mathbf{B}_{dd}^{LCL} & \mathbf{A}_{dd}^{LCL}\mathbf{B}_{dd}^{LCL} & \left(\mathbf{A}_{dd}^{LCL}\right)^2 \mathbf{B}_{dd}^{LCL} & \left(\mathbf{A}_{dd}^{LCL}\right)^3 \mathbf{B}_{dd}^{LCL} \end{bmatrix} A_{cl}(\mathbf{A}_{dd}^{LCL}),$$

where A_{cl} is the characteristic polynomial, whose roots are the desired closed-loop poles of the system. The expression of A_{cl} evaluated at $\mathbf{A}_{dd}^{LCL}$ is

$$A_{cl}\left(\mathbf{A}_{dd}^{LCL}\right) \;\; = \;\; \left(\mathbf{A}_{dd}^{LCL} - p_1^{cl}\mathbf{I_4}\right)\left(\mathbf{A}_{dd}^{LCL} - p_2^{cl}\mathbf{I_4}\right)\left(\mathbf{A}_{dd}^{LCL} - p_3^{cl}\mathbf{I_4}\right)\mathbf{A}_{dd}^{LCL}.$$

When the feedback path is closed using the previously calculated feedback gain $\mathbf{K_c}$, cf. Figure 55, the resultant closed-loop system is

$$\mathbf{x}_{dd}^{LCL}(k+1) \;\; = \;\; \overbrace{\left(\mathbf{A}_{dd}^{LCL} - \mathbf{B}_{dd}^{LCL}\mathbf{K_c}\right)}^{\mathbf{A}_{cl}^{LCL}} \mathbf{x}_{dd}^{LCL}(k) + K_f\mathbf{B}_{dd}^{LCL}i_1^*(k)$$
$$i_1(k) \;\; = \;\; \mathbf{C}_{dd}^{LCL}\mathbf{x}_{dd}^{LCL}(k). \tag{64}$$

Such system has the following closed-loop transfer function from its reference $i_1^*(k)$ to its output $i_1(k)$:

$$T(f) \;\; = \;\; K_f\mathbf{C}_{dd}^{LCL}\left(e^{j2\pi fT_s}\mathbf{I_4} - \mathbf{A}_{cl}^{LCL}\right)^{-1}\mathbf{B}_{dd}^{LCL}. \tag{65}$$

In order to achieve unity gain at the nominal grid frequency, e.g., $T(f_g) = 1$, the feedforward gain K_f is

$$K_f \;\; = \;\; \frac{1}{\mathbf{C}_{dd}^{LCL}\left(e^{j2\pi f_gT_s}\mathbf{I_4} - \mathbf{A}_{cl}^{LCL}\right)^{-1}\mathbf{B}_{dd}^{LCL}}. \tag{66}$$

This concludes the design of the compensator.

Concerning the design of the observer, now the system model in (63) has a high order. Consequently, it is not easy to design the observer as in [1] (a Luenberger observer with direct discrete-time pole placement) and achieve a robust system, as further explained in Section 4.3. In order to avoid this problem and simplify the design process, a Kalman filter [54] is used in this section.

The Kalman filter consists of the following two equations. The first one is a prediction equation that estimates the state $\hat{\mathbf{x}}_{add}^{LCL}(k)$ based on the previous state estimate $\hat{\mathbf{x}}_{add}^{LCL}(k-1)$ and the last actuation on the plant $u_{sat}(k-1)$:

$$\hat{\mathbf{x}}_\mathbf{p}(k) \;\; = \;\; \mathbf{A}_{add}^{LCL}\hat{\mathbf{x}}_{add}^{LCL}(k-1) + \mathbf{B}_{add}^{LCL}u_{sat}(k-1). \tag{67}$$

The second one is a correction equation that modifies this prediction $\hat{\mathbf{x}}_\mathbf{p}(k)$ based on the most recent measurement of the grid-side current $i_1(k)$:

$$\hat{\mathbf{x}}_{add}^{LCL}(k) \;\; = \;\; \hat{\mathbf{x}}_\mathbf{p}(k) + \mathbf{K_o}[i_1(k) - \mathbf{C}_{add}^{LCL}\hat{\mathbf{x}}_\mathbf{p}(k)] \tag{68}$$

where $\mathbf{K_o}$ is the Kalman gain.

This constant gain can be obtained in two different ways: by calculating its analytic expression [81] or by executing an iterative algorithm. Due to its simplicity, the authors recommend using the algorithm given in Section 4.6.

In order to calculate $\mathbf{K_o}$, two parameters need to be defined: the measurement (or sensor) noise N and the process (or plant) noise $\mathbf{Q}$. The first parameter, N, can be easily obtained from the grid-side current measurement i_1 when the voltage source converters (VSCs) is on and disconnected from the grid:

$$N \;=\; \mathcal{E}\{|i_1(k)|^2\} \tag{69}$$

where $\mathcal{E}\{\circ\}$ denotes mathematical expectation [54] and can be approximated by a time average of its argument. The second parameter, the process noise $\mathbf{Q}$, represents the uncertainty in the system model and disturbances. The relation between N and $\mathbf{Q}$ determines the bandwidth of the observer. A higher observer bandwidth is obtained if N is reduced (the grid-side current measurements are accurate) or if $\mathbf{Q}$ is increased (the disturbances vary a lot, e.g., the amplitude of voltage harmonics changes quickly). In the next section, the effect of $\mathbf{Q}$ is analyzed and a value for this parameter is proposed. The details for computing the Kalman gain $\mathbf{K_o}$ using N and $\mathbf{Q}$ are given in Section 4.6. The computational complexity of the control algorithm depending on the number of controlled harmonics is analyzed in detail in Section 4.7. This study shows that the computational load of the control algorithm is suitable for an implementation using a microcontroller.

4.3.   Performance Analysis of the Proposed Controller

The observer proposed in the previous section can, theoretically, eliminate as many harmonics as desired because the number n of frequencies where a resonant action (infinite gain) [1] can be placed is not limited. The only obvious practical limitation is the computational burden. In any case, current processors can execute the proposed control equations, which consist only of simple additions and multiplications (cf. Figure 55 and Section 4.7), without any problems even for large orders [cf. (63)]; hence, this constraint is virtually eliminated. Unfortunately, the disturbance rejection capability and the robustness of the grid-tied inverter is restricted by some fundamental limitations that are common to all linear controllers. In the following, these fundamental constraints are analyzed. A good understanding of them also helps to evaluate and choose a convenient value of $\mathbf{Q}$.

First a qualitative analysis, using the sensitivity function, of the tradeoffs involved in the design of the multi-frequency observer is presented in Section 4.3.1. Then, in Section 4.3.2, a quantitative analysis that relates $\mathbf{Q}$ with the position of the system poles is adopted to solve such tradeoffs. Finally, the advantage of the adopted reference-input structure (state-command) over the reference-input structure typically used with resonant controllers (output-error command) is studied in Section 4.3.3.

4.3.1.   Sensitivity Function of the System

The sensitivity function $S(f)$ of the system shows how the controller responds to disturbances [54]. It indicates how much the controller modifies (amplifies or attenuates) the
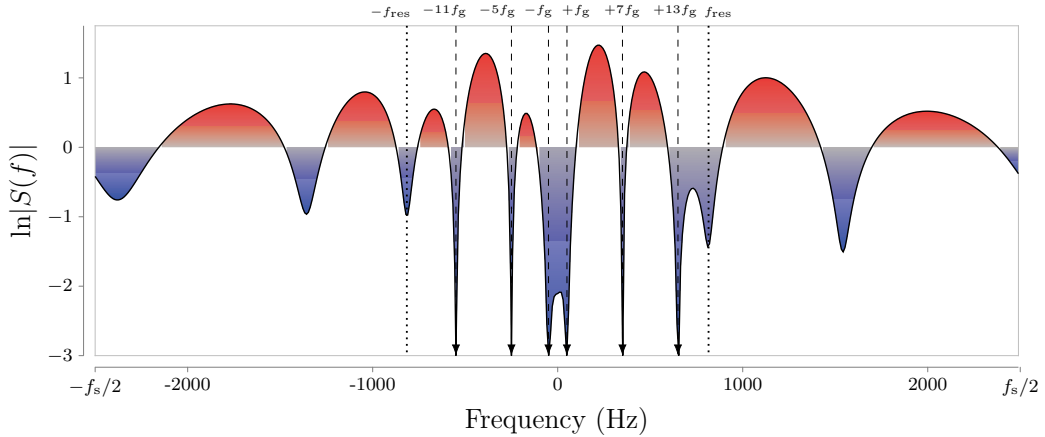
Figure 56. Graphical interpretation of the Bode integral [cf. (70)], for a multi-frequency controller, that shows a restriction that applies to the sensitivity function. In this example, the controller uses a Luenberger observer with dynamics that are twice as fast as the dominant pole of the compensator [1].

effect of disturbances (e.g., the grid voltage v_g, voltage source converters (VSCs) nonlinearities, and plant model mismatches) on the grid-side current with respect to the open-loop response. The calculation process to obtain $S(f)$ is given in Section 4.8.

Under normal operating conditions [111], the orders of the larger-amplitude harmonics in the per-phase grid voltage are $3, 5, 7, 9, 11,$ and 13. In addition, the harmonic orders associated to the voltage source converters (VSCs) nonlinearities coincide with those of the grid [112]. These voltage disturbances, under balanced conditions, correspond to the harmonic orders $h = -5, +7, -11,$ and $+13$ in the $\alpha\beta$ frame. The third and ninth harmonics are mapped to the zero-sequence component, and they do not cause any current circulation in a balanced or three-wire system. Furthermore, the negative sequence of the fundamental grid voltage ($h = -1$) should also be included in the disturbance model. The reason is that, although the unbalance of the fundamental component shall be within the range 0% to 3% during normal operation [111], it can be significantly bigger and become the main voltage disturbance under a fault condition, such as a voltage sag [111].

In this manner, a multi-frequency controller achieves zero sensitivity $S(f)$ at a set of arbitrarily specified frequencies [$S(f_g h_1) = S(f_g h_2) = \cdots = S(f_g h_n) = 0$], so as to eliminate the distortion, and a low sensitivity at the resonant frequency of the LCL f_{res}, in order to improve the lack of attenuation of the LCL filter around this frequency region and damp the resonance. Figure 56 shows $\ln|S(f)|$ when f_s is $10\,\text{kHz}$ and the harmonics $+1, -1, -5, +7, -11, +13$ are controlled. This is accomplished by placing observer open-loop poles at the desired frequencies [cf. (59)] in conjunction with the model of the plant, [cf. (55)], as done in (63). In the following, it is shown that if the number of harmonics controlled with zero steady-state error augments (n increases), then the sensitivity of the system at other frequencies is amplified. Therefore, the aforementioned set of main harmonic orders correspond to the frequencies among which the low-sensitivity regions of the controller should be distributed in order to maximize the performance.

The sensitivity function must satisfy two requirements [113]: an analytic and an algebraic design tradeoff. The first requirement (the analytic design tradeoff) states that, in the case of a system model with no open-loop poles outside the unit circle, such as (63), the average attenuation and amplification of disturbances over the complete frequency range where the controller operates $(-f_s/2, f_s/2)$ is zero, where f_s is the sampling frequency:

$$\int_{-f_s/2}^{f_s/2} \ln |S(f)| \, df \;\; = \;\; 0. \tag{70}$$

Thus, the choice of the sensitivity function $S(f)$ at one frequency affects its value at other frequencies. This effect is illustrated in Figure 56. The area above the curve must be equal to the area below the curve according to (70). Consequently, if the designer increases the number of frequencies with low sensitivity (to cancel more harmonics), the sensitivity at other frequencies also increases.

To try to overcome the previous constraint, a higher sampling rate f_s could be used. If the frequency band where the integration is performed widens, the new frequency region could be used to spread the area associated to sensitivities greater than one and yield a lower peak magnitude of the sensitivity function. Therefore, a double-update strategy is recommended because it increases f_s, compared to a conventional single-update strategy, and maintains the same switching frequency. Unfortunately, this approach (increasing f_s) cannot be used indefinitely. There is no significant improvement in sampling faster than a certain frequency, because of the second requirement, as explained next.

The second requirement (the algebraic design tradeoff) states that the sensitivity function $S(f)$ and the complementary sensitivity function $T(f)$ are related at all frequencies [54]:

$$S(f) + T(f) \;\; = \;\; 1. \tag{71}$$

The complementary sensitivity function $T(f)$ is the transfer function that relates the grid-side current i_1 with its reference i_1^* when an output-error feedback structure is used. The calculation process to obtain $T(f)$ is given in Section 4.8. This transfer function should be close to zero for frequencies above the resonant frequency of the LCL filter, due to the low-pass behavior of the plant (the LCL filter); otherwise, a high controller effort would be required, which would cause overmodulation in the voltage source converters (VSCs). From (71), as $T(f)$ approaches zero, $S(f)$ must approach one [i.e., $\ln|S(f)|$ goes to zero]. Therefore, although the designer could be tempted to spread the area with sensitivity greater than one in Figure 56 over a wide frequency range up to $\pm f_s/2$ to reduce the sensitivity peak, in reality this compensation has to take place in a narrower bandwidth, as $\ln |S(f)|$ must be close to zero beyond the available bandwidth (the resonant frequency of the LCL filter) of the closed-loop system.

There is another important reason to avoid spreading the red area (sensitivities greater than one) over high frequencies. The sensitivity function describes how much the controller modifies (amplifies or attenuates) the effect of disturbances. In order to achieve this control action, the controller relies on the system model. Nevertheless, this model usually presents deviations from the real plant, which are especially significant at high frequencies, where

unmodeled dynamics are more common. Therefore, if the controller responds to distur-
bances in such frequency ranges (i.e., the red area extends to high frequencies), then the
resultant system presents a greater sensitivity to plant and parameter variations.

4.3.2.   System Sensitivity with a Luenberger Observer and with a Kalman Filter

Section 4.3.1 has presented two restrictions that the sensitivity function has to meet. These
restrictions limit the performance of the controller by imposing a tradeoff between the
disturbance-rejection capability and the sensitivity of the system to parameter variations.
In what follows, the previous fundamental constraints are analyzed when a Luenberger ob-
server or a Kalman filter are used. In the case of the Kalman filter, the effect of the process
noise parameter $\mathbf{Q}$ on the observer poles and on the system sensitivity is shown.

   Conventionally, the design of the observer is carried out using frequency-domain tech-
niques and the dynamics of the observer are usually faster than those of the compen-
sator [81]. Nonetheless, although this frequency-domain design approach is convenient
when a small and fixed number of frequencies are controlled, it can result in a bad design
in terms of robustness when applied to a multi-frequency controller.

   The physical explanation of this problem that occurs with a conventional design is as
follows. When a complicated (high-order) voltage disturbance is estimated, unmodeled
disturbances in the grid-side current measurements and plant parameter variations cause
greater error in the estimation; therefore, a larger sensitivity is obtained. This problem is
further illustrated and analyzed in the next example.

   Figure 56 shows the sensitivity function of a controller designed for the system param-
eters that are used in the experimental setup (cf. Table 8). The harmonics $+1$, -1, $+7$,
-5, $+13$, -11 are controlled with zero steady-state error with a Luenberger observer that
is designed using the criteria included in [1], which are based on the frequency domain.
The system has fourteen closed-loop poles: four poles related to the plant model of the
compensator $p^p_{1,\cdots,4}$ and ten observer poles $p^o_{2,\cdots,10}$ (four from the plant model and six from
the disturbance model). The observer poles are placed at twice the frequency of the dom-
inant pole p^p_4 (cf. Figure 57) [1]. These closed-loop pole locations give a high sensitivity
(red areas in Figure 56) at frequency ranges above the resonant frequency, which yields
a low robustness. Another inconvenient is the presence of useless low-sensitivity areas
outside the targeted frequencies, which contribute to worsen the performance at other fre-
quencies. An optimum sensitivity function should have sensitivities lower than unity only
at the frequency regions of the targeted harmonics and at the resonant frequency of the LCL
filter. In addition, the sensitivities greater than one should be spread evenly in the rest of
the frequency range where the controller operates, i.e., below the cut off frequency of the
LCL filter. From the previous example it is clear that a better closed-loop pole-placement
strategy is needed when a multi-frequency controller is considered.

   Instead of designing the observer according to its dynamic characteristics, which re-
sults in a high sensitivity, a time-domain approach that minimizes the estimation error is
adopted. This method is particularly useful in this case, where a multi-frequency observer
is considered, because it frees the designer from defining the multiple required closed-loop
pole locations. In this manner, $\mathbf{K_o}$ is selected to give estimates of the plant state $\hat{\mathbf{x}}_\mathbf{2}$ and the
grid voltage $\hat{w}$ that minimize the estimation error under some assumptions. The Kalman
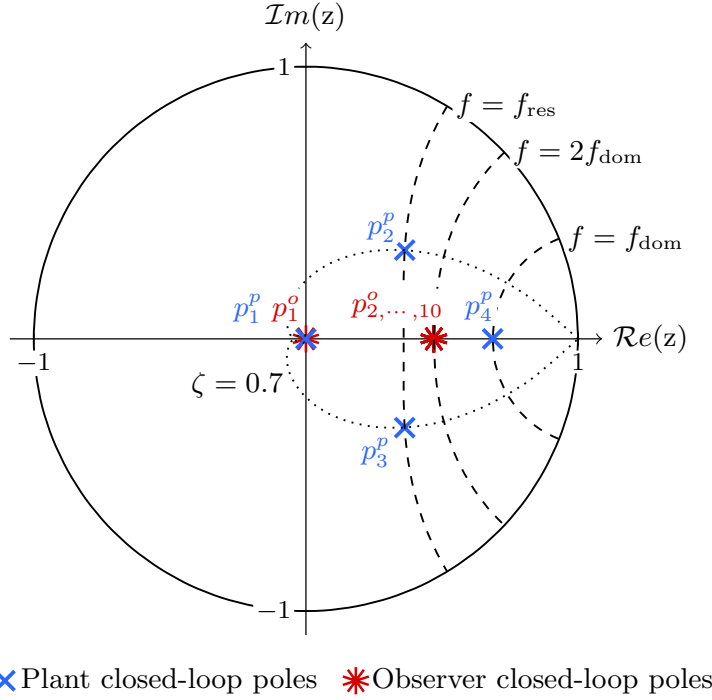
Figure 57. Closed-loop poles of the system using a direct discrete-time pole-placement strategy (a Luenberger observer).

filter (cf. Figure 55) is a solution to this minimization problem. This filter minimizes the mean square error of the estimated state vector $\hat{\mathbf{x}}_3$ assuming that the unmodeled disturbances that affect the plant $\mathbf{Q}$ and the measurement noise of the sensors N are random and of a certain mean square value. If these two assumptions are valid, then the proposed solution (the Kalman filter) is also optimal. The uncertainty about the characteristics of the grid voltage, the plant parameters, and the converter nonlinearities prevents from having the true N and $\mathbf{Q}$ values accurately and obtaining the optimal solution. Nevertheless, in application of the central limit theorem [114], the combined result of all the small remaining unmodeled effects (e.g., plant model mismatches and other small voltage harmonics) can be described as random. Therefore, the previous two assumptions are a reasonable approximation to describe all the aforementioned uncertainties without resorting to a complex nonlinear time-variable model. The process noise parameter $\mathbf{Q}$ assigns a quantitative value to all these unmodeled effects. The effect of $\mathbf{Q}$ is further illustrated in the following.

Figure 58 shows the sensitivity function of the proposed controller (cf. Figure 55) designed for the system parameters that are used in the experimental results (cf. Table 8). This sensitivity function achieves a better (compared to Figure 56) distribution of the low- and high-sensitivity frequency regions. In this manner, a more robust system to plant variations, namely, the grid impedance and the LCL filter parameters, is also obtained. In the following, the proposed Kalman filter is further analyzed and a value of $\mathbf{Q}$ is recommended.

Figure 59a shows the closed-loop roots of the sensitivity transfer function $S(f)$ for a sweep in the process noise $\mathbf{Q}$. When $\mathbf{Q}$ increases, the observer closed-loop poles move away from the disturbance zeros. Conversely, as $\mathbf{Q}$ approaches zero, the poles get closer to the disturbance zeros. The Kalman filter reallocates the rest of the observer zeros so as to yield an optimal sensitivity function for the values of N and $\mathbf{Q}$ provided. A detail of their effect on the magnitude is shown in Figure 59b. The value of $\mathbf{Q}$ is changed from 0.01% to 0.2%. The bandwidth of a multi-frequency observer is determined by the width of the low-sensitivity regions around the frequencies of interest (cf. Figure 58). Wide low-sensitivity frequency regions eliminate the targeted disturbances fast. The Kalman observer automatically adjusts the bandwidth of the observer (depending on the values of N and $\mathbf{Q}$ provided) by controlling the distance between the closed-loop poles of the observer and the zeros associated to the disturbances rejected with zero-steady state error, i.e., the disturbance zeros z_h^d. Based on the results of this analysis, a value of 0.1% is here recommended to be used in the design. This value can be modified from the proposed one to improve the performance depending on the particular conditions where the voltage source converters (VSCs) is installed. If, e.g., the voltage fluctuates significantly (at the fundamental or at harmonic frequencies) a higher value of $\mathbf{Q}$ is recommended. Conversely, if the voltage source converters (VSCs) is connected to a weak grid (the plant parameters vary significantly from the nominal model), then a lower $\mathbf{Q}$ yields a more robust controller.
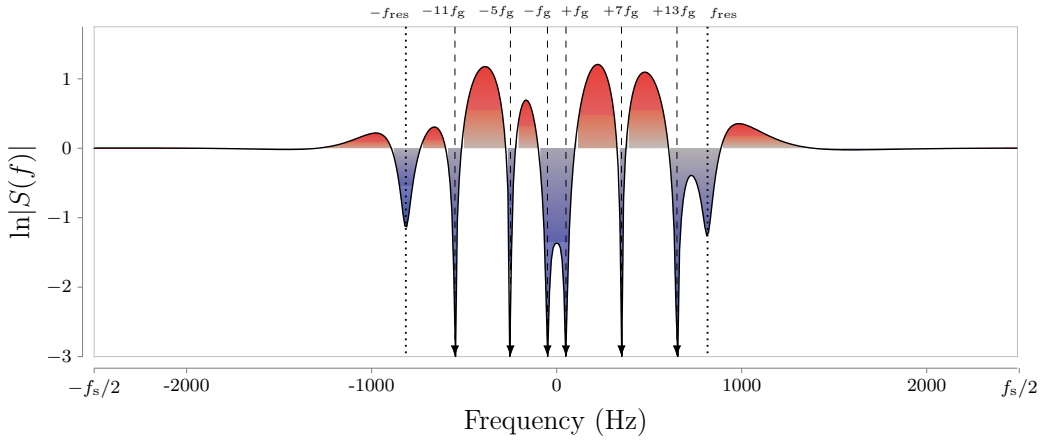

Figure 58. Graphical interpretation of the Bode integral for the proposed multi-frequency controller.

Furthermore, the plant closed-loop poles $p_{1,2,3,4}^p$ do not move, as expected from the pole-placement strategy adopted for the compensator [1]. This permits to obtain a constant reference-tracking performance irrespectively of the number of harmonics controlled and the bandwidth selected for the observer. A detailed analysis concerning this fact is given in Section 4.3.3.

Finally, it is important to notice that the proposed controller and the limitations presented do not depend on the LCL filter values because the design takes into account the parameters of the plant to be controlled. The described solution can operate with a resonant frequency of the LCL filter above or below $f_s/6$, i.e., the threshold above which
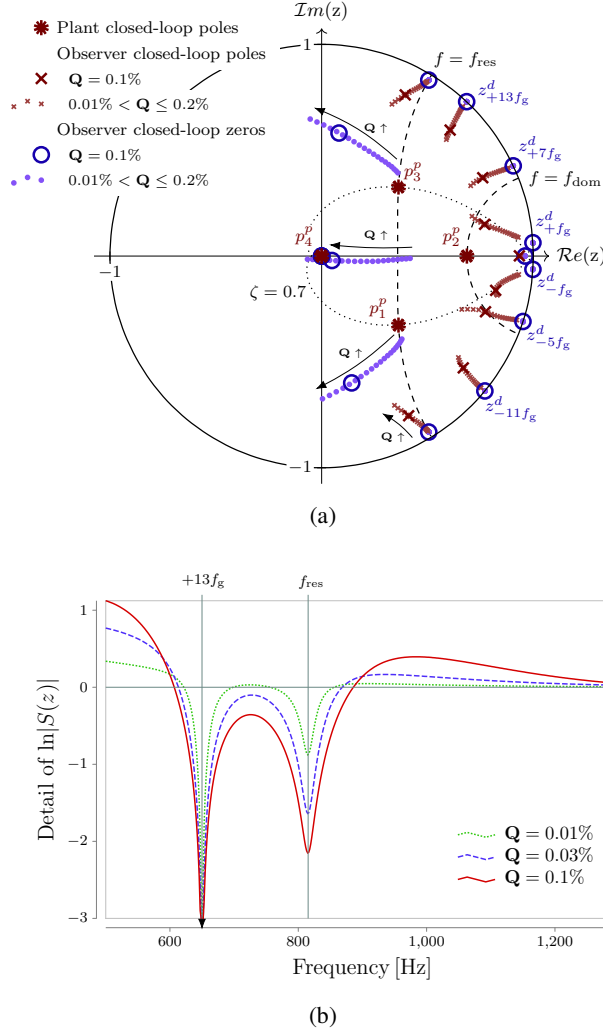
(a)

(b)

Figure 59. Sensitivity function $S(f)$ using a Kalman filter in the observer, and a direct discrete-time pole-placemente strategy [1] to design the compensator. a Closed-loop poles and zeros. b Detail of the magnitude at one of the controlled harmonics $(+13)$ and at the resonant frequency of the LCL filter.

conventional controllers have stability problems [47]. The achievable performance depends on the measured value of N (sensor noise) and the selected value of $\mathbf{Q}$ (process noise), which should be selected in accordance with the amount of unmodeled disturbances that the current controller has to deal with.

4.3.3. Analysis of the Reference-Tracking Performance of the Proposed Multi-Frequency Controller

The transfer function from the current reference i_1^* to the grid-side current i_1 is determined by the reference input structure selected. This section analyzes the advantage of the state-

command structure (the adopted solution) for a multi-frequency current controller over the traditional output-error feedback. The output-error feedback structure is typically used in classic transfer-function design [35, 99, 41], where the controller transfer function is driven by an error signal $e = i_1 - i_1^*$.
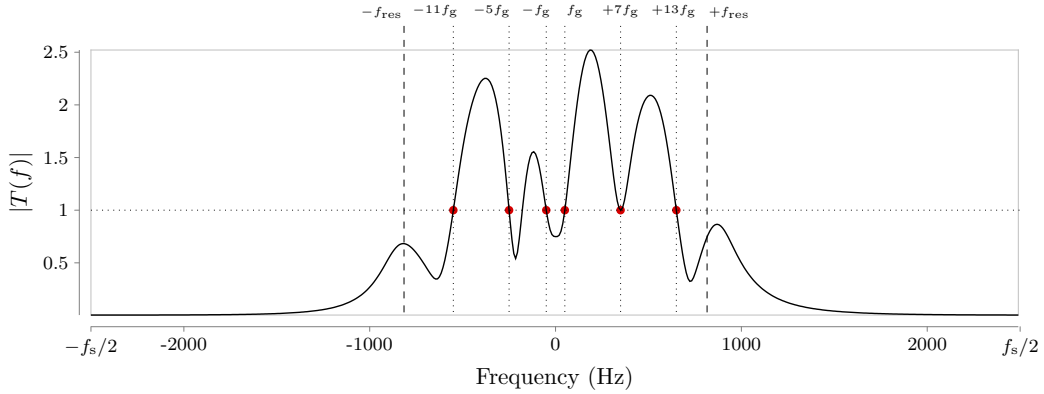

Figure 60. Magnitude of the complementary sensitivity function $T(f)$ (the transfer function that relates the current reference input i_1^* to the grid-side current reference i_1) when an output-error-command structure is used in a multi-frequency controller designed with the proposed Kalman observer.

On the one hand, when an output-error feedback is chosen, the reference-to-output transfer function is the complementary sensitivity function $T(f)$ (cf. Figure 60). This transfer function has unity gain at the frequencies controlled with zero steady-state error; however, it does not have a flat frequency response. In the particular case of a multi-frequency controller, there are several closed-loop poles at low frequencies [the observer poles in a state-space controller, cf. Figure 59a, or the controller poles in a classic transfer-function design] that significantly degrade the transient response to reference commands (non flat frequency response, cf. Figure 60). Depending on the harmonics controlled, the response would also vary because the denominator of this transfer function includes the closed-loop poles of the observer [cf. Figure 59a] or the closed-loop poles of the controller transfer function in a classic design.

On the other hand, if a state-command structure is used, the reference-to-output transfer function is not $T(f)$. Now the transfer function only contains the closed-loop poles of the plant, irrespectively of the number of harmonics controlled [81]. Hence, this transfer function has a flat frequency response below the cutoff frequency (cf. Figure 61), as expected from the plant closed-loop pole locations [1], and mainly determined by the dominant pole. The cutoff frequency ($-3dB$) is slightly smaller than f_{dom} due to the effect of the other three non-dominant closed-loop poles of the plant. In this manner, contrarily to a conventional resonant controller, the state-command structure does not modify or degrade the reference-tracking capability, irrespectively of the order of the observer [54]. Therefore, this reference-input structure presents an increasing advantage over the traditional solution as the number of harmonics controlled n augments.
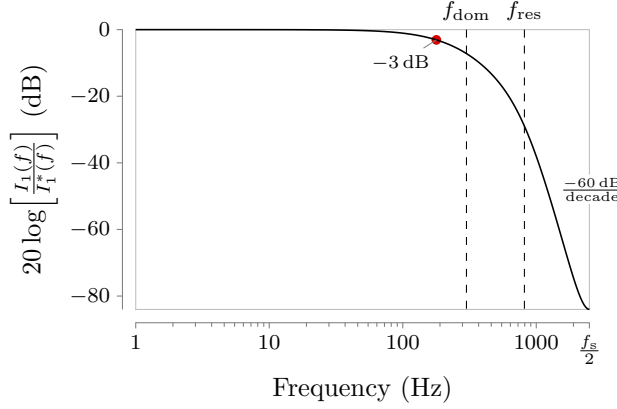
Figure 61. Magnitude of the transfer function that relates the current reference input i_1^* to the grid-side current reference i_1 when a state-command structure is used in a multi-frequency controller designed with the proposed Kalman observer.

4.4. Robustness to Grid Impedance Variations

The analysis presented in the previous section explains how the design process determines the achieved robustness. As explained, in order to obtain a high robustness, the control action should be focused only at the frequencies where disturbances are expected, namely, low-order grid-frequency harmonics. However, the previous theoretical analysis does not indicate the range of grid impedance values where the controller can operate. In this section, a numerical analysis is carried out to evaluate the stability of the controller for a wide range of grid impedance values.

The stability is assessed by calculating the time constant of the poles of the closed-loop system when the grid impedance is increased. This permits to easily assess the change in the transient response, which is determined by the pole with the slowest time constant. The time constant (or decay time-constant) of a pole at frequency f and damping ratio ζ is $\tau = 1/(2\pi f \zeta)$. Therefore, a time constant with a negative value indicates an unstable pole, i.e., a pole with negative damping.

In the case of a weak grid, the robustness of the controller can be modified depending on the feedforward gain implemented [115]. Since the proposed controller does not rely on a voltage feedforward to achieve stability, the analysis presented in this section was performed assuming that K_{ff} is zero so as to study the robustness of the current controller isolated from such effect.

Figure 62 shows regions of grid impedance, whose colors denote the value of the largest time constant τ_{max} in the system, that is, the time constant of the pole with the slowest dynamics. The relation between each color and its corresponding time constant interval is indicated in the label at the right of the figure. Both the resistive and the reactive components of the grid impedance (R_g and L_g respectively) are changed from zero to a value of 1 p.u., cf. base values in Table 8. Three different values of the design parameter $\mathbf{Q}$ are tested, namely, the recommended value of $0.1\,\%$ (cf. Section IV-B) and the two limit values shown in Figure 59a ($0.2\,\%$ and $0.01\,\%$).
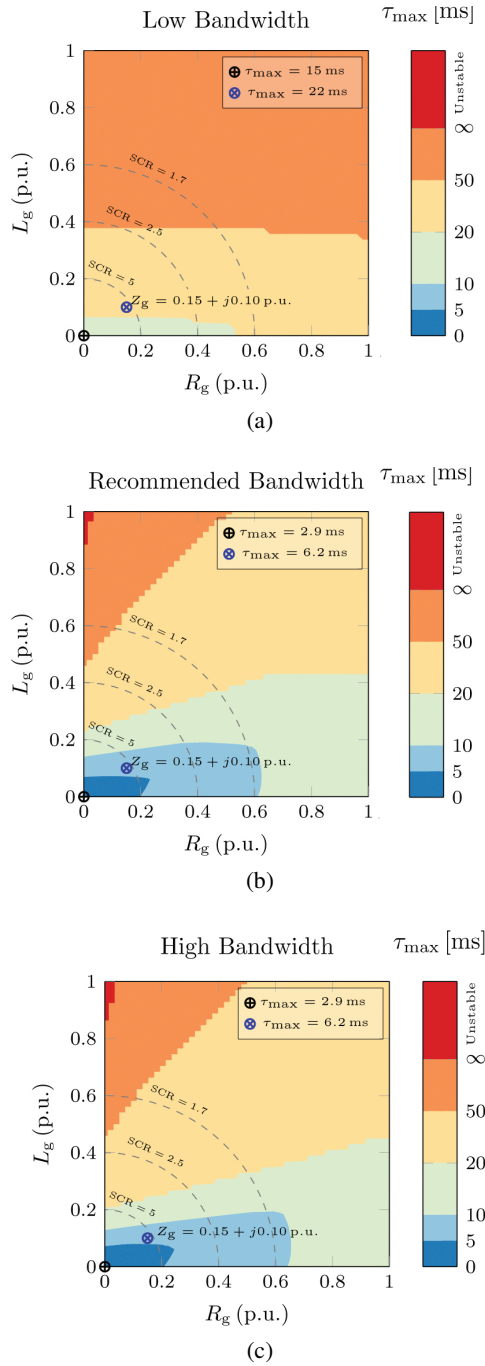
Low Bandwidth

Recommended Bandwidth

High Bandwidth

Figure 62. Stability regions as a function of the grid impedance. a Low bandwidth ($Q = 0.01\%$). b Recommended bandwidth ($Q = 0.1\%$). c High bandwidth ($Q = 0.2\%$).

When $\mathbf{Q}$ is set to $0.01\,\%$ [low bandwidth, cf. Figure 62a], the resultant design has a slower response to disturbances compared to the recommended value of $\mathbf{Q} = 0.1\,\%$ due to its larger time constant under nominal conditions ($R_\mathrm{g} = L_\mathrm{g} = 0$). Nevertheless, this design

has a high robustness and is always stable in spite of changes in the grid impedance value $(R_{\mathrm{g}}, L_{\mathrm{g}} \leq 1 \, \mathrm{p.u.})$.

If $\mathbf{Q}$ is set to $0.1\,\%$ (recommended bandwidth), a faster rejection of disturbances is obtained under nominal conditions ($Z_{\mathrm{g}} = 0 \, \mathrm{p.u.}$). However, τ_{max} increases faster, compared to the previous case, as the grid short circuit ratio (SCR) is increased, cf. Figure 62b. In particular, τ_{max} doubles when the inverter is tied to a weak grid with impedance $Z_{\mathrm{g}} = 0.15 + j0.1 \, \mathrm{p.u.}$, cf. Table 8. Nevertheless, the controller remains stable for values of the grid inductance L_{g} smaller than $0.8 \, \mathrm{p.u.}$, cf. Figure 62b. When the grid impedance becomes greater than such a large value, e.g., during islanded operation, a voltage controller should be used in place of a current controller.

Finally, when $\mathbf{Q}$ is set to $0.2\,\%$, no further improvements are obtained under nominal conditions. Nevertheless, the obtained grid-impedance region with a time constant smaller than $20 \, \mathrm{ms}$ is smaller than in the previous case because the system is less robust to changes in the plant parameters.

4.5.   Experimental and Simulation Results

The proposed multi-frequency controller is tested in a voltage source converters (VSCs) working as an inverter connected to a three-phase grid. A three-phase ac voltage source was used so as to generate the distorted grid voltage and the voltage sags. The switching frequency is $2.5 \, \mathrm{kHz}$ and a double-update scheme is used, yielding a sampling frequency of $f_{\mathrm{s}} = 5 \, \mathrm{kHz}$. Such low switching frequency reduces switching losses in the VSC and it represents a worst-case scenario in terms of the effect of the computation and modulation delays. The setup parameters are summarized in Table 8. The LCL filter was designed according to [83], resulting in a high-performance filter with reduced reactive values. The grid voltage has the harmonics presented in Table 9 and a total harmonic distortion (THD) of 10.5%. The controller was designed according to the proposed method. The PLL presented in [107] is used. Figures 63a and 63b show a diagram and a photograph of the experimental setup, respectively.

The first test shows the effect of the resonant action of the observer. If $\hat{w}$ is zero in the control law (cf. Figure 55), the resonant action of the observer is stopped. Figure 64a shows the effect of enabling $\hat{w}$ in the controller. Figure 64b displays the grid-side current spectrum before and after the activation of $\hat{w}$. As expected, when the resonant action is enabled, zero steady-state error is obtained at the controlled harmonics.

In the second test, the reference-tracking capability of the voltage source converters (VSCs) is evaluated. Figure 65a shows a reference step $i^*_{1,dq}$ in the positive-sequence dq frame (dq+ frame). The measured grid-side current $i_{1,abc}$ is transformed into the synchronous dq+ frame obtaining $i_{1,dq}$. Contrarily to the abc representation, the dq profiles allow to easily visualize the rise time, settling time, overshoot, steady-state error, and axis cross coupling in the response of the current controller. The 10%–90% rise time is approximately $1.5ms$, as expected from the bandwidth of the system $[T_{10\%-90\%} = \ln|9| / (2\pi f_{\mathrm{dom}}) = 1.2ms]$. This is in accordance with [1], where a f_{dom} of $150 \, \mathrm{Hz}$ (and other LCL filter) was used and a rise time of $2.5ms$ was obtained. In addition, negligible overshoot and good axis decoupling is attained because the response is not affected by the observer poles, as intended.
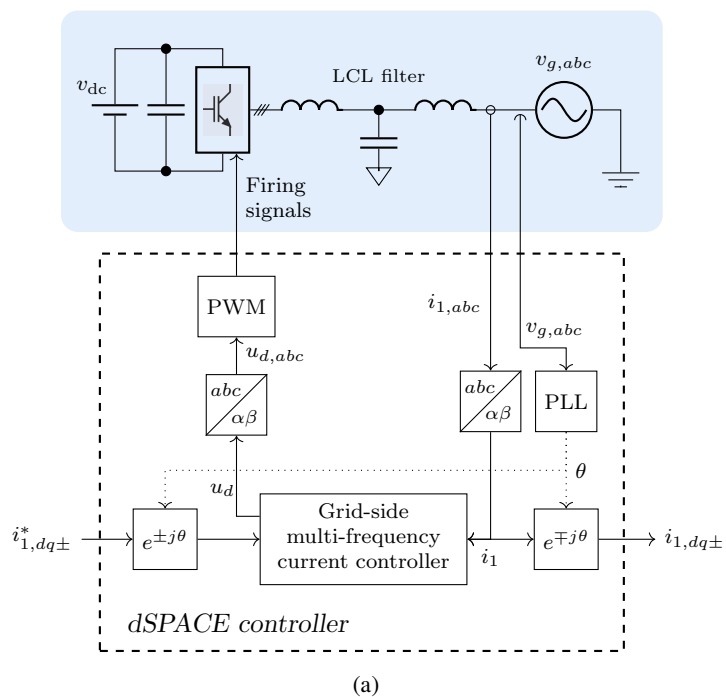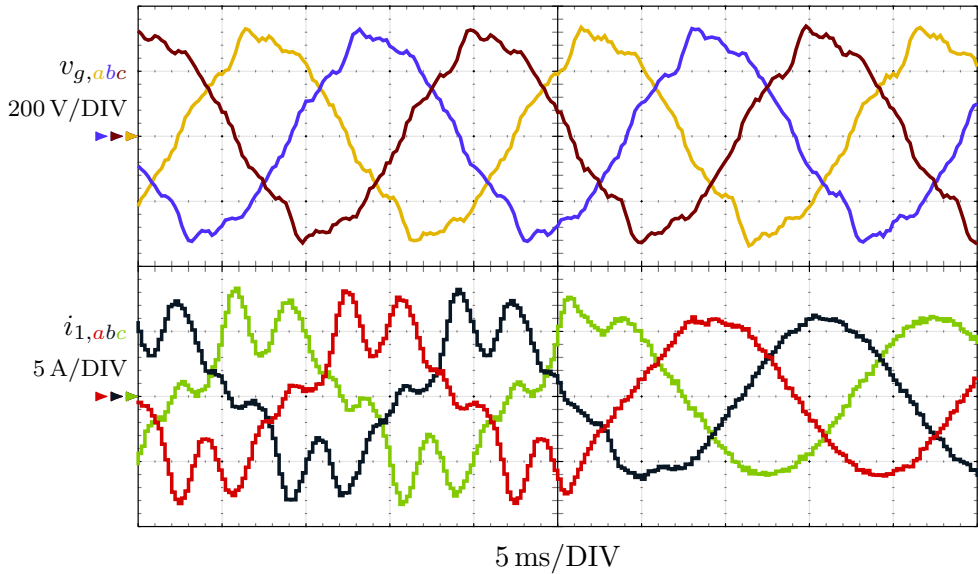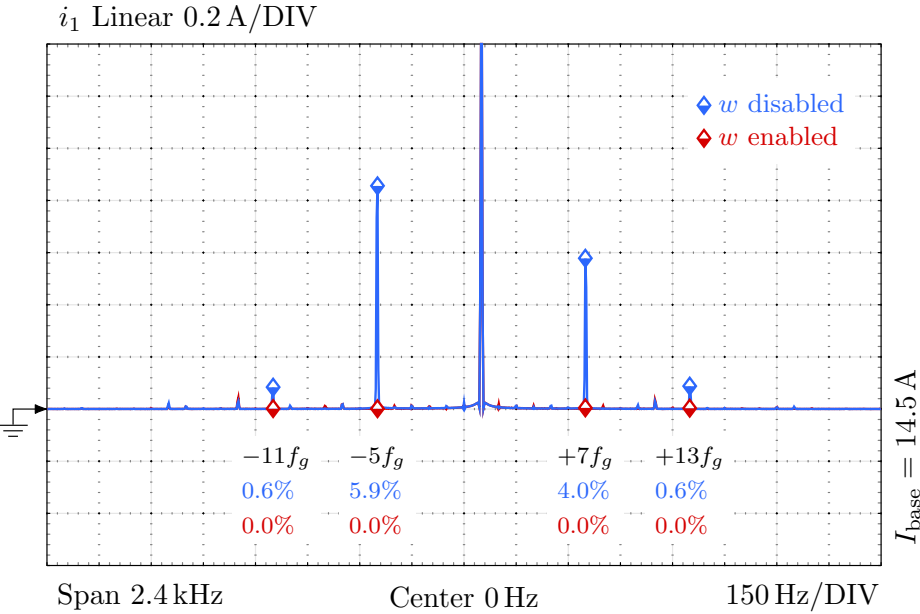
(a)
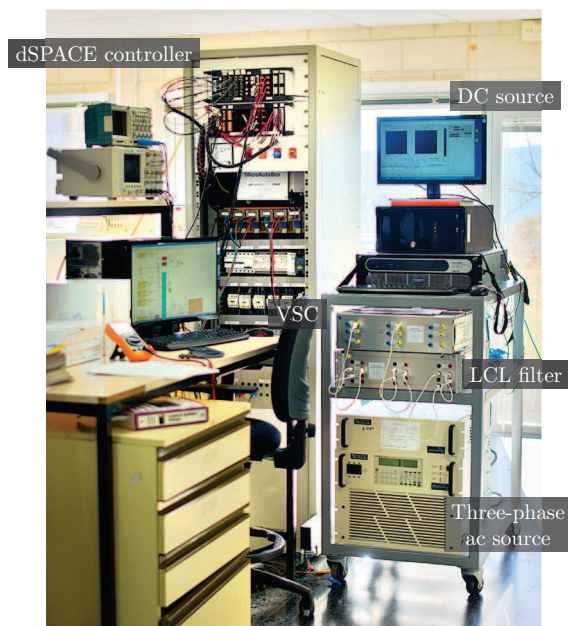
(b)

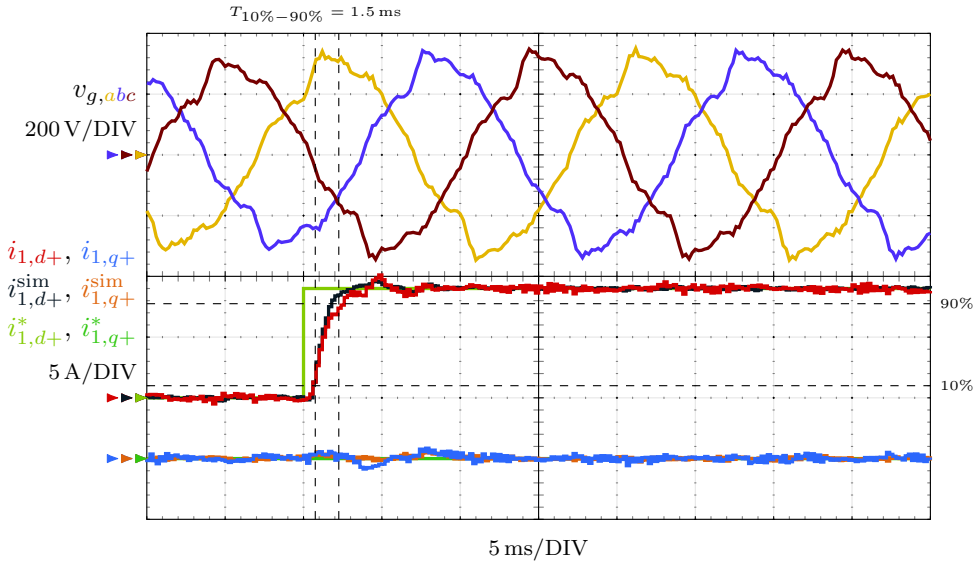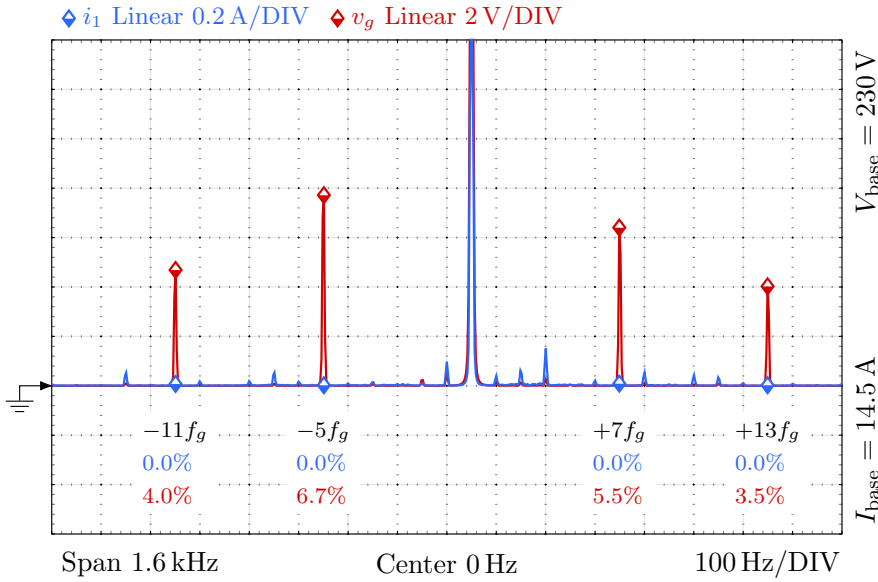Figure 63. Experimental setup. a Diagram. b Photograph.

(a)

(b)

Figure 64. Activation of the resonant action of the controller. a Time domain. b Frequency domain.

$T_{10\%-90\%} = 1.5\,\mathrm{ms}$

$v_{g,abc}$

$200\,\mathrm{V/DIV}$

$i_{1,d+},\ i_{1,q+}$
$i_{1,d+}^{\mathrm{sim}},\ i_{1,q+}^{\mathrm{sim}}$
$i_{1,d+}^{*},\ i_{1,q+}^{*}$

$5\,\mathrm{A/DIV}$

90%

10%

$5\,\mathrm{ms/DIV}$

(a)

◇ i_1 Linear $0.2\,\mathrm{A/DIV}$ ◇ v_g Linear $2\,\mathrm{V/DIV}$

$V_{\mathrm{base}} = 230\,\mathrm{V}$

$I_{\mathrm{base}} = 14.5\,\mathrm{A}$

$-11f_g$	$-5f_g$	$+7f_g$	$+13f_g$
0.0%	0.0%	0.0%	0.0%
4.0%	6.7%	5.5%	3.5%

Span $1.6\,\mathrm{kHz}$ Center $0\,\mathrm{Hz}$ $100\,\mathrm{Hz/DIV}$

(b)

Figure 65. Normal operation: the voltage harmonics are balanced. a Experimental and simulation waveforms ($i_{1,dq}$ and $i_{1,dq}^{\mathrm{sim}}$, respectively) for a reference step $i_{1,q+}^{*}$ in the positive synchronous frame dq+ rotating at the fundamental grid frequency f_g. b Experimental spectrum of the grid-side current and the grid-side voltage in the $\alpha\beta$ frame (i_1 and v_g, respectively).

Figure 65b shows the spectrum of the grid-side current $i_1(f)$ and the grid voltage $v_g(f)$ in the $\alpha\beta$ frame (both axis use a linear scale). As expected, the substantial voltage distortion ($-11, -5, -1, +7, +13$ harmonics) does not cause any current circulation due to the action of the proposed multi-frequency controller.

Figure 66 shows the grid-side current waveforms in the abc frame $i_{1,abc}$ and their corresponding experimental and simulation waveforms in the dq frame ($i_{1,dq}$ and $i_{1,dq}^{\text{sim}}$, respectively) during the previously described reference step test.

The third test evaluates the robustness of the controller to sags in the grid voltage. Sags usually cause unbalanced voltage grid conditions. In particular, a 40%-depth type-C sag [85] is generated. The response to voltage sags in different depth can be easily derived because the system is composed of a linear controller and a plant that can be described with a linear model, cf. Figure 55; therefore, the resultant closed-loop system is also linear. Using the scaling property of linear systems, it can be seen that scaling the input (changing the depth of a voltage sag) scales the output by the same factor. This type of sag contains both fundamental voltage sequences (±1) in addition to the harmonics described in Table 9. Figure 67a shows the transient response of the current controller to this voltage sag. The current reference $i_{1,dq+}^{*}$ is kept constant so as to observe the response to the sag isolated from other actions that also cause transients in the grid-side current. A transient time of $10ms$ is obtained due to the dynamics of the Kalman observer [cf. the observer poles in Fig 59a]. The increase in the disturbance-rejection transient duration (compared to $6ms$ in [1]) is an unavoidable limitation, as explained in Section 4.3, because now six frequencies are being controlled with zero steady-state error instead of just two as in [1]. Notwithstanding, the resulting response is in any case relatively fast.

Figure 67b shows the response in the frequency domain of the controller during the sag (the spectrum starts being measured $15ms$ after the sag event to capture the steady-state regime). In this case, due to the unbalanced grid voltage, both positive and negative sequences of the harmonic voltages from Table 9 arise in the $\alpha\beta$ frame. The controller continues eliminating the targeted disturbances, including the negative sequence of the fundamental (harmonic -1). The new grid-voltage harmonics ($-7, +5$, and ±3) are associated to the unbalance and are not eliminated; hence, they cause some undesirable current circulation (cf. Figure 58). This explains the increased error during the sag fault [cf. Figures 65 and 67]. Of course, the designer could also include these harmonic frequencies in the design and eliminate them, at the expense of increasing the sensitivity at other frequencies, as it has been described in Section 4.3. Nevertheless, the main voltage harmonics, as well as the fundamental unbalance $v_g(-f_{\text{g}})$, which is now the most important voltage disturbance, are still rejected with zero steady-state error.

Figure 68 shows the grid-side current waveforms in the abc frame $i_{1,abc}$ and their corresponding experimental and simulation waveforms in the dq frame ($i_{1,dq}$ and $i_{1,dq}^{\text{sim}}$, respectively) during the previously described 40%-depth type-C sag [85].

The fourth test shows the effect of modifying $\mathbf{Q}$. Two values of $\mathbf{Q}$ are tested: the recommended value of 0.1% and one an order of magnitude smaller (0.01%). As aforementioned, $\mathbf{Q}$ controls the width of the blue (low sensitivity) frequency regions shown in Figure 58. In Figure 69, the grid voltage is changed from a low-distortion situation to the highly-distorted voltage defined in Table 9. The transient duration in Figure 69b increases with respect to Figure 69a, as expected, because the observer has a lower bandwidth (cf. Figure 59 and 62).
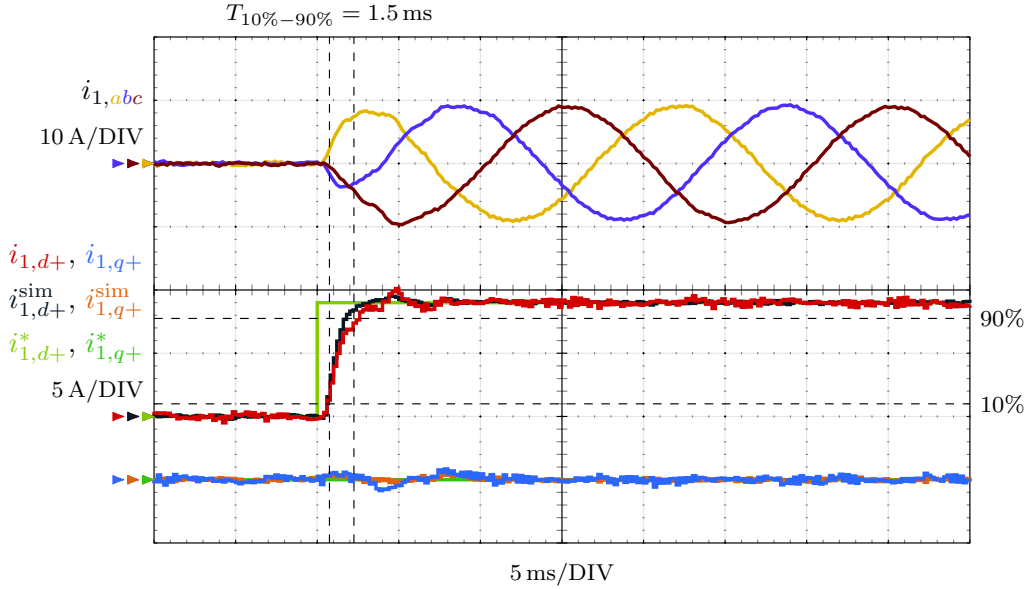
Figure 66. Grid-side current waveforms in the abc frame $i_{1,abc}$ and their corresponding experimental and simulation waveforms in the dq frame ($i_{1,dq}$ and $i^{\text{sim}}_{1,dq}$, respectively). for a reference step $i^*_{1,q+}$ in the positive synchronous frame dq+ rotating at the fundamental grid frequency f_g during normal operation, e.g., the voltage harmonics are balanced.

Figure 70 shows the grid-side current waveforms in the abc frame $i_{1,abc}$ and their corresponding experimental and simulation waveforms in the dq frame ($i_{1,dq}$ and $i^{\text{sim}}_{1,dq}$, respectively) during the previously described grid-voltage distortion-step test.

In order to assess the robustness of the proposal when connected to a weak grid, the fifth and last test shows the operation of the controller under the same conditions as in the third test (a 40%-depth type-C sag with harmonic distortion) but connected to a weak grid. The weak grid is emulated by an impedance in series with the grid voltage. Now the grid has an impedance Z_g with a value of $0.1 + j0.15$ p.u., cf. Table 8. This grid impedance value is also denoted with a cross mark in Figure 62. Such change causes a small reduction of the damping of the system, cf. Figure 62b. In particular, when Z_g is $0.1 + j0.15$ p.u., the smallest damping of the system is lower than 0.05 (orange region); whereas, under nominal conditions, the minimum damping is higher than 0.05 (blue region). According to the analysis presented in Section 4.3, the stability is not lost when the grid impedance is changed. Furthermore, the transient dynamics are not significantly modified, as expected from the small change in the damping of the system. Figure 71a shows the response of the current controller to the previously described voltage sag. A 5-A overshoot in both dq axis is obtained, which is slightly smaller than the the 8-A overshoot measured in the nominal case, see Figure 67a. Such reduction in the current overshoot is due to the increase in the grid-impedance value, which limits the current during the fault event. Concerning the settling time, both cases show a settling time of approximately 10-ms. An exact value cannot be measured because the uncontrolled unbalanced harmonics that appear during
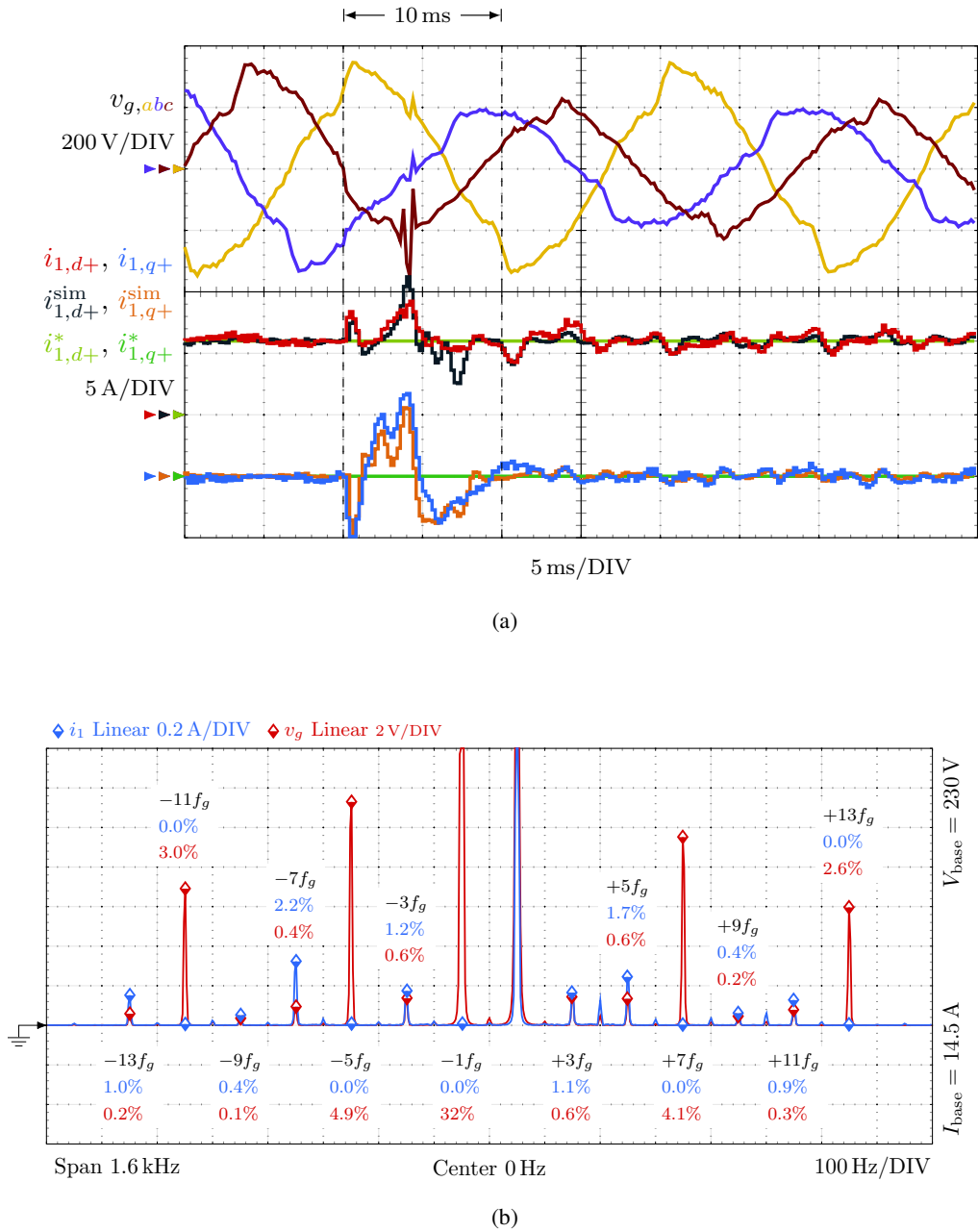
(a)

(b)

Figure 67. Operation during a 40%-depth type-C sag [85]. a Experimental and simulation waveforms ($i_{1,dq}$ and $i_{1,dq}^{\mathrm{sim}}$, respectively). b Experimental spectrum of the grid-side current and the grid-side voltage in the $\alpha\beta$ frame (i_1 and v_g, respectively). Notice that during the sag $v_g(-f_g) \neq 0$ and the voltage harmonics are unbalanced (the spectrum starts being measured 15 ms after the sag event to capture the steady-state regime).
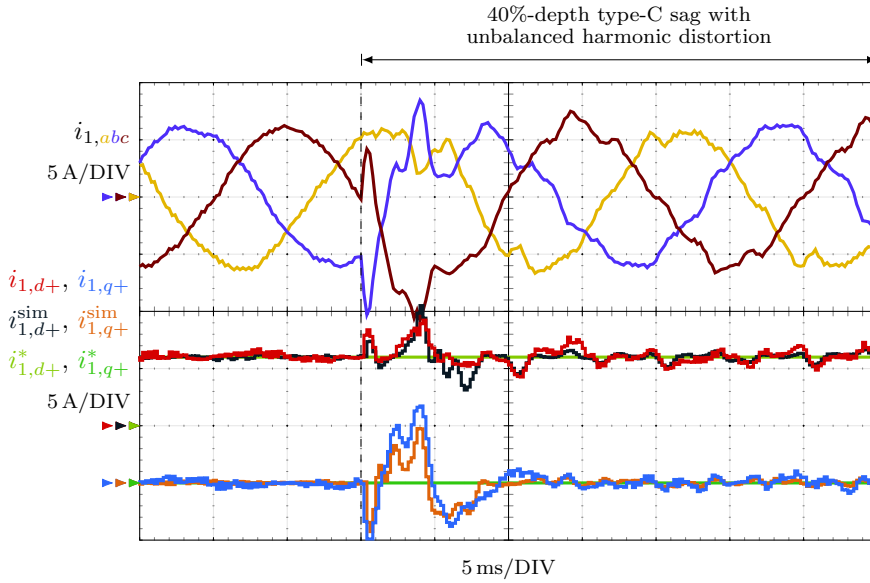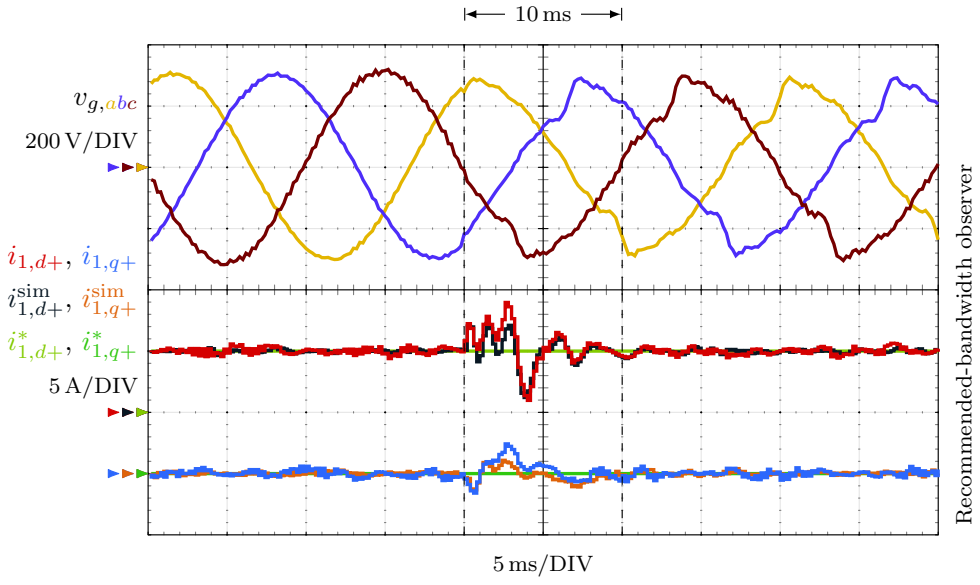
Figure 68. Grid-side current waveforms in the abc frame $i_{1,abc}$ and their corresponding experimental and simulation waveforms in the dq frame ($i_{1,dq}$ and $i_{1,dq}^{\mathrm{sim}}$, respectively) during a 40%-depth type-C sag [85]. Notice that during the sag $v_g(-f_g) \neq 0$ and the voltage harmonics are unbalanced.

the sag event cause an additional steady-state error. Contrarily to Figure 67a, now the measured voltage at the PCC $v_{\mathrm{g},abc}$ contains more switching noise because a voltage divider is formed by the LCL filter and the grid impedance, cf. Figure 72. Therefore, some of the large switching harmonics created by the VSC appear at the PCC. Nevertheless, there is no current circulation at the design selected frequencies in spite of the change in the grid impedance, cf. Figure 71b, due to the resonant action of the observer.

The next test assesses the response to a step in the reference when an inductive load is connected to the output. Figure 116 shows the output voltage in the abc frame $v_{C,abc}^{\mathrm{sim}}$ and in the positive synchronous frame dq+ rotating at the fundamental output frequency $v_{C,dq}^{\mathrm{sim}}$ for a reference step $v_{C,dq}^*$ from zero to the rated voltage. Compared to the unloaded condition, cf. Figure 112, the transient response is slightly modified because the plant model changes with respect to the nominal model when a load is connected. Nonetheless, such change in the response is small because the proposed design offers a large robustness to plant parameter variations.

Figure 73a and 73b show the response of the proposed current controller with and without a feedforward of v_{g}, respectively, to a 40%-depth type-C sag [85] when the voltage source converters (VSCs) is connected to the previously indicated weak grid. In both cases, a stable operation is obtained. In order to reduce this switching distortion in the visualization, these new oscilloscope captures display the voltage at the PCC $v_{\mathrm{g},abc}$ without its zero-sequence component v_0, as explained above. Figure 74 shows the grid-side current waveforms in the abc frame $i_{1,abc}$ and their corresponding experimental and simulation
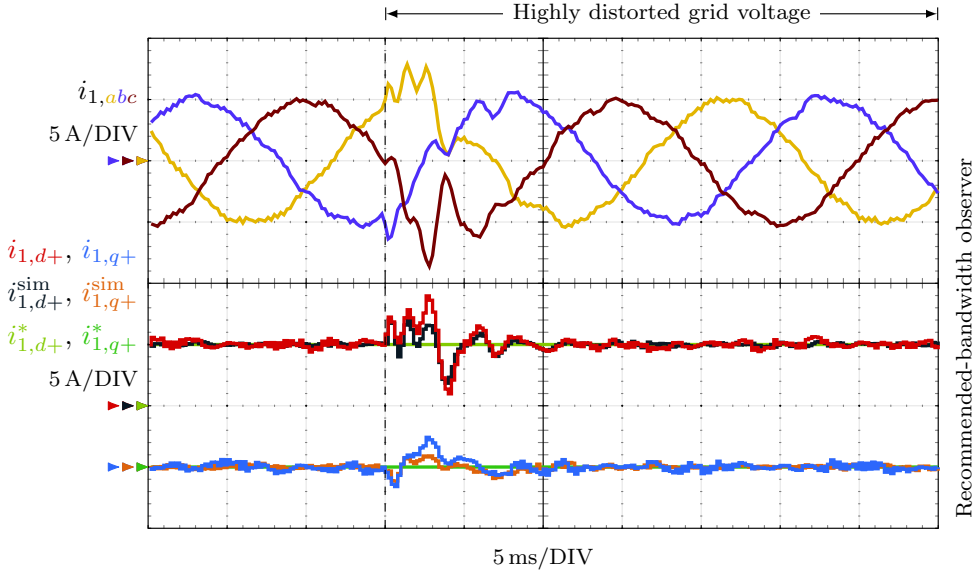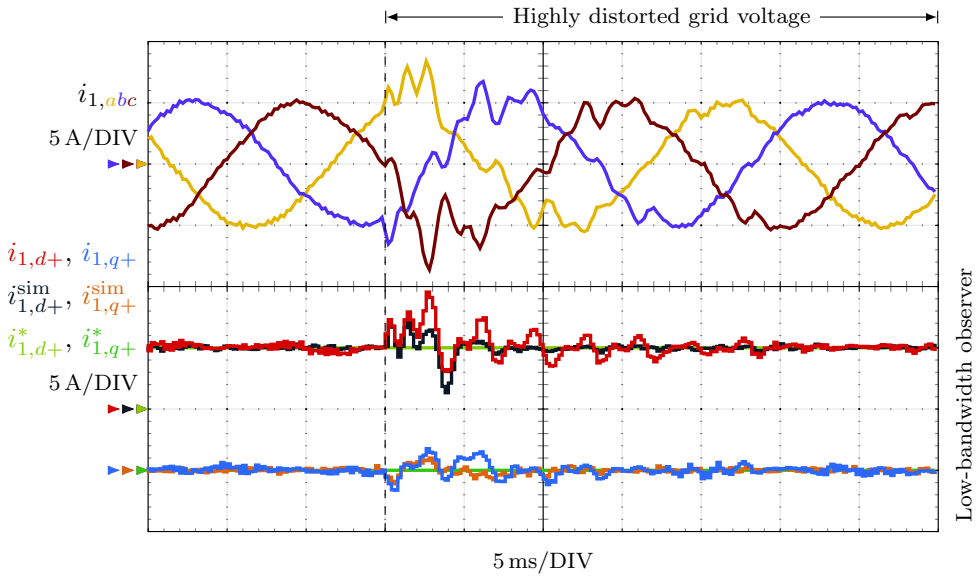
(a)
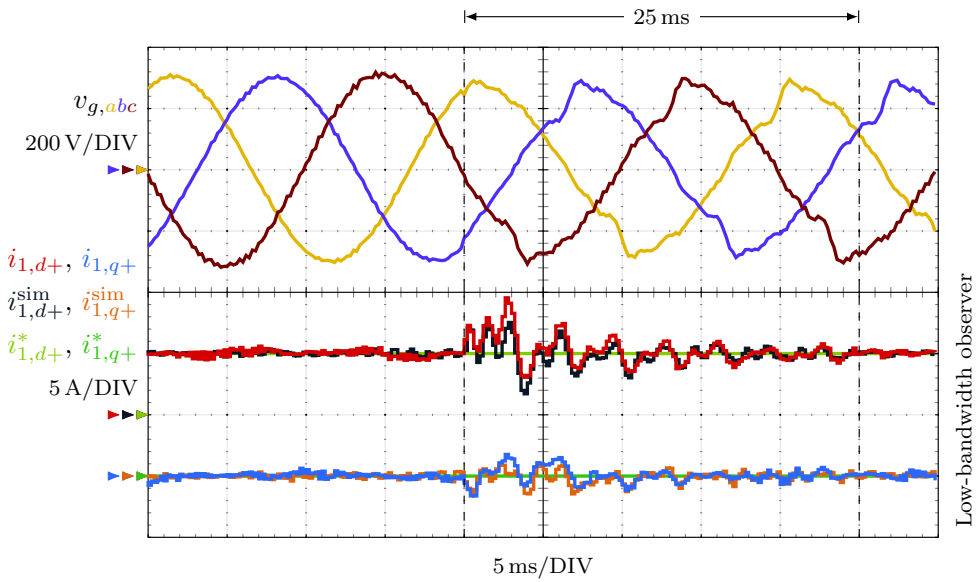
(b)

Figure 69. The grid voltage is changed from a low-distortion situation to the highly distorted voltage defined in Table 9. a Recommended-bandwidth observer ($\mathbf{Q} = 0.1\%$). b Low-bandwidth observer ($\mathbf{Q} = 0.01\%$).

Figure 70. Grid-side current waveforms in the abc frame $i_{1,abc}$ and their corresponding experimental and simulation waveforms in the dq frame ($i_{1,dq}$ and $i_{1,dq}^{sim}$, respectively) when the grid voltage is changed from a low-distortion situation to the highly distorted voltage defined in Table 9. a Recommended-bandwidth observer ($\mathbf{Q} = 0.1\%$). b Low-bandwidth observer ($\mathbf{Q} = 0.01\%$).
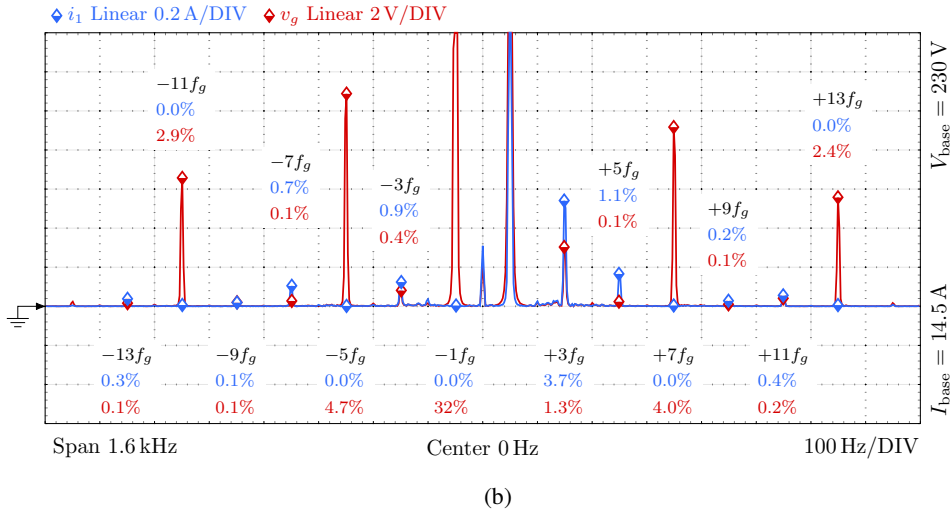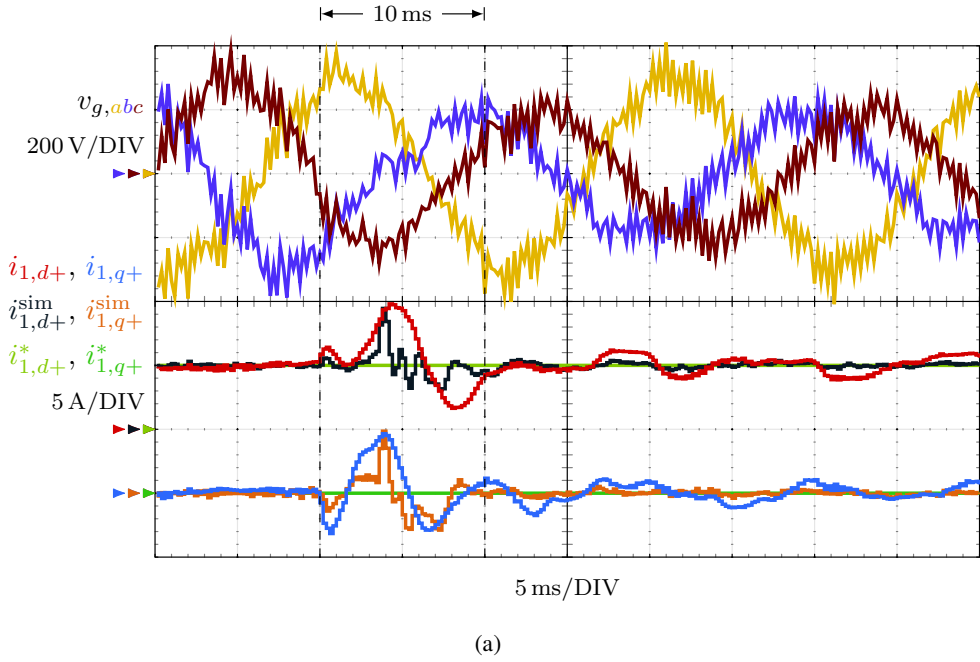
(a)

(b)

Figure 71. Operation during a 40%-depth type-C sag [85] with grid impedance of $Z_\mathrm{g} = 0.15 + j0.10$ p.u. a Experimental and simulation waveforms ($i_{1,dq}$ and $i_{1,dq}^\mathrm{sim}$, respectively). b Experimental spectrum of the grid-side current and the grid-side voltage in the $\alpha\beta$ frame (i_1 and v_g, respectively). The spectrum starts being measured 15 ms after the sag event to capture the steady-state regime.
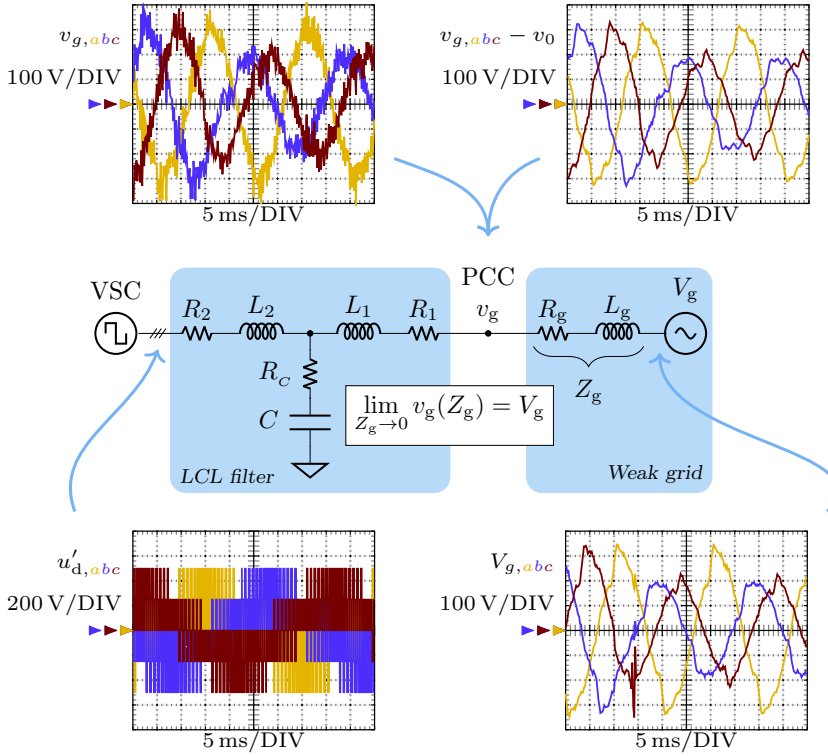
Figure 72. The voltage at the PCC is the output of a voltage divider formed by the LCL filter and the grid impedance Z_g.

waveforms in the dq frame ($i_{1,dq}$ and $i_{1,dq}^{\mathrm{sim}}$, respectively) during the previously described voltage sag.

4.5.1.   Experimental Comparison between the Proposed Controller and a Traditional Multi-Frequency Current Controller

An experimental comparison between the proposed controller and a traditional multi-frequency current controller is presented below. The new experimental results show the advantages of the proposed multi-frequency current controller compared to a transfer-function-based controller. Both the reference-tracking performance and the robustness to parameter variations are compared. The implemented transfer-function-based controller is composed of a PR controller tuned at the grid frequency in the $\alpha\beta$ frame (± 1 harmonics), and two resonant controllers tuned at the sixth and twelfth harmonics in a synchronous dq frame rotating at the grid frequency. These last two resonant controllers eliminate the -5 and $+7$, and the -11, $+13$ harmonics, respectively, in the $\alpha\beta$ frame. The design of these three resonant controllers was performed according to [37]. The first experimental test shows the reference-tracking performance of the previously described transfer-function-based current controller. The same setup parameters are used, cf. Table 8, in order to obtain a valid comparison. Such parameters result in a resonant frequency close to the critical resonant frequency where a controller cannot stabilize the system [47] ($f_{\mathrm{res}} = f_{\mathrm{s}}/6.1$).
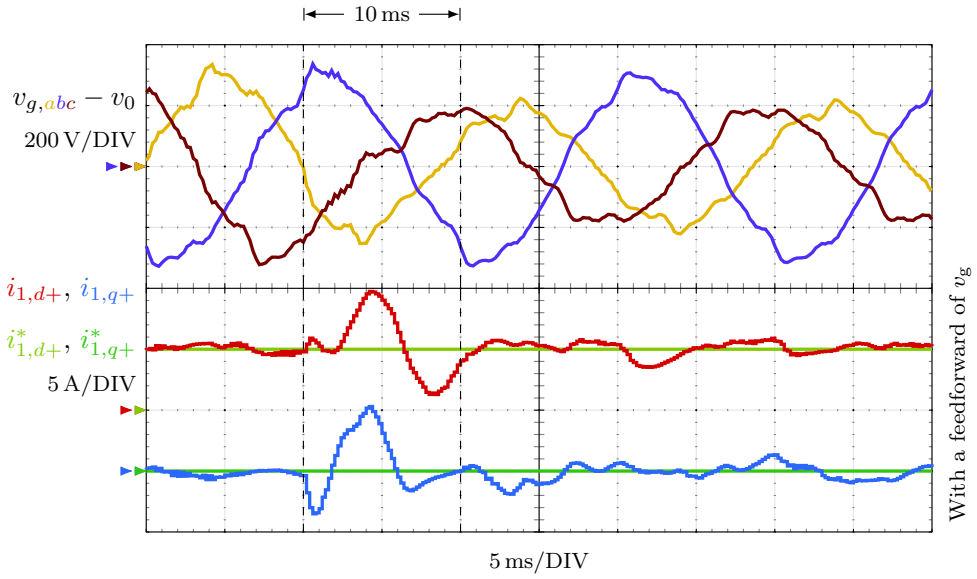
(a)
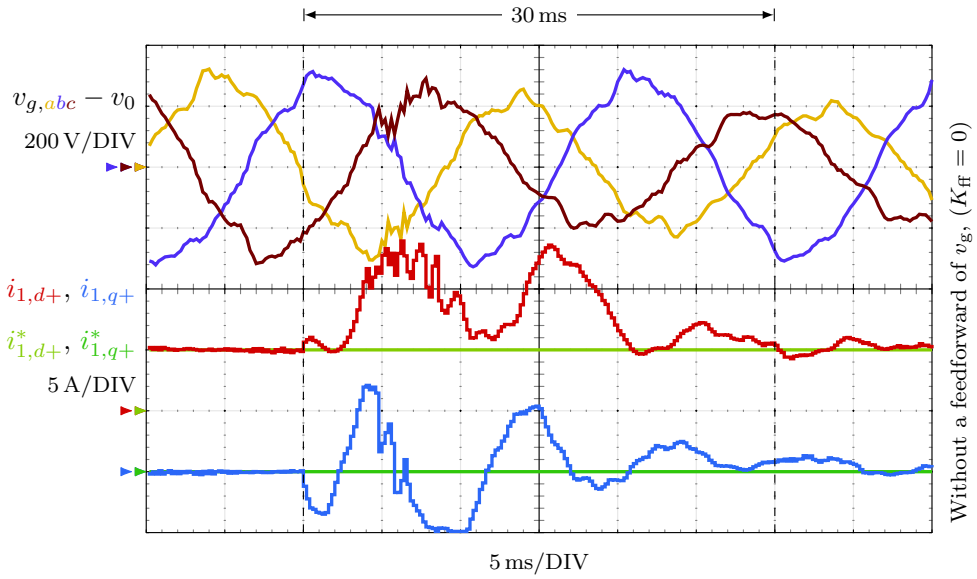
(b)

Figure 73. Effect in the grid-side current $i_{1,dq}$ of the voltage feedforward when the voltage source converters (VSCs) is connected to a weak grid with an impedance value of $0.15 + j0.10$ p.u. and a 40%-depth type-C sag [85] occurs. a With the recommended feedforward. b Without a feedforward of the voltage at the PCC ($K_{\text{ff}} = 0$).

Figure 74. Grid-side current waveforms in the abc frame $i_{1,abc}$ and their corresponding experimental and simulation waveforms in the dq frame ($i_{1,dq}$ and $i_{1,dq}^{\text{sim}}$, respectively) when the grid impedance is increased to a value of $Z_{\text{g}} = 0.15 + j0.10\,\text{p.u.}$ and a 40%-depth type-C sag [85] occurs. a With the recommended feedforward. b Without a feedforward of the voltage at the PCC ($K_{\text{ff}} = 0$).

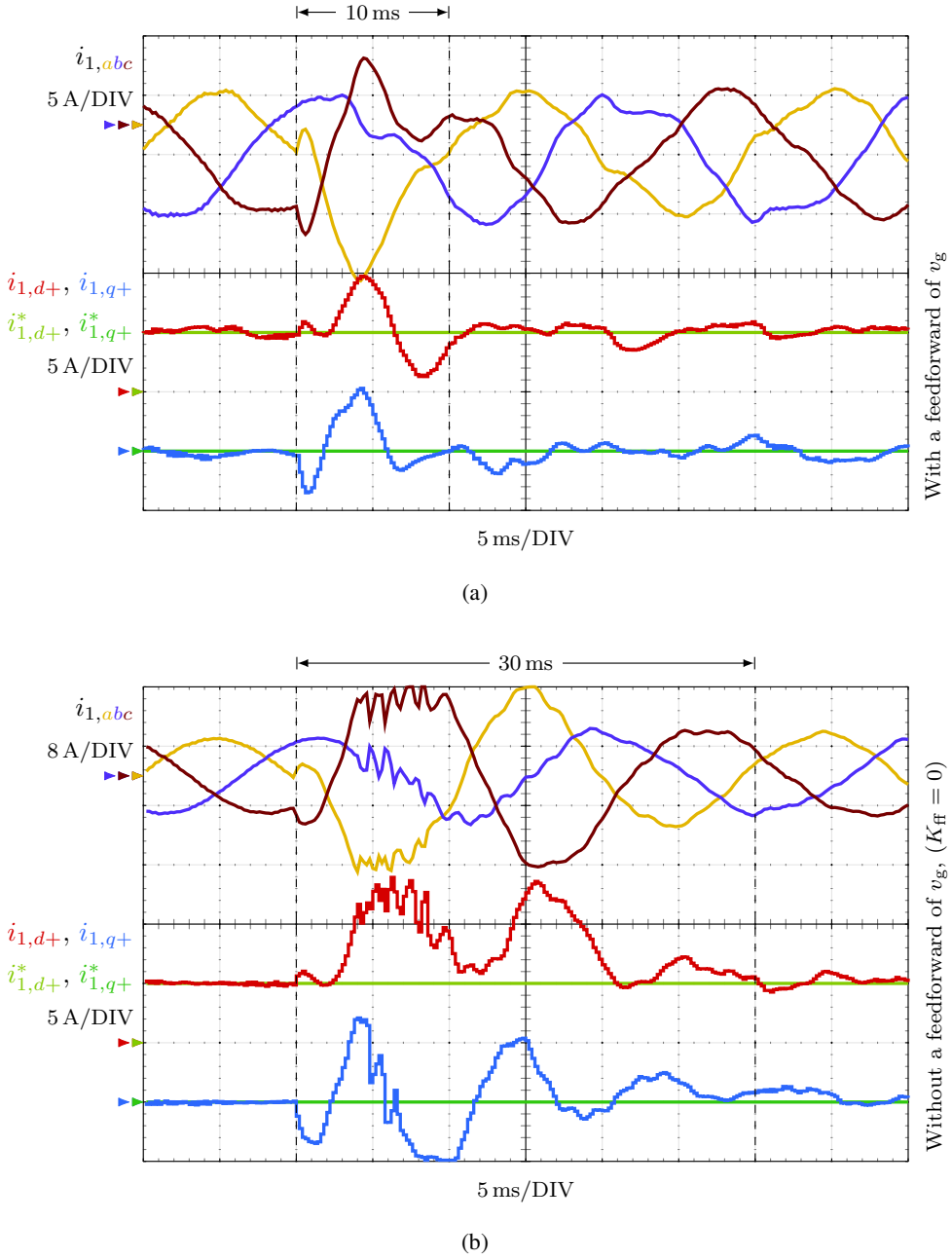Transfer-function-based controller ($f_{\text{res}} = f_{\text{s}}/6.1$)

Figure 75. Grid-side current waveforms in the abc frame $i_{1,abc}$ and their corresponding experimental and simulation waveforms in the dq frame ($i_{1,dq}$ and $i_{1,dq}^{\text{sim}}$, respectively) when commutation begins ($C = 30\mu F$, $f_{\text{res}} = f_{\text{s}}/6.1$) and a transfer-function-based controller is used.

Transfer-function-based controller ($f_{\text{res}} = f_{\text{s}}/5.6$)

(a)

Figure 76. Continued on next page.

Transfer-function-based controller ($f_{\mathrm{res}} = f_{\mathrm{s}}/5.0$)

$i_{1,abc}$

5 A/DIV

$i_{1,d+}$, $i_{1,q+}$
$i_{1,d+}^{\mathrm{sim}}$, $i_{1,q+}^{\mathrm{sim}}$
$i_{1,d+}^{*}$, $i_{1,q+}^{*}$

5 A/DIV

5 ms/DIV

(b)
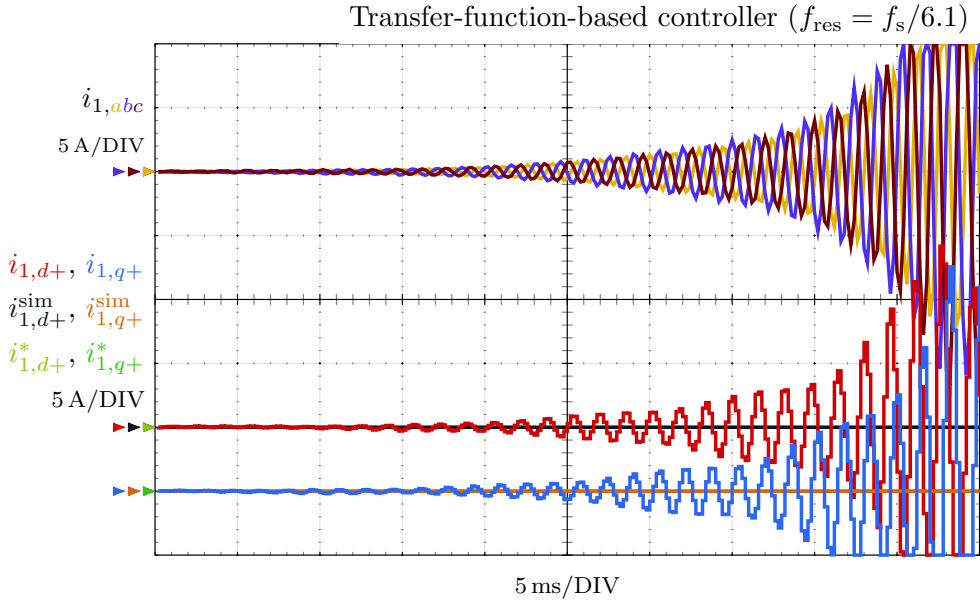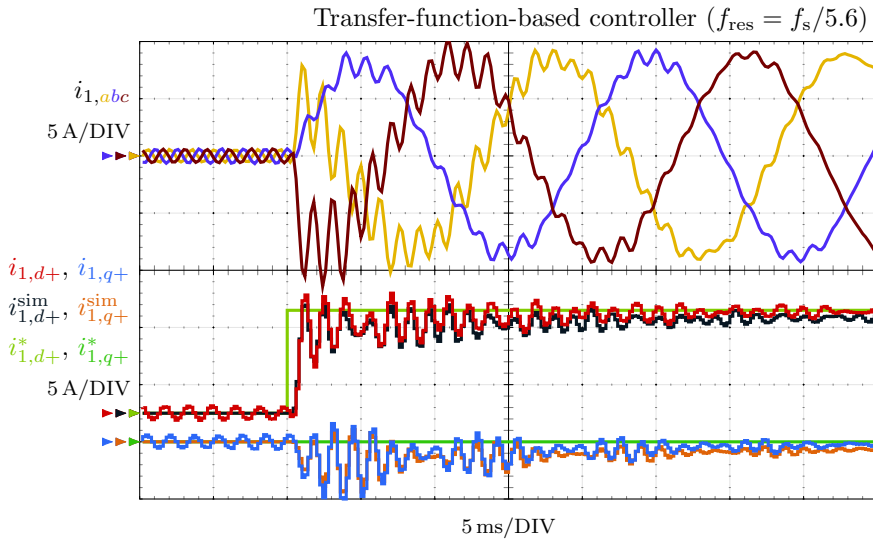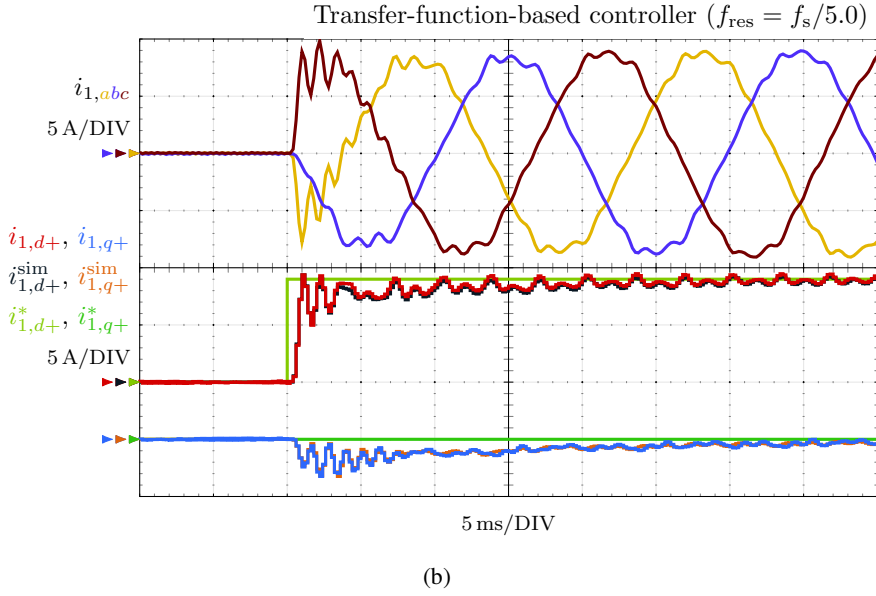
Figure 76. Grid-side current waveforms in the abc frame $i_{1,abc}$ and their corresponding experimental and simulation waveforms in the dq frame ($i_{1,dq}$ and $i_{1,dq}^{\mathrm{sim}}$, respectively) for a reference step $i_{1,d+}^{*}$ in the positive synchronous frame dq+ rotating at the fundamental grid frequency f_g. A transfer-function-based controller is used. a $C = 25\mu F$, $f_{\mathrm{res}} = f_{\mathrm{s}}/(5.6)$. b $C = 20\mu F$, $f_{\mathrm{res}} = f_{\mathrm{s}}/(5.0)$.

Transfer-function-based controller ($f_{\mathrm{res}} = f_{\mathrm{s}}/5.0$)

$i_{1,abc}$

5 A/DIV

$i_{1,d+}$, $i_{1,q+}$
$i_{1,d+}^{*}$, $i_{1,q+}^{*}$

5 A/DIV

$Z_{\mathrm{g}} = 0.15 + j0.02\,\mathrm{p.u.}$ ($2.5\,\Omega$, $1.2\,\mathrm{mH}$)
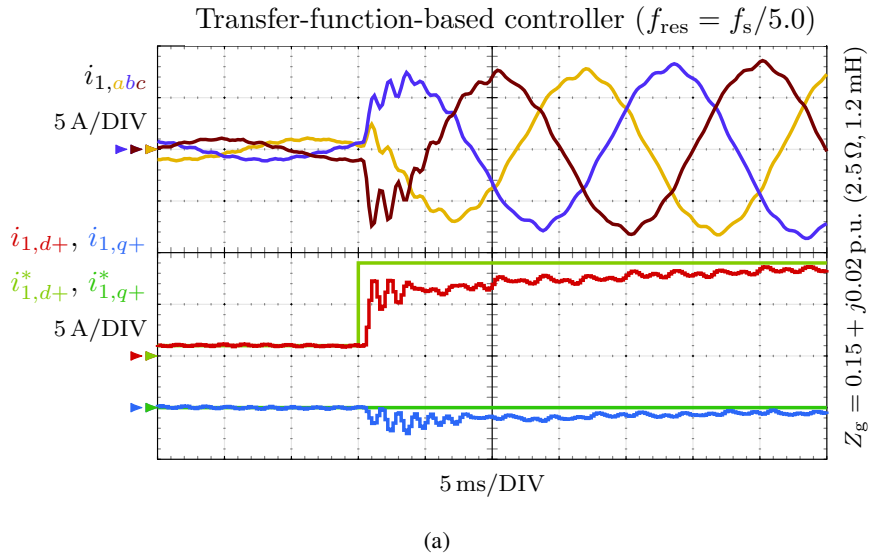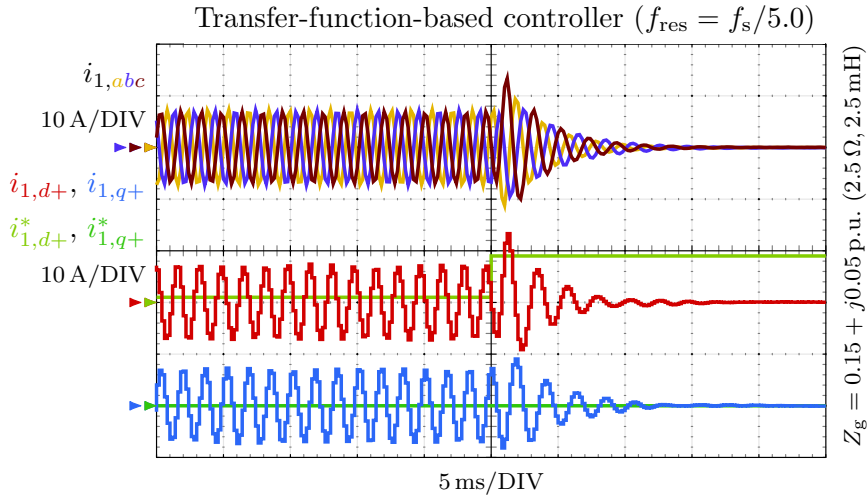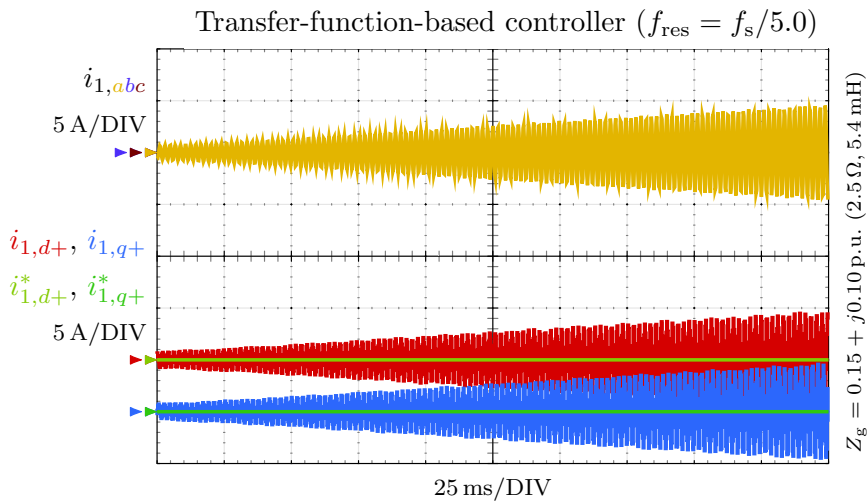
5 ms/DIV

(a)

Figure 77. Continued on next page.

(b)

(c)

Figure 77. Grid-side current waveforms in the abc frame $i_{1,abc}$ and their corresponding waveforms in the dq frame $i_{1,dq}$ during weak-grid operation for a reference step $i_{1,d+}^*$ in the positive synchronous frame dq+ rotating at the fundamental grid frequency f_g for different values of grid impedance. A transfer-function-based controller is used. a $Z_g = 0.15 + j0.02$ p.u. ($R_g = 2.5\,\Omega$, $L_g = 1.2\,\text{mH}$). b $Z_g = 0.15 + j0.05$ p.u. ($R_g = 2.5\,\Omega$, $L_g = 2.5\,\text{mH}$). c $Z_g = 0.15 + j0.10$ p.u. ($R_g = 2.5\,\Omega$, $L_g = 5.4\,\text{mH}$).

Figure 75 shows the grid-side current when the voltage source converters (VSCs) is turned on. The results show that the system is unstable. Contrarily to these results, the proposed current controller does not have a critical frequency where additional active damping techniques are required to avoid instability, cf. Figure 64-69.

In the next test, cf. Figure 76, f_{res} is increased by lowering the filter capacitance C so as to achieve stability. Two values are tested: $C = 25\mu F, f_{\text{res}} = f_{\text{s}}/(5.6)$, and $C = 20\mu F, f_{\text{res}} = f_{\text{s}}/(5.0)$. As f_{res} rises, the dynamic performance improves. Nevertheless, the transient response to reference commands contains some high-frequency lightly-damped oscillations and some axis cross-coupling. Contrarily to these results, the proposed controller provides a first-order response with the desired rise time, see Figures 65a.

The second experimental test assesses the robustness to variations in the grid impedance. Now the most stable configuration from the previous test, $C = 20\mu F$, is used. Figure 77 shows the reference tracking performance of the transfer-function-based current controller for three values of grid impedance: $Z_{\text{g}} = 0.15 + j0.02\,\text{p.u.}\,(2.5\,\Omega, 1.2\,\text{mH})$, $Z_{\text{g}} = 0.15 + j0.05\,\text{p.u.}\,(2.5\,\Omega, 2.5\,\text{mH})$, and $Z_{\text{g}} = 0.15 + j0.10\,\text{p.u.}\,(2.5\,\Omega, 5.4\,\text{mH})$.

When $Z_{\text{g}} = 0.15 + j0.02\,\text{p.u.}$, the system preserves stability. Nonetheless, a slower response, compared to Figure 76b, is obtained. If Z_{g} is set to a value of $0.15 + j0.05\,\text{p.u.}$, a marginally stable system is obtained. During steady-state, a high-frequency sustained oscillation appears due to the large sensitivity of the system at such frequency. When the reference step is commanded, overcurrent occurs and the voltage source converters (VSCs) commutation is stopped. Finally, when $Z_{\text{g}} = 0.15 + j0.10\,\text{p.u.}$, the system is unstable. Contrarily to these results, the proposed controller offers a stable operation for a larger range of grid impedance values, cf. Section 4.4.

4.6.   Steady-State Kalman-Filter Gain

In the following, the procedure to calculate the observer gain $\mathbf{K_o}$ (cf. Figure 55) is detailed.

Since the system model is linear and stationary, the algorithm that calculates the Kalman gain $\mathbf{K_o}$ converges to a steady-state value [54]. The computation of this gain can be performed offline to reduce the computational load of the controller.

A simple iterative numerical solution is shown in Algorithm 1.

Algorithm 1 Calculation of the Kalman Gain $\mathbf{K_o}$

Inputs: $N, \mathbf{Q}, \mathbf{A}_{add}^{LCL}, \mathbf{C}_{add}^{LCL}, \epsilon$

1: **while** $\|\mathbf{K_o}(k+1) - \mathbf{K_o}(k)\|_2 \geq \epsilon$ **do**

2:     Update values from previous iteration

3:     $\mathbf{P}(k) \leftarrow \mathbf{P}(k+1)$

4:     $\mathbf{K_o}(k) \leftarrow \mathbf{K_o}(k+1)$

5:     Project the error covariance ahead

6:     $\mathbf{P_p} \leftarrow \mathbf{A}_{add}^{LCL}\mathbf{P}(k)\mathbf{A}^{LCL\text{T}_{add}} + \mathbf{Q}$

7:     Compute the Kalman gain

8:     $\mathbf{K_o}(k+1) \leftarrow \mathbf{P_p}\mathbf{C}^{LCL\text{T}_{add}}/(\mathbf{C}_{add}^{LCL}\mathbf{P_p}\mathbf{C}^{LCL\text{T}_{add}} + N)$

9:     Update the error covariance

10:     $\mathbf{P}(k+1) \leftarrow (\mathbf{I} - \mathbf{K_o}(k+1)\mathbf{C}_{add}^{LCL})\mathbf{P_p}$

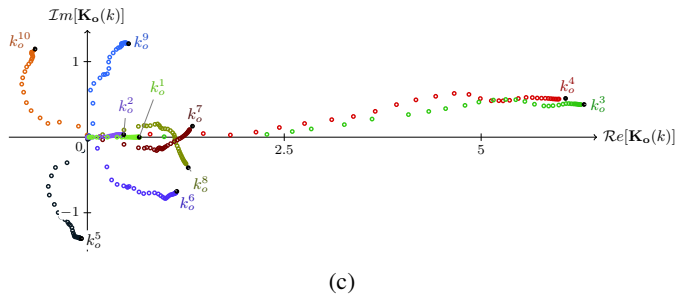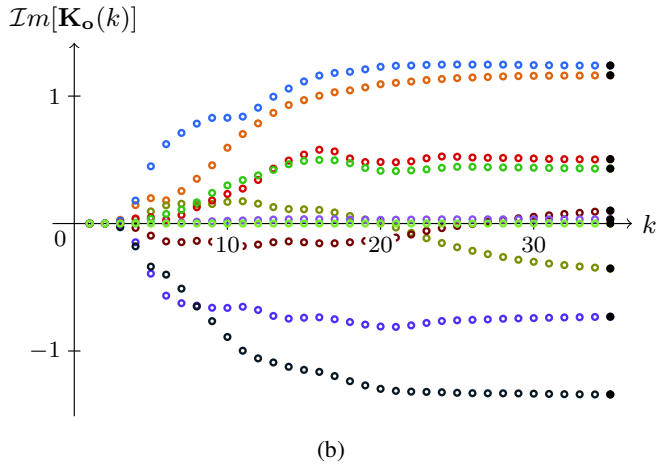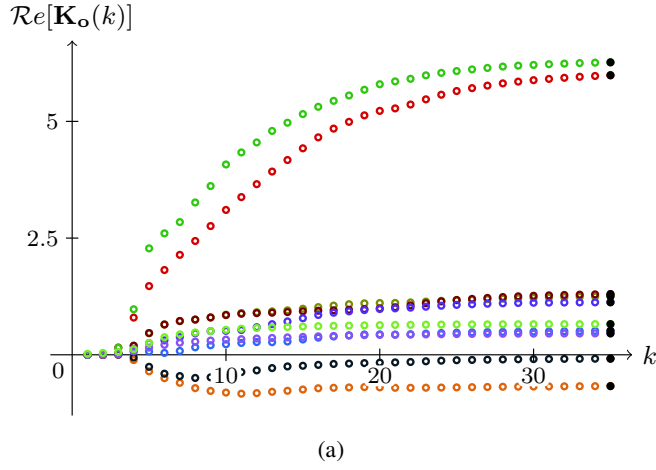11: **end while**

(a)

(b)

(c)

Figure 78. Result of the first 35 iterations of Algorithm 1 when applied to a system with the parameters shown in Table 8. a Real component of the elements of the vector $\mathbf{K_o}$. b Imaginary component of the elements of the vector $\mathbf{K_o}$. c Plot in the complex plane of the elements of the vector $\mathbf{K_o}$.

Table 8. Experimental Setup Parameters

Base values		
Nominal power	P_{base}	10 kW
Phase voltage	V_{base}	230 V
Nominal current	I_{base}	14.5 A
Grid frequency	f_{g}	50 Hz
LCL filter		
Grid-side inductance	L_1	2.5 mH (5 %)
Converter-side inductance	L_2	2.5 mH (5 %)
Filter capacitance	C	30μ F (14 %)
Filter resonance	f_{res}	815 Hz
Weak grid		
Grid inductance	L_{g}	5.4 mH (10 %)
Grid resistance	R_{g}	2.5Ω (15 %)
VSC		
Switching frequency		2.5 kHz
Dead time		3μ s
DC-bus voltage	v_{dc}	750 V
Controller		
Sampling frequency	f_{s}	5 kHz
Dominant frequency	f_{dom}	300 Hz
Measurement noise	N	0.01A^2
Process noise	$\mathbf{Q}$	0.1%

The input parameters of the algorithm are the measurement noise N [cf. (69)]; the process noise $\mathbf{Q}$, for which a value of 0.1% is recommended (cf. Section 4.3)

$$
\mathbf{Q} = \frac{0.1}{100}
\begin{bmatrix}
I_{\text{base}} & 0 & 0 & 0 & 0 & \cdots & 0 \\
0 & I_{\text{base}} & 0 & 0 & 0 & \cdots & 0 \\
0 & 0 & V_{\text{base}} & 0 & 0 & \cdots & 0 \\
0 & 0 & 0 & V_{\text{base}} & 0 & \cdots & 0 \\
0 & 0 & 0 & 0 & V_{\text{base}} & \cdots & 0 \\
\vdots & \vdots & \vdots & \vdots & \vdots & \ddots & \vdots \\
0 & 0 & 0 & 0 & 0 & \cdots & V_{\text{base}}
\end{bmatrix}; \qquad (72)
$$

the model of the plant and the disturbance $\mathbf{A}_{add}^{LCL}$ and $\mathbf{C}_{add}^{LCL}$ [cf. (63)]; and a tolerance ϵ, which is used in the stop condition to detect when convergence is achieved. A value of $\epsilon = 10^{-10}$ ensures a good precision in the coefficients.

Table 9. Grid Voltage Parameters

Order	Sequence*	h	Magnitude
1	+	+1	230V
3	0		5 %
5	−	−5	6 %
7	+	+7	5 %
9	0		1.5 %
11	−	−11	3.5 %
13	+	+13	3 %
THD			10.5 %

* When the sag occurs, the harmonic
voltages are unbalanced (all sequences
are present for each harmonic).

An analytical solution can be found in [81] and its implementation is available in the Matlab function `kalman`. Figure 78 shows the result of the first 35 iterations of Algorithm 1 when applied to a system with the parameters shown in Table 8. In this case, the design selected frequencies are the grid-frequency harmonics $+1, -1, -5, +7, -11, +13$; therefore, the obtained gain $\mathbf{K_o}$ is a vector with ten elements: one element for each of the selected frequencies and four elements for the plant model, cf. (55) and (63):

$$\mathbf{K_o} = \begin{bmatrix} k_o^1 & k_o^2 & \cdots & k_o^{10} \end{bmatrix}. \tag{73}$$

It should be noticed that when the selected frequencies are not symmetric with respect to zero hertz, the resultant vector $\mathbf{K_o}$ is complex valued.

4.7. Computational Load of the Multi-Frequency Controller

The control equation is (cf. Figure 55)

$$u(k) = K_f i_1^*(k) + K_{ff} v_g(k) - \mathbf{K_c} \hat{\mathbf{x}}_{dd}^{LCL}(k) - w(k). \tag{74}$$

Therefore, the number of operations that the control law requires is 6 complex multiplications and 6 complex additions. Since a complex multiplication requires 6 two floating-point operations (flops) and a complex addition is performed in two flops, the control law has a constant complexity of 48 flops.

On the other hand, the observer equations are (67) and (68). The state vector of the augmented plant model $\mathbf{x}_{add}^{LCL}(k)$ increases its size for every new harmonic that is included in the disturbance model. The size of $\mathbf{x}_{add}^{LCL}(k)$ is $n + 4$, e.g., it has three state variables associated to the LCL filter, one to the computational delay, and n to the disturbance model. Thus, the observer requires $2n^2 + 18n + 40$ complex multiplications and $n^2 + 11n + 26$ complex additions. This results in a total of $14n^2 + 130n + 292$ flops for the observer.

Therefore, the total number of two flops per second that the current controller executes is $f_s(14n^2 + 130n + 340)$, which is constant for a given number n of controlled harmonics, and increases with n. In the presented implementation ($n = 6$ and $f_s = 5\,\mathrm{kHz}$), a figure of 8.1 mega flops per second is obtained, which is well below the capability of modern micro-controllers.

4.8. Derivation Process of the Sensitivity and Complementary Sensitivity Functions
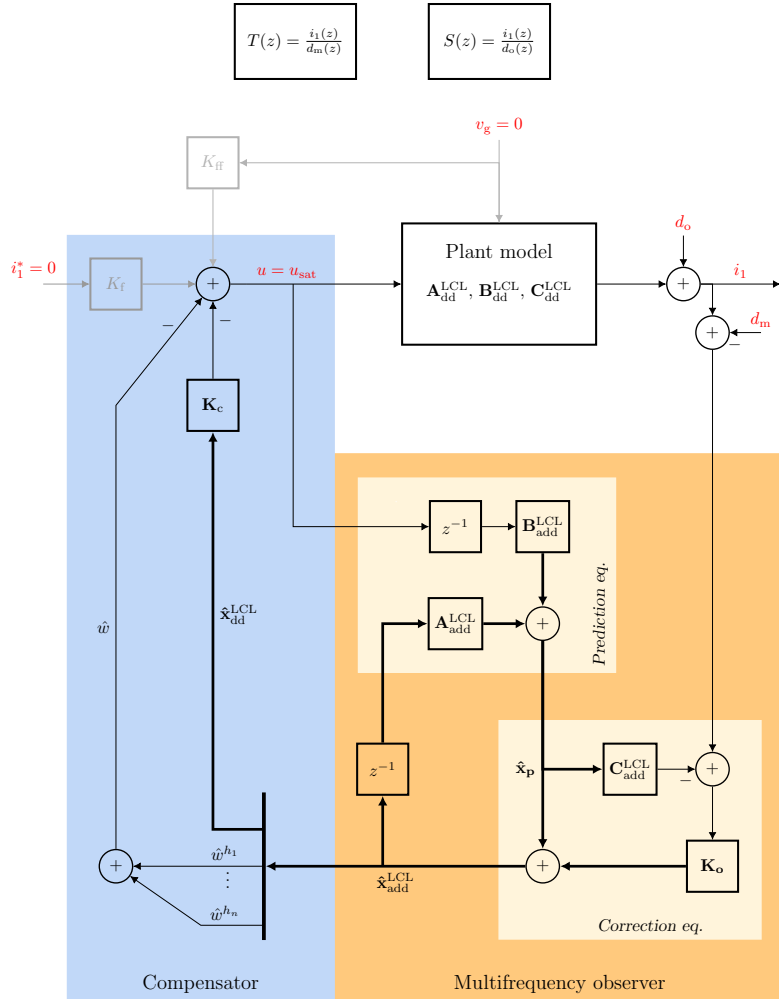
Figure 79. Block diagram representation of the closed-loop system used to obtain the sensitivity function $S(f)$ and the complementary sensitivity function $T(f)$.

The derivation process to obtain the sensitivity function $S(f)$ and the complementary sensitivity function $T(f)$ is detailed below. In order to obtain a transfer function between two variables (an input and an output) the output is calculated as a function of the desired input, assuming the remaining inputs of the system equal to zero.

$$
\underbrace{\begin{bmatrix} \mathbf{x}_{dd}^{LCL}(k+1) \\ \mathbf{x}_{dd}^{LCL}(K+1) \\ u_{\mathrm{d}}(k+1) \end{bmatrix}}_{\mathbf{x}_{cl}^{LCL}(k+1)} = \underbrace{\begin{bmatrix} \mathbf{A}_{dd}^{LCL} - \mathbf{B}_{dd}^{LCL}\mathbf{K_c}\mathbf{K_o}\mathbf{C}_{dd}^{LCL} & -\mathbf{B}_{dd}^{LCL}\mathbf{K_c}\left(\mathbf{A}_{add}^{LCL} - \mathbf{K_o}\mathbf{C}_{add}^{LCL}\mathbf{A}_{add}^{LCL}\right) & -\mathbf{B}_{dd}^{LCL}\left(\mathbf{K_c}\mathbf{B}_{add}^{LCL} + \mathbf{K_o}\mathbf{C}_{add}^{LCL}\mathbf{B}_{add}^{LCL}\right) \\ \mathbf{K_o}\mathbf{C}_{dd}^{LCL} & \mathbf{A}_{add}^{LCL} - \mathbf{K_o}\mathbf{C}_{add}^{LCL}\mathbf{A}_{add}^{LCL} & \mathbf{B}_{add}^{LCL} - \mathbf{K_o}\mathbf{C}_{add}^{LCL}\mathbf{B}_{add}^{LCL} \\ -\mathbf{K_c}\mathbf{K_o}\mathbf{C}_{dd}^{LCL} & -\mathbf{K_c}\left(\mathbf{A}_{add}^{LCL} - \mathbf{K_o}\mathbf{C}_{add}^{LCL}\mathbf{A}_{add}^{LCL}\right) & -\mathbf{K_c}\left(\mathbf{B}_{add}^{LCL} - \mathbf{K_o}\mathbf{C}_{add}^{LCL}\mathbf{B}_{add}^{LCL}\right) \end{bmatrix}}_{\mathbf{A}_{cl}^{LCL}}
\underbrace{\begin{bmatrix} \mathbf{x}_{dd}^{LCL}(k) \\ \mathbf{x}_{add}^{LCL}(k) \\ u_{\mathrm{d}}(k) \end{bmatrix}}_{\mathbf{x}_{cl}^{LCL}(t)}
$$

$$
+ \underbrace{\begin{bmatrix} -\mathbf{B}_{dd}^{LCL}\mathbf{K_c}\mathbf{K_o} \\ \mathbf{K_o} \\ -\mathbf{K_c}\mathbf{K_o} \end{bmatrix}}_{\mathrm{B}_{cl,d_o}^{LCL}} d_{\mathrm{o}}(k) + \underbrace{\begin{bmatrix} \mathbf{B}_{dd}^{LCL}\mathbf{K_c}\mathbf{K_o} \\ -\mathbf{K_o} \\ \mathbf{K_c}\mathbf{K_o} \end{bmatrix}}_{\mathrm{B}_{cl,d_m}^{LCL}} d_{\mathrm{m}}(k)
$$

$$
i_1(k) = \underbrace{\begin{bmatrix} \mathbf{C}_{dd}^{LCL} & \mathbf{0} \end{bmatrix}}_{\mathbf{C}_{cl}^{LCL}} \underbrace{\begin{bmatrix} \mathbf{x}_{dd}^{LCL}(k) \\ u_{\mathrm{d}}(k) \end{bmatrix}}_{\mathbf{x}_{cl}^{LCL}(t)} + d_{\mathrm{o}}(k).
$$

(75)

On the one hand, the sensitivity function $S(f)$ relates a disturbance d_o in the grid current with the grid current i_1, see Figure 79. On the other hand, the complementary sensitivity function $T(f)$ is the ratio of i_1 to a disturbance d_m in the measured grid current. Using the block-diagram representation shown in Figure 79, the state-space model given in (75) on the top of the next page is obtained. Such model relates $i_1(k)$ with $d_\mathrm{o}(k)$ and $d_\mathrm{m}(k)$.

Therefore, the resultant sensitivity function is

$$
S(f) \quad = \quad \frac{i_1}{d_o} = \mathbf{C}_{cl}^{LCL} \left(e^{j2\pi f T_\mathrm{s}} \mathbf{I} - \mathbf{A}_{cl}^{LCL} \right)^{-1} \mathbf{B}_{\mathrm{cl},\mathbf{d_o}}^{\mathrm{LCL}} + 1.
$$

In addition, the complementary sensitivity function is

$$
T(f) \quad = \quad \frac{i_1}{d_m} = \mathbf{C}_{cl}^{LCL} \left(e^{j2\pi f T_\mathrm{s}} \mathbf{I} - \mathbf{A}_{cl}^{LCL} \right)^{-1} \mathbf{B}_{\mathrm{cl},\mathbf{d_m}}^{\mathrm{LCL}} = -S(f) + 1,
$$

which agrees with the fundamental relation in (71).

4.9.   Summary

This section has presented a multi-frequency current controller based on a direct discrete-time pole-placement strategy and a Kalman filter for grid-tied converters with LCL filter.

In addition to the advantages of previously proposed harmonic-current controllers, the presented solution responds to commands with a constant, damped, and fast response independently of the LCL filter used or the targeted harmonics. The rise-time value for reference changes is determined by the selected dominant frequency f_dom of the compensator.

Concerning the disturbance-rejection capability, the proposed scheme achieves zero steady-state error in the grid-side current at a set of arbitrarily specified harmonic currents. Contrarily to the previously proposed solutions, the controller offers an infinite impedance at these frequencies without altering the response to reference commands or affecting the stability and robustness of the system, when several current harmonics are being controlled.

It has also been shown that the response to disturbances cannot be simultaneously improved in the steady-state operation and during transients. If the number of controlled harmonics increases (to reduce the steady-state error), then the transient response to disturbances of the controller is degraded. This is an unavoidable tradeoff that applies to all linear controllers.

The proposal has also been proved robust against alterations in the grid impedance. Stability is maintained with minimal change in the transient dynamics of the system regardless of the grid-impedance variation.

The design and the theoretical outcomes have been verified by simulations and experiments.

5. Grid-Tied Inverter With AC-Voltage Sensorless Synchronization and Soft-Start

This section presents a novel grid synchronization method with bumpless start which requires minimal computational load and can selectively track the positive sequence of the grid voltage in an unbalanced and distorted three-phase weak grid. Only twelve two floating-point operations (flops) are required to obtain the in-phase and quadrature components that define a synchronous frame which tracks the positive sequence of the grid voltage. Contrarily to a phase-locked loop (PLL), the presented scheme does not require to measure any ac voltages. Therefore, this sensorless method is particularly suitable in weak-grid conditions in which the voltage at the point of common coupling (PCC) is different from the grid voltage and may contain significant noise. The error in the estimated phase depends on the accuracy of the plant model. If the grid-impedance is assumed to be zero and the LCL filter parameters are known, both the proposal and a PLL-based scheme result in the same steady-state error. Experimental results show the advantages of the proposal compared to a moving average filter (MAF)-based PLL.

Grid-connected converters usually require a phase measurement system in order to synchronize with the grid voltage. Several techniques have been proposed to detect the phase of the grid voltage [117]. Among these techniques, voltage-sensorless methods are gaining popularity due to advantages such as cost reduction and increased reliability, specially when a weak grid is considered [118, 119]. Furthermore, some voltage-sensorless methods can estimate the grid voltage at remote points that cannot be measured, hence improving the performance of the converter when connected to a weak grid in which the voltage at the point of common coupling (PCC) is different from the grid voltage.

Different grid voltage estimation techniques have been proposed in the literature. Virtual flux (VF) methods [120, 121, 122] are commonly applied to grid-tied inverters with an L filter; but they result in a complex synchronization scheme when they are used in a system with an LCL filter. Methods based on instantaneous power measurements [123, 124] provide a simple structure that does not require any integral, derivative, or trigonometric operations. Nevertheless, they do not completely eliminate steady-state errors caused by a distorted grid voltage. Observer-based synchronization schemes provide an excellent performance [125, 126, 127, 128]. However they present a higher computational load compared to previous solutions. In [126] and [127], an external loop with an adaptation law is added to the current controller in order to synchronize the estimated reference frame with the positive sequence of the grid voltage. Nonetheless, the plant model used in [126] and [127] does not include resistive components. Such simplification introduces an steady-state estimation error, specially during weak-grid conditions. In [128], a continuous-time extended-state observer is used in combination with a phase-locked loop (PLL) and a PI current controller. Such design has a slower response compared to a conventional PLL that directly receives the grid voltage measurements. In [129], a novel controller structure that

uses a PLL connected to the measured grid current is presented. Such solution removes steady-state errors that model-based grid voltage estimation methods have when plant parameter variations are considered; but it requires a known load value to be connected at the dc bus.

The contribution of this section is a novel grid synchronization method which requires minimal computational load and provides a fast and accurate estimation of the grid voltage when connected to a weak grid. The presented synchronization method selectively tracks the positive sequence of the grid voltage in an unbalanced and distorted three-phase grid. Moreover, contrarily to a PLL, the presented scheme does not require to measure the grid voltage, which could affect the performance when connected to a weak grid because the voltage at the PCC can be different from the grid voltage depending on the grid-side current value. The proposed structure avoids this interaction between the current controller and the synchronization mechanism, resulting in a more robust system. Furthermore, it also removes the grid voltage feedforward. This improves the stability and robustness of the current controller because it eliminates an additional path for disturbances and noise to enter the system, a common problem of feedforward schemes.

Concerning the implementation, only twelve two floating-point operations (flops) are required to obtain the in-phase and quadrature components that define a synchronous frame which tracks the positive sequence of the grid voltage. The proposed method employs the information available in the estimated system state vector and it is optimized for a grid-tied inverter that uses an state-space controller with disturbance estimation [81]; however, it can be easily adapted to other types of current controllers.

The error in the estimated phase depends on the accuracy of the identified grid impedance. When the current controller assumes that the grid impedance is zero, both the proposal and a PLL-based scheme have the same steady-state error. A change in the LCL filter parameters with respect to their nominal values also introduces an estimation error. Nevertheless, such error is negligible for the typical component tolerances due to the low sensitivity of the proposal to variations in the plant parameters. The transient response is improved compared to a controller that measures the voltage at the PCC because there is no interaction between the current controller and the synchronization scheme.

The rest of the section is organized as follows. Section 5.1 introduces the proposed controller structure. Then, in Section 5.2, the operation of the synchronization scheme is described. Next, in Section 5.3, the robustness of the proposal to plant parameter variations is assessed. Section 5.4 explains the steady-state and transient performance of the presented sensorless synchronization method. Section 5.5 describes the bumpless start capability. In Section 5.6, the theory is validated by simulation and experimental results. Finally, Section 5.7 summarizes the work.

5.1.   Proposed Controller Structure

In order to obtain the best performance, current controllers from modern control theory use all prior knowledge available at the design stage. In the case of a grid-tied inverter with an LCL filter, cf. Figure 80, the current controller uses a plant model that represents the dynamics of the LCL filter, the PWM, and the computational delay. Such discrete-time model relates the grid-side current i_1 with the nominal controller output voltage v
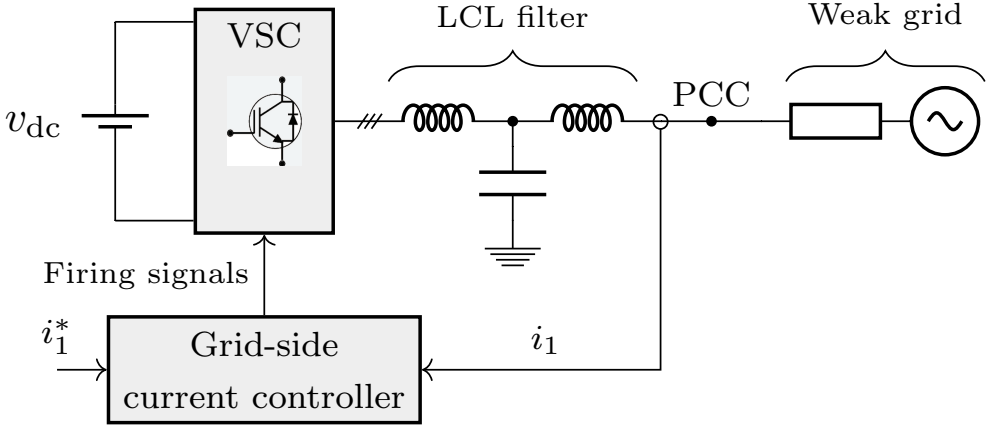
Figure 80. Voltage source converters (VSCs) with a grid-side current controller connected to a weak grid with an LCL filter.

when the grid voltage is assumed to be zero and the voltage source converters (VSCs) is not overmodulating. The mathematical process to obtain such model is presented in the following.

Figure 80 depicts the physical plant, which consists of a voltage source converters (VSCs) connected to the grid using an LCL filter. A block diagram representation of the plant model in the $\alpha\beta$ frame is shown in Figure 81, where L_1, L_2, and C are the values of the reactive elements of the LCL filter. R_1, R_2, and R_c model the equivalent series resistances of the filter and the voltage source converters (VSCs) [15]. $v_{g,abc}$ is the grid voltage at the PCC. R_g and L_g are the values of the resistive and inductive components of the grid impedance Z_g. Since these values are usually unknown, they are assumed to be zero to design the controller. $i_{1,abc}$ and $i^*_{1,dq}$ denote the measured grid-side current in the abc frame and the grid-side current reference in the dq frame, respectively. If the subscript in a variable does not specify a reference frame, the $\alpha\beta$ frame is assumed. The signal v is the nominal controller output voltage; u_{sat} is the saturated controller output voltage; u_d is the PWM voltage reference, e.g., it is the one-sample-delayed saturated controller output voltage; and u'_d is the voltage source converters (VSCs) output voltage.

The discrete-time modeling process that describes the LCL filter, the PWM, and the computational delay of this system was presented in section 3. Such modeling process takes place in several steps; each step adds features to the model obtained in the previous stage. The final model relates the grid-side current $i_1(k)$ to the nominal controller output voltage $v(k)$ in the plant shown in Figure 81 when the grid voltage v_g and the resonant action w are zero.

$$
\begin{aligned}
\mathbf{x}^{LCL}_{dd}(k+1) &= \mathbf{A}^{LCL}_{dd}\,\mathbf{x}^{LCL}_{dd}(k) + \mathbf{B}^{LCL}_{dd}v(k) \\
i_1(k) &= \mathbf{C}^{LCL}_{dd}\,\mathbf{x}^{LCL}_{dd}(k). \\
\mathbf{x}^{LCL}_{dd}(k) &= \begin{bmatrix} i_1 & i_2 & v_C & u_d \end{bmatrix}^{\mathrm{T}}.
\end{aligned}
\tag{76}
$$

From the current controller perspective, the grid voltage v_g is an unknown disturbance that affects the value of the grid-side current. Commonly, such disturbance is canceled by
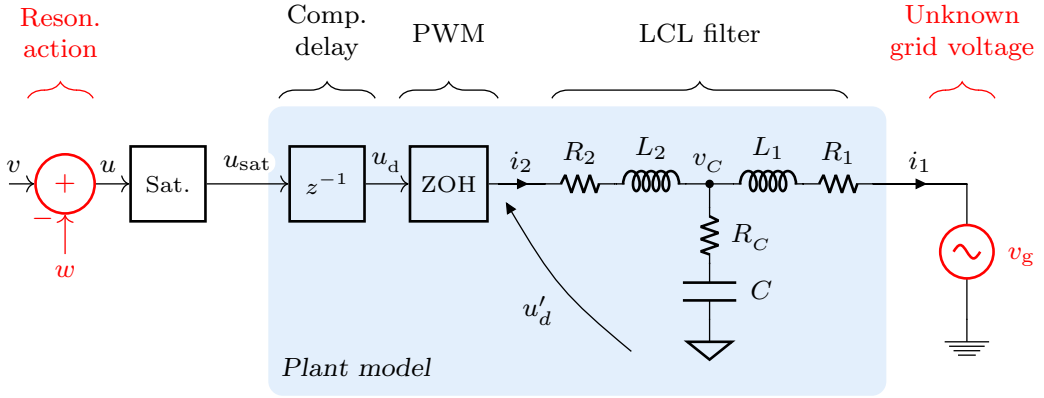
Figure 81. The augmented plant model includes an input-equivalent disturbance w that cancels the effect of the unmeasured grid voltage v_{g} on the grid-side current i_1 when it is subtracted from the plant model input. The controller output voltage u contains two terms, namely, the nominal output voltage v and an input equivalent voltage disturbance w. The observer estimates w so as to cancel the effect of disturbances such as v_{g} on the grid-side current i_1. When v_{g} is zero, w is also zero.

adding a feedforward of the voltage at the PCC in combination with a PI or a PR controller to remove any remaining error during steady state. Contrarily to this approach, state-space controllers with disturbance estimation [81] achieve zero steady-state error by augmenting the plant model with a disturbance model [1, 8]. Such disturbance model (so called resonant action) represents an input equivalent disturbance w that is subtracted from the nominal controller output voltage v to cancel the effect of the grid voltage on the controlled grid-side current, as shown in Figure 81.

Figure 82 illustrates the complete controller structure [8]. The observer estimates an augmented state vector $\hat{\mathbf{x}}_{add}^{LCL}$, which contains an estimation of the plant state vector $\hat{\mathbf{x}}_{dd}^{LCL}$ and of the input equivalent disturbance $\hat{w}$:

$$\hat{\mathbf{x}}_{add}^{LCL} = \begin{bmatrix} \hat{\mathbf{x}}_{dd}^{LCL} & \hat{w}^{+} & \hat{w}^{-5} & \cdots & \hat{w}^{+13} \end{bmatrix}^{\mathrm{T}}, \tag{77}$$

where $\hat{w}^{+}, \hat{w}^{-5}, ...\hat{w}^{+13}$ are the components of $\hat{w}$. Typically, such components are tuned at the fundamental grid frequency ($\pm f_{\mathrm{g}}$) and at its main low-order harmonics ($-11f_{\mathrm{g}}$, $-5f_{\mathrm{g}}$, $+7f_{\mathrm{g}}$, and $+13f_{\mathrm{g}}$).

In order to achieve an ac voltage sensorless operation, the controller structure shown in Figure 83 is proposed. Compared to Figure 82, this scheme replaces the PLL with a synchronization algorithm. Contrarily to the PLL, which uses the measured voltage at the PCC v_{PCC}, the proposed synchronization algorithm utilizes the signal $\hat{w}^{+}$ estimated by the observer. Such signal is the symmetrical component of $\hat{w}$ that cancels the positive sequence of the grid voltage v_{g}^{+}. The next section describes the relation between w^{+} and v_{g}^{+}. Such relation is used to synchronize the voltage source converters (VSCs) with the fundamental component of the grid frequency.

The start-up sequence is also changed in order to achieve a bumpless start without measuring v_{PCC}. In a conventional controller, the observer is reset (the accumulators are
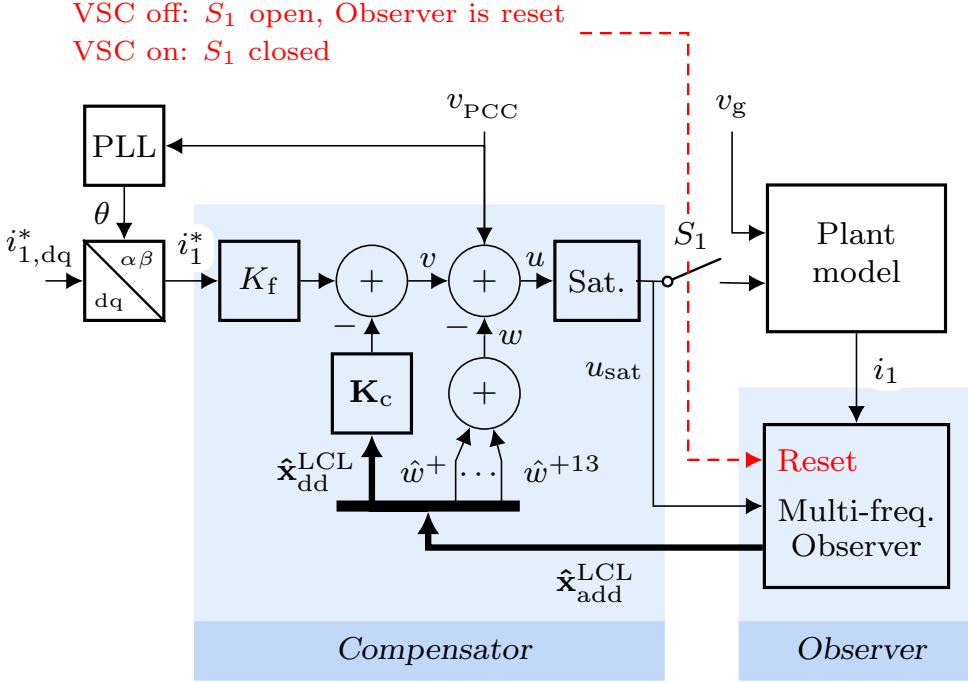
Figure 82. A conventional state-space current controller is composed of a compensator and an observer, cf. [8, Figure 3].

set to zero) while the PLL is always running before the voltage source converters (VSCs) begins commutation in order to avoid wind-up and to obtain the required phase information for the start-up. The switch included in Figure 82 illustrates this start-up sequence: if the switch is open, the observer and the PWM are disabled; when the switch closes, a voltage is applied to the plant (commutation begins) and the observer starts estimating the plant state $\mathbf{x}_{dd}^{LCL}(k)$ and the input equivalent disturbance w that cancels any remaining steady-state error in the grid-side current at the frequencies where a resonant action has been included.

Contrarily to a conventional controller, the proposal maintains the observer always running, cf. Figure 83. A block named bumpless-start generates a voltage $\hat{u}_{\text{sat}}$ that allows the observer to estimate the correct system state before commutation begins. This is illustrated in Figure 83 by a double-throw switch that passes such voltage to the observer when the voltage source converters (VSCs) is off and the controller output voltage u_{sat} is not applied to the plant, e.g., the PWM is disabled. Section 5.5 explains the theory of operation of the bumpless observer, which contains a transfer function $G_{\text{bl}}(z)$, and details the design steps to obtain such transfer function.

5.2. AC-Voltage Sensorless Synchronization

This section describes the proposed ac-voltage sensorless synchronization scheme. First, the mathematical relation between the input-equivalent disturbance w and the grid volt-

age v_g is calculated. Then, the structure of the synchronization algorithm, which uses the previous relation, is detailed. Finally a performance analysis is presented.
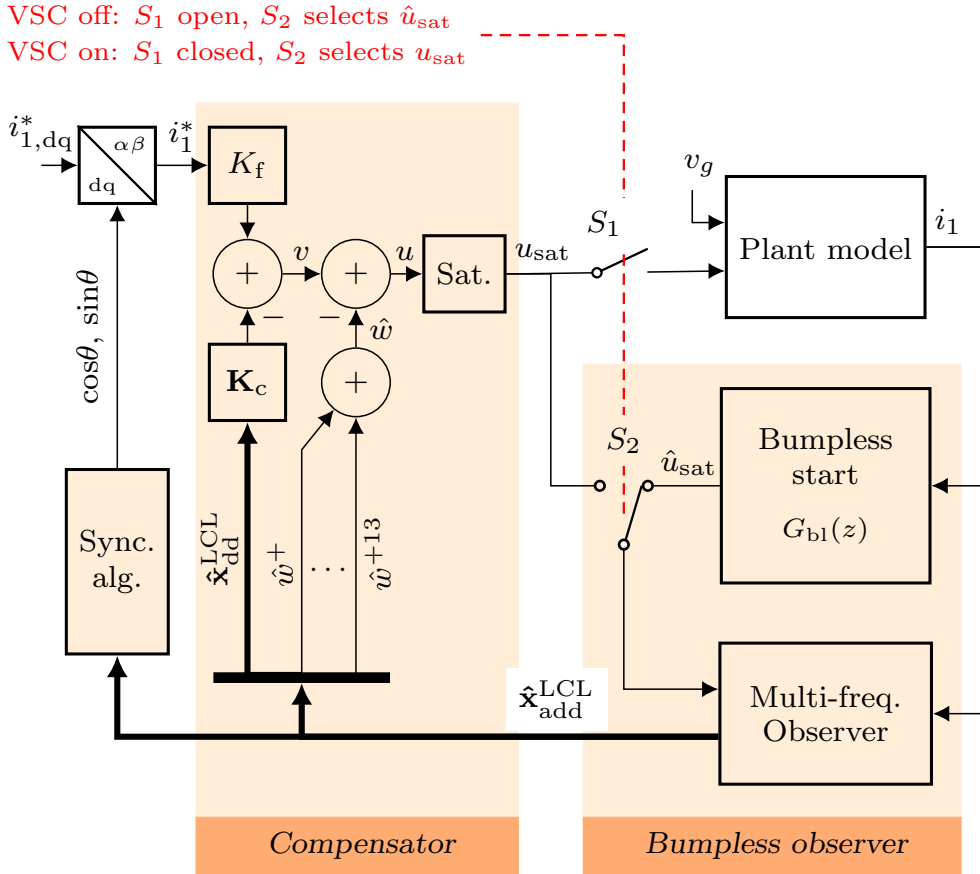

Figure 83. Proposed ac-voltage sensorless state-space current controller.

5.2.1. Relation between w and v_g

The control law that gives the PWM voltage reference u_sat when the saturator operates in its linear range is

$$u_\mathrm{sat} = \overbrace{K_\mathrm{f}i_1^* - \mathbf{K}_c\hat{\mathbf{x}}_{dd}^{LCL}}^{v} - \hat{w}, \qquad (78)$$

which contains three terms, namely, a feedforward term $K_\mathrm{f}i_1^*$, a feedback term $\mathbf{K}_c\hat{\mathbf{x}}_{dd}^{LCL}$, and a resonant action term $\hat{w}$, cf. Figure 83. The feedback and feedforward terms constitute the nominal controller output voltage v.

The goal of the resonant action $\hat{w}$ is to cancel the effect on the grid-side current of any unmodeled disturbances such as an unknown grid voltage v_g, cf. Figure 81. The design of the observer was presented in [8], but for the purpose of this section, it suffices to say

that the observer adjusts the amplitude and phase of each of the components of $\hat{w}$ ($\hat{w} = \hat{w}^+ + \hat{w}^- + \hat{w}^{-5} + \hat{w}^{+7} + \hat{w}^{-11} + \hat{w}^{+13}$) so as to achieve zero steady-state error in the grid-side current at the frequencies where such components are tuned; typically, the fundamental grid frequency and the main low-order harmonics.

Therefore, the grid voltage can be estimated by filtering $\hat{w}$ with a discrete-time model that relates such input-equivalent disturbance with v_g. In order to obtain such model, the grid-side impedance of the LCL filter is assumed to be an open circuit because w cancels any errors (current circulation) in the grid-side current caused by v_g. In such condition, the capacitor voltage v_C is equal to v_g, see Figure 84b. Therefore the required model relates the capacitor voltage v_C with the input equivalent voltage disturbance w and includes the PWM and modulation delays, as shown in Figure 84b. In the following, the derivation process to obtain such model is presented.

The mathematical modeling process takes place in several steps. Each step adds features to the model equations obtained in the previous stage. In the first place, a continuous-time model of the LC filter in the $\alpha\beta$ frame, including losses, is presented. This model relates the capacitor voltage v_C to the the averaged PWM output voltage u'_d for the LC filter of the plant shown in Figure 84. The first-order differential equations in the continuous domain (written in state-space form) are

$$\frac{\mathrm{d}\mathbf{x}^{LC}(t)}{\mathrm{d}t} = \underbrace{\begin{bmatrix} \frac{-R_C}{L_2} & \frac{-R_C R_2}{L_2} + \frac{1}{C} \\ \frac{-1}{L_2} & \frac{-R_2}{L_2} \end{bmatrix}}_{\mathbf{A}^{LC}} \mathbf{x}^{LC}(t) + \underbrace{\begin{bmatrix} \frac{R_C}{L_2} \\ \frac{1}{L_2} \end{bmatrix}}_{\mathbf{B}^{LC}} u'_d(t)$$

$$v_C(t) = \underbrace{\begin{bmatrix} 1 & 0 \end{bmatrix}}_{\mathbf{C}^{LC}} \mathbf{x}^{LC}(t)$$

$$\mathbf{x}^{LC}(t) = \begin{bmatrix} v_C & i_2 \end{bmatrix}^{\mathrm{T}}. \tag{79}$$

Boldface denotes a vector or a matrix. Equation (79) does not include the effect of a load current i_o in the state variables. This disturbance is studied later.

Next, (79) is discretized by using a ZOH equivalent [81]. Such discretization method takes into account the half a sample delay added by the PWM [15].
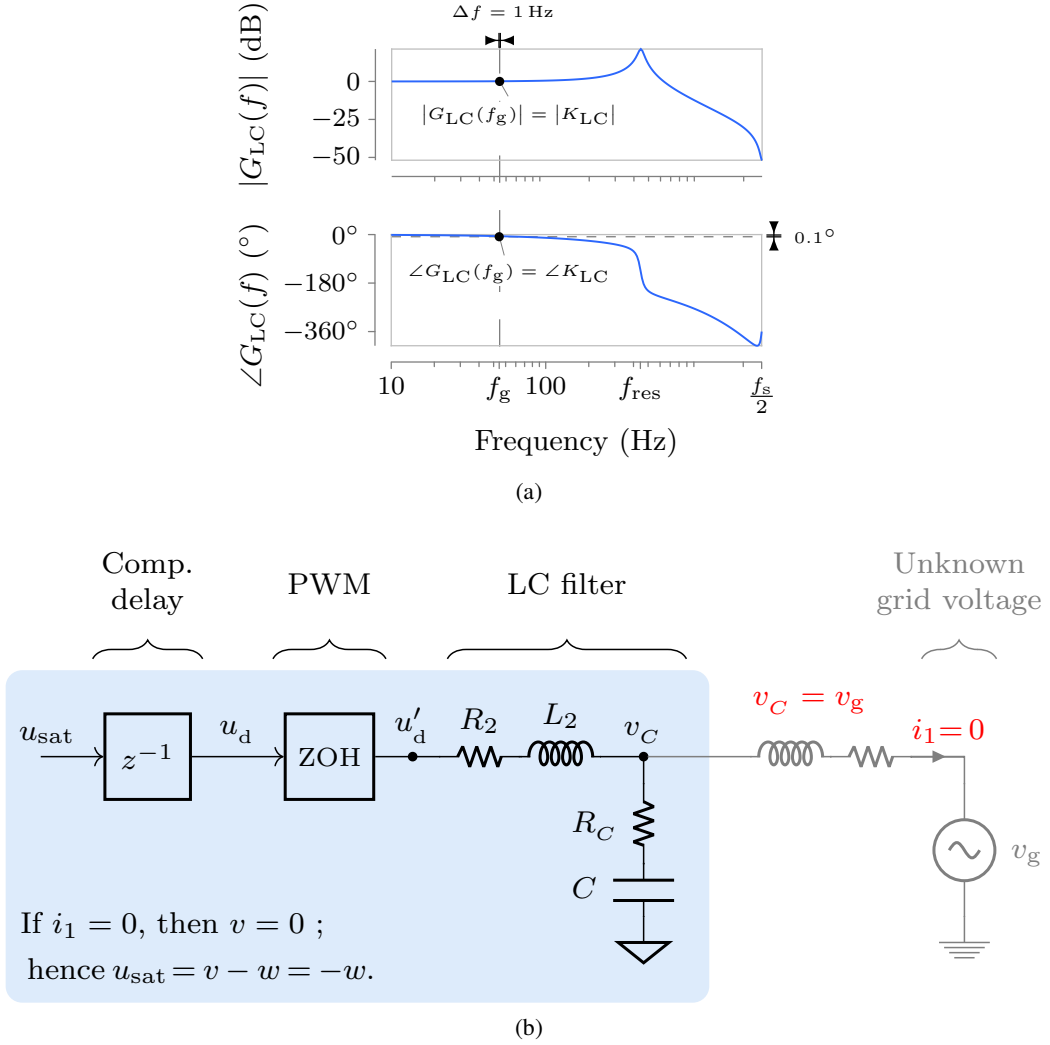
$$\mathbf{A}_d^{LC} = e^{\mathbf{A}^{LC} T_s}$$
$$\mathbf{B}_d^{LC} = \left(\mathbf{A}^{LC}\right)^{-1} \left(e^{\mathbf{A}^{LC} T_s} - \mathbf{I}\right) \mathbf{B}$$
$$\mathbf{C}_d^{LC} = \mathbf{C}^{LC}. \tag{80}$$

The resulting model relates the the PWM voltage reference u_d with the sampled capacitor voltage:

$$\mathbf{x}_d^{LC}(k+1) = \mathbf{A}_d^{LC} \mathbf{x}_d^{LC}(k) + \mathbf{B}_d^{LC} u_d(k)$$
$$v_C(k) = \mathbf{C}_d^{LC} \mathbf{x}_d^{LC}(k). \tag{81}$$

Then, a one-sample (computational) input delay is added, cf. Figure 99. The model of this delay on the controller output voltage v is

$$u_d(k+1) = u(k). \tag{82}$$

(a)

(b)

Figure 84. Relation between w and v_g: b Bode diagram. a Block diagram.

In this manner, combining (81) and (82), the plant model that takes the computational delay into account is

$$\underbrace{\begin{bmatrix} \mathbf{x}_d^{LC}(k+1) \\ u_d(k+1) \end{bmatrix}}_{\mathbf{x}_{dd}^{LC}(k+1)} = \underbrace{\begin{bmatrix} \mathbf{A}_d^{LC} & \mathbf{B}_d^{LC} \\ \mathbf{0} & 0 \end{bmatrix}}_{\mathbf{A}_{dd}^{LC}} \underbrace{\begin{bmatrix} \mathbf{x}_d^{LC}(k) \\ u_d(k) \end{bmatrix}}_{\mathbf{x}_{dd}^{LC}(k)} + \underbrace{\begin{bmatrix} \mathbf{0} \\ 1 \end{bmatrix}}_{\mathbf{B}_{dd}^{LC}} u(k)$$

$$v_C(k) = \underbrace{\begin{bmatrix} \mathbf{C}_d^{LC} & 0 \end{bmatrix}}_{\mathbf{C}_{dd}^{LC}} \underbrace{\begin{bmatrix} \mathbf{x}_d^{LC}(k) \\ u_d(k) \end{bmatrix}}_{\mathbf{x}_{dd}^{LC}(k)}$$

$$\mathbf{x}_{dd}^{LC}(k) = \begin{bmatrix} v_C & i_L & u_d \end{bmatrix}^{\mathrm{T}}. \tag{83}$$

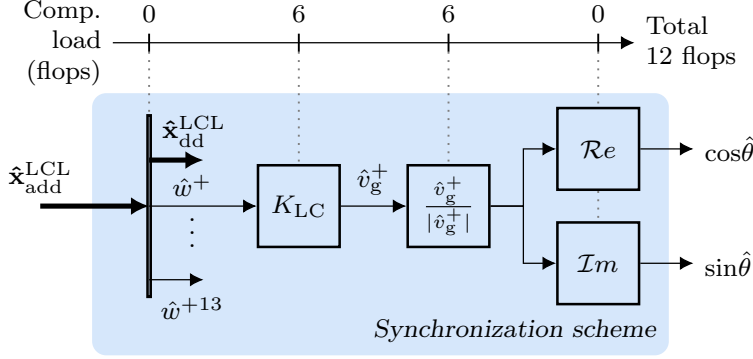The resultant model relates the inverter output voltage $v_C(k)$ to the controller output voltage

Figure 85. Block diagram of the synchronization scheme.

$u(k)$, cf. Figure 100a. Equation (83) is the nominal plant model and it is used in Section 6.2 to design the controller.

In order to reduce the computational load when implemented in a real-time platform, this third-order state-space model is expressed as a transfer function:

$$G_{\mathrm{LC}}(z) \;=\; \frac{v_c(z)}{w(z)} = \mathbf{C}_{dd}^{LC}\left(z\mathbf{I} - \mathbf{A}_{dd}^{LC}\right)^{-1}\mathbf{B}_{dd}^{LC}. \tag{84}$$

Figure 84a shows the bode of (84).

Since the phase curve does not significantly change in the frequency range centered at f_{g}, the real-time implementation replaces the third-order transfer function (84) with a constant gain so as to further reduce the computational load:

$$K_{\mathrm{LC}} \;=\; G_{\mathrm{LC}}(e^{j2\pi f_{\mathrm{g}}T_{\mathrm{s}}}). \tag{85}$$

Such simplification does not significantly degrade the performance of the grid-tied inverter because the maximum phase error introduced, which occurs for a maximum frequency deviation [130], is comparable to the accuracy of a commercial current sensor ($< 0.1°$). Section 5.3 presents a detailed analysis of the effect of plant parameter variations in the estimation accuracy.

5.2.2. Synchronization Scheme

The proposed synchronization algorithm consists of four steps, cf. Figure 85. First, the positive-sequence component of the estimated input-equivalent voltage disturbance $\hat{w}^+$ is selected from the augmented state vector provided by the observer $\hat{\mathbf{x}}_{add}^{LCL}$. Then, this signal is multiplied by K_{LC} to obtain the estimated positive-sequence component of the grid voltage $\hat{v}_{\mathrm{g}}^+$. Next, $\hat{v}_{\mathrm{g}}^+$ is normalized to yield a space vector with unity magnitude. Finally, the real and imaginary components of such vector are the in-phase and quadrature signals ($\cos\theta$ and $\sin\theta$) which define a synchronous frame that is synchronized with the positive sequence of the fundamental component of the grid voltage.

Figure 86 shows a representation of the signals involved in the synchronization scheme during steady-state operation. In this example, the design-selected harmonic frequencies

were the fundamental component with a 40% imbalance and the main low-order harmonics of the grid voltage, namely, $-5f_{\mathrm{g}}$, $+7f_{\mathrm{g}}$, $-11f_{\mathrm{g}}$, and $+13f_{\mathrm{g}}$. Figure 86c shows a polar representation of $\hat{v}_{\mathrm{g}}$ and two of its symmetrical components $\hat{v}_{\mathrm{g}}^{+}$ and $\hat{v}_{\mathrm{g}}^{-}$, respectively. It should be noted that, when the sampling period is small compared to a grid fundamental period, the frequency response of (84) is close to one at low frequencies; therefore, both $\hat{w}^{+}$ and $\hat{v}_{\mathrm{g}}^{+}$ have a similar magnitude and phase. Contrarily, $\hat{w}^{-11}$ has a smaller amplitude than $\hat{v}_{\mathrm{g}}^{-11}$ because such component is tuned at a frequency ($11f_{\mathrm{g}}$) close to the resonant frequency of the LC circuit; hence Equation (84) introduces a high gain at such frequency.
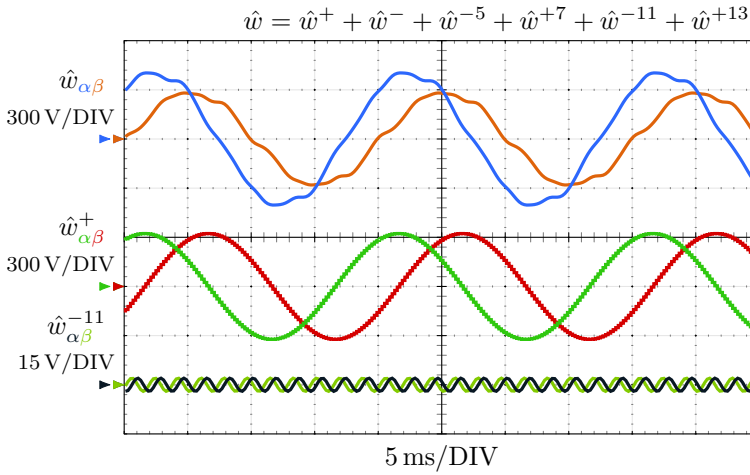
(a)
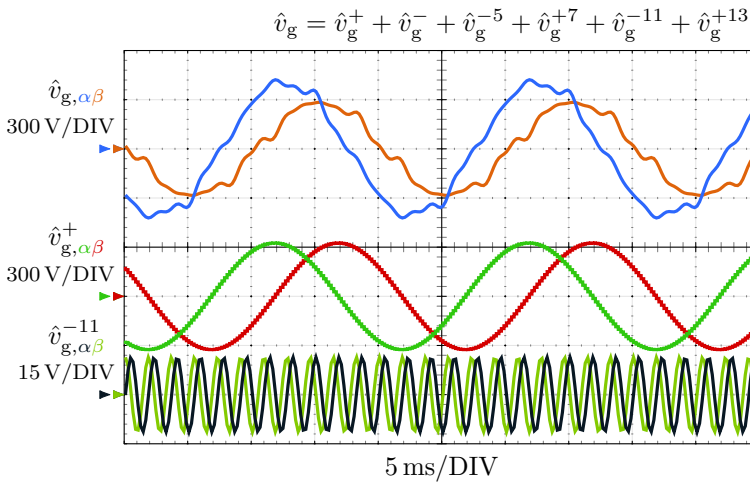
(b)
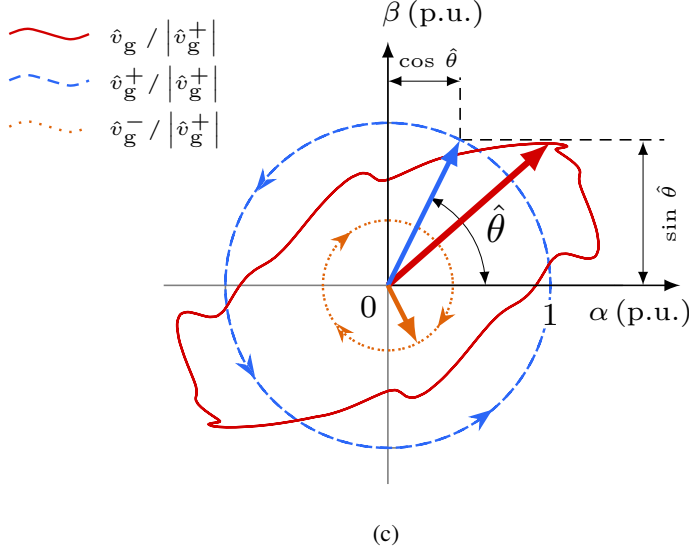
Figure 86. Continued on next page.

(c)

Figure 86. Input equivalent voltage disturbance w and grid voltage v_g waveforms in the $\alpha\beta$ frame. a Time-domain representation of w and two of its symmetrical components w^+ and w^{-11}. b Time-domain representation of v_g and two of its symmetrical components v_g^+, and v_g^{-11}. c Space-vector trajectories of v_g and its main symmetrical components v_g^+ and v_g^-.

5.3. Sensitivity of the Estimated Phase to Plant Modeling Errors

This section gives a bound on the error of the estimated phase θ_err when the plant parameters or the grid impedance change with respect to the nominal values. The estimated phase error is

$$\theta_\mathrm{err} = \hat{\theta} - \theta_\mathrm{actual}, \tag{86}$$

where $\hat{\theta}$ is the estimated phase and θ_actual is the phase of the positive sequence of the grid voltage.

The proposed grid-synchronization method uses two models, namely, G_LCL and G_LC. G_LCL is a discrete-time model of the LCL filter plus the computational delay that relates the grid-side current with the plant input voltage when no disturbances, such as the grid voltage, are considered:

$$G_\mathrm{LCL}(z) = \frac{i_1}{v} = \left.\frac{i_1}{u_\mathrm{sat}}\right|_{[\,]\,v_\mathrm{g}=0}. \tag{87}$$

This model is used by the observer to calculate the input-equivalent voltage disturbance $\hat{w}$ and the controller output voltage u_sat. The mathematical process to derive such model was presented in [8, Sec. II] and it requires the nominal values of the LCL filter parameters L_1, R_1, L_2, R_2, C, and R_C.

The second model G_LC is used by the proposed synchronization scheme, cf. (85) and describes the relation between w and v_g.
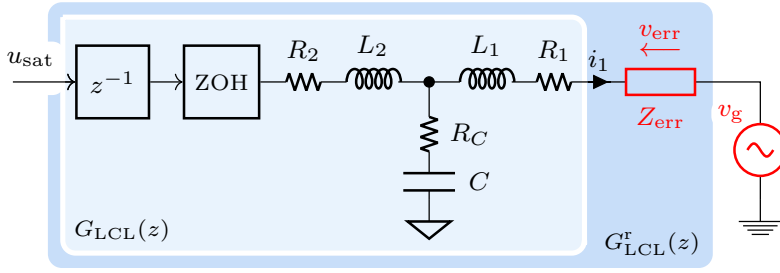
Figure 87. Nominal plant model G_{LCL} used by the current controller and real plant model $G_{\text{LCL}}^{\text{r}}$. Plant modeling errors are represented by an impedance Z_{err}.

In order to study the sensitivity of the system to plant parameter variations, the presented study is organized into two parts. First, a theoretical relation between plant modeling errors and θ_{err} is introduced. Then, the maximum value of θ_{err} is calculated for a 50% variation in the plant parameters and for a sweep in the grid impedance value. It should be noticed that a variation in the grid impedance can be modeled as a change in L_1 or R_1, cf. Figure 81, because the grid-side inductor of the LCL filter is in series with the grid impedance and the proposed controller does not measure the voltage at the PCC.

The real LCL model relates the grid-side current with the plant input voltage when the grid voltage is zero and the filter parameters are L_1^{r}, R_1^{r}, L_2^{r}, R_2^{r}, C^{r}, and R_C^{r}:

$$G_{\text{LCL}}^{\text{r}}(z) \quad = \quad \frac{i_1}{v + v_{\text{errr}}}. \tag{88}$$

Similarly, the real LC model $G_{\text{LC}}^{r}(z)$ represents the relation between w and v_g when the real filter parameters are considered instead of the nominal values.

Using (87) and (88) the following relation is obtained:

$$\frac{1}{G_{\text{LCL}}^{\text{r}}(z)} \quad = \quad \frac{v + v_{\text{err}}}{i_1} = \frac{1}{G_{\text{LCL}}(z)} + Z_{\text{err}}, \tag{89}$$

where the impedance Z_{err} represents a change in the plant model caused by any plant parameter variations, cf Figure 87. It should be noticed that Z_{err} represents a variation in any of the plant parameters in spite of it being an impedance in series with the grid-side inductance; hence Z_{err} has a magnitude and phase that depends on the choice of plant parameter variations.

Figure 88 illustrates (84) and (89) evaluated at the positive sequence of the grid voltage frequency f_{g} when the filter parameters vary a $\pm 50\%$ with respect to their nominal values. As shown in Figure 88, the resistive component of Z_{err} is mainly determined by the resistive plant modeling error $R_{\text{err}} = R_1 - R_1^{\text{r}} + R_2 - R_2^{\text{r}}$. The reactive component of Z_{err} primarily depends on the reactive plant modeling error $L_{\text{err}} = L_1 - L_1^{\text{r}} + L_2 - L_2^{\text{r}}$. Moreover, Z_{err} evaluated at f_g is not significantly affected by modeling errors on C or R_C. Therefore, an approximation of the magnitude of Z_{err} is

$$|Z_{\text{err}}| \quad \approx \quad \sqrt{R_{\text{err}}^2 + (2\pi f_{\text{g}} L_{\text{err}})^2}. \tag{90}$$

For a $\pm 50\%$ parameter variation, the following bounds on the resistive and reactive modeling errors are obtained:

$$|R_{\mathrm{err}}| \leq \max\,(R_1, R_2) \quad \text{and} \quad |L_{\mathrm{err}}| \leq \max\,(L_1, L_2)\,. \qquad (91)$$

When such upper bounds are evaluated with the experimental setup parameters used in this section ($L_1 = L_2 = 0.05$ p.u., $R_1 = R_2 = 0.015$ p.u.), the value of Z_{err} is approximately 0.05 p.u. (1Ω, cf. Figure 88).

Concerning the LC model (84), G_{LC} presents a low sensitivity to parameter variations at low frequencies. A negligible change in G_{LC} occurs at the grid frequency when a 50% variation in the nominal LC parameters L_2, R_2, C, and R_c is performed, cf. Figure 88. Such robustness is a consequence of the large impedance difference between the series inductor and the parallel capacitor at the grid frequency: $2\pi f_{\mathrm{g}} L_2 \ll 1/(2\pi f_{\mathrm{g}} C)$. This impedance difference is maintained even in the presence of large parameter variations and causes the resulting transfer function to always have a magnitude close to one. Therefore, a small modeling error is introduced by using K_{LC} in the proposed synchronization scheme, in spite of it being computed offline using the nominal plant parameters.
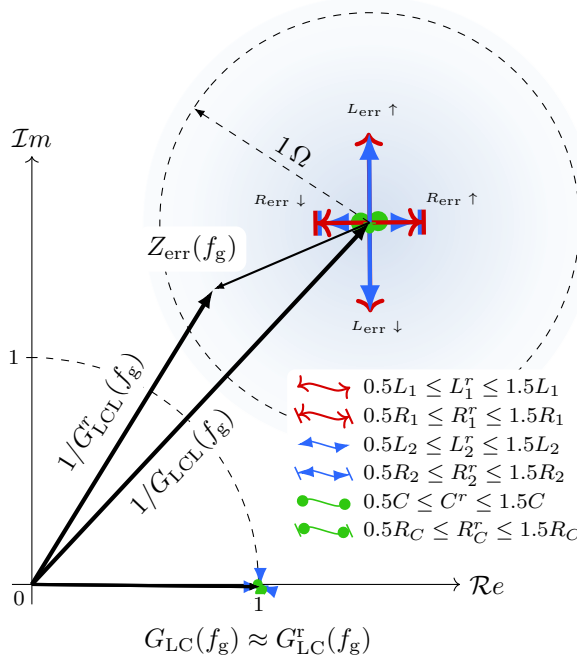

Figure 88. Nominal LCL filter impedance $1/G_{\mathrm{LCL}}$, cf. (87); real LCL filter impedance $1/G_{\mathrm{LCL}}^{\mathrm{r}}$, cf. (88); nominal LC gain G_{LC}, cf. (84); and real LC gain $G_{\mathrm{LC}}^{\mathrm{r}}$ at the grid frequency f_{g} when a $\pm 50\%$ variation in the nominal plant parameters L_1, L_2, R_1, R_2, C, and R_C is considered.

When there are plant modeling errors, i.e., $Z_{\mathrm{err}} \neq 0$, the observer estimates an input equivalent voltage disturbance $\widehat{w}$ that cancels the effect of v_{g} and of v_{err}. At the positive
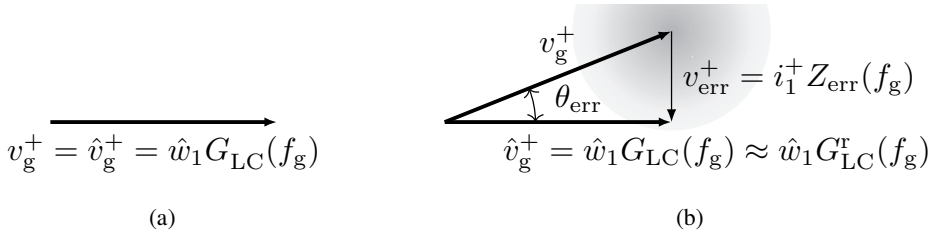
Figure 89. Phase estimation error: a Nominal case. b Worst case.

sequence of the fundamental grid frequency, such cancellation is expressed as:

$$\widehat{v}_{\mathrm{g}}^{+} \;=\; \widehat{w}_1 G_{\mathrm{LC}}(f_{\mathrm{g}}) = v_{\mathrm{g}}^{+} + v_{\mathrm{err}}^{+}. \tag{92}$$

Equation (92) uses the nominal LC model G_{LC} instead of the real model G_{LC}^{r} because plant parameter variations do not significantly affect the response of such model at the fundamental grid frequency, as explained previously.

In the nominal case, Z_{err} and v_{err} are zero; therefore, $\widehat{v}_{\mathrm{g}}^{+}$ is equal to v_{g}^{+} and θ_{err} is zero, cf. Figure 89a. When the plant parameters vary, θ_{err} can be non zero depending on the magnitude and phase of v_{err}, as illustrated in Figure 89b. The maximum θ_{err} is obtained when the amplitude of v_{err} is maximum and the phase is 90° with respect to $w^{+}G_{\mathrm{LC}}^{r}$, cf. Figure 89b. Such condition results in the following upper bound for the error in the estimated phase

$$\theta_{\mathrm{err}} \;\leq\; \sin^{-1}\left|\frac{v_{\mathrm{err}}}{v_{\mathrm{g}}}\right| \leq \sin^{-1}\frac{i_{\mathrm{base}}|Z_{\mathrm{err}}|}{v_{\mathrm{base}}}. \tag{93}$$

When Z_{err} represents an unmodeled grid impedance Z_g, the error in the estimated phase (93) can be expressed in terms of the grid short circuit ratio (SCR), $\mathrm{SCR} = Z_{\mathrm{base}}/|Z_{\mathrm{g}}|$:

$$\theta_{\mathrm{err}} \;\leq\; \sin^{-1}\frac{1}{\mathrm{SCR}}. \tag{94}$$

Equation (94) is shown in Figure 90 and is explained in detail in the next section.

5.4. Performance Analysis of the Proposal

The proposed synchronization scheme provides a robust operation under distorted or unbalanced grid conditions thanks to the symmetrical component decomposition performed by the observer.

Concerning the steady-state performance, the presented method provides the same estimation accuracy as a PLL if the LCL filter parameters are known and the grid impedance value is considered zero. In such conditions, both solutions provide the phase of the voltage at the PCC, which can be different than the phase of the grid voltage depending on the value of the grid impedance and the grid-side current. Nonetheless, if the grid impedance value is added to the grid-side impedance (L_1 and R_1) in the plant model, cf. (87), then the proposed method yields the actual phase of the grid voltage θ_{actual}. In this manner, the proposal avoids the phase estimation error that a PLL introduces due to the grid impedance.
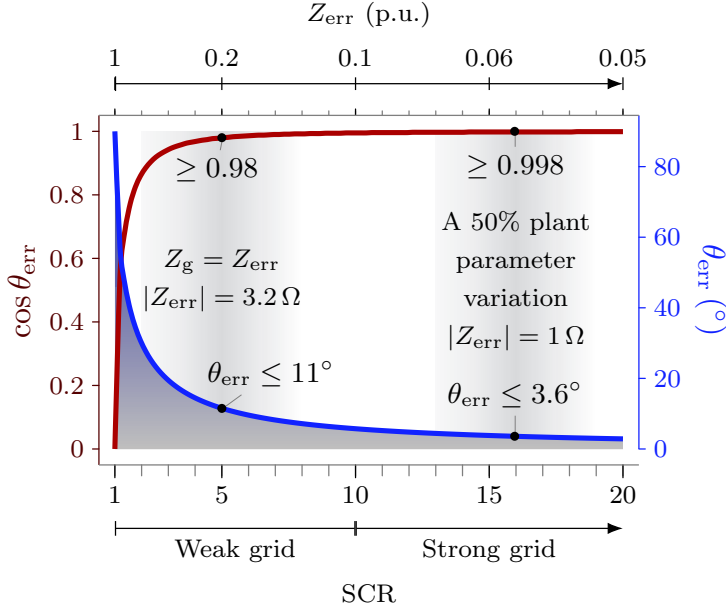
Figure 90. Maximum phase estimation error θ_{err} and minimum achievable power factor $\cos \theta_{\mathrm{err}}$ as a function of the grid short circuit ratio (SCR) when the grid impedance is not included in the model used by the current controller.

On the other hand, when the LCL filter parameters are not known, the proposed method introduces an steady-state estimation error. The error introduced is equivalent to an error caused by an unmodeled grid impedance of value $R_{\mathrm{err}} + j2\pi L_{\mathrm{err}}$. As mentioned previously, changes in the nominal capacitor parameters C and R_C have a negligible effect on the estimation error.

Grid-tied inverters are usually required to operate at unity power factor. Nonetheless, when a phase estimation error occurs, the inverter operates at a lower power factor. Figure 90 plots θ_{err}, cf. (94), and the resultant power factor $\cos \theta_{\mathrm{err}}$ for a sweep in the magnitude of Z_{err} from 0.05 p.u. to a value of 1 p.u. When a 50% variation in the plant parameters is considered, the magnitude of Z_{err} is smaller than $1\,\Omega$, as explained previously, and the estimation error in such condition is negligible ($\cos \theta_{\mathrm{err}} \leq 0.98$), cf. Figure 90. Moreover, the estimated phase error is not significant for short circuit ratio (SCR) values greater than 5.

Regarding the transient performance, the proposed scheme has the same bandwidth as the current controller because both systems use the same state vector $\hat{\mathbf{x}}_{add}^{LCL}$; hence, the observer determines the dynamics of both the current controller and the synchronization scheme. Therefore, when a transient, such as a voltage sag, occurs in the grid voltage, both the current controller and the proposed synchronization method converge at the same rate to the new steady-state regime. Further increasing the bandwidth of the synchronization mechanism does not provide any real benefit because the performance is ultimately limited by the current controller dynamics.

It should be noticed that, contrary to a PLL-based scheme [118, 119], there is no interaction between the current controller and the synchronization algorithm because the voltage at

the PCC is not measured and the dynamics of both systems are determined by the observer.

The frequency range where synchronization occurs is established by the bandwidth of the resonant action in the current controller. In this manner the locking range of the synchronization algorithm is matched to the frequency range where the current controller operates.

Finally, the proposal requires a minimal computational load. Only a complex multiplication and a complex division (12 flops) are required, cf. Figure 85, because the synchronization scheme employs the information available in the state-vector of the current-controller observer.

5.5.   Bumpless Start

This section explains how to obtain a bumpless start without measuring the voltage at the PCC. The proposed method can be applied to any observer-based current controller with disturbance estimation [81] that measures the grid-side current.

When the voltage source converters (VSCs) is on, wind-up occurs if the plant input u_{sat} is different from the controller output u, e.g., when overmodulation occurs. In this situation, the controller estimated states do not correspond with the actual system states. Contrarily to PI and PR controllers, observer-based controllers avoid this inconsistency by feeding back the saturated controller output u_{sat} when the voltage source converters (VSCs) is on (the switch S_1 is closed, cf. Figure 82).

However, when the voltage source converters (VSCs) is off, the signal applied to the plant input is not determined by the controller or the converter because the voltage source converters (VSCs) output is in a high-impedance mode. This is represented by the switch S_1 in the open position in Figure 82. Traditionally, the current controller is reseted (the accumulators are set to zero) when the voltage source converters (VSCs) is off so as to avoid wind-up problems, as illustrated by the the dashed line in Figure 82.

Contrarily to this approach, the proposed ac-voltage sensorless controller maintains the observer active when the converter is off. Figure 83 illustrates the proposed start up sequence. Before commutation begins (S_1 is open), the observer receives a virtual voltage $\hat{u}_{\text{sat}}$ obtained by filtering the measured grid-side current with a transfer function $G_{\text{bl}}(z)$ that provides the estimation of the plant model input voltage $\hat{u}_{\text{sat}}$. In this manner, the observer estimates the correct plant state $\mathbf{x}_{dd}^{LCL}(k)$ and the input equivalent disturbance w that allows for a bumpless start. In the following, the derivation process to obtain $G_{\text{bl}}(z)$ is detailed.

As illustrated in Figure 91a, the output of the voltage source converters (VSCs) is in a high impedance state before the converter starts switching because the switching transistors are all off. Therefore, the voltage at the output of the voltage source converters (VSCs) u_{d}' is equal to the capacitor voltage v_C because the converter-side current is zero.

$$u_{\text{d}}' \quad = \quad -\frac{i_1}{sC}. \tag{95}$$

However, the observer requires the plant model input voltage u_{sat}, cf. Figure 81, in order to estimate the system state. This signal is a time-shifted version of u_{d}', which includes the effect of the computational (one sample) and the modulation (half a sample) delays. Therefore, the continuous-time transfer function that relates the grid-side current with u_{sat}

is

$$G_{\mathrm{bl}}(s) = \frac{u_{\mathrm{sat}}}{i_1} \quad = \quad \frac{1}{sC} e^{s1.5T_{\mathrm{s}}}. \tag{96}$$

In order to implement (96) in a real-time controller, two problems should be addressed, namely, its non-causality and its infinite gain at dc. The discrete-time equivalent of the causal part of (96) using using a backward rectangular rule is

$$G'_{\mathrm{bl}}(z) = \frac{u_{\mathrm{sat}}}{i_1} \quad = \quad \frac{T_{\mathrm{s}}}{C} \frac{z}{z-1}. \tag{97}$$

The discrete backward rule introduces a phase roll-up at high frequencies which helps to model the non-causal delay, cf. Figure 91b. Finally, the dc pole of (97) is moved to a higher frequency f_{low} in order to clip the low-frequency gain. The authors recommend a value of 10 Hz for f_{low}. The resultant first-order discrete-time transfer function is

$$G_{\mathrm{bl}}(z) = \frac{u_{\mathrm{sat}}}{i_1} \quad = \quad \frac{T_{\mathrm{s}}}{C} \frac{z}{z - e^{j2\pi f_{\mathrm{low}}T_{\mathrm{s}}}}. \tag{98}$$

Figure 91b shows the bode of (98) and compares it to (96). As expected, both transfer functions have a similar response at the fundamental component and the main low order harmonics of the grid frequency, which are located within the shaded region. Furthermore, at low frequencies, the gain is limited to reduce the sensitivity to noise and to a dc offset in the current measurement. At high frequencies, a phase modeling error appears due to the non-causal delay in (96). Nevertheless, such high frequency modeling error has a negligible effect in the performance as verified in the experimental results.

5.6.   Experimental Results

The proposed ac-voltage sensorless method is tested in a 10-kW voltage source converters (VSCs) working as an inverter and connected to a 400-V line-to-line 50-Hz three-phase grid. A three-phase ac voltage source was used to generate transient events in the grid voltage, such as a sag and phase and frequency jumps. The grid voltage has the harmonics presented in Table 14. The performance of the proposal is compared with that of a moving average filter (MAF)-based PLL [131] which uses the measured voltage at the PCC v_{PCC}. Table 19 summarizes the setup parameters. Figures 92a and 92b show a diagram and a photograph of the experimental setup, respectively.

The first test assesses the operation of the proposed synchronization scheme when connected to a weak grid with a distorted voltage. The weak grid is emulated by an impedance in series with the grid voltage. The grid impedance is $Z_{\mathrm{g}} = 10\Omega$ (SCR = 1.6). Figure 93a shows the estimated phase $\hat{\theta}$ and the phase of the positive sequence of the fundamental component of the grid voltage θ_{actual}, which is directly obtained from the three-phase ac source. The proposal provides zero phase error $\hat{\theta} - \theta_{\mathrm{actual}}$, whereas a PLL introduces an error $\theta_{\mathrm{PLL}} - \theta_{\mathrm{actual}}$ due to the change in the voltage at the PCC $v_{\mathrm{PCC},abc}$ as the grid-side current $i_{1,abc}$ increases. Figure 93b shows the spectrum of $\hat{\theta}$ and θ_{PLL}. Both solutions achieve an excellent performance with a low distortion in spite of the large grid voltage distortion thanks to the moving average filter (MAF) in the case of the PLL and to the resonant action
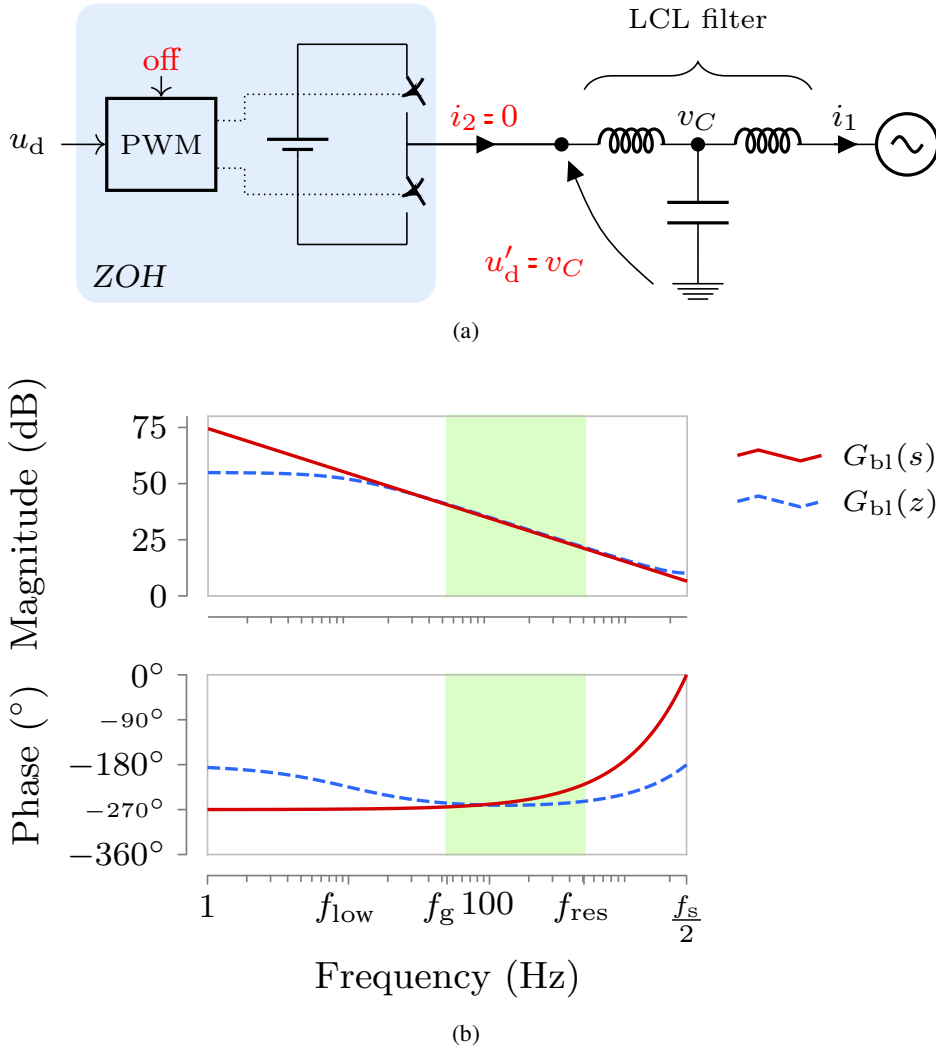
(a)

(b)

Figure 91. Plant model before the converter starts switching. a Block diagram. The voltage at the output of the ZOH is equal to the capacitor voltage. b Bode diagrams.

of the current controller as regards the proposal. The presented method has a non-zero noise amplitude compared to the PLL at the harmonic frequencies that are not controlled by the current controller, such as unbalanced grid harmonics $-7f_g$, $\pm 3f_g$, $+5f_g$ and even grid harmonics. Nevertheless, at the frequencies where the resonant action of the current controller is tuned $-11f_g$, $-5f_g$, $\pm f_g$, $+7f_g$, and $+13f_g$, the proposal achieves a greater attenuation compared to the moving average filter (MAF)-based PLL due to its higher bandwidth.

The second test assesses the sensitivity of the proposal to parameter variations. Figure 94a shows the synchronization performance when the grid impedance value Z_g is included in the plant model. Now the PLL yields a larger error, compared to Figure 93a, because the current reference step is generated in the q axis instead of the d axis. Such current reference results in a grid-side current with a different phase angle. As explained

(a)

(b)

Figure 92. Experimental setup of the grid-connected inverter. a Diagram. b Photograph.
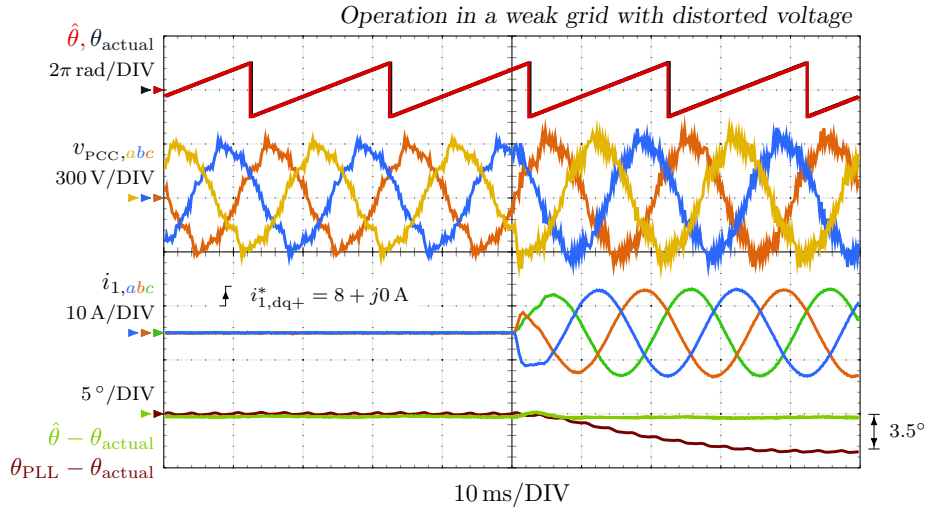
(a)
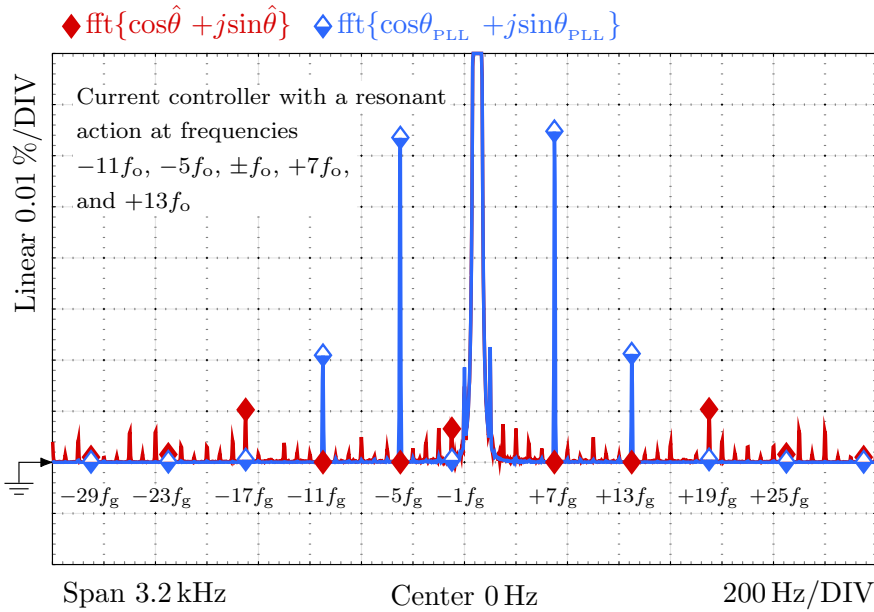
(b)

Figure 93. Synchronization performance when connected to a weak grid with a distorted grid voltage at the PCC $v_{\mathrm{PCC},abc}$. a Time domain waveforms: estimated phase $\hat{\theta}$, phase of the positive sequence of the fundamental component of the grid voltage θ_{actual}, estimation error $\hat{\theta} - \theta_{\mathrm{actual}}$, PLL error $\theta_{\mathrm{PLL}} - \theta_{\mathrm{actual}}$, and grid-side current $i_{1,abc}$. b Spectrum of the estimated phase fft$\{\cos\hat{\theta} + j\sin\hat{\theta}\}$ and of a moving average filter (MAF)-based PLL [131] fft$\{\cos\theta_{\mathrm{PLL}} + j\sin\theta_{\mathrm{PLL}}\}$.

Table 10. Grid Voltage Parameters

Order	Sequence[*]	h	Magnitude
1	+	+1	230 V
3	0		5 %
5	−	−5	6 %
7	+	+7	5 %
9	0		1.5 %
11	−	−11	3.5 %
13	+	+13	3 %
THD			10.5 %

[*] When a sag occurs, the harmonic voltages are unbalanced (all sequences are present for each harmonic).

in Section 5.3, the estimation error depends on the value of the grid-side current, cf. Figure 89b. Contrarily to a PLL, the proposed synchronization scheme does not introduce an error in the estimated phase when the grid-side current is increased provided that the grid impedance value is included in the plant model used to design the controller. If the grid impedance value is not included in the plant model, then both solutions result in the same steady-state error, cf. Figure 94b.

The third test, cf. Figure 95, shows the transient response to a $40°$ phase step and to a 2-Hz frequency jump in the grid-voltage. When a $40°$ phase step occurs in the the grid voltage, cf. Figure 95a, the proposed sensorless method converges to the new phase in one fundamental cycle of the grid voltage and has a faster transient response compared to a moving average filter (MAF)-based PLL. In addition, the phase estimation error is eliminated at the same rate as the grid-side current error generated by the voltage transient because the dynamics of both signals are determined by the observer. When a 2-Hz frequency jump that switches between the grid-frequency limits according to [111] is generated, cf. Figure 95b, the proposed sensorless method yields a smaller estimation error compared to the PLL due to its higher bandwidth and a similar transient response duration.

The forth test assesses the voltage sag ride-through capability of the synchronization scheme, cf. Figure 96. During a sag with a distorted voltage, the estimation error $\hat{\theta} - \theta_{\mathrm{actual}}$ slightly increases due to the appearance of unbalanced voltage harmonics in the grid voltage which are not eliminated by the current controller. Contrarily to the proposal, the PLL does not introduce an additional error thanks to the moving average filter (MAF) filter. Nevertheless, the fundamental unbalance is successfully eliminated from the estimated phase $\hat{\theta}$, which is the main voltage disturbance, and both schemes provide an adequate phase signal with negligible steady-state error. Furthermore, a sensorless scheme avoids measuring and introducing into the controller a distorted voltage $v_{\mathrm{PCC},abc}$, which can degrade the perfor-

**Table 11. Experimental Setup Parameters**

| Base values		
Nominal power	P_{base}	10 kW
Phase voltage	V_{base}	230 V
Nominal current	I_{base}	14.5 A
Grid frequency	f_{g}	50 Hz
LCL filter		
Grid-side inductance	L_1	2.5 mH (0.05 p.u.)
Converter-side inductance	L_2	2.5 mH (0.05 p.u.)
Filter capacitance	C	$30\mu F$ (0.14 p.u.)
Grid-side ESR	R_1	0.25Ω (0.015 p.u.)
Converter-side ESR	R_2	0.25Ω (0.015 p.u.)
Capacitor ESR	R_C	0.1Ω (0.006 p.u.)
Filter resonance	f_{res}	815 Hz
Weak grid		
Grid impedance	Z_{g}	10Ω (0.6 p.u.)
Short circuit ratio	SCR	1.6
voltage source converters (VSCs)		
Switching frequency		2.5 kHz
Sampling frequency		5 kHz
Dead time		$3\mu s$
DC-bus voltage	v_{dc}	700 V

mance of the controller.

The fifth test evaluates the proposed bumpless start scheme. When the voltage source converters (VSCs) is off, an uncontrolled grid-side current circulates through the circuit formed by the grid-side inductance and the capacitor of the LCL filter. A large current distortion is observed because some of the grid voltage harmonics are close to the resonant frequency of the resultant LC circuit. Figure 97 displays the voltage at the PCC and the grid-side current when the voltage source converters (VSCs) is turned on with its current reference $i^*_{1,\text{dq}}$ set to zero. As expected from the theoretical analysis, a smooth start is obtained without measuring $v_{\text{PCC},abc}$ in spite of the highly distorted grid voltage. A one-cycle transient is obtained, which is in accordance with the bandwidth of the current controller.

5.7.   Summary

This section has presented a sensorless grid synchronization method which requires minimal computational load and provides a fast and accurate estimation of the grid voltage when
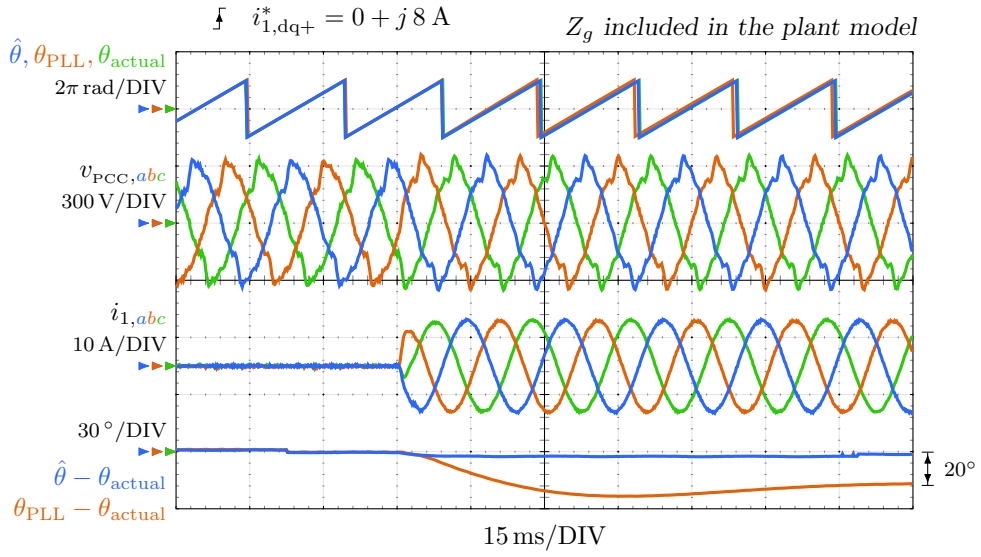
(a)
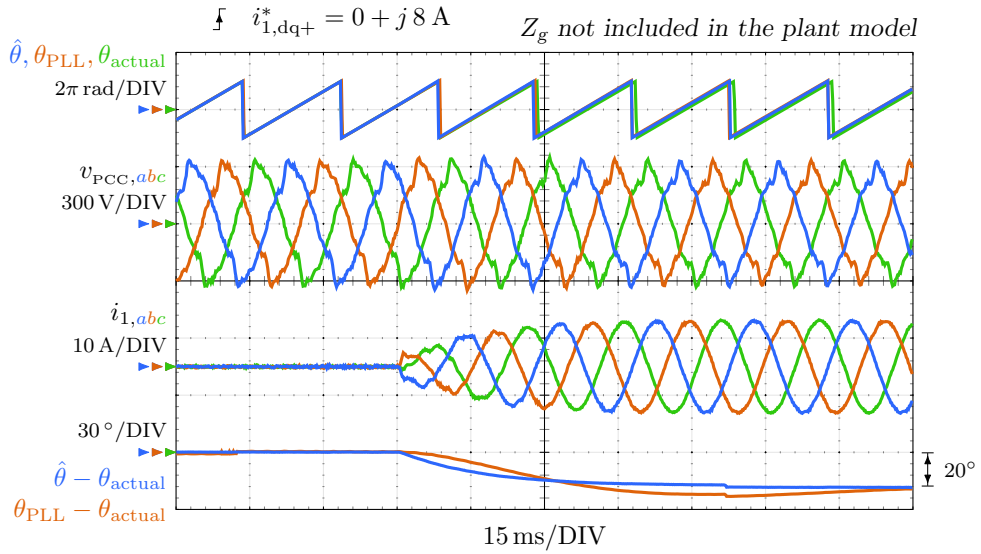
(b)

Figure 94. Synchronization performance when connected to a weak grid with an impedance of value $Z_\mathrm{g} = 10\,\Omega$ and a distorted grid voltage at the PCC $v_{\mathrm{PCC},abc}$. Estimated phase $\hat{\theta}$, phase calculated by a moving average filter (MAF)-based PLL θ_{PLL}, phase of the positive sequence of the fundamental component of the grid voltage θ_{actual}, estimation error $\hat{\theta} - \theta_{\mathrm{actual}}$, PLL error $\theta_{\mathrm{PLL}} - \theta_{\mathrm{actual}}$, and grid-side current $i_{1,abc}$. a The grid impedance value Z_g is included in the plant model used to design the controller. b The grid impedance value Z_g is not included in the plant model; the controller considers Z_g is zero.
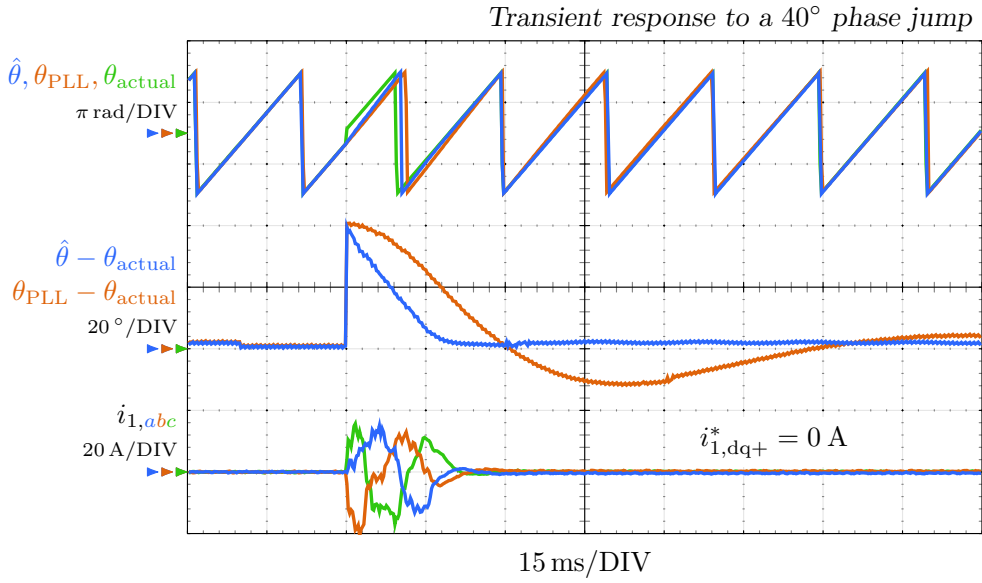
(a)
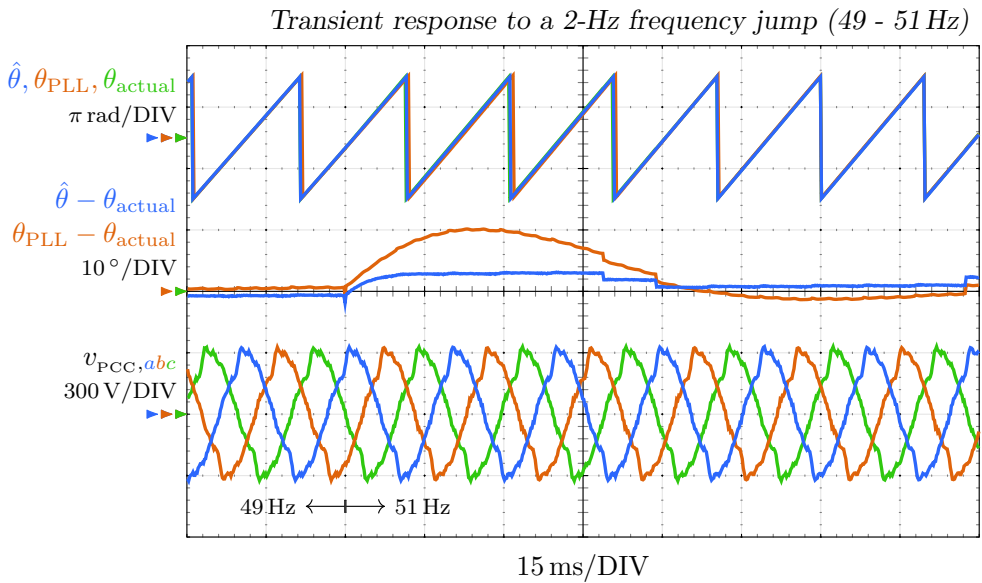
(b)

Figure 95. Estimated phase $\hat{\theta}$, phase calculated by a moving average filter (MAF)-based PLL θ_{PLL}, phase of the positive sequence of the fundamental component of the grid voltage θ_{actual}, estimation error $\hat{\theta} - \theta_{\mathrm{actual}}$, PLL error $\theta_{\mathrm{PLL}} - \theta_{\mathrm{actual}}$, grid-side current $i_{1,abc}$, and voltage at the PCC $v_{\mathrm{PCC},abc}$. a A $40°$ phase jump. b A 2-Hz frequency step.

connected to a weak grid. The interaction between the proposed synchronization method and the current controller is avoided in spite of them having the same bandwidth. A small
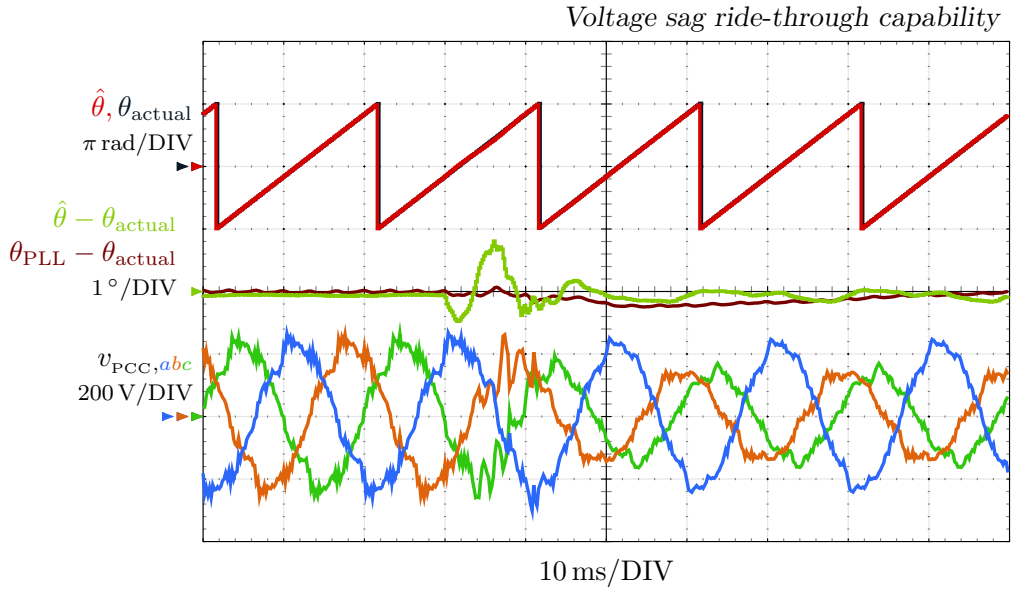
Figure 96. Estimated phase $\hat{\theta}$, phase of the positive sequence of the fundamental component of the grid voltage θ_{true}, estimation error $\hat{\theta} - \theta_{\text{true}}$, PLL error $\theta_{\text{PLL}} - \theta_{\text{true}}$, and voltage at the PCC $v_{\text{PCC},abc}$ before and during a 40%-depth type-C sag.
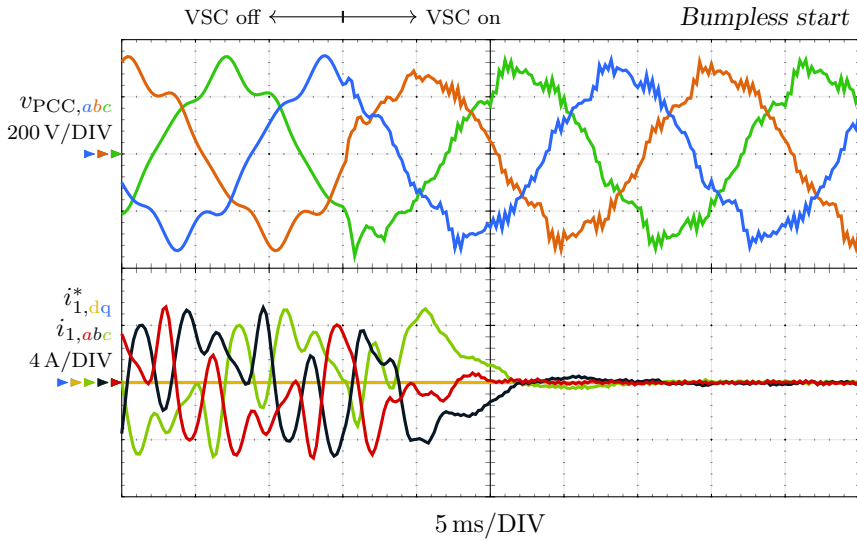

Figure 97. Grid-side current $i_{1,abc}$ and voltage at the PCC $v_{\text{PCC},abc}$ when the voltage source converters (VSCs) is turned on with a zero current reference $i_{1,dq}^*$.

estimation error is obtained due to the low sensitivity of the proposal to plant modeling errors. If the grid-impedance is assumed to be zero, both the proposal and a PLL-based scheme result in the same steady-state error. Contrarily to a PLL, the presented scheme

does not require to measure the grid voltage, which could affect the performance under weak grid conditions, when the voltage at the PCC is different from the grid voltage and it is coupled to the grid-side current. A bumpless start capability provides a soft start and a sensorless operation in any grid conditions.

6.   AC-Voltage Harmonic Control for Stand-Alone and Weak-Grid-Tied Converter

This section presents an ac voltage controller with a high robustness to plant model variations which can operate under a wide range of loads. A robust voltage controller is required in a droop-controlled inverter which operates in island mode with other generators or is connected to a grid. In such modes of operation, the voltage source converters (VSCs) can experience large load impedance variations depending on the number of parallel generators or the grid impedance value. The transient performance is improved by selectively minimizing the output impedance of the system at the frequencies which typically contain the largest components of the output current. Complete harmonic control is achieved due to its zero output impedance at a set of design-selected frequencies. The proposed controller only measures the output voltage; hence, it uses a single-loop structure that uses all available bandwidth. The design process only requires, as input parameters, the LC filter values, the sampling frequency, and a set of harmonics where load-current circulation is expected.

Voltage controllers are an essential component in the performance of a voltage source converters (VSCs) that operates in island operation mode[57] or connected to a microgrid (MG) using a droop control [14, 132, 133].

In order to regulate the ac voltage, inverters commonly use a double-loop [55, 56] or a single-loop controller [52]. Double-loop structures provide a stable system using simple (low-order) proportional-integral (PI) or PR controllers because they divide the complex plant model into two parts. An inner current loop simplifies the plant model seen by the voltage controller. The inner current controller assumes an L filter, whereas the outer voltage loop mainly sees a capacitive plant in the low frequency range where it operates. Typically, the bandwidth of the current controller is larger than the bandwidth of the voltage controller so as to avoid interaction between both loops. Nevertheless, such extra bandwidth of the current controller does not provide any improvements to the system performance besides the desired decoupling between controllers [56]. Actually, the output impedance of the system augments when the bandwidth of the current loop increases [134], as expected from the fact that good current sources have a high output impedance. Furthermore, double loop controllers have stability problems when controlling frequency components close or above the critical frequency ($f_s/6$), where f_s denotes the sampling frequency [57].

Single loop structures with classical transfer-function-based controllers [58] offer a simple design process. Nevertheless, they lack the flexibility, modularity and robustness to

parameter variations of double-loop controllers [59]. Moreover, they may need to measure additional variables, such as the converter current for protection against a short circuit or the capacitor current to achieve stability [52]. In particular, single-loop control cannot stabilize the system when the resonance frequency of the LC filter is less than one-fourth of the sampling frequency [60]. For these reasons, a multiloop structure is typically adopted.

Concerning the type of controller, transfer-function-based solutions are commonly adopted. The voltage loop typically implements PR or synchronous reference frame (SRF)-PI controllers to achieve zero steady-state error in the output voltage at the fundamental frequency and at the main low-order harmonics under different loads [52]. The current loop usually contains a simple P controller [56] so as to reach a high bandwidth and obtain a good decoupling between the two loops. Nevertheless, these solutions do not optimize the performance of the voltage controller in terms of the achievable bandwidth or the robustness against a large variation in the load impedance, in particular when the resonant frequency of the LCL filter is above the critical frequency (a sixth of the sampling frequency) [57]. Contrarily to these solutions, state-space controllers from modern control theory have proven to have a high robustness[61, 62, 63]. Such robustness is convenient during grid-connected mode or during parallel operation, because the inverter sees a low load impedance [64], which is the parallel equivalent of the load impedance and the coupling impedance. The voltage controller presented in [62] incorporates an integral action to remove steady-state error at the fundamental output frequency. In [61], a voltage controller is designed using a pole-placement technique. Such design [61] provides a stable operation in parallel configurations with a grid impedance down to short circuits and intermodule coupling impedances as low as 1%. The solution presented in [63] uses a pole-placement strategy and improves the reference tracking performance compared to transfer function based controllers.

This section proposes an ac voltage controller with a high robustness to changes in the plant model. Plant model changes can occur due to LC filter parameter variations or when the voltage source converters (VSCs) switches the mode of operation. The proposed controller can operate with small load impedances and output power factors smaller than that of previously proposed controllers without significantly degrading the transient performance.

In order to maximize the performance, the proposal uses all the information available at the design stage, namely, a high-order model which describes the installed LC filter, the computational delay, and the expected harmonic disturbances. The transient performance is improved by selectively minimizing the output impedance of the system at a set of design-selected frequencies. Complete harmonic control is achieved due to its zero output impedance at the previous set of frequencies. The controller only measures the output voltage; hence, it uses a single-loop structure with all the available bandwidth. An independent converter-current monitor provides short-circuit protection using the saturated PWM voltage reference and the measured output voltage.

The design process offers a simple tuning and only requires, as input parameters, the values of the LC filter elements, the sampling frequency, and a set of frequencies where load-current circulation is expected. Moreover, the indicated properties are maintained irrespectively of the LC filter installed or the sampling frequency used, provided that over-modulation of the voltage source converters (VSCs) is avoided and the resonant frequency of the LC filter is lower than the Nyquist frequency of the digital controller.

The rest of the section is organized as follows. Section 6.1 introduces the model of

the plant and the disturbances. This model is used in Section 6.2 to design the proposed controller. Next, in Section 6.3, the robustness of the proposal is assessed. In Section 6.3.1, the performance under different load conditions is studied. In Section 6.5, the theory is validated by simulation and experimental results. Finally, Section 8.6 summarizes the work.

6.1.   Modeling of the Plant and the Disturbances

This section presents a mathematical model of the plant and of the design-selected disturbances that are being controlled. Figure 98 shows a diagram of the physical system, where $v_{C,abc}$ is the measured load voltage and v_C^* is the load voltage reference in the $\alpha\beta$ frame. When no reference frame in a subscript of a variable is detailed, the $\alpha\beta$ frame with an amplitude-invariant transformation is assumed.
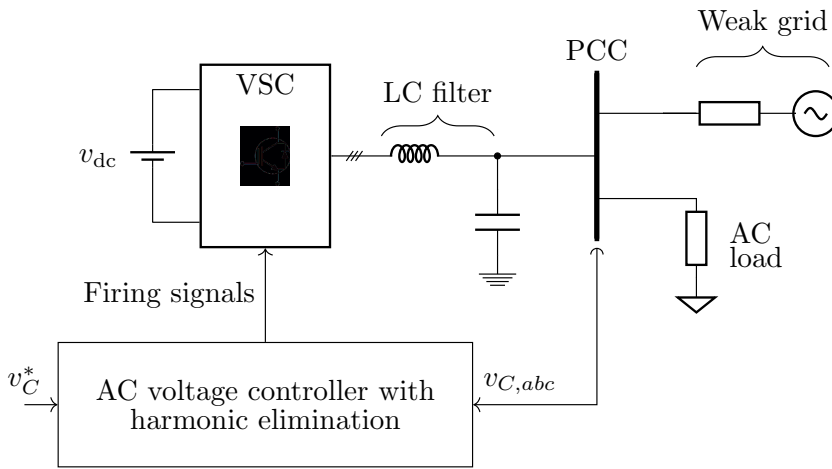

Figure 98. Grid-connected voltage source converters (VSCs) with an LCL filter and a grid-side current controller.

The plant model required to design the proposed voltage controller relates the controller output voltage v with the capacitor voltage v_C. Figure 100a shows a detailed block diagram in the $\alpha\beta$ frame of such plant model, where L and C denote the values of the LC filter reactive elements; R_L^{ESR}, R_C, and $R_{\text{VSC}}^{\text{ESR}}$ represent the ESRs of the filter and the voltage source converters (VSCs) [15]; the ZOH block models the PWM by introducing a half-sample delay; the z^{-1} block symbolizes a one-sample computational delay; and Z_{load} models the impedance of an unknown load connected at the output. A one-sample computational delay appears in the PWM reference voltage v when it is implemented in a real-time controller, as shown in Figure 99. The voltage reference computed using the measurements at instant kT_s is executed by the PWM at instant $(k+1)T_s$. The signals v_C and i_L are the LC-filter state variables (the capacitor voltage and the inductor current, respectively); v_{dl} is the PWM voltage reference, which is the one-sample delayed controller output voltage; and v_{PWM} is the averaged PWM output voltage. It should be noticed that v does not exist in the real system because, by the time the controller output voltage is computed, a one-sample computational delay has already passed; hence the value provided by the embedded controller is v_{dl}.
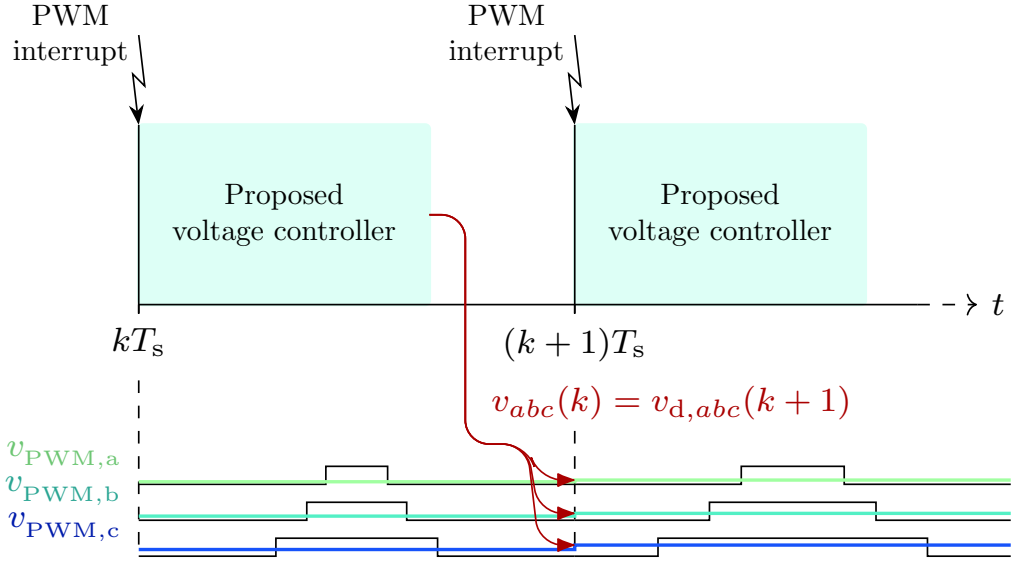
Figure 99. Chronogram of the execution.

Such model depends on the current demanded by a load connected at the output i_{o}. Figure 100b shows the frequency response of this plant model when a linear load is connected. Three different types of linear loads are considered, namely, a resistive, a capacitive, and an inductive load. A resistively load damps the resonance of the LC filter, that is, it lowers the gain of the plant model at the resonant frequency. Inductive and capacitive loads shift the resonant frequency of the system.

The proposed design aims to give a good performance under a wide range of loads because the load value is usually unknown at the design stage and often variable and nonlinear. The nominal plant model assumes that the load is an open circuit (no load). This is the model used to design the controller. Such choice minimizes the plant modeling error when both capacitive and inductive loads are considered, cf. Figure 100b. Moreover, at low frequencies, the open-loop output voltage usually decreases when a load is connected at the output due to the loading effect, i.e., the gain of the model diminishes when the load impedance lowers; hence, stability is usually improved with respect to the nominal case. A thorough study of the load effect in the system performance is analyzed in Section 6.3.1.

6.1.1. Model of the Plant for the Compensator

The mathematical modeling process takes place in several steps. Each step adds features to the model equations obtained in the previous stage. In the first place, a continuous-time model of the LC filter in the $\alpha\beta$ frame, including losses, is presented. This model relates the capacitor voltage v_C to the the averaged PWM output voltage u'_d for the LC filter of the plant shown in Figure 100a. The first-order differential equations in the continuous domain
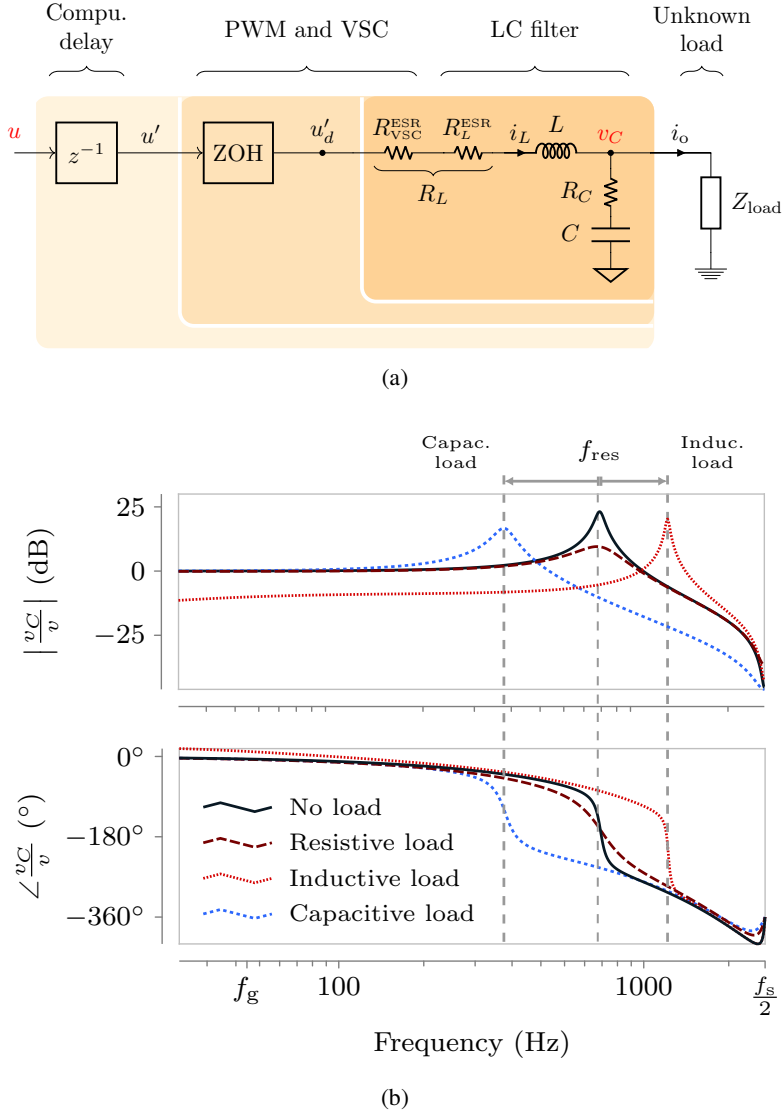
(a)

(b)

Figure 100. Model of the plant. a Plant diagram in the $\alpha\beta$ frame when a load is connected at the output: LC filter, PWM (modeled as a ZOH), and one-sample computation delay. b Bode of the plant model (v_C/v) under different load conditions.

(written in state-space form) are

$$\frac{\mathrm{d}\mathbf{x}^{LC}(t)}{\mathrm{d}t} = \underbrace{\begin{bmatrix} \frac{-R_C}{L} & \frac{-R_C R_L}{L} + \frac{1}{C} \\ \frac{-1}{L} & \frac{-R_L}{L} \end{bmatrix}}_{\mathbf{A}^{LC}} \mathbf{x}^{LC}(t) + \underbrace{\begin{bmatrix} \frac{R_C}{L} \\ \frac{1}{L} \end{bmatrix}}_{\mathbf{B}^{LC}} u_d'(t)$$

$$v_C(t) = \underbrace{\begin{bmatrix} 1 & 0 \end{bmatrix}}_{\mathbf{C}^{LC}} \mathbf{x}^{LC}(t)$$

$$\mathbf{x}^{LC}(t) = \begin{bmatrix} v_C & i_L \end{bmatrix}^{\mathrm{T}}. \tag{99}$$

Boldface denotes a vector or a matrix. Equation (99) does not include the effect of a load current i_o in the state variables. This disturbance is studied later.
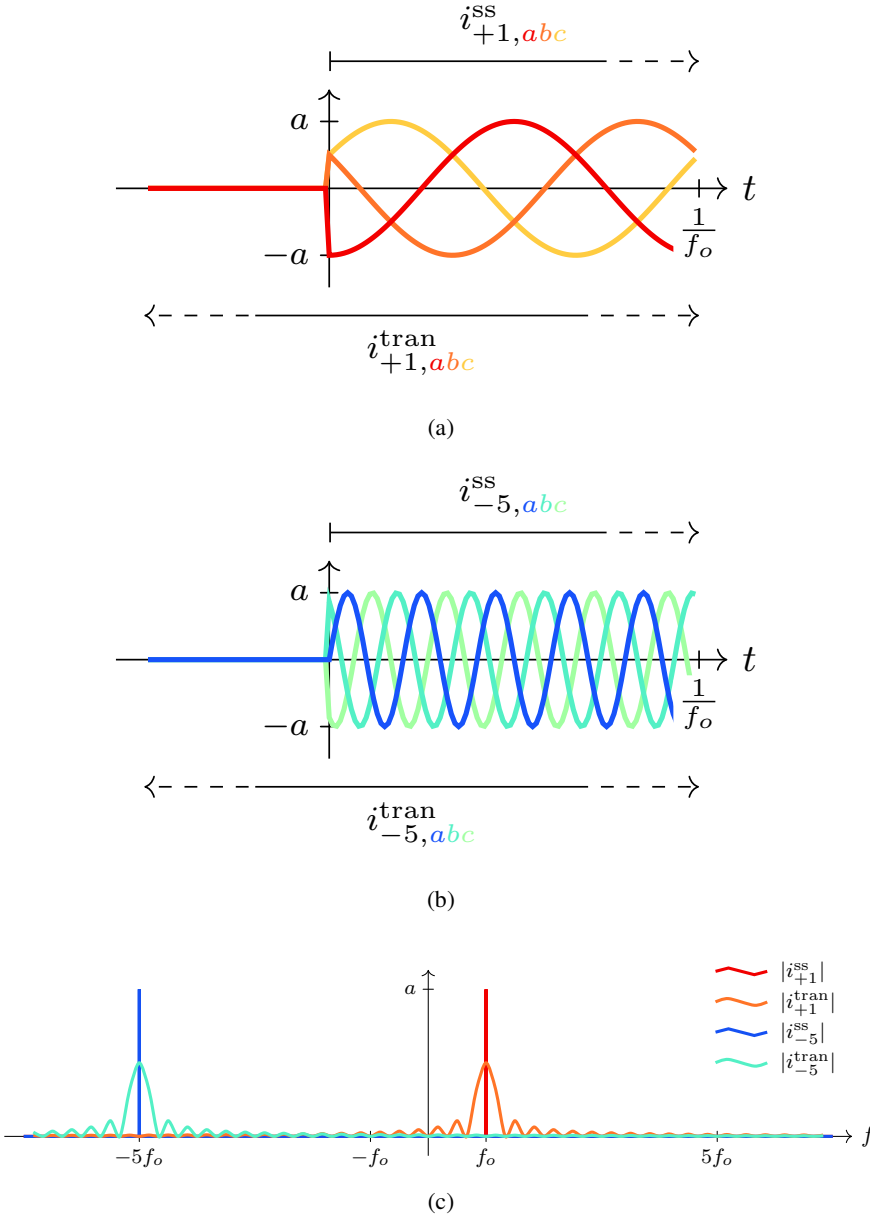

(a)

(b)

(c)

Figure 101. Example of current components demanded by a load. a Positive sequence of the fundamental (first-harmonic) current component $i_{+1,abc}$. b Negative sequence of the fifth-harmonic current component $i_{-5,abc}$. c Magnitude of the spectrum of the previous two current components in the $\alpha\beta$ frame during steady state and during a transient event.

Next, (99) is discretized by using a ZOH equivalent [81]. Such discretization method takes into account the half a sample delay added by the PWM [15].

$$\begin{aligned}
\mathbf{A}_d^{LC} &= e^{\mathbf{A}^{LC}T_s} \\
\mathbf{B}_d^{LC} &= \left(\mathbf{A}^{LC}\right)^{-1}\left(e^{\mathbf{A}^{LC}T_s} - \mathbf{I}\right)\mathbf{B} \\
\mathbf{C}_d^{LC} &= \mathbf{C}^{LC}.
\end{aligned} \tag{100}$$

The resulting model relates the the PWM voltage reference u_d with the sampled capacitor voltage:

$$\begin{aligned}
\mathbf{x}_d^{LC}(k+1) &= \mathbf{A}_d^{LC}\mathbf{x}_d^{LC}(k) + \mathbf{B}_d^{LC}u_d(k) \\
v_C(k) &= \mathbf{C}_d^{LC}\mathbf{x}_d^{LC}(k).
\end{aligned} \tag{101}$$

Then, a one-sample (computational) input delay is added, cf. Figure 99. The model of this delay on the controller output voltage v is

$$u_d(k+1) = u(k). \tag{102}$$

In this manner, combining (101) and (102), the plant model that takes the computational delay into account is

$$\underbrace{\begin{bmatrix} \mathbf{x}_d^{LC}(k+1) \\ u_d(k+1) \end{bmatrix}}_{\mathbf{x}_{dd}^{LC}(k+1)} = \underbrace{\begin{bmatrix} \mathbf{A}_d^{LC} & \mathbf{B}_d^{LC} \\ \mathbf{0} & 0 \end{bmatrix}}_{\mathbf{A}_{dd}^{LC}} \underbrace{\begin{bmatrix} \mathbf{x}_d^{LC}(k) \\ u_d(k) \end{bmatrix}}_{\mathbf{x}_{dd}^{LC}(k)} + \underbrace{\begin{bmatrix} \mathbf{0} \\ 1 \end{bmatrix}}_{\mathbf{B}_{dd}^{LC}} u(k)$$

$$v_C(k) = \underbrace{\begin{bmatrix} \mathbf{C}_d^{LC} & 0 \end{bmatrix}}_{\mathbf{C}_{dd}^{LC}} \underbrace{\begin{bmatrix} \mathbf{x}_d^{LC}(k) \\ u_d(k) \end{bmatrix}}_{\mathbf{x}_{dd}^{LC}(k)}$$

$$\mathbf{x}_{dd}^{LC}(k) = \begin{bmatrix} v_C & i_L & u_d \end{bmatrix}^{\mathrm{T}}. \tag{103}$$

The resultant model relates the inverter output voltage $v_C(k)$ to the controller output voltage $u(k)$, cf. Figure 100a. Equation (103) is the nominal plant model and it is used in Section 6.2 to design the controller.

6.1.2. Disturbance Model for the Observer

The proposed controller includes a multi-frequency resonant action in order to eliminate steady-state errors in the controlled capacitor voltage v_C caused by non linear loads or any other unmodeled nonlinearity in the system. The resonant action is obtained by placing open-loop poles in the observer at the targeted frequencies. Since the proposed controller operates in the $\alpha\beta$ frame, both the positive- and the negative-sequence voltage harmonics, cf. Figure 101, can be controlled independently by placing the observer poles in the positive or the negative frequencies, respectively.

In order to implement such resonant action in the observer, the model of the plant in (103) is augmented with a high-order disturbance model. An h-order harmonic voltage disturbance as a function of time $w^h(t)$ in the $\alpha\beta$ frame has the following expression:

$$w^h(t) = A_h e^{j(2\pi f_o ht + \phi_h)} \tag{104}$$

where A_h and ϕ_h are the amplitude and initial phase, respectively; f_o is the fundamental output frequency; and the sign of h defines the sequence (positive or negative) of the harmonic disturbance [36].

A multi-frequency disturbance $w(t)$ that is composed of n harmonics $(h_1, h_2, \ldots, h_n)$ is modeled using (104) as

$$w(t) = w^{h_1}(t) + w^{h_2}(t) + \cdots + w^{h_n}(t). \tag{105}$$

This disturbance equation models all the harmonics (and the fundamental components, for $h = \pm 1$) that are to be rejected with zero steady-state error.

The single-frequency disturbance $w^h(t)$ in (104) is a solution of the following differential equation:

$$\frac{\mathrm{d}w^h(t)}{\mathrm{d}t} = j\,\omega_g\,h\,w^h(t). \tag{106}$$

Hence, the multi-frequency disturbance in (105) can be expressed in matrix notation as a solution of

$$\frac{\mathrm{d}\mathbf{r}(t)}{\mathrm{d}t} = \underbrace{\begin{bmatrix} j\omega_g h_1 & 0 & \cdots & 0 \\ 0 & j\omega_g h_2 & \cdots & 0 \\ \vdots & \vdots & \ddots & \vdots \\ 0 & 0 & \cdots & j\omega_g h_n \end{bmatrix}}_{\mathbf{A}^{dis}} \mathbf{r}(t)$$

$$w(t) = \underbrace{\begin{bmatrix} 1 & 1 & \cdots & 1 \end{bmatrix}}_{\mathbf{C}^{dis}} \mathbf{r}(t) \tag{107}$$

where

$$\mathbf{r}(t) = \begin{bmatrix} w^{h_1} & w^{h_2} & \cdots & w^{h_n} \end{bmatrix}^{\mathrm{T}}. \tag{108}$$

Then, the model in (107) is discretized by using a ZOH equivalent [81] (to model the PWM effect) [1]:

$$\begin{aligned} \mathbf{A}_d^{dis} &= e^{\mathbf{A}^{dis}T_s} \\ \mathbf{C}_d^{dis} &= \mathbf{C}^{dis}. \end{aligned} \tag{109}$$

The nominal plant model (103) is augmented with this input disturbance model (107) to obtain the augmented system model:

$$\underbrace{\begin{bmatrix} \mathbf{x}_{dd}^{LC}(k+1) \\ \mathbf{r}(k+1) \end{bmatrix}}_{\mathbf{x}_{add}^{LC}(k+1)} = \underbrace{\begin{bmatrix} \mathbf{A}_{dd}^{LC} & \mathbf{B}_{dd}^{LC}\mathbf{C}_d^{dis} \\ \mathbf{0} & \mathbf{A}_d^{dis} \end{bmatrix}}_{\mathbf{F_3}} \underbrace{\begin{bmatrix} \mathbf{x}_{dd}^{LC}(k) \\ \mathbf{r}(k) \end{bmatrix}}_{\mathbf{x}_{add}^{LC}(k)} + \underbrace{\begin{bmatrix} \mathbf{B}_{dd}^{LC} \\ \mathbf{0} \end{bmatrix}}_{\mathbf{B}_{add}^{LC}} u(k)$$

$$i_1(k) = \underbrace{\begin{bmatrix} \mathbf{C}_{dd}^{LC} & \mathbf{0} \end{bmatrix}}_{\mathbf{C}_{add}^{LC}} \underbrace{\begin{bmatrix} \mathbf{x}_{dd}^{LC}(k) \\ \mathbf{r}(k) \end{bmatrix}}_{\mathbf{x}_{add}^{LC}(k)}. \tag{110}$$

This model is used in the next section to develop the observer of the proposed controller.

6.2.   Design of the Controller

This section describes the proposed controller. First, single and dual loop structures are compared in order to explain the advantages of the adopted structure. Then, the controller design process is presented. Such controller uses a single voltage loop and contains three modules: a compensator, an observer, and an ac-side converter-current estimator for over-current protection, cf. Figure 103.
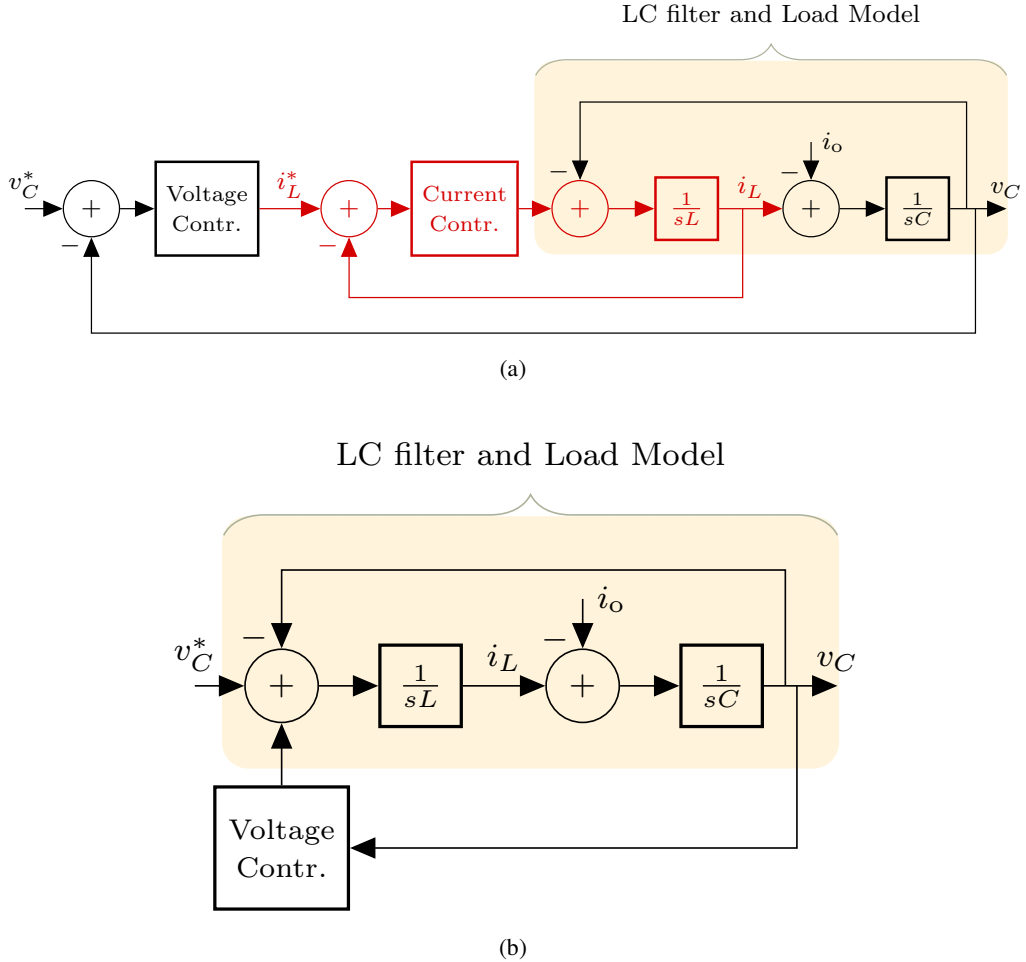

(a)

(b)

Figure 102. Comparison of controller structures. a Typical double-loop (or cascaded) structure. b Simplified diagram of the proposed structure, which consists on a single controller in the feedback path.

6.2.1.   Analysis of Single- and Dual-Loop Structures

This section discusses the advantages and disadvantages of a dual-loop structure compared to a single-loop structure, cf. Figure 102. The model of an LC filter introduces a two-pole lagging phase shift $(180°)$, which requires compensation. Furthermore, an additional

phase lag appears when such plant model is discretized and a one-sample computational delay is considered, cf. Figure 100a. To add a bit more complexity into an already complex situation, multiple resonant controllers are usually included to ensure zero-steady state error at both sequences of the fundamental grid frequency and at the main low-order harmonics.

Double-loop structures provide a stable system using simple (low-order) PI or PR controllers because they divide the complex plant model into two parts. An inner current loop simplifies the plant model seen by the voltage controller. The inner current controller assumes an L filter, whereas the outer voltage loop mainly sees a capacitive plant in the low frequency range where it operates. Typically, the bandwidth of the current controller is larger than the bandwidth of the voltage controller so as to avoid interaction between both loops. Nevertheless, such extra bandwidth does not provide any improvements to the system performance besides the desired decoupling between controllers [61]. Actually, the output impedance of the system augments when the bandwidth of the current loop increases [134], as expected from the fact that good current sources have a high output impedance.

The proposal implements a single-loop high-order voltage controller, which is placed in the feedback path. The presented controller only measures the output voltage v_C without compromising the stability of the system and offering a reliable protection against an output short circuit. The resultant controller can be used with a wide range of LC filters.

6.2.2. Proposed Controller Structure

The proposal implements a single-loop high-order voltage controller, which is placed in the feedback path. The presented controller only measures the output voltage v_C without compromising the stability of the system and offering a reliable protection against an output short circuit. The resultant controller can be used with a wide range of LC filters.

In order to carry out the design of the proposed controller, the principle of separation of estimation and control is applied. In this manner, the design of the observer and the design of the compensator are performed independently and, when combined, they keep their properties [54]. Figure 103 shows a detailed scheme of the proposed controller structure.

On the one hand, the compensator is designed to provide a good transient response to reference changes. The designer specifies the desired bandwidth and the compensator provides a damped response equivalent to a first-order system with such bandwidth. The maximum bandwidth that can be achieved is limited by the sampling rate and the available bandwidth in the physical system (where overmodulation does not occur) [2, Sec. III-A]. The compensator also includes a saturator so as to provide the observer a more accurate value of the voltage source converters (VSCs) output voltage when overmodulation occurs. With such controller structure, the wind-up problem is avoided by feeding back the saturated control signal v_{sat} to the observer rather than the control output v. In this manner, the estimated states are correct and the consistency between the observer and the real plant states is maintained. This eliminates wind-up problems in the observer when the voltage source converters (VSCs) is commanded with a reference that cannot be achieved [1, 54].

On the other hand, the observer is designed to cancel the effect on the capacitor voltage of current harmonics generated by a nonlinear load or a distorted grid voltage and to provide a sinusoidal waveform with the desired output frequency. Therefore, the observer reduces the output impedance of the voltage source converters (VSCs) at the frequencies where
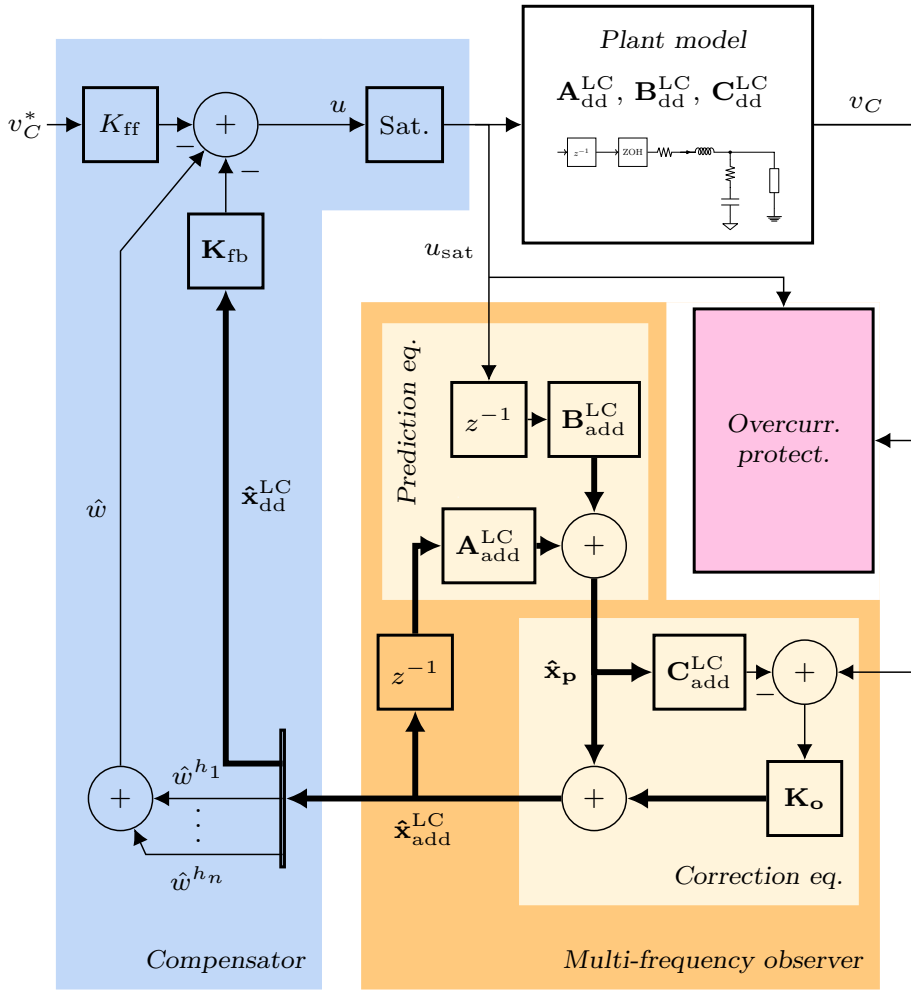
Figure 103. Detailed scheme of the proposed controller structure.

the load is expected to demand current. Moreover, it also has a high robustness against changes in the load impedance in order to maintain the performance when different loads are connected.

6.2.3. Design of the Compensator

The compensator contains two gains, namely, a feedback gain K_{fb} and a reference feedforward gain K_{ff}. In the following, the required steps to obtain such gains are detailed. The proposed design method uses a direct discrete-time pole-placement strategy which only depends on the the resonant frequency of the LC filter f_{res}, the sampling period of the digital controller T_{s}, and the desired bandwidth of the controller f_{BW}.

In order to obtain a damped response, the open-loop resonant poles of the LC filter $p^{\mathrm{ol}}_{1,2}$ are moved to a more damped region $p^{\mathrm{cl}}_{1,2}$ using a radial projection [81], cf. Figure 104a. A damping factor ζ of 0.7 is used because it provides enough damping while requiring a low
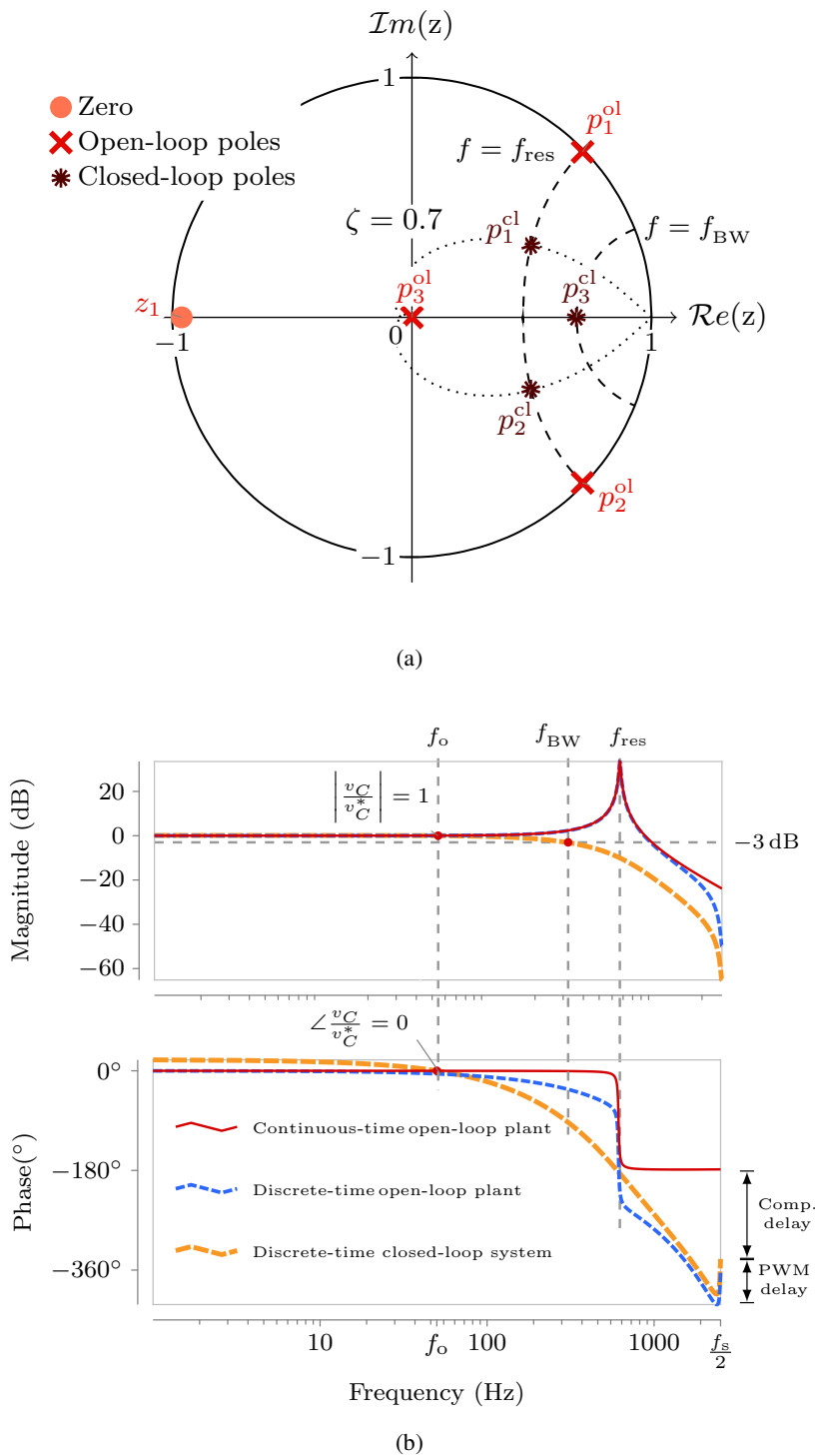
(a)

(b)

Figure 104. Frequency domain models of the nominal plant and of the closed-loop system. a Discrete-time pole-zero map. b Bode diagram.

Table 12. Direct Discrete-Time Pole Placement of the Plant Poles

Poles	Position in the z-plane	
	Open-loop	**Closed-loop**
LC filter	Radial projection of resonant poles to $\zeta = 0.7$.	
	$p_{1,2}^{ol} = e^{\pm j\omega_{res}T_s}$	$p_{1,2}^{cl} = e^{-\left(\zeta\omega_{res}\pm j\omega_{res}\sqrt{1-\zeta^2}\right)T_s}$
Comp. delay	Moved to make it the dominant pole, and set the desired bandwidth.	
	$p_3^{ol} = 0$	$p_3^{cl} = e^{-2\pi f_{dom}T_s}$

controller effort. The computational delay pole p_3^{ol} is moved to a lower frequencty p_3^{cl} in order to make it the dominant pole, and set the desired bandwidth, cf. Figure 104b. Such pole locations are summarized in Table 12.

The plant model also contains a fast zero z_1. Such zero is caused by the capacitor ESR of the LC filter. Since it is located at a high frequency, it does not require compensation. Figure 104a shows a pole-zero map of the open-loop and the closed-loop roots of the plant.

Then, Ackerman formula is applied to compute the gain K_{fb} that yields a closed-loop system with the specified closed-loop poles:

$$K_{fb} = \begin{bmatrix} 0 & 0 & 1 \end{bmatrix} \begin{bmatrix} \mathbf{B}_{dd}^{LC} & \mathbf{A}_{dd}^{LC}\mathbf{B}_{dd}^{LC} & \left(\mathbf{A}_{dd}^{LC}\right)^2 \mathbf{B}_{dd}^{LC} \end{bmatrix} A_{cl}\left(\mathbf{A}_{dd}^{LC}\right), \tag{111}$$

where $A_{cl}\left(\mathbf{A}_{dd}^{LC}\right)$ is the characteristic polynomial, whose roots are the desired closed-loop poles of the system, evaluated at $\mathbf{A}_{dd}^{LC}$:

$$A_{cl}\left(\mathbf{A}_{dd}^{LC}\right) = \left(\mathbf{A}_{dd}^{LC} - p_1^{cl}\mathbf{I}\right)\left(\mathbf{A}_{dd}^{LC} - p_2^{cl}\mathbf{I}\right)\left(\mathbf{A}_{dd}^{LC} - p_3^{cl}\mathbf{I}\right).$$

When the feedback path is closed using the previously calculated feedback gain K_{fb}, cf. Figure 103, the resultant closed-loop system is:

$$\mathbf{x}_{dd}^{LC}(k+1) = \overbrace{\left(\mathbf{A}_{dd}^{LC} - \mathbf{B}_{dd}^{LC}\mathbf{K}_{fb}\right)}^{\mathbf{A}_{cl}^{LC}}\mathbf{x}_{dd}^{LC}(k) + K_{ff}\mathbf{B}_{dd}^{LC}v_C^*(k)$$
$$v_C(k) = \mathbf{C}_{dd}^{LC}\mathbf{x}_{dd}^{LC}(k). \tag{112}$$

Such system has the following closed-loop transfer function from its reference $v_C^*(k)$ to its output $v_C(k)$:

$$T_{LC}^*(f) = K_{ff}\mathbf{C}_{dd}^{LC}\left(e^{j2\pi fT_s}\mathbf{I} - \mathbf{A}_{cl}^{LC}\right)^{-1}\mathbf{B}_{dd}^{LC}. \tag{113}$$

In order to achieve unity gain at the nominal output frequency, e.g., $T_{LC}^*(T_{LC}^*(f_o)) = 1$, the feedforward gain K_{ff} is

$$K_{ff} = \frac{1}{\mathbf{C}_{dd}^{LC}\left(e^{j2\pi T_{LC}^*(f_o)T_s}\mathbf{I} - \mathbf{A}_{cl}^{LC}\right)^{-1}\mathbf{B}_{dd}^{LC}}. \tag{114}$$

The resultant closed-loop transfer function is shown in Figure 104b in comparison with the continuous- and discrete-time open-loop transfer functions of the nominal plant model.

6.2.4.   Design of the Observer

Two types of linear observers can be implemented, namely, a Luenberger observer and a Kalman filter. A Kalman filter offers some advantages over a Luenberger observer in terms of robustness and simplicity of design when a high-order system, such as the proposed voltage controller, is considered. This point is explained in detail in Section 6.3.

The Kalman gain $\mathbf{K}_o$ is computed off-line using the iterative numerical solution described in [8, Algorithm I]. The input parameters of the algorithm are the measurement noise N, the process noise $\mathbf{Q}$, and the augmented model of the system $\mathbf{A}_{add}^{LC}$ and $\mathbf{C}_{add}^{LC}$, cf. (110).

The proposed ac voltage controller only measures the capacitor voltage; therefore, the measurement noise N is obtained from the capacitor voltage measurements v_C when the voltage source converters (VSCs) is on and the capacitor is discharged:

$$N = \mathcal{E}\{|v_C(k)|^2\} \tag{115}$$

where $\mathcal{E}\{\circ\}$ denotes mathematical expectation [54] and can be approximated by a time average of its argument. In our setup, N is $0.1V^2$. The second parameter, $\mathbf{Q}$, represents the uncertainty in the amplitude and phase of the disturbances. The diagonal of $\mathbf{Q}$ contains the variance of each state variable in the observer state vector $\mathbf{x}_{add}^{LC}(k)$. It is a measure of how much this state variables change from its steady state value due to unmodeled disturbances. A physical interpretation of this parameter has been presented in [8]. This parameters define the bandwidth of the observer by controlling the distance between the closed-loop poles and the disturbance ceros of the system. The authors recommend using a value of 0.1%, as proposed and justified in [8].

$$\mathbf{Q} = \frac{0.1}{100} \begin{bmatrix} V_o & 0 & 0 & \cdots & 0 \\ 0 & \frac{P_o}{3V_o} & 0 & \cdots & 0 \\ 0 & 0 & V_o & \cdots & 0 \\ \vdots & \vdots & \vdots & \ddots & \vdots \\ 0 & 0 & 0 & \cdots & V_o \end{bmatrix}; \tag{116}$$

Figure 105 shows the root locus of $S(f)$ for a sweep in $\mathbf{Q}$ when the design selected frequencies are are both sequences of the fundamental output frequency $\pm f_o$ and the main low-order harmonics $-11f_o$, $-5f_o$, $+7f_o$, and $+13f_o$.

On the one hand, some of the roots of S are in fixed locations irrespectively of the value of $\mathbf{Q}$. The disturbance zeros $z_{hf_g}^d/h \in \{-11, -5, \pm1, +7, +13\}$ are always placed over the unit circumference at the design selected frequencies to ensure that the sensitivity is always zero at such frequencies. The so called plant-model zeros z_{delay}^p and $z_{\pm f_{res}}^p$ are placed at the location of the plant-model poles. In addition, the plant closed-loop poles $p_{1,2,3}^{ol}$ are also at a fixed position, cf. Table 12 because of the direct pole-placement strategy applied to design the compensator. On the other hand, the rest of the poles and zeros are automatically placed by the proposed observer design method. The Kalman filter automatically places
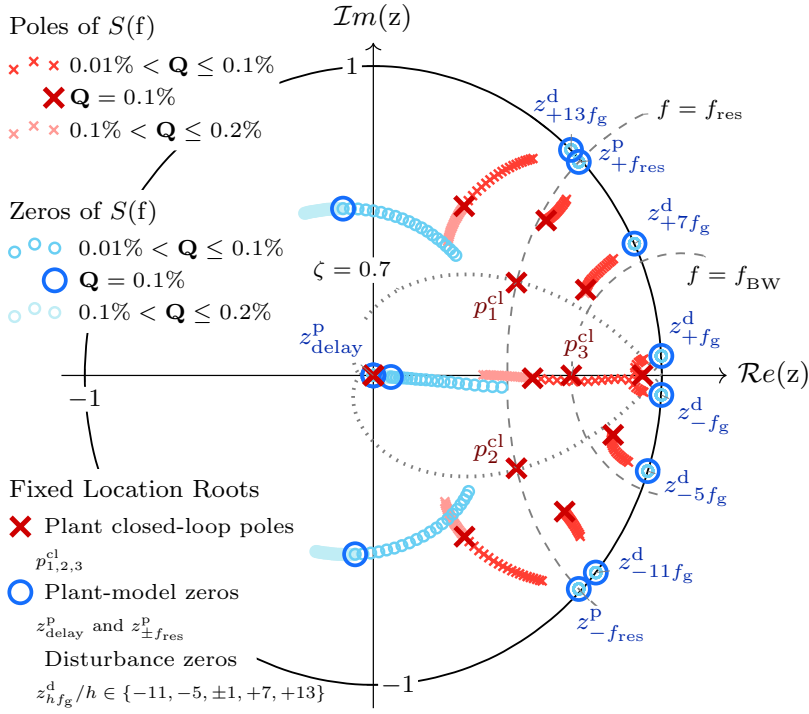
Roots of the Sensitivity Transfer Function $S(\mathrm{f})$

Figure 105. Roots of the sensitivity tranfer function for a sweep in the design parameter **Q**.

them in locations which provide a robust system and a high bandwidth. The parameter **Q** determines the resultant observer bandwidth (and consequently the robustness [8] of the system) by changing the distance between the poles and the zeros of $S(f)$. A detailed study of such effect was presented in [8].

6.2.5. Design of the Overcurrent Protection

In this section, a fast software overcurrent protection is presented. First, the principle of operation is described. Then, the overcurrent protection structure is presented.

The converter current i_L is computed by low-pass filtering the measured capacitor voltage v_C and the PWM voltage reference v_{dl}, with a model of the impedance of the L branch of the LC filter, cf. Figure 100a. The discrete-time transfer function that relates i_L with v_C and u_d is

$$Z_L(z) \;=\; \frac{i_L}{u_d - v_C} = \frac{a}{z - b}, \tag{117}$$

where

$$a = -\frac{e^{-(R_L/L)T_s} - 1}{R_L}$$

$$b = e^{(-R_L/L)T_s}. \tag{118}$$

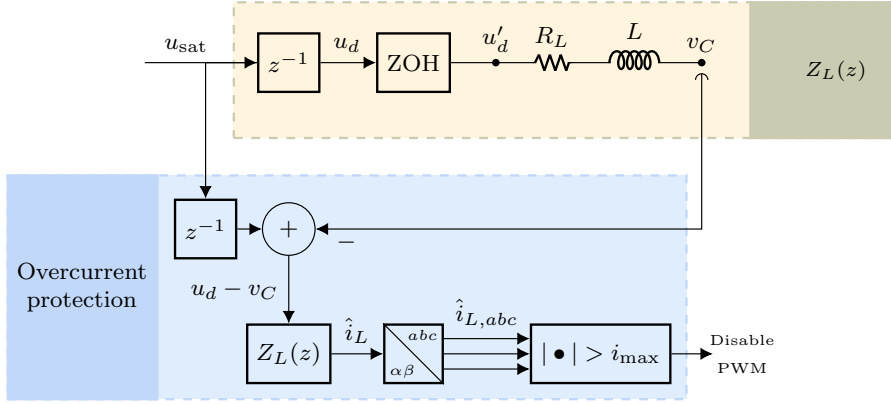The proposed overcurrent protection scheme is shown in Figure 106.

Figure 106. Detailed scheme of the proposed overcurrent protection.

Since this protection scheme operates in the digital domain, it cannot detect a change in the output voltage caused by a disturbance, such as a short circuit at the output, until the next sample is acquired. Therefore, a one-sample error in the estimated converter current can appear depending on the relative position of the disturbance event with respect to the sample instant. In the following, the maximum change in the converter current between two samples is calculated in order to assess the performance of this protection.

The slew rate S_r (defined as the rate of change of current per unit of time, i.e., the time differentiation of i_L) that an output short circuit ($v_L = 0$) generates in the grid-side current is

$$S_r(z) = \underbrace{\frac{z-1}{T_s}}_{\text{Time diff.}} i_L(z) = \frac{z-1}{T_s} \underbrace{u_d \frac{z}{z-1}}_{\text{Voltage step}} Z_L(z). \tag{119}$$

In the time domain, (119) results in a slew rate that exponentially decays to zero because $|b| < 1$:

$$S_r(t = kT_s) = \frac{au_d}{T_s} b^k, \tag{120}$$

Therefore, the maximum value of S_r is obtained when the voltage disturbance appears, i.e., at $t = 0$:

$$S_{r,\text{max}} = \frac{au_d}{T_s}, \tag{121}$$

Hence the maximum change in the converter current that can occur between two samples is $S_{r,\text{max}}T_s = av_{dl}$. This value is an upper bound of the intersample uncertainty of the

proposed discrete-time overcurrent protection, e.g., the maximum difference that can appear between the true continuous current waveform i_L and its sampled estimation $\hat{i}_L$. It should be noticed that the grid-side current limit $i_{\max}$ should always be set lower than the filter inductance saturation current.

6.3.   Relation between Robustness and Output Impedance

This section explains how the presented controller enhances the steady state and transient performance of the system. To obtain a good performance during steady state and transient events, the output impedance of the system Z_{out} should be as low as possible.

In a voltage source converters (VSCs), a low output impedance can be achieved in two different ways: using an LC filter with reactive elements that have a low impedance [cf. $Z_{\mathrm{out}}^{\mathrm{ol}}$ in Figure 107a], or designing a controller that lowers the output impedance of the system formed by the converter and LC filter. Figure 107b shows the output impedance $Z_{\mathrm{out}}^{\mathrm{ol}}$ of an inverter that operates without a closed-loop controller to regulate the output voltage (the waveform is clamped for values greater than 10Ω). Such output impedance achieves very low values at dc and at high frequencies, namely, R_L and R_C. However, $Z_{\mathrm{out}}^{\mathrm{ol}}$ increases in the mid-frequency range and it tends to infinity at f_{res}. If the value of L is reduced and the value of C increased, a lower impedance is obtained maintaining the same resonant frequency [cf. 107a] at the expense of increasing the inductor current ripple and the capacitor size. In addition, this approach has the following problems. It does not provide a true zero output impedance at any frequency and the impedance around f_{res} is always too high.

In order to solve these limitations, the proposed controller reduces the output impedance. This is accomplished by lowering the sensitivity of the system at a set of design-selected frequencies. The sensitivity function of the system S describes how the controller responds to disturbances [54]. The controller modifies (amplifies or attenuates) the effect of a disturbance (e.g., the load current) on the controlled variable (the capacitor voltage) with respect to the open-loop response, according to the value of S. In other words, it represents the change in the output impedance when a closed-loop controller is installed:

$$Z_{\mathrm{out}}^{\mathrm{cl}} \quad = \quad S Z_{\mathrm{out}}^{\mathrm{ol}}. \tag{122}$$

Figure 107c shows the change in the output impedance caused by the proposed closed-loop controller. The proposal provides a zero output impedance at a set of arbitrarily selected frequencies ($-11, -5, \pm 1, +7$, and $+13$ in this example). Since the spectrum of the load current in the $\alpha\beta$ frame typically contains such sequences, this design improves the transient and steady-state responses of the voltage controller because the output voltage distortion is minimized.

The design presented in the previous section can, theoretically, provide a zero output impedance at as many frequencies as desired because the number of frequencies where a resonant action (infinite gain) [1] can be placed is unlimited, provided that they are below the Nyquist frequency of the digital controller $f_{\mathrm{s}}/2$. The only obvious practical limitation is the computational burden. In any case, current processors can execute the proposed control equations, which consist only of simple additions and multiplications (cf. Figure 103), without any problems even for large orders [cf. (110)]; hence, this constraint is virtually
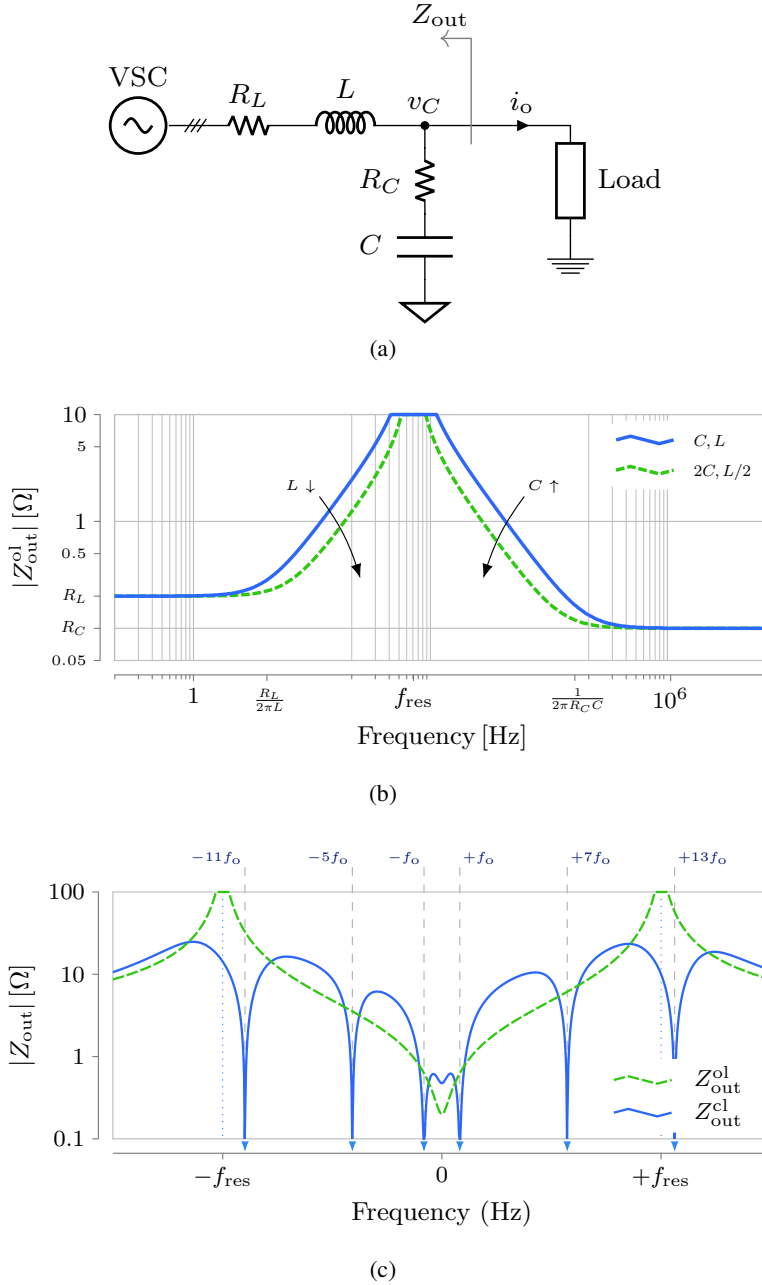
(a)

(b)

(c)

Figure 107. Output impedance of a voltage source converters (VSCs) with an LC filter. a Circuit diagram of an inverter without a closed-loop controller. b Change in the magnitude of the output impedance $Z_{\text{out}}^{\text{ol}}$ of an inverter without a closed-loop controller when the values of the LC filter are modified. c Change in the output impedance when the proposed controller is implemented.

eliminated. Unfortunately, the robustness of the system to load changes or parameter variations is restricted by a fundamental limitation that is common to all linear controllers,

namely, Bode's integral theorem.

Bode's integral theorem states that the average attenuation and amplification of disturbances over the complete frequency range where the controller operates $(-f_s/2, f_s/2)$ is zero, where f_s is the sampling frequency:

$$\int_{-f_s/2}^{f_s/2} \ln|S(f)|\, df \;=\; 0. \tag{123}$$

Thus, the choice of the sensitivity function $S(f)$ at one frequency affects its value at other frequencies. This effect is illustrated in Figures 108a and 109a. The area above the frequency axis must be equal to the area below the frequency axis according to (123). Consequently, if the designer increases the number of frequencies with low sensitivity, the sensitivity at other frequencies also increases.

The previous mathematical result has an important physical and practical consequence because the sensitivity function is related to the output impedance of the system according to (122). Therefore, if a controller reduces the output impedance in some frequency range, then the output impedance must be increased at some other frequencies, cf. Figures 108b and 109b.

For this reason, the output impedance should be reduced only at the frequencies where the load is expected to demand current. The Kalman filter optimizes the performance of the system by reducing the sensitivity only at the design-selected frequencies and the resonant frequency of the filter.

When the plant model is modified with respect to the nominal model, e.g., when a load is connected, some of the roots of the sensitivity are moved from the previously described locations. Therefore, the sensitivity function and the output impedance are changed [134]. Figures 109b and 108b illustrate this change when the load impedance value is swept from infinity (no load) to a value of 0.1 p.u. Nevertheless, the proposed controller always provides a zero output impedance at the design-selected frequencies because the disturbance zeros, cf. Figure 105, do not move irrespectively of the change in the plant model.

To design a robust controller, this change in the output impedance of the system should be minimized. This is accomplished by reducing the range where the controller responds to disturbances, i.e., the range where $S(f) \neq 1$. This range can be reduced in two ways. The first one is by selecting a lower value of $\mathbf{Q}$ [8]; hence reducing the bandwith of the observer. The second one is by reducing the set of design-selected frequencies where a zero output impedance is requested, i.e., where $S(f) = 0$.

The previous analysis gives a qualitative insight into the relation between the robustness of the controller to plant parameter variations and the output impedance of the inverter using the sensitivity function. However, such analysis does not provide a quantitative indication of the range of load impedance values where transient performance requirements are met. In the following section, a quantitative analysis of the stability of the system as a function of the load impedance is presented; both inductive and capacitive loads are considered.

6.3.1. Analysis of the Stability of the System as a Function of the Load

Although the load is usually modeled as a current disturbance, this common practice is an approximation that does not take into account the change in the system dynamics. Only
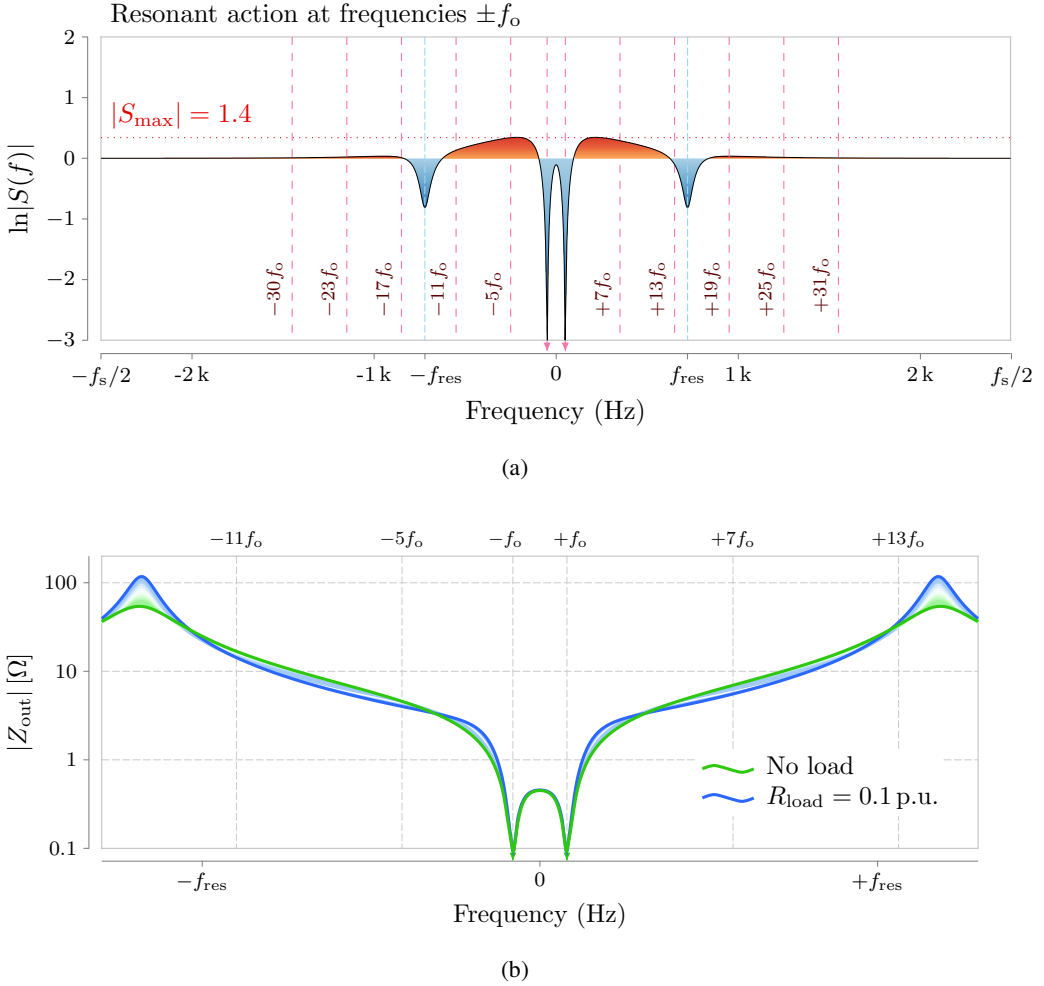
(a)

(b)

Figure 108. A design with resonant action at the positive- and the negative-sequence of the fundamental output frequency $\pm f_{\mathrm{o}}$. a Graphical interpretation of Bode's integral theorem. b Output impedance $Z_{\mathrm{load}}^{\mathrm{cl}}$ when a resistive load R_{load} is connected, $R_{\mathrm{load}} > 0.1\,\mathrm{p.u.}$

when the load is a true current source (with infinite output impedance), it is accurate to model it as a disturbance. Therefore, the effect of a load should be analyzed as a change in the plant model in order to determine the stability margins and transient performance, specially when large changes in the load impedance are considered.

From the control point of view, two factors determine the range of loads that can be connected to the system before the performance is significantly degraded. The first one is the robustness of the controller. A robust controller can tolerate a severe change in the plant model (caused by connecting a low impedance load) without changing its steady-state and transient performance significantly. The second factor is the impedance of the LC filter installed. For a given LC filter, a smaller change is obtained in the plant model, cf. Figure 100b when the impedance of the load Z_{load} is large compared to the impedance of the filter, e.g., when $Z_{\mathrm{load}} \gg j\omega L$ and $Z_{\mathrm{load}} \gg 1/(j\omega C)$. Hence, for a given load power
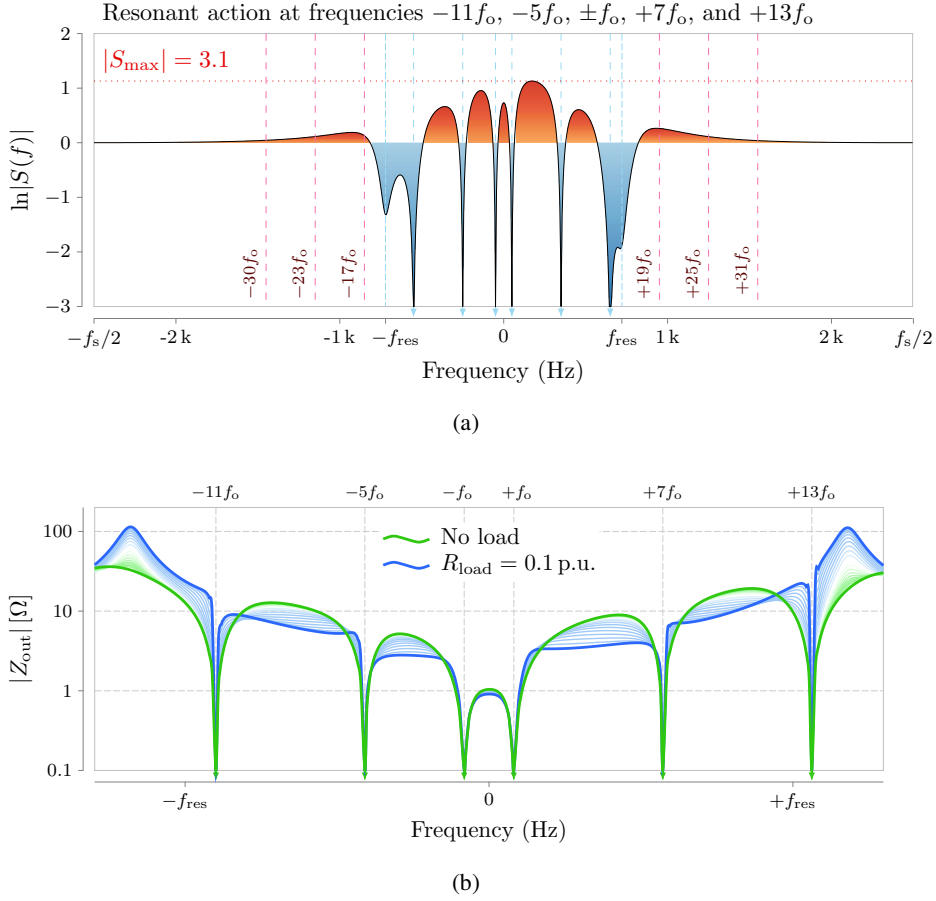
Figure 109. A design with resonant action at the main low-order harmonic sequences $-5f_o, +7f_o, -11f_o, +13f_o$ and at the positive- and the negative-sequence of the fundamental output frequency $\pm f_o$. a Graphical interpretation of Bode's integral theorem: on average, the amplification (red areas) and reduction (blue areas) of the output impedance is zero. b Change in the output impedance Z_{load}^{cl} when a resistive load R_{load} is connected, $R_{load} > 0.1$ p.u.

factor, stability is most affected when the load impedance is minimum.

Two parameters are commonly used to specify the range of loads which can be connected to the system during islanded operation: the nominal output power P_o and the rated output power factor $\cos\phi$ [135]. The nominal output power P_o sets a lower bound in the magnitude of the load impedance during islanded operation.

$$|Z_{load}^{nom}| = 3V_o^2/P_o, \tag{124}$$

where V_o is the rated output voltage. The rated output power factor describes the ratio of the maximum active and apparent loading that the converter can handle, that is, the maximum admissible load impedance angle during nominal power operation.

Nevertheless, when the inverter operates in grid-connected mode, cf. Figure 98, a much lower load impedance can be seen by the inverter without exceeding its power limit because

the load impedance in such configuration is the parallel equivalent of the grid impedance with the local load impedance whereas the power transfer depends on the relation between the grid voltage and the converter output voltage. As explained previously, the worst case in terms of stability and plant parameter variations corresponds to a setup with a low impedance load, such as during grid-connected mode, because the nominal model [used to design the controller, cf. (103)] assumes an infinite load impedance value (no load). For such reason, this section analyzes the stability of the system when the load impedance is changed from 0 p.u. (a short circuit) to a value of 10 p.u.. For load impedance values greater than 10 p.u., the performance is almost identical to the nominal case, when no load is connected.
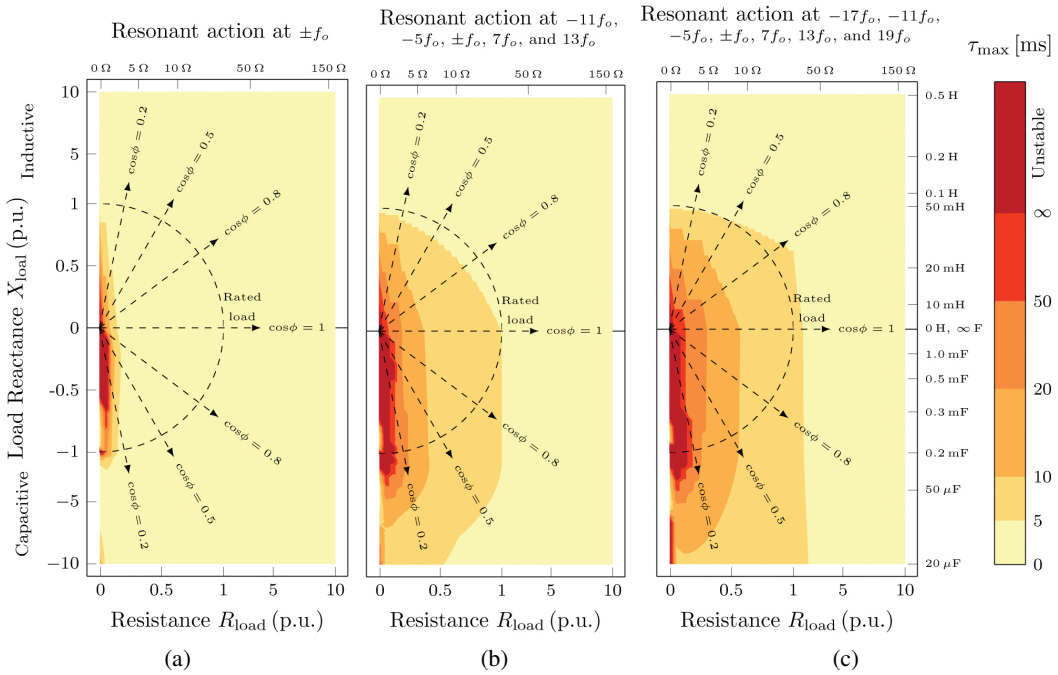
Figure 110. Regions of load impedance, whose colors denote the value of the largest time constant $\tau_{\max}$ in the system, that is, the time constant of the pole with the slowest dynamics. a Zero output impedance is requested only at the fundamental output frequency $\pm f_o$. b Zero output impedance is requested at the fundamental output frequency $\pm f_o$ and at the following main low-order harmonics $-11f_o$, $-5f_o$, $+7f_o$, and $+13f_o$. c Zero output impedance is requested at the fundamental output frequency $\pm f_o$ and at the following main low-order harmonics $-17f_o$, $-11f_o$, $-5f_o$, $+7f_o$, $+13f_o$, and $+19f_o$.

The presented analysis studies the robustness of the proposal by calculating the time constant of the poles of the closed-loop system for different values of load impedance. The time constant (or decay time-constant) of a pole at frequency f and damping ratio ζ is $\tau = 1/(2\pi f\zeta)$. Figure 110 shows regions of load impedance whose colors denote the value of the largest time constant $\tau_{\max}$ in the system, that is, the time constant of the pole with the slowest dynamics. The load time constant has been excluded from the calculation.

The relation between each color and its corresponding time constant interval is indicated in the label at the right of the figure. Both the resistive and the reactive components of the load impedance (R_{load} and X_{load} respectively) are changed from a light load condition ($R_{\text{load}} = 10$ p.u., $X_{\text{load}} = \pm 10$ p.u.) to a short-circuit situation ($R_{\text{load}} = X_{\text{load}} = 0$, cf. base values in Table 19.

Since the proposed controller allows the designer to arbitrarily specify a set of frequencies where a zero output impedance is obtained, three different designs with zero-output impedance at different sets of frequencies are tested, namely, at the nominal output frequency$\pm f_{\text{o}}$, cf. Figure 110a; at the nominal output frequency $\pm f_{\text{o}}$ plus at the main low-order harmonics $-11 f_{\text{o}}, -5 f_{\text{o}}, +7 f_{\text{o}}, +13 f_{\text{o}}$, cf. Figure 110b; and at all the previous frequencies plus at $-17 f_{\text{o}}, +19 f_{\text{o}}$, cf. Figure 110c. As expected from the study included in Section 6.3, the robustness of the controller is reduced when the number of frequencies where a zero-output impedance is increased. This is a fundamental limitation, cf. Bode's integral theorem, that applies to any linear controller. Nonetheless, the achieved performance is acceptable even when a large set of frequencies are controlled with zero steady-state, cf. Figure 110c.

In summary, the proposal can operate connected to a wide range of loads without significantly degrading its performance and without requiring a low-impedance LC filter or a high switching frequency. This analysis has considered RL and RC loads, which assess the operation when the output current lags or leads, respectively, the output voltage. Figure 111 shows the range of load magnitude and phase values that where tested. Therefore, this analysis can be extrapolated to the case of a complex (high-order) impedance network, such as a an LC load, whose impedance is comprised in the shaded regions shown in Figure 111.
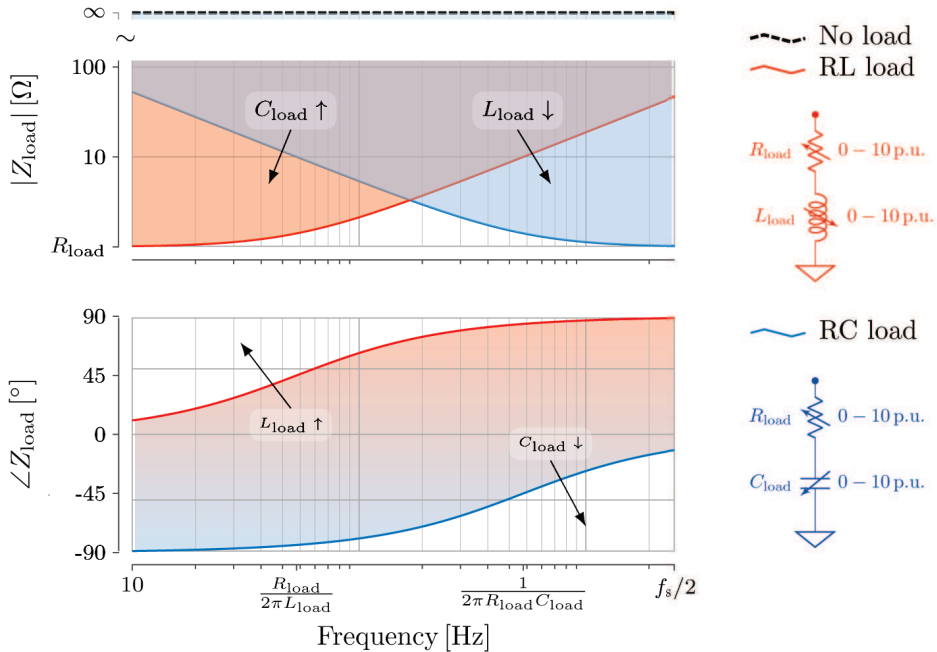

Figure 111. Magnitude and phase of the loads used to assess the performance of the proposal.

6.4.   Simulation Results

Before the proposed voltage controller is experimentally tested, the response to reference commands and load steps is simulated using Matlab. The controller is designed according to the proposed method and the set of design-selected frequencies with zero output impedance is $-11f_o$, $-5f_o$, $+7f_o$, $+13f_o$, and both sequences of the fundamental frequency $\pm f_o$.

The first simulation assess the response to a step in the reference. Figure 112 shows the output voltage in the abc frame $v_{C,abc}^{\text{sim}}$ and in the positive synchronous frame dq+ rotating at the fundamental output frequency $v_{C,dq}^{\text{sim}}$ for a reference step $v_{C,dq}^{*}$ from zero to the rated voltage. As expected, a first-order response with negligible axis crosscoupling is obtained. The rise time is determined by the design-selected bandwidth f_{bw}.

The next test simulates a short circuit condition at the output of the voltage source converters (VSCs) in order to evaluate the fault clearing response of the proposed overcurrent protection. Figure 113 shows the output voltage $v_{C,abc}^{\text{sim}}$ and the load current $i_{\text{load},abc}^{\text{sim}}$ during an output short circuit condition. The short circuit is modeled by an impedance with a value of $0.1\,\Omega$. The voltage source converters (VSCs) quickly stops commutation when the output current exceeds the current limit i_{max}, in order to mitigate the fast overcurrent transient event.

A step in the reference without a load connected at the output

$v_{C,abc}^{\text{sim}}$
200 V/DIV

$v_{C,d+}^{\text{sim}}$, $v_{C,q+}^{\text{sim}}$
$v_{C,d+}^{*}$, $v_{C,q+}^{*}$
200 V/DIV

5 ms/DIV
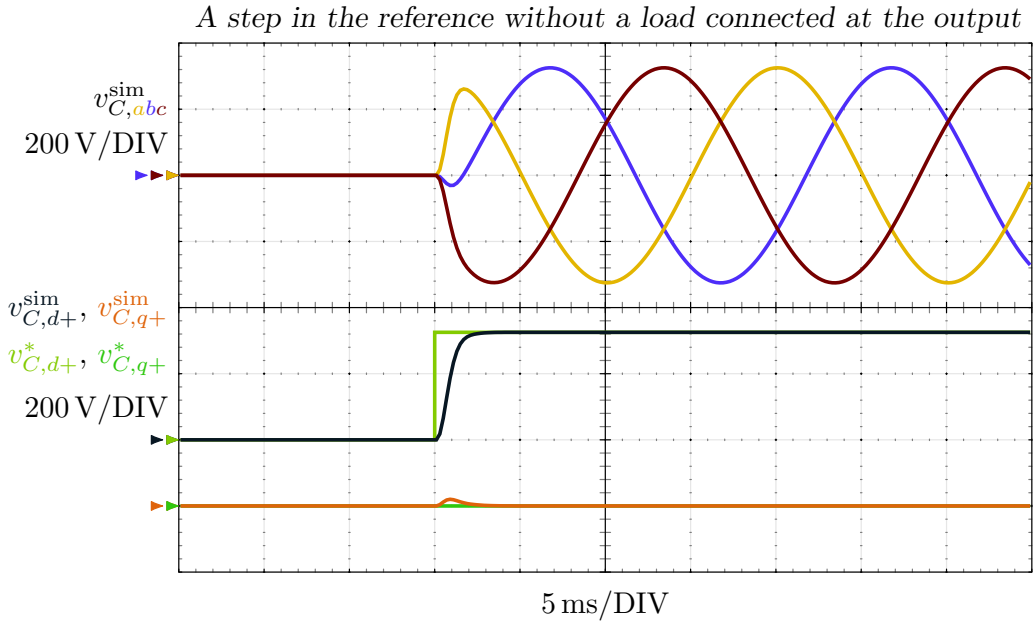
Figure 112.   Simulated output voltage in the abc frame $v_{C,abc}^{\text{sim}}$ and in the positive synchronous frame dq+ rotating at the fundamental output frequency $v_{C,dq}^{\text{sim}}$ for a reference step $v_{C,dq}^{*}$ when the converter is not connected to a load.

The next tests evaluate the operation of the voltage controller when different loads are connected to the output of the LC filter. Both linear and nonlinear loads are tested. In particular, two types of linear loads are considered, namely, inductive and capacitive loads.
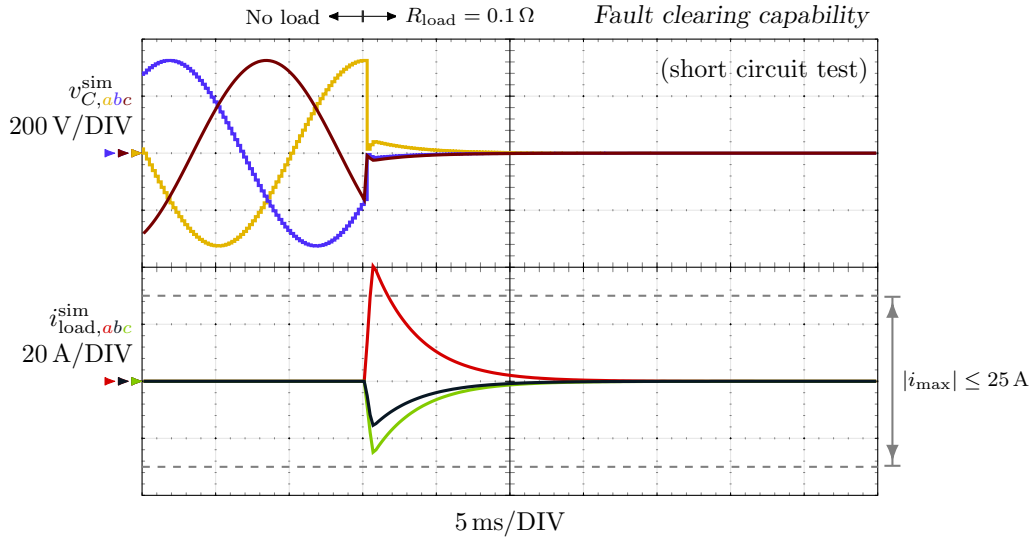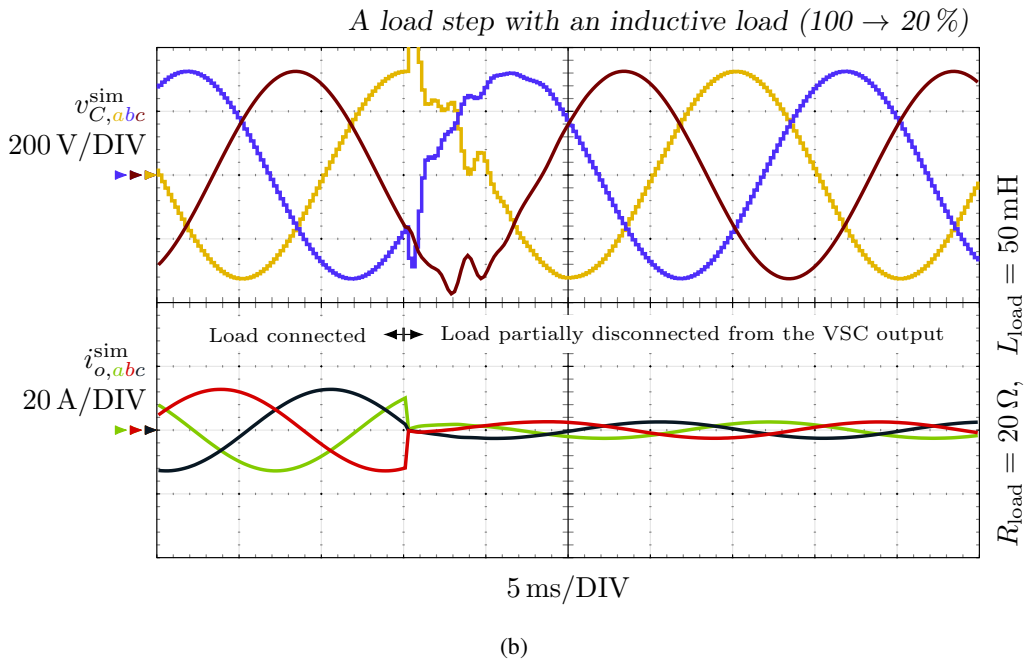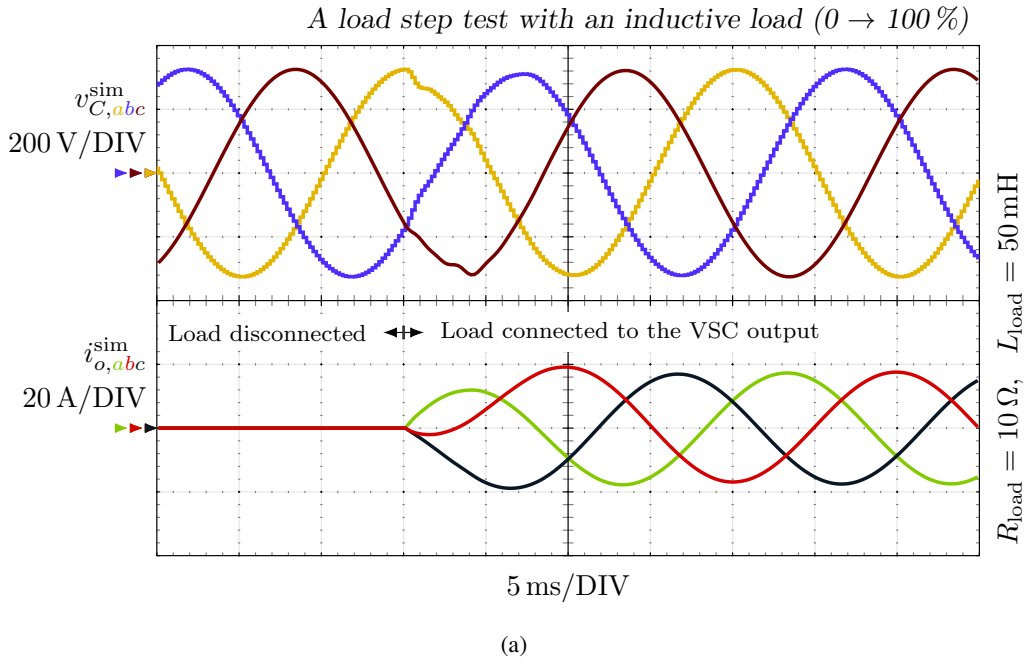
Figure 113. Simulated output voltage $v_{C,abc}^{\text{sim}}$ and simulated load current $i_{\text{load},abc}^{\text{sim}}$ during an output short circuit condition. The short circuit is modeled by an impedance with a value of $0.1\,\Omega$.

The simulated nonlinear load models a full-wave rectifier with an inductive load.

Figure 114 shows the simulated response to an inductive load step test. The load is composed of a resistive component R_{load} with a value of $10\,\Omega$ in series with an inductive component L_{load} of value $50\,mH$. As expected from the theoretical analysis, cf. Figure 110, stability is maintained when the load is connected, as shown in Figure 114a. The connection event causes a smaller transient in the output voltage $v_{C,abc}^{\text{sim}}$ compared to the disconnection event because the output current $i_{o,abc}$ changes smoothly when the load is connected due to the inductive component.

Figure 115 shows the simulated voltage deviation $v_{C,abc}^{*} - v_{C,abc}^{\text{sim}}$ over time for the previous load step test and compares it to the limits defined in [135]. The simulated design marginally meets a class 3 limit [135]. Nevertheless, it should be noted that the limits defined in [135] are constant and they do not depend on the parameters of the voltage source converters (VSCs) or the LC filter used. Therefore, a designer can improve the transient response by decreasing the impedance of the LC filter elements, i.e., increasing the value of capacitance and reducing the inductance.

After the operation of the converter with an inductive load has been simulated, the previous reference and load step tests are repeated with a capacitive load. The capacitive load is composed of a resistive component R_{load} with a value of $10\,\Omega$ in series with a capacitive component C_{load} of value $0.1\,mF$. Figure 117 shows the simulated transient response when the previously described capacitive load is connected, cf. Figure 117a, and disconnected, cf. Figure 117a. As expected from the theoretical analysis, cf. Figure 110, stability is maintained when the load is connected. Contrarily to the inductive load case, now the the connection event causes a larger transient in the output voltage $v_{C,abc}^{\text{sim}}$ compared to the disconnection event because the output current $i_{o,abc}$ changes abruptly when the load is

A load step test with an inductive load (0 → 100 %)

$v_{C,abc}^{\mathrm{sim}}$

200 V/DIV

Load disconnected ◄►► Load connected to the VSC output

$i_{o,abc}^{\mathrm{sim}}$

20 A/DIV

$L_{\mathrm{load}} = 50\,\mathrm{mH}$

$R_{\mathrm{load}} = 10\,\Omega,$

5 ms/DIV

(a)

A load step with an inductive load (100 → 20 %)

$v_{C,abc}^{\mathrm{sim}}$

200 V/DIV

Load connected ◄►► Load partially disconnected from the VSC output

$i_{o,abc}^{\mathrm{sim}}$

20 A/DIV

$L_{\mathrm{load}} = 50\,\mathrm{mH}$

$R_{\mathrm{load}} = 20\,\Omega,$

5 ms/DIV

(b)

Figure 114. Simulated output voltage $v_{C,abc}^{\mathrm{sim}}$ and simulated load current $i_{\mathrm{load},abc}^{\mathrm{sim}}$ during an inductive load step. The load is composed of a resistive component R_{load} with a value of 10Ω in series with an inductive component L_{load} of value $50mH$. a Connection test: load step from 0 % to 100 % of the load rated value. b Disconnection test: load step from 100 % to 20 % of the load rated value.
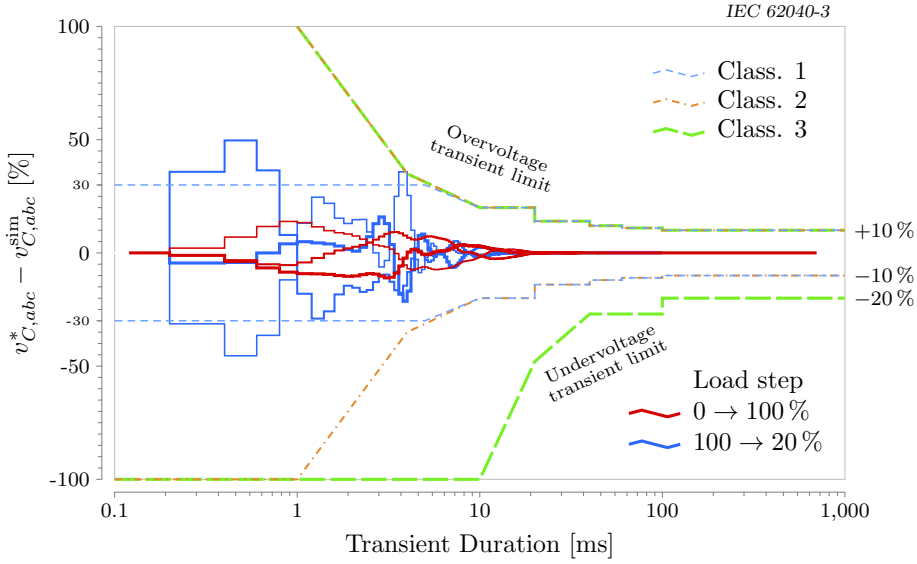
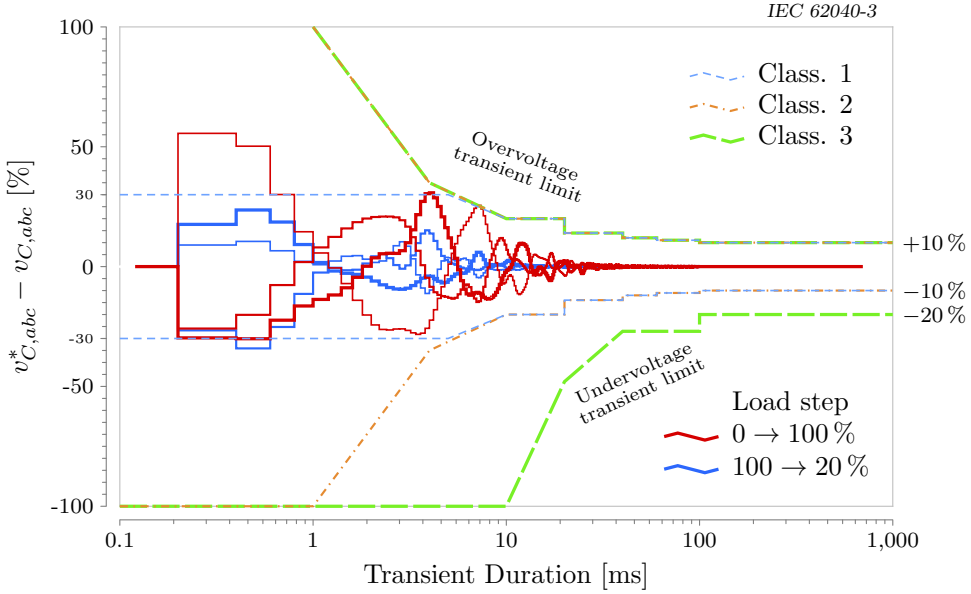Figure 115. Simulated voltage deviation $v_{C,abc}^* - v_{C,abc}^{sim}$ over time when a load step is generated using an inductive load. The load is composed of a resistive component R_{load} with a value of 10Ω in series with an inductive component L_{load} of value $50mH$. Both connection and partial disconnection of the described load events are represented. The limits defined in [135] are included for reference.
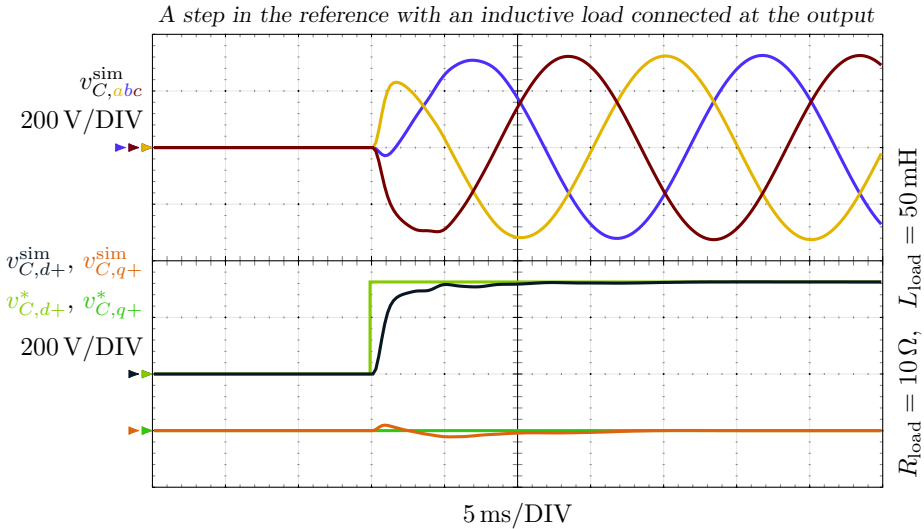

Figure 116. Simulated output voltage in the abc frame $v_{C,abc}^{sim}$ and in the positive synchronous frame dq+ rotating at the fundamental output frequency $v_{C,dq}^{sim}$ for a reference step $v_{C,dq}^*$ when the converter is connected to a inductive load.
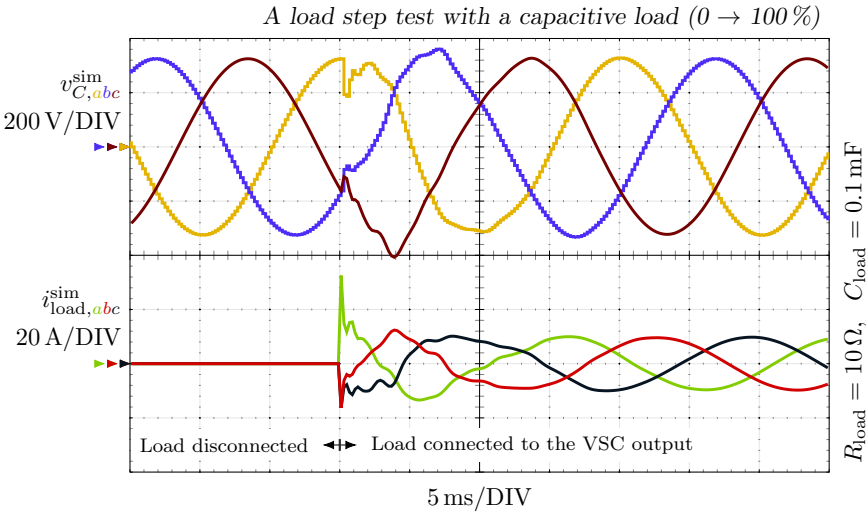
(a)
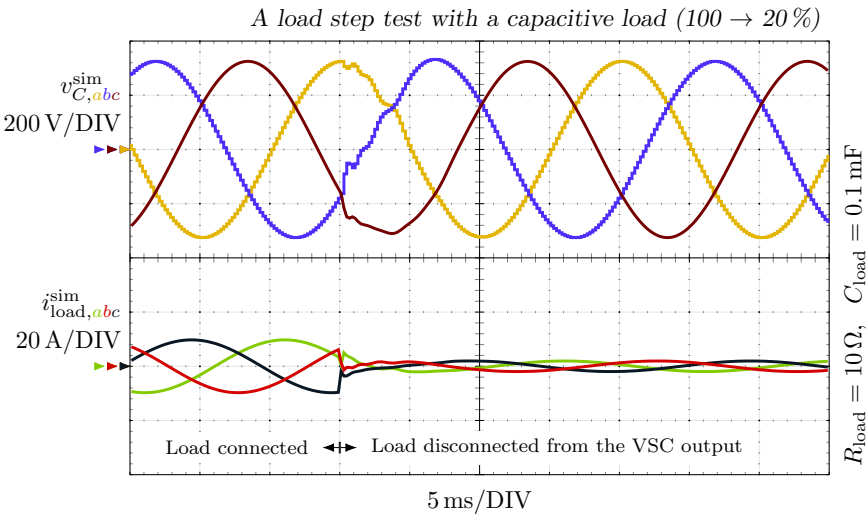
(b)

Figure 117. Performance of the proposal when connected to an inductive load. a Connection test: load step test from 0 % to 100 % of rated power. b Disconnection test: load step test from 100 % to 20 % of rated power.

Figure 118. Simulated voltage deviation $v_{C,abc}^* - v_{C,abc}^{sim}$ over time when a load step is generated using a capacitive load. The load is composed of a resistive component R_{load} with a value of 10Ω in series with a capacitive component C_{load} of value $0.1mF$. Both connection and partial disconnection of the described load events are represented. The limits defined in [135] are included for reference.
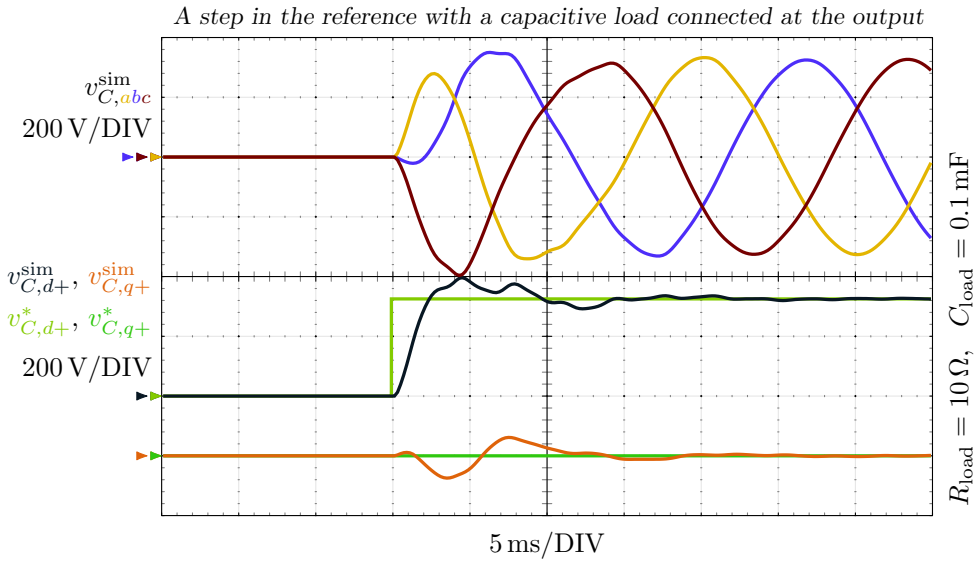
Figure 119. Performance of the proposal when connected to a capacitive load. A reference step with an amplitude equal to the rated voltage under full load.
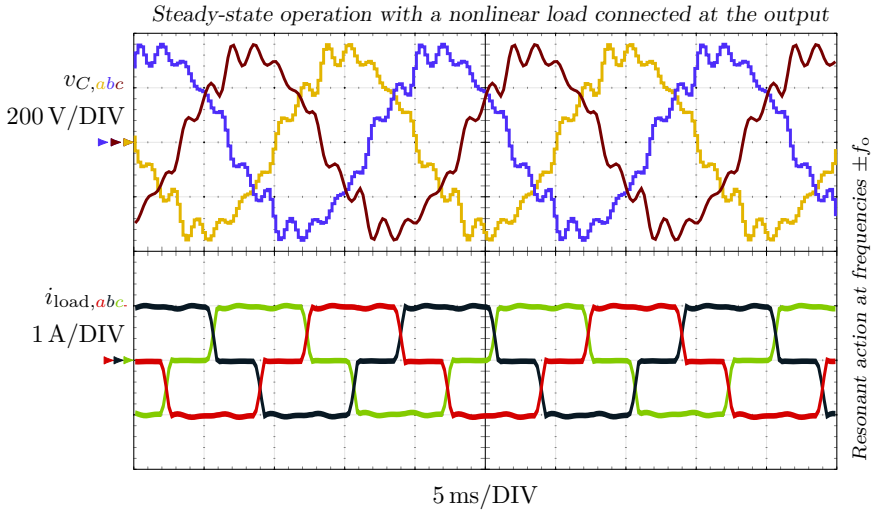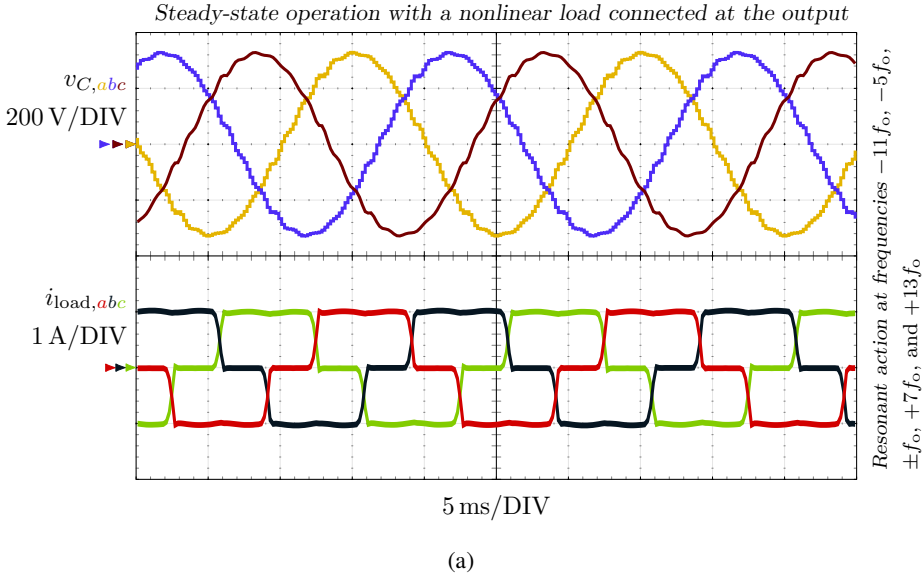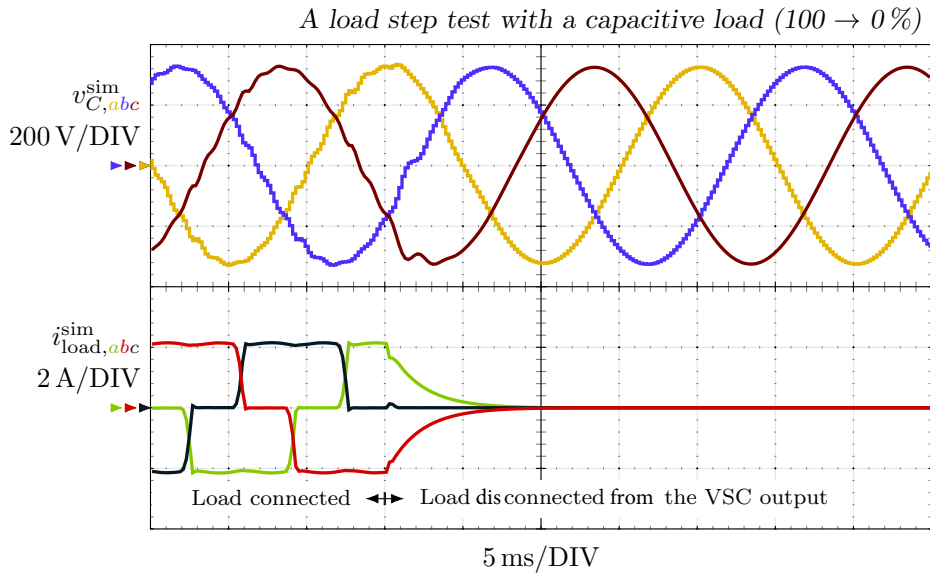
(a)
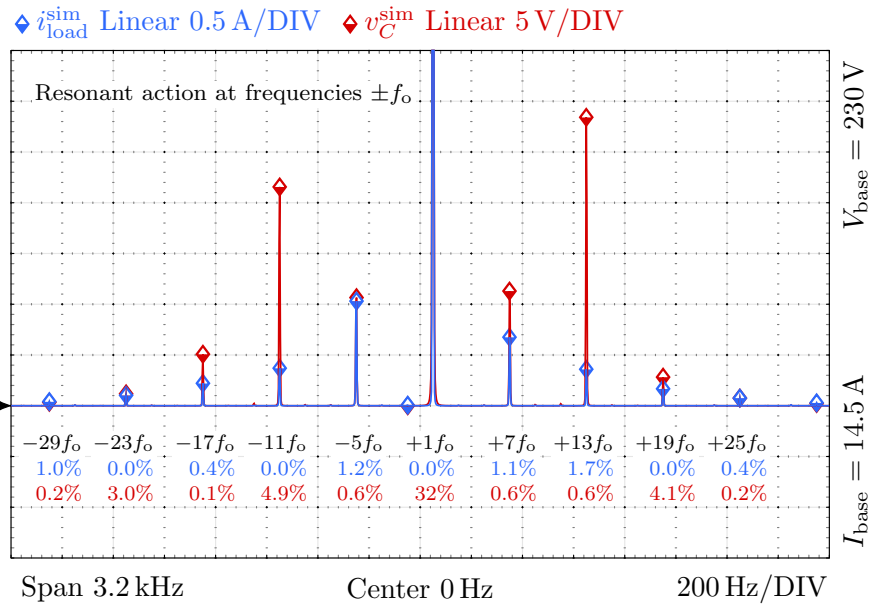
(b)

Figure 120. Steady-state performance of the proposal when connected to a nonlinear load. Design with zero output impedance only at the nominal output frequency$\pm f_{\mathrm{o}}$. a Time-domain Waveforms. b Frequency spectrum of the output voltage v_{C_f} and of the load current i_{load}.

Steady-state operation with a nonlinear load connected at the output

$v_{C,abc}$
200 V/DIV

$i_{\text{load},abc}$
1 A/DIV

5 ms/DIV

Resonant action at frequencies $-11f_o$, $-5f_o$, $\pm f_o$, $+7f_o$, and $+13f_o$

(a)

$i_{\text{load}}^{\text{sim}}$ Linear 0.2 A/DIV v_C^{sim} Linear 2 V/DIV

Resonant action at frequencies
$-11f_o$, $-5f_o$, $\pm f_o$, $+7f_o$,
and $+13f_o$

$V_{\text{base}} = 230$ V

$I_{\text{base}} = 14.5$ A

	$-29f_o$	$-23f_o$	$-17f_o$	$-11f_o$	$-5f_o$	$+1f_o$	$+7f_o$	$+13f_o$	$+19f_o$	$+25f_o$
	1.0%	0.0%	0.4%	0.0%	1.2%	0.0%	1.1%	1.7%	0.0%	0.4%
	0.2%	3.0%	0.1%	4.9%	0.6%	32%	0.6%	0.6%	4.1%	0.2%

Span 3.2 kHz   Center 0 Hz   200 Hz/DIV

(b)
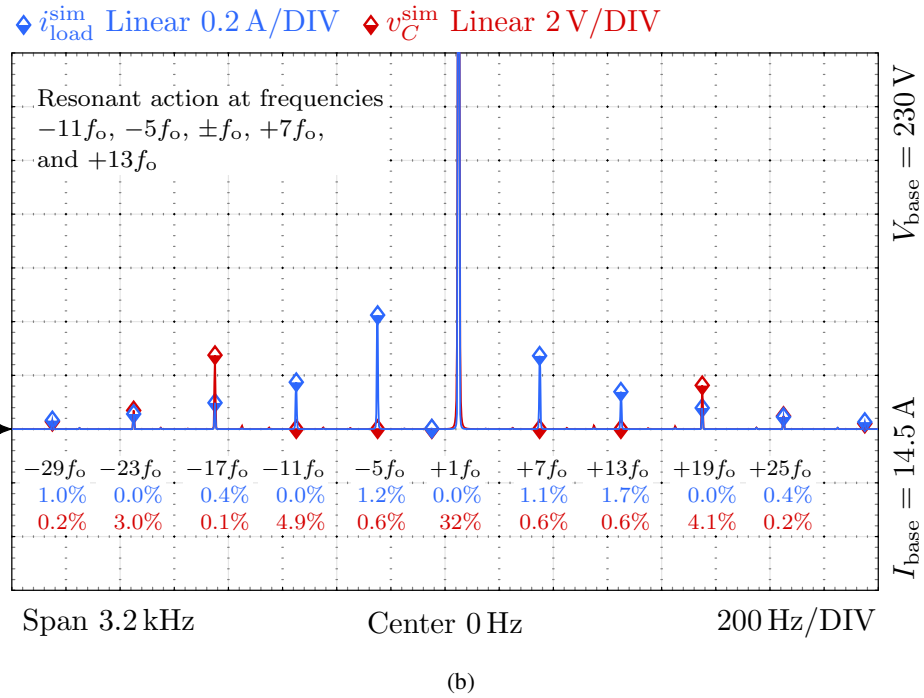
Figure 121.   Steady-state performance of the proposal when connected to a nonlinear load. Design with zero output impedance at the nominal output frequency $\pm f_o$ plus at the main low-order harmonics $-11f_o$, $-5f_o$, $+7f_o$, $+13f_o$. a Time-domain Waveforms. b Frequency spectrum of the output voltage v_{C_f} and of the load current i_{load}.

A load step test with a capacitive load (100 → 0 %)

$v_{C,abc}^{\mathrm{sim}}$

200 V/DIV

$i_{\mathrm{load},abc}^{\mathrm{sim}}$

2 A/DIV

Load connected ◄► Load disconnected from the VSC output

5 ms/DIV

Figure 122. Dynamic performance of the proposal when connected to a nonlinear load. Disconnection test: load step test from 100 % to 0 % of rated power.

A step in the reference with a nonlinear load connected at the output

$v_{C,abc}^{\mathrm{sim}}$

200 V/DIV

$v_{C,d+}^{\mathrm{sim}},\ v_{C,q+}^{\mathrm{sim}}$

$v_{C,d+}^{*},\ v_{C,q+}^{*}$

200 V/DIV

5 ms/DIV
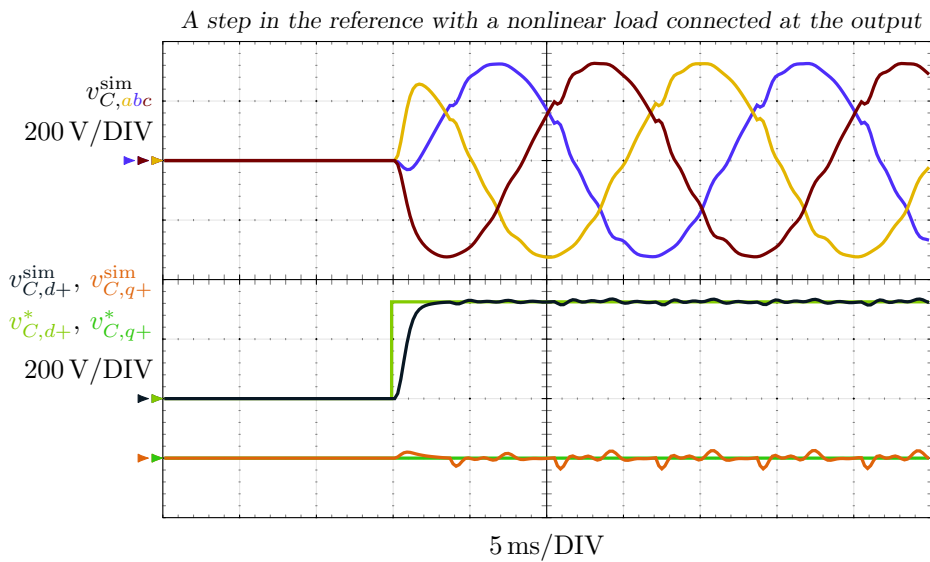
Figure 123. Dynamic performance of the proposal when connected to a nonlinear load. A reference step of the rated amplitude under full load.

connected due to the capacitive component and affects the output voltage.

Figure 118 shows the simulated voltage deviation $v_{C,abc}^* - v_{C,abc}^{\text{sim}}$ over time for the previous load step test and compares it to the limits defined in [135]. The obtained results are similar to the inductive load step test, cf. Figure 115, because the proposed design uses a nominal model that assumes a no load condition.

Figure 119 shows the output voltage in the abc frame $v_{C,abc}^{\text{sim}}$ and in the positive synchronous frame dq+ rotating at the fundamental output frequency $v_{C,dq}^{\text{sim}}$ for a reference step $v_{C,dq}^*$ from zero to the rated voltage. Similarly to the inductively loaded test, cf. Figure 116, the transient response is slightly modified, compared to the no load condition, due to the plant model change with respect to the nominal model.

Finally, in order to conclude the presentation of the simulation results, the performance of the proposed controller is studied with a non-linear load. Figure 120 shows the steady-state performance when the design provides zero output impedance only at the nominal output frequency $\pm f_o$. The large current distortion demanded by the nonlinear load causes a large output voltage distortion, cf. the time-domain waveforms and the frequency spectrum of the output voltage v_{C_f} and of the load current i_{load} in Figure 120.

In order to eliminate the previous voltage distortion, a designer can reduce the output impedance of the system at the main harmonic frequencies. Figure 121 shows the steady-state performance when the design provides zero output impedance at the nominal output frequency $\pm f_o$ plus at the main low-order harmonics $-11 f_o, -5 f_o, +7 f_o, +13 f_o$. As expected, a negligible output voltage distortion is obtained thanks to the lower impedance at the main harmonic frequencies.

After the steady-state performance has been simulated, the last two simulation tests analyze the dynamic performance of the proposal when connected to the same nonlinear load. Figure 122 shows a load disconnection test. Similarly to the linear load case, the controller provides a fast and stable regulation when a load step from $100\,\%$ to $0\,\%$ of the rated power is generated. Figure 123 shows the response to a reference step of the rated amplitude under full load. As illustrated, the response time is similar to the linear load case thanks to the robustness of the proposal.

6.5.   Experimental Results

The proposed ac voltage controller has been tested in a 10-kW voltage source converters (VSCs) working in both stand-alone and grid-connected modes. An LC filter designed according to [136] is used. The filter reactive values are $L = 2.5mH$ and $C = 30\mu F$ ($f_{\text{res}} = 580\,\text{Hz}$). The switching frequency is $f_{\text{sw}} = 2.5\,\text{kHz}$, and the dead-time is $3\,\mu s$. A low switching frequency reduces switching losses in the voltage source converters (VSCs) and it represents a worst-case scenario in terms of the effect of the computation and modulation delays. A double-update sampling strategy is used, resulting in a sampling frequency f_s of $5\,\text{kHz}$. The implemented controller is designed using the proposed method and the set of design-selected frequencies with zero output impedance is $-17 f_o, -11 f_o, -5 f_o, +7 f_o, +13 f_o, +19 f_o$ and both sequences of the fundamental frequency $\pm f_o$. This validates the operation of the proposal when controlling harmonics close to the resonant frequency of the LC filter. The bandwidth of the controller f_{bw} is set to $300\,\text{Hz}$. It should be noticed that, the compensator bandwidth is limited to f_{bw} in order to

reduce the controller effort and avoid overmodulation when a reference step is commanded. Nonetheless, the low-sensitivity regions of the controller are placed at frequencies above and below f_{bw}; hence, the controller can cancel disturbances above its reference-tracking bandwidth. The setup parameters are summarized in Table 19. Figures 124a and 124b show a diagram and a photograph of the experimental setup, respectively. Figure 125 illustrates the execution order of the proposed controller and indicates the computational load as a function of the number of design-selected frequencies where a zero output impedance is requested n. The implementation of the proposed AC voltage controller contains three main parts that are executed sequentially during a sampling period: the overcurrent protection, which controls the PWM-enable signal; the multi-frequency observer, which provides the state of the plant and the estimated disturbances; and the compensator which executes the control law, i.e., it computes the controller output voltage using a state feedback and a reference feedforward, cf. Figure 103.

6.5.1. Islanded Operation

In order to asses the operation in an islanded configuration (S_2 open in Figure 124), a nonlinear load is used. The nonlinear load consists of a three-phase full-wave thyristor rectifier with an inductive load and a displacement power factor (DPF) of 0.3.

The first test, cf. Figures 126a and 126b, shows the reference tracking capability of the proposal under no load and with a nonlinear load connected at the output, respectively. In Figures 126b, a small voltage is applied before the step is commanded so as to ensure that the nonlinear load is operating during the transient event because the response of the voltage controller is faster than the start-up time of the nonlinear load. When no load is connected at the output, the plant model used to design the controller (103) accurately describes the physical system because the nominal model used to design the compensator assumes a no load condition. Therefore, the response precisely follows the transient response of a first-order system of the design selected bandwidth f_{bw}, as expected from the proposed direct discrete-time pole-placement strategy adopted for the compensator. When a nonlinear load is connected at the output, the response is not significantly modified, compared to Figure 126a, in spite of the plant model change caused by the load because of the robustness of the proposal, as explained in Section 6.3.

The second test evaluates the performance of the controller to a load step. Both connection and disconnection events are tested. Figures 127a and 127b shows the output voltage $v_{C,abc}$ and the load current $i_{o,abc}$ during a connection and a disconnection event, respectively. In order to asses the dynamic output performance, Figure 127c displays the voltage error $v^*_{C,abc} - v_{C,abc}$ in comparison to the limits defined in [135] for the two previous load step tests. The proposal meets such specification using an LC filter with reduced reactive values and a low switching frequency because the presented design optimizes the transient response, cf. Section 6.3. During steady-state, Figure 127c show a small high-frequency voltage error which is the 400-μs switching ripple of the voltage source converters (VSCs), see Figures 127aand 127b.

Figure 127d shows the magnitude of the spectrum of the output voltage v_C and of the load current i_o. As expected, no output voltage distortion appears at the main low-order harmonics due to the resonant action of the controller.
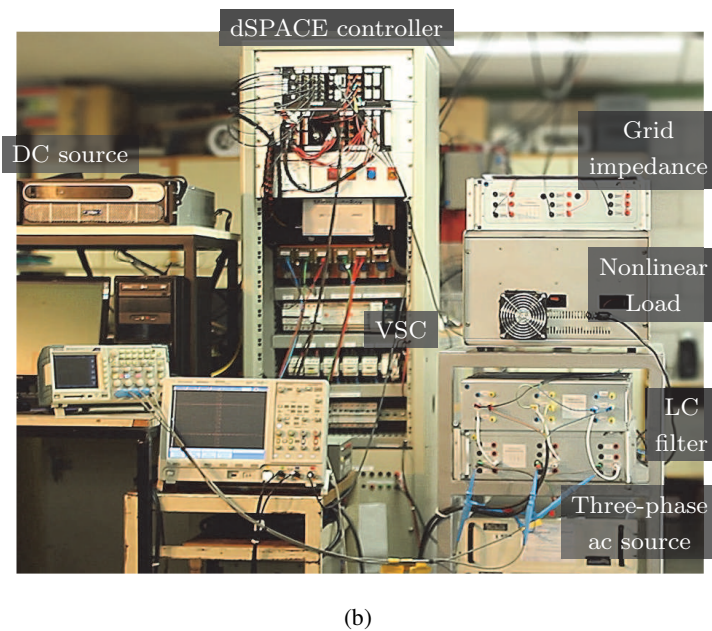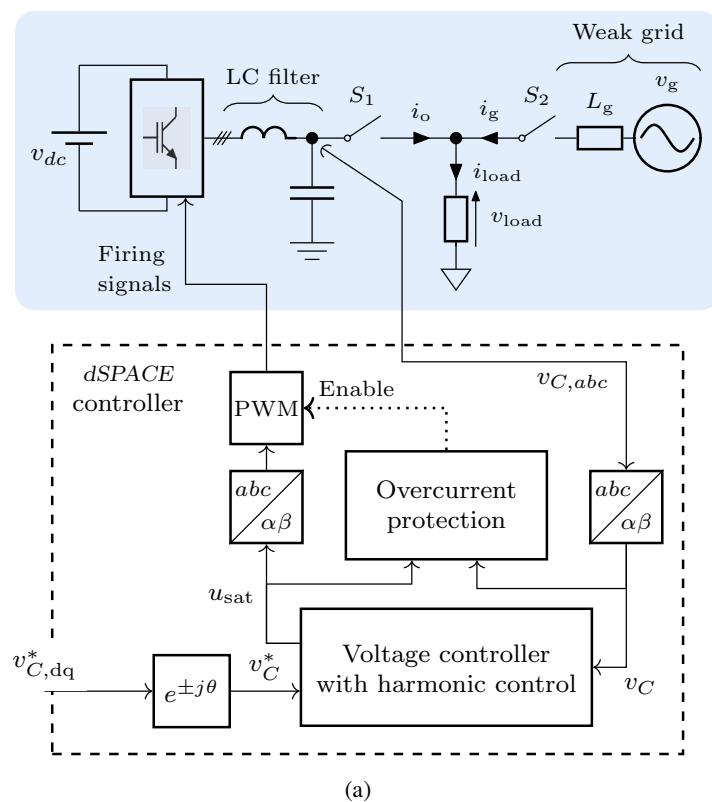
(a)

(b)

Figure 124. Experimental setup of the grid-connected inverter. a Diagram. b Photograph.

Table 13. Experimental Setup Parameters

Base values			
Nominal output power	P_{o}	10	[kW]
Nominal output voltage	V_{oRMS}	230	[V]
Minimum load power factor	$\cos\phi$	$0.2^{\dagger}$	
Output frequency	f_{o}	50	[Hz]
LC filter			
Filter inductance	L_{f}	2.5, 0.05	[mH, p.u.]
Filter capacitance	C_{f}	30, 0.14	[μF, p.u.]
Filter resonance	f_{res}	581	[Hz]
VSC			
Switching frequency		2.5	[kHz]
Dead time		3	[μs]
DC bus voltage	v_{dc}	700	[V$_{\text{DC}}$]
Controller			
Sampling frequency	f_{s}	5	[kHz]
Bandwidth	f_{dom}	300	[Hz]
Measurement noise	N	0.01	[A^2]
Process noise	$\mathbf{Q}$	0.1	[%]

[†] Minimum load power factor depends on the number of voltage harmonics controlled with zero steady-state error, c.f. Figure 1.110.

The next test assesses the fault clearing capability of the proposal. The maximum change in the converter current that can occur between two samples, cf. (121), is 15A. An output overload condition is generated by suddenly connecting a 12Ω load. Figure 128 shows the estimated inductor current $\hat{i}_{L,abc}$ and compares it to the measured inductor current $i_{L,abc}$. Two time bases are used ($5ms$/DIV and $1ms$/DIV) to clearly visualize the discrete samples when the transient occurs. The voltage source converters (VSCs) quickly disables the PWM, cf. Figure 128, when $\hat{i}_{L,abc}$ exceeds the 15-A current limit, in order to stop the overcurrent transient. After the voltage source converters (VSCs) stops commutation, $\hat{i}_{L,abc}$ is not an accurate estimation of $i_{L,abc}$ because the controller output voltage v_{sat} is not applied to the plant, cf. Figure 106.

6.5.2. Grid Connected Operation

In order to asses the operation in a grid-connected configuration (S_2 closed), the proposed voltage controller is connected to a three-phase grid through a coupling impedance L_{g} of

Table 14. Grid Voltage Harmonics

Order	Sequence	h	Magnitude
1	$+$	$+1$	230V
3	0		5 %
5	$-$	-5	6 %
7	$+$	$+7$	5 %
9	0		1.5 %
11	$-$	-11	3.5 %
13	$+$	$+13$	3 %
THD			10.5 %

value $5.4mH$ (0.1 p.u.). A three-phase ac voltage source is used to generate a distorted grid voltage. The grid voltage v_g has a total harmonic distortion (THD) of 10.5% and the harmonic content is indicated in Table 14. The nonlinear load described in the previous section is used as a local load, as shown in Figure 124.

Figure 129 shows the experimental waveforms in the abc frame during the connection event of the voltage source converters (VSCs) to such distorted grid. Before the voltage source converters (VSCs) is switched to grid-connected mode (S_1 is open and S_2 is closed), the load voltage v_{load} has a large distortion caused by the nonlinear load current i_{load} and the distorted grid voltage v_g. When S_1 is closed, the voltage source converters (VSCs) output voltage v_C is maintained sinusoidal in spite of the distorted output current i_o delivered to the nonlinear load i_{load} and to the distorted grid i_g.

6.6.   Summary

This section has presented an ac voltage controller with a high robustness to variations in the load. Both islanded operation and grid-connected mode have been tested. The proposed controller uses a single-loop structure that improves the transient performance by selectively minimizing the output impedance of the system at a set of design-selected frequencies. This set of frequencies can contain any frequency below the Nyquist frequency of the digital controller, including the resonant frequency of the LC filter and frequencies above the critical frequency of the system $f_{s/6}$, where previous proposals have stability problems. Complete harmonic control is achieved due to the zero output impedance at such set of frequencies. System stability has been demonstrated for a wide range of load values. Moreover, the above properties are maintained irrespectively of the LC filter installed, or the sampling frequency used, provided that overmodulation of the voltage source converters (VSCs) is avoided and the resonant frequency of the LC filter is lower than the Nyquist frequency.
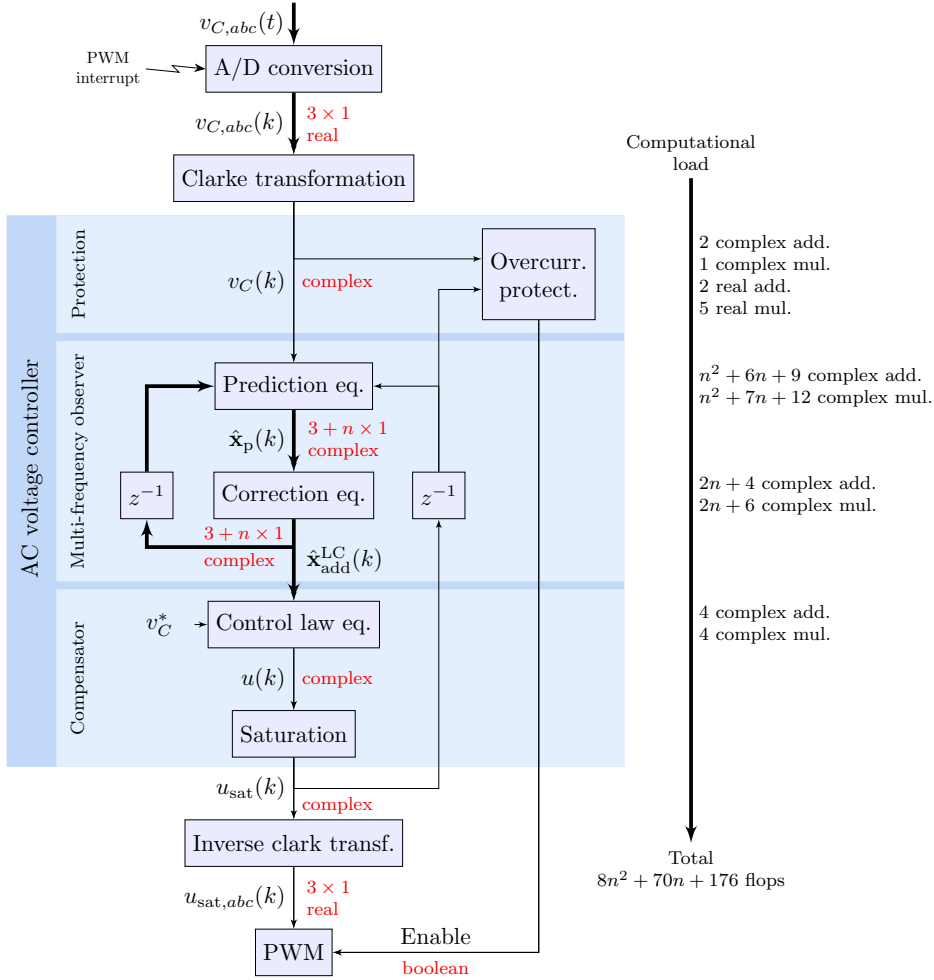
Figure 125. Execution chronogram of the proposed controller and computational load as a function of the number of design-selected frequencies where a zero output impedance is requested.

7. A Finite-Control-Set Linear Current Controller with Fast Transient Response and Low Switching Frequency for Grid-Tied Inverters

This section presents a linear current controller for a grid-tied inverter with L or LCL filter that uses a finite control set (FCS) operation. Thanks to the FCS operation, the proposed controller provides a very fast transient response, similarly to an FCS model predictive controller (MPC), while needing a low switching frequency and a low computational load. Contrarily to MPC solutions, the proposal uses a linear control structure. Such linear structure offers a straightforward implementation and stability assessment compared to an MPC, which usually requires complex optimization algorithms and Lyapunov functions that are a

(a)

(b)
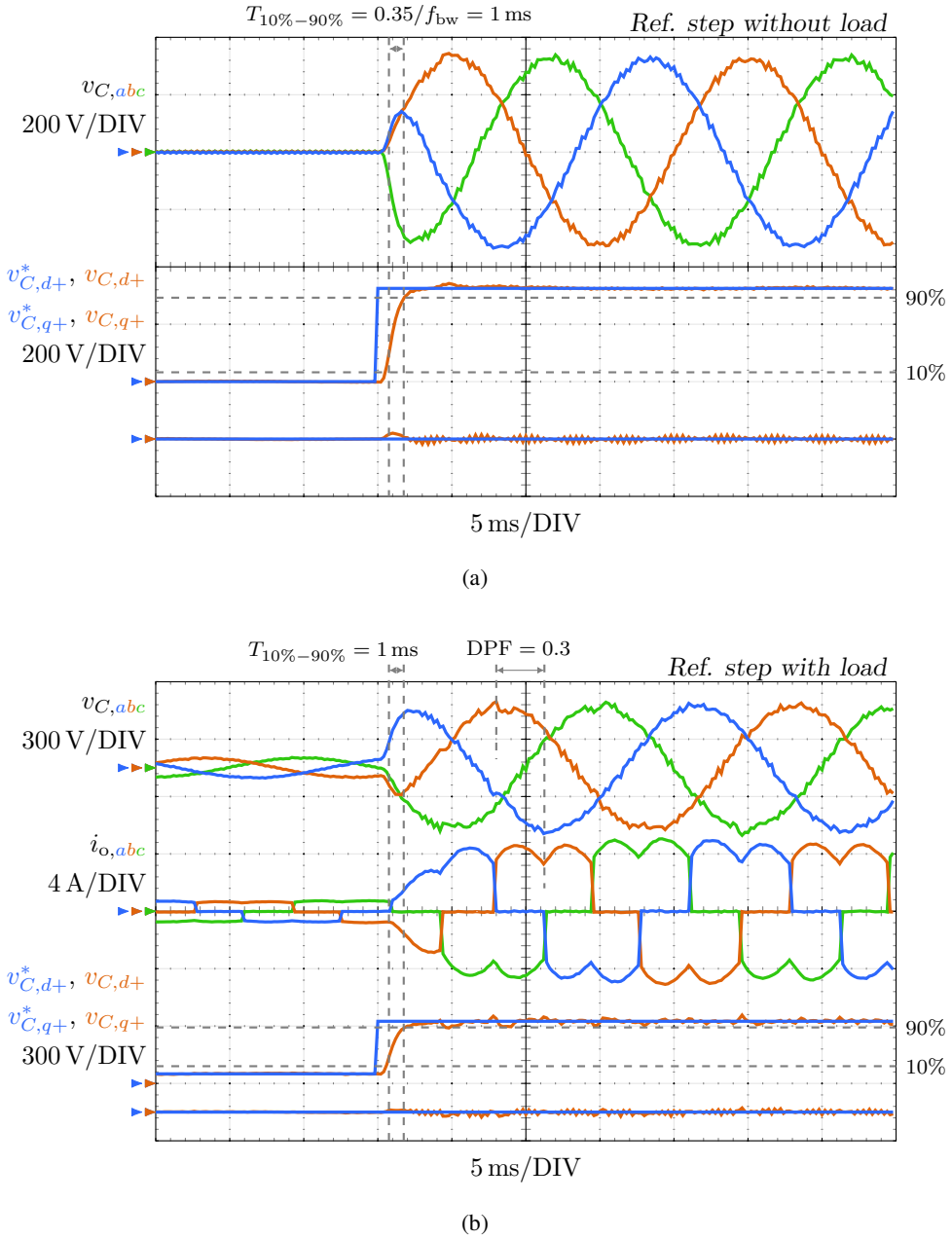
Figure 126. Experimental output voltages in the abc frame $v_{C,\text{abc}}$ and in the positive synchronous frame dq+ rotating at the fundamental output frequency f_o $v_{C,\text{dq+}}$ for a reference step $v_{C,\text{dq+}}^*$. a Without a load. b With a nonlinear load connected at the output.

Nonlinear load step (0 → 100 %)

$v_{C,abc}$
200 V/DIV

$i_{o,abc}$
4 A/DIV

5 ms/DIV

(a)

Nonlinear load step (100 → 0 %)

$v_{C,abc}$
200 V/DIV

$i_{o,abc}$
4 A/DIV

5 ms/DIV

(b)
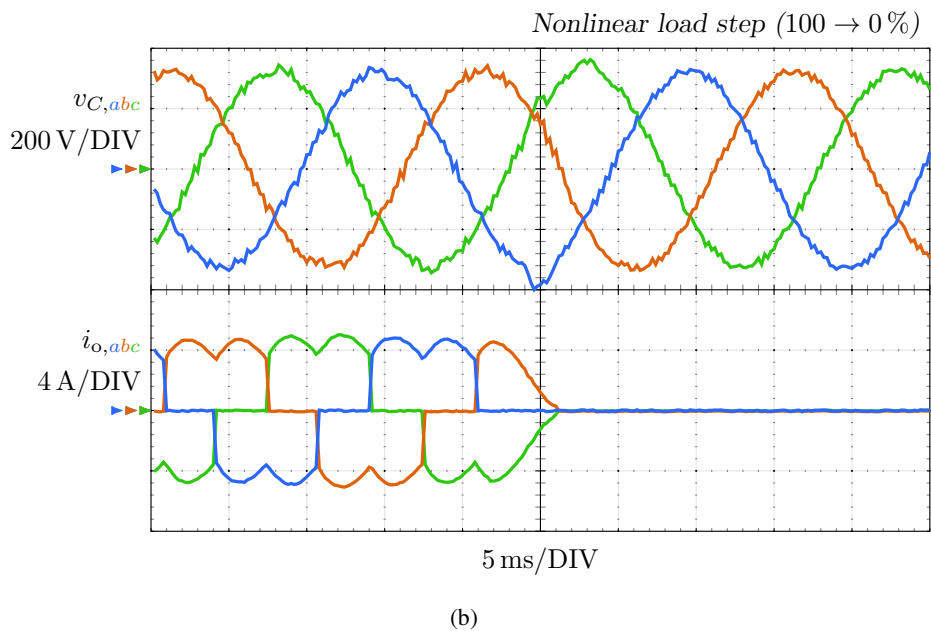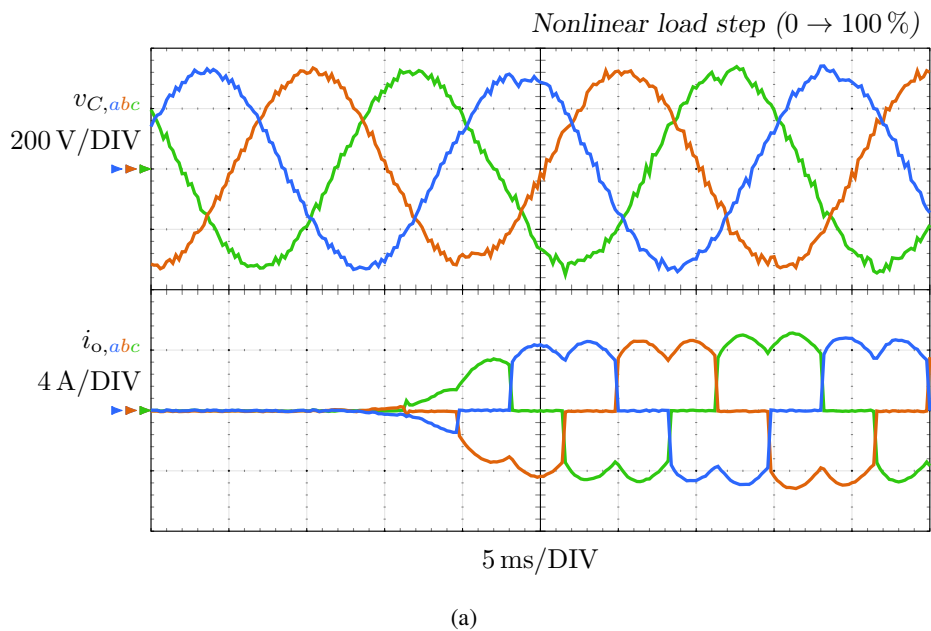
Figure 127. Continued on next page.

(c)

(d)
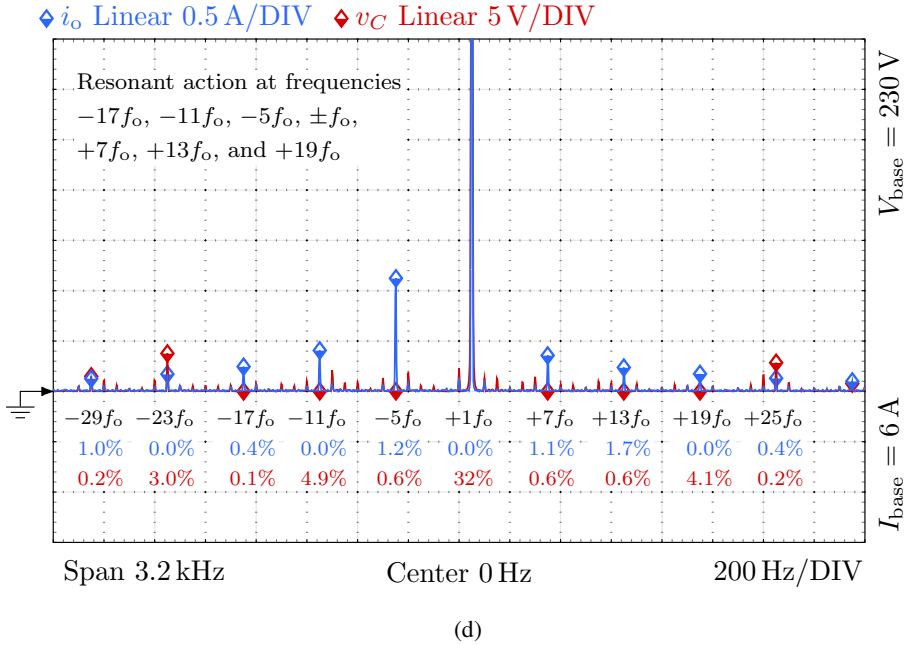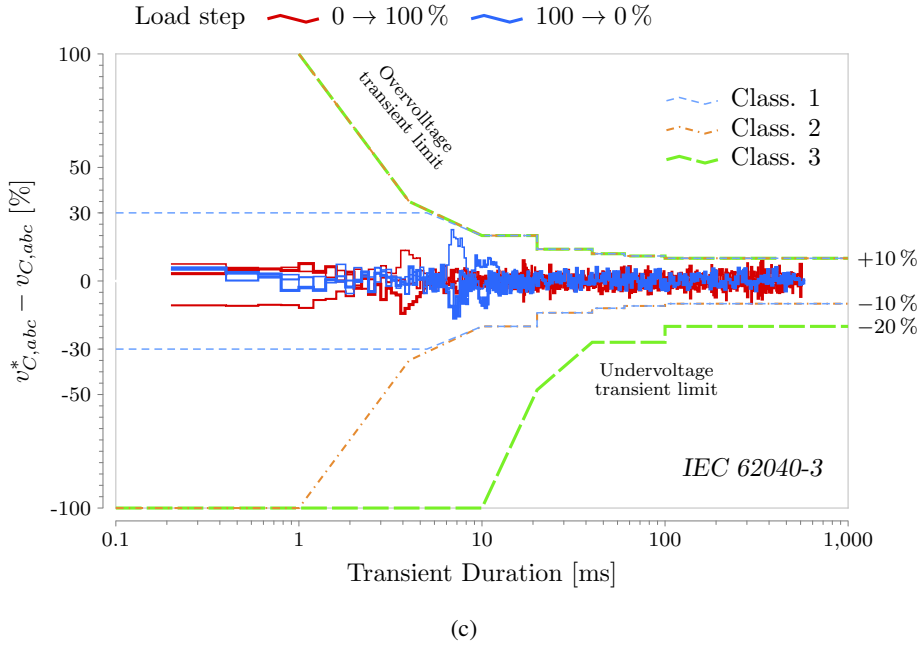
Figure 127. Transient response to a nonlinear load step. a Connection test: load step test from 0 % to 100 % of rated power. b Disconnection test: load step test from 100 % to 0 % of rated power. c Dynamic output performance according to [135]. d Magnitude of the spectrum of the output voltage v_C and of the load current i_o.
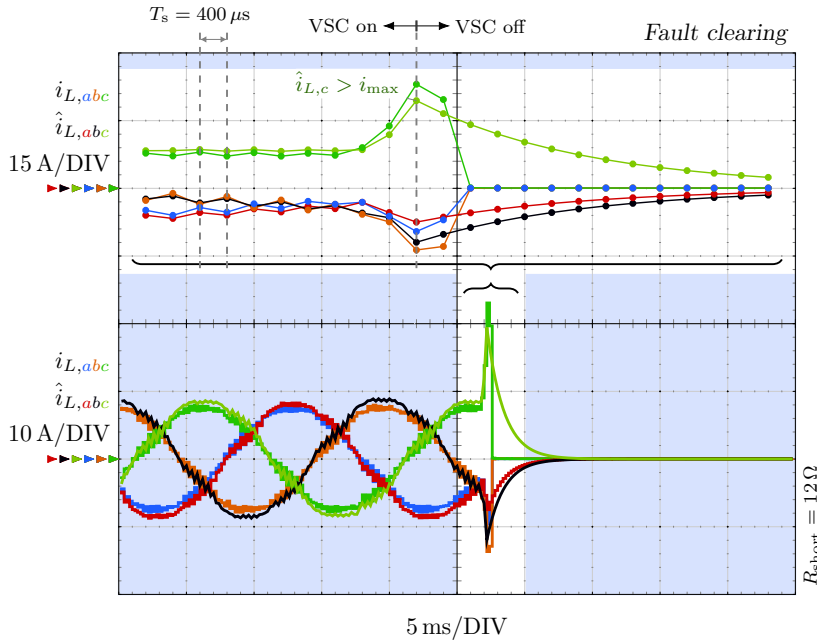
Figure 128. Turn-off process due to a converter current amplitude that exceeds the converter current limit (15 A). Measured inductor current $i_{L,\text{abc}}$ and its estimate $\hat{i}_{L,\text{abc}}$.

field of study in its own right. The proposal does not generate any switching or low-order harmonics. By design, the switching noise is evenly spread at all frequencies instead of it being concentrated at some harmonic frequencies like in the case of PWM-based controllers. This reduces the risk of exciting resonances in the utility grid and facilitates the operation of multiple inverters in parallel. In particular, the proposal is shown to achieve compliance with stringent grid harmonic codes using an L filter in a multimegawatt application where previous proposals required an LCL filter with the same total inductance.

Linear current controllers with pulse width modulators (PWMs) are commonly used in grid-tied inverters with L filter or LCL filter. Among the different types of linear current controllers, state-space solutions are an interesting choice thanks to their high robustness combined with fast and damped transient dynamics. State-space controllers can achieve zero steady-state error in the controlled variable, which is typically the grid current, even in the presence of voltage disturbances and plant modeling errors, by incorporating a disturbance model. This disturbance model, which is also named integral or resonant action, can be introduced into the controller in two different places, namely, in the forward path [98] or in the feedback path, as part of an observer [29, 8]. Such modularity of state-space controllers provides some advantages compared to more traditional transfer-function-based
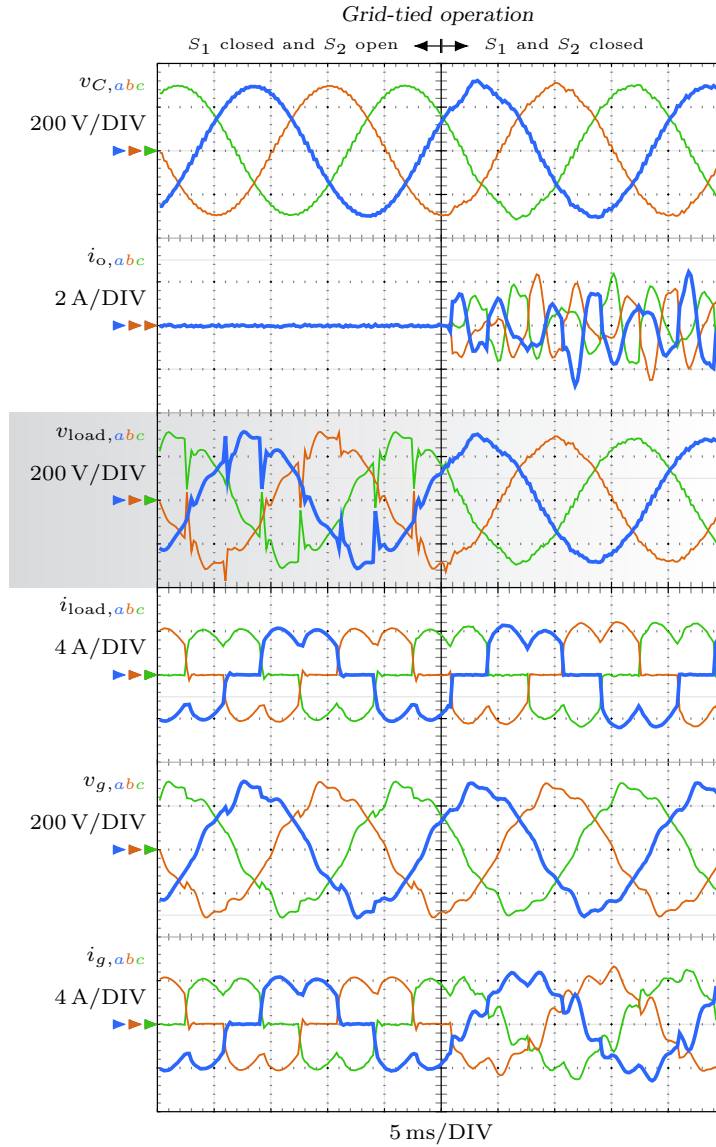
Figure 129. Experimental waveforms in the abc frame during the connection event of the voltage source converters (VSCs) to a distorted grid.

designs [98, 29, 8].

Recently, a different kind of controllers, which are based on optimization techniques, have been acquiring popularity in power electronic applications thanks to the growth in computational power of embedded controllers, which makes feasible to solve in real time a complex optimization problem. This new type of controllers are commonly referred as model predictive controllers (MPCs) [16, 17, 18, 19, 20, 21, 22, 23, 24, 25, 26] or direct-sequence controllers [27, 28]. The main advantage of model predictive controllers (MPCs) is a fast transient response with a low switching frequency. These nonlinear controllers per-

mit to improve the performance of linear controllers because they offer additional degrees of freedom. In power converter applications, where the controller effort must be limited in order to avoid overmodulation of the converter, a nonlinear solution can achieve a faster response while avoiding windup and robustness problems. When a linear controller is used, there is always a trade off between the disturbance rejection capability of the controller and its robustness to plant model variations, namely, Bode's sensitivity integral. Such trade off does not apply to nonlinear systems. These advantages of nonlinear control techniques permit to achieve a lower total harmonic distortion (THD) than linear controllers with a PWM [24], specially for low switching frequencies.

There is a vast literature of model predictive controllers (MPCs), which can be classified into two main categories depending on the domain where the optimization problem is solved, namely, continuous control set (CCS) and finite control set (FCS) methods. CCS methods use a PWM in order to synthesize the solution of the optimization problem whereas FCS methods carry out the optimization only over the discrete switching states of the power converter. Additionally, CCS-model predictive controller (MPC) can be subdivided into two types depending on whether the optimization algorithm finds an unconstrained solution or includes the constraints that limit the converter output voltage when it enters into overmodulation.

On the one hand, the unconstrained MPC has been found to be equivalent to a linear quadratic (LQ) state-space controller when the control and the prediction horizon of the MPC approach infinity [137]. Nonetheless, if constraints are ignored during the optimization process and the resultant control law is saturated, then the design is likely to give a poor closed-loop response and may lead to instability. These limitations also apply to linear deadbeat controllers [21]. In order to deal with this nonlinear characteristic of the power converter, a designer can use a constrained MPC or a linear controller with an antiwind-up scheme [98, 29, 8].

On the other hand, to the authors' knowledge, FCS methods do not have an equivalent or similar alternative in the classical linear control theory field. Linear controllers are frequently adopted as current controllers in power applications because they offer a simple design process and their performance and stability can be easily studied using linear analysis tools [138]; hence, a linear or classical design is frequently more valuable for practicing power-electronic engineers and researchers. However, linear controllers have never been implemented in a grid-tied inverter with an FCS operation. In particular, PI and PR controllers cannot be used without a PWM. This limits the applicability of an FCS operation to only FCS-model predictive controllers (MPCs). However, FCS-model predictive controllers (MPCs) usually require complex numerical algorithms that are a field of study in its own right. Their robustness and stability to plant model variations is also hard to assess due to their nonlinear characteristics. Stability, from a practical viewpoint [18], i.e., by guaranteeing a maximum error in the controlled output, has been studied in [18, 19] using Lyapunov theory. These studies provide a sound and precise stability analysis for a wide range of applications of model predictive controllers (MPCs) but they require a higher complexity, compared to classical linear controllers. Such complexity burden associated to FCS-model predictive controllers (MPCs) constraints the use of an FCS operation.

This section is an extension of the conference presentation [13], which introduced the proposed linear FCS controller and demonstrated its operation with an L filter by means
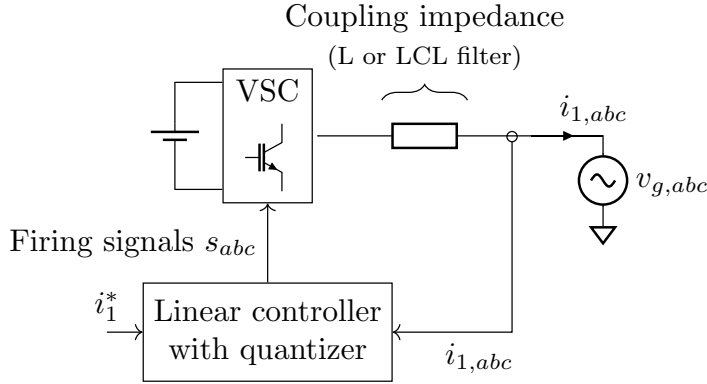
Figure 130. Grid-tied voltage source converters (VSCs) with a grid current controller and an coupling filter.

of simulation results. The presented work completes the theoretical presentation and experimentally verifies the operation using both L and LCL filters. In summary, this section presents a linear FCS current controller for grid-tied inverters with L or LCL filter that combines the advantages of linear controllers with the performance of complex FCS-MPC solutions. The presented controller provides a fast transient response (high bandwidth) with a low switching frequency, similarly to a FCS-MPC. Nonetheless, it uses a simple linear controller structure that results in a simple design process and a straightforward implementation. Due to its high bandwidth in combination with an integral action, the proposal achieves zero steady-state error at the fundamental grid frequency, equivalently to a PI controller, and minimizes the current distortion at the main low-order harmonics. Thanks to the FCS operation, the proposal does not generate any switching or low-order harmonics. It generates a spread-spectrum output voltage similar to that of a FCS-MPC [19]. The switching noise is evenly spread at all frequencies instead of it being concentrated at some harmonic or interharmonic frequencies. This reduces the risk of exciting resonances in the grid and facilitates the operation of multiple inverters in parallel; therefore, grid codes such as [110, 139, 130] can be more easily met, even during weak-grid conditions.

After this introduction, a model of the plant including the grid-voltage disturbance is defined. Then, the design of the proposed FCS controller is proposed in Section 7.2. The capability of the proposal to avoid exciting grid resonances is explained in Section 7.3. Finally, Section 7.4 presents some experimental results that validate the proposal in a setup representative of a multimegawatt low-voltage application with a two-level voltage source converters (VSCs).

7.1. Modeling of the Plant

This Section presents three mathematical models that are used in the next Section to design the proposed controller. The first two models describe the plant dynamics. There is a model for a grid-tied inverter with an L filter and another model for a grid-tied inverter with an LCL filter. The third model is a disturbance model that represents the grid voltage.

The grid-tied inverter shown in Figure 130 can be accurately modeled in the discrete-time domain by a transfer function or a state-space model that describes the dynamics of the coupling filter, the computational delay of the embedded controller, and the modulation delay of the voltage source converters (VSCs). When an L filter is used, such plant model is a second-order system as shown in Figure 131a. The discrete-time state-space model that relates the controller output voltage v to the grid current i_1 is:

$$
\begin{aligned}
\mathbf{x}_{dd}^L(k+1) &= \mathbf{A}_{dd}^L \mathbf{x}_{dd}^L(k) + \mathbf{B}_{dd}^L v(k) \\
i_1(k) &= \mathbf{C}_{dd}^L \mathbf{x}_{dd}^L(k). \\
\mathbf{x}_d^L(k) &= \begin{bmatrix} i_1(k) & v_{\mathrm{d}}(k) \end{bmatrix}^{\mathrm{T}},
\end{aligned}
\tag{125}
$$

where $\mathbf{x}_d^L(k)$ is the system state vector, which contains two state variables, namely, the grid current i_1 and the one-sample-delayed plant input voltage v_d. The latter models a one-sample computational delay in the embedded controller. The mathematical derivation of the system, input, and output matrices $\mathbf{A}_{dd}^L$, $\mathbf{B}_{dd}^L$, and $\mathbf{C}_{dd}^L$ is given in Section 7.5.

During the study of the proposed controller characteristics, a transfer function representation of the plant without considering the effect of the grid voltage v_g is also needed. Such discrete-time transfer function can be directly obtained from the previous state-space model.

$$
G_{\mathrm{plant}}^{\mathrm{L}}(z) = \left.\frac{i_g}{v}\right|_{v_g=0} = \mathbf{C}_{dd}^L \left(z\mathbf{I} - \mathbf{A}_{dd}^L \right)^{-1} \mathbf{B}_{dd}^L.
\tag{126}
$$

Alternatively, when an LCL filter is used, the plant model is a forth-order system as shown in Figure 131b. The resultant state-space model is

$$
\begin{aligned}
\mathbf{x}_{dd}^{LCL}(k+1) &= \mathbf{A}_{dd}^{LCL} \mathbf{x}_{dd}^{LCL}(k) + \mathbf{B}_{dd}^{LCL} v(k) \\
i_1(k) &= \mathbf{C}_{dd}^{LCL} \mathbf{x}_{dd}^{LCL}(k). \\
\mathbf{x}_{dd}^{LCL}(k) &= \begin{bmatrix} i_1 & i_2 & v_C & v_{\mathrm{d}} \end{bmatrix}^{\mathrm{T}},
\end{aligned}
\tag{127}
$$

where now the system state vector $\mathbf{x}_{dd}^{LCL}(k)$ contains four state variables, namely, the grid current i_1, the converter current i_2, the capacitor voltage v_C, and the one-sample-delayed plant intput voltage v_d. The mathematical calculation of the system, input, and output matrices $\mathbf{A}_{dd}^{LCL}$, $\mathbf{B}_{dd}^{LCL}$, and $\mathbf{C}_{dd}^{LCL}$ as a function of the plant parameters is given in Section 7.5.

Similarly to the L filter case, a transfer function representation of the plant with an LCL filter and without considering the effect of the grid voltage v_g can be directly obtained from (127) as

$$
G_{\mathrm{plant}}^{\mathrm{LCL}}(z) = \left.\frac{i_g}{v}\right|_{v_g=0} = \mathbf{C}_{dd}^{LCL} \left(z\mathbf{I} - \mathbf{A}_{dd}^{LCL} \right)^{-1} \mathbf{B}_{dd}^{LCL}.
\tag{128}
$$

The proposed current controller does not contain a feedforward of the grid voltage v_g in order to compensate its effect on the grid current; instead, it contains a linear model of the grid voltage. Specifically, the grid voltage is described as a sinusoidal disturbance. More complete disturbance models that also take harmonic components into account are not considered in this section, whose scope is to demonstrate the capabilities of this new
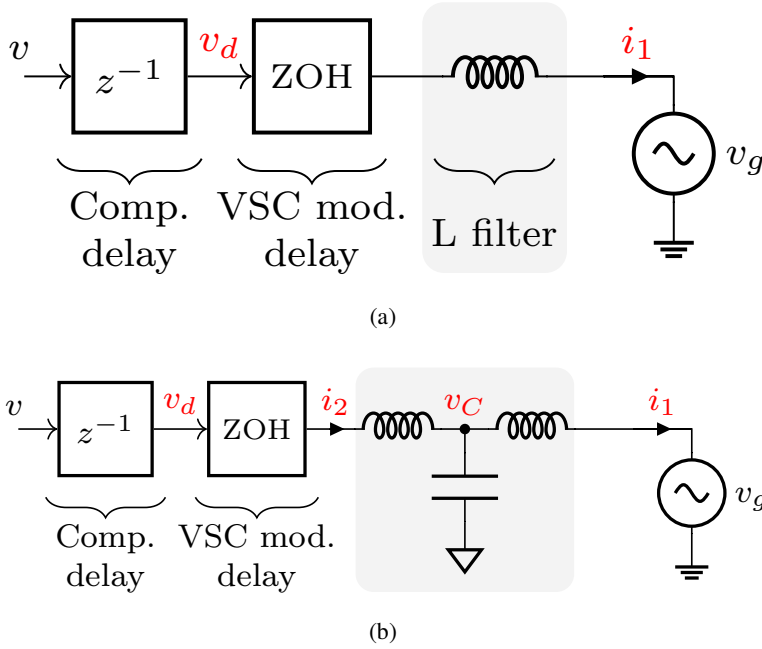
(a)

(b)

Figure 131. Two models of a grid-tied voltage source converters (VSCs) with a coupling filter. The plant state variables are denoted in red. a The coupling filter is an L filter. b The coupling filter is an LCL filter.

controller; however, thanks to the large bandwidth of the proposal, the main low-order harmonic disturbances are successfully attenuated without having to explicitly include them in the disturbance model. According to the internal model principle, a controller can reject the effect of a disturbance if a disturbance model is included in the control loop. In order to achieve zero steady-state error in the grid current at the fundamental grid frequency, a resonant action is added to the controller. The grid voltage space vector can be described by a complex exponential disturbance $\mathbf{x}^{dis}(t)$ of frequency f_g [8, Sec. II]. Such disturbance is a solution of the following equation:

$$\frac{\mathrm{d}\mathbf{x}^{dis}(t)}{\mathrm{d}t} = -j2\pi f_g \mathbf{x}^{dis}(t). \tag{129}$$

Using a ZOH equivalent, the resultant discrete-time state-space disturbance model is obtained:

$$\mathbf{x}_d^{dis}(k+1) = \mathbf{A}_d^{dis}\mathbf{x}_d^{dis}(k) + \mathbf{B}_d^{dis}[i_1^*(k) - i_1(k)]. \tag{130}$$

7.2. Design of the Current Controller

This section introduces the proposed current controller. First, an overview of the controller architecture and its theory of operation is presented. Next, the detailed controller architecture and design process is explained. Both L- and LCL-filtered grid-tied inverters are considered. The design process employs the disturbance model (130) and the plant model (125) or (127) depending on the installed filter.
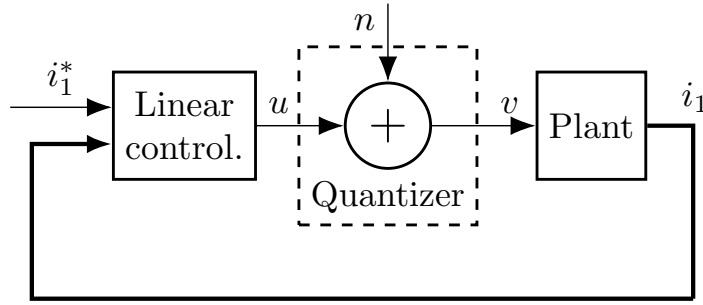
Figure 132. Simplified block diagram of the proposed current controller.

Theory of Operation

The proposed controller operates in the $\alpha\beta$ frame and it only receives as inputs the measured grid current $i_{1,abc}$ and the desired grid current reference i_1^*. Using these two signals, the proposed controller directly generates the firing signals s_{abc}, as shown in Figure 130. It should be noted that grid-tied converters often measure the grid voltage v_g in order to synchronize with the grid, unless a sensorless grid synchronization mechanism is employed [126, 4]; however, such measurements are not required by the proposed current controller.

The proposed controller consists of two main parts, namely, a linear controller and a quantizer. A simplified block diagram representation of the controller structure in the $\alpha\beta$ frame is shown in Figure 132. For simplicity, the subscript that denotes the $\alpha\beta$ frame, which is the reference frame where the controller operates, is omitted in the variable names.

The linear controller calculates a reference voltage u to command the voltage source converters (VSCs); however, the voltage source converters (VSCs) can only generate a reduced set of voltages at its output. In the case of a two-level voltage source converters (VSCs), there are eight switching states v_i with $i = 1, 2, \cdots, 8$, see Figure 133; therefore, an error or switching-noise voltage n appears at the plant input, see Figure 132, when the voltage vector v closest to u is hold for one sampling period at the plant input instead of the commanded voltage u. This process of selecting the switching state that results in an output voltage v that is closest to the commanded linear controller voltage u is denoted quantization and it is carried out by the quantizer, cf. Figure 132. Figure 133 shows a representation of this quantization error (or switching noise) in the $\alpha\beta$ frame and the regions associated to each of the switching states, also known as Voronoi regions in the mathematical field.

The switching-noise voltage n is a disturbance that affects the grid current. Contrarily to a PWM-based controller, the value of such disturbance is known by the proposed controller because $n = v - u$. This is something unique to a FCS operation and it permits the controller to receive in real time all the information about the switching noise generated by the voltage source converters (VSCs). Using such knowledge of n, the controller is able to accurately calculate the actual state of the plant and compensate the effect of the switching noise on the grid current. Moreover, a PWM-based controller forces the average value of n over every switching period to be equal to zero. Such deterministic or repetitive behavior is the cause of harmonics in the output voltage. Alternatively, the quantizer achieves the same average value of n but over a variable time period. Ideally the transfer function from the switching
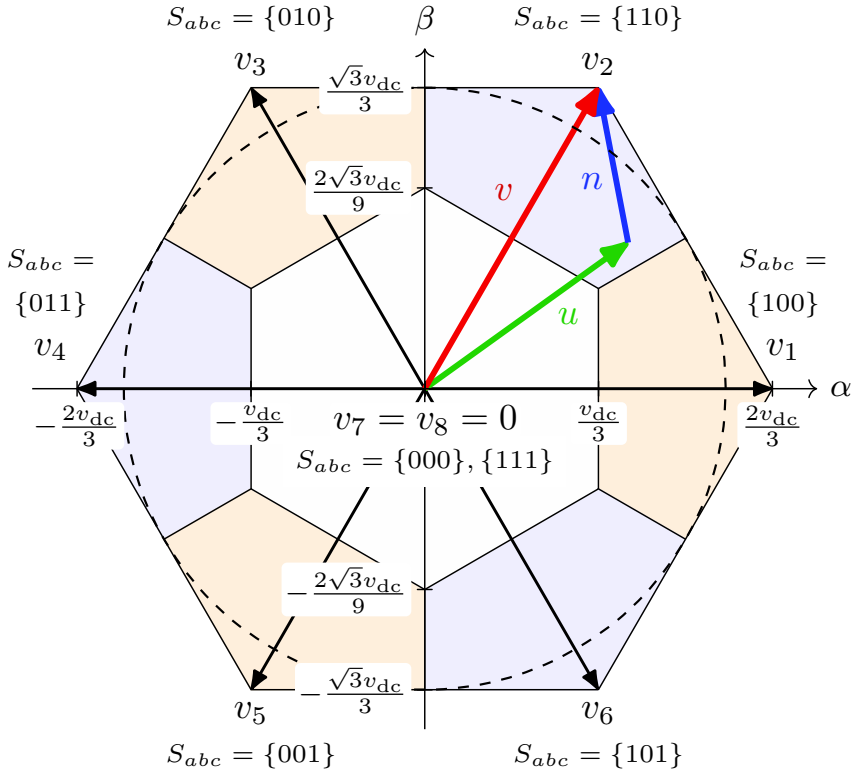
Figure 133. Graphical representation in the $\alpha\beta$ frame of the Voronoi regions associated to each of the switching states v_i with $i = 1, 2, \cdots, 8$ of a two-level voltage source converters (VSCs) and example of the complex-valued signals involved in the quantization process, namely, the linear controller output voltage u, the voltage source converters (VSCs) output voltage v, and the switching (or quantization) noise n.

noise input n to the grid current output i_1 in Figure 132 should be zero. The response of the closed-loop system from the input n to the output i_1 is denominated in the following as the noise transfer function (NTF). In order to achieve the best performance (lowest current noise), the magnitude of the NTF should be as small as possible. This ensures that the switching noise generated by the converter has the least effect on the grid current.

In order to achieve the previous goal, the proposed linear controller design optimizes the NTF frequency response. At high frequencies, the coupling filter (L filter or LCL filter) already provides a good attenuation of the switching noise n due to its low-pass characteristic; therefore the linear controller need not perform any compensation action at such high frequencies in order to meet current distortion requirements. Figure 134a shows the magnitude of the open-loop plant response $G_{\text{plant}}^{\text{L}}$ in the case of a voltage source converters (VSCs) with an L filter. As shown in the bode plot, the plant successfully attenuates high frequency components. But it does not provide enough attenuation at low frequencies. This limitation is addressed by incorporating a linear controller that improves the disturbance

rejection at low frequencies, cf. NTF in Figure 134a. Ideally, the resultant NTF has a flat frequency response with a magnitude close to zero thanks to the linear controller, which shapes the magnitude of the noise transfer function by changing the location of the plant and disturbance poles. Without a controller, the disturbance pole p_3 and the filter pole p_1 are located at low frequencies, as shown in Figure 134b, resulting in a frequency response with a low-pass behavior. During closed-loop operation, one of the plant poles p_1 is moved to a higher frequency, as shown in Figure 134c, yielding the desired flat frequency response. Additionally, the disturbance model introduces a zero z_1^{cl} that eliminates any steady-state error at the fundamental grid frequency f_g.
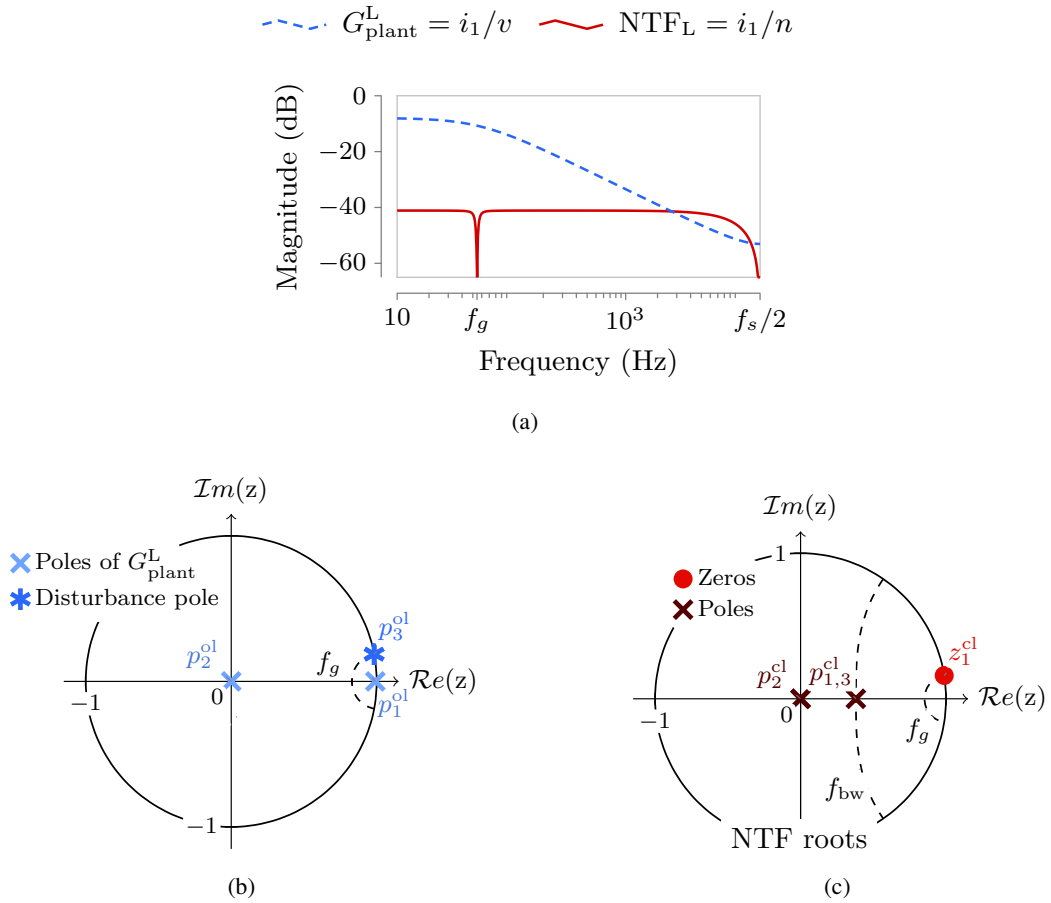
Figure 134. Effect of the proposed controller on the plant dynamics (L filter). a Magnitude of the plant model G_{plant}^L and magnitude of the noise transfer function (NTF). b Pole-zero map of the plant model G_{plant}^L. c Pole-zero map of the NTF.

Design of the Quantizer

The proposed current controller is composed of two components, namely a linear controller and a quantizer. A quantizer is a memoryless device defined by its input-output character-

istics. It chooses the output vector v, or voltage source converters (VSCs) switching state, that results in the least switching noise being generated at each sampling period:

$$v \quad = \quad \arg \min_{v_i} |u - v_i| . \qquad (131)$$

Such choice defines the Voronoi regions associated to each of the switching states of the voltage source converters (VSCs). The selected sequence of output vectors does not necessary constitute the optimum sequence, which generates the least grid current error. In order to calculate the optimum sequence, there is no other option than to solve a complex optimization problem. However, such optimization problem cannot be easily calculated in real time due to the high computational load required [21]. Therefore, model predictive controllers (MPCs) often use heuristics in order to reduce the computational load required, at the expense of not guaranteeing an optimal solution. Similarly to most MPC, the proposal does not guarantee an optimal performance; but it offers a simpler design process and requires a lower computational load than model predictive controllers (MPCs), even when heuristics are used.

The quantizer only depends on the type of voltage source converters (VSCs) and on the reference frame in which it operates. In particular, the proposal is implemented in a two-level three-phase voltage source converters (VSCs) and the current controller operates in the $\alpha\beta$ frame. The resultant regions associated to each of the discrete switching states (Voronoi regions) are shown in Figure 133. It should be noticed that a newly selected Voronoi region does not have to be consecutive to the previously selected one. Furthermore, there are two different switching states $S_{abc} = \{000\}$ and $S_{abc} = \{111\}$ that yield the same output voltage in the $\alpha\beta$ frame; hence they share a common Voronoi region. When the linear controller commands a voltage reference that is contained within such Voronoi region, the quantizer selects the one that minimizes the number of commutations depending on the current switching state, i.e., if the current switching state is $S_{abc} = \{000\}$, $\{001\}$, $\{010\}$, or $\{100\}$, then it selects the switching state $\{000\}$; otherwise, it selects $\{111\}$.
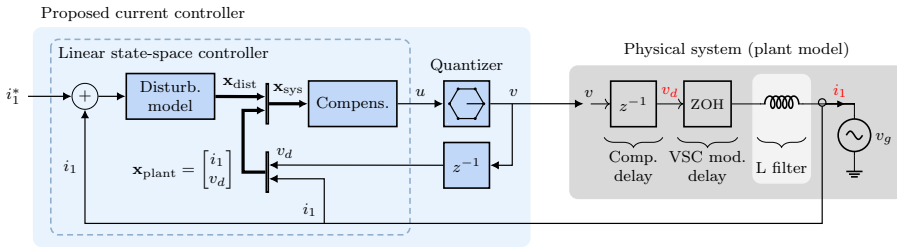

Figure 135. Detailed structure of the proposed current controller when an L filter is used.

Design of the Linear Controller

The proposed linear controller architecture employs a conventional state-space structure, which is composed of a compensator and a disturbance model. Figure 135 shows a detailed block diagram of the proposed controller architecture connected to the plant model

of an L-filtered grid-tied inverter. Such model comprises the grid voltage v_g, the L filter, the modulation delay of the voltage source converters (VSCs), and the one-sample computational delay of the embedded controller. The union of the plant state vector $\mathbf{x}_{\text{plant}}$ and the disturbance state variable x_{dist} conforms the system state vector $\mathbf{x}_{\text{sys}}$. When an L filter is employed, only the filter current is fed back to the current controller. Nevertheless, in order to generate a grid current reference i_1^*, additional elements may be required depending on the reference generation strategy adopted, such as a PLL and grid-voltage sensors.
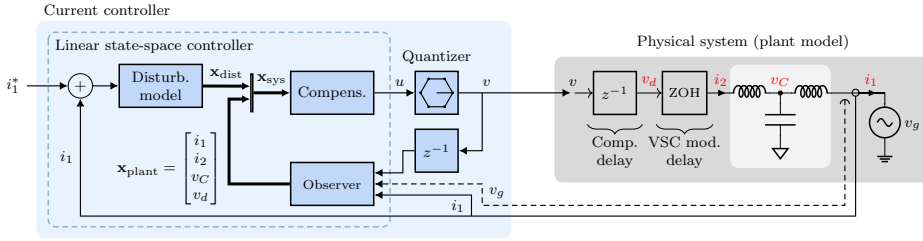
Figure 136. Detailed structure of the proposed current controller when an LCL filter is used.

If an LCL filter is employed in place of an L filter, the detailed controller architecture is slightly modified, compared to the L filter case, as shown in Figure 136. An observer is added in order to estimate the new plant state variables that are not directly measured, which are the capacitor voltage v_C and the converter-side current i_2. In addition to measuring the grid current, the observer may measure the grid voltage in order to improve the state estimation speed when a sudden change in the grid voltage occurs, such as a sag or an interruption. It should be noted that, contrarily to previous proposals [8], now the disturbance model cannot be part of the observer. The reason is that the observer cannot calculate the grid current error $i_1^* - i_1$ because the observer is unaware of the current reference i_1^*. The chosen observer type is a classical Kalman filter, which calculates the plant state $\mathbf{x}_{dd}^{LCL}(k)$ according to the following two equations:

$$\mathbf{x}_{dd}^{LCL}(k) = \mathbf{x}_{\text{pred}}(k) + \mathbf{K_o}[i_1(k) - \mathbf{C}_{dd}^{LCL}\mathbf{x}_{\text{pred}}(k)], \qquad (132)$$

where $\mathbf{K_o}$ is the Kalman gain and $\mathbf{x}_{\text{pred}}$ is the predicted state. The predicted state equation is

$$\mathbf{x}_{\text{pred}}(k) = \mathbf{A}_{dd}^{LCL}\mathbf{x}_{\text{dd}}^{\text{LCL}}(k-1) + \mathbf{B}_{dd}^{LCL}v(k-1). \qquad (133)$$

This type of observer has been extensively used in the literature and it has been successfully used for controlling a grid-tied inverter [8]. The observer gain $\mathbf{K_o}$ calculation process is given in [8, Appendix A].

In both cases (L and LCL filter), the shape of the NTF is determined solely by the disturbance model and the compensator. The disturbance model (130), eliminates the grid current error at the fundamental grid frequency. This is achieved by introducing a disturbance zero in the NTF that is located at the grid fundamental frequency, see z_1^{cl} in Figure 134c and Figure 137c. In addition, the disturbance model increases the order of the system, i.e., it adds a pole to the NTF; hence the NTF is a third-order transfer function when an L filter is used and a fifth-order transfer function if an LCL is employed.
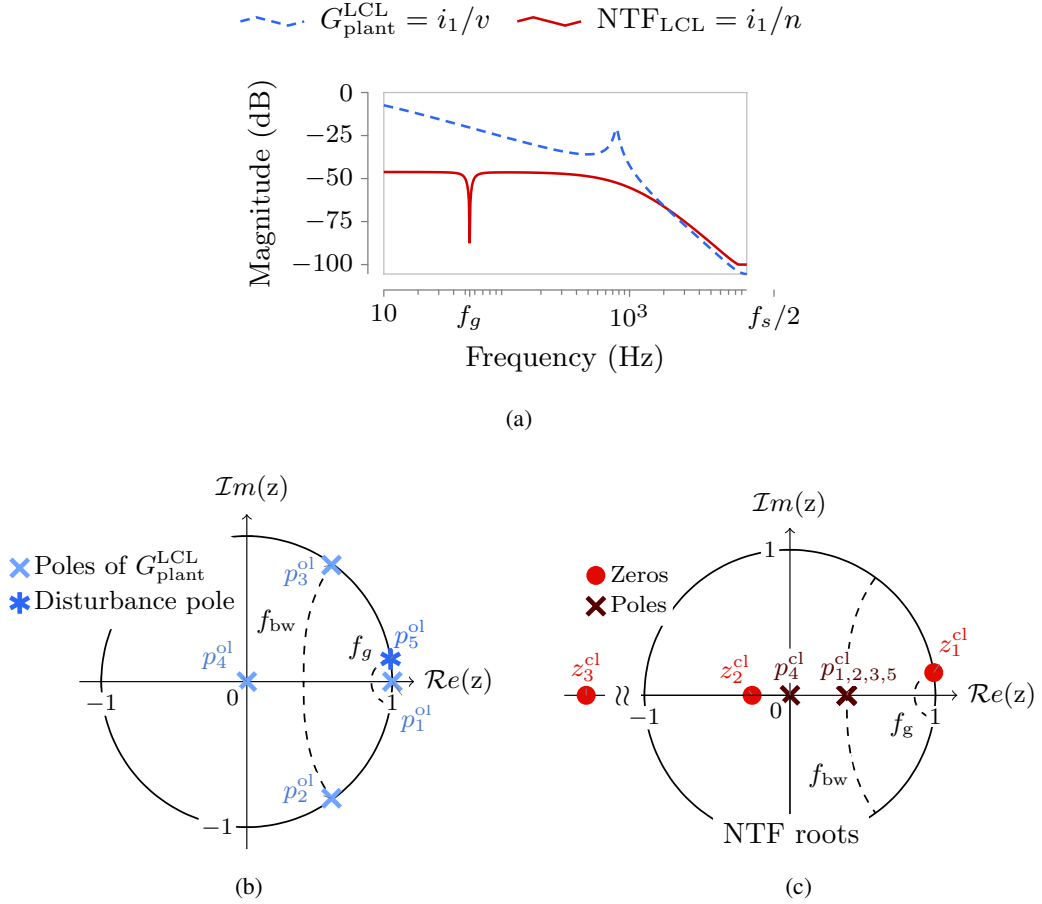
Figure 137. Effect of the proposed controller on the plant dynamics (LCL filter). a Magnitude of the plant model $G_{\text{plant}}^{\text{L}}$ and magnitude of the noise transfer function (NTF). b Pole-zero map of the plant model $G_{\text{plant}}^{\text{L}}$. c Pole-zero map of the NTF.

The location of the poles of the NTF is established by the compensator. The compensator consists of a vector gain $\mathbf{K}_{\text{c}}$ that multiplies the system state vector $\mathbf{x}_{\text{sys}}$. The result of such operation is the linear controller output voltage

$$u = \mathbf{K}_{\text{c}}\mathbf{x}_{\text{sys}}. \tag{134}$$

The compensator gain has the same number of elements as the order of the system; therefore it has three elements when an L filter is used and five elements if an LCL filter is employed. The value of such elements determines the closed-loop pole locations of the system, which are the same as those of the NTF. The proposal uses a direct discrete-time pole-placement strategy to calculate the compensator gain. This permits to directly control the shape of the NTF and achieve the design objective of minimizing the magnitude of the NTF at all frequencies.

Table 15. Compensator Design for L Filtered Converters

Poles	Position in the z-plane	
	Open-loop	**Closed-loop**
Plant model $G_{\text{plant}}^{\text{L}}$	L-filter pole is moved to a high frequency f_{bw}.	
	$p_1^{ol} = 1$	$p_1^{cl} = \exp[2\pi f_{\text{bw}} T_s]$
	Computational delay pole is not moved.	
	$p_2^{ol} = 0$	$p_2^{cl} = 0$
Disturb. model	Disturbance pole is moved to a high freq. f_{bw}.	
	$p_3^{ol} = \exp[j\, 2\pi f_g\, T_s]$	$p_3^{cl} = \exp[2\pi f_{\text{bw}} T_s]$

The compensator gain $\mathbf{K}_{\text{c}}$ is calculated applying Ackerman's formula:

$$\mathbf{K}_{\text{c}} \;=\; \begin{bmatrix} 0 & 0 & 1 \end{bmatrix} \begin{bmatrix} \mathbf{B} & \mathbf{AB} & (\mathbf{A})^2\,\mathbf{B} \end{bmatrix} A_{\text{cl}}(\mathbf{A}), \tag{135}$$

where $\mathbf{A}$ is the augmented-model state matrix:

$$\mathbf{A} \;=\; \begin{bmatrix} \mathbf{A}_d^{dis} & \mathbf{B}_d^{dis}\mathbf{C}_{dd}^{L} \\ \mathbf{0} & \mathbf{A}_{dd}^{L} \end{bmatrix}; \tag{136}$$

$\mathbf{B}$ is the augmented-model input matrix

$$\mathbf{B} \;=\; \begin{bmatrix} \mathbf{0} \\ \mathbf{B}_{dd}^{L} \end{bmatrix}; \tag{137}$$

$A_{\text{cl}}(\mathbf{A})$ is the characteristic polynomial, whose roots are the desired closed-loop poles of the system p_1^{cl}, p_2^{cl}, and p_3^{cl} evaluated at $\mathbf{A}$:

$$A_{\text{cl}}(\mathbf{A}) \;=\; \left(\mathbf{A} - p_1^{\text{cl}}\mathbf{I}\right)\left(\mathbf{A} - p_2^{\text{cl}}\mathbf{I}\right)\left(\mathbf{A} - p_3^{\text{cl}}\mathbf{I}\right); \tag{138}$$

and $\mathbf{I}$ is the identity matrix of size 3×3. The equations presented here are particularized for the L filter case. For the LCL filter case, the same equations are used, but replacing the L filter model matrices $\mathbf{A}_{dd}^{L}$, $\mathbf{B}_{dd}^{L}$, and $\mathbf{C}_{dd}^{L}$ with those of the LCL filter model $\mathbf{A}_{dd}^{LCL}$, $\mathbf{B}_{dd}^{LCL}$, and $\mathbf{C}_{dd}^{LCL}$, respectively. Section 7.5 details how to calculate such plant model matrices. The selected closed-loop pole locations p_i^{cl} are detailed in the following for both L- and LCL-filtered converters.

L-Filtered Converters

The dc pole of the L filter [see p_1^{ol} in Figure 134b] is moved to a high frequency f_{bw} [see p_1^{cl} in Figure 134c]. The pole that models the one-sample computational delay [see p_2^{ol} in Figure 134b] is maintained at the origin of the z plane [see p_2^{cl} in Figure 134c]. The remaining open-loop pole, the disturbance pole p_3^{ol}, is moved to the same location as p_1^{cl}. Table 15 summarizes the proposed closed-loop pole locations. The previously described pole-placement strategy results in the NTF shown in Figure 134a, which provides a high attenuation of the switching noise at all frequencies. Furthermore, this NTF provides zero steady-state error in the grid current at the fundamental grid frequency, thanks to the disturbance zero introduce by the disturbance model.
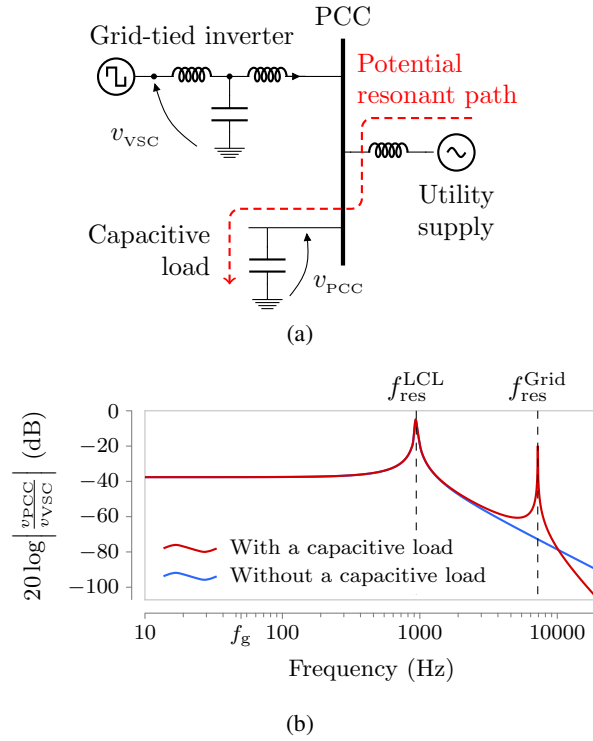
Figure 138. Potential parallel resonant situation. a Circuit diagram. b Transmission of the switching noise from the voltage source converters (VSCs) to the point of common coupling (PCC).

LCL-Filtered Converters

The LCL filter increases the order of the system by two compared to the L filter case. Therefore, two new closed-loop pole locations need to be specified. The dc pole p_1^{ol}, the two resonant poles of the LCL filter p_2^{ol} and p_3^{ol}, and the pole of the disturbance model p_5^{ol}, see Figure 137b, are moved to a higher frequency f_{bw} [see p_1^{cl}, p_2^{cl}, p_3^{cl}, and p_5^{cl} in Figure 137c]. The open-loop computational delay pole p_4^{ol} is maintained at the origin of the z plane [see p_4^{cl} in Figure 137c]. Table 16 summarizes the proposed closed-loop pole locations. The previously described pole-placement strategy results in the NTF shown in Figure 137a, which similarly to the L-fiter case, achieves a high attenuation of the switching noise at all frequencies.

7.3.   Avoiding Grid Resonances

Effective integration of power converters into the utility grid is becoming more difficult to achieve as a result of increasing switching frequencies and more complex grid topologies [37]. Ineffective filtering can lead to excessive voltage noise at the point of common coupling (PCC). For example, the combination of a grid inductance and a capacitive load significantly changes the grid impedance seen at the PCC, compared to that of an ideal voltage source. An impedance spike at the PCC can be caused by a parallel resonant net-

Table 16. Compensator Design for LCL Filtered Converters

Poles	Position in the z-plane	
	Open-loop	**Closed-loop**
Plant model $G_{\text{plant}}^{\text{LCL}}$	DC pole is moved to a high frequency f_{bw}.	
	$p_1^{ol} = 1$	$p_1^{cl} = \exp[2\pi f_{\text{bw}} \, T_s]$
	Resonant poles are moved to a higher and more damped frequency.	
	$p_{2,3}^{ol} = \exp[\pm j \, 2\pi f_{\text{res}} \, T_s]$	$p_{2,3}^{cl} = \exp[2\pi f_{\text{bw}} \, T_s]$
	Computational delay pole is not moved.	
	$p_4^{ol} = 0$	$p_4^{cl} = 0$
Disturb. model	Disturbance pole is moved to a high freq. f_{bw}.	
	$p_5^{ol} = \exp[j \, 2\pi f_g \, T_s]$	$p_5^{cl} = \exp[2\pi f_{\text{bw}} \, T_s]$

work [140], as illustrated in Figure 138. If some switching harmonics from a PWM appear at or near the frequency of these spikes, then the resonance is excited and the voltage noise at the PCC dramatically increases causing a grid voltage quality problem.

7.3.1. Analysis of the Switching-Noise and Switching Frequency

In the strict sense, the presented controller does not generate any switching or low-order harmonics thanks to the proposed NTF design in combination with the FCS operation. In order to explain this point, the spectrum of the switching noise generated by the proposed FCS linear current controller is analyzed and compared to that of a linear current controller with a PWM. The presented analysis is performed in the $\alpha\beta$ frame instead of the abc frame (where all symmetrical components are present) in order to simplify the study. No loss of generality occurs by omitting the homopolar (or zero-sequence) component because the impedance of a three-phase three-wire system in the homopolar component is infinite.

Figure 139 shows the spectrum of the controller output voltage v (a discrete-time signal) and of the voltage source converters (VSCs) output voltage v_{VSC} (a continuous-time signal) when a PWM with regular sampling and a 2-level voltage source converters (VSCs) is employed. As shown, the spectrum of v does not contain information about the switching noise. Therefore, the digital controller cannot compensate for the effect of the switching noise in the grid current. Nonetheless, the voltage source converters (VSCs) output voltage v_{VSC}, which is approximately equal to v_{PWM} when the ESR of the converter is small, shows large amplitude switching harmonics concentrated close to multiples of the switching frequency. The amplitude of such harmonics also depends on the particular waveform being generated, e.g., the switching harmonics change their amplitude if the PWM modulation index is reduced or low-order harmonics are added so as to compensate the grid-voltage distortion [141]. This is an undesirable effect because it changes the performance of the voltage source converters (VSCs) (the amount of current ripple generated) depending on the particular operating conditions.

Contrarily to a design that employs a PWM, the presented solution spreads the switch-
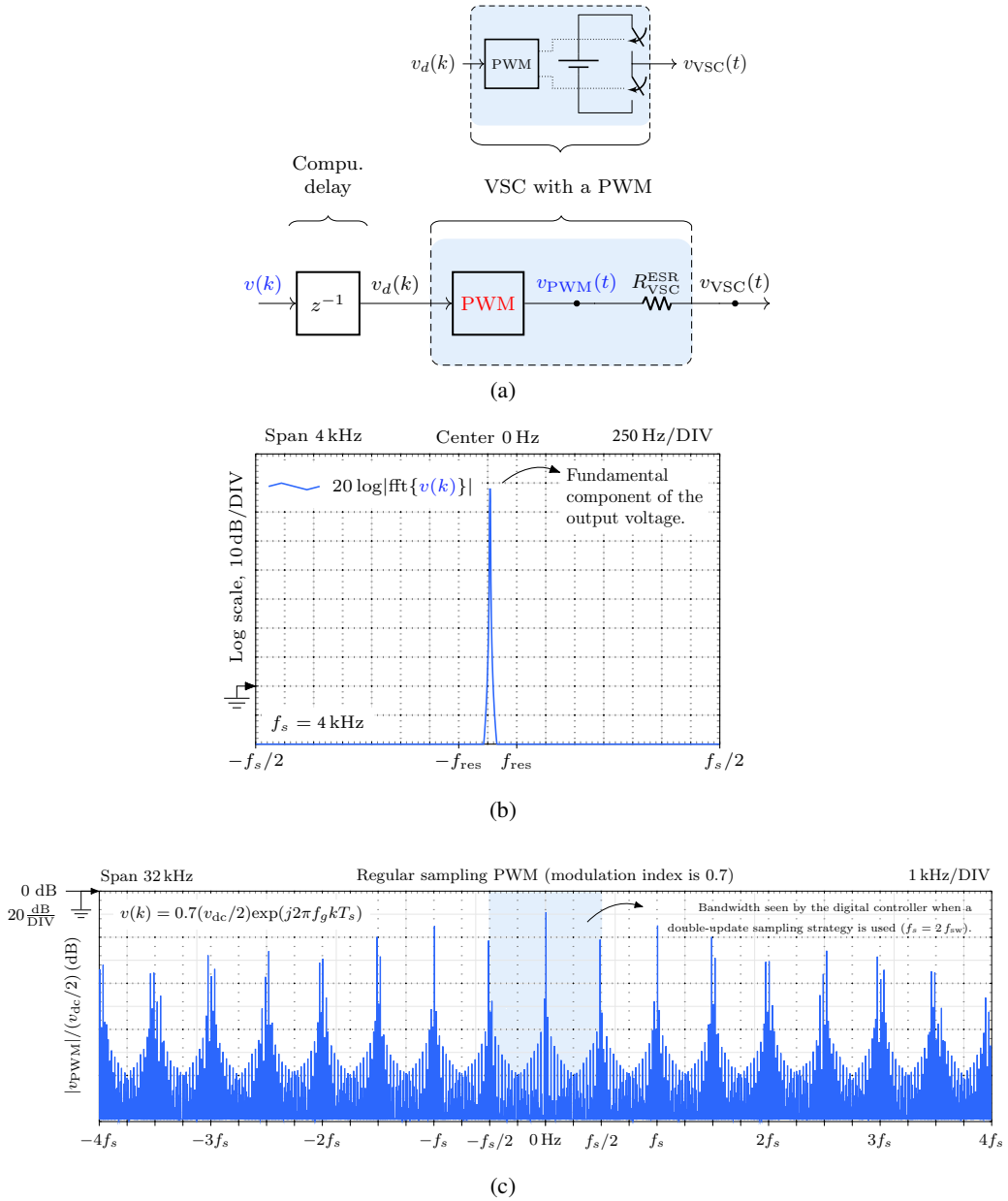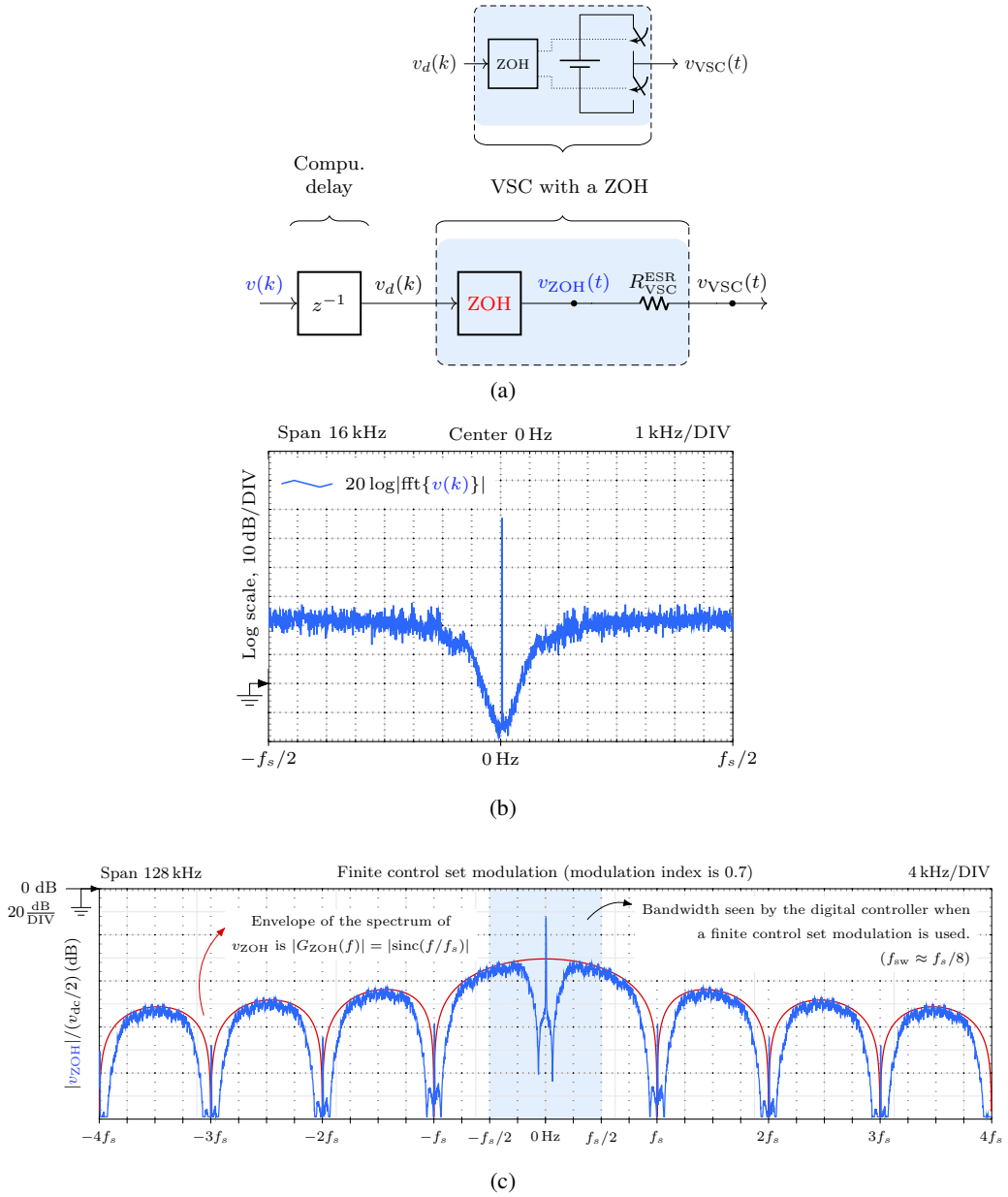
(a)

(b)

(c)

Figure 139. A voltage source converters (VSCs) commanded by a PWM with regular sampling. a Block diagram model. b Spectrum of the discrete-time controller output voltage $v(k)$. c Spectrum of the continuous-time voltage source converters (VSCs) output voltage $v_{\mathrm{PWM}}(t)$.

ing noise across wide frequency regions, instead of concentrating it at certain frequencies. In electrical terms this means that the power spectral density of the converter output voltage is very low. This reduces the risk of the grid-tied inverter exciting any potential resonances in the power system. Figure 140 shows the spectrum of the discrete-time controller voltage

(a)

(b)

(c)

Figure 140. A voltage source converters (VSCs) commanded by a FCS current controller. a Block diagram model. b Spectrum of the discrete-time controller output voltage $v(k)$. c Spectrum of the continuous-time voltage source converters (VSCs) output voltage $v_{\text{ZOH}}(t)$.

reference $v(k)$ and of the continuous-time voltage source converters (VSCs) output voltage $v_{\text{ZOH}}(t)$ during closed-loop operation. As shown, the proposed discrete-time FCS current controller generates a voltage v that contains complete information about the switching noise that is present in the continuous-time voltage waveform v_{VSC}. The reason is that the element that performs the conversion from discrete-time to continuous time, which is

a ZOH block, does not introduce new harmonics. The ZOH only repeats the discrete-time spectrum at multiples of the sampling frequency and multiplies it by the frequency response of a ZOH G_{zoh}, which is a sinc function. This enables, for example, the implementation of novel grid-impedance identification techniques that do not require to inject additional current components into the grid [142].

The switching frequency is chosen indirectly by selecting a sampling frequency. The proposed FCS controller has a lower ratio of switching to sampling frequency, compared to a PWM-based solutions with a single or a double update sampling strategies. This can be easily understood by observing Figure 141. Figure 141a shows the simulated grid current in the abc frame $i_{1,abc}$ and in the dq frame $i_{1,dq}$ during a 10-A reference step $i_{1,dq}^*$ in the d axis of the +dq frame, and Figure 141b displays the previous transient event in greater detail. Figure 141b also shows the firing signals s_{abc}, which permit to assess the switching frequency of the voltage source converters (VSCs), and the controller sampling instants, which are denoted by points in the current waveforms. As shown, the firing signals only commutate once every sampling period at most; but, on average, they commutate at a lower frequency because there are many sampling periods that do not generate commutations.

7.4.   Experimental Results

The experimental results are carried out in a 5-kW voltage source converters (VSCs) working as an inverter with a 700-V dc bus v_{dc} and connected to a 400-V line-to-line 50-Hz three-phase grid. In addition to the actual grid, a three-phase grid emulator is employed to simulate adverse grid conditions such as a type-C sag, an interruption, and a highly distorted grid voltage. Table 17 details the grid voltage distortion. The controller is executed in a MicroAutoBox from the manufacturer dSPACE. An unmodeled resonance in the grid is created by introducing a grid inductance of value L_g and a capacitive load of value C_{load}, which create a resonance at a frequency of $7.9\,\text{kHz}$.

In order to assess and compare the performance of the proposal to a commonly adopted solution, a high-performance PWM-based controller that consist of a synchronous PI controller with axis decoupling, a grid voltage feedforward compensation, a double-update sampling scheme, and a space vector modulation is selected. The comparison is carried out using both L and LCL filters. A common switching frequency has been established for both solutions. In all tests the switching frequency is $2\,\text{kHz}$, unless stated otherwise. Since the proposal presents a low switching to sampling frequency ratio thanks to the FCS operation [22, 23], the sampling frequency of the proposal must be higher than that of the PWM based design. The proposed FCS controller is executed with a sampling frequency of $16\,\text{kHz}$, which yields the desired switching frequency of $2\,\text{kHz}$. It should be noted that a small variation of approximately $200\,\text{Hz}$ is observed when changing the point of operation of the inverter from rated power to a no load condition. The filter impedance values are indicated in Table 18. These filter parameter values and the selected switching frequency value are commonly employed in multimegawatt low-voltage applications with two-level VSCs [143, 144, 145, 146]. With a $2\,\text{kHz}$ switching frequency, some of the PWM switching harmonics are below the 50th harmonic; therefore, they have to meet stringent grid codes, such as IEC [147], IEEE [110], and VDEW [148]. This configuration represents a worst case condition in terms of current distortion compliance; however, the obtained results can
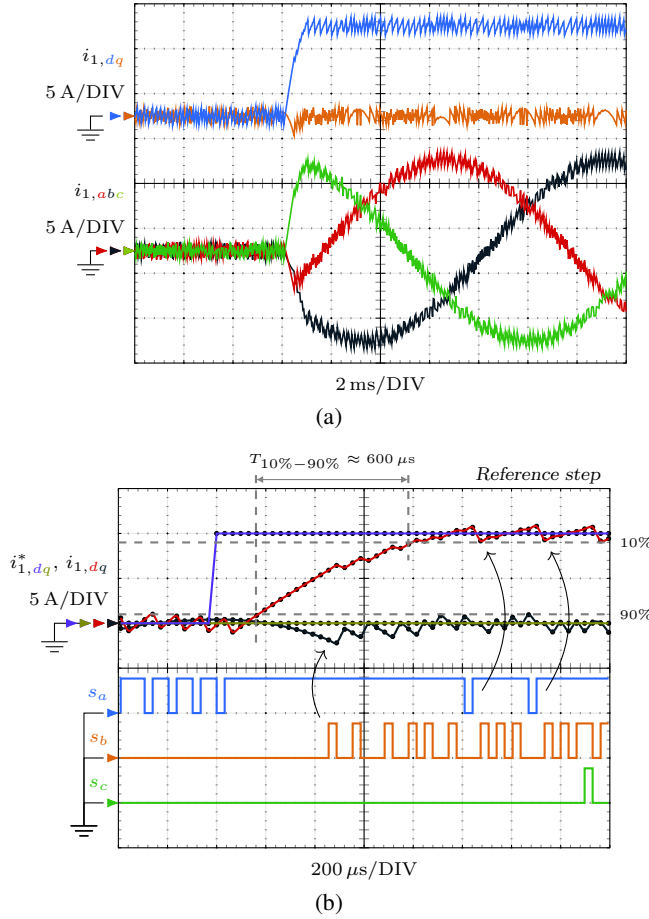
Figure 141. Simulation waveforms during a 10-A reference step in the d axis of the +dq frame when an L filter is employed. a Grid current in the dq frame $i_{1,\mathrm{dq}}$ and in the abc frame $i_{1,\mathrm{abc}}$. a Detail of the reference step event that shows the firing signals s_{abc}, the measured grid current in the dq frame $i_{1,\mathrm{dq}}$, and grid current reference $i_{1,\mathrm{dq}}^{*}$.

be also applied to other configurations in which a higher switching frequency and lower p.u. filter values are employed. Table 18 details the values of the setup parameters and Figure 142 shows a diagram and a photo of the setup.

　　The experimental comparison is organized into three parts. First, a frequency-domain study measures the switching distortion of the proposal and compares it to that of a PWM-based controller and to the limits defined in IEC [147], IEEE [110], and VDEW [148]. Next, a time-domain study analyzes the dynamic response of the proposal to a reference step and to disturbances, including low-order grid harmonics, a voltage sag, and an interruption in the grid voltage. Finally, the last test assesses the operation of the proposal when the grid contains an unmodeled resonance and compares it to that of PWM-based controller.
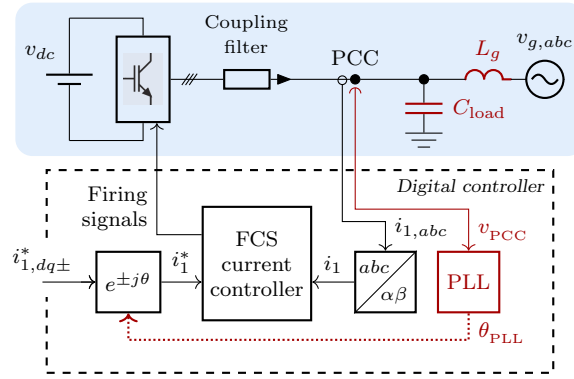
(a)
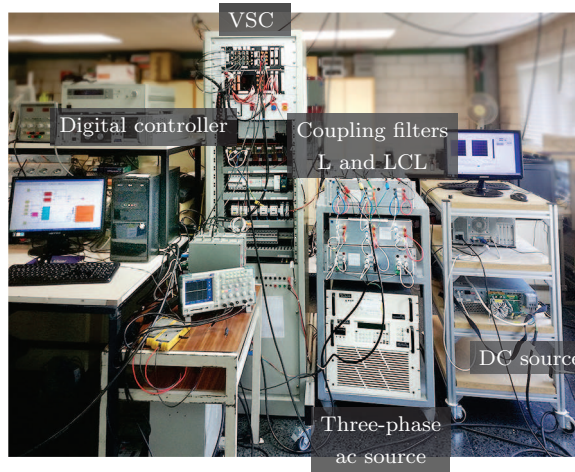
(b)

Figure 142. Experimental setup. a Diagram. b Photograph.

7.4.1.   Frequency Distortion Comparison

The switching distortion created by a PWM-controlled voltage source converters (VSCs) is different from the switching distortion generated during FCS operation. This yields different types of distortion in the grid current. The proposal generates a current noise density, which should be integrated over a certain bandwidth, usually denoted as noise bandwidth (NBW), in order to obtain a value for the noise amplitude, as shown in Figure 143a, whereas PWM-based controllers produce switching noise harmonics, cf. 143b. A small value of noise bandwidth (NBW) provides a high spectral resolution, which permits to accurately locate any frequency component in the spectrum. In order to perform a meaningful comparison between a narrow band signal (PWM harmonics) and a spread-spectrum signal (FCS switching noise), the switching distortion of the converter is measured according to [149]. This standard groups (or integrates) the switching noise measured over 50-Hz frequency bands in order to provide harmonic amplitudes that are equivalent to the measured noise, irrespectively of the nature of the current distortion.
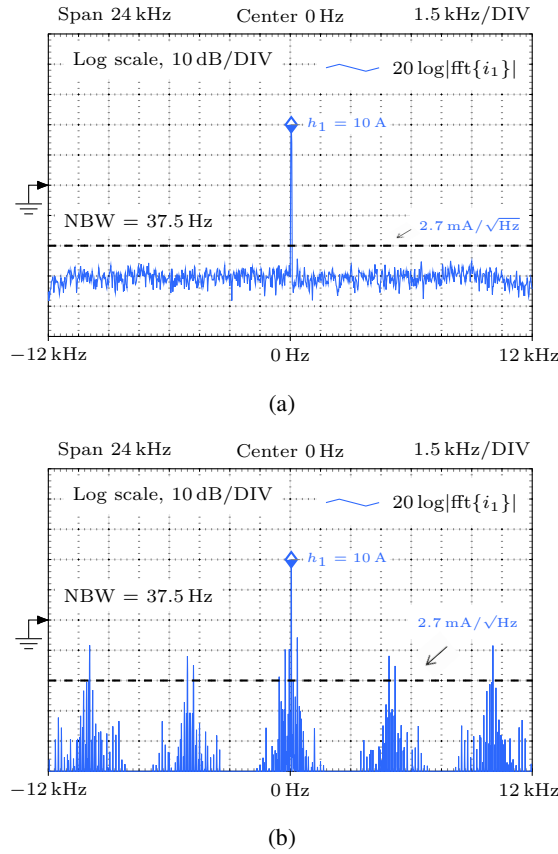
Figure 143. Current distortion measured by a spectrum analyzer with a noise bandwidth (NBW) of 37.5 Hz. a Proposal. b PWM-based controller.

Figure 144 shows the grid current distortion during PWM and FCS operation measured according to [149] and compares it to the grid-current harmonic limits defined in IEC [147], IEEE [110], and VDEW [148]. These standards define different limits for odd and even harmonics. The even harmonic limits are denoted in red and the odd harmonic limits are displayed in blue. Both L and LCL filter cases are considered for comparison.

On the one hand, when an L filter is employed, the proposal is able to meet the harmonic limits established in IEC [147] whereas the PWM-based solution in the same conditions does not meet such limits, in spite of also having a low grid current THD. The reason is that the PWM-based controller concentrates a large part of the switching distortion in the harmonics that are located around the 40th harmonic, failing compliance with the IEC [147] at such frequencies. Conversely, the proposal spread the switching distortion evenly, which enables compliance at all frequencies.

On the other hand, if an LCL filter is installed, both the PWM-based design and the proposal are able to meet the harmonic limits established in IEC [147]. The LCL filter significantly attenuates the harmonic distortion above its resonant frequency ($f_{res}^{LCL} = 790$ Hz) compared to the L filter case. This higher attenuation improves compliance with more stringent standards, such as the IEEE [110] or the German standard VDEW [148]. How-

Table 17. Grid Voltage Parameters

Order	Sequence*	Magnitude
1	+	230 V
3	0	5 %
5	−	6 %
7	+	5 %
9	0	1.5 %
11	−	3.5 %
13	+	3 %
THD		10.5 %

* When the sag occurs, the harmonic voltages are unbalanced (all sequences are present for each harmonic).

ever the PWM-based design still does not comply with the VDEW standard [148] at the 35th, 37th, and 41th harmonics. Similarly, the proposal exceeds the even harmonic limits in the frequency region located between the 10th and 28th harmonics.

It should be noticed that these standards impose very low limits for the even harmonics compared to the odd harmonic. When using a PWM-based controller, such low limits for even harmonics can be met, while still having a high current distortion, by selecting a value for the switching frequency that is an odd multiple of the fundamental frequency. But with a FCS operation, the current distortion should be low at both even and odd harmonics in order to achieve full compliance [150].

When an LCL filter is used, a PWM-based design provides a lower THD than the proposal. Nonetheless, compared to the PWM-based design, the proposed controller does not generate switching harmonics, as explained in Section 7.3. This reduces the risk of exciting any unmodeled resonances that may appear in the grid and is particularly convenient when the converter operates connected to a weak grid with a complex topology, in which resonances may occur at unknown or variable frequencies, depending on the state of the grid.

In order to compare the performance of the proposal to that of a FCS-MPC, the design presented in [26] was selected due to its popularity and simple implementation. Such solution [26] requires a lower computational load compared to more advanced FCS-model predictive controllers (MPCs) published in the literature, which contain complex optimization algorithms. Figure 145 shows the measured grid current distortion of a grid-tied inverter with a FCS-MPC [26] in comparison to the current harmonic limits defined in IEC [147], IEEE [110], and VDEW [148] for two values of the grid voltage v_g, namely, $v_g = 115$V and $v_g = 230$V. The same setup parameters used to test the proposal are also used in the FCS-MPC implementation. Similarly to the proposal [cf. Figure 144a], a FCS-MPC generates a more uniform distribution of the switching noise, compared to a

Table 18. Experimental Setup Parameters

Base values			
Nominal power	P_o	5	$[\text{kW}]$
Grid voltage	v_g	230	$[\text{V}_{\text{phase}}^{\text{RMS}}]$
Grid frequency	f_g	50	$[\text{Hz}]$
LCL filter (designed according to [83])			
Converter-side inductance	L_2	0.16	$[\text{p.u.}]$
Grid-side inductance	L_1	0.16	$[\text{p.u.}]$
Filter capacitance	C_f	0.05	$[\text{p.u.}]$
Filter resonance	f_{res}	790	$[\text{Hz}]$
L filter (same inductance as LCL filter)			
Filter inductance	L_f	0.32	$[\text{p.u.}]$
Grid resonance			
Grid inductance	L_g	0.003	$[\text{p.u.}]$
Capacitive load	C_{load}	0.05	$[\text{p.u.}]$
Grid resonance	$f_{\text{res}}^{\text{grid}}$	7.9	$[\text{kHz}]$
VSC			
Sampling freq. (FCS)		16	$[\text{kHz}]$
Sampling freq. (PWM)		4	$[\text{kHz}]$
Switching freq.		2	$[\text{kHz}]$
DC bus voltage	v_{dc}	700	$[\text{V}_{\text{DC}}]$

PWM-based controller [cf. Figure 144b]. However, the FCS-MPC results in a higher THD compared to the proposal in the same conditions and it does not meet IEC [147] harmonic limits, cf. Figure 145b and Figure 144a. If the grid voltage is reduced to a value of 115 V, see Figure 145a, the FCS-MPC meets IEC [147] harmonic limits by a close margin, which indicates that the performance of the MPC controller improves as the modulation index of the converter decreases. A detailed study of the current error and the switching frequency of the proposal for different modulation indexes in comparison to the FCS-MPC is presented in Section 7.4.4.

In summary, the obtained results show that the proposal provides a greater advantage when an L filter is employed, whereas the PWM-based controller performs better, in terms of current harmonic distortion, when an LCL filter is used.
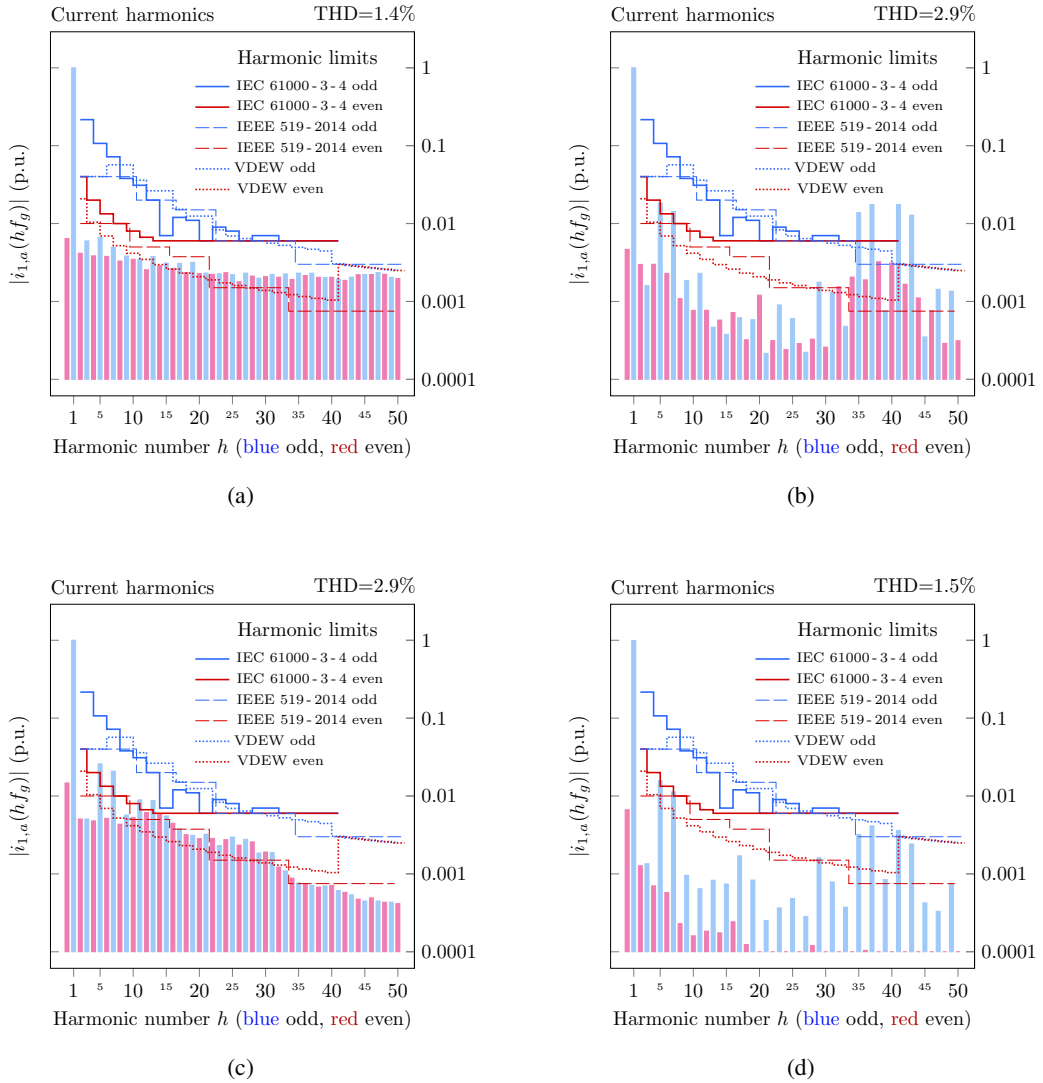
Figure 144. Measured grid current distortion in comparison to the grid current harmonic limits defined in IEC [147], IEEE [110], and VDEW [148]. a FCS operation with L filter. b PWM operation with L filter. c FCS operation with LCL filter. d PWM operation with LCL filter.

7.4.2. Transient Response Comparison

The proposal offers fast transient dynamics, similarly to an MPC, as expected from its FCS operation. In the following the dynamic response of the proposal is assessed and compared to that of a PWM-based controller. An L filter is employed to connect the inverter to the grid in all following tests.

Figure 146 shows the reference-tracking response to a reference step that is commanded in the q axis of a dq frame which tracks the positive sequence of the grid voltage. Fig-
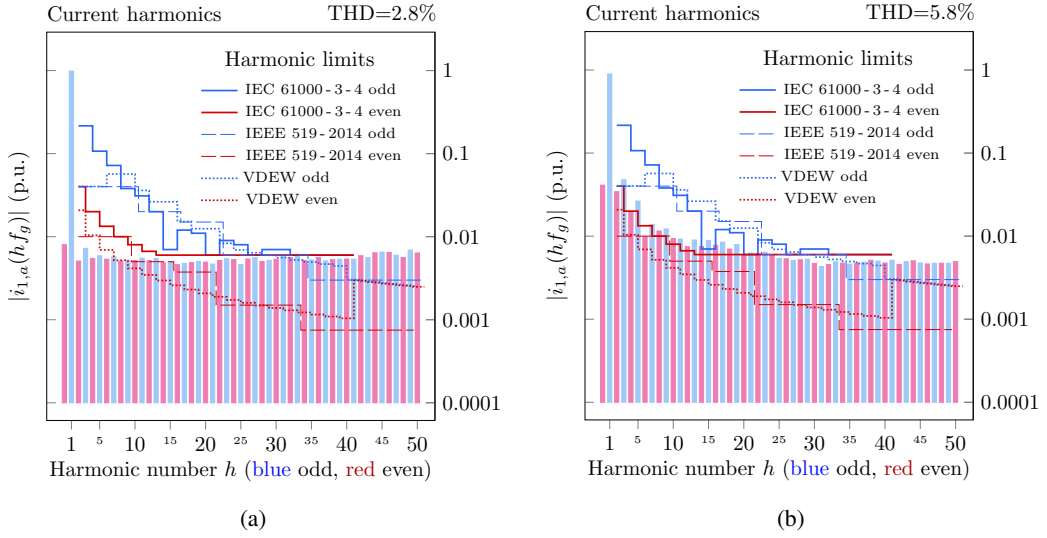
Figure 145. Measured grid current distortion of a FCS-MPC [26] with L filter in comparison to the grid current harmonic limits defined in IEC [147], IEEE [110], and VDEW [148]. a $v_g = 115\text{V}$. b $v_g = 230\text{V}$.

ure 146a corresponds to the proposed controller and Figure 146b to the PWM-based controller. The proposal achieves a fast rise time $(T_{10\%-90\%} \approx 1ms)$ while a low average switching frequency is required $(f_{\text{sw}} \approx 2\,\text{kHz})$ due to the FCS operation. The PWM-based controller offers a slower response, as expected from the exponential convergence of the PI controller. Both controllers achieve a damped response with no axis cross-coupling. It should be noted that the proposal appears to have noisier grid-current waveforms $i_{1,\text{dq}}$ compared to the PWM-based controller. This is a result of the fact that, during FCS operation, the switching ripple in the grid current is measured and observed by the digital controller; however, when a PWM is employed with a double-update sampling scheme, the switching ripple in the grid current is not present in the measurements taken by the controller due to the synchronous sampling scheme. This point is explained in detail in Section 7.2.

Figure 147 shows the disturbance-rejection response to a 40%-depth type-C sag and a highly distorted grid voltage. The type-C sag introduces a large unbalance in the grid voltage, i.e., a negative sequence component at the fundamental grid frequency. The grid-current reference i_1^* is set to zero in order to clearly see the grid current error, $i_1^* - i_1 = -i_1$. Figure 147a corresponds to the proposed controller and Figure 147b to the PWM-based controller. Due to the large bandwidth of the proposal, the low-order grid voltage harmonics and the fundamental component unbalance are effectively rejected. The PWM-based controller does not achieve such high rejection and a higher grid current distortion appears, specially during the sag fault.

A large disturbance rejection bandwidth also permits to minimize the overcurrent transient that occurs due to a sudden interruption in the grid voltage. Figure 148 shows the response of both controllers to an interruption in the grid voltage. As shown, the proposal tightly controls the grid current, even when the interruption occurs, in spite of not using
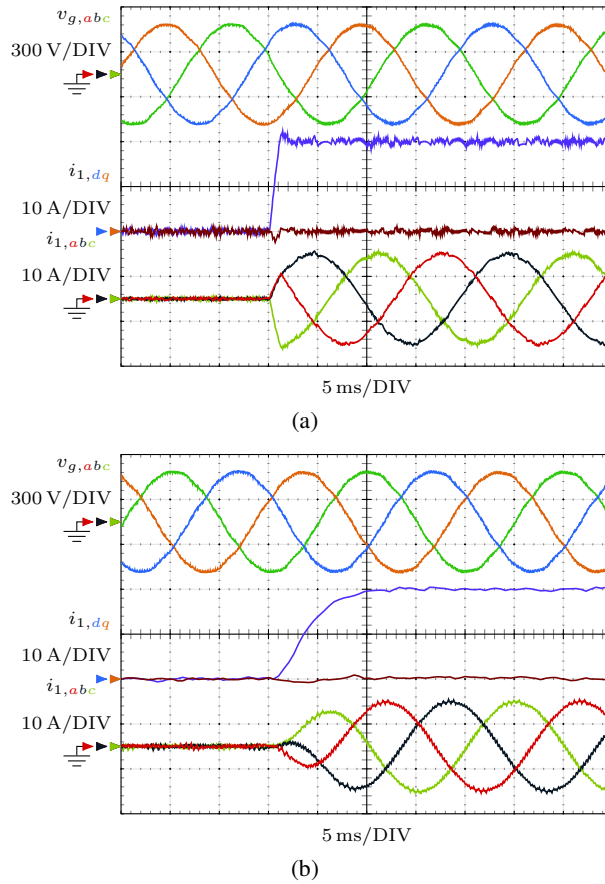
Figure 146. Experimental waveforms during a 10-A reference step in the q axis of the +dq frame when an L filter is employed to connect the inverter to the grid. Measured grid current in the dq frame $i_{1,\mathrm{dq}}$, in the abc frame $i_{1,\mathrm{abc}}$, and measured grid voltage v_g. a FCS-based controller. b PWM-based controller.

a feedforward of the grid voltage to improve the disturbance rejection. The PWM-based controller yields a 0.4 p.u. current transient and a larger overcurrent would occur if the grid voltage feedforward were disabled.

In summary, the proposal achieves a faster reference-tracking and disturbance rejection responses than a PWM-based controller operating at the same switching frequency.

7.4.3.   Operation in a Grid with an Unmodeled Resonance

This last test shows the response of the proposal and of the PWM-based controller when the grid contains an unmodeled resonance. The grid resonance is formed by a grid inductance L_g and a capacitive load C_{load}, as shown in Figure 142. Such plant model change modifies the location of the closed-loop poles of the system with respect to their nominal locations. However, the performance of the proposal is not significantly affected because linear state-space controllers offer a high robustness to plant parameter variations [126]. The resultant

40%-depth type-C sag

$v_{g,abc}$
250 V/DIV

$i_{1,abc}$
3 A/DIV
$i_1^* = 0\,\mathrm{A}$

5 ms/DIV

(a)

40%-depth type-C sag

$v_{g,abc}$
250 V/DIV

$i_{1,abc}$
3 A/DIV
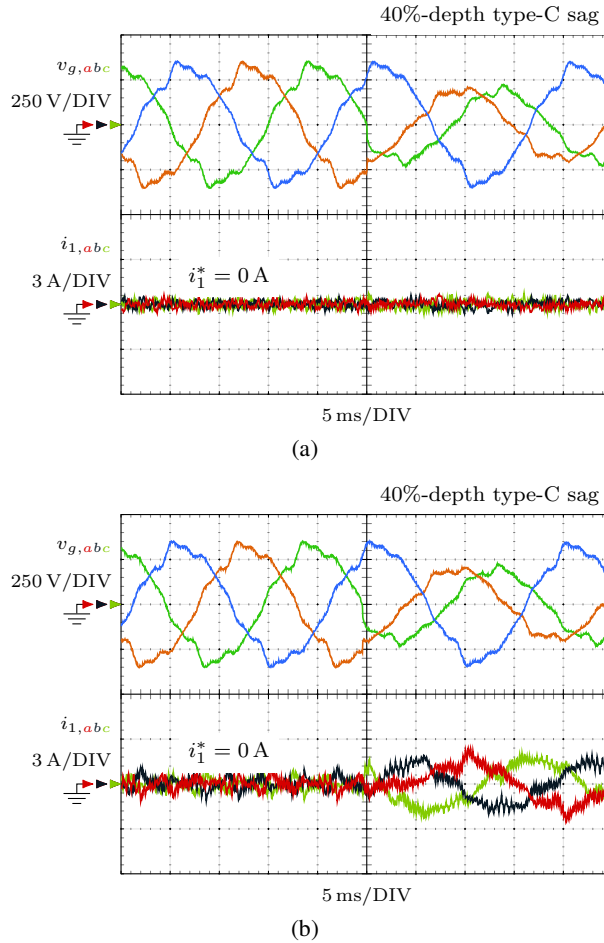$i_1^* = 0\,\mathrm{A}$

5 ms/DIV

(b)

Figure 147. Experimental waveforms during a 40%-depth type-C sag. An L filter is employed to connect the inverter to the grid and the grid current reference i_1^* is set to zero. Measured grid current in the dq frame $i_{1,\mathrm{dq}}$, in the abc frame $i_{1,\mathrm{abc}}$, and measured grid voltage v_g. a FCS-based controller (no grid voltage feedforward). b PWM-based controller (with grid voltage feedforward).

resonance is located at a frequency of 7.9 kHz. At such frequency, both designs produce a large voltage distortion at the output of the voltage source converters (VSCs). In particular, the proposal generates a high switching noise density, cf. Figure 140c, and the PWM-based design generates some switching harmonics, cf. Figure 139c. In order to avoid equipment damage when the grid resonance is excited, the amplitude of the switching distortion produced by the voltage source converters (VSCs) is lowered an order of magnitude by reducing its dc bus voltage to 70V and setting the amplitude of the grid voltage to zero. In this manner, the voltage measured at the PCC directly corresponds to the noise distortion caused by the voltage source converters (VSCs).

Figure 149 shows the measured voltage at the PCC $v_{\mathrm{PCC},abc}$ when the grid-tied inverter is coupled to the grid using an L filter and the grid-current reference i_1^* is set to two amps.
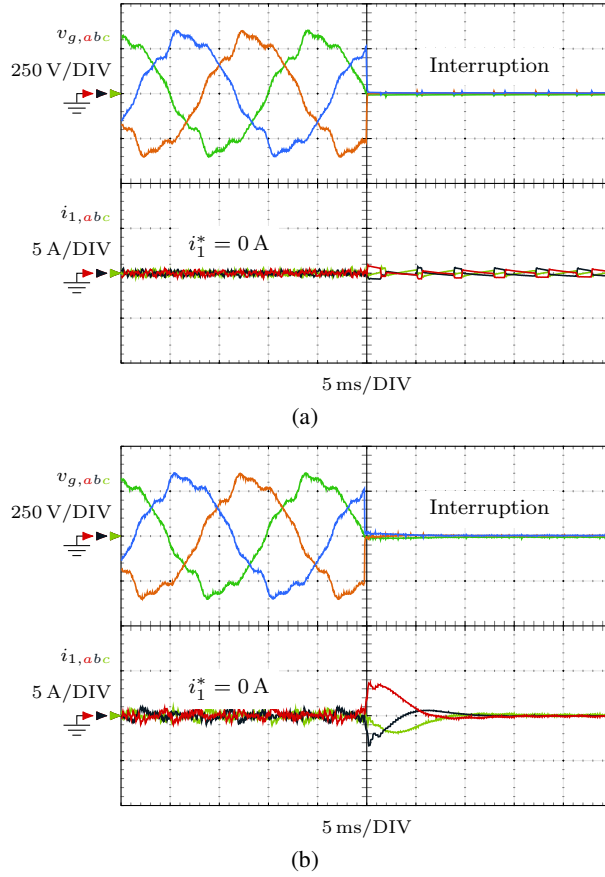
Figure 148. Experimental waveforms during an interruption in the grid voltage. An L filter is employed to connect the inverter to the grid and the grid current reference i_1^* is set to zero. Measured grid current in the dq frame $i_{1,dq}$, in the abc frame $i_{1,abc}$, and measured grid voltage v_g. a FCS-based controller (no grid voltage feedforward). b PWM-based controller (with grid voltage feedforward).

As shown, the proposal [Figure 149a] results in a much lower voltage distortion compared to the PWM-based controller [Figure 149b] in the same conditions. The PWM-based controller excites the grid resonance when some of its switching harmonics are close to the resonant frequency, as explained in Section 7.3, whereas the proposal excites the resonance less because it produces a low switching noise density instead of switching harmonics. The resonance is not manifested in the controlled grid current i_1 because the coupling filter is not part of the resonant path formed by the grid impedance and the capacitive load, cf. Figure 138. Such characteristic of the proposal facilitates the operation of a grid-tied inverter during weak grid conditions.
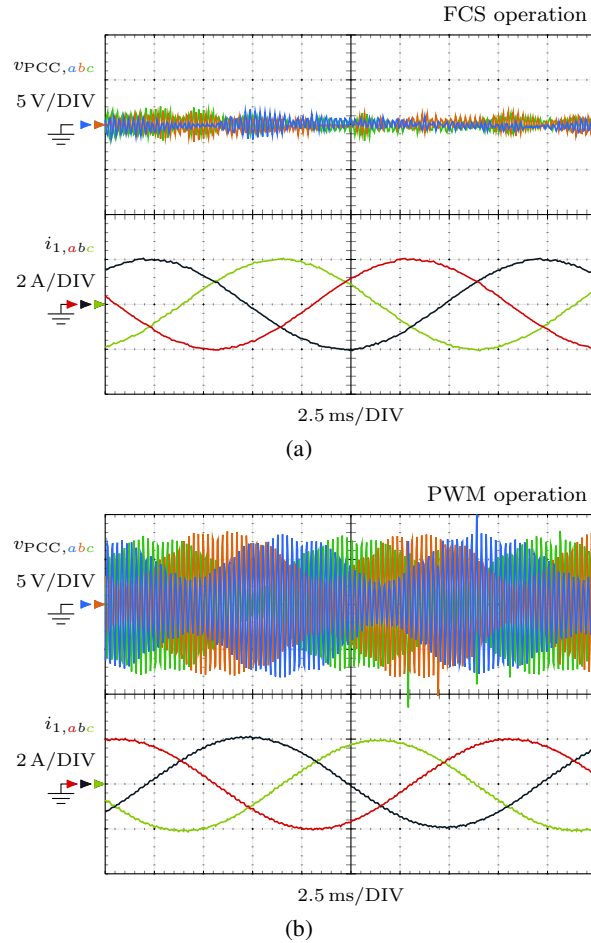
Figure 149. Voltage distortion at the PCC $v_{\text{PCC},abc}$ and inverter output current i_1 when the grid contains an unmodeled resonance. a FCS-based controller. b PWM-based controller.
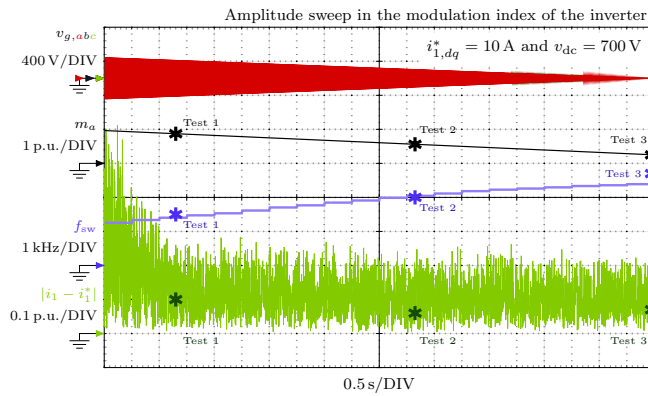
7.4.4. Switching Frequency and Current Error as a Function of the Modulation Index

The switching frequency depends on the modulation index of the converter. Such characteristic is also shared with other FCS controllers [22]. In a grid-tied inverter, the modulation index typically experiences small variations compared to other applications of power converters, such as motor drives [22, 23].

Figure 150 shows the switching frequency f_{sw} and the current error $|i_1 - i_1^*|$ of the proposed controller for a large variation in the modulation index m_a of the power converter and compares the results to that of a FCS-MPC [26]. In order to produce a large change in the modulation index of the power converter, the grid voltage amplitude v_g is slowly swept from a value 15% greater than nominal to zero, while the dc bus voltage and the grid current reference are maintained constant ($v_{\text{dc}} = 700$V and $i_{1,dq}^* = 10$A). Since the grid voltage amplitude is slowly reduced over a long period of time (10 s) compared to the fast dynamics of the current controller, the obtained results provide a close approximation to the
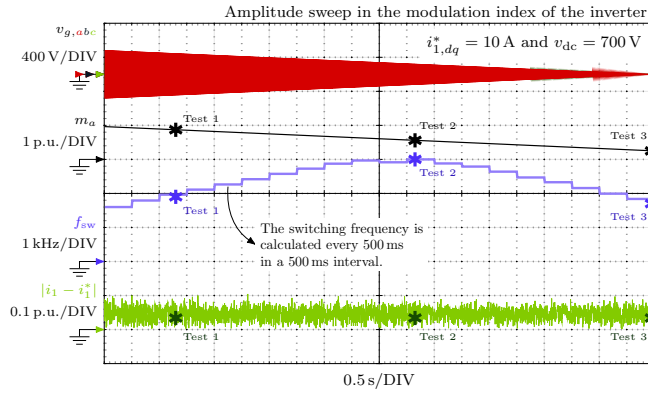
Figure 150. Switching frequency f_{sw}, magnitude of the current error $|i_1 - i_1^*|$, and modulation index m_a of the power converter for an amplitude sweep in the grid voltage $v_{g,abc}$. a Proposed controller. b An FCS-MPC controller [26].

performance during steady-state for different values of m_a.

The results show that the switching frequency is minimum ($1.7\,\text{kHz}$) at high and low modulation index levels. Specifically, the switching frequency is minimized when the space vector orbits close to the voltage source converters (VSCs) output voltage vectors. At intermediate modulation index levels, the switching frequency increases to a maximum value of $3\,\text{kHz}$. The FCS-MPC [26] manifest a different behavior. The switching frequency monotonically increases from a value of $1.3\,\text{kHz}$ to a value of $2.4\,\text{kHz}$ when the modulation index is reduced.

Both the proposal and the FCS-MPC [26] maintain a constant current error when the modulation index is reduced. However, the FCS-MPC [26] significantly degrades its performance for high values of m_a. Moreover, the proposal result in a lower current error than the FCS-MPC [26] in the same conditions.

In order to experimentally verify the simulation results previously presented, the proposed controller and the FCS-MPC [26] have been tested at three different operating points,
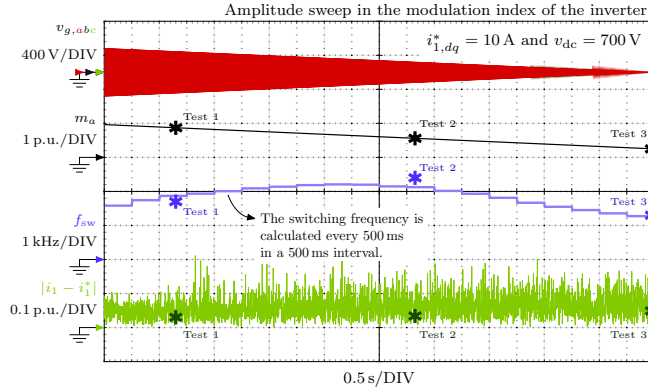
Figure 151. Switching frequency f_{sw}, magnitude of the current error $|i_1 - i_1^*|$, and modulation index m_a of the power converter for an amplitude sweep in the grid voltage $v_{g,abc}$ and consecutive-region mode of operation of the controller.

namely, at a high, an intermediate, and a low modulation index level. The first test (Test 1) corresponds to a normal operation of a grid-tied inverter with rated grid voltage ($m_a = 0.87 p.u.$). The second test (Test 2) corresponds to an operation with an intermediate modulation index ($m_a = 0.56 p.u.$), which is obtained when the grid voltage is reduced to a value of 115V. The third test (Test 3) corresponds to an operation with a low modulation index ($m_a = 0.25 p.u.$), which is caused by an interruption in the grid voltage ($v_g = 0$V). In all these tests, the current reference is set to a value of 10A. The obtained switching frequency and current error are denoted by asterisk marks in Figure 150. Since the current error during steady-state operation is an stochastic process, the indicated current error value represented by the asterisk corresponds to the mean value of the current error $|i_1 - i_1^*|$ during steady-state operation for each operating point.

As shown, the measured switching frequency closely matches the simulation results. The largest difference is observed during Test 1 and Test 3 with the FCS-MPC. In such tests, the measured experimental frequencies are slightly larger (1.5 kHz and 2.7 kHz) than the theoretical values (1.4 kHz and 2.4 kHz). It should be noted that the current error does not follow a uniform distribution; therefore, the mean value of the current error is not located exactly between the maximum and the minimum simulated current error values. As expected from the simulation, the FCS-MPC increases the mean current error from a value of 0.6 p.u. to a value of 0.9 p.u. for large values of m_a.

7.4.5. Consecutive-Region Mode of Operation

The quantizer does not force a newly selected Voronoi region to be consecutive to the previously selected one. However, such feature can be incorporated to the proposal by further restricting the set where the quantizer operates, cf. (131). During the development of the proposal, the indicated modification was considered and evaluated. In the following, we refer to this mode of operation as consecutive-region mode. In the such mode, the converter never commutates more than one branch every sampling period.

Figure 151 shows the switching frequency f_sw, the magnitude of the current error $|i_1 - i_1^*|$, and the modulation index m_a of the power converter for an amplitude sweep in the grid voltage $v_{g,abc}$ when the proposed controller is modified to operate in a consecutive-region mode. Since the grid voltage amplitude is slowly reduced over a long period of time (10 s) compared to the fast dynamics of the current controller, the obtained results provide a close approximation to the performance during steady-state for different values of m_a.

The obtained results show a reduction in the switching frequency and an increase in the current noise, compared to the normal operation of the proposed controller, cf. Figure 150a. The switching frequency is significantly reduced for intermediate and low modulation index values. The minimum switching frequency with consecutive-region mode of operation is 1.3 kHz and the maximum switching frequency is 2.5 kHz. Such values correspond to a 24% and a 17% reduction of the switching frequency, compared to the normal mode of operation.

In order to experimentally verify this simulation results, the modified controller with a consecutive-region mode of operation has been experimentally tested at three different operating points, namely, at a high, an intermediate, and a low modulation index level. The first test (Test 1) corresponds to a normal operation of a grid-tied inverter with rated grid voltage ($m_a = 0.87 p.u.$). The second test (Test 2) corresponds to an operation with an intermediate modulation index ($m_a = 0.56 p.u.$), which is obtained when the grid voltage is reduced to a value of 115 V. The third test (Test 3) corresponds to an operation with a low modulation index ($m_a = 0.25 p.u.$), which is caused by an interruption in the grid voltage ($v_g = 0$V). In all these tests, the current reference is set to a value of 10 A. The obtained switching frequency and current error are denoted by asterisk marks in Figure 151. Since the current error during steady-state operation is an stochastic process, the indicated current error value represented by the asterisk corresponds to the mean value of the current error $|i_1 - i_1^*|$ during steady-state operation for each operating point.

As shown, the measured switching frequency closely matches the simulation results. The largest difference is observed during Test 1 and Test 2. In such tests, the measured experimental frequencies are slightly lower (1.7 kHz) and larger (2.4 kHz) than the theoretical values (1.9 kHz and 2.1 kHz). It should be noted that the current error does not follow a uniform distribution; therefore, the mean value of the current error is not located exactly between the maximum and the minimum simulated current error values. As expected from the simulation, the mean current error slightly increases from a value of 0.03 p.u. (Test 1) to a value of 0.04 p.u. (Test 3) as the value of m_a decreases.

7.5.   Calculation of the Plant Model Matrices

This Section details the calculation process to obtain the plant model matrices that define the state-space models (125) and (127). The calculation process consists of three steps. The first step defines a continuous-time model that relates the grid current $i_1(t)$ to the voltage source converters (VSCs) output voltage $v_\text{VSC}(t)$. Next, such model is discretized using a ZOH equivalent in order to account for the FCS operation of the voltage source converters (VSCs) and the sampling process carried out by the digital controller. Finally, a one-sample delay is added to the model so as to describe the effect of the computational delay.

For the L filter case, the continuous-time plant model is

$$\frac{d\,i_1(t)}{dt} \;=\; \frac{1}{L_{\mathrm{f}}}v_{\mathrm{VSC}}(t). \tag{139}$$

Hence, in state-space notation, the system state matrix $\mathbf{A}^L$ is zero; the input matrix $\mathbf{B}^L$ is $1/L_{\mathrm{f}}$; the output matrix $\mathbf{C}^L$ is equal to one; and the state vector $\mathbf{x}^L(t)$ only contains one state variable, the grid current $i_1(t)$.

For the LCL filter case, the continuous-time plant model is

$$\frac{d\,x^{LCL}(t)}{dt} \;=\; \underbrace{\begin{bmatrix} 0 & 0 & \frac{1}{L_1} \\ 0 & 0 & \frac{-1}{L_2} \\ \frac{-1}{C_f} & \frac{1}{C_f} & 0 \end{bmatrix}}_{A^{LCL}} x^{LCL}(t) + \underbrace{\begin{bmatrix} 0 \\ \frac{1}{L_2} \\ 0 \end{bmatrix}}_{B^{LCL}} v_{\mathrm{VSC}}(t)$$

$$i_1(t) \;=\; \underbrace{\begin{bmatrix} 1 & 0 & 0 \end{bmatrix}}_{C^{LCL}} x^{LCL}(t), \tag{140}$$

where the state vector $x^{LCL}(t)$ is composed of three state variables: the grid current i_1, the converter current i_2, and the capacitor voltage v_c.

Next, the continuous-time models (139) and (140) are discretized using a ZOH equivalent [81]. The resultant matrices of the discrete-time state-space model for the L filter case are:

$$\begin{aligned} \mathbf{A}_d^L &= 1 \\ \mathbf{B}_d^L &= T_s/L_{\mathrm{f}} \\ \mathbf{C}_d^L &= 1. \end{aligned} \tag{141}$$

For the LCL filter case, the model matrices are:

$$\begin{aligned} A_d^{LCL} &= \exp\left\{A^{LCL}\,T_s\right\} \\ B_d^{LCL} &= A^{LCL^{-1}}(A_d^{LCL} - \mathbf{I_3})B^{LCL} \\ C_d^{LCL} &= C^{LCL}, \end{aligned} \tag{142}$$

where $\mathbf{I_3}$ is the 3×3 identity matrix.

Finally, a one-sample input (computational) delay is added to the discrete-time model. For the L filter case, the augmented system model is

$$\underbrace{\begin{bmatrix} \mathbf{x}_d^L(k+1) \\ v_d(k+1) \end{bmatrix}}_{\mathbf{x}_{dd}^L(k+1)} \;=\; \underbrace{\begin{bmatrix} \mathbf{A}_d^L & \mathbf{B}_d^L \\ \mathbf{0} & 0 \end{bmatrix}}_{\mathbf{A}_{dd}^L} \underbrace{\begin{bmatrix} \mathbf{x}_d^L(k) \\ v_d(k) \end{bmatrix}}_{\mathbf{x}_{dd}^L(k)} + \underbrace{\begin{bmatrix} \mathbf{0} \\ 1 \end{bmatrix}}_{\mathbf{B}_{dd}^L} v(k)$$

$$i_1(k) \;=\; \underbrace{\begin{bmatrix} \mathbf{C}_d^L & 0 \end{bmatrix}}_{\mathbf{C}_{dd}^L} \underbrace{\begin{bmatrix} \mathbf{x}_d^L(k) \\ u_d(k) \end{bmatrix}}_{\mathbf{x}_{dd}^L(k)}. \tag{143}$$

Similarly, the following state-space model is obtained for the LCL filter case:

$$
\underbrace{\begin{bmatrix} \mathbf{x}_d^{LCL}(k+1) \\ v_d(k+1) \end{bmatrix}}_{\mathbf{x}_{dd}^{LCL}(k+1)} = \underbrace{\begin{bmatrix} A_d^{LCL} & B_d^{LCL} \\ \mathbf{0} & 0 \end{bmatrix}}_{\mathbf{A}_{dd}^{LCL}} \underbrace{\begin{bmatrix} \mathbf{x}_d^{LCL}(k) \\ v_d(k) \end{bmatrix}}_{\mathbf{x}_{dd}^{LCL}(k)} + \underbrace{\begin{bmatrix} \mathbf{0} \\ 1 \end{bmatrix}}_{\mathbf{B}_{dd}^{LCL}} v(k)
$$

$$
i_1(k) = \underbrace{\begin{bmatrix} C_d^{LCL} & 0 \end{bmatrix}}_{\mathbf{C}_{dd}^{LCL}} \underbrace{\begin{bmatrix} \mathbf{x}_d^{LCL}(k) \\ u_d(k) \end{bmatrix}}_{\mathbf{x}_{dd}^{LCL}(k)}. \tag{144}
$$

7.6. Computational Complexity of the FCS Controller

The computational load of the proposed FCS controller in number of two floating-point operations (flops) is detailed in the following. The results correspond to a grid-tied inverter with an LCL filter because the number of operations is greater when an LCL filter is employed compared to an L filter due to the additional observer required to estimate all unmeasured plant state variables.

The proposed controller consists of an observer, a compensator, and a quantizer, as shown in Figure 136. The disturbance model (130) carries out two complex additions and two complex products, which require 16 real flops. The observer is a Kalman filter, which consists of the following two equations. The first one is a prediction equation that calculates the current state $\mathbf{x}_{\text{pred}}(k)$ using the previous state estimate $\mathbf{x}_{dd}^{\text{LCL}}(k-1)$ and the last voltage source converters (VSCs) switching state $v(k-1)$:

$$
\mathbf{x}_{\text{pred}}(k) = \underbrace{\mathbf{A}_{dd}^{LCL}}_{4\times4} \underbrace{\mathbf{x}_{dd}^{\text{LCL}}(k-1)}_{4\times1} + \underbrace{\mathbf{B}_{dd}^{\text{LCL}}}_{4\times1} \underbrace{v(k-1)}_{1\times1}. \tag{145}
$$

The second one is a correction equation that updates the previous prediction $\mathbf{x}_{\text{pred}}(k)$ using the most recent measurement of the grid current $i_1(k)$:

$$
\mathbf{x}_{dd}^{\text{LCL}}(k) = \underbrace{\mathbf{x}_{\text{pred}}(k)}_{4\times1} + \underbrace{\mathbf{K_o}}_{4\times1} [\underbrace{i_1(k)}_{1\times1} - \underbrace{\mathbf{C}_{dd}^{\text{LCL}}}_{1\times4} \underbrace{\mathbf{x}_{\text{pred}}(k)}_{4\times1}] \tag{146}
$$

where $\mathbf{K_o}$ is the Kalman gain. Thus, the observer executes 28 complex multiplications and 24 complex additions, which require 216 real flops.

The compensator equation is

$$
u(k) = \underbrace{\mathbf{K_c}}_{1\times5} \underbrace{\begin{bmatrix} x_d^{\text{dist}} \\ \mathbf{x}_{dd}^{\text{LCL}} \end{bmatrix}}_{5\times1}. \tag{147}
$$

Such vector multiplication requires four complex additions and five complex multiplications; hence the compensator executes 38 real flops.

The quantizer (131) carries out seven complex subtractions in order to obtain the noise associated to each switching state $n_i = u - v_i$. Next, the quantizer computes the squared magnitude of each of the noise vectors by multiplying each noise vector n_i by its complex

conjugate. Finally, six comparison operations are necessary to find the index i of the noise vector with the smaller magnitude. Therefore, the quantizer executes 62 real flops.

In the presented implementation ($f_s = 16$ kHz), a constant computational load with a value of 5.1 mega flops per second is obtained, which is lower than that of model predictive controllers (MPCs) [151, 16]. This figure is also significantly lower than the computational power of typical microcontrollers, such as the TMS320F335 from the manufacturer Texas Instruments. Figure 152 summarizes the computational load results given in this section.
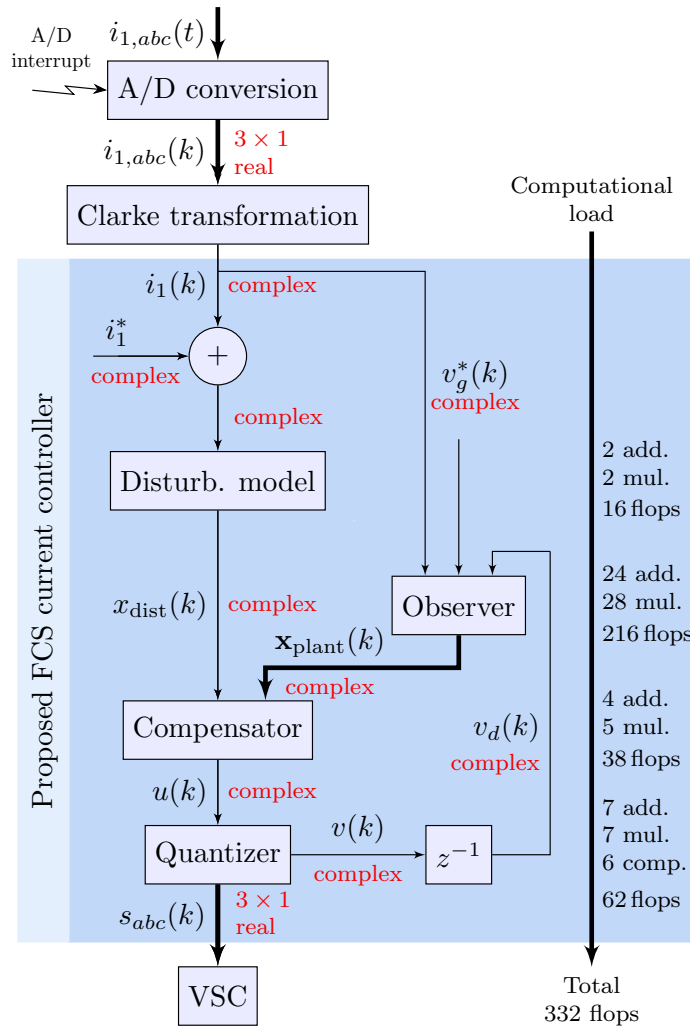
Figure 152. Execution chronogram of the proposed controller and computational load associated to each component.

7.7. Summary

This section has presented a linear current controller for a grid-tied inverter with an L or an LCL filter that provides a very fast transient response with low switching frequency,

similarly to a FCS-MPC but without requiring complex optimization algorithms. This fast dynamic, compared to a classical design, permits to rapidly follow reference commands and reject disturbances, such as an interruption in the grid voltage. Thus, this solution is a valuable alternative to FCS-model predictive controllers (MPCs) for practicing power-electronic engineers and researchers due to the use of linear control theory, which simplifies the design and assessment of the performance and stability, compared to Lyapunov techniques often required in MPC stability sutdies. Contrarily to PWM-based solutions, the proposal does not generate any switching or low-order harmonics thanks to the FCS operation and the proposed noise transfer function (NTF) design. By design, the switching noise is evenly spread at all frequencies instead of it being concentrated at some harmonics. This reduces the risk of exciting resonances in the grid and facilitates the operation of multiple inverters in parallel.

The proposed method improves the compliance of a grid-tied inverter with standards that limit the grid current distortion. These standards define different limits for even and odd harmonics; however, since the proposal distributes the distortion evenly, only the most stringent limits, which are the even harmonic limits, need to be considered for compliance. The experimental results have shown that the proposal is able to meet IEC harmonic limits using an L filter when a PWM-based controller requires an LCL filter with the same total inductance value; hence reducing the cost of the filter by eliminating the capacitor and improving the system reliability.

8.   A Model Predictive Current Controller with Improved Robustness against Measurement Noise and Plant Model Variations

This section improves the robustness of a finite control set (FCS)-model predictive controller (MPC) for grid-tied inverters and motor drives applications to plant parameter variations and noise, without reducing its bandwidth or affecting its excellent transient response to disturbances and reference commands. The proposed modification adds an observer to the MPC controller structure, which does not significantly increase the computational burden on the embedded controller. Traditionally, observers are employed to estimate unmeasured variables and cancel the effect of disturbances, but this section employs the observer to estimate a measured variable, the converter output current. This solution leverages the benefits of observers from linear controller theory in order to remove undesired components in the measured current and improve the robustness of the controller; hence it is a valuable solution for practicing power-electronic engineers and researchers in the field of grid-tied inverters and motor drives due to its simplicity compared to some advanced techniques often required in more complex MPC designs.

In power electronic applications, model predictive controllers (MPCs) are growing in popularity thanks to an increasing computational capability in embedded controllers and an

enormous research effort throughout the last two decades [152, 153]. Compared to traditional error-driven solutions, such as proportional-integral (PI) and proportional-resonant (PR) controllers, a model predictive controller (MPC) can potentially offer better performance because it incorporates a model of the dynamics and constraints in the plant. A model-based controller calculates the best converter response in terms of an objective or cost function while taking into account the nonlinear converter response due to its switching operation.

There are two main categories of model predictive controllers (MPCs), namely, finite control set (FCS)-MPC and continuous control set (CCS)-MPC. A FCS-MPC directly selects a switching state and maintains it during a whole sampling period whereas a CCS-MPC uses a PWM to generate the firing signals that drive the power converter. The former design is more popular among researchers in the field of power conversion [154] and it is the type of MPC considered in this section.

Compared to other applications with slower dynamics [155], converter control applications have to meet sub-millisecond execution times, which challenges the implementation of complex MPC formulations and favors the use of simpler control laws [156]. Current proposals of CCS-model predictive controllers (MPCs) that solve a high-order quadratic programming (QP) or linear programming (LP) optimization problem in real time require a high computational load [157]. Similarly, a FCS-MPC with a long prediction horizon and several state variables [16] is still difficult to implement due to the extremely high computational load required to solve an integer optimization problem. Nonetheless, as indicated in [154], long prediction horizons [158, 24, 159] offer performance improvements, despite the fact that their advantages are often misunderstood due to a poor formulation of the optimization goal. Recent proposals [160, 161, 24, 162] have achieved promising results using a novel algorithm [163] borrowed from the digital telecommunication field. Moreover, the development of solvers for online optimization continue to be an active field of research that has already provided several solutions, as summarized in [152].

Due to the previous limitations, practical implementations of FCS-model predictive controllers (MPCs) often use a short prediction horizon. Frequently, a one-sample[164, 165, 166, 167, 168, 169] prediction is selected. The one-sample prediction is often modified [168, 169] to compensate for the effect of the computational delay. Since FCS-model predictive controllers (MPCs) often use a high sampling frequency compared to PWM-based designs, a one- or two-sample prediction horizon spans a negligible time interval compared to a fundamental grid cycle. Such short prediction horizon can be significantly affected by the measurement noise and plant model deviations. Previous literature has studied the operation under distorted grid conditions [170] and the effect of plant model deviations [171] for CCS-MPC. However, very little progress has been done in studying how the noise affects the robustness of FCS-model predictive controllers (MPCs) in spite of a large research effort [172, 165, 173, 174] due to the complex nonlinear studies often required to assess the robustness and stability of FCS-model predictive controllers (MPCs).

This section analyzes the limitations of the one-step ahead FCS-MPC current controller in terms of robustness to plant model deviations and measurement noise and proposes an observer that can be used in conjunction with the one-step ahead FCS-MPC to improve its robustness with a minimal increase in computational load and without affecting the transient dynamics. Observers are frequently used in the control of electric drives [175] and grid-tied

inverters [126, 4]. Depending on the application, an observer can perform different tasks. For example, in electric drive applications an observer can be used to estimate unmeasured variables, such as the rotor flux orientation and speed, or the temperature of internal elements in a motor [176]. Hence, the observer permits to obtain information about system variables without requiring additional sensors, which may be difficult or costly to install. Another common application of observers is the estimation of disturbances that can affect the performance of the system. Such disturbance observers [175] permit to compensate the effect of parameter mismatches and nonlinearities [177, 178]. Traditionally, disturbance observers estimate an input-equivalent disturbance that, if subtracted from the plant input, cancels the effect of disturbances in the plant [179, 180, 181].

This proposal differentiates from the previous two applications because it uses an observer to estimate a measured variable, instead of estimating a disturbance or an unmeasured variable. The estimation improves the actual measurement in the presence of noise and plant model mismatches [81] because it is able to eliminate undesired components in the measurement and enhance the robustness of the controller. Moreover, the previously mentioned solutions can be used in conjunction with the proposal, i.e., a dual observer design, in order to benefit from the advantages of each observer.

The main contribution of this section is an improvement in the performance of the one-step ahead FCS-MPC in the presence of noise in the current measurements. To the author's knowledge, there are no previous proposals that have studied the effect of measurement noise in the current distortion for the one-step ahead FCS-MPC. The proposal reduces the current distortion by calculating an estimation of the measured current, without increasing the switching frequency of the voltage source converters (VSCs) and with a moderate increase in computational load. The proposed modification does not affect the transient dynamics of the one-step ahead FCS-MPC and preserves a fast reference tracking and disturbance rejection responses.

The concept presented in this section can also be implemented using other observer structures, such as a Luenberger observer. The proposal selected a Kalman filter due to its popularity, simple design process, and good performance. However, an equivalent performance can be obtained with a Luenberger observer that is designed using a direct pole placement strategy if the observer poles are placed in the same locations as the poles of the Kalman filter [81]. It should also be noted that the design or tuning of the observer is not critical in this application, the proposal uses the same observer design for all tests, although it is also possible to adjust the observer design according to the expected noise intensity.

The rest of this paper is organized in the following manner. Section II describes the plant model and cost function employed by the MPC. Section III presents the controller architecture and design process, including the proposed observer. Section IV presents a theoretical analysis that compares the performance of the proposal to a conventional FCS-MPC. In Section V, experimental results that validate the theory are presented. Finally, Section VI summarizes this section.

8.1.   Modeling of the Plant and the Cost Function

In order to design an MPC, a plant model and a cost function needs to be defined. In the case of a current controller, the plant model allows the controller to predict the achievable future
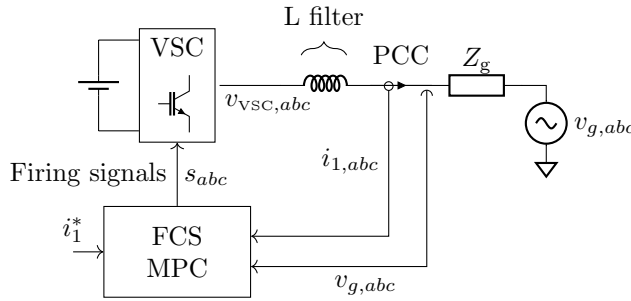
Figure 153. Grid-tied voltage source converter (VSC) connected at the PCC and controlled by a grid current model predictive controller (MPC) with a FCS operation.

plant states for the different controller actions. The cost function permits the controller to choose the best controller action so as to follow a given reference signal.

This section considers a discrete-time second-order plant model, which is frequently used in applications such as motor control and grid-tied inverters with an L filter. A simplified block diagram representation of a grid-tied inverter with an L filter is shown in Figure 153. The controller measures the grid voltage v_{g} and the grid current i_1 and generates the voltage source converter (VSC) firing-signals. In a grid-tied application, the grid current is usually measured at the PCC. The three-phase grid is modeled by a grid impedance Z_{g} and a grid voltage v_{g}. If present, the grid impedance can also model additional filter elements [182]. The control problem is formulated in the grid-aligned $\alpha\beta$ frame. If no reference frame is denoted in a variable or parameter, the $\alpha\beta$ reference frame is assumed. Such a model can be described by the following first-order differential equation:

$$\frac{\mathrm{d}\, i_1(t)}{\mathrm{d}t} \quad = \quad -\frac{R_{\mathrm{f}}}{L_{\mathrm{f}}}i_1(t) + \frac{1}{L_{\mathrm{f}}}v_{\mathrm{VSC}}(t) - \frac{1}{L_{\mathrm{f}}}v_{\mathrm{g}}(t). \tag{148}$$

where the variable v_{VSC} denotes the converter output voltage, and the parameters R_{f} and L_{f} denote the resistive and reactive components, respectively, of the L filter.

In state-space notation, Equation (148) can be rewritten as

$$\frac{\mathrm{d}\, \mathbf{x}^L(t)}{\mathrm{d}t} \quad = \quad \mathbf{A}^L\, \mathbf{x}^L(t) + \mathbf{B}^L \begin{bmatrix} v_{\mathrm{VSC}}(t) \\ v_{\mathrm{g}}(t) \end{bmatrix}$$
$$i_1(t) \quad = \quad \mathbf{C}^L\, \mathbf{x}^L(t), \tag{149}$$

where $\mathbf{x}^L(t)$ is the system state vector, which only contains one state variable, the grid current in a grid-tied inverter $i_1(t)$, or the motor current in a motor drive application. The system state matrix $\mathbf{A}^L$ is $-R_{\mathrm{f}}/L_{\mathrm{f}}$; the input matrix $\mathbf{B}^L$ is $[1/L_{\mathrm{f}}, \; -1/L_{\mathrm{f}}]$; the output matrix $\mathbf{C}^L$ is equal to one.

Since an MPC is executed in an embedded controller at a constant sampling frequency, the continuous-time model (149) is discretized using a ZOH equivalent and a sampling period of value T_s. Although the ZOH equivalent is an exact discretization that requires a higher computational load compared to other approximations, such as the Euler method, this operation does not add up to the computational load of the controller algorithm because

it is performed offline, during the design process of the controller. The discrete-time state-space model matrices are:

$$
\begin{aligned}
\mathbf{A}_d^L &= \exp\left\{\mathbf{A}^L T_s\right\} \\
\mathbf{B}_d^L &= \mathbf{A}^{L-1}(\mathbf{A}_d^L - 1)\,\mathbf{B}^L \\
\mathbf{C}_d^L &= \mathbf{C}^L.
\end{aligned}
\tag{150}
$$

A ZOH accurately describes the FCS operation of the VSC, which introduces a half sample delay. The resultant discrete-time state-space model is

$$
\begin{aligned}
\mathbf{x}_d^L(k+1) &= \mathbf{A}_d^L\,\mathbf{x}_d^L(k) + \mathbf{B}_d^L\begin{bmatrix} v_{\mathrm{d}}(k) \\ v_{\mathrm{g}}(k) \end{bmatrix} \\
i_1(k) &= \mathbf{C}_d^L\,\mathbf{x}_d^L(k).
\end{aligned}
\tag{151}
$$

The subscripts "cont" and "disc" denote a continuous-time and a discrete-time model parameter or variable, respectively. It should be noted that the resultant discrete-time state-space model is observable, but not controllable because one of the inputs, the grid voltage v_{g}, is an uncontrolled variable.

Finally, the discrete-time model (151) is augmented so as to also model a one sample delay in the plant input, which describes the effect of a computational delay, i.e., $v_{\mathrm{d}}(k+1) = v(k)$. The resultant plant model is

$$
\underbrace{\begin{bmatrix} \mathbf{x}_d^L(k+1) \\ v_{\mathrm{d}}(k+1) \end{bmatrix}}_{\mathbf{x}_{dd}^L(k+1)} = \underbrace{\begin{bmatrix} \mathbf{A}_d^L & \mathbf{B_1} \\ 0 & 0 \end{bmatrix}}_{\mathbf{A}_{dd}^L} \underbrace{\begin{bmatrix} \mathbf{x}_d^L(k) \\ v_{\mathrm{d}}(k) \end{bmatrix}}_{\mathbf{x}_{dd}^L(k)} + \underbrace{\begin{bmatrix} 0 & \mathbf{B_2} \\ 1 & 0 \end{bmatrix}}_{\mathbf{B}_{dd}^L}\begin{bmatrix} v(k) \\ v_{\mathrm{g}}(k) \end{bmatrix}
$$

$$
i_1 = \underbrace{\begin{bmatrix} \mathbf{C}_d^L & 0 \end{bmatrix}}_{\mathbf{C}_{dd}^L} \underbrace{\begin{bmatrix} \mathbf{x}_d^L(k) \\ v_{\mathrm{d}}(k) \end{bmatrix}}_{\mathbf{x}_{dd}^L(k)}
$$

$$
\mathbf{x}_{dd}^L(k) = \begin{bmatrix} i_1 & v_{\mathrm{d}} \end{bmatrix}^{\mathrm{T}},
\tag{152}
$$

where $\mathbf{B_1}$ and $\mathbf{B_2}$ are the first and second elements, respectively, of $\mathbf{B}_d^L$. This model relates the output vector $v(k)$ selected by the controller to the the grid current $i_1(k)$ in the plant shown in Figure 154.

The selected cost function measures the one-step ahead current error using the following l_1 norm:

$$
\begin{aligned}
J(k) &= \|i_{1,\alpha}^*(k+1) - i_{1,\alpha}(k+1)\| + \tag{153} \\
&\quad + \|i_{1,\beta}^*(k+1) - i_{1,\beta}(k+1)\|, \tag{154}
\end{aligned}
$$

where $i_{1,\alpha}^*$ and $i_{1,\beta}^*$ are the current references in the $\alpha\beta$ frame. More complex cost functions have been defined in the literature, at the expense of a higher computational load and increased design complexity associated to the calculation of the weighting factors [183]. Recent proposals [154] advocate towards including in the cost function a penalty on the switching transitions. Such modification frequently results in a sampling frequency two
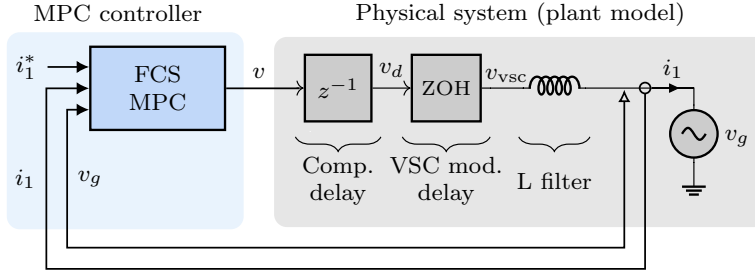
Figure 154. Structure of a conventional FCS-MPC.

orders of magnitude greater than the switching frequency [154], which significantly increases the computational load of the controller. In this section, a simple cost function is selected due to its popularity [169, 184, 26] and low computational load compared to an FCS-MPC with a long prediction horizon. However, the proposed solution is not affected by the complexity of the selected cost function and can also be applied to an MPC with a more elaborated cost function.

8.2. Design of the Current Controller

Compared to a PWM-based controller, an FCS-MPC operates directly with actual switching signals (firing signals and current measurements) instead of their average values, as illustrated in Figure 154. The switching signals contain a much larger frequency content (higher bandwidth) than their average value counterparts; therefore, an FCS-MPC operates over a much larger frequency range than a traditional PWM-based design. In fact, an FCS-MPC is regulating the switching noise that is generated by the VSC during operation at the same time as it controls the fundamental component and the low-order harmonics. As a result of such high bandwidth, the FCS-MPC inherently achieves a fast transient response. However, a high bandwidth also reduces the robustness of the controller to noise and plant model deviations. This problem is explained in the following.

Since the controller commands actions at high frequencies, it relies on a plant model that describes the plant response at high frequencies. However, a plant parameter variation is more noticeable at high frequencies than at low frequencies. For example, a one-sample delay introduces a negligible phase error at the fundamental frequency. But it causes a polarity inversion at half the sampling frequency. Similarly, a parameter deviation in an inductive component results in an impedance deviation that increases linearly with frequency. Moreover, unmodeled effects such as core losses, skin effect, and measurement noise can become significant at the high frequencies that the MPC operates.

In order to reduce the sensitivity of the controller to plant parameter variations and measurement noise, the proposal introduces an observer, as shown in Figure 155. Observers are frequently used in the literature; however, to the authors knowledge, an observer has not been previously used in the field of MPC for power converter applications in order to obtain an estimation of the grid current $\hat{i}_1$ that improves the actual measurement i_1. The observer computes every sampling period an estimation of the instantaneous current value $\hat{i}_1$ using
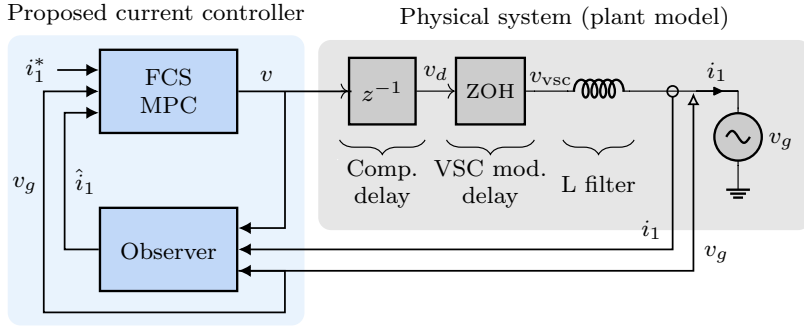
Figure 155. Structure of the proposed current controller, which includes an observer.

all information available, namely, the measured grid current, the previously commanded switching states, and the measured grid voltage.

The observer selected is the steady-state solution of a Kalman filter for a linear time-invariant system, due to its simple design and popularity across numerous research fields. Such Kalman filter for a linear system with a constant variance noise model consists of the following two equations. The first one is a prediction equation that estimates the state $\hat{\mathbf{x}}_{\mathbf{p}}(k)$ from the previous state estimate $\hat{\mathbf{x}}_{\text{disc}}(k-1)$ and the last actuation on the plant $v(k-1)$. The subscript "p" denotes predicted.

$$\hat{\mathbf{x}}_{\mathbf{p}}(k) \quad = \quad \mathbf{A}_{dd}^{L}\,\hat{\mathbf{x}}_{\text{plant}}(k-1) + \mathbf{B}_{dd}^{L}\begin{bmatrix} v(k-1) \\ v_{\text{g}}(k-1) \end{bmatrix}. \tag{155}$$

The second one is a correction equation that modifies the prediction $\hat{\mathbf{x}}_{\mathbf{p}}(k)$ based on the most recent current measurement $i_1(k)$:

$$\hat{\mathbf{x}}_{\text{plant}}(k) \quad = \quad \hat{\mathbf{x}}_{\mathbf{p}}(k) + \mathbf{K_o}\left[i_1(k) - \hat{\mathbf{x}}_{\mathbf{p}}(k)\right], \tag{156}$$

where $\mathbf{K_o}$ is the Kalman gain. The procedure to calculate the Kalman gain is given in Section 8.5.

Figure 156 shows an execution chronogram of the proposed FCS-MPC plus observer that illustrates the operations executed by the embedded controller every sampling period. As shown, the proposed solution does not significantly increases the computation burden on the embedded controller compared to a classical FCS-MPC.

8.2.1. Computational Complexity

The computational load of the proposal in number of two floating-point operations (flops) is detailed in the following and the obtained figure is compared to a typical FCS-MPC.

The proposed controller consists of an observer and a one-step ahead FCS-MPC, as shown in Figure 155. The observer consists of two equations, namely, (155) and (156). Such equations contain four complex additions and four complex products in total. Since a complex product requires six real flops and a complex addition requires two real flops, the total computational load of the observer is 32 real flops.
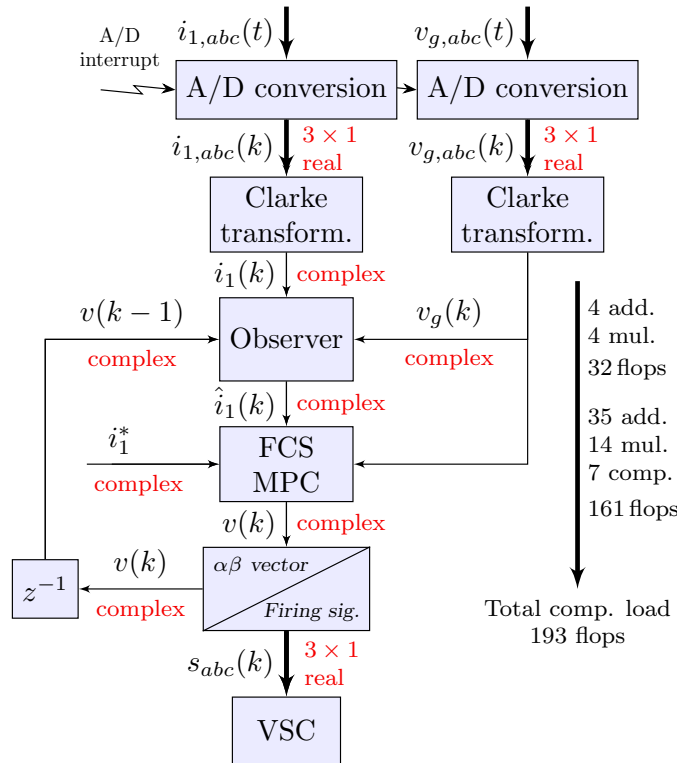
Figure 156. Execution chronogram of the proposed FCS-MPC plus observer and computational load associated to each component.

The FCS-MPC carries out an optimization loop that calculates the current error associated to each of the eight switching states of a two-level VSC. In order to obtain the current error, it computes the plant model (152) and the associated current error (154) for every possible VSC output vector. The switching state with a lower current error is selected. This optimization executes five complex additions, two multiplications, and a comparison operation every loop iteration. Since there are seven different VSC output vectors in the $\alpha\beta$ frame, the FCS-MPC executes 161 real two flops.

In the presented implementation ($f_s = 16\,\text{kHz}$), a constant computational load with a value of 3.1 mega flops per second is obtained for the proposal and a value of 2.6 mega flops per second for the conventional FCS-MPC alone. As a reference for benchmark, these figures are lower than the computational power of typical microcontrollers, such as the TMS320F335 from the manufacturer Texas Instruments. Figure 156 summarizes the computational load results.

8.3. Current Distortion

This section analyzes how the current distortion changes when the proposed observer is included in the controller. The performance is studied by simulating the operation of a grid-tied inverter during steady-state for different intensities of measurement noise and comput-
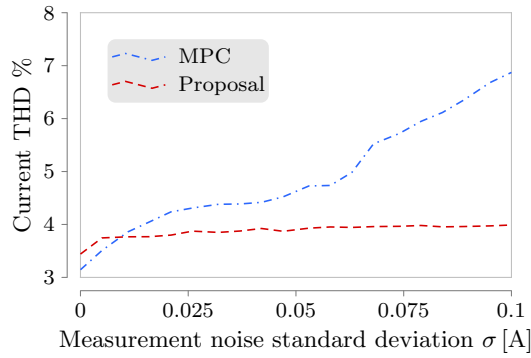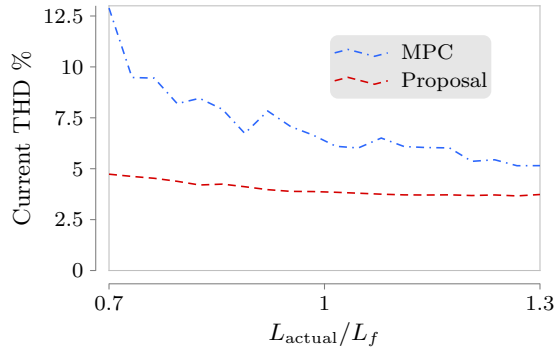
(a)
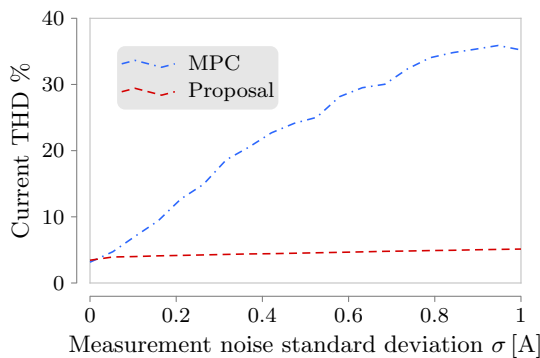
(b)

Figure 157. Comparison of the current total harmonic distortion (THD) of a conventional FCS-MPC and the proposal for different intensities of measurement noise. a Measurement noise standard deviation sweeps from 0 to 0.1 A. b Measurement noise standard deviation sweeps from 0 to 1 A.

ing the current THD. The measurement noise is added to the grid current measurements before they are sent to the controller. The current THD in a grid-tied inverter with an FCS-MPC depends on multiple parameters in addition to the type of controller, such as the filter parameter values, the switching frequency, and the DC bus voltage. In order to assess any improvement in performance between a conventional FCS-MPC and the proposal, the setup parameters are maintained constant in all the presented tests. The simulated setup parameters used in this section are the same as the parameters of the experimental setup presented in Section 8.4.

Figure 157 shows a comparison of the current THD of a conventional one-step ahead FCS-MPC and the proposal for different intensities of measurement noise and no plant parameter deviations. In Figure 157a, the standard deviation of the measurement noise is changed from zero (no noise) to a value of 0.1A, and in Figure 157b, the standard deviation of the measurement noise is changed from zero (no noise) to a value of 1A. As shown, in a conventional FCS-MPC, the THD rapidly increases as the measurement noise augments. Contrarily, the proposal maintains a consistent performance independently of

Figure 158. Comparison of the current total harmonic distortion (THD) of a conventional FCS-MPC and the proposal for a plant model variation that consists of a change in the actual filter impedance value L_{actual} from the nominal value L_{f} and an additional one-sample computational delay.

the measurement noise intensity and the current THD is maintained below a 4%.

Figure 158 shows the current THD for a plant model variation that consists of a change in the L filter impedance and a one sample delay. The actual filter impedance L_{actual} is changed from a value 30% smaller than the nominal value L_{f} to a value 30% greater than nominal. For the nominal condition $L_{\text{actual}}/L_{\text{f}} = 1$, the proposal provides a lower THD than a conventional MPC. When the impedance of the L filter is diminished without updating the controller, the conventional MPC experiments a faster increase in current THD than the proposal due to its lower robustness to plant parameter variations. On the other hand, the current THD diminishes in both cases when the filter impedance increases due to the additional attenuation provided by a filter with a greater inductance value.

It should be noted that, in a traditional electrical grid, the presence of even harmonics indicates an unbalance between the positive half of the current or voltage waveform and the negative half. Those even harmonic components cause unequal positive and negative peak values, which are called waveform asymmetry. Waveform asymmetry has a harmful impact on the loads sensitive to voltage or current peaks. Converters with an FCS operation, such as FCS-MPC, generate switching noise that is spread throughout a wide and continuous frequency range. Therefore a direct application of the harmonic limits defined in [110, 147] can be difficult. This problem has been recognized in [154], where the use of an FCS-MPC is not recommended for grid-tied inverters due to the difficulty of meeting the even harmonic limits established for current waveforms with a periodic distortion.

8.4. Experimental Results

This section experimentally validates the previous simulation results. The experimental results are carried out in a 5-kW VSC working as an inverter with a 700-V dc bus v_{dc} and connected to a 400-V line-to-line 50-Hz three-phase grid. In addition to the actual grid, a three-phase grid emulator is employed to simulate adverse grid condition that consists of a highly distorted grid voltage an a sudden interruption. The controller (see Figure 156) is executed in real-time at a sampling frequency of 16 kHz, which results in an average switching

(a)

(b)
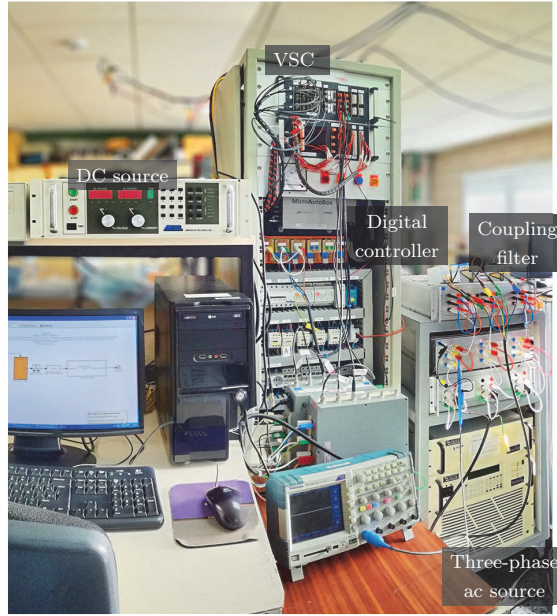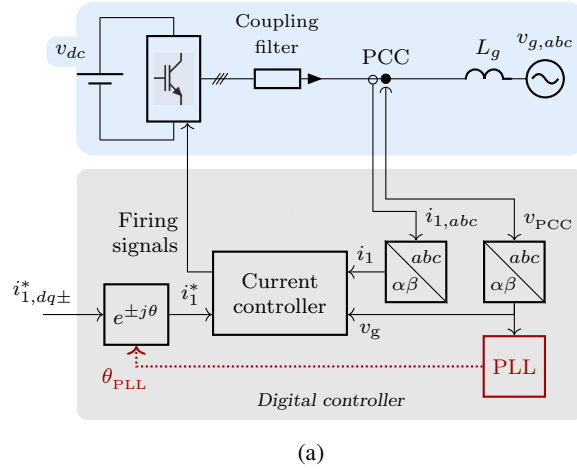
Figure 159. Experimental setup. a Diagram. b Photograph.

frequency of 2 kHz, in an embedded hardware control platform from the German manufacturer dSpace. This platform is programmed using Simulink programming language, Matlab scripts, and C code and it also provides a large number of analogue input channels, compared to a traditional oscilloscope. By adding the required external voltage and current sensors, this platform is able to record in the same time base, i.e. simultaneously, the three-phase grid voltages, the three-phase grid currents, and signals internal to the controller such as the grid-current in the dq frame or the grid current estimation provided by the observer. Such feature is employed to record the experimental results shown in this section.

The L filter impedance value is indicated in Table 19. The selected filter inductance

Table 19. Experimental Setup Parameters

Base values			
Nominal power	P_o	5	$[\text{kW}]$
Grid voltage	v_g	230	$[\text{V}^{\text{RMS}}_{\text{phase}}]$
Grid frequency	f_g	50	$[\text{Hz}]$
L filter			
Filter inductance	L_f	0.32	$[\text{p.u.}]$
VSC			
Sampling frequency	f_s	16	$[\text{kHz}]$
DC bus voltage	v_{dc}	700	$[\text{V}_{\text{DC}}]$

value and the switching frequency are commonly employed in low-voltage applications with two-level VSCs [143, 144, 145, 146]. The tests presented in the section show the performance of the proposed controller for two different grid impedance conditions. For the reference tracking tests the grid-tied inverter is connected to the three-phase grid available in the lab. For the disturbance rejection tests the inverter is connected to a three-phase grid emulator, configured to generate a highly distorted voltage and an interruption. In these two configurations, the value of the grid impedance is assumed to be low compared to the impedance of the L filter.

It should be noticed that, since the grid impedance is in series with the L filter, a variation in the grid impedance can be approximated by a variation in the filter impedance. However, this is only an approximation because, contrarily to a deviation in the L filter value, an increase in the grid impedance also causes a coupling between the grid current and the voltage at the PCC, which can affect the grid synchronization mechanism. This feature is beyond the scope of this section; however, there are numerous references that analyze this problem in detail [117, 118]. In order to synchronize the VSC with the grid, a synchronous reference frame PLL with additional filtering to enhance its robustness to low-order harmonics is used [185]. Figures 159a and 159b show a diagram and a photograph, respectively, of the experimental setup.

Figure 160 shows the experimental waveforms during a 10-A reference step in the d axis of the +dq frame for different intensities of measurement noise. The experimental results show that the the FCS-MPC presents a higher current noise during steady-state operation compared to the proposal. The difference in performance is larger as the measurement noise increases, as explained in the previous section. Nevertheless, the transient response is extremely fast, with a rise time of $2.5ms$ and negligible overshoot in both cases.

Figure 161 shows the experimental waveforms during an interruption in the grid voltage for different intensities of measurement noise. For this test, the VSC is connected to a three-phase ac source that has been programmed to generate a highly distorted grid voltage
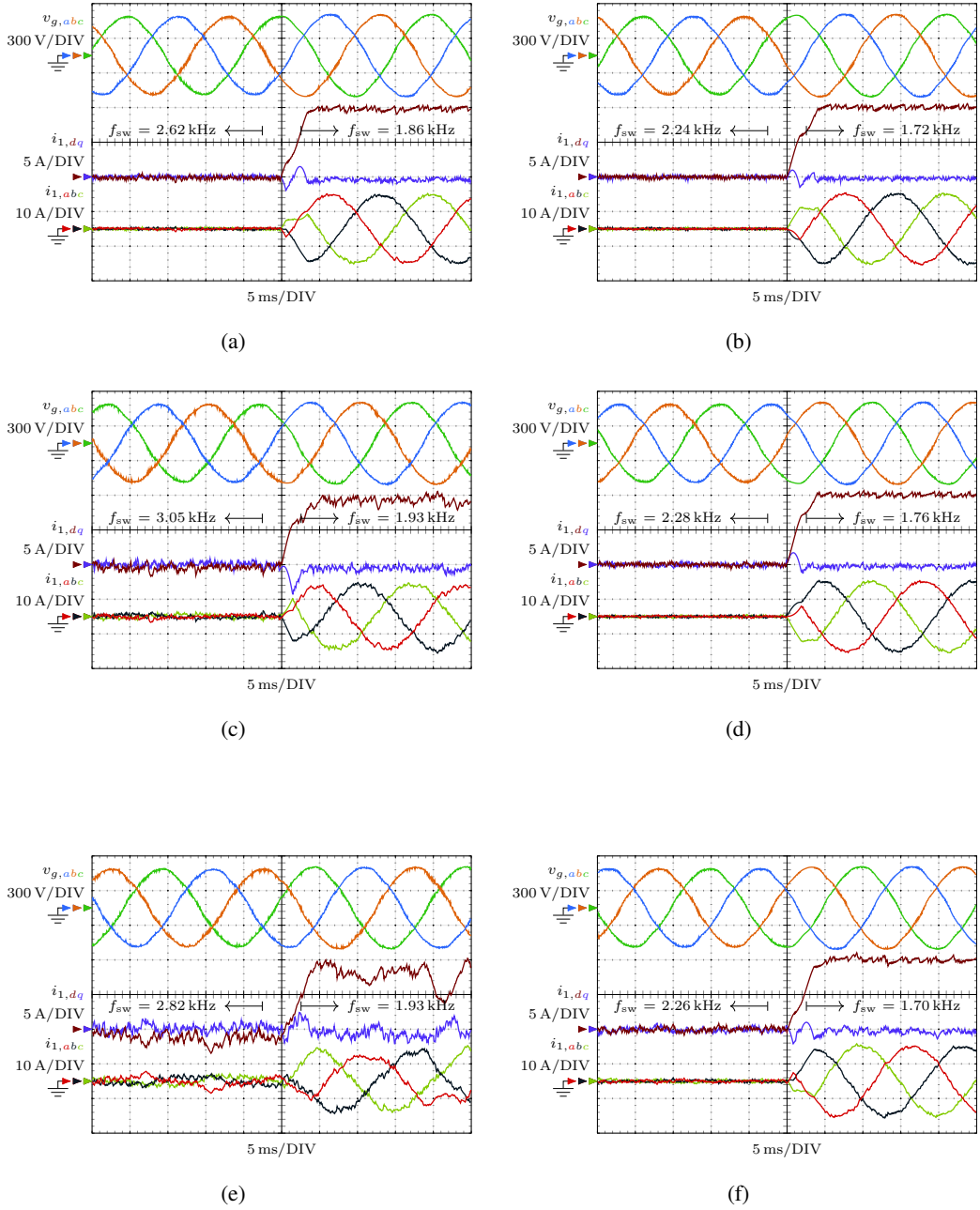
(a)

(b)

(c)

(d)

(e)

(f)

Figure 160. Experimental waveforms during a 10-A reference step in the d axis of the +dq frame for different intensities of measurement noise. Measured grid current in the dq frame $i_{1,dq}$, in the abc frame $i_{1,abc}$, and measured grid voltage v_g. a FCS-MPC controller with a measurement noise intensity of 0.1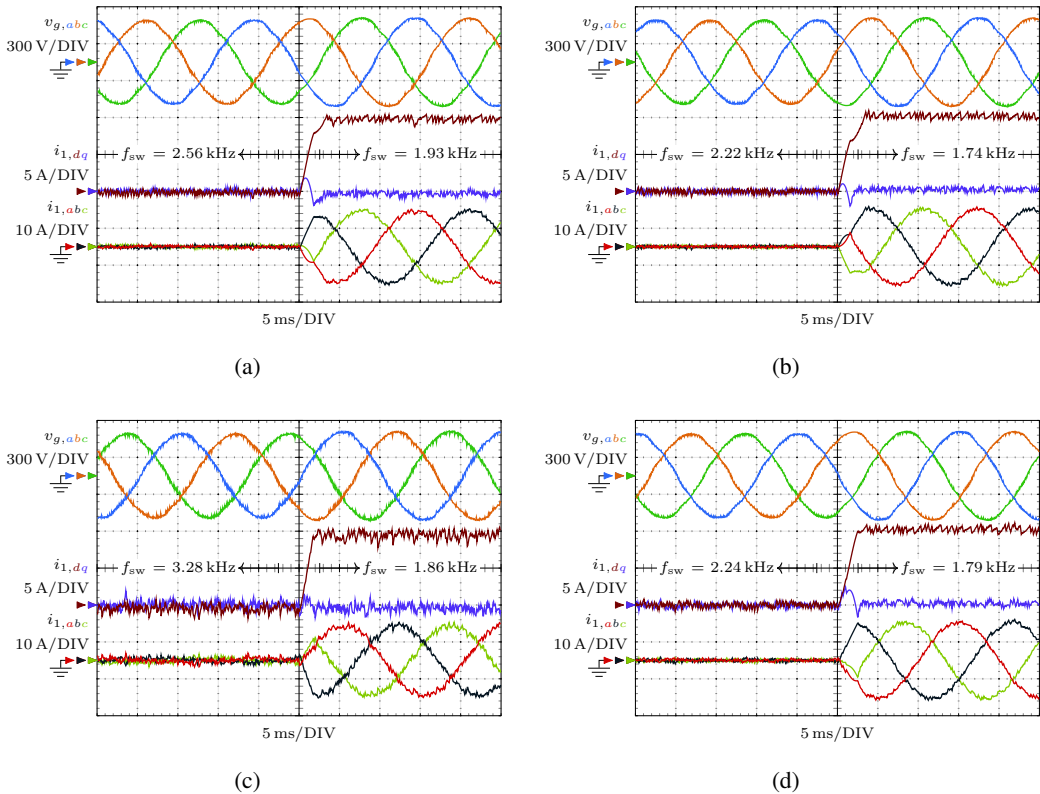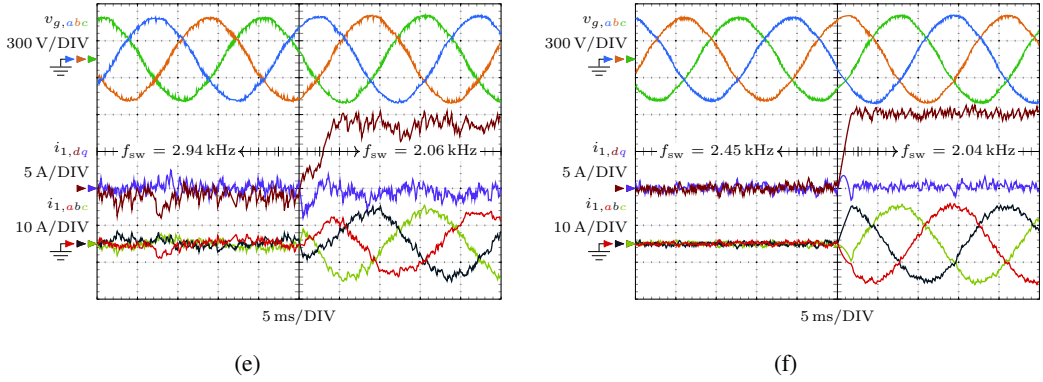A. **??** Proposal with a measurement noise intensity of 0.1A. c FCS-MPC controller with a measurement noise intensity of 0.5A. d Proposal with a measurement noise intensity of 0.5A. e FCS-MPC controller with a measurement noise intensity of 1.0A. f Proposal with a measurement noise intensity of 1.0A.

(a)

(b)

(c)

(d)

(e)

(f)
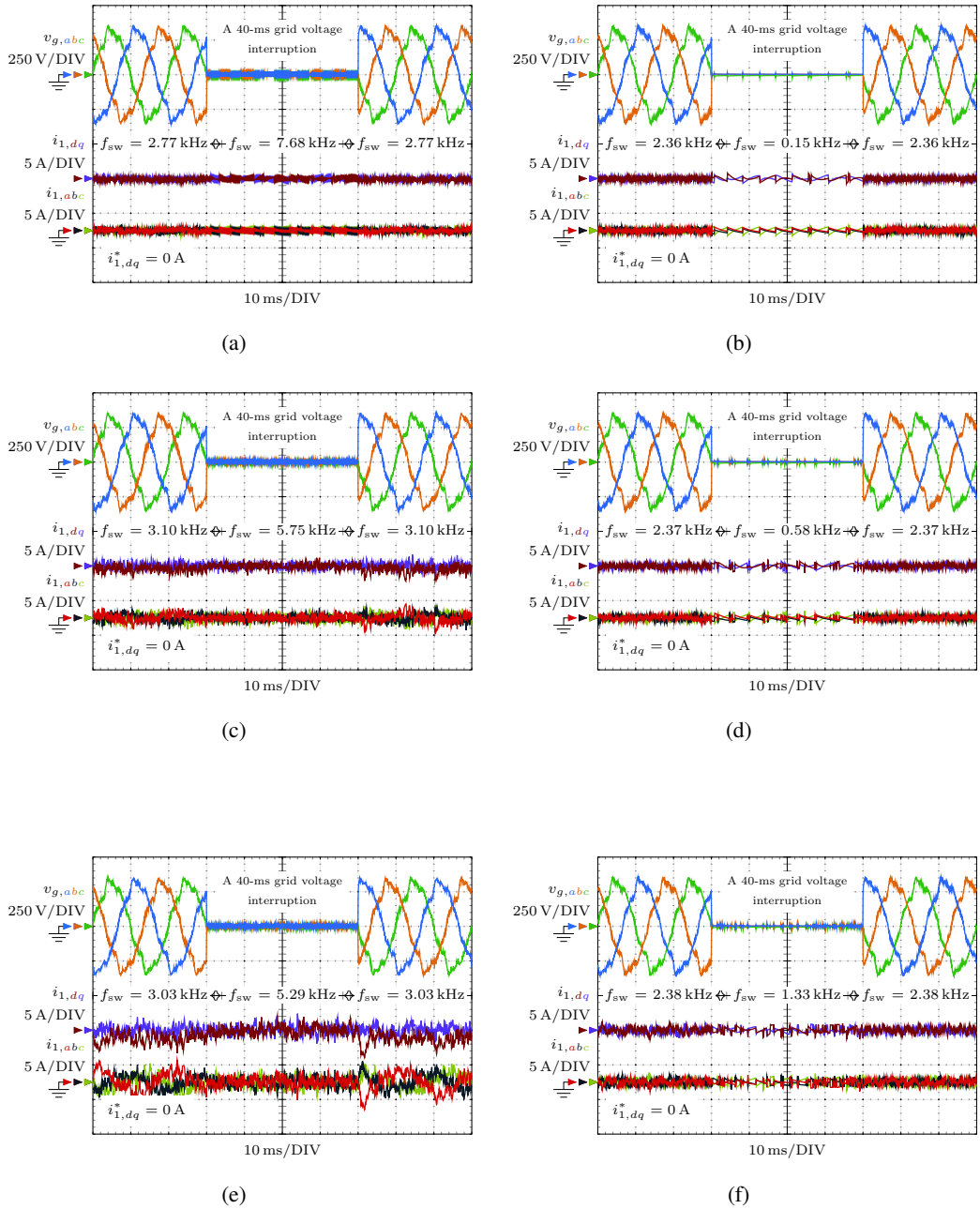
Figure 161. Experimental waveforms during a 40-ms grid voltage interruption for different intensities of measurement noise. Measured grid current in the dq frame $i_{1,\mathrm{dq}}$, in the abc frame $i_{1,\mathrm{abc}}$, and measured grid voltage v_{g}. a FCS-MPC controller with a measurement noise intensity of $0.1\mathrm{A}$. b Proposal with a measurement noise intensity of $0.1\mathrm{A}$. c FCS-MPC controller with a measurement noise intensity of $0.5\mathrm{A}$. d Proposal with a measurement noise intensity of $0.5\mathrm{A}$. e FCS-MPC controller with a measurement noise intensity of $1.0\mathrm{A}$. f Proposal with a measurement noise intensity of $1.0\mathrm{A}$.

before the interruption occurs. The current reference of the grid-tied inverter is set to zero; therefore, the measured current is equal to the current error.

As shown, the current noise of the conventional FCS-MPC is severely affected as the amplitude of the measurement noise increases. Conversely, the proposal maintains a more consistent performance for the different intensities of measurement noise. Similarly to the reference tracking test, both the proposal and the conventional FCS-MPC show an excellent disturbance rejection capability. No transient events appear in the current in spite of the large and sudden voltage disturbance. It should be noticed that the shape of the current ripple changes when the grid voltage interruption occurs. This effect results from the fact that a FCS-MPC varies its switching frequency depending on the modulation index value, and when the interruption occurs, there is a large change in the modulation index of the VSC.

Figure 162 repeats the previous reference tracking test but the filter inductance value is a 30% lower than its nominal value. As expected from the theoretical analysis, cf. Figure 158, the conventional MPC experiences a greater degradation compared to the proposal. A plant parameter mismatch causes steady-state error in addition to a greater distortion if no corrective actions, such as including a disturbance observer, are incorporated to the controller. The proposed observer is not a disturbance observer; therefore, it does not completely eliminate steady-state errors that may appear due to plant model variations or noise.

Figure 162. Continued on next page.

(e) (f)
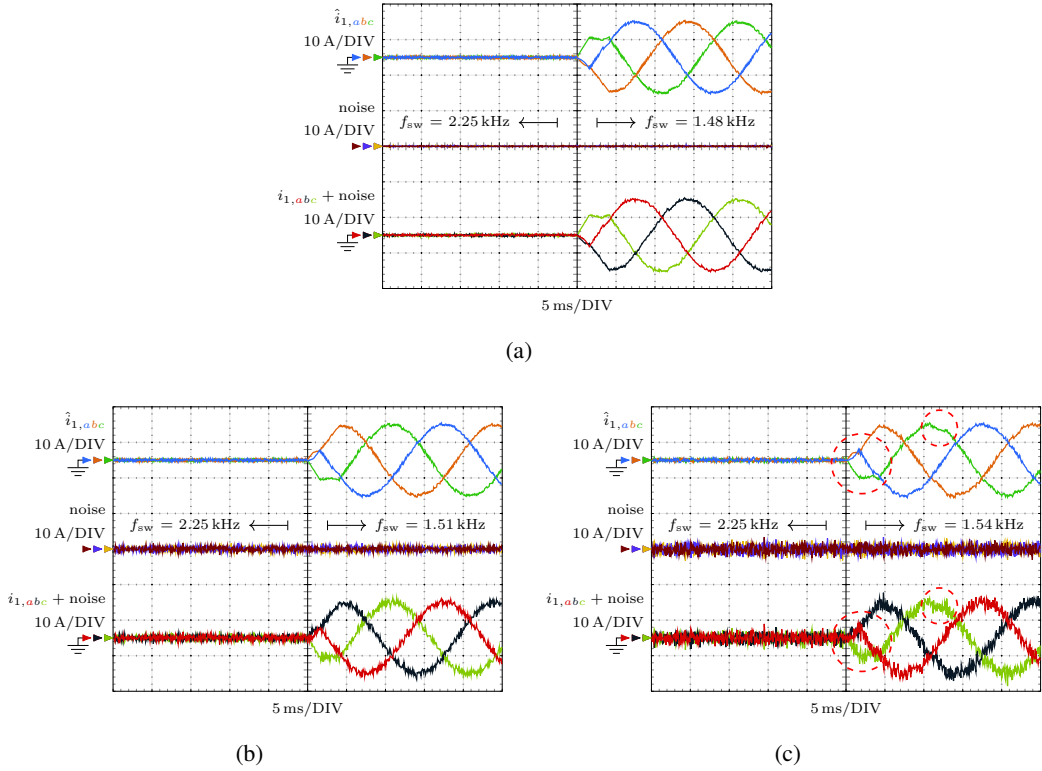
Figure 162. Experimental waveforms during a 10-A reference step in the d axis of the +dq frame for different intensities of measurement noise and a plant model variation that consists of a 30-% reduction in the filter impedance value. Measured grid current in the dq frame $i_{1,dq}$, in the abc frame $i_{1,abc}$, and measured grid voltage v_g. a FCS-MPC controller with a measurement noise intensity of 0.1A. b Proposal with a measurement noise intensity of 0.1A. c FCS-MPC controller with a measurement noise intensity of 0.5A. d Proposal with a measurement noise intensity of 0.5A. e FCS-MPC controller with a measurement noise intensity of 1.0A. f Proposal with a measurement noise intensity of 1.0A.

Figure 160 and Figure 162 show that the steady-state error in the proposal is lower than in the case of the conventional FCS-MPC. The proposal helps to improve the reference-tracking steady-state error in the presence of noise.

Figure 163 shows the difference between the estimated currents $\hat{i}_1$ and the measured currents i_1 plus the noise. As shown, the observer is able to remove most of the measurement noise from the current measurements, without removing the high frequency components that are actually in the current waveform when the current reference is changed. This feature is most noticeable in Figure 163c, where it is highlighted using dashed red circles.

In addition to the voltage and current waveforms, all oscilloscope captures detail the switching frequency of the VSC. Since the oscilloscope captures show different transient events, the average switching frequency is reported before the transient event and after the transient event. In order to measure the average switching frequency, an interval of duration equal to 15 power line cycles (PLC) is used, except for the measurement of the switching frequency during the grid interruption event (Figure 161), which only lasts 40 ms; hence a two PLC interval is used instead. The results show that the proposal achieves a reduction in the current noise compared to a conventional FCS-MPC in the same conditions, without increasing the switching frequency. This effect is most noticeable during the grid voltage interruption shown in Figure 161. Ideally, the switching frequency should fall to zero when the interruption occurs because the current reference is set to zero. However, the switching frequency is not zero due to the effect of noise.

In summary, when the observer is added, the transient dynamics of the controller to reference commands and disturbances are not affected, in spite of the additional filtering provided by the observer during steady-state. The reason is that the observer selectively fil-

(a)

(b)

(c)

Figure 163. Experimental waveforms during a 10-A reference step in the d axis of the +dq frame for different intensities of measurement noise. Estimated grid current in the abc frame $\hat{i}_{1,\text{abc}}$, measurement noise, and measured grid current $i_{1,\text{abc}}$ plus noise. a Proposal with a measurement noise intensity of 0.1A. b Proposal with a measurement noise intensity of 0.5A. c Proposal with a measurement noise intensity of 1A.

ters out the unmodeled dynamics and the measurement noise, but it preserves the frequency components associated to sudden changes in the current reference or the grid voltage. This is possible because the observer receives as inputs the VSC switching state v, the measured voltage at the PCC v_{g}, and the measured current i_1. The presented experimental results validate the theoretical analysis and the previous simulation results.

8.5.   Calculation of the Kalman Gain

This section details the procedure to calculate the Kalman gain $\mathbf{K_o}$ required to implement the Kalman filter equations [54] presented in Section 8.2. This method has also been applied to calculate the Kalman gain of a disturbance observer in [8].

The computation of the Kalman gain is performed offline to reduce the computational load of the controller. The calculation process consists of the steps shown in Algorithm I. Such Algorithm converges, after a few iterations, towards a constant value in $\mathbf{K_o}$.

The input parameters of the algorithm are the measurement noise N, the process noise Q, the plant model matrices $\mathbf{A}_{\text{plant}}$ and $\mathbf{C}_{\text{plant}}$ [cf. (152)], and a tolerance ϵ, which is used in

---

Algorithm 2 Calculation of the Kalman Gain $\mathbf{K_o}$

Inputs: $N, Q, \mathbf{A}_{\text{plant}}, \mathbf{C}_{\text{plant}}, \epsilon$

1: **while** $\|\mathbf{K_o}(k+1) - \mathbf{K_o}(k)\|_2 \geq \epsilon$ **do**

2:     Update values from previous iteration
3:     $\mathbf{P}(k) \leftarrow \mathbf{P}(k+1)$
4:     $\mathbf{K_o}(k) \leftarrow \mathbf{K_o}(k+1)$
5:     Project the error covariance ahead
6:     $\mathbf{P_p} \leftarrow \mathbf{A}_{\text{plant}}\mathbf{P}(k)\mathbf{A}_{\text{plant}}{}^{\text{T}} + Q$
7:     Compute the Kalman gain
8:     $\mathbf{K_o}(k+1) \leftarrow \mathbf{P_p}\mathbf{C}_{\text{plant}}{}^{\text{T}}/(\mathbf{C}_{\text{plant}}\mathbf{P_p}\mathbf{C}_{\text{plant}}{}^{\text{T}} + N)$
9:     Update the error covariance
10:     $\mathbf{P}(k+1) \leftarrow (\mathbf{I} - \mathbf{K_o}(k+1)\mathbf{C}_{\text{plant}})\mathbf{P_p}$

11: **end while**

---

the stop condition to detect when convergence is achieved. A value of $\epsilon = 10^{-10}$ ensures a good precision in the coefficients.

The parameters N and Q permit to tune the observer to the amount of noise in the plant. However, all the tests presented in the section have been carried out using the same observer gain. A value of one is selected for the measurement noise N and a value of one percent is used for the process noise parameter Q. These values provide a good performance for the range of noise intensities that have been tested. For the setup parameters used in the section, the obtained Kalman gain $\mathbf{K_o}$ is the following vector:

$$\mathbf{K_o} = \begin{bmatrix} 0.1287 & 0.0087 \end{bmatrix}. \tag{157}$$

8.6. Summary

This section has presented an improvement for an finite control set (FCS)-MPC controller that provides a higher robustness to plant parameter variations and measurement noise, without reducing the bandwidth of the controller or affecting its excellent transient response to reference steps and disturbances. The proposal reduces the current distortion and the steady-state error of a an FCS-MPC controller in the presence of noise. The proposed modification does not significantly increase the computational burden on the embedded controller nor increases the switching frequency of the VSC. This solution leverages the convenience of observers from linear controller theory; hence it is a valuable solution for practicing power-electronic engineers and researchers due to its simplicity compared to some advanced techniques often required in more complex MPC designs.

Conclusion

This Chapter addresses the primary control of power converters in a microgrid (MG). Its main conclusions are summarized below.

- An enhanced current controller for grid-tied converters with LCL filter. The developed method is based on a direct discrete-time pole placement strategy from the clas-

sical control theory, involving two extra filters. It provides a simple design process of the controller for a wide range of LCL filter values and it ensures stable operation without additional damping methods. The frequency of the dominant pole in the system is set in accordance with the available system bandwidth. As a result, a fast reference-tracking capability with negligible overshoot and acceptable controller effort are attained in combination with a fast disturbance rejection. The sensitivity to variations in the grid inductance is low due to the proposed pole-placement strategy. The proposed controller also has the well-known characteristics of conventional resonant controllers (RCs), e.g., zero steady-state error at both fundamental sequences, and a simple implementation with a low computational load compared to state-space controllers from modern control theory.

- A current controller of both positive and negative grid-side current sequences for grid-tied converters with LCL filter. Similarly to the previous proposal, this controller offers fast reference-tracking capability with negligible overshoot and low controller effort, regardless of the switching frequency and LCL filter used: f_{res} above or below $f_s/6$. The controller has also been proved to be robust to disturbances such as voltage sags and low-order voltage harmonics, even when combined with reference changes in both sequences. A low sensitivity to parameter variations is obtained, as verified with stability-region maps, root-locus diagrams, time domain simulation, and experimental tests. In addition to the advantages of the previous controller, this design avoids wind-up problems thanks to its state-feedback structure. This facilitates the bumpless start of the converter and permits to operate the VSC close to its performance limits, reaching saturation during transient events, in order to obtain the fastest response that the physical setup permits, similarly to a model predictive controller.

- A multi-frequency current controller based on a direct discrete-time pole-placement strategy and a Kalman filter for grid-tied converters with LCL filter. In addition to the advantages of previously proposed controllers, this design achieves a reference-tracking response with a consistent, damped, and fast response independently of the LCL filter used or the targeted harmonics. The rise-time value for reference changes is determined by the selected dominant frequency f_{dom} of the compensator, which can approach the available bandwidth available in the physical system. Concerning the disturbance-rejection capability, the proposed scheme achieves zero steady-state error in the grid-side current at a set of arbitrarily specified harmonic frequencies. Contrarily to the previously proposed solutions, the controller offers an infinite impedance at these frequencies without altering the response to reference commands or affecting the stability and robustness of the system, when several current harmonics are being controlled. It has also been shown a fundamental tradeoff that exists between the robustness of the controller and the response to disturbances in the steady-state operation and during transients. If the number of controlled harmonics increases (to reduce the steady-state error), then the robustness or the transient response to disturbances of the controller should be degraded. This is an unavoidable tradeoff that applies to all linear controllers. The recommended design has also been proved robust against alterations in the grid impedance. Stability is maintained with minimal change in the transient dynamics of the system regardless of the grid-impedance vari-

ation.

- A sensorless grid synchronization method which requires minimal computational load and provides a fast and accurate estimation of the grid voltage when connected to a weak grid. The proposed synchronization method eliminates any interaction with the current controller. A small estimation error is obtained due to the low sensitivity of the proposal to plant modeling errors. If the grid-impedance is assumed to be zero, both the proposal and a PLL-based scheme result in the same steady-state error. Contrarily to a PLL, the presented scheme does not require to measure the grid voltage, which could affect the performance under weak grid conditions, when the voltage at the PCC is different from the grid voltage and it is coupled to the grid-side current. A bumpless start capability provides a soft start and a sensorless operation in any grid conditions, including the start-up of the VSC.

- An ac voltage controller with a high robustness to variations in the load that allows it to operate in islanded and grid-connected mode. The proposed controller uses a single-loop structure that improves the transient performance by selectively minimizing the output impedance of the system at a set of design-selected frequencies. This set of frequencies can contain any frequency below the Nyquist frequency of the digital controller, including the resonant frequency of the LC filter and frequencies above the critical frequency of the system $f_{s/6}$, where previous proposals have stability problems. Complete harmonic elimination is achieved due to the zero output impedance at such set of frequencies. System stability has been studied for all values of R, RL, and RC loads. Moreover, the above properties are maintained irrespectively of the LC filter installed, or the sampling frequency used, provided that overmodulation of the VSC is avoided and the resonant frequency of the LC filter is lower than the Nyquist frequency.

References

[1] Pérez-Estévez D., Doval-Gandoy J., Yepes A. G., López O., and Baneira F., Enhanced resonant current controller for grid-connected converters with LCL filter, *IEEE Trans. Power Electron.*, vol. 33, no. 5, pp. 37653778, May 2018.

[2] Pérez-Estévez D., Doval-Gandoy J., Yepes A. G., and López O., Positive- and negative-sequence current controller with direct discrete-time pole placement for grid-tied converters with LCL filter, *IEEE Trans. Power Electron.*, vol. 32, no. 9, pp. 7207 7221, 2017.

[3] Pérez-Estévez D., Doval-Gandoy J., Yepes A. G., López O., and Baneira F., Generalized multi-frequency current controller for grid-tied converters with LCL filter, *IEEE Trans. Ind. Appl.*, vol. 54, no. 5, pp. 45374553, Sep. 2018.

[4] Pérez-Estévez D. and Doval-Gandoy J., Grid-tied inverter with AC voltage sensorless synchronization and soft start, *IEEE Trans. Ind. Appl.*, vol. 55, no. 5, pp. 49204933, Sep./Oct. 2019.

[5] Pérez-Estévez D., Doval-Gandoy J., and Guerrero J. M., AC-voltage harmonic control for stand-alone and weak-grid-tied converter, *IEEE Trans. Ind. Appl.*, vol. 56, no. 1, pp. 403421, 2020.

[6] Pérez-Estévez D. and Doval-Gandoy J., A finite-control-set linear current controller with fast transient response and low switching frequency for grid-tied inverters, *IEEE Trans. Ind. Appl.*, vol. 56, no. 6, pp. 65466564, 2020.

[7] Pérez-Estévez D. and Doval-Gandoy J., A model predictive current controller with improved robustness against measurement noise and plant model variations, *IEEE Open J. Ind. Appl.*, vol. 2, pp. 131142, 2021.

[8] Pérez-Estévez D., Doval-Gandoy J., Yepes A. G., Lopez O., and Baneira F., Improved resonant current controller for grid-tied converters, in *IEEE Energy Conv. Congress and Exp.*, Oct. 2017, pp. 38773884.

[9] Pérez-Estévez D., Doval-Gandoy J., Yepes A. G., Lopez O., and Baneira F., Positive- and negative-sequence current control based on direct discrete-time pole placement for grid-connected converters with lcl filter, in *IEEE Energy Conversion Congress and Exposition (ECCE)*, Sep. 2016, pp. 18.

[10] Pérez-Estévez D., Doval-Gandoy J., Yepes A. G., Lopez O., and Baneira F., Multi-frequency current controller for grid-tied converters, in *IEEE Energy Conv. Congress and Exp. (ECCE)*, Oct 2017, pp. 38973904.

[11] Pérez-Estévez D. and Doval-Gandoy J., AC voltage sensorless method with bumpless start for current-controlled converters connected to microgrids, in *IEEE Energy Conv. Congress and Exp.*, Sep. 2018, pp. 194201.

[12] Pérez-Estévez, Doval-Gandoy J., and Guerrero J. M., Robust AC voltage controller with harmonic elimination for stand-alone and weak-grid-connected operation, in *IEEE Energy Conv. Congress and Exp.*, Sep. 2018, pp. 48764883.

[13] Pérez-Estévez and Doval-Gandoy J., Linear current controller with fast transient response and low switching frequency, in *IEEE Energy Conv. Congress and Exp. (ECCE)*, Sep./Oct. 2019, pp. 69226928.

[14] Guerrero J. M., Vasquez J. C., Matas J., de Vicuna L. G., and Castilla M., Hierarchical control of droop-controlled AC and DC microgrids a general approach toward standardization, *IEEE Trans. Ind. Electron.*, vol. 58, no. 1, pp. 158172, Jan. 2011.

[15] Vidal A., Yepes A. G., Freijedo F. D., Malvar J., Lpez O., and Doval-Gandoy J., A technique to estimate the equivalent loss resistance of grid-tied converters for current control analysis and design, *IEEE Trans. Power Electron.*, vol. 30, no. 3, pp. 17471761, Mar. 2015.

[16] Karamanakos P., Geyer T., and Aguilera R. P., Long-horizon direct model predictive control: Modified sphere decoding for transient operation, *IEEE Trans. Ind. Appl.*, vol. 54, no. 6, pp. 60606070, Nov./Dec. 2018.

[17] Stellato B., Geyer T., and Goulart P. J., High-speed finite control set model predictive control for power electronics, *IEEE Trans. Power Electron.*, vol. 32, no. 5, pp. 40074020, May 2017.

[18] Aguilera R. P. and Quevedo D. E., Stability analysis of quadratic MPC with a discrete input alphabet, *IEEE Trans. Automat. Contr.*, vol. 58, no. 12, pp. 31903196, 2013.

[19] , Predictive control of power converters: Designs with guaranteed performance, *IEEE Trans. Ind. Inform.*, vol. 11, no. 1, pp. 5363, 2015.

[20] Karamanakos P., Geyer T., and Kennel R., On the choice of norm in finite control set model predictive control, *IEEE Trans. Power Electron.*, vol. 33, no. 8, pp. 71057117, 2018.

[21] Karamanakos P. and Geyer T., Guidelines for the design of finite control set model predictive controllers, *IEEE Trans. Power Electron.*, vol. 35, no. 7, pp. 74347450, 2020.

[22] Geyer T., Papafotiou G., and Morari M., Model predictive direct torque controlpart i: Concept, algorithm, and analysis, *IEEE Trans. Ind. Electron.*, vol. 56, no. 6, pp. 18941905, 2009.

[23] Geyer T. and Mastellone S., Model predictive direct torque control of a five-level ANPC converter drive system, *IEEE Trans. Ind. Appl.*, vol. 48, no. 5, pp. 15651575, 2012.

[24] Geyer T. and Quevedo D. E., Performance of multistep finite control set model predictive control for power electronics, *IEEE Trans. Power Electron.*, vol. 30, no. 3, pp. 16331644, 2015.

[25] Rodriguez J., Kazmierkowski M. P., Espinoza J. R., Zanchetta P., Abu-Rub H., Young H. A., and Rojas C. A., State of the art of finite control set model predictive control in power electronics, *IEEE Trans. Ind. Informat.*, vol. 9, no. 2, pp. 10031016, 2013.

[26] Rodriguez J., Pontt J., Silva C. A., Correa P., Lezana P., Cortes P., and Ammann U., Predictive current control of a voltage source inverter, *IEEE Trans. Ind. Electron.*, vol. 54, no. 1, pp. 495503, Feb. 2007.

[27] Chatterjee D. and Mazumder S. K., Switching-sequence control of a higher-order power-electronic system driving a pulsating load, *IEEE Trans. Power Electron.*, Early access 2019.

[28] Tajfar A. and Mazumder S. K., Sequence-based control of an isolated DC/AC matrix converter, *IEEE Trans. Power Electron.*, vol. 31, no. 2, pp. 17571773, Feb 2016.

[29] Busada C. A., Gmez Jorge S., and Solsona J. A., Full-state feedback equivalent controller for active damping in LCL-filtered grid-connected inverters using a reduced number of sensors, *IEEE Trans. Ind. Electron.*, vol. 62, no. 10, pp. 59936002, Oct. 2015.

[30] Wu X., Li X., Yuan X., and Geng Y., Grid harmonics suppression scheme for LCL-type grid-connected inverters based on output admittance revision, *IEEE Trans. Sust. Energy*, vol. 6, no. 2, pp. 411421, Mar./Apr. 2015.

[31] Abeyasekera T., Johnson C. M., Atkinson D. J., and Armstrong M., Suppression of line voltage related distortion in current controlled grid connected inverters, *IEEE Trans. Power Electron.*, vol. 20, no. 6, pp. 13931401, Nov. 2005.

[32] P. Xiao, K. A. Corzine, and G. K. Venayagamoorthy, Multiple reference frame-based control of three-phase PWM boost rectifiers under unbalanced and distorted input conditions, *IEEE Trans. Power Electron.*, vol. 23, no. 4, pp. 20062017, Jul. 2008.

[33] Chapman P. L. and Sudhoff S. D., A multiple reference frame synchronous estimator/regulator, *IEEE Trans. Energy Convers.*, vol. 15, no. 2, pp. 197202, Jun. 2000.

[34] Limongi L. R., Bojoi R., Griva G., and Tenconi A., Digital current-control schemes, *IEEE Ind. Electron. Mag.*, vol. 3, no. 1, pp. 2031, Mar. 2009.

[35] Rocabert J., Luna A., Blaabjerg F., and Rodrguez P., Control of power converters in ac microgrids, *IEEE Trans. Power Electron.*, vol. 27, no. 11, pp. 47344749, Nov. 2012.

[36] Harnefors L., Yepes A. G., Vidal A., and Doval-Gandoy J., Passivity-based stabilization of resonant current controllers with consideration of time delay, *IEEE Trans. Power Electron.*, vol. 29, no. 12, pp. 62606263, Dec. 2014.

[37] , Passivity-based controller design of grid-connected VSCs for prevention of electrical resonance instability, *IEEE Trans. Ind. Electron.*, vol. 62, no. 2, pp. 702710, Jan./Feb. 2015.

[38] Briz F., Garca P., Degner M. W., Daz-Reigosa D., and Guerrero J. M., Dynamic behavior of current controllers for selective harmonic compensation in three-phase active power filters, *IEEE Trans. Ind. Appl.*, vol. 49, no. 3, pp. 14111420, May/Jun. 2013.

[39] Li B., Yao W., Hang L., and Tolbert L. M., Robust proportional resonant regulator for grid-connected voltage source inverter (VSI) using direct pole placement design method, *IET Power Electron.*, vol. 5, no. 8, pp. 13671373, Sep. 2012.

[40] Vidal A., Freijedo F. D., Yepes A. G., Malvar J., Lpez O., and Doval-Gandoy J., Transient response evaluation of stationary-frame resonant current controllers for grid-connected applications, *IET Power Electron.*, vol. 7, no. 7, pp. 17141724, Jul. 2014.

[41] Liserre M., Teodorescu R., and Blaabjerg F., Stability of photovoltaic and wind turbine grid-connected inverters for a large set of grid impedance values, *IEEE Trans. Power Electron.*, vol. 21, no. 1, pp. 263272, Jan. 2006.

[42] Eldeeb H., Massoud A., Abdel-Khalik A. S., and Ahmed S., A sensorless kalman filter-based active damping technique for grid-tied vsi with LCL filter, *Int. J. Electr. Power Energy Syst.*, vol. 93, no. Supplement C, pp. 146 155, 2017.

[43] Xin Z., Mattavelli P., Yao W., Yang Y., Blaabjerg F., and Loh P. C., Mitigation of grid-current distortion for lcl-filtered voltage-source inverter with inverter-current feedback control, *IEEE Trans. Power Electron.*, vol. 33, no. 7, pp. 62486261, 2018.

[44] Li B., Zhang M., Huang L., Hang L., and Tolbert L. M., A new optimized pole placement strategy of grid-connected inverter with LCL-filter based on state variable feedback and state observer, in *App. Power Electron. Conf. and Exp. (APEC)*, Mar. 2013, pp. 29002906.

[45] Chen D., Zhang J., and Qian Z., An improved repetitive control scheme for grid-connected inverter with frequency-adaptive capability, *IEEE Trans. Ind. Electron.*, vol. 60, no. 2, pp. 814823, Feb. 2013.

[46] Buso S., Caldognetto T., and Brandao D. I., Dead-beat current controller for voltage-source converters with improved large-signal response, *IEEE Trans. Ind. Appl.*, vol. 52, no. 2, pp. 15881596, Mar. 2016.

[47] Parker S. G., McGrath B. P., and Holmes D. G., Regions of active damping control for LCL filters, IEEE Trans. Ind. Appl., vol. 50, no. 1, pp. 424432, Jan./Feb. 2014.

[48] Wang J., Yan J. D., Jiang L., and Zou J., Delay-dependent stability of single-loop controlled grid-connected inverters with LCL filters, *IEEE Trans. Power Electron.*, vol. 31, no. 1, pp. 743757, Jan. 2016.

[49] Dannehl J., Fuchs F. W., Hansen S., and Thogersen P. B., Investigation of active damping approaches for PI-based current control of grid-connected pulse width modulation converters with LCL filters, *IEEE Trans. Ind. Appl.*, vol. 46, no. 4, pp. 15091517, Jul./Aug. 2010.

[50] Wang X., Blaabjerg F., and Loh P. C., Grid-current-feedback active damping for LCL resonance in grid-connected voltage-source converters, *IEEE Trans. Power Electron.*, vol. 31, no. 1, pp. 213223, Jan. 2016.

[51] Xu J., Xie S., and Tang T., Active damping-based control for grid-connected LCL-filtered inverter with injected grid current feedback only, *IEEE Trans. Ind. Electron.*, vol. 61, no. 9, pp. 47464758, Sep. 2014.

[52] He J. and Li Y.W., Generalized closed-loop control schemes with embedded virtual impedances for voltage source converters with LC or LCL filters, *IEEE Trans. Power Electron.*, vol. 27, no. 4, pp. 18501861, Apr. 2012.

[53] Wang X., Li Y.W., Blaabjerg F., and Loh P. C., Virtual-impedance-based control for voltage-source and current-source converters, *IEEE Trans. Power Electron.*, vol. 30, no. 12, pp. 70197037, Dec 2015.

[54] Goodwin G. C., Graebe S. F., and Salgado M. E., *Control System Design*, 1st ed. Prentice Hall, 2001, p. 355.

[55] Vasquez J. C., Guerrero J. M., Savaghebi M., Eloy-Garcia J., and Teodorescu R., Modeling, analysis, and design of stationary-reference-frame droop-controlled parallel three-phase voltage source inverters, *IEEE Trans. Ind. Electron.*, vol. 60, no. 4, pp. 12711280, Apr. 2013.

[56] de Bosio F., de Souza Ribeiro L. A., Freijedo F. D., Pastorelli M., and Guerrero J. M., Effect of state feedback coupling and system delays on the transient performance of stand-alone vsi with lc output filter, *IEEE Trans. Ind. Electron.*, vol. 63, no. 8, pp. 49094918, Aug. 2016.

[57] Wang X., Loh P. C., and Blaabjerg F., Stability analysis and controller synthesis for single-loop voltage-controlled VSIs, *IEEE Trans. Power Electron.*, vol. 32, no. 9, pp. 73947404, Sep. 2017.

[58] Li Z., Li Y., Wang P., Zhu H., Liu C., and Gao F., Single-loop digital control of high-power 400-Hz ground power unit for airplanes, *IEEE Trans. Ind. Electron.*, vol. 57, no. 2, pp. 532543, Feb 2010.

[59] Buso S. and Mattavelli P., Digital Control in Power Electronics, J. Hudgins, Ed. Morgan & Claypool, 2006.

[60] Geng Y., Yun Y., Chen R., Wang K., Bai H., and Wu X., Parameters design and optimization for LC-type off-grid inverters with inductor-current feedback active damping, *IEEE Trans. Power Electron.*, vol. 33, no. 1, pp. 703715, Jan. 2018.

[61] Turner R., Walton S., and Duke R., Robust high-performance inverter control using discrete direct-design pole placement, *IEEE Trans. Ind. Electron.*, vol. 58, no. 1, pp. 348357, Jan. 2011.

[62] Kim H. S., Jung H. S., and Sul S. K., Discrete state-space voltage controller for voltage source inverters with LC filter based on direct pole-zero placement design, in *Applied Power Elec. Conf. and Exp.*, Mar. 2017, pp. 27512758.

[63] Quan X., Dou X., Wu Z., Hu M., Song H., and Huang A. Q., A novel dominant dynamic elimination control for voltage-controlled inverter, *IEEE Trans. Ind. Electron.*, vol. 65, no. 8, pp. 68006812, Aug. 2018.

[64] Jensen U. B., Blaabjerg F., and Pedersen J. K., A new control method for 400-Hz ground power units for airplanes, *IEEE Trans. Ind. Appl.*, vol. 36, no. 1, pp. 180187, Jan. 2000.

[65] Bose B. K., Global energy scenario and impact of power electronics in 21st century, *IEEE Trans. Ind. Electron.*, vol. 60, no. 7, pp. 26382651, Jul. 2013.

[66] Grnbaum R., Voltage and power quality control in wind power, in *Proc. Powergen Europe*, Brussels, 2001.

[67] Vidal A., Freijedo F. D., Yepes A. G., Malvar J., Lpez O., and Doval-Gandoy J., Transient response evaluation of stationary-frame resonant current controllers for grid-connected applications, IET Power Electron., vol. 7, no. 7, pp. 17141724, Jul. 2014.

[68] Bahrman M. P., Johansson J. G., and Nilsson B. A., Voltage source converter transmission technologies: the right fit for the application, in *Proc. IEEE Power Eng. Soc. Gen. Meeting*, vol. 3, Jul. 2003, p. 1847 Vol. 3.

[69] Channegowda P. and John V., Filter optimization for grid interactive voltage source inverters, *IEEE Trans. Ind. Electron.*, vol. 57, no. 12, pp. 41064114, Dec. 2010.

[70] Shen G., Zhu X., Zhang J., and D. Xu, A new feedback method for PR current control of LCL-filter-based grid-connected inverter, *IEEE Trans. Ind. Electron.*, vol. 57, no. 6, pp. 20332041, Jun. 2010.

[71] Yepes A. G., Freijedo F. D., Lpez O., and Doval-Gandoy J., Analysis and design of resonant current controllers for voltage-source converters by means of Nyquist diagrams and sensitivity function, *IEEE Trans. Ind. Electron.*, vol. 58, no. 11, pp. 52315250, Nov. 2011.

[72] Citro C., Siano P., and Cecati C., Designing inverters current controllers with resonance frequencies cancellation, *IEEE Trans. Ind. Electron.*, vol. 63, no. 5, pp. 30723080, May 2016.

[73] Huang L., Li B., Lu Z., Hang L., and Tolbert L., PR controller for grid-connected inverter control using direct pole placement strategy, in *Proc. IEEE ISIE*, May 2012, pp. 469474.

[74] Jia Y., Zhao J., and Fu X., Direct grid current control of LCL-filtered grid-connected inverter mitigating grid voltage disturbance, *IEEE Trans. Power Electron.*, vol. 29, no. 3, pp. 15321541, Mar. 2014.

[75] Komurcugil H., Altin N., Ozdemir S., and Sefa I., Lyapunov-function and proportional-resonant-based control strategy for single-phase grid-connected VSI with LCL filter, *IEEE Trans. Ind. Electron.*, vol. 63, no. 5, pp. 28382849, May 2016.

[76] Pan D., Ruan X., Bao C., Li W., and Wang X., Optimized controller design for LCL-type grid-connected inverter to achieve high robustness against grid-impedance variation, *IEEE Trans. Ind. Electron.*, vol. 62, no. 3, pp. 15371547, Mar. 2015.

[77] Busada C. A., Jorge S. G., and Solsona J. A., Resonant current controller with enhanced transient response for grid-tied inverters, *IEEE Trans. Ind. Electron.*, vol. 65, no. 4, pp. 29352944, 2018.

[78] Pea-Alzola R., Liserre M., Blaabjerg F., Sebastin R., Dannehl J., and Fuchs F. W., Analysis of the passive damping losses in LCL-filter-based grid converters, *IEEE Trans. Power Electron.*, vol. 28, no. 6, pp. 26422646, Jun. 2013.

[79] Tang Y., Loh P. C., Wang P., Choo F. H., Gao F., and Blaabjerg F., Generalized design of high performance shunt active power filter with output LCL filter, *IEEE Trans. Ind. Electron.*, vol. 59, no. 3, pp. 14431452, Mar. 2012.

[80] Hanif M., Khadkikar V., Xiao W., and Kirtley J. L., Two degrees of freedom active damping technique for LCL filter-based grid connected PV systems, *IEEE Trans. Ind. Electron.*, vol. 61, no. 6, pp. 27952803, Jun. 2014.

[81] Franklin G. F., Powell J. D., and Workman M. L., *Digital Control of Dynamic Systems*, 2nd ed. Addison Wesley Longman, Inc, 1990, p. 261.

[82] Astrom K. J., P. Hagander, and Sternby J., Zeros of sampled systems, *Automatica*, vol. 20, no. 1, pp. 31 38, 1984.

[83] Liserre M., Blaabjerg F., and Hansen S., Design and control of an LCL-filter-based three-phase active rectifier, *IEEE Trans. Ind. Appl.*, vol. 41, no. 5, pp. 12811291, Sep./Oct. 2005.

[84] Rodrguez P., Timbus A. V., Teodorescu R., Liserre M., and Blaabjerg F., Flexible active power control of distributed power generation systems during grid faults, *IEEE Trans. Ind. Electron.*, vol. 54, no. 5, pp. 25832592, Oct. 2007.

[85] Bollen M. H., *Understanding Power Quality Problems: Voltage Sags and Interruptions*, 1st ed. Wiley, 1999, p. 194.

[86] Etxeberria-Otadui I., Heredia A. L. D., Gaztanaga H., Bacha S., and Reyero M. R., A single synchronous frame hybrid (SSFH) multifrequency controller for power active filters, *IEEE Trans. Ind. Electron.*, vol. 53, no. 5, pp. 16401648, Oct. 2006.

[87] Yepes A. G., Vidal A., Lpez O., and Doval-Gandoy J., Evaluation of techniques for cross-coupling decoupling between orthogonal axes in double synchronous reference frame current control, *IEEE Trans. Ind. Electron.*, vol. 61, no. 7, pp. 35273531, Jul. 2014.

[88] Pea-Alzola R., Liserre M., Blaabjerg F., Sebastin R., Dannehl J., and Fuchs F. W., Systematic design of the lead-lag network method for active damping in LCL-filter based three phase converters, *IEEE Trans. Ind. Informat.*, vol. 10, no. 1, pp. 4352, Feb. 2014.

[89] Wu E. and Lehn P. W., Digital current control of a voltage source converter with active damping of LCL resonance, *IEEE Trans. Power Electron.*, vol. 21, no. 5, pp. 13641373, Sep. 2006.

[90] Bahrani B., Vasiladiotis M., and Rufer A., High-order vector control of grid-connected voltage-source converters with LCL-filters, *IEEE Trans. Ind. Electron.*, vol. 61, no. 6, pp. 27672775, Jun. 2014.

[91] Meyer R., Zlotnik A., and Mertens A., Fault ride-through control of medium-voltage converters with LCL filter in distributed generation systems, *IEEE Trans. Ind. Appl.*, vol. 50, no. 5, pp. 34483456, Sep./Oct. 2014.

[92] Panten N., Hoffmann N., and Fuchs F. W., Finite control set model predictive current control for grid-connected voltage-source converters with LCL filters: A study based on different state feedbacks, *IEEE Trans. Power Electron.*, vol. 31, no. 7, pp. 51895200, Jul. 2016.

[93] Nishida K., Ahmed T., and Nakaoka M., A novel finite-time settling control algorithm designed for grid-connected three-phase inverter with an LCL-type filter, *IEEE Trans. Ind. Appl.*, vol. 50, no. 3, pp. 20052020, May/Jun. 2014.

[94] Mohamed Y. A. R. I., Rahman M. A., and Seethapathy R., Robust line-voltage sensorless control and synchronization of LCL-filtered distributed generation inverters for high power quality grid connection, *IEEE Trans. Power Electron.*, vol. 27, no. 1, pp. 8798, Jan. 2012.

[95] Massing J. R., Stefanello M., Grundling H. A., and Pinheiro H., Adaptive current control for grid-connected converters with LCL filter, *IEEE Trans. Ind. Electron.*, vol. 59, no. 12, pp. 46814693, Dec. 2012.

[96] Gabe I. J., Montagner V. F., and Pinheiro H., Design and implementation of a robust current controller for VSI connected to the grid through an LCL filter, *IEEE Trans. Power Electron.*, vol. 24, no. 6, pp. 14441452, Jun. 2009.

[97] Xue M., Zhang Y., Kang Y., Yi Y., Li S., and Liu F., Full feedforward of grid voltage for discrete state feedback controlled grid-connected inverter with LCL filter, *IEEE Trans. Power Electron.*, vol. 27, no. 10, pp. 42344247, Oct. 2012.

[98] Kukkola J. and Hinkkanen M., Observer-based state-space current control for a three-phase grid-connected converter equipped with an LCL filter, IEEE Trans. Ind. Appl., vol. 50, no. 4, pp. 27002709, Jul./Aug. 2014.

[99] Kukkola J., Hinkkanen M., and Zenger K., Observer-based state-space current controller for a grid converter equipped with an LCL filter: Analytical method for direct discrete-time design, *IEEE Trans. Ind. Appl.*, vol. 51, no. 5, pp. 40794090, Sep./Oct. 2015.

[100] Dannehl J., Fuchs F. W., and Thogersen P. B., PI state space current control of grid-connected PWM converters with LCL filters, *IEEE Trans. Power Electron.*, vol. 25, no. 9, pp. 23202330, Sep. 2010.

[101] Ramos C., Martins A., and Carvalho A., Complex state-space current controller for grid-connected converters with an LCL filter, in *Proc. IEEE IECON*, Nov. 2009, pp. 296301.

[102] Maccari L. A., Massing J. R., Schuch L., Rech C., Pinheiro H., Oliveira R. C. L. F., and Montagner V. F., LMI-based control for grid-connected converters with LCL filters under uncertain parameters, *IEEE Trans. Power Electron.*, vol. 29, no. 7, pp. 37763785, Jul. 2014.

[103] Maksimovic D. and Zane R., Small-signal discrete-time modeling of digitally controlled PWM converters, *IEEE Trans. Power Electron.*, vol. 22, no. 6, pp. 25522556, Nov. 2007.

[104] de Sype D. M. V., Gusseme K. D., Belie F. M. L. L. D., den Bossche A. P. V., and Melkebeek J. A., Small-signal z-domain analysis of digitally controlled converters, *IEEE Trans. Power Electron.*, vol. 21, no. 2, pp. 470478, Mar. 2006.

[105] Zhang X., Spencer J. W., and Guerrero J. M., Small-signal modeling of digitally controlled grid-connected inverters with LCL filters, *IEEE Trans. Ind. Electron.*, vol. 60, no. 9, pp. 37523765, Sep. 2013.

[106] Li Y. W. and Kao C. N., An accurate power control strategy for power-electronics-interfaced distributed generation units operating in a low-voltage multibus microgrid, IEEE Trans. Power Electron., vol. 24, no. 12, pp. 29772988, Dec. 2009.

[107] Freijedo F. D., Doval-Gandoy J., Lpez O., and Acha E., Tuning of phase-locked loops for power converters under distorted utility conditions, *IEEE Trans. Ind. Appl.*, vol. 45, no. 6, pp. 20392047, Nov./Dec. 2009.

[108] Davari M. and Mohamed Y. A.-R. I., Robust vector control of a very weak-grid-connected voltage-source converter considering the phase-locked loop dynamics, *IEEE Trans. Power Electron.*, vol. 32, no. 2, pp. 977994, 2017.

[109] Dong D., Wen B., Boroyevich D., Mattavelli P., and Xue Y., Analysis of phase-locked loop low-frequency stability in three-phase grid-connected power converters considering impedance interactions, *IEEE Trans. Ind. Electron.*, vol. 62, no. 1, pp. 310321, Jan. 2015.

[110] IEEE, Recommended practice and requirements for harmonic control in electric power systems, *IEEE Std 519-2014*, pp. 129, Jun. 2014.

[111] Voltage characteristics of electricity supplied by public distribution systems, CENELEC EN 50160 Std.

[112] Yepes A. G., Malvar J., Vidal A., Lpez O., and Doval-Gandoy J., Current harmonics compensation based on multiresonant control in synchronous frames for symmetrical n-phase machines, *IEEE Trans. Ind. Electron.*, vol. 62, no. 5, pp. 27082720, May 2015.

[113] Mohtadi C., Bodes integral theorem for discrete-time systems, *IEE Proceedings D - Control Theory and Applications*, vol. 137, no. 2, pp. 5766, Mar. 1990.

[114] Papoulis A. and Pillai S. U., *Probability, Random Variables and Stochastic Processes*, McGraw-Hill, Ed. McGraw-Hill, 2002.

[115] Lu M., Wang X., Blaabjerg F., Muyeen S. M., Al-Durra A., and Leng S., Grid-voltage-feedforward active damping for grid-connected inverter with LCL filter, in *App. Power Electron. Conf. and Exp. (APEC)*, Mar. 2016, pp. 19411946.

[116] Prez-Estvez D. and Doval-Gandoy J., Grid-tied inverter with AC voltage sensorless synchronization and soft start, *IEEE Trans. Ind. Appl.*, vol. 55, no. 5, pp. 49204933, 2019.

[117] Boyra M. and Thomas J. L., A review on synchronization methods for grid-connected three-phase VSC under unbalanced and distorted conditions, in *Eur. Conf. on Pow. Electron. and App.*, Aug. 2011, pp. 110.

[118] Zhou S., Zou X., Zhu D., Tong L., Zhao Y., Kang Y., and Yuan X., An improved design of current controller for LCL-type grid-connected converter to reduce negative effect of PLL in weak grid, *IEEE J. Emerg. Sel. Topics Power Electron.*, vol. 6, no. 2, pp. 648663, Jun. 2018.

[119] Zhang X., Xia D., Fu Z., Wang G., and D. Xu, An improved feedforward control method considering pll dynamics to improve weak grid stability of grid-connected inverters, *IEEE Trans. Ind. Appl.*, vol. 54, no. 5, pp. 51435151, 2018.

[120] Roslan N. F., Suul J. A., Rocabert J., and Rodriguez P., A comparative study of methods for estimating virtual flux at the point of common coupling in grid-connected voltage source converters with LCL filter, *IEEE Trans. Ind. Appl.*, vol. 53, no. 6, pp. 57955809, Nov.-Dec. 2017.

[121] Suul J. A., Luna A., Rodriguez P., and Undeland T., Voltage-sensor-less synchronization to unbalanced grids by frequency-adaptive virtual flux estimation, *IEEE Trans. Ind. Electron.*, vol. 59, no. 7, pp. 29102923, Jul. 2012.

[122] Malinowski M., Kazmierkowski M. P., Hansen S., Blaabjerg F., and Marques G. D., Virtual-flux-based direct power control of three-phase PWM rectifiers, *IEEE Trans. Ind. Appl.*, vol. 37, no. 4, pp. 10191027, Jul.-Aug. 2001.

[123] Gholami-Khesht H. and Monfared M., Novel grid voltage estimation by means of the newton-raphson optimisation for three-phase grid connected voltage source converters, *IET Pow. Electron.*, vol. 7, no. 12, pp. 29452953, Dec. 2014.

[124] Gholami-Khesht H., Monfared M., and Golestan S., Low computational burden grid voltage estimation for grid connected voltage source converter-based power applications, *IET Pow. Electron.*, vol. 8, no. 5, pp. 656664, May 2015.

[125] Jorge S. G., Solsona J. A., and Busada C. A., Control scheme for a single-phase grid-tied voltage source converter with reduced number of sensors, *IEEE Trans. Power Electron.*, vol. 29, no. 7, pp. 37583765, Jul. 2014.

[126] Kukkola J. and Hinkkanen M., State observer for grid-voltage sensorless control of a converter under unbalanced conditions, *IEEE Trans. Ind. Appl.*, vol. 54, no. 1, pp. 286297, 2018.

[127] Kukkola J. and Hinkkanen M., State observer for grid-voltage sensorless control of a converter equipped with an LCL filter: Direct discrete-time design, *IEEE Trans. Ind. Appl.*, vol. 52, no. 4, pp. 31333145, Jul. 2016.

[128] Wang B., Xu Y., Shen Z., Zou J., Li C., and Liu H., Current control of grid-connected inverter with LCL filter based on extended-state observer estimations using single sensor and achieving improved robust observation dynamics, *IEEE Trans. Ind. Electron.*, vol. 64, no. 7, pp. 54285439, Jul. 2017.

[129] Ketzer M. B. and Jacobina C. B., Sensorless control technique for PWM rectifiers with voltage disturbance rejection and adaptive power factor, *IEEE Trans. Ind. Electron.*, vol. 62, no. 2, pp. 11401151, Feb 2015.

[130] IEEE standard for interconnecting distributed resources with electric power systems, *IEEE Std 1547-2003*, pp. 128, Jul. 2003.

[131] Freijedo F. D., Doval-Gandoy J., O. Lopez, and Acha E., Tuning of phase-locked loops for power converters under distorted utility conditions, *IEEE Trans. Ind. Appl.*, vol. 45, no. 6, pp. 20392047, Nov. 2009.

[132] He J., Li Y. W., Wang R., and Zhang C., Analysis and mitigation of resonance propagation in grid-connected and islanding microgrids, *IEEE Trans. Energy Conv.*, vol. 30, no. 1, pp. 7081, Mar. 2015.

[133] He J., Li Y. W., and Blaabjerg F., Flexible microgrid power quality enhancement using adaptive hybrid voltage and current controller, *IEEE Trans. Ind. Electron.*, vol. 61, no. 6, pp. 27842794, Jun. 2014.

[134] Wen B., Boroyevich D., R. Burgos, and Mattavelli P., Modeling the output impedance of three-phase uninterruptible power supply in D-Q frame, in *Energy Conv. Congress and Exp. (ECCE)*, Sep. 2014, pp. 163169.

[135] Uninterruptible power systems (UPS) - Part 3: Method of specifying the performance and test requirements, *IEC 62040-3 Std.*

[136] Kim H.-S. and Sul S.-K., A novel filter design for output LC filters of PWM inverters, *J. Power Electron.*, vol. 11, Jan. 2011.

[137] Camacho E., Bordons C., and Alba C., Model Predictive Control, ser. *Advanced Textbooks in Control and Signal Processing*. Springer London, 2004.

[138] Busada C. A., Jorge S. G., and Solsona J. A., A synchronous reference frame PI current controller with dead beat response, *IEEE Trans. Power Electron.*, vol. 35, no. 3, pp. 30973105, Mar. 2020.

[139] Electromagnetic compatibility (emc) - part 3-2: Limits - limits for harmonic current emissions (equipment input current ¡16 a per phase), *IEC 61000-3-2*, pp. 173, Jan. 2018.

[140] IEEE recommended practice for industrial and commercial power systems analysis (Brown Book), *IEEE Std 399-1997*, pp. 1488, Aug 1998.

[141] Holmes D. G. and Lipo T. A., Pulse Width Modulation for Power Converters: Principles and Practice. *IEEE*, 2003.

[142] Prez-Estvez D. and Doval-Gandoy J., Grid impedance identification using the VSC switching ripple, in *IEEE Energy Conv. Congress and Exp. (ECCE)*, Sep./Oct. 2019.

[143] Rockhill A. A., Liserre M., Teodorescu R., and Rodriguez P., Grid-filter design for a multimegawatt medium-voltage voltage-source inverter, *IEEE Trans. Ind. Electron.*, vol. 58, no. 4, pp. 12051217, Apr. 2011.

[144] Zabaleta M., Burguete E., Madariaga D., Zubimendi I., Zubiaga M., and Larrazabal I., LCL grid filter design of a multimegawatt medium-voltage converter for offshore wind turbine using shepwm modulation, *IEEE Trans. Power Electron.*, vol. 31, no. 3, pp. 19932001, Mar. 2016.

[145] Kantar E. and Hava A. M., Optimal design of grid-connected voltage-source converters considering cost and operating factors, *IEEE Trans. Ind. Electron.*, vol. 63, no. 9, pp. 53365347, Sep. 2016.

[146] Park K., Kieferndorf F. D., Drofenik U., Pettersson S., and Canales F., Weight minimization of LCL filters for high-power converters: Impact of PWM method on power loss and power density, *IEEE Trans. Ind. Appl.*, vol. 53, no. 3, pp. 22822296, May 2017.

[147] Electromagnetic compatibility (EMC) - part 3-4: Limits - limitation of emission of harmonic currents in low-voltage power supply systems for equipment with rated current greater than 16 a, *IEC 61000-3-4*, pp. 129, Oct. 1998.

[148] E. am mittelspannungsnetz, *Verlags- und wirtschaftsgesellschaft der elecktrizitätswerke m.b.h.VWEW*, Frankfurt, Germany, pp. 129, Dec. 1998.

[149] "Electromagnetic compatibility (emc) - part 4-7: Testing and measurement techniques - general guide on harmonics and interharmonics measurements and instrumentation, for power supply systems and equipment connected thereto," *IEC 61000-4-7*, pp. 114, Jan. 2018.

[150] Nahalparvari M., Karamanakos P., and Geyer T., Gradient-based fixed switching frequency direct model predictive control for grid-connected converters with LCL filters, in *European Conf. on Power Electron. and Applications*, 2019, pp. P.1P.10.

[151] Dorfling T., du Toit Mouton H., Geyer T., and Karamanakos P., Long-horizon finite-control-set model predictive control with nonrecursive sphere decoding on an FPGA, *IEEE Trans. Power Electron.*, vol. 35, no. 7, pp. 75207531, 2020.

[152] Karamanakos P., Liegmann E., Geyer T., and Kennel R., Model predictive control of power electronic systems: Methods, results, and challenges, *IEEE Open J. Ind. Appl.*, vol. 1, pp. 95114, 2020.

[153] Vazquez S., Rodriguez J., Rivera M., Franquelo L. G., and Norambuena M., Model predictive control for power converters and drives: Advances and trends, *IEEE Trans. Ind. Electron.*, vol. 64, no. 2, pp. 935947, 2017.

[154] Karamanakos P. and Geyer T., Guidelines for the design of finite control set model predictive controllers, *IEEE Trans. Power Electron.*, vol. 35, no. 7, pp. 74347450, 2020.

[155] Bonab S. A. and Emadi A., Mpc-based energy management strategy for an autonomous hybrid electric vehicle, *IEEE Open J. Ind. Appl.*, vol. 1, pp. 171180, 2020.

[156] Dewar D., Rohten J., Formentini A., and Zanchetta P., Decentralised optimal controller design of variable frequency three-phase power electronic networks accounting for sub-system interactions, *IEEE Open J. Ind. Appl.*, vol. 1, pp. 270282, 2020.

[157] Karamanakos P., Nahalparvari M., and Geyer T., Fixed switching frequency direct model predictive control with continuous and discontinuous modulation for grid-tied converters with LCL filters, *IEEE Trans. Control Sys. Tech.*, pp. 116, 2020.

[158] Karamanakos P., Geyer T., N. Oikonomou, Kieferndorf F. D., and S. Manias, Direct model predictive control: A review of strategies that achieve long prediction intervals for power electronics, *IEEE Ind. Electron. Mag.*, vol. 8, no. 1, pp. 3243, 2014.

[159] Geyer T., Karamanakos P., and Kennel R., On the benefit of long-horizon direct model predictive control for drives with lc filters, in *2014 IEEE Energy Conversion Congress and Exposition (ECCE)*, 2014, pp. 35203527.

[160] Dorfling T., du Toit Mouton H., Geyer T., and Karamanakos P., Long-horizon finite-control-set model predictive control with nonrecursive sphere decoding on an FPGA, *IEEE Trans. Power Electron.*, vol. 35, no. 7, pp. 75207531, 2020.

[161] Geyer T. and Quevedo D. E., Multistep finite control set model predictive control for power electronics, *IEEE Trans. Power Electron.*, vol. 29, no. 12, pp. 68366846, 2014.

[162] Andersson A. and Thiringer T., Assessment of an improved finite control set model predictive current controller for automotive propulsion applications, *IEEE Trans. Ind. Electron.*, vol. 67, no. 1, pp. 91100, 2020.

[163] Hassibi B. and Vikalo H., On the sphere-decoding algorithm i. expected complexity, *IEEE Transs on Signal Process.*, vol. 53, no. 8, pp. 28062818, 2005.

[164] Han Y., Gong C., Yan L., Wen H., Wang Y., and Shen K., Multiobjective finite control set model predictive control using novel delay compensation technique for PMSM, *IEEE Trans. Power Electron.*, vol. 35, no. 10, pp. 11 19311 204, 2020.

[165] Parvez Akter M., Mekhilef S., Mei Lin Tan N., and Akagi H., Modified model predictive control of a bidirectional ac-dc converter based on lyapunov function for energy storage systems, *IEEE Trans. Ind. Electron.*, vol. 63, no. 2, pp. 704715, 2016.

[166] Dragicevic T., Model predictive control of power converters for robust and fast operation of AC microgrids, *IEEE Trans. Power Electron.*, vol. 33, no. 7, pp. 63046317, 2018.

[167] Zhang Y., Liu J., Yang H., and Fan S., New insights into model predictive control for three-phase power converters, *IEEE Trans. Ind. Appl.*, vol. 55, no. 2, pp. 19731982, 2019.

[168] Rohten J. A., Espinoza J. R., Munoz J. A., Perez M. A., Melin P. E., Silva J. J., Espinosa E. E., and Rivera M. E., Model predictive control for power converters in a distorted three-phase power supply, *IEEE Trans. Ind. Electron.*, vol. 63, no. 9, pp. 58385848, 2016.

[169] Cortes P., Rodriguez J., Silva C., and Flores A., Delay compensation in model predictive current control of a three-phase inverter, *IEEE Trans. Ind. Electron.*, vol. 59, no. 2, pp. 13231325, 2012.

[170] Xue C., Ding L., Li Y., and Zargari N. R., Improved model predictive control for high-power current-source rectifiers under normal and distorted grid conditions, *IEEE Trans. Power Electron.*, vol. 35, no. 5, pp. 45884601, 2020.

[171] Wallscheid O. and Ngoumtsa E. F. B., Investigation of disturbance observers for model predictive current control in electric drives, *IEEE Trans. Power Electron.*, vol. 35, no. 12, pp. 13 56313 572, 2020.

[172] Zhang X., Zhang L., and Zhang Y., Model predictive current control for pmsm drives with parameter robustness improvement, *IEEE Trans. Power Electron.*, vol. 34, no. 2, pp. 16451657, 2019.

[173] Alam K. S., Akter M. P., Xiao D., Zhang D., and Rahman M. F., Asymptotically stable predictive control of grid-connected converter based on discrete space vector modulation, *IEEE Trans. Ind. Inform.*, vol. 15, no. 5, pp. 27752785, 2019.

[174] Yaramasu V., Rivera M., Wu B., and Rodriguez J., Model predictive current control of two-level four-leg invertersPart I: Concept, algorithm, and simulation analysis, *IEEE Trans. Power Electron.*, vol. 28, no. 7, pp. 34593468, 2013.

[175] Wallscheid O. and Ngoumtsa E. F. B., Investigation of disturbance observers for model predictive current control in electric drives, *IEEE Trans. Power Electron.*, vol. 35, no. 12, pp. 13 56313 572, 2020.

[176] Wallscheid O., Specht A., and Bocker J., Observing the permanent-magnet temperature of synchronous motors based on electrical fundamental wave model quantities, *IEEE Trans. Ind. Electron.*, vol. 64, no. 5, pp. 39213929, 2017.

[177] Li J., Huang X., Niu F., You C., Wu L., and Fang Y., Prediction error analysis of finite-control-set model predictive current control for IPMSMs, *Energies*, vol. 11, no. 8, 2018.

[178] Jia C., Wang X., Liang Y., and Zhou K., Robust current controller for IPMSM drives based on explicit model predictive control with online disturbance observer, *IEEE Access*, vol. 7, pp. 45 89845 910, 2019.

[179] Yin Z., Han X., Du C., Liu J., and Zhong Y., Research on model predictive current control for induction machine based on immune-optimized disturbance observer, *IEEE J. Emerg. Sel. Topics Power Electron.*, vol. 6, no. 4, pp. 16991710, 2018.

[180] Abdelrahem M., Hackl C. M., Kennel R., and Rodriguez J., Efficient direct-model predictive control with discrete-time integral action for PMSGs, *IEEE Transactions on Energy Conversion*, vol. 34, no. 2, pp. 10631072, 2019.

[181] Wang J., Wang F., Zhang Z., Li S., and Rodriguez J., Design and implementation of disturbance compensation-based enhanced robust finite control set predictive torque control for induction motor systems, *IEEE Trans. Ind. Informat.*, vol. 13, no. 5, pp. 26452656, 2017.

[182] Harnefors L., Yepes A. G., Vidal A., and Doval-Gandoy J., Multifrequency current control with distortion-free saturation, *IEEE J. Emerg. Sel. Topics Power Electron.*, vol. 4, no. 1, pp. 3743, Mar. 2016.

[183] Norambuena M., Rodriguez J., Zhang Z., Wang F., Garcia C., and Kennel R., A very simple strategy for high-quality performance of AC machines using model predictive control, *IEEE Trans. Power Electron.*, vol. 34, no. 1, pp. 794800, 2019.

[184] Acuna P., Moran L., Rivera M., Aguilera R., Burgos R., and Agelidis V. G., A single-objective predictive control method for a multivariable single-phase three-level npc converter-based active power filter, *IEEE Trans. Ind. Electron.*, vol. 62, no. 7, pp. 45984607, 2015.

[185] Wang X., Taul M. G., Wu H., Liao Y., Blaabjerg F., and Harnefors L., Grid-synchronization stability of converter-based resourcesan overview, *IEEE Open J. Ind. Appl.*, vol. 1, pp. 115134, 2020.

Chapter 2

State-of-the-Art Multi-Phase Windings Types

Ayman Samy Abdel-Khalik[1,*]**, Mohamed Y. Metwly**[1]**,**
Ahmed Massoud[2] **and Shehab Ahmed**[3]
[1]Department of Electrical Engineering, Alexandria University, Alexandria, Egypt
[2]Department of Electrical Engineering, Qatar University, Doha, Qatar
[3]CEMSE Division, King Abdullah University of Science and Technology,
Saudi Arabia

Abstract

Multiphase machines have attracted significant attention in academic and industrial sectors as candidates for high-power safety-critical applications and wind energy conversion systems. Premierly, this chapter introduces the state-of-the-art in multiphase machine winding topologies. This typically considers the winding layouts employed in multiphase induction machines with prime phase and multiple three-phase orders. This chapter also provides some recent winding topologies that offer better machine characteristics in terms of torque density, efficiency, and fault-tolerance capability. One of the major problems when dealing with a prime number of phases, either in academic research or industrial applications, is the special stator design. Thus, a general technique to rewind standard off-the-shelf three-phase stator frames with any general prime phase order is introduced while preserving the same copper volume.

Keywords: multi-phase induction machine, quadruple three-phase winding, high-power machines, stator winding configuration, fault-tolerant operation, optimal slot/pole combination

1. Introduction

Employing polyphase machines with high phase order in high-power safety-critical applications has attracted the attention of both academia and industry in the last two decades. This was driven by the concurrent need for high-performance drive systems and rigorous reliability standards [1, 2]. Multiphase machines are advantageous over their three-phase counterparts in many ways. The converter rating per phase is reduced by splitting the power

---
*Corresponding Author's Email: ayman.abdel-khalik@alexu.edu.eg.

among more phases while offering improved fault tolerance [3]. Moreover, when compared to three-phase machines, multiphase machines offer a similar high-quality magnetomotive force (MMF) flux distribution, while the number of slots per pole per phase is reduced. It is worth mentioning that winding layouts with a single-coil per pole per phase are known as concentrated overlapping winding.

Multiphase induction machines (IMs) can be modeled as multiple decoupled sequence planes after using an appropriate transformation [4, 5, 6]. Each plane corresponds to a particular sequence. For an odd number of phases, n, the corresponding number of planes is $(n-1)/2$, with one zero sequence. However, $n/2$ planes correspond to even number of phases. For a six-phase system, the number of orthogonal subspaces will be three, namely, the fundamental $\alpha\beta$ subspace, the secondary xy subspace, and the zero-sequence $0^+ \, 0^-$ subspace. It is well known that each subspace gives rise to a different air gap flux distribution, which is highly dependent on the winding layout [7]. For example, the fundamental $\alpha\beta$ subspace produces an air gap flux with a fundamental flux distribution and is mostly considered as the dominant torque/flux producing subspace. On the other hand, both secondary xy and $0^+ \, 0^-$ subspaces produce zero magnetizing flux, while they only correspond to small leakage flux components. This assumption has been predominately used to simplify the machine modeling, although the generalization of this assumption to any winding layout yields notable inaccuracies [8].

Several winding layouts, with either a single- or double-layer, have been proposed in the literature, shedding light on the fundamental winding factor, flux distribution, and winding simplicity [9, 10, 11, 12, 13]. Single-layer winding layouts are commonly used for multiphase machines of prime phase order, e.g., five-, seven-, and eleven-phase machines. However, multiple three-phase machines employ double-layer winding configurations, e.g., six- and nine-phase machines. One of the main operating challenges of machines with conventional six-phase double-layer winding layouts, when supplied from a voltage source inverter, is the significant amplitude of the induced circulating harmonic current components due to the relatively low impedance of the secondary x-y subspace [14]. This problem is commonly mitigated in the literature by employing multilevel inverters [15] and proper PWM modulation techniques [16, 17]. In [18], the nine-phase six-terminal (9P6T) winding recently emerged as an effective winding topology to employ single-layer winding layouts in medium voltage high-power IMs. This layout offers a more straightforward winding construction for such high-power machines, improving the fundamental winding factor of approximately 5% over the traditional asymmetrical six-phase (A6P) winding with the same copper volume. Stators with a single-layer winding also allow for a higher possible filling factor and more resilient insulation requirements. Interestingly enough, the circulating harmonic currents were highly suppressed when the 9P6T winding is used, owing to the relatively higher secondary subspace impedance when a single-layer winding is employed [19].

This chapter introduces several winding layouts proposed in the literature for multiphase induction machines, as shown in Figure 1. Since multiphase machines are mainly proposed for high-power applications, improved fundamental winding factor and flux distribution, and simple winding layout are amongst the main design objectives of such machines. Due to their high-quality flux production, double-layer winding layouts are commonly employed with conventional three-phase induction machines. However, increasing

the number of phases stands as a simple technique to ensure a high-quality air gap flux distribution while a single-layer winding layout is preserved. This point is first explained in detail, and the most suitable winding layouts for different phase orders are also presented. Another important aspect related to the multiphase system is its high fault tolerance capability. Some other innovative winding layouts are introduced to suppress the flux components of the secondary subspace, which degrade the machine performance. Eventually, a simple technique to rewind standard three-phase stator frames with any n-phase symmetrical prime phase order winding is elaborated.

2.   Conventional Multiphase Winding Layouts

Multiphase winding configurations are classified into single- and double-layer windings with a further classification by the spatial phase shift between the winding sets δ: dual n-phase ($\delta = 0^0$), symmetrical n-phase ($\delta = 2\pi/n$), and asymmetrical n-phase ($\delta = \pi/n$) configurations. Basically, the stators with prime phase order adopt single-layer winding arrangements; however, stators with composite phase orders usually employ double-layer winding layouts. The former generally offers a better torque/current production; therefore, the maximum achievable torque will be higher than other possible alternatives [20, 21]. Besides, the fault-tolerance capability can be further enhanced through different stator winding connections [22]. On the other hand, it is fair to acknowledge that induction machines (IMs) with prime phase order entail custom-made power converters and stator cores with special designs, where the number of stator slots should be an integer multiple of the phase order. Unfortunately, the most available standard three-phase stator frames cannot be rewound with another balanced winding with a prime phase order in a simple and direct manner. Therefore, the application of multiphase machines with prime phase order still has not met a considerable interest in practical industrial sectors. However, the stators with composite phase orders can simply utilize the readily commercial off-the-shelf three-phase power converters [23]. That was mainly the reason behind the widespread utilization of six-phase machines in practical industrial sectors. Recent literature also proposed simple techniques to rewind standard three-phase stators with multiphase windings without many practical constraints [9, 23].

The design of multiphase windings constitutes assigning coils in the stator slots to several phases, defining the current direction in coil sides, selecting coil connection per phase and between phases, and measuring number of turns per coil and conductor size [24].

2.1.   Single-Layer-Based Conventional Winding Design with Prime Phase Order

When designing a single-layer-based winding configuration for a multiphase IM with a prime phase order, it is crucial to determine the number of slots per pole per phase q:

$$q = \frac{S}{2p.m} \tag{1}$$

where S is the number of slots, p number of pole pairs. The optimal value of q for both five- and seven-phase IMs is 2. However, q is preferably set to 1 for eleven-phase IM. For ex-
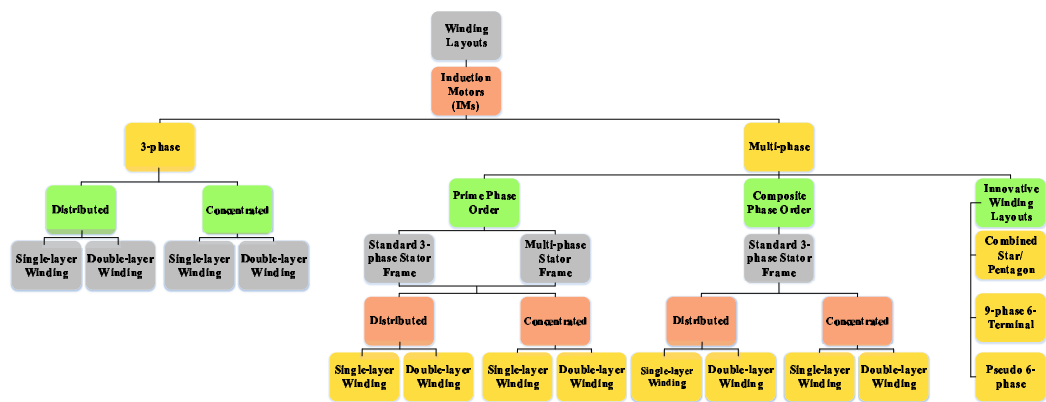
Figure 1. Induction machine winding layouts.

ample, the number of slots for 2-pole five- and seven-phase IM are 20 and 28, respectively. The corresponding winding layouts are shown in Figure 2.
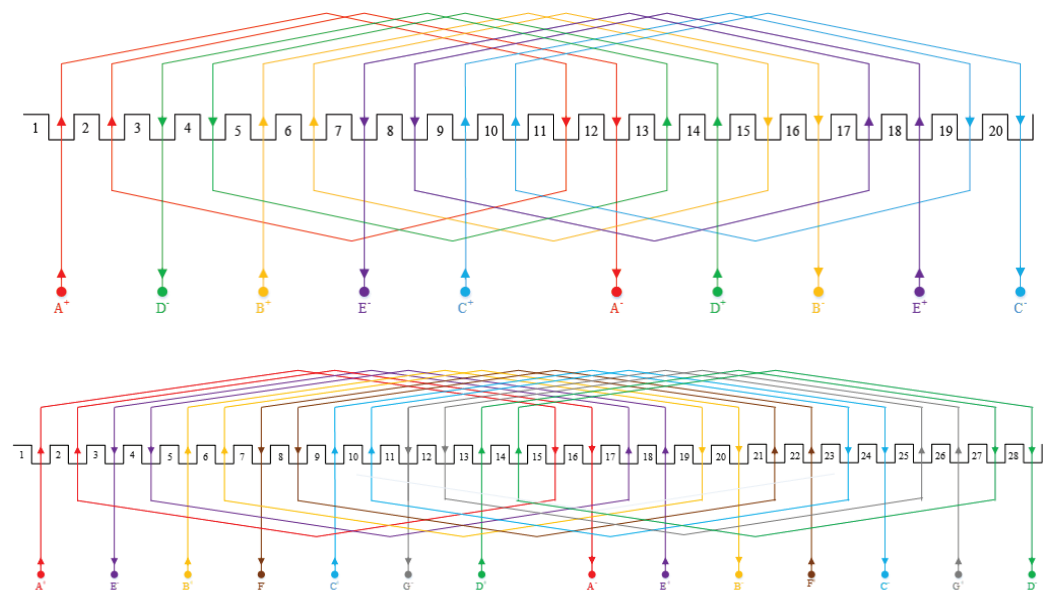
Figure 2. Conventional prime-phase-based winding layouts. (upper) five-phase. (bottom) seven-phase.

This subsection presents the design of several multiphase IMs with prime phase order, namely three-, five-, seven-, and eleven-phase IMs [25]. This is supported by introducing a mathematical means of calculating the parameters of equivalent multiphase machines with any number of phases based on the knowledge of an existing machine. To facilitate the evaluation of the various stator designs, the same phase current, as well as flux per pole, is

used in all machines. Additionally, a set of constant volume and identical lamination design rotors differing only in their value of bar skew angle for compatibility with the various machines are utilized [6]. The rotor design ensures proper operation without parasitic torque or cogging problems. The rotor parameters calculation technique, introduced in [26, 27], has also been generalized to the n-phase case to investigate the effect of increasing the stator number of phases on the machine's parameters. The design procedure follows the steps given in reference [24] but with a single-layer stator winding and 30 rotor bars. Moreover, torque enhancement in multiphase induction machines using harmonic current injection has been extensively addressed in [25]. The four designs and their corresponding winding layouts are shown in Figure 3.
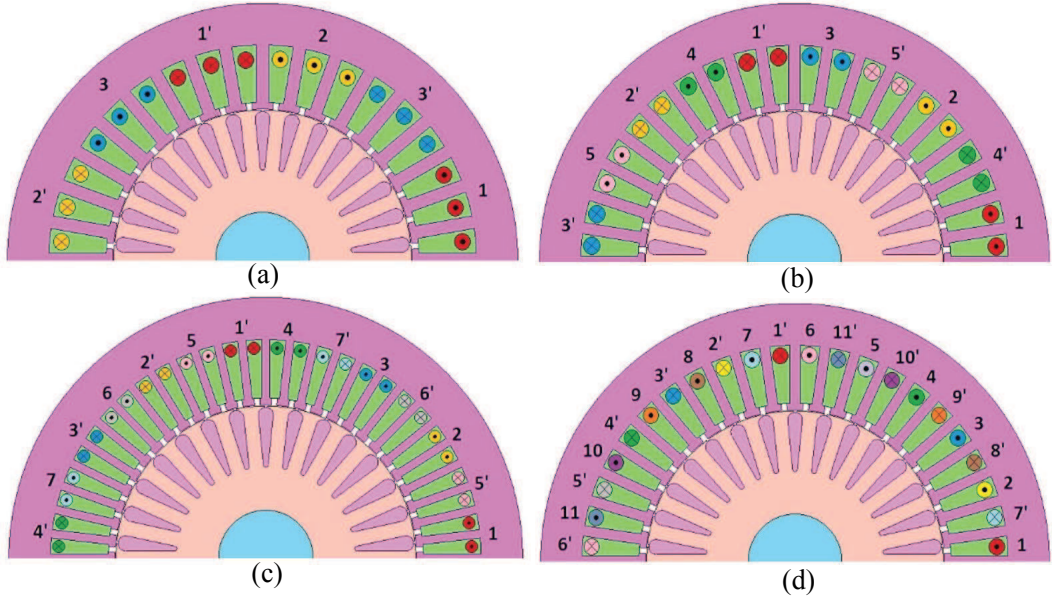
Figure 3. Several multiphase winding layouts with prime phase order. (a) Three-phase. (b) Five-phase. (c) Seven-phase. (d) Eleven-phase.

2.1.1. Effect of Number of Phases on Machine Parameters

In this subsection, the effect of the number of phases on different machine parameters is proven mathematically. An equivalent multiphase machine can be derived from another existing multiphase machine based on the derived relations. With a constant volt-ampere S_s and current, the required number of turns per phase N_{ph} is given by (2).

$$N_{ph} = \frac{V}{4.44 f \phi k_w} = \frac{S_s}{4.44 n I f \phi k_w} \propto \frac{1}{n} \tag{2}$$

where are V and I are the per-phase voltage and current, respectively. ϕ is maximum flux per pole, K_w is the winding factor, and f is the frequency. For a certain current rating, the conductor cross-sectional area a_c is constant, hence the stator resistance R_s can be

calculated by (3):

$$R_s = \frac{\rho L_e N_{ph}}{a_c} \propto \frac{1}{n} \tag{3}$$

Where ρ Is the electric resistivity, L_e is the conductor length, and n is the number of phases. The multiphase induction machine can be modeled as multiple decoupled sequence planes after using an appropriate transformation [4, 5, 6]. Each plane corresponds to a certain sequence. For an odd number of phases, the corresponding number of planes will be $\frac{1}{2(n-1)}$, with one zero sequence. The stator parameters are common between all sequences. However, the magnetizing inductance and the referred rotor parameters depend on the sequence number.

The magnetizing inductance L_m is proportional to the square of the number of turns per phase and the number of phases; where $k = 1, 3, ..., \frac{1}{2(n-1)}$.

$$L_{m(k)} \propto n\frac{N_{ph}^2}{k^2} \propto \frac{1}{n} \tag{4}$$

The rotor resistance R'_r referred to the stator is given by (5),

$$R'_{r(k)} = \frac{4n}{S_r} R_{be} \left(\frac{k_{w(k)} N_{ph}}{k_{skew(k)}}\right)^2 \propto \frac{1}{n} \tag{5}$$

Where the skew angle K_{skew} and winding factor are given by (6) and (7), respectively,

$$k_{skew(k)} = \frac{\sin(k\beta/2)}{k\beta/2} \tag{6}$$

$$k_{w(k)} = \frac{\sin(qk^{\gamma_s}/2)}{q\sin(k^{\gamma_s}/2)} \tag{7}$$

Where S_r is the number of rotor bars. β and γ_s are the rotor bars skewing angle and angle between two successive slots, respectively. The number of slots per pole per phase is q. In addition, the equivalent rotor bar resistance R_{be} is given by (8) [24],

$$R_{be(k)} = R_b + \frac{R_e}{2\sin^2\left(\frac{1}{2}k\gamma_r\right)} \tag{8}$$

Where R_b and R_e are the rotor bar and end ring resistances, respectively. The number of pole pairs is p and the angle between two successive rotor bars γ_r is calculated as follows:

$$\gamma_r = \frac{2\pi}{S_r}p \tag{9}$$

Similarly, the referred rotor leakage reactance l'_r is given by (10),

$$l'_{r(k)} = \frac{4n}{S_r} l_{be} \left(\frac{k_{w(k)} N_{ph}}{k_{skew(k)}}\right)^2 \propto \frac{1}{n} \tag{10}$$

where, l_{be} is the equivalent bar inductance, as given by (11) [24],

$$l_{be(k)} = l_b + \frac{l_e}{2\sin^2\left(\frac{1}{2}k\gamma_r\right)} \tag{11}$$

Where l_b and l_e are the rotor bar and end ring inductances, respectively. The maximum machine torque T_{max} can be approximated as follows [24]:

$$T_{max} = \frac{nV_s^2}{2\omega_s X} \tag{12}$$

Where V_s and ω_s are the stator phase voltage and machine synchronous speed, respectively. X represents the equivalent reactance. Thus, for two different stator designs with a number of phases n_1 and n_2, the corresponding ratio between maximum machine torques can be expressed as follows:

$$\frac{T_{max(n_1)}}{T_{max(n_2)}} = \frac{n_1}{n_2} \cdot \left(\frac{V_{n_1}}{V_{n_2}}\right)^2 \cdot \frac{X_{n_2}}{X_{n_1}} = \frac{n_1}{n_2} \cdot \left(\frac{n_2}{n_1}\right)^2 \cdot \frac{n_1}{n_2} = 1 \tag{13}$$

This shows that the machine will give the same maximum torque for any number of phases. Additionally, the total machine impedance Z_{total} at any slip s is governed by (14):

$$\frac{Z_{total(n_1)}}{Z_{total(n_2)}} = \frac{n_2}{n_1} \tag{14}$$

Thus, from a mathematical point of view, the n-phase machine develops similar output torque and power to its equivalent three-phase machine with identical characteristics. However, practical constraints may cause differences in dimensions and deviations in the machine parameters from the derived relations.

2.1.2.   Analysis of Single-Layer Multiphase Winding Layouts

In this subsection, the characteristic steady-state curves of the four multiphase machines using the machine parameters in [25] without harmonic injection are compared. Additionally, a transient simulation using MATLAB/SIMULINK and finite element analysis (FEA) is investigated. With the rated voltage applied to each stator winding at a specific time instant, the machine MMF flux density distributions using JMAG-studio 10 are shown in Figure 4. The flux density distribution for the four machines is approximately the same, with a 1.6 T peak value, which proves that the four designs are equivalent.

Figure 5(a) shows that the torque-speed characteristics of the different machines are almost identical up to the rated value of 1757 rpm. This confirms (12) where the maximum torque is approximately constant for the four machines. Figure 5(b) shows that the machine current is approximately the same for all machines at the rated operating point. Figure 5(c) presents the machine power factor, while Figure 5(d) depicts the machine efficiency.

Furthermore, transient simulation results using the conventional dq model for a multiphase machine are obtained using MATLAB/SIMULINK and compared with the transient simulation using the JMAG software. This validates the mathematical model given in the previous subsection for motor parameter calculations. As an illustrative example, a five-phase machine is simulated, supplying the stator with a fundamental sinusoidal voltage. The machine is assumed to run steadily at a constant speed of 1757 rpm, i.e., the full load speed. Figure 6 shows the simulation results for the phase current and motor torque. An agreement between the mathematical and analytical solutions is highlighted in Figure 6. These results support the method for parameter determination using FEA and hence prove the relations given in the previous subsection.
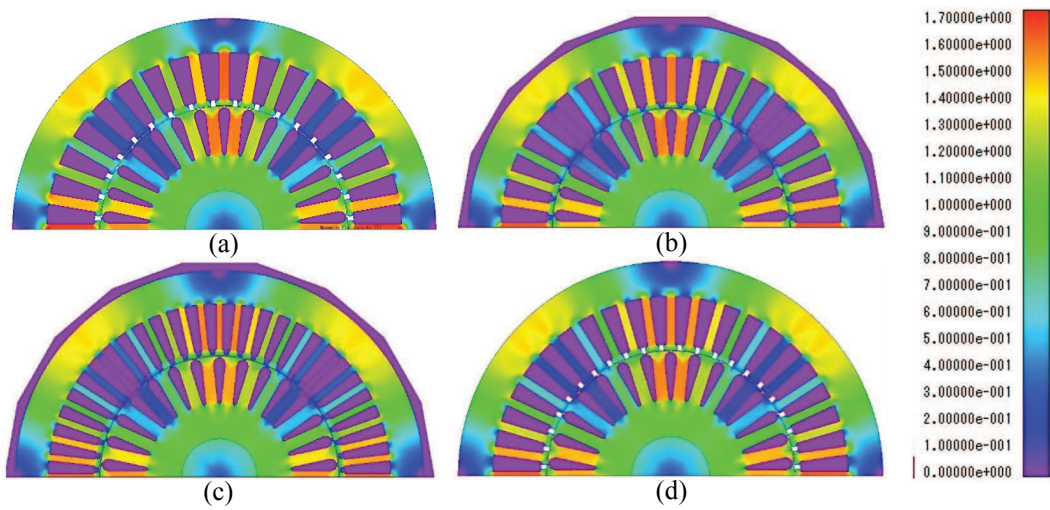
Figure 4. MMF flux density distributions. (a) Three-phase. (b) Five-phase. (c) Seven-phase. (d) Eleven-phase.
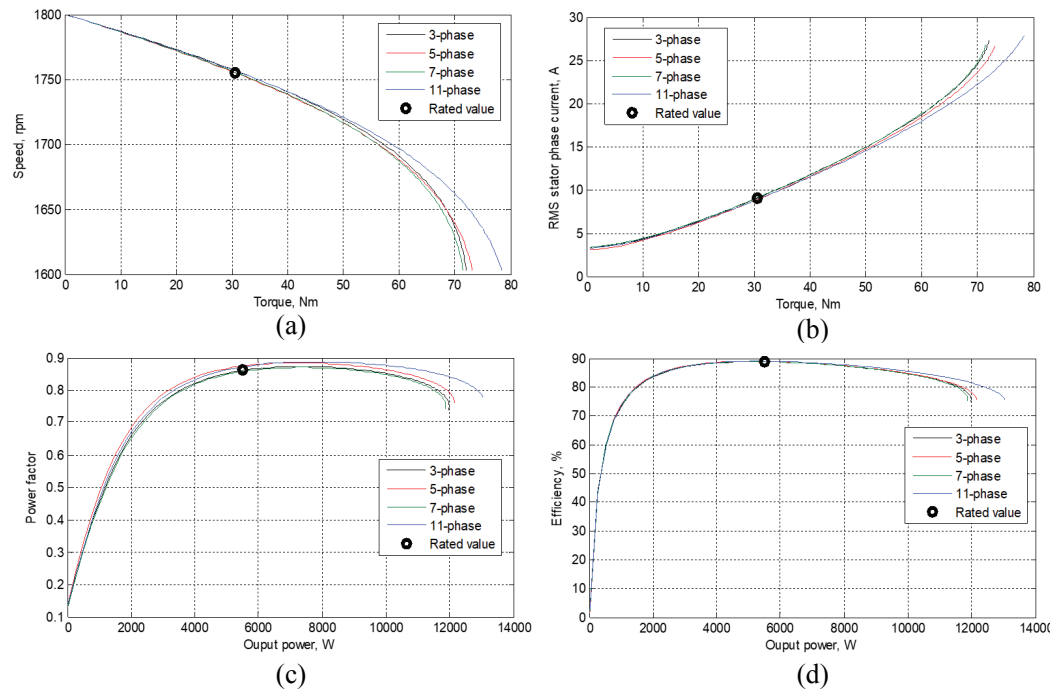
Figure 5. Characteristic curves (a) torque-speed characteristics, (b) torque-current characteristics, (c) output power versus power factor, and (d) output power versus efficiency.

2.2. Double-Layer-Based Conventional Winding Design with Composite Phase Order

Multiphase machines with multiple three-phase winding designs, e.g., six-, nine-, and twelve-phase IMs, have been introduced in the literature for several applications [28, 29,
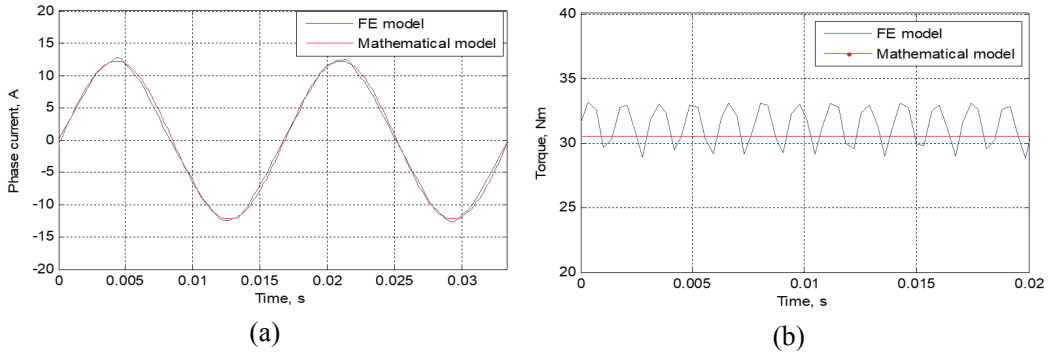
Figure 6. Transient performance using MATLAB/SIMULINK and an FE-JMAG transient model. (a) phase current. (b) developed torque.

30, 31]. Six- and twelve-phase IMs usually adopt a double-layer winding layout. However, nine-phase IMs can employ either double-layer or preferably single-layer winding topology. Figure 7 depicts the winding layouts of six- and twelve-phase IMs.

Moreover, a three-phase double layer winding can simply be converted into a six-phase winding by employing a four-layer stator winding design. Each two layers represent one three-phase double layer winding. This winding layout is denoted as a "true" six-phase distribution. However, this complex winding design entails an extra coil side insulation [32]. In most practical six-phase IM, the traditional double layer winding distribution is used by splitting the 60^0 phase belt of a conventional three-phase winding into two portions, thus employing a 12-slot/pole pair stator or its multiples. To ensure a high-quality flux distribution while minimizing the stator leakage inductance, a winding pitch of $5/6$ is commonly used.

As an illustrative example, several six-phase winding configurations, namely, dual three-phase (D3P), symmetrical six-phase (S6P), and asymmetrical six-phase (A6P) winding layouts, are presented, as shown in Figure 8 [33]. These three winding configurations are compared by investigating the air gap flux distributions under different excitations and the equivalent parameters of the three orthogonal subspaces of a six-phase system. The same stator is utilized to provide a fair comparison, so the study is performed for the same copper volume. This is carried out by rewinding a 24-slot/4-pole three-phase machine into a 12-phase stator by simply splitting the coils under each pole pair, i.e., splitting each phase into separate coils, as illustrated in Figure 9. A double-layer winding with a chorded winding of a $5/6$ coil span is used. All terminals are made externally available at the machine's terminal box to allow reconfiguration. The obtained 12-phase stator can then be reconfigured into one of the six-phase winding arrangements by connecting the 12 -phases in different manners, as depicted in Figure 10. Since the conclusion made in [34], which argued in favor of the A6P induction machine, most high power practical variable speed drive systems have been based on the asymmetrical winding layout.
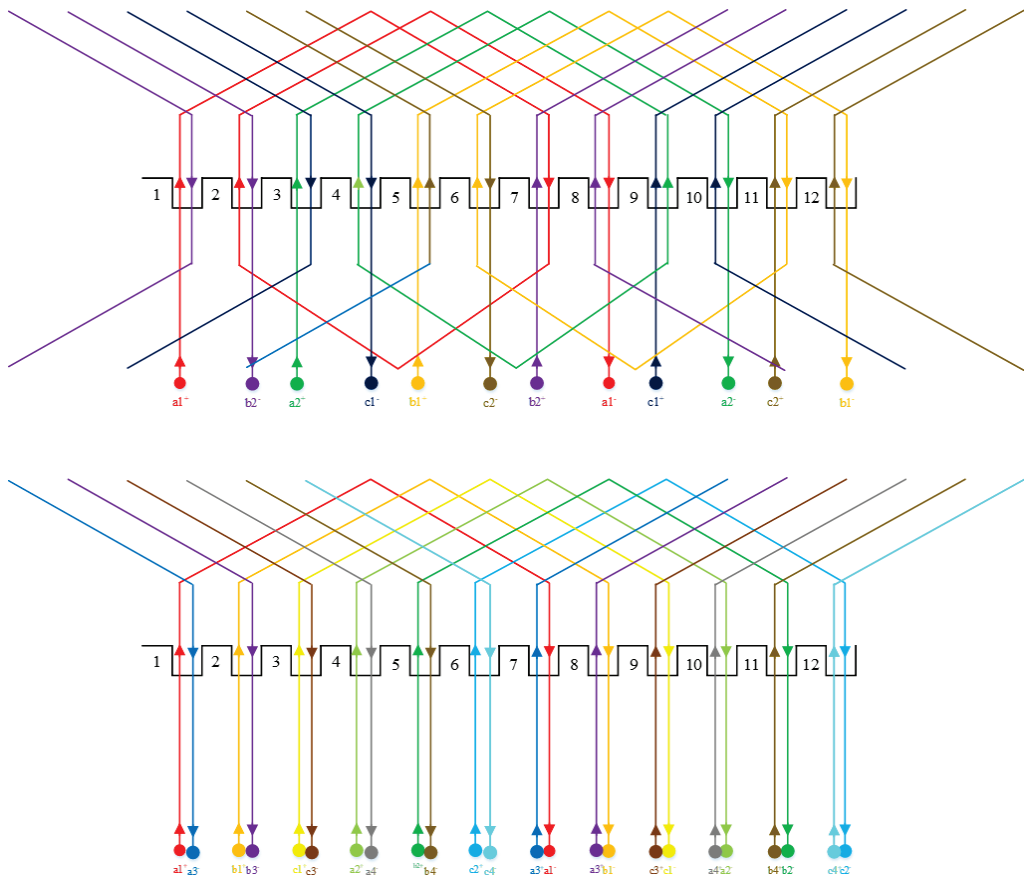
Figure 7.   Conventional prime-phase-based winding layouts.   (Upper) five-phase. (lower) seven-phase.
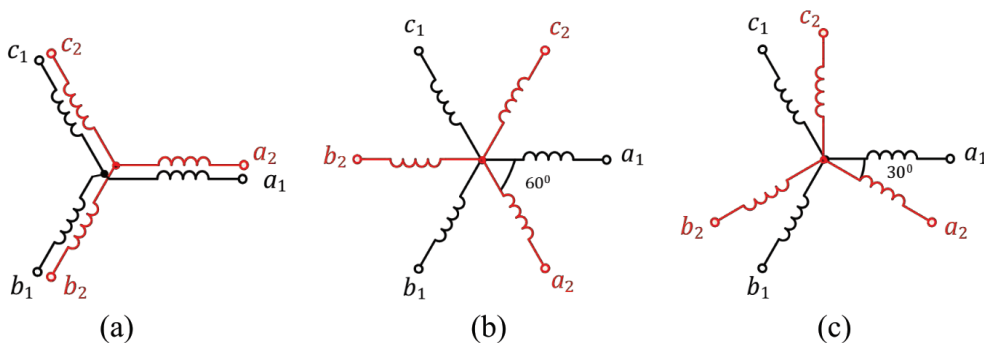
Figure 8. Different six-phase winding configurations (a) D3P. (b) S6P. (c) A6P.

Slot	1	2	3	4	5	6	7	8	9	10	11	12	13	14	15	16	17	18	19	20	21	22	23	24
Top layer	1 +	2 +	3 +	4 +	5 +	6 +	7 +	8 +	9 +	10 +	11 +	12 +	1 +	2 +	3 +	4 +	5 +	6 +	7 +	8 +	9 +	10 +	11 +	12 +
Down layer	8 −	9 −	10 −	11 −	12 −	1 −	2 −	3 −	4 −	5 −	6 −	7 −	8 −	9 −	10 −	11 −	12 −	1 −	2 −	3 −	4 −	5 −	6 −	7 −

Figure 9. The winding layout of the 4-pole 12-phase stator.
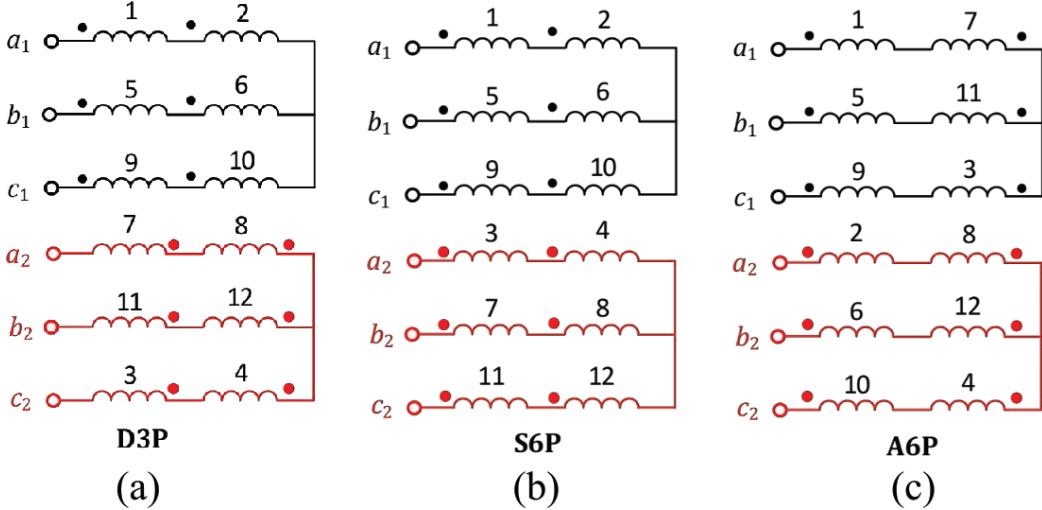
Figure 10. Stator connections for different six-phase arrangements. (a) D3P. (b) S6P. (c) A6P.

2.2.1. Vector Space Decomposition and Harmonic Mapping

Multiphase machines are preferably modeled using the Vector Space Decomposition (VSD) modeling technique, where the n-phase Clarke's transformation is used to decompose the phase quantities (i.e., current, voltage, and flux linkage) into orthogonal stationary subspaces [2]. Six-phase systems have three orthogonal subspaces. The general VSD matrix for a six-phase machine with an arbitrary angular displacement δ between the two three-phase winding sets is given in [21]. The effect of stator winding connection on the harmonic mapping is investigated by plotting the MMF distributions and their harmonic spectra under different excitations for the three available connections. Figure 11-Figure 13 show the simulation results for the MMF distributions and their spectra in per-unit values under different excitations by taking the dual three-phase case as a benchmark. The following conclusions can be drawn:

- Under $\alpha\beta$ excitation, the MMF distribution and the corresponding spectrum will be the same for D3P and S6P with small 5th and 7th space harmonics present in the airgap flux. However, these two low-order harmonics are eliminated under the A6P connection, while the fundamental torque-producing component is enhanced by approximately 3% over the other two connections.

- Under xy excitation, the 5th and 7th MMF space harmonics are mapped to this sub-space when A6P is employed. While the D3P and S6P correspond to small even order space harmonics as a result of using chorded coils. If a "true" six-phase winding [32] is employed, these even harmonics are likely canceled.

- Under zero-sequence excitation, the total magnetizing flux is completely canceled when D3P is used. On the other hand, both S6P and A6P connections correspond to pulsating third harmonic flux distribution of the same magnitude.
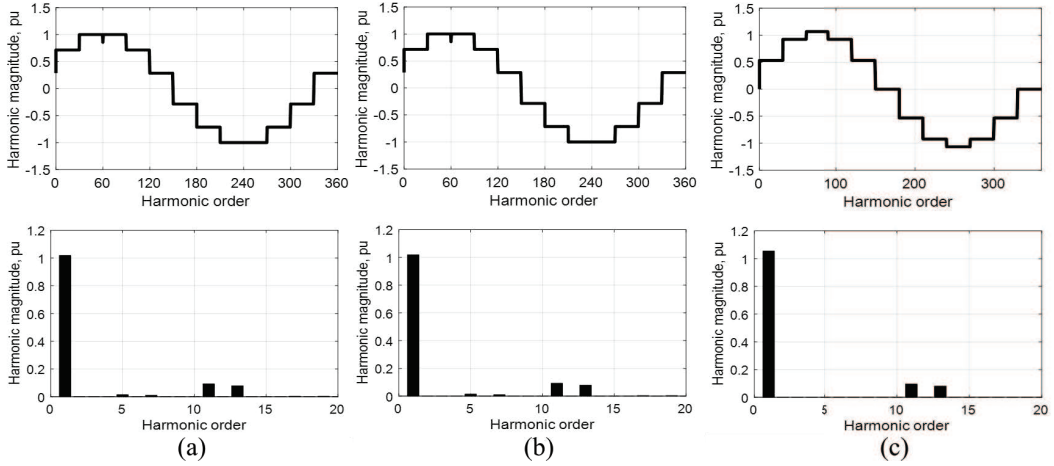
Figure 11. Stator MMF under $\alpha\beta$ excitation. (a) D3P. (b) S6P. (c) A6P.
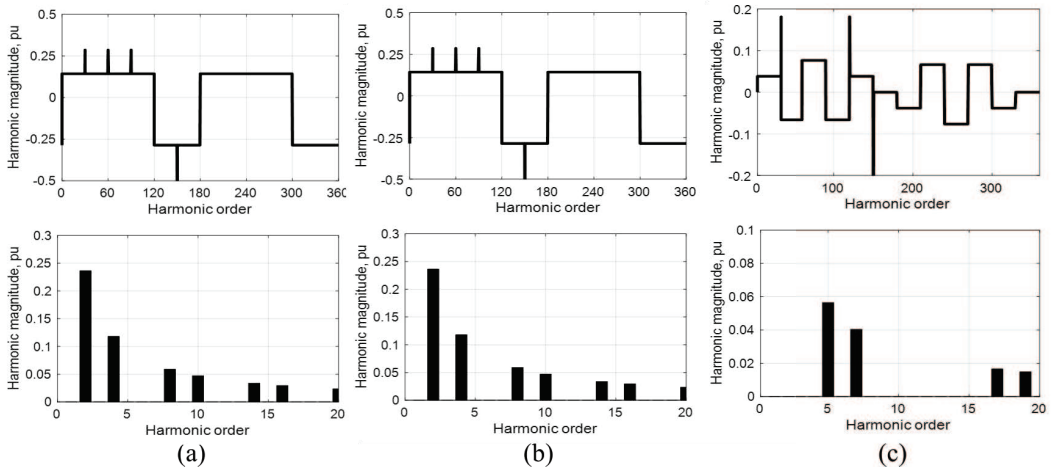
Figure 12. Stator MMF under xy excitation. (a) D3P. (b) S6P. (c) A6P.
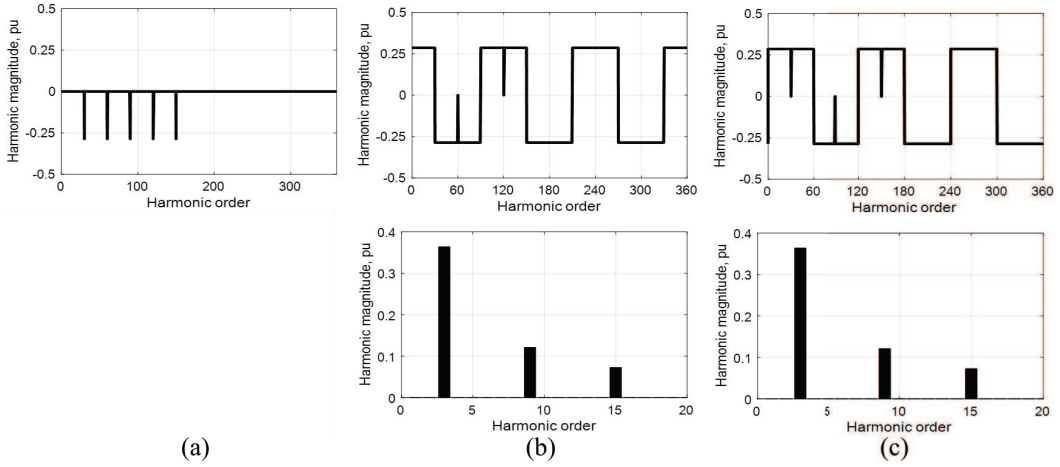
Figure 13. Stator MMF under zero-sequence excitation. (a) D3P. (b) S6P. (c) A6P.

2.2.2. Analysis of Double-Layer Six-Phase Winding Layouts

The different configurations are experimentally assessed under open-loop control while fed at rated voltage and frequency [33]. Figure 14 compares the characteristic curves corresponding to the three connections. Figure 14(a) shows the torque versus rotor speed characteristic. Both the D3P and S6P have almost the same characteristic curves since the equivalent circuits of the torque producing $\alpha\beta$ subspace of both connections are quite similar. The A6P, however, corresponds to a higher equivalent machine reactance due to the effect of the mutual leakage inductance between stator layers. This yields a higher machine slip for the same developed torque. The torque versus RMS phase current characteristic is shown in Figure 14(b), which slightly differs amongst different connections. Although the S6P exhibits the lowest phase current magnitude for the same torque, the difference in current magnitudes between different connections may be insignificant. This is especially true when the effect of the induced stator harmonics on the total RMS phase current is considered. The machine efficiency versus output power curve is shown in Figure 14(c). Clearly, the D3P has the best efficiency among all connections, while the lowest efficiency is obtained with the machine connected as an A6P.

The full-load phase current waveforms corresponding to the three connections are shown in Figure 15. Under the D3P and S6P connections, the current ripple component at switching frequency is much lower than the A6P case. This conclusion can be explained by the fact that the latter connection has a smaller L_{ls}^{xy}, which causes a high current ripple component (36% of rated current magnitude). On the other hand, the current waveforms of the D3P and S6P machines experience a superimposed high-frequency current component due to the slotting effect [35]. This rotor slot harmonic (RSH) component mainly depends on the employed combination of stator slots and the number of rotor bars [36]. The frequency, f_h, of RSH component depends on the rotor speed and is given by (15):

$$f_h = f_s \left((N_r/p)(1-s) \pm 1 \right) \tag{15}$$

where, f_s is the supply frequency and s is the rotor slip. The RSH component can simply be avoided by properly selecting the number of rotor bars based on the number of stator slots and phase belt harmonics of the stator MMF [36].

(a)   (b)   (c)
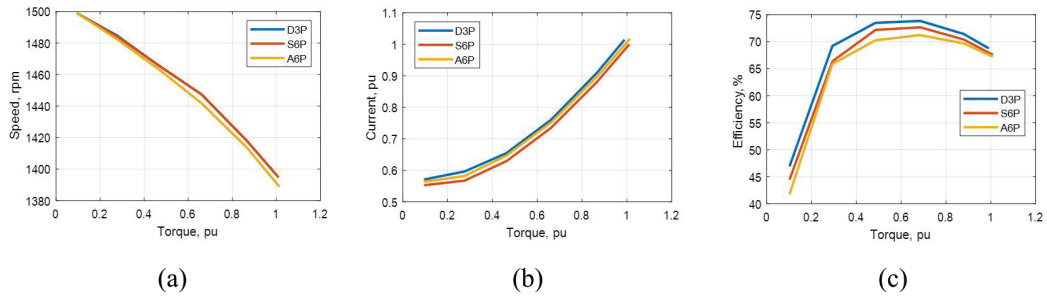
Figure 14. Machine open-loop characteristic curves under different stator connections.

3.   Winding Layouts for Fault-Tolerance Enhancement

One of the main merits offered by multiphase machines is their high fault-tolerance capability. Literature has demonstrated that the employed stator winding connection affects the performance of multiphase induction machines under fault conditions. Although six-phase machines use conventional three-phase converters, five-phase machines offer better performance under fault conditions and effectively support higher mechanical loads. In the case of induction machines with one phase open and under optimal current control, previous work shows that the machine can maintain approximately 70% of its rated load in the case of a five-phase machine [37] and only 66% in the case of an asymmetrical six-phase machine [30]. However, these maximum allowable loading ratios can be increased under open-loop control [37] but with a corresponding higher torque ripple magnitude and unbalanced winding currents [38]. This section presents innovative winding layouts aiming to improve fault-tolerance capability [10, 18, 39].

3.1.   Combined Star/Pentagon Single-Layer Stator Winding Connection

For a multiphase machine with an odd number of phases n, there are $(n+1)/2$ connection alternatives. For example, a five-phase stator winding has three types of winding configurations, namely, star (S5P), pentagon (P5P), and pentacle connections [40]. Recent papers show that the pentagon connection presents a better performance over the star connection under open phase conditions for both permanent magnet [41] and induction [37] machines. Moreover, it can retain a higher maximum loading ratio than a star-connected stator under fault conditions. On the other hand, for the healthy case, the star connection avoids the induced zero sequence component in the pentagon connection, which decreases the copper loss and, hence, enhances the machine efficiency.

This subsection introduces a new combined star/pentagon five-phase (SP5P) single-layer winding layout that combines the advantages of both star and pentagon connections
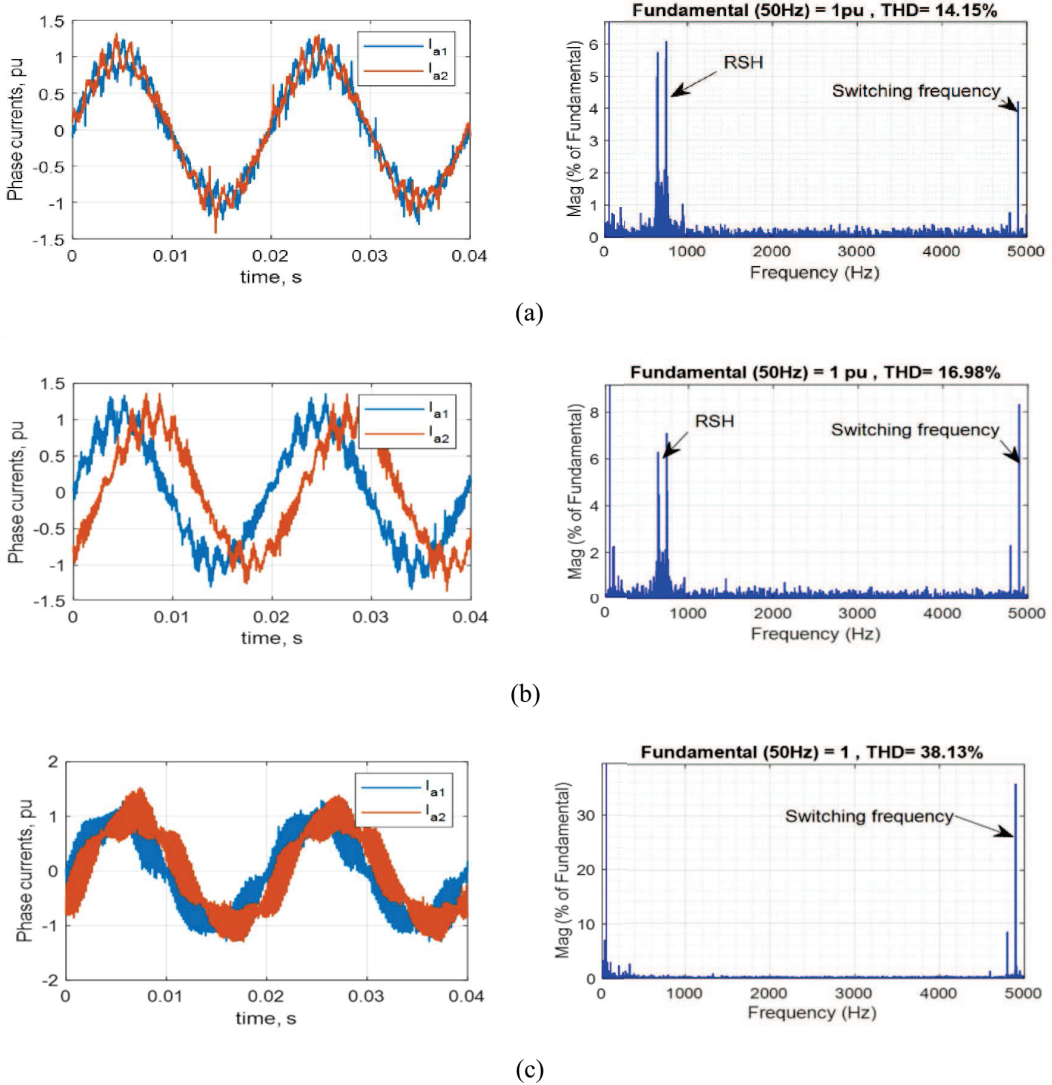
Figure 15. Full load current waveform under different stator connections.

for a five-phase induction machine. Although this winding is intrinsically an asymmetrical 10-phase machine, its connection allows for only five-phase terminals. A conventional 4-pole five-phase stator with the number of slots per pole per phase equal two is shown in Figure 16(a). Each phase contains two coils for each pole pair with a total of 4 coils for a 4-pole winding. Each two nonadjacent series coils are represented using one coil in Figure 17, and all coils are connected in series and have the same number of turns. Different phases can be connected either in star or pentagon connections, as shown in Figure 17(a and b), respectively. This winding can be modified into a split-phase dual five-phase winding [20] and can be considered an asymmetrical 10-phase winding shown in Figure 16(b). The coils $A1$, $B1$, $C1$, $D1$, and $E1$ represent the first five-phase winding group with a number of

turns per coil N_{c1}, while coils $A2$, $B2$, $C2$, $D2$, and $E2$ represent the second five-phase winding group with a number of turns per coil N_{c2}. Both winding groups are shifted in space by one slot or $18°$ electrical degrees. Each winding has $q = 1$, which corresponds to a unity winding factor. To benefit from splitting the winding phase belt into two halves to reduce space harmonics, the two winding groups should be fed from two five-phase current groups shifted in time by an angle of $18°$ [42]. Furthermore, the total ampere turn of both windings should be equal. Hence, two separate five-phase inverters should be employed.

Moreover, the proposed winding not only yields better flux distribution than a conventional single-layer winding but also provides a complete cancellation of the third-order harmonic flux component caused by the induced third sequence currents due to the saturation effect and/or under unbalanced operation. Hence, the machine losses are decreased, which improves the overall machine efficiency. It has been shown in [42] that the combined star/pentagon connection, when applied to a 20-slot/18-pole PM machine, can be an effective alternative to produce the same MMF distribution of a dual five-phase fractional slot winding while requiring only a single five-phase inverter. Hence, the same concept is applied to multiphase single-layer induction machine stators for a full-pitch concentrated winding. Thus, one of the two winding groups is connected in pentagon, and the other between the inverter and the pentagon connection terminals, as shown in Figure 17(c).

Generally, in a pentagon connection, the relation between phase and line currents is given by (16) [40].

$$I_{Line} = 2\sin\frac{\pi}{5}I_{phase} = 1.1756I_{phase} \tag{16}$$

Hence, to obtain the same MMF magnitudes from the two winding sets, the relation between the number of turns per phase for the star winding group (N_1) and the pentagon winding group (N_2) is given by (17).

$$N_2 = 1.1756N_1 \tag{17}$$

This yields the same copper volume as in a conventional five-phase winding as the conductor cross-sectional area for the pentagon section will be less by the same ratio, as depicted by the current ratio given by (16).
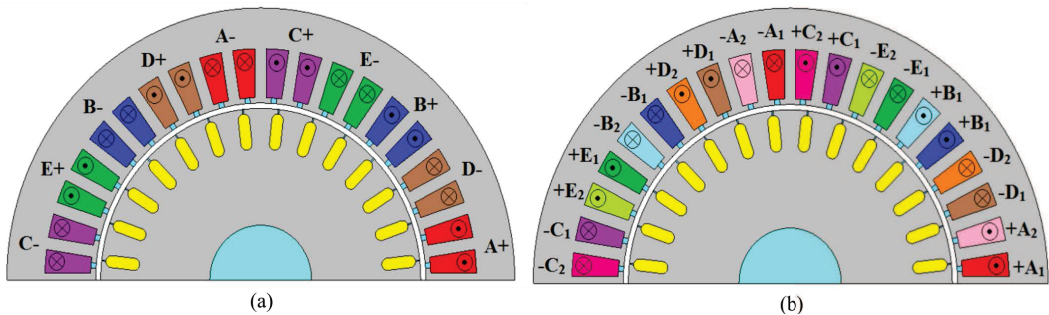
Figure 16. Winding arrangement of a 4-pole five-phase induction machine. (a) Single five-phase winding. (b) Split-phase dual five-phase winding.
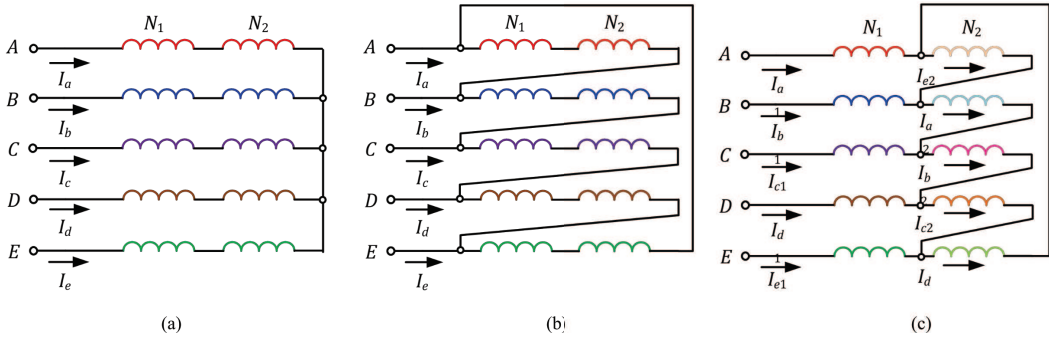
Figure 17. Winding connection of a five-phase induction machine. (a) Star $N_1 = N_2$. (b) Pentagon $N_1 = N_2$. (c) Combined star/pentagon $N_2 = 1.1756N_1$.

3.1.1. MMF Flux Distribution

For the star/pentagon connection, the phase shift angle between the two current groups in the two windings will depend mainly on the applied stator sequence. With the fundamental current sequence applied to the supply terminals, the angle between different phase currents in any group is $72°$, while the phase shift between the two current groups is $18°$, as shown in Figure 18(a). On the other hand, with the third sequence applied, the angle between different phase currents is $216°$, while the phase shift between the two current groups is $-126°$, as shown in Figure 18(b). Based on the current relations shown in Figure 17(c), it can be easily shown that the relation between the ampere-turn phasors of both winding groups will be as shown in Figure 18 for both fundamental and third supply phase current sequences.

The effect of the star/pentagon winding layout on the MMF spectrum can be simply investigated using the winding function theory [43]. The Fourier series of the turn functions of the two phases $A1$ and $A2$, shown in Figure 19, can be expressed as in (18) and (19):

$$N_{A1}(\theta) = \sum_{k=1,3,\dots}^{\infty} \frac{2N_{c1}}{k\pi} \sin k\theta \tag{18}$$

$$N_{A2}(\theta) = \sum_{k=1,3,\dots}^{\infty} \frac{2N_{c2}}{k\pi} \sin k(\theta - \pi/10) \tag{19}$$

where, N_{c1} and N_{c2} are the number of turns per coil for the two phases $A1$ and $A2$, respectively, and θ is the stator peripheral angle. Similarly, the turn functions of other phases can be obtained.

In S5P and P5P winding connections shown in Figure 17(a or b), the two winding groups have the same number of turns per coil, $N_{c1} = N_{c2} = N_c$, and are connected in series while fed from a single five-phase supply. Hence, the MMF produced by each winding section is given by (20) and (21):

$$F_{1c}(\theta, t) = \sum_{k=1,-9,11,\dots}^{\infty} \frac{5N_c I_{m11}}{k\pi} \cos(k\theta - \omega t) \tag{20}$$
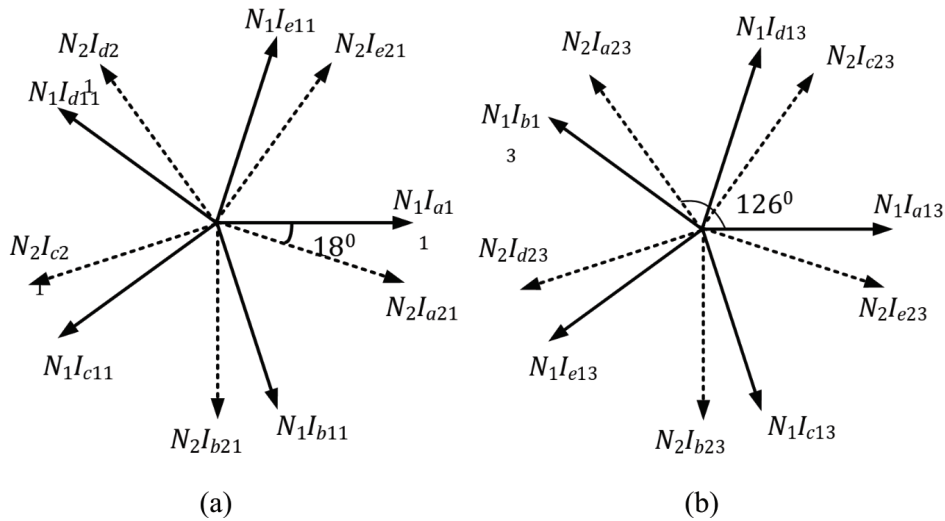
Figure 18. Phasor diagram of MMFs produced by the two winding sets of the introduced connection. (a) Fundamental sequence. (b) Third sequence. (The first and second subscript numbers indicate the winding section and the sequence number, respectively.)
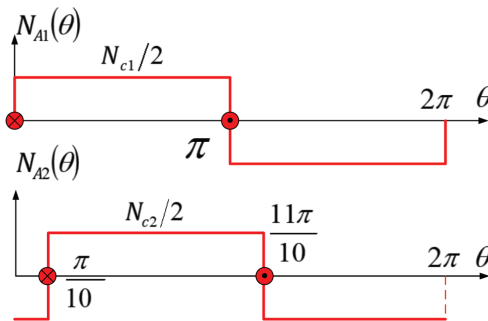
Figure 19. Winding functions for the two phases $A1$ and $A2$.

$$F_{2c}(\theta, t) = \sum_{k=1,-9,11,\ldots}^{\infty} \frac{5 N_c I_{m21}}{k\pi} \cos\left[(k(\theta - \pi/10) - \omega t)\right] \tag{21}$$

where, I_{m11} and I_{m21} are the peak magnitudes of the phase currents with fundamental sequence applied to both stator windings, while ω is the angular frequency. The sign of the harmonic k indicates the flux direction of the corresponding harmonic sequence. For a conventional connection, $I_{m11} = I_{m21}$, where both winding sections are connected in series, as shown in Figure 18(a or b). Hence, the total air gap MMF distribution can be

simply given as shown in (22):

$$
\begin{aligned}
F_{tc}(\theta, t) &= F_{1c}(\theta, t) + F_{2c}(\theta, t) \\
&= \sum_{k=1,-9,11,\ldots}^{\infty} \frac{10 N_c I_{m11}}{k\pi} . \cos\left(\frac{k\pi}{20}\right) . \cos\left(k\theta - \omega t - \frac{k\pi}{20}\right)
\end{aligned}
\tag{22}
$$

For the star/pentagon connection shown in Figure 17(c) and with fundamental sequence applied, the two winding groups carry two balanced 5-phase current groups shifted in time by $\pi/10$, as shown in Fig 18(a). The rotating MMF generated by each winding group can be expressed using (23) and (24):

$$
F_{1p}(\theta, t) = \sum_{k=1,-9,11,\ldots}^{\infty} \frac{5 N_{c1} I_{m11}}{k\pi} \cos(k\theta - \omega t)
\tag{23}
$$

$$
F_{2p}(\theta, t) = \sum_{k=1,-9,11,\ldots}^{\infty} \frac{5 N_{c2} I_{m21}}{k\pi} \cos\left[(k(\theta - \pi/10) - (\omega t - \pi/20)\right]
\tag{24}
$$

where, I_{m11} and I_{m21} are the peak currents of phases $A1$ and $A2$ respectively, assuming a fundamental current sequence. For equal ampere turn for both windings, $N_{c1} I_{m11} = N_{c2} I_{m21}$, the total air gap MMF distribution is given by (25):

$$
F_{tp}(\theta, t) = \sum_{k=1,-9,11,\ldots}^{\infty} \frac{10 N_{c1} I_{m11}}{k\pi} . \cos\left(\frac{(k-1)\pi}{20}\right) . \cos\left(k\theta - \omega t - \frac{(k-1)\pi}{20}\right)
\tag{25}
$$

The MMF distribution and harmonic spectra of both conventional and presented windings are shown in Figure 20(a and b), respectively, assuming a set of five-phase currents with 1 A peak and fundamental sequence is applied to the stator terminals. For the conventional winding, the main dominant low order harmonics are the 9th, 11th, 19th, and 21st. In the new winding, the 9th and 11th harmonics are completely canceled, while the fundamental component is slightly increased by approximately 1.25% as the fundamental winding factor increases from 0.9877 to unity.

With the third sequence applied to the stator terminals, the two current groups are shifted in time by $7\pi/10$, as shown in Figure 18(b). The MMF generated by each winding group can be expressed using (26) and (27):

$$
F_{1p}(\theta, t) = \sum_{k=3,-7,\ldots}^{\infty} \frac{5 N_{c1} I_{m13}}{k\pi} \cos(k\theta - \omega t)
\tag{26}
$$

$$
F_{2p}(\theta, t) = \sum_{k=3,-7,\ldots}^{\infty} \frac{5 N_{c2} I_{m23}}{k\pi} \cos\left[\left(k\left(\theta - \frac{\pi}{10}\right) - \left(\omega t + \frac{7\pi}{10}\right)\right)\right]
\tag{27}
$$

where, I_{m13} and I_{m23} are the peak currents of the two winding groups respectively and with the third sequence applied. The total air gap MMF distribution is given by (28):

$$
F_{tp}(\theta, t) = \sum_{k=3,-7,\ldots}^{\infty} \frac{10 N_{c1} I_{m13}}{k\pi} \cos\left(\frac{(k+7)\pi}{20}\right) \cos\left(k\theta - \omega t - \frac{(k+7)\pi}{20}\right)
\tag{28}
$$

The MMF distribution and harmonic spectra of both the conventional and star/pentagon windings are shown in Figure 20(c and d), respectively. For the conventional five-phase winding, the third harmonic component is 30% of the fundamental component. However, for the star/pentagon winding, the third harmonic component adds to zero, as depicted by (28) when $k = 3$. Although the seventh harmonic is increased in the star/pentagon winding, however, its effect on the induced rotor currents and hence the torque production is negligible. This is because the corresponding magnetizing inductance of the seventh harmonic is inversely proportional to the square of the harmonic order [44]. The main MMF harmonic components for both conventional and star/pentagon windings are given in Table 1.
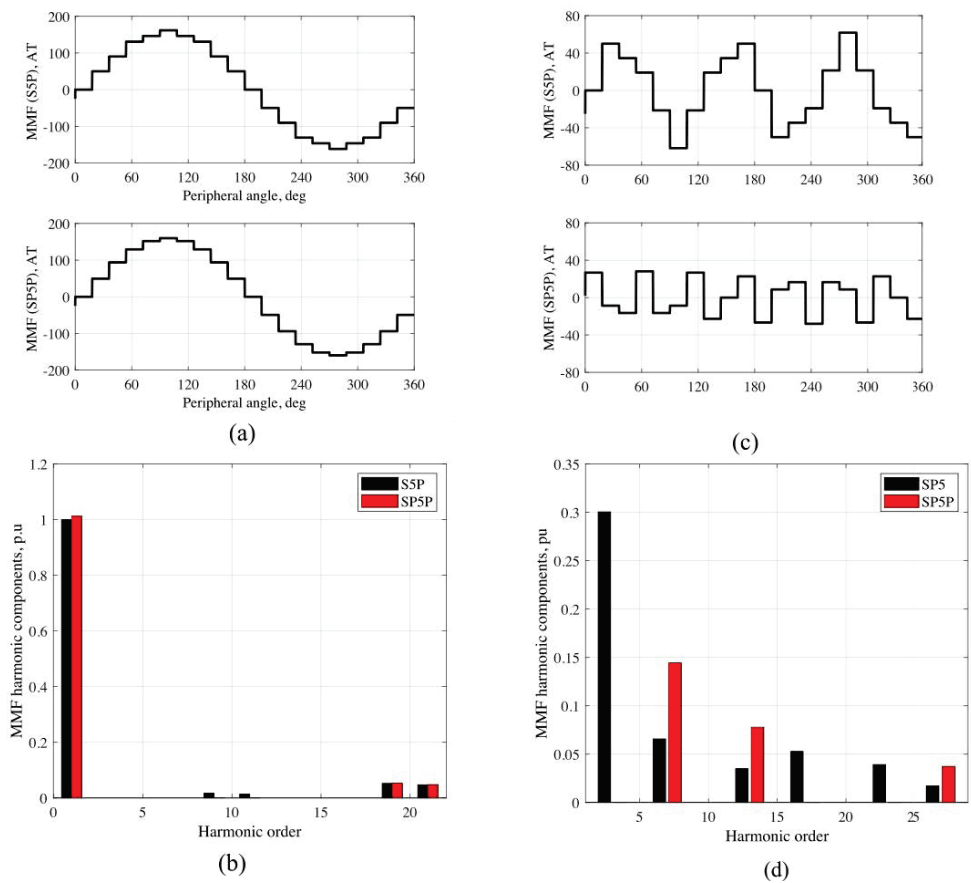
Figure 20. MMFs for both conventional and star/pentagon windings with ((a) and (b)) fundamental sequence and ((c) and (d)) third sequence. (The base value is 157.2 AT).

Table 1. MMF harmonic components percentage for both conventional and star/pentagon winding with different current sequences.

		Fundamental		Sequence	
Harmonic order	1	9	11	19	21
Conventional winding	100	1.78	1.42	5.26	4.76
Star/pentagon winding	101.25	0	0	5.32	4.85
		Fundamental		Sequence	
Harmonic order	3	7	13	17	23
Conventional winding	30	6.6	3.5	5.3	1.7
Star/pentagon winding	0	14.4	7.8	0	3.7

3.1.2. Analysis of the SP5P Winding Connection

Figure 21(a)-(c) shows the current waveforms with one-line open under open-loop control for the same three connections, shown in Figure 17. Compared with the waveforms obtained for conventional connections, the current waveform in the star/pentagon connection is generally sinusoidal. Moreover, the line currents of the star/pentagon connection are much approximate to the conventional star case, but with a significant reduction in the harmonic distortion due to the cancellation of the induced third harmonic component caused by core saturation. With optimal current control employed, the magnitudes of the line currents become equal, and for the same load current, they are 1.382 times the current magnitude of the healthy case, as shown in Figure 21(d to f). It was explained before in [37] that the star-connected stator gives better performance and better current waveform than a conventional pentagon-connected stator. The star/pentagon connection is similar to a conventional star-connected stator. Since simple optimal current control is employed and harmonic current compensation is not applied, for simplicity, the current waveforms experience some distortion, which is generally expected in multiphase drives due to machine and converter nonlinearities [45].

For open-loop control with one line open, the relations between machine torque and phase currents in the healthy phases for the three connections are shown in Figure 22. Although the conventional pentagon connection ensures minimum current diversion, the star/pentagon connection is better than the star case in this regard. In addition, the phase currents of the star/pentagon connection are higher under light loads; however, the machine draws less current magnitude when approaching full load, which in turn significantly improves the machine efficiency. Thus, for the same full-load speed, the star/pentagon connection can support higher loads at higher efficiency than conventional star and pentagon connections.

With one line open and optimal current control applied, the line currents are approximately equal. The torque-speed characteristic is very close to the healthy case, but at lower efficiency due to the increase in the line current by a factor of 1.382 with respect to the healthy case, which increases the copper loss. When comparing the obtained results for optimal current control with those obtained from conventional connections [37], the star/pentagon connection can support higher mechanical loads for the same total copper loss.
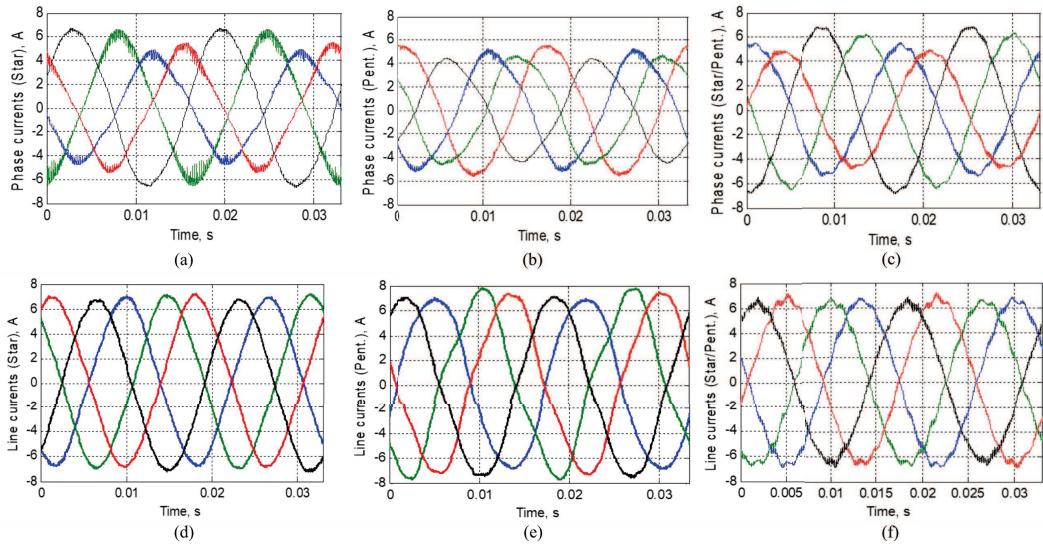
Figure 21. Experimental current waveforms for different connections under open line conditions. ((a) star, (b) pentagon, and (c) star/pentagon) Open-loop control. ((d) star, (e) pentagon, and (f) star/pentagon) Optimal current control.
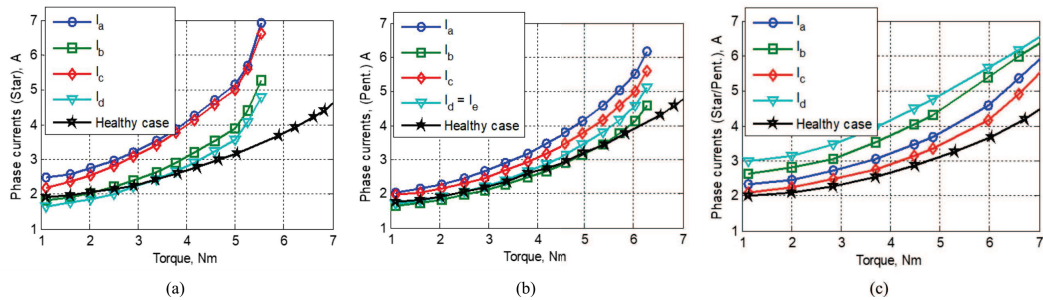
Figure 22. Experimental characteristic curves under different conditions for different stator connections. (a) Torque/current char. (star one line open). (b) Torque/current char. (pent. one line open). (c) Torque/current char. (Star/pent. one line open).

3.1.3. Derating Factor Calculation

The derating factor is defined as the factor by which the machine should be derated to avoid overheating under fault conditions. In [37], these factors are determined for conventional star and pentagon stator connections. The obtained derating factors for the combined Star/Pentagon winding connection are compared with those given in [37]. The output-load percentage corresponding to rated copper loss under healthy conditions will represent the machine's maximum load power. Since the same copper volume is used with the new connection, the same value of copper loss of the conventional connection under rated current is assumed. These values are found for different connections and given in Table 2. It is

clear that the combined Star/Pentagon winding connection can support higher loads than the other two connections in all operational cases.

Table 3 reveals the machine output torque that corresponds to a rated speed of 1700 rpm. It is also clear that the new winding connection gives higher output torque for the same speed, indicating the machine pull-out stability limit torque improvement.

Table 2. Output Power in PU For Same Rated Copper Loss (Base Power is 1000 **W).**

Connection	Star	Pentagon	Star/Pentagon
Healthy case	1	0.92	1
Open line and open loop control	0.77	0.84	0.89
Open line and optimal loop control	0.7	0.83	0.88

Table 3. Output Torque in PU Under Rated Speed (Base Torque 5.24 **Nm).**

Connection	Star	Pentagon	Star/Pentagon
Healthy case	1.04	0.96	1.01
Open line and open loop control	0.82	0.89	0.94
Open line and optimal loop control	1.05	0.98	1.03

3.2.   Nine-Phase Six-Terminal Concentrated Single-layer Winding Layout

The idea of exploiting the same performance of a higher-order multiphase machine while providing a less number of machine terminals has been recently presented in some papers, which is carried out based on either static winding transformations [46] or through special stator winding connections [39, 42, 47].

This subsection introduces an emerging winding layout for high-power medium-voltage nine-phase IMs based on a single-layer concentrated winding layout having a unity winding factor [18]. The machine is fundamentally an asymmetrical nine-phase IM, where phases are connected in such a way as to provide six terminals that are fed from two three-phase inverters. Compared to a conventional asymmetrical six-phase IM with the same stator and copper volumes, it provides improved torque density, a higher torque/current ratio, and a simpler winding layout. A nine-phase winding can be either symmetrical or asymmetrical. Generally, an asymmetrical winding layout corresponds to a higher number of phase belts per pole, increasing the order of the lowest harmonic [48]. The asymmetrical nine-phase winding, shown in Figure 23(a), simply comprises three three-phase winding sets with a spatial phase shift of $20°$. The three winding sets are fed by three three-phase current sets shifted in time by $20°$. The required number of stator slots per pole pair for the nine-phase six-terminal (9P6T) winding layout is 18 slots, as shown in Figure 24. Since each coil under a pole pair represents one phase, the winding factor will be unity.

If the coils of the nine phases are connected as in Figure 23(b), then the machine will have only six terminals. In this connection, if the phase shift between the first current group

I_{abc1} and the second current group I_{abc2} is $40°$, the current phase shift of the third group I_{abc3} should be $20°$. However, the current magnitude in the winding set I_{abc3} is higher by a factor of 1.88, as depicted by (29).

$$\overline{I}_{a3} = \overline{I}_{a1} + \overline{I}_{a2} = I_{ph}\angle 0° + I_{ph}\angle - 40° = 1.88 I_{ph}\angle - 20° \tag{29}$$

where, I_{ph} is the machine phase current magnitude. To maintain the same ampere-turn from all winding sets, the number of turns of the winding set $abc3$ should be reduced by 1.88, and the cross-sectional area should be increased by the same factor allowing for the same copper volume.
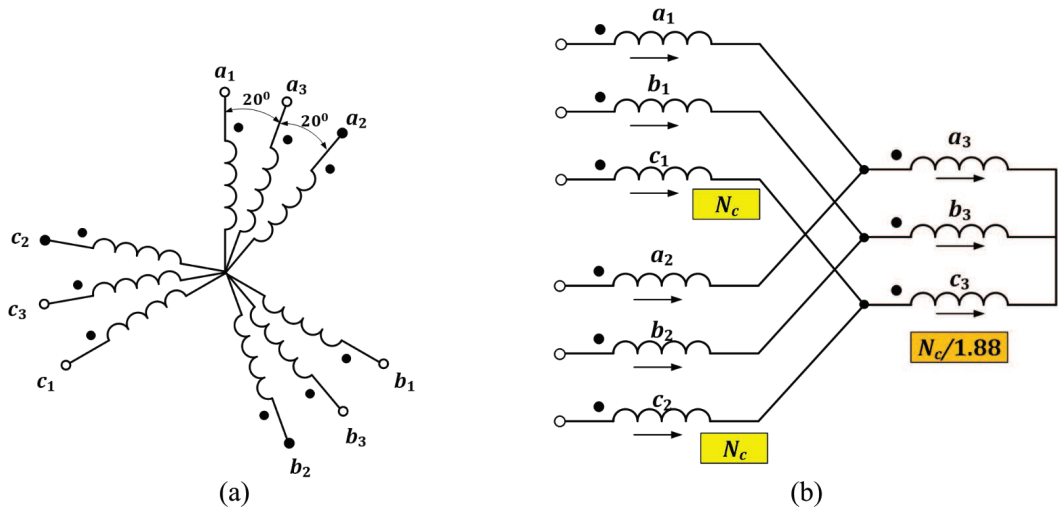
Figure 23. (a) Conventional asymmetrical nine-phase winding. (b) Six-terminal connection.
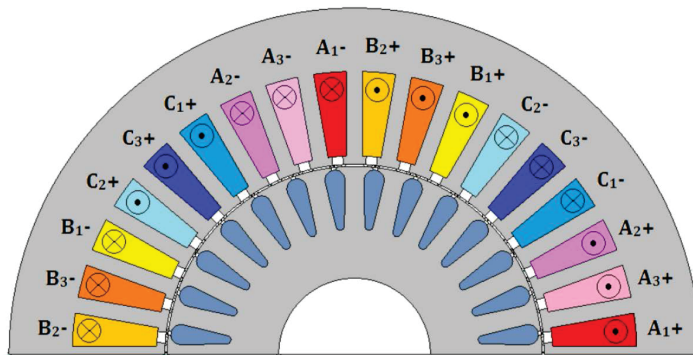
Figure 24. Winding layout for the nine-phase six-terminal IM.

In order to determine the required voltage phase shift between the two three-phase volt-

age sets applied to windings $abc1$ and $abc2$ while ensuring a current phase shift of $40°$, the per-phase equivalent circuit for the three three-phase sets is used, as shown in Figure 25. To simplify the analysis, all sources of winding asymmetries are neglected. Since phases a_1 or a_2 have the same number of turns, their equivalent per phase impedances is equal:

$$\overline{Z}_{a1} = \overline{Z}_{a2} = \overline{Z}_{ph} \tag{30}$$

where $\overline{Z}_{ph}$ represents the impedance of each three-phase set, including the mutual effect between different sets. Since the winding impedance is generally proportional to the square of the number of turns, the impedance of phase a_3 as a function of the impedance of other phases can be given by (31):

$$\overline{Z}_{a3} = \overline{Z}_{ph}/1.88^2 = 0.283\overline{Z}_{ph} \tag{31}$$

As shown in Figure 25, the voltage across the phase a3 is given by (32):

$$\overline{V}_{a3} = \overline{Z}_{a3}\overline{I}_{a3} = 0.283\overline{Z}_{ph}1.88\overline{I}_{ph}\angle - 20° = 0.532\overline{Z}_{ph}\overline{I}_{ph}\angle - 20° \tag{32}$$

Hence, the applied phase voltages from the two three-phase inverters are given by (33) and (34).

$$\overline{V}_{a1} = \overline{V}_{a3} + \overline{Z}_{a1}\overline{I}_{a1} = 1.51\overline{Z}_{ph}I_m\angle - 6.92° \tag{33}$$

$$\overline{V}_{a2} = \overline{V}_{a3} + \overline{Z}_{a2}\overline{I}_{a2} = 1.51\overline{Z}_{ph}I_m\angle - 33.08° \tag{34}$$
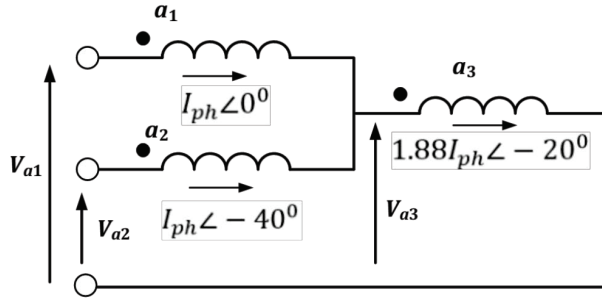
Figure 25. Per phase equivalent circuit for the three three-phase sets.

It is clear that both sets correspond to the same phase voltage magnitudes. However, the phase shift between the two applied three-phase voltage sets will be $-26.16°$ for a corresponding current phase shift of $40°$. This conclusion is based on the complete symmetry between the two windings. Nonetheless, in the practical case, the actual shift angle and voltage magnitudes may be slightly different. Experimental investigation shows that the current magnitude in each three-phase inverter and the phase shift between the two three-phase current sets are highly affected by the shift angle between the applied three-phase voltages and their relative voltage magnitudes.

3.2.1. Comparison between Nine-Phase Six-Terminal and Asymmetrical Six-Phase IMs

In this subsection, the MMF distributions of conventional A6P and 9P6T winding layouts are compared, assuming a unity phase current. The MMF distributions and their spectra are shown in Figure 26. Generally, the MMF distribution is of high quality, and the lowest order harmonics are the 17th and 19th. An approximate 5 % gain in the fundamental torque-producing flux component is achieved with the 9P6T winding employed. Hence, for the same magnetizing current, the fundamental air gap flux component is increased by the same factor. The gain in the phase voltage will be proportional to the flux gain multiplied by the gain in the winding factor. Since the phase voltage will be slightly different, and for a fair assessment, the comparison is carried out for the same magnetizing current. The relation between the phase voltages of the nine-phase and asymmetrical six-phase stators is given by (35).

$$\frac{V_{ph}^9}{V_{ph}^6} = \frac{N_{ph}^9}{N_{ph}^6} \cdot \frac{\phi^9}{\phi^6} \cdot \frac{K_w^9}{K_w^6} = \frac{1}{1.5} \cdot \frac{1.05}{1} \cdot \frac{1}{0.9598} = 0.73 \tag{35}$$

where, N_{ph} is the number of turns per phase, ϕ is the average flux per pole, and K_w is the winding factor. Ideally, when converting a six-phase IM into an equivalent nine-phase IM for the same phase current, the voltage ratio should be 0.667, which gives an additional gain of 9.4 % for the 9P6T winding, as clear from (35) [25]. The applied inverter voltage for the nine-phase six-terminal IM should be 1.51 times its phase voltage, as depicted by (33) and (34). Therefore, the applied inverter voltage across the 9P6T winding layout will be $1.51 \times 0.73 = 1.1$ times the phase voltage in a conventional six-phase IM to ensure the same magnetizing current. It is worth noting that the increase in the winding factor to unity for the 9P6T winding layout will also yield an increase in the magnetizing inductance and the equivalent rotor resistance referred to stator side by the square of this factor.

(a)

(b)
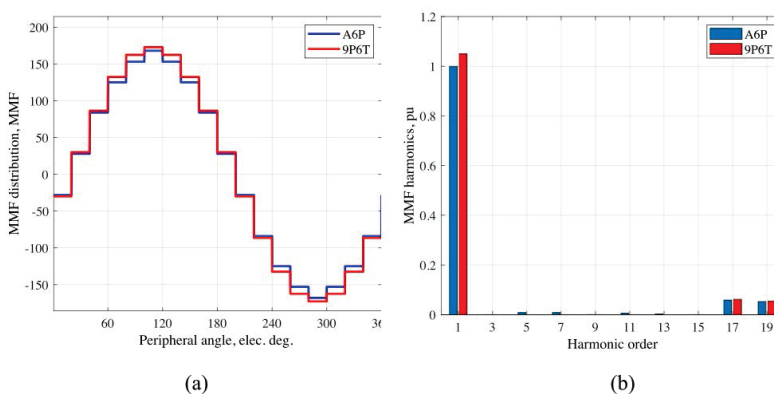
Figure 26. MMF distributions and their spectra. (a) conventional A6P. (b) 9P6T winding layouts.

3.2.2. Analysis of the 9P6T Concentrated Single-Layer Winding Layout

In this subsection, two FE models using JMAG Studio-10 software have been built with the 9P6T and conventional winding layouts assuming the same stator, rotor, and cage dimensions. The transient module is used to estimate different IM variables under different speeds. The machine characteristic curves under these two winding layouts are then compared. Since the equivalent IM impedance and phase voltage are higher in the new 9P6T winding layout, the line current will be less for the same speed. The gain in the fundamental flux will expectedly improve the machine torque density. To this end, the torque-speed and torque-current characteristics are compared in Figure 27(a and b), respectively.

As shown in Figure 27(a), the 9P6T connection corresponds to a 15 % increase in the pull-out torque. This is due to the increase in the fundamental flux component and the winding factor under the same magnetizing current. Moreover, the maximum torque corresponds to a higher slip due to the increase in the equivalent rotor resistance. As a result, the starting torque is also enhanced by approximately 37 %. Figure 27(b) illustrates the torque-current characteristics, while Figure 27(c) shows the torque gain versus machine per unit torque. It is evident that the torque/current ratio is prominently enhanced, which improves the machine torque density, and a torque gain of approximately 11 % is obtained under rated torque. Of course, the previous values, especially the maximum and starting torques, will mainly depend on the circuit parameters; however, they can be used as a general clue to the expected improvements in the machine performance.

(a) (b) (c)
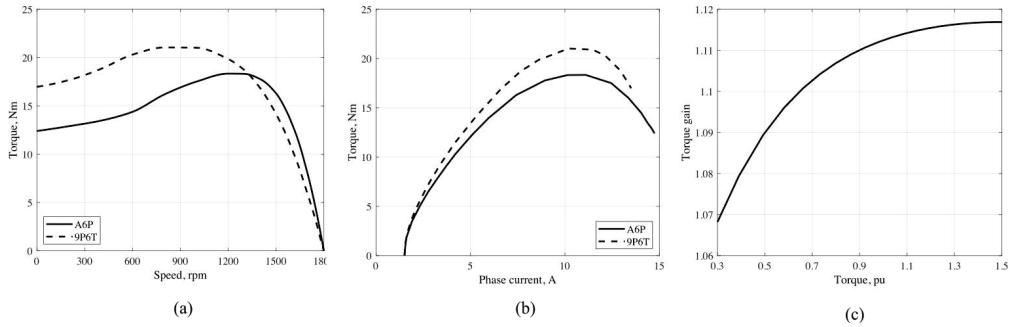
Figure 27. Characteristic curves using FEA for the conventional A6P and 9P6T IMs. (a) Torque versus speed. (b) Torque versus current. (c) Torque gain versus per unit torque.

In order to investigate the machine derating factors under single voltage source converter (VSC) mode, two scenarios may be applied, namely, same rated current or same stator copper loss scenarios. The former is a much conservative scenario and yields a significant reduction in the maximum achievable torque. While, in the latter scenario, the machine is loaded until rated stator copper loss is reached. In order to find this maximum loading point, the rated stator copper loss under the healthy case, P_{cs}^n, is first determined from (36):

$$P_{cs}^n = 9I_n^2 R_s \tag{36}$$

where, R_s is the stator resistance of either phase $a1$ or $a2$ and I_n is the rated phase current.

Under a single converter operation, assuming $abc1$ is only functional, the currents in the winding group $abc2$ will be zero, while the phase currents in the first and third groups, $abc1$ and $abc3$ respectively, will be equal. Hence, the machine total stator copper loss is then given by (37):

$$P_{cs} = 3I_d^2 R_s + 3I_d^2(0.283R_s) = 3.85I_d^2 R_s \qquad (37)$$

where, I_d is the phase current under this derated operation. The phase current that yields the same rated stator copper loss, P_{cs}^n, is then given by (38):

$$I_d = \sqrt{\frac{9}{3.85}}I_n = 1.53I_n \qquad (38)$$

Furthermore, the healthy and the single VSC mode cases are compared to determine the maximum output load corresponding to the condition given by (38). The machine characteristic curves under the healthy case and single VSC mode are shown in Figure 28. The same phase voltage is assumed in all cases. The torque-speed characteristic is shown in Figure 28(a). For the same rated speed, 1700 rpm, the achievable torque under the same phase voltage is reduced by approximately 31 % when a single VSC mode is enabled. The torque-current characteristic is shown in Figure 28(b). Under single VSC mode, the machine developed torque is reduced to 30 % and 64 % of the rated torque under the same current and same copper loss scenarios, respectively. These values are comparable to the conventional six-phase case [30], which justifies its practicality. The machine efficiency versus output power is shown in Figure 28(c). The maximum efficiency is approximately 78 % for the healthy case. This relatively low-efficiency value is mainly because of the low power rating of the employed prototype machine. The typical efficiencies for standard induction motors with high power ratings and energy-efficient designs can be increased up to approximately 96 % [24]. Under light loads (< 0.4 pu), single VSC mode corresponds to a better efficiency, which promoted its application even under healthy condition by simply disabling one of the converters. Since machine overheating, and consequently the required derating, mainly depends on the total losses rather than the stator copper loss only, the relation between the machine total losses versus the output power is shown in Figure 28(d). This figure shows that the maximum achievable output power can be extended up to 70 % of the rated output power, which is a better conclusion than the value obtained based on considering stator copper loss only.

3.3. Pseudo Six-Phase IM Using a Quadruple Three-Phase Stator

A pseudo six-phase (P6P) winding layout suitable for medium-voltage high-power induction machines, which employs quadruple three-phase stator winding sets while providing the same terminal behavior of a 9P6T winding, has been recently introduced, as shown in Figure 29 [49]. In this emerging winding layout, the middle winding group $abc3$ of the 9P6T winding, shown in Figure 29, is replaced by two separate three-phase winding sets, namely $abc3$ and $abc4$, sharing the same stator slots. This way, the stator will house four three-phase winding sets. To maintain the single-layer winding layout advantages of the 9P6T winding, the coils of these two winding groups $abc3$ and $abc4$ are wound together and placed in the corresponding slots at the same time as if they are one coil. The four three-phase winding sets are then connected, as shown in Figure 29(b). The winding groups $abc1$
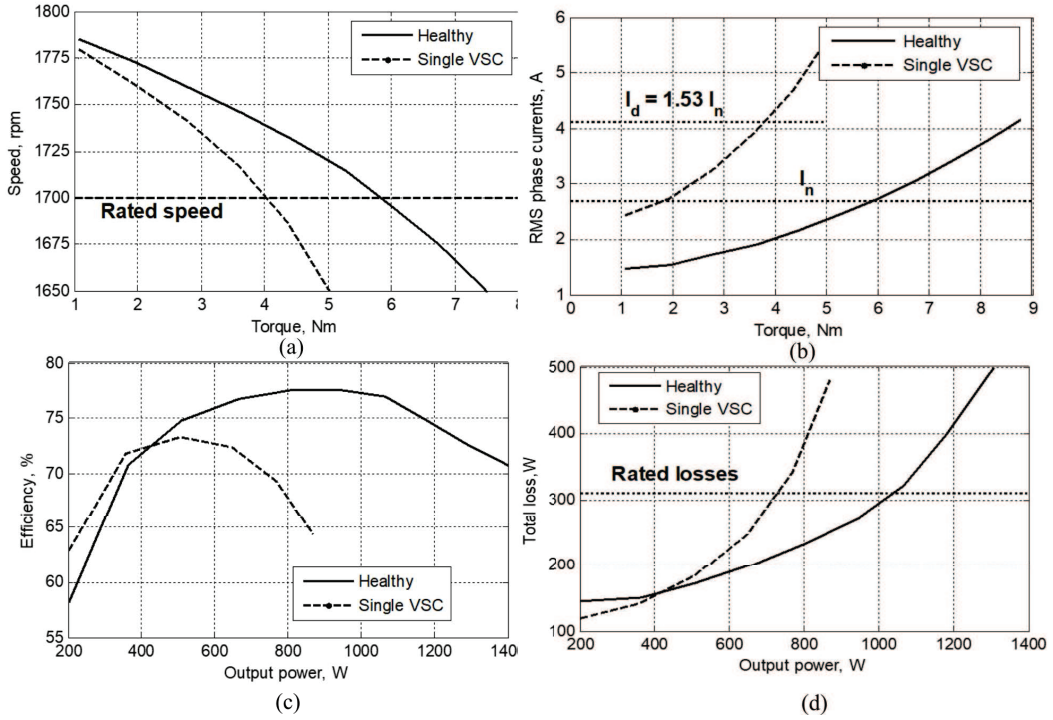
Figure 28. Machine experimental characteristic curves. (a) Torque versus speed. (b) Torque versus phase current. (c) Output power versus efficiency. (d) Output power versus total losses.

and $abc3$ are connected in series forming the first equivalent three-phase group of the P6P stator winding. While the remaining two winding groups $abc2$ and $abc4$ are also connected in series to provide the second equivalent three-phase winding group. This way, the stator will be architecturally equivalent to a traditional asymmetrical six-phase (A6P) stator. Unlike the 9P6T winding, all phases should have the same conductor diameter since all winding groups will carry the same current magnitude. In order to maintain the same MMF production, the total AT of the two winding groups $abc3$ and $abc4$ should also be $1.5N_cI_m$ AT. Hence, the number of turns of these two winding groups should be 0.532 times the number of turns of the winding groups $abc1$ and $abc2$. This can be proven using (39):

$$
\begin{aligned}
\overline{F}^{P6P}_{abc3} &= \frac{3}{2}\left(0.532N_ce^{-j20°}\right)\left(I_me^{-j0°}\right) + \frac{3}{2}\left(0.532N_ce^{-j20°}\right)\left(I_me^{-j40°}\right) \\
&= \frac{3}{2}\left(0.532N_ce^{-j20°}\right)\left(I_me^{-j0°} + I_me^{-j40°}\right) \\
&= \frac{3}{2}0.532N_ce^{20°}1.88I_me^{-j20°} \\
&= \frac{3}{2}N_cI_me^{-j0°}
\end{aligned}
\tag{39}
$$

where, I_m is the phase current amplitude and N_c represents the number of turns. With the AT of the other two winding sets, $abc1$ and $abc2$ is equal to $1.5N_cI_m$ AT each, the total

MMF magnitude of the four sets will be $4.5N_cI_m$, which is the same as the 9P6T winding. Hence, the two winding layouts will be equivalent. Figure 30 shows the MMF harmonic spectra of both 9P6T and P6P windings in two cases, namely, the $\alpha\beta$ subspace excitation at which the current phase angle $\gamma = 40°$ and x-y subspace excitation at which $\gamma = 206.16°$. As shown in Figure 29(a), the slots which house the coil sides of the winding groups $abc3$ and $abc4$ will have a slightly higher number of conductors (approximately 6 %). This also yields an approximate 2 % increase in the total copper volume compared to the 9P6T winding to produce the same air gap flux magnitude, which may be considered a slight increase and can be neglected. Clearly, the P6P winding can be configured with either a single neutral (1N) or an isolated neutral (2N) arrangement. With the former neutral arrangement, the stator winding will be identical to a 9P6T winding.

(a)   (b)
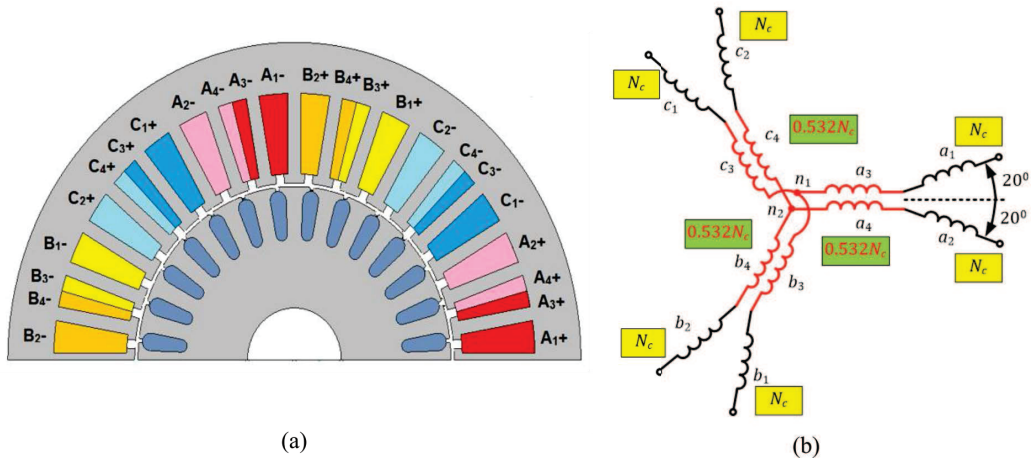
Figure 29. Pseudo six-phase machine. (a) winding layout. (b) connection of different phases.

(a)   (b)
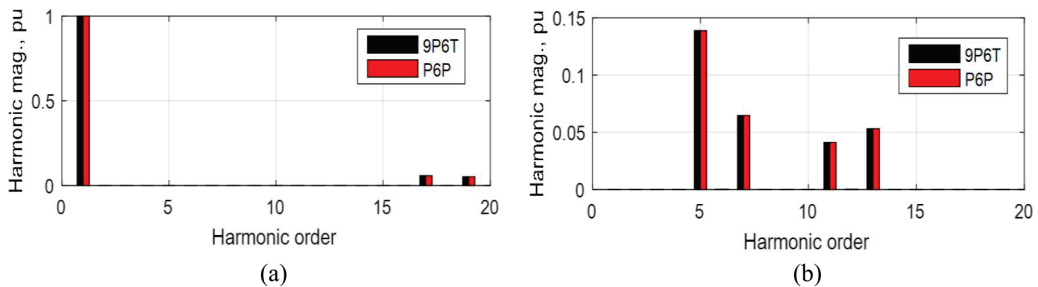
Figure 30. MMF spectra of 9P6T and P6P windings. (a) $\alpha\beta$ excitation with $\gamma = 40°$. (b) $x - y$ excitation with $\gamma = 206.16°$.

3.3.1. Comparison with Conventional A6P Winding

It has been proven in [19] that the 9P6T winding outperforms an equivalent A6P winding under fault conditions. Since the P6P is equivalent to a 9P6T winding, the study is extended herein to derive the required optimal currents and postfault control under one phase open (line a_1 will be assumed open in the following). With the stator winding configured with a 1N arrangement, the same optimal currents for a 9P6T derived in [19] will, therefore, be maintained for the P6P winding. The derivation will consequently be given in this section for the 2N arrangement. The required set of currents that produce rated flux and torque with line a_1 open will be derived under the two well-known optimization criteria, namely, maximum torque (MT) and minimum loss (ML) [30]. For the sake of comparison, the derived optimal currents are compared with those of a traditional A6P winding to highlight the improvement in the torque/current ratio under different strategies.

The optimal currents under one phase open for the P6P are compared with those of a conventional A6P winding, which are derived in [30]. The comparison is made for both possible scenarios, namely MT and ML modes, and under the two possible neutral arrangements. As explained before, the optimal currents for the P6P with 1N will be the same as those derived for the 9P6T winding. Figure 31 reveals this comparison for both neutral arrangements assuming a 5 % gain in the fundamental winding factor of the P6P over the A6P case, with the latter taken as a reference case, as proved in [18]. This will better highlight the improved gained in the machine torque density when the P6P is employed. The comparison shows the optimal currents, the expected copper loss for rated output, P_{loss}, and the maximum achievable torque, T_x, when all healthy phases are limited to 1 pu. The maximum achievable torque is theoretically obtained from the reciprocal of the phase that carries maximum current under rated output torque [30]. This assumption is typically employed to avoid undesirable winding hotspots. In the case of the P6P, T_x is multiplied by the expected 5 % gain in the fundamental winding factor. This rough assumption assumes a linear torque current relation and neglects the effect of the magnetizing current component, I_d. Needless to say, this assumption was roughly used in literature for the sake of comparison between different cases rather than obtaining an accurate torque value, noting that the actual torque current curve is a parameter dependent relationship. Clearly, the P6P winding layout outperforms the conventional A6P winding under different winding arrangements since it corresponds, in general, to a lower copper loss for the same rated output power and a higher maximum achievable torque for the same rated line current. Under the MT strategy, the gain in torque/current ratio of the P6P seems to be higher under the 2N arrangement. On the other hand, a higher torque/current ratio improvement is noted for the 1N arrangement under the ML mode.

3.3.2. Analysis of the P6P Winding Layout

This subsection gives experimental results under healthy and for different postfault scenarios with the two possible neutral arrangements. The machine characteristic curves in per-unit values for both the 9P6T and novel P6P layouts under healthy conditions are shown in Figure 32. In that case, the P6P is configured with two isolated neutrals to avoid the circulating zero-sequence current components, while the 9P6T possesses a single neutral point. The rated efficiency under rated output power and speed is approximately 81%. With

Neutral arrangement	2N		1N	
Winding	P6P	A6P [30]	P6P (Similar to 9P6T [50])	A6P [30]
Max. Torque (MT)				
Optimal line currents, pu	$\begin{bmatrix}\bar{i}_{a1}\\\bar{i}_{b1}\\\bar{i}_{c1}\\\bar{i}_{a2}\\\bar{i}_{b2}\\\bar{i}_{c2}\end{bmatrix}=\begin{bmatrix}0\\1.723\angle-93.1^0\\1.723\angle86.9^0\\1.723\angle-6.92^0\\1.723\angle-186.9^0\\0\end{bmatrix}\cdot e^{j\omega_s t}$	$\begin{bmatrix}\bar{i}_{a1}\\\bar{i}_{b1}\\\bar{i}_{c1}\\\bar{i}_{a2}\\\bar{i}_{b2}\\\bar{i}_{c2}\end{bmatrix}=\begin{bmatrix}0\\1.732\angle-90^0\\1.732\angle90^0\\1.732\angle0^0\\1.732\angle-180^0\\0\end{bmatrix}\cdot e^{j\omega_s t}$	$\begin{bmatrix}\bar{i}_{a1}\\\bar{i}_{b1}\\\bar{i}_{c1}\\\bar{i}_{a2}\\\bar{i}_{b2}\\\bar{i}_{c2}\end{bmatrix}=\begin{bmatrix}0\\1.472\angle-88.9^0\\1.472\angle143.2^0\\1.472\angle-18.4^0\\1.472\angle171.5^0\\1.472\angle34.7^0\end{bmatrix}\cdot e^{j\omega_s t}$	$\begin{bmatrix}\bar{i}_{a1}\\\bar{i}_{b1}\\\bar{i}_{c1}\\\bar{i}_{a2}\\\bar{i}_{b2}\\\bar{i}_{c2}\end{bmatrix}=\begin{bmatrix}0\\1.44\angle-85.4^0\\1.44\angle145.9^0\\1.44\angle-13^0\\1.44\angle178.5^0\\1.44\angle39.4^0\end{bmatrix}\cdot e^{j\omega_s t}$
P_{loss}, pu	**1.98**	2	**1.8**	1.73
T_x, pu	0.5803 × 1.05 = **0.61**	0.5774	0.679 × 1.05 = **0.713**	**0.694**
Min. Loss (ML)				
Optimal line currents, pu	$\begin{bmatrix}\bar{i}_{a1}\\\bar{i}_{b1}\\\bar{i}_{c1}\\\bar{i}_{a2}\\\bar{i}_{b2}\\\bar{i}_{c2}\end{bmatrix}=\begin{bmatrix}0\\0.866\angle-90^0\\0.866\angle90^0\\1.784\angle-21.1^0\\1.803\angle-169.1^0\\0.9906\angle83.8^0\end{bmatrix}\cdot e^{j\omega_s t}$	$\begin{bmatrix}\bar{i}_{a1}\\\bar{i}_{b1}\\\bar{i}_{c1}\\\bar{i}_{a2}\\\bar{i}_{b2}\\\bar{i}_{c2}\end{bmatrix}=\begin{bmatrix}0\\0.866\angle-90^0\\0.866\angle90^0\\1.803\angle-16.1^0\\1.803\angle-163.9^0\\1\angle90^0\end{bmatrix}\cdot e^{j\omega_s t}$	$\begin{bmatrix}\bar{i}_{a1}\\\bar{i}_{b1}\\\bar{i}_{c1}\\\bar{i}_{a2}\\\bar{i}_{b2}\\\bar{i}_{c2}\end{bmatrix}=\begin{bmatrix}0\\1.005\angle-120.6^0\\1.005\angle120.4^0\\1.817\angle-20.7^0\\1.197\angle-163.4^0\\1.091\angle64.6^0\end{bmatrix}\cdot e^{j\omega_s t}$	$\begin{bmatrix}\bar{i}_{a1}\\\bar{i}_{b1}\\\bar{i}_{c1}\\\bar{i}_{a2}\\\bar{i}_{b2}\\\bar{i}_{c2}\end{bmatrix}=\begin{bmatrix}0\\1.146\angle-130.9^0\\1.146\angle130.9^0\\1.867\angle-15.5^0\\0.943\angle-148^0\\1.12\angle63.4^0\end{bmatrix}\cdot e^{j\omega_s t}$
P_{loss}, pu	**1.49**	1.5	**1.32**	1.37
T_x, pu	0.554 × 1.05 = **0.582**	0.554	0.55 × 1.05 = **0.578**	0.536

Figure 31. Optimal Currents under Different Postfault Strategies for The P6P and the Traditional A6P Windings.

all tests carried out at a reference speed of 1000 rpm due to dc-link voltage limitation, the machine efficiency for the same rated output torque is expected to be relatively lower. As depicted in Figure 32, the two windings seem equivalent, especially under loads near the rated load torque. A slight improvement in the machine efficiency and a smaller phase current magnitude is noted under light loads when the machine is equipped with the P6P winding layout. This improvement is due to the complete elimination of the circulating zero-sequence current component since the P6P is configured with a 2N arrangement. Under light loads, the effect of core saturation causes a notable increase in the induced third harmonic current with the machine equipped with a 9P6T winding. This effect significantly decreases as the machine is mechanically loaded, and the two winding layouts offer similar performance.

Moreover, the performance of the novel P6P machine under different postfault strategies with a one-phase open condition is investigated based on the adopted postfault strategy and neutral arrangement. Figure 33 shows the measured steady-state current waveforms and their sequence components in per-unit for the MT and ML modes, and the two neutral arrangements. Clearly, under MT mode, the remaining healthy currents are equal in magnitude with a per-unit current magnitude of 1.723 pu and 1.44 pu for the 2N and 1N neutral arrangements, respectively, under rated load torque. While, under ML mode, the remaining healthy current magnitudes are generally unequal. A general conclusion drawn from
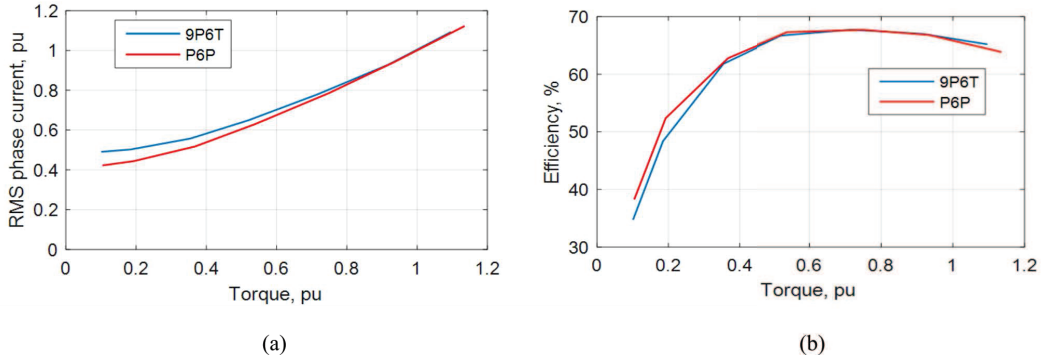
Figure 32. Comparison between the healthy steady-state characteristic for 9P6T and P6P winding layouts at 1000 rpm. (a) Torque-current curve. (b) Torque-efficiency curve. (Rated torque = 6 Nm, Rated current = 2.7 A).

the obtained current waveforms is that a higher quality current is achieved when the P6P winding is configured with a 2N arrangement. The current waveform for the two postfault strategies seems to be more sinusoidal without the need for employing harmonic compensation techniques. This is simply because the circulating zero-sequence current component between the two inverters, experienced under the 1N arrangement, is completely avoided.

The effect of neutral arrangement on machine steady-state performance under postfault operation is also assessed by plotting the machine characteristic curves for the full torque loading range. The healthy case is used for benchmarking. Figure 34 shows the machine curves in per-unit values with the base values given in the figure caption. Under fault conditions, machine derating is inevitably experienced by limiting the line currents to their rated values to avoid possible excessive overheating [30]. However, the full loading range will preferably be displayed in this study to indicate to what extent the machine developed torque and the corresponding efficiency can reach under different modes with respect to the healthy case. Generally, the ML mode offers better efficiency than the MT mode due to the fact that stator loss is minimized under this mode. On the other hand, the 1N arrangements generally correspond to better steady-state efficiency at lower current magnitudes for the same developed torque for both MT and ML modes. Furthermore, the torque profiles under both the healthy case and the four postfault strategies are shown in Figure 35. The simulated average torque, as well as the percentage torque ripple, are given in Table 4. Clearly, for the healthy case, the machine exhibits an almost ripple-free torque profile. With the machine controlled to draw the reference optimal currents under one phase open, the average torque magnitudes are approximately equal rated torque for all cases. Interestingly, the percentage torque ripple is less than 5 %, which safely falls within the acceptable limits, but with no notable improvement among different postfault operation cases.

By comparing the obtained results with those for a conventional A6P given in [30], it can be concluded that the operation of the emerging P6P winding layout seems equivalent to a conventional A6P while providing enhanced performance due to the improvement in machine winding factor. The full comparison between A6P and 9P6T (equivalent to P6P
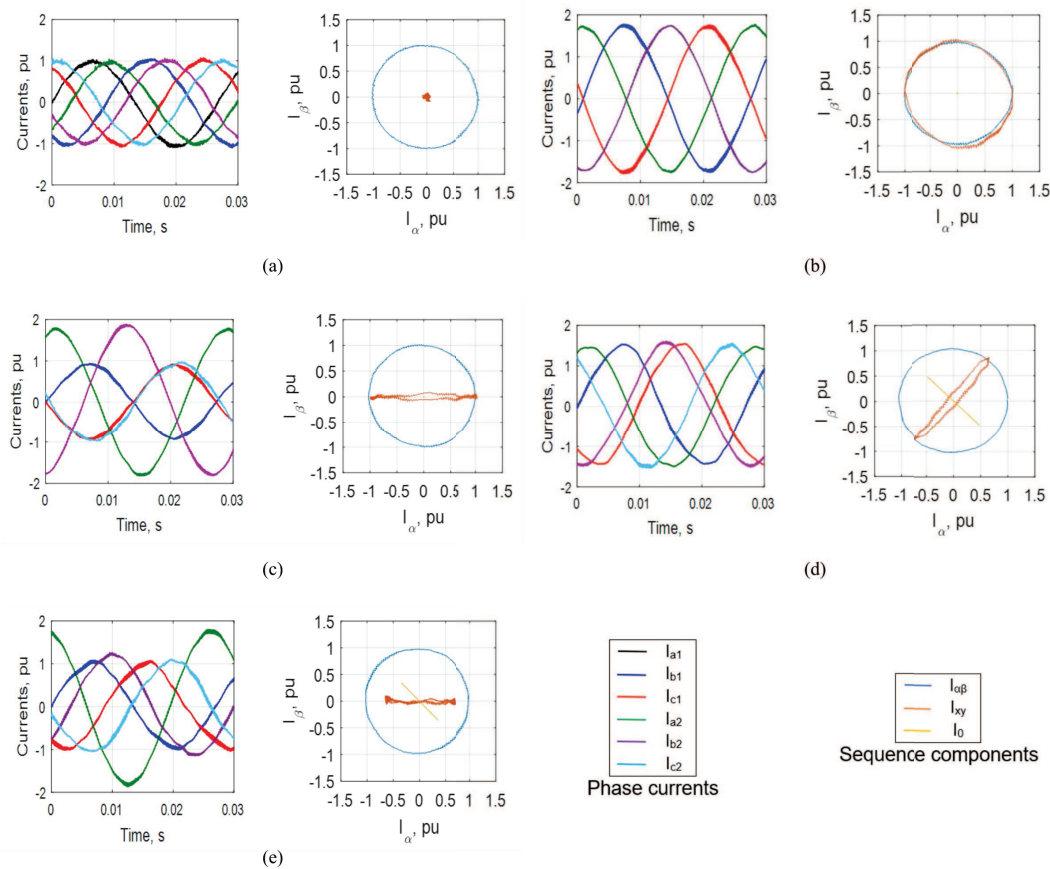
Figure 33. Steady-state current waveforms and their sequence components in per unit at 1000 rpm and full load torque. (a) Healthy. (b) MT2N. (c) ML2N. (d) MT1N. (e) ML1N.

Table 4. FE Simulation Results for Torque Profiles under Different Postfault Strategies.

Mode	H	MT2N	ML2N	MT1N	ML1N
T_{av}, pu	1	0.986	0.994	0.988	0.995
$\%\Delta T$	0.75	4.9	4.3	4.85	4.25

with 1N) was already given in [19]. Therefore, the same improvement gained under P6P with a 2N arrangement will inevitably be obtained.
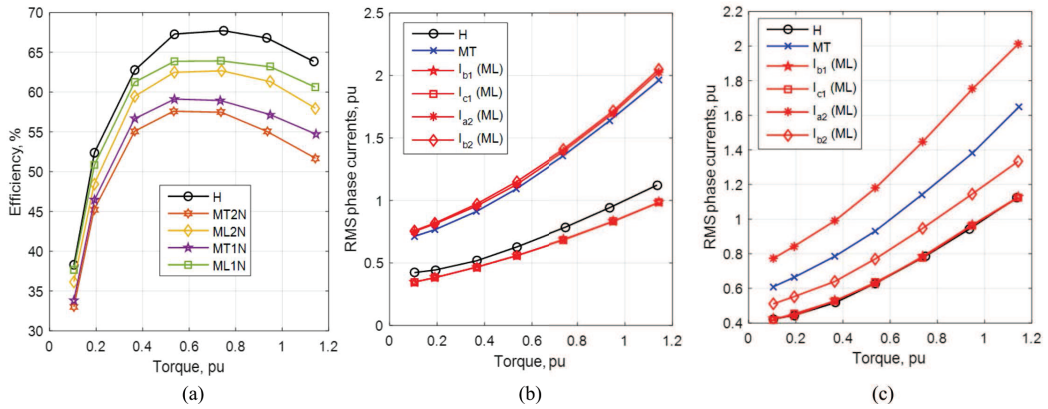
Figure 34. Steady-state characteristic curves at 1000 rpm. (a) Torque-efficiency curve. (b) Torque-current curve (2N). (c) Torque-current curve (1N). (Rated torque = 6 Nm, Rated current = 2.7 A).
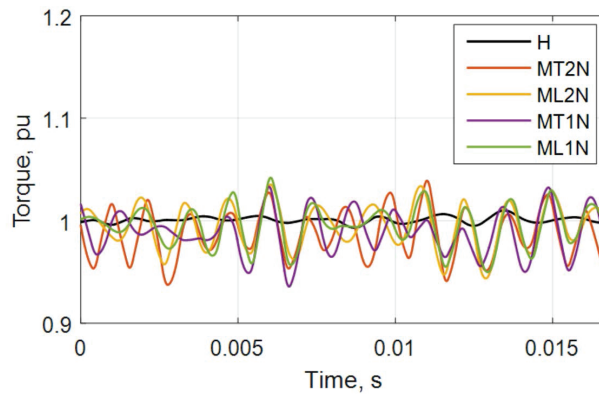
Figure 35. Torque profiles under different postfault strategies (Rated torque = 6 Nm).

4. Building Multiphase Winding with Standard Three-Phase Stators

Although multiphase machines with multiple three-phase winding sets have been favored in many applications, literature has shown that machines with a prime number of phases, such as five-phase machines, generally outperform other phase orders, especially in terms of machine torque density. One of the major problems when dealing with a prime number of phases, either in academic research or industrial applications, is the special stator design. To overcome this issue, a simple technique to rewind standard three-phase stator frames with any n-phase symmetrical prime phase order winding is investigated [51]. The new winding layout design is derived based on the star of slots, which proved to be an appropriate design tool for designing different winding layouts [52]. The star of slots drawing

is widely explained in the literature and can simply be formed for any existing stator by drawing a number of phasors equals the number of stator slots, S. Each phasor represents the fundamental emf component induced in the coil side located in each corresponding slot. The angle between different phasors, therefore, represents the angle between adjacent slots in electrical degrees. Since most existing three-phase IMs have a number of slots corresponding to a symmetrical winding distribution, the presented analysis will be limited to this case. The given concept also assumes the same number of poles for the new winding to ensure the same machine output power and avoid core saturation.

Taking an 18-slot/2-pole three-phase stator as an example, the corresponding star of slots, represented using black-colored phasors, is shown in Figure 36. For this case, the electrical angle between each slot, γ, will be 20°. In this example, it is required to rewind this stator with an equivalent five-phase symmetrical winding, where the angle between each phase is 72°. For a conventional five-phase symmetrical winding, the number of slots per pole is preferably selected to be 10, which corresponds to a number of slots per pole per phase, q, of 2 [44]. Hence, for the given 9-slot/pole stator and over the same figure, the magnetic axes of the five phases of the new winding are also drawn using the single-pole symmetry, which works equally well for either odd or even phase order [53]. For this representation, the magnetic axis of each phase may be positive or negative, as shown in Figure 36. The magnetic axis of phase a and the star of slots phasor of slot 1 are assumed collinear. For simplicity, each slot comprises a single coil side as a first assumption. Now, each phase of the five-phase winding can simply be constructed using the two adjacent phasors of the star of slots of the existing three-phase stator. For example, phase b can be obtained from the coils occupying slots 4 and 5.
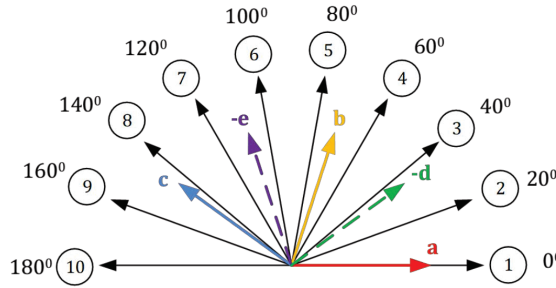
Figure 36. The star of slots for an 18-slot/2-pole stator.

To generalize the presented case, the following angle vectors are defined. First, the elements of the vector W_n represent the angles of the magnetic axes of the new n-phase winding.

$$W_n = [\alpha_1 \quad \alpha_2 \quad \ldots \quad \alpha_j \quad \ldots \quad \alpha_n] \tag{40}$$

While the elements of the vectors d_1 and d_2 represent the angles of the two adjacent phasors of the existing three-phase star of slots to each phase of the new n-phase winding.

$$d_1 = [\delta_{11} \quad \delta_{12} \quad \ldots \quad \delta_{1j} \quad \ldots \quad \delta_{1n}] \tag{41}$$

$$d_2 = [\delta_{21} \quad \delta_{22} \quad \ldots \quad \delta_{2j} \quad \ldots \quad \delta_{2n}] \tag{42}$$

For the given 18-slot stator, these vectors are defined as follows:

$$W_5 = \begin{bmatrix} 0° & 72° & 144° & 36° & 108° \end{bmatrix}$$
$$d_1 = \begin{bmatrix} 0° & 60° & 140° & 20° & 100° \end{bmatrix} \qquad (43)$$
$$d_2 = \begin{bmatrix} 0° & 80° & 160° & 40° & 120° \end{bmatrix}$$

Each phasor of the new n-phase winding can be constructed as the phasor summation of the two nearest black-colored phasors located in the two adjacent slots in Figure 36. However, this technique will yield coils with a different number of turns. The main criterion to obtain the required number of turns of each coil is to obtain equal emf waveforms across all phases, with a displacement angle of $2\pi/n$ among phases. If the effective number of turns per pole of each phase is N_{ph}, the number of turns, N_{1j} and N_{2j}, of the coils located in the two adjacent slots to phase j can simply be obtained from

$$\begin{bmatrix} N_{phj} \\ 0 \end{bmatrix} = \begin{bmatrix} \cos(\alpha_j - \delta_{1j}) & \cos(\alpha_j - \delta_{2j}) \\ \sin(\alpha_j - \delta_{1j}) & \sin(\alpha_j - \delta_{2j}) \end{bmatrix} \begin{bmatrix} N_{1j} \\ N_{2j} \end{bmatrix} \qquad (44)$$

Equation (44) is solved using the angles corresponding to each phase, as defined by (40)-(42). For the five-phase example, the calculated number of conductors per slot and hence the suggested winding layout under one pole are shown in Figure 37.

Phase (j)		A		b		c		d		e
Slot (i)	1	2	3	4	5	6	7	8	9
$\dfrac{N_{ij}}{N_{ph}}$	1 ⊙	0.2 ⊗	0.8 ⊗	0.4 ⊙	0.6 ⊙	0.6 ⊗	0.4 ⊗	0.8 ⊙	0.2 ⊙
N_{ci}/N_{ph}	1	0.2	0.8	0.4	0.6	0.6	0.4	0.8	0.2

Figure 37. Number of Cond./Slot for A Single-layer Five-phase 18-Slot/2-Pole Stator.

Clearly, for the obtained single-layer winding using the proposed technique, the diversion between the maximum and minimum number of conductors per slot is significant ($N_{ph} - 0.2N_{ph} = 0.8N_{ph}$), which yields a poor filling factor. To improve this drawback, a double-layer winding layout would be an ideal proposition, which can simply be obtained using the concept of stator winding shifting [54]. This concept implies that two identical stator windings are combined after shifting the second one with a certain mechanical angle β. To maintain the same number of stator slots, this angle should be a multiple of γ. The simplest case is to shift the winding shown in Figure 38 by one slot, hence $\beta = \gamma$. This will yield the winding layout shown in Figure 38. The maximum percentage difference in the number of conductors between different slots for this latter case will be 20%, which is much better than the initial single-layer design.

To minimize the difference between the number of conductors per slot in different slots, a preceding step can be done before shifting the stator winding. Since phase a comprises one coil per pole, it is clear from Figure 37 that slot 1 has the largest number of conductors among different slots. The slots, which have the next highest number of conductors

Slot (i)		1	2	3	4	5	6	7	8	9
$\dfrac{N_{ij}}{N_{ph}}$	U	1 ⊙	0.2 ⊗	1	0.4 ⊙	1	0.6 ⊗	1	0.8 ⊙	1
	L	0.2 ⊗	1 ⊙	⊗	0.8 ⊗	1 ⊙	0.6 ⊙	⊗	0.4 ⊗	⊙
mN_{ci}/N_{ph}		1.2	1.2	1	1.2	1	1.2	1	1.2	1
N_{ci}/N_c^3		1.08	1.08	0.9	1.08	0.9	1.08	0.9	1.08	0.9

Figure 38. Number of Cond./Slot For A Double-layer Five-Phase 18-Slot/2-Pole Stator By Applying Stator Winding Shifting.

($0.8N_{ph}$), are slots 3 and 8. The number of conductors in slot 1 can then be reduced to $0.8N_{ph}$ by moving the extra conductors ($N_{ph} - 0.8N_{ph} = 0.2N_{ph}$) of this phase to be placed in the two adjacent slots. This is done by sharing these extra conductors equally between adjacent slots 2 and 9 (or 18 under the second pole). This way, the total number of turns per phase is preserved. Since the magnetic axis of these two adjacent slots is shifted by the angle γ, the actual number of conductors that belong to phase a in these adjacent slots to maintain the same MMF magnitude from this phase will be given by:

$$\Delta N_\alpha = \left(\frac{1-0.8}{2}\right)\frac{N_{ph}}{\cos\gamma} = 0.1064N_{ph} \tag{45}$$

which can be approximated to $0.1N_{ph}$ for $\gamma = 20°$. The stator winding shifting is then applied to further improve the filling factor, as explained before. The final winding layout is then shown in Figure 39. The extra conductors sharing concept defined by (45) can also be applied to increase the number of conductors in certain slots from other coils that belong to the same phase and located in adjacent slots. For a higher number of stator slots, the concept of stator shifting can be repeated h times by shifting the obtained winding layout, with one slot in each step, to minimize the diversion between the number of conductors in different slots. However, this will yield a more complicated winding, a higher number of coils per phase, and may be a higher number of layers. Hence, the final optimal design is subjected to a trade-off between the winding complexity and the acceptable air gap flux distribution quality.

The last step in this design is to select the suitable number of turns per phase per pole, N_{ph}, of the new n-phase winding, keeping in mind that applying the stator winding shifting concept will double the number of turns per phase each time. Therefore, the employed criterion in this study is to maintain the same copper volume of the existing three-phase winding. If it is assumed that the number of conductors per slot and the corresponding cross-section area of the existing three-phase stator are N_c^3 and a_c^3, respectively, N_{ph} can be obtained by equating the total number of conductors in both cases.

$$\sum_{i=1}^{S} N_{ci}\, a_c^n = S\, N_c^3\, a_c^3 \tag{46}$$

Slot (i)		1	2	3	4	5	6	7	8	9
$\dfrac{N_{ij}}{N_{ph}}$	U	0.9 ⊙	0.2 ⊗	1 ⊗	0.35 ⊙	1.1	0.55 ⊗	1.1	0.8 ⊙	0.1 ⊗
	L	0.2 ⊗	0.9 ⊙	0.1 ⊙	0.8 ⊗	⊙	0.55 ⊙	⊗	0.35 ⊗	1 ⊙
mN_{ci}/N_{ph}		1.1	1.1	1.1	1.15	1.1	1.1	1.1	1.15	1.1
N_{cj}/N_c^3		1	1	1	1.04	1	1	1	1.04	1

Figure 39. Number of Cond./Slot for A Double-layer Five-Phase 18-Slot/2-Pole Stator And Better Filling Factor.

where, a_c^n is the cross-section area of the n-phase winding. For the winding given by Figure 39, for example, and by applying (46), where the number of winding shifts, h, is 1 (i.e., $m = 2$), hence;

$$a_c^n \frac{Nph}{2}\left(5 \times 1.2 + 4 \times 1\right) = 9N_c^3 a_c^3 \tag{47}$$

Assuming same conductor size ($a_c^n = a_c^3$), hence $N_{ph} = 1.8N_c^3$. The ratios between the required number of turns of each slot N_{ci} to the initial number of conductors of the three-phase machine N_c^3 are also given in Figure 38 and Figure 39 for both suggested winding layouts. For both winding layouts, the maximum number of conductors will be 8 % and 4 % above the initial three-phase machine, respectively. Other slots will have a smaller number of conductors; however, the same copper volume is preserved. Although the winding given by Figure 39 gives a better distribution for the number of conductors among different slots, it corresponds to a higher number of coils per phase. Finally, the two winding layouts can offer approximate gains in the fundamental MMF component of 2 % and 1.5 %, respectively, compared with a conventional single-layer three-phase winding having $q = 3$, which represents an additional merit gained when upgrading the three-phase stator to a higher phase order.

4.1. General n-Phase Winding

In this subsection, the concept is extended to a general phase order with different number of slots. The final winding layouts for the well-known seven- and eleven-phase symmetrical windings are also given. For a given n-phase winding, there will be a minimum number of slots that would optimize the air gap flux distribution. Optimally, if standard three-phase stator frames are used, the number of stator slots should be close to the required number of slots for a standard symmetrical n-phase stator. In conventional five- and seven-phase windings, q is commonly selected to be 2 [25], which entails a number of slots per pole of 10 and 14 for the two cases, respectively. The nearest number of slots per pole for these numbers using standard three-phase stator frames will be 9 and 12 for the five- and seven-phase cases, respectively. In the case of an 11-phase winding, concentrated single-layer winding with $q = 1$ was proved to ensure a perfect sinusoidal flux distribution [55], which

entails an 11-slot/pole stator. The nearest number of slots per pole for this latter case will be 12.

As mentioned in the previous subsection, the final winding design will be subjected to certain constraints. The suggested constraints to decide the final design will be as follows:

- To simplify the winding process, all designs are limited to double-layer winding layouts.

- The fundamental MMF component is maximized.

- The difference between the maximum and minimum number of conductors N_c^{max} and N_c^{min} among different slots should be minimized to ensure approximate equal end turn volumes.

- (N_c^3) should be less than 1.28. This is based on the ratio between the recommended filling factor limit values of IMs ($0.35 - 0.45$) [24, 25].

Based on these constraints, Figure40 gives the optimal designs for the most common slots per pole of standard three-phase stator frames assuming the same copper volumes. According to Table 40, the most available standard stator frames can be used to build a five-phase machine. On the other hand, the minimum number of slots per pole to build a seven-phase machine will be 9, corresponding to an approximate 3 % gain in the fundamental component. For this slot number, the optimal winding design is directly obtained from the initial design based on (44) without applying the stator shifting. Increasing the number of slots will correspond to a better air gap flux distribution but at the cost of a more complex winding with a higher number of layers. For a 12-slot/pole stator, an acceptable seven-phase winding design can be obtained while considering the above-mentioned constraints with the stator shifting concept applied a single time. Finally, in case of 11-phase, the first valid standard three-phase stator is the 12-slot/pole one. The obtained MMF fundamental gain is 3.7 %, which is the highest among different phase orders. A higher number of slots can be used; however, the obtained winding layouts will necessitate a higher number of layers. Some winding layout examples are given in Figure 41-Figure 43. It is worth mentioning that the sequence components of magnetizing flux and stator leakage flux are extensively explained in [9].

Phase S/pole	Five-phase				Seven-phase				Eleven-phase			
	Shift	N_c^{max}/N_c^3	N_c^{min}/N_c^3	% Gain	Shift	N_c^{max}/N_c^3	N_c^{min}/N_c^3	% Gain	Shift	N_c^{max}/N_c^3	N_c^{min}/N_c^3	% Gain
6	0	1.064	0.96	0.8%	Invalid				Invalid			
9	1	1.08	0.9	2%	0	1.096	0.92	2.9%	Invalid			
12	2	1.19	0.96	2%	1	1.11	0.857	2.8%	0	1.034	0.99	3.7%
18	5	1.167	0.85	2.3%	3	1.056	0.92	3%	Complex winding			

Figure 40. Possible N-Phase Winding Layouts for Different Slot Numbers.

Phase (j)		a	b	c	d	e	f	g		
Slot		1	2	3	4	5	6	7	8	9
N_{ij}/N_{ph}	U	a (0.86)	-e (0.72)	b (0.44)	-f (0.15)	-f (0.86)	c (0.86)	-g (0.58)	d (0.29)	-a (0.08)
	L		a (0.08)	-e (0.29)	b (0.58)			c (0.15)	-g (0.44)	d (0.72)
mN_{ci}/N_{ph}		0.86	0.8	0.73	0.73	0.86	0.86	0.73	0.73	0.8
N_{ci}/N_c^3		1.096	1.01	0.92	0.92	1.096	1.096	0.92	0.92	1.01

Figure 41. Seven-Phase Winding Using A 9-Slot/Pole Stator.

Phase (j)		a	b	c	d	e	f	g					
Slot		1	2	3	4	5	6	7	8	9	10	11	12
N_{ij}/N_{ph}	U	a (0.72)	-e (0.22)	-e (0.78)	b (0.45)	b (0.78)	-f (0.66)	c (0.12)	c (0.78)	-g (0.33)	-g (0.78)	d (0.56)	-a (0.06)
	L	-d (0.22)	a (0.72)	a (0.06)	-e (0.56)		b (0.33)	-f (0.78)	-f (0.12)	c (0.66)		-g (0.45)	d (0.78)
mN_{ci}/N_{ph}		0.94	0.94	0.84	1.01	0.78	0.99	0.9	0.9	0.99	0.78	1.01	0.84
N_{ci}/N_c^3		1.033	1.033	0.923	1.11	0.857	1.088	0.99	0.99	1.088	0.857	1.11	0.923

Figure 42. Seven-Phase Winding Using A 12-Slot/Pole Stator.

Phase (j)		a	b	c	d	e	f	g	h	i	j	k	
Slot		1	2	3	4	5	6	7	8	9	10	11	12
N_{ij}/N_{ph}	U	a (0.91)	-g (0.91)	b (0.82)	-h (0.73)	c (0.64)	-i (0.55)	d (0.46)	-j (0.37)	e (0.28)	-k (0.19)	f (0.1)	-a (0.05)
	L		a (0.05)	-g (0.1)	b (0.19)	-h (0.28)	c (0.37)	-i (0.46)	d (0.55)	-j (0.64)	e (0.73)	-k (0.82)	f (0.91)
N_{ci}/N_c^3		0.995	1.034	0.99	0.992	0.994	0.995	0.995	0.995	0.994	0.992	0.99	1.034

Figure 43. Eleven-Phase Winding Using A 12-Slot/Pole Stator.

4.2. Analysis of Multiphase Windings Based on Standard Three-Phase Stators

The addressed winding layouts are corroborated by rewinding a standard 1 Hp, 4-pole, 400V, 50Hz, 36-slot three-phase IM as five- and seven-phase machines. The existing three-phase machine has a single-layer winding with a number of conductors per slot $N_c^3 = 84$ and a conductor diameter of 0.56 mm. The total number of turns per phase will be 252 turns. The same stator is rewound using the five-phase and seven-phase windings given by Figure 38 and Figure 41, assuming the same conductor diameter. Therefore, the total number of turns per phase will be 150 and 108 for the five-phase and seven-phase windings, respectively. The numbers of conductors for different slots of the prototype machine are shown in Figure 44 and Figure 45, respectively.

The new phase voltages will be $(3/5) \times 230$ V 138 V and $(3/7) \times 230$ V 98.6 V for the five- and seven-phase stators, respectively [25]. While same rated RMS current of 2.1 A is maintained at a full load speed of 1320 rpm. A simulation study based on finite element simulations is carried out to compare the new five- and seven-phase winding layouts with the conventional three-phase case. A comparative study with standard five- and seven-phase distributed windings is also included. While the experimental verification is performed for

| Phase (j)	a		b		c		d		e
Slot (i)	1	2	3	4	5	6	7	8	9
N_{ij} U	75	15	75	30	75	45	75	60	75
N_{ij} L	15	75	75	60	75	45	75	30	75
N_{ci}	90	90	75	90	75	90	75	90	75

Figure 44. Experimental Five-Phase Winding.

Phase (j)	a		b		c		d		e		f		g
Slot (i)	1	2	3	4	5	6	7	8	9
N_{ij} U	91	77	46	16	91	91	61	31	8
N_{ij} L	91	8	31	61	91	91	16	46	77
N_{ci}	91	85	77	77	91	91	77	77	85

Figure 45. Equivalent Seven-Phase Winding.

the five-phase winding under different operational conditions.

To verify that the three-phase-based new winding layouts will perfectly yield a symmetrical n-phase machine, finite element simulations are employed in this subsection using JMAG-Studio 10. The simulation study will be carried out under normal n-phase sinusoidal excitation and with a third harmonic injection applied. The latter case will expectedly yield a trapezoidal air gap flux distribution, better core utilization, and, eventually, a torque density enhancement [55, 56]. In the following part, the machine stator phase currents, induced rotor bar currents, and torque profiles will be compared for the three cases. Under sinusoidal excitation, the machine is simulated at a rated speed of 1320 rpm. While under third harmonic injection, the machine speed is adjusted such that same rated RMS line current of 2.1 A is maintained, which corresponds to a rotor speed of 1365 rpm.

Figure 36(a) firstly depicts the MMF harmonic spectra of the five- and seven-phase windings, obtained based on winding function for a unit stator current, in comparison to the standard three-phase case while assuming sinusoidal balanced stator currents. While the corresponding MMF distributions are also shown in Figure 46(b and c). It is evident that the recent windings, while offering 2 % and 3 % gains in the fundamental component for the five- and seven-phase windings, respectively, the MMF spectra seem to be even better than the conventional three-phase case. With the third harmonic injection applied, flat-topped MMF distributions are obtained, as desired, in the two cases.

The machine flux density distributions under different cases are shown in Figure 47. Comparing the equivalent five- and seven-phase winding layouts with the three-phase case, the machine flux distributions are better than the three-phase case, as a known salient feature of multiphase winding in general. When a third harmonic injection is applied, the flux densities of different slots under a certain pole (dashed red area in Figure 47) tend to be approximately equal, as indicated by the more teeth/pole having the same color code (green).
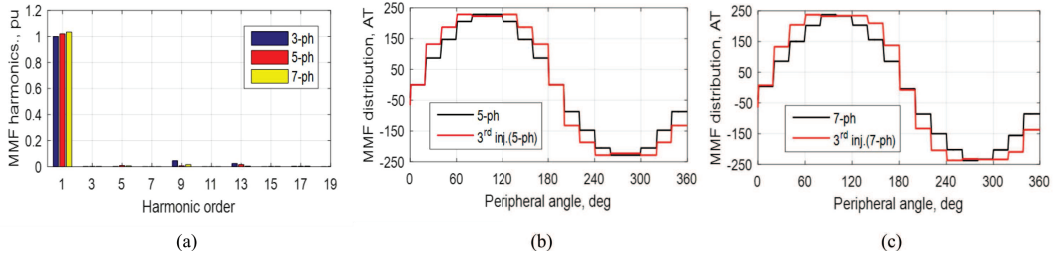
(a)

(b)

(c)

Figure 46. MMF harmonic spectra for all windings with sinusoidal current excitation. (b) MMF distribution of 5-ph winding. (c) MMF distribution of 7-ph winding.

This, therefore, indicates a quasi-square air gap flux distribution. It is worth mentioning that the stator back-iron flux will slightly be increased when a third-harmonic injection is applied. However, for the considered case, the flux density is still below the saturation level to yield undesirable effects. Otherwise, the applied voltage should be reduced.

(a)

(b)

(c)

(d)

(e)
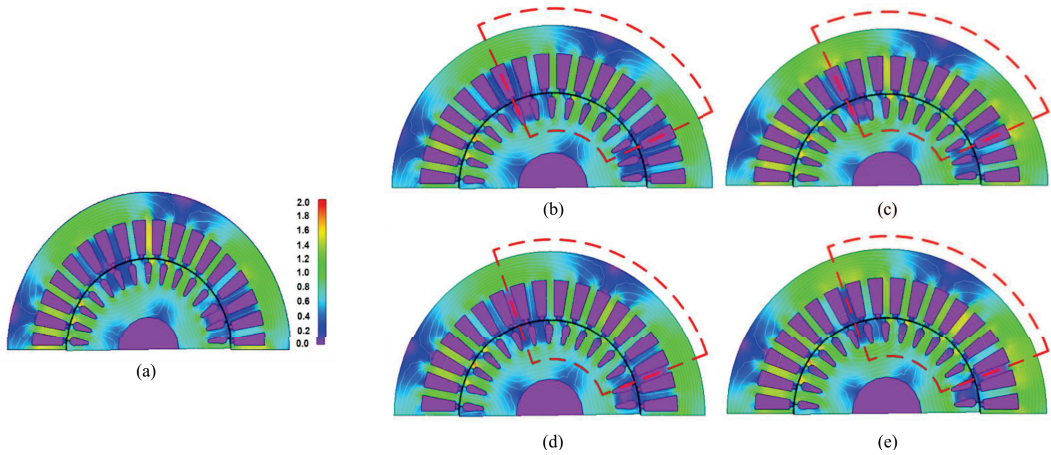
Figure 47. Flux density distribution. (a) 3-ph. (b) 5-ph. (c) 5-ph with 3rd harmonic injection. (d) 7-ph. (e) 7-ph with 3rd harmonic injection.

Figure 48(a and b) show the stator phase currents for the five-phase winding for a conventional sinusoidal supply and with third harmonic injection employed, respectively. The same is shown in Figure 48(c and d) for the seven-phase winding. In both five-phase and seven-phase windings, a small unbalance component, but higher in the seven-phase case is observed in the current waveforms. This is due to the difference in the leakage stator inductance between different phases due to the uneven distribution of different coils sides between the upper and lower layers of different phases. This can be much improved if the number of stator slots is selected to be close enough to the conventional n-phase case. Hence, building a seven-phase stator using a 12-slot/pole stator will be a better option to minimize this impedance mismatch. Nevertheless, this small current unbalance does not give rise to a notable torque ripple component since the secondary subspace can be assumed

as a non-torque/flux producing subspace, as clear from Figure 48(e). Needless to say, this small current unbalance is even expected in conventional symmetrical n-phase winding due to different unavoidable machine and/or inverter asymmetries.
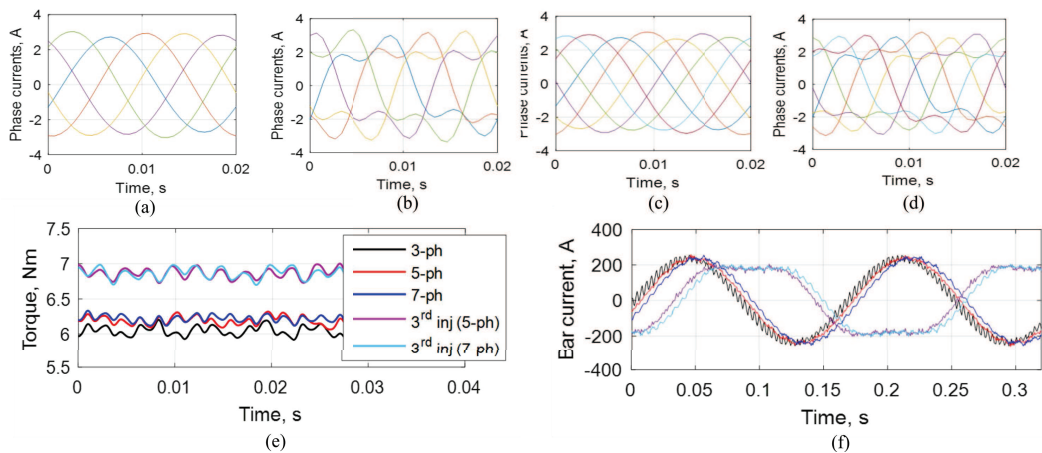

Figure 48. Finite element results for different stator winding layouts. (a) 5-ph. (b) 5-ph with 3rd harmonic injection. (c) 7-ph. (d) 7-ph with 3rd harmonic injection. (e) Torque profiles. (f) Induced bar current.

The simulated results to the average torque and the percentage torque ripple are given in Table 5. For a sinusoidal input supply, the five- and seven-phase windings offer a torque gain of 2.3 % and 2.8 % over the conventional three-phase case, respectively. When a third harmonic current injection is applied, an extra 10 % gain is obtained, similar to conventional five- and seven-phase windings [25], which ends up with a total torque gain of 13.4 % and 13.5 % over the initial three-phase winding for the five-phase and seven-phase winding, respectively. The induced rotor bar current is shown in Figure 48(f). Clearly, the induced current ripple in the bar current waveform is reduced in the five-phase and seven-phase cases compared to the original three-phase case. This is, of course, a direct result of the relative improvement in the air gap flux distribution, reflecting the torque ripple magnitude, as depicted by Figure 48(e). Under the third harmonic injection, the rotor current has a flat-topped waveform due to the quasi-square air gap flux distribution.

Table 5. Simulation Results to The Prototype Machine Torque Under Different Winding Layouts.

Case	3-ph	5-ph	7-ph	5-ph with harmonic injection	7-ph with harmonic injection
T_{av}, Nm	6.05	6.19	6.22	6.86	6.87
$\%\Delta T$	2.3	2	1.4	2.2	2.1

To co-support the validity of the presented winding layouts, a comparison with the conventional n-phase windings is also carried out in this subsection. The five- and seven-phase windings based on the standard three-phase frame are compared with equivalent standard five- and seven-phase stators having $q = 2$ with the same total number of conductors. For the original 4-pole machine, the required number of stator slots to build a standard five-phase and seven-phase stators are 40 (10-slot/pole) and 56 (14-slot/pole), respectively. Since the existing prototype machine has 36 slots, the equivalent winding layout, in Figure 44, will be employed. In order to maintain the same total number of conductors, the number of turns per coil for the 40-slot stator with standard five-phase winding will be 75 turns.

For the seven-phase case, the nearest standard three-phase stator frame will have a 48-slot. The winding layout shown in Figure 42 seems, therefore, appropriate for this comparison. For the same number of conductors, the number of turns per coil for the standard 56-slot stator will be 54 turn/coil, while the number of turns of different coils of the equivalent seven-phase winding using the 48-slot stator is given in Figure 49.

Phase (j)		a	b	c	d	e	f	g					
Slot		1	2	3	4	5	6	7	8	9	10	11	12
N_{ij}	U	49+	16-	53-	31+	55+	46-	9+	53+	22-	55-	39+	5-
N_{ph}	L	16-	49+	5+	39-		22+	53-	9-	46+		31-	53+
N_{ci}		65	65	58	70	55	58	62	62	58	55	70	58

Figure 49. Equivalent Seven-phase winding with the Same Copper Volume using a 12-slot/pole stator.

The MMF produced by the four machines and their spectra is plotted in Figure 50 for a unit stator current, while the gain in the fundamental MMF component against the original 36-slot three-phase stator is given in Table 6. Although the standard n-phase windings provide an approximate 1 % higher fundamental component, the harmonic spectra of the new windings seem to be the same. Finite element models are also built to simulate the machine average torque of different stators, and the simulation results are also given in Table 6. Since all machines have the same cage rotor with the same stator copper volume, the average torques under standard n-phase windings are slightly higher thanks to their higher fundamental MMF components.

Table 6. Comparison with Standard n-phase Distributed Winding in Terms of Fund. MMF magnitude And Average torque.

Case	5-ph		7-ph	
	Prop. 9-slot/pole	Stand. 10-slot/pole	Prop. 9-slot/pole	Stand. 10-slot/pole
Fund. MMF gain	2%	3%	3%	4%
T_{av}, Nm	6.19	6.21	6.22	6.27

Furthermore, the presented concept is experimentally verified by rewinding a 36-slot stator with a five-phase winding, as shown in Figure 51. Moreover, the prototype machine
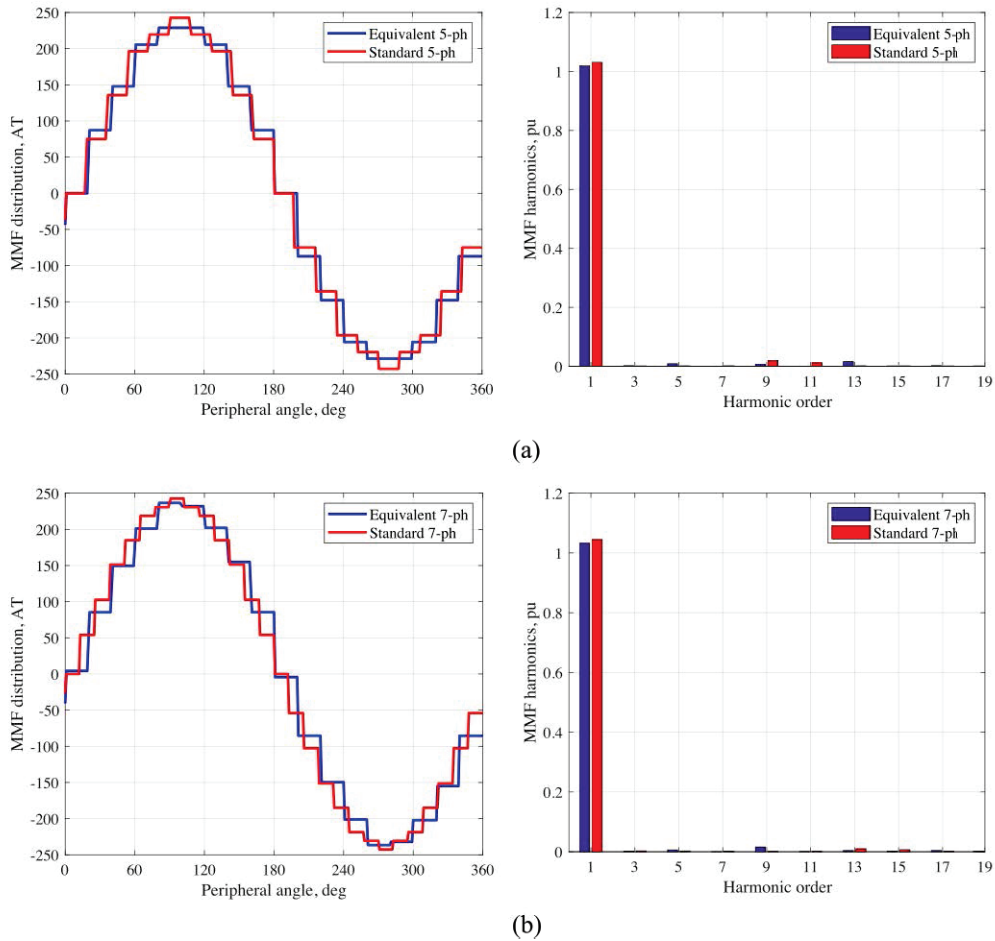
(a)

(b)

Figure 50. MMF distributions and their harmonic spectra for the equivalent and the standard n-phase windings. (a) 5-ph winding. (b) 7-ph winding.

and the power converter are shown in Figure 52. To verify that the machine will pursue a conventional five-phase machine, the machine is first tested under open-loop V/f control by plotting its characteristic curves under different cases. The machine performance under standard indirect rotor field oriented control (IRFOC) is then carried out under both healthy and open-phase cases. The machine parameters are estimated based on the identification technique given in [44].

Figure 53 compares the simulated and experimentally obtained characteristic curves under three cases, namely, a healthy case with sinusoidal excitation only, a healthy case with third harmonic injection, and an open-phase condition with sinusoidal excitation. The continuous curves represent the simulation results, while experimental readings are represented using discrete points. In all these cases, open-loop V/f control [37] is simply used by applying rated input supply voltage at a rated frequency of 50 Hz, while the machine is mechanically loaded using the coupled PM generator. The machine output torque is estimated
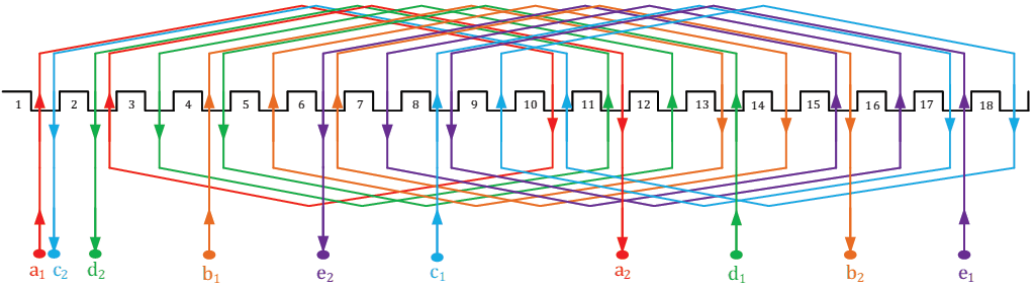
Figure 51. Stator winding layout of the prototype five-phase induction machine.
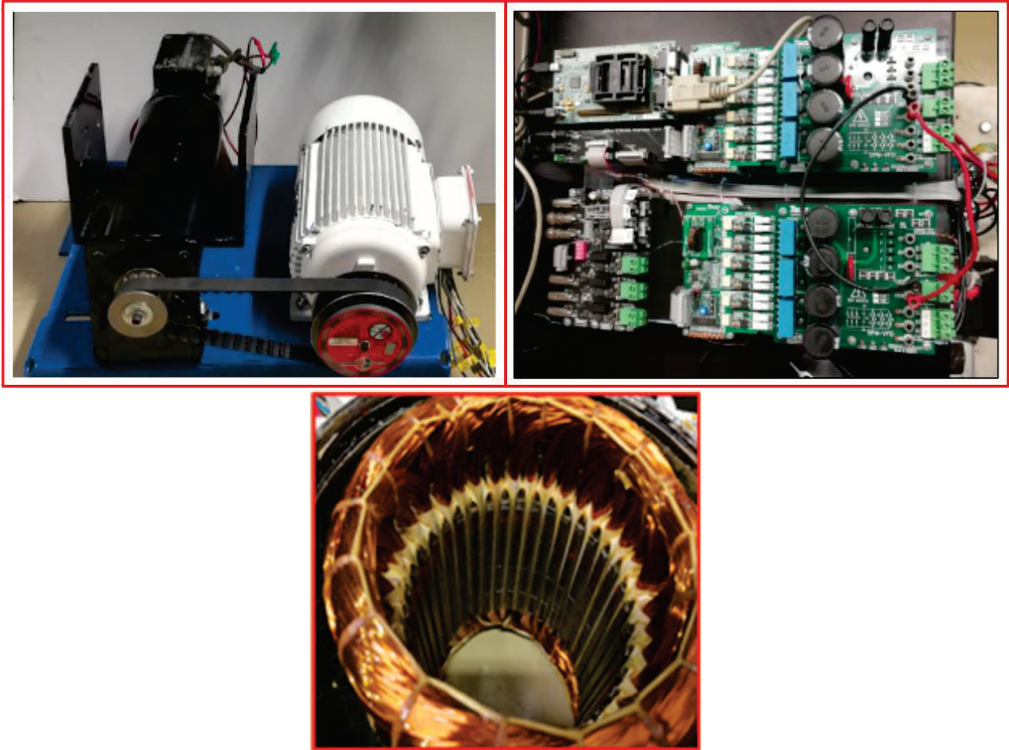

Figure 52. The prototype five-phase IM and the multiphase converter.

from the PM generator side after compensating for different loss components. For the sinusoidal excitation case, the modulation index is set to unity at a dc supply of 400 V, and the reference frequency is 50 Hz. Under third harmonic injection, the reference modulating signal for any phase j is given by:

$$M_j = 1.1547 \left[\sin \theta_j + \frac{1}{6} \sin 3\theta_j \right] \tag{48}$$

where $\theta_j = \omega t - \frac{2\pi}{5}(j-1)$, ω is the reference angular frequency and $j = 1$ to 5. It is well-known that torque enhancement using third-harmonic injection represents one of the potential merits of a five-phase system, where machine torque density can be improved by approximately 10 % for the same rated current [25, 56]. The sinusoidal and third harmonic injection cases are shown in Figure 53(a and b), respectively. The agreement between simulation and experimental results proves that the emerging winding can perfectly behave as a conventional five-phase symmetrical winding. To highlight the effect of third harmonic injection on torque production and machine efficiency, the experimental characteristic curves are compared in Figure 53(c). Under rated current, the actual improvement in the machine torque/current gain is approximately 7 %. Similar to the third harmonic injection applied to conventional five-phase machines, the machine performance under third harmonic injection only outperforms the sinusoidal excitation case when the load exceeds a certain loading point [56]. Hence, operating under sinusoidal excitation will be better for light loads in terms of efficiency and torque/current ratio. Under open phase conditions, the machine phase currents will be unbalanced, and the machine developed torque will be reduced for the same motor speed. Figure 53(d) shows the machine curves assuming phase a disconnected, where the current magnitude diversion between phases is the same as a conventional star-connected five-phase IM [37].

Figure 54(a and b) show the steady-state full load current waveforms under healthy conditions with sinusoidal excitation only, and the third harmonic injection applied, respectively. The current waveforms perfectly match those obtained from conventional multiphase IM while the same controller is applied [57]. Since simple PI current controllers are employed in this study, a notable distortion in the current waveform due to the effect of third and seventh space harmonics and the slot harmonics is observed. This effect can generally be compensated by employing a multiple resonant current controller structure, as detailed in [58]. Under fault conditions, the steady-state current waveforms are shown in Figure 53(c) under rated load torque. Phases b and c are in phase opposition with phases d and e, while the current magnitudes of all phases are approximately equal to 1.38 times rated current, which is identically the same in a conventional five-phase machine [37].

The steady-state performance under different operational conditions proved that the machine works equally well as a conventional five-phase machine presented in literature. While producing a high-quality flux distribution, the new winding layouts based on standard three-phase stator frames correspond to a more complicated winding structure at a higher cost than standard winding layouts. They also yield small secondary sequence current components due to the difference in the leakage stator inductances of different phases. However, this latter problem can simply be mitigated through current control.
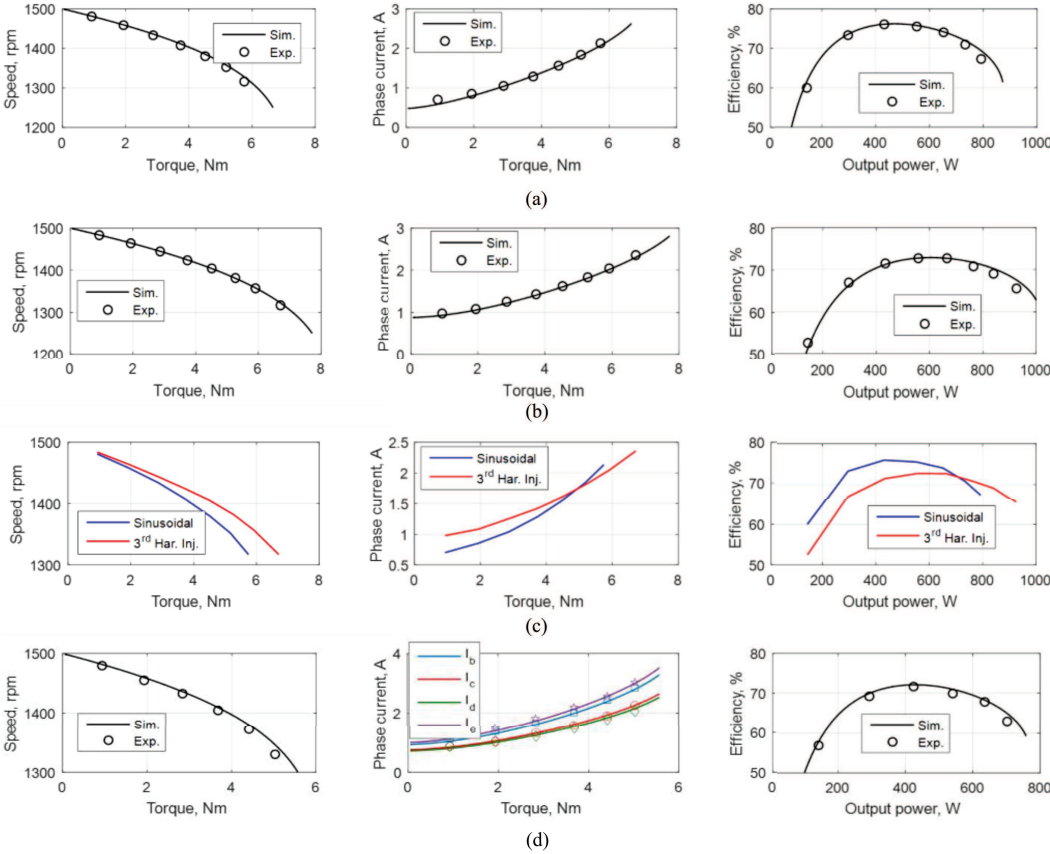
Figure 53. Machine characteristic curves. (a) Healthy case with sinusoidal excitation. (b) Healthy case with third harmonic injection. (c) Comparison between experimental characteristic curves of sinusoidal and third harmonic injection cases. (d) Open phase with sinusoidal excitation.
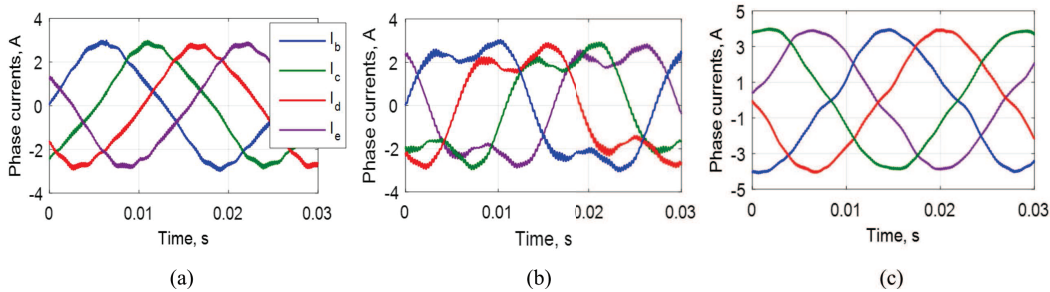

Figure 54. Machine characteristic curves. (a) Healthy case with sinusoidal excitation. (b) Healthy case with third harmonic injection. (c) Comparison between experimental characteristic curves of sinusoidal and third harmonic injection cases. (d) Open phase with sinusoidal excitation.

Conclusion

This chapter surveyed the state-of-the-art in multi-phase IM winding layouts for high-power applications. Various types of windings were discussed, while investigating their advantages and limitations. Additionally, innovative winding arrangement for improving fault-tolerance capability have been discussed. Eventually, the construction of multi-phase machines with general n-phase using standard three-phase stator frames has been elaborated. The following conclusions can be drawn:

- Single-layer winding layouts are preferably used with a machine with a prime number of phases. These winding layouts offer much simpler construction for high-power machines, improved fundamental winding factor, low insulation requirement, and relatively high secondary subspace impedance.

- Double-layer windings are usually used with multiple three-phase machines with even phase numbers. These winding layouts have a high-quality flux production. However, they require higher insulations and offers low secondary subspace impedance.

- For six-phase-based winding arrangements, the A6P gives enhanced fundamental torque producing component by approximately 3%. However, it gives a lower maximum torque due to its high sequence stator leakage inductance. Therefore, the D3P outperforms the other six-phase winding layouts from an efficiency perspective and under faulty cases.

- A combined star/pentagon connection is presented for better fault-tolerant capability and when compared to the star and pentagon ones, it improves the fundamental flux component.

- The emerging nine-phase six-terminal winding topology is also elaborated for a better fault-tolerance capability. The 9P6T corresponds to a 5 % gain in the fundamental torque producing flux component while using a single layer winding.

- The novel P6P winding layout is introduced, offering several merits over both the 9p6T and conventional A6P layouts. These merits include a simpler single-layer stator winding construction, a unity winding factor, an improved torque density, and a higher stator current quality.

- Clear steps of how to build multiphase winding with standard three-phase stators are extensively presented.

References

[1] Barrero F. and Duran M. J., "Recent advances in the design, modeling, and control of multiphase machines-Part I," *IEEE Trans. Ind. Electron.*, vol. 63, no. 1, pp. 449-458, 2015.

[2] Levi E., Bojoi R., Profumo F., Toliyat H., and Williamson S., "Multiphase induction motor drives-a technology status review," *IET Electr. Power Appl.*, vol. 1, no. 4, pp. 489-516, 2007.

[3] Levi E., "Multiphase Electric Machines for Variable-Speed Applications," *IEEE Trans. Ind. Electron.*, vol. 55, no. 5, pp. 1893-1909, 2008.

[4] Jones M., "A literature survey of state-of-the-art in multiphase ac drives," in *Proc. UPEC*, 2002.

[5] Apsley J., Williamson S., Smith A., and Barnes M., "Induction motor performance as a function of phase number," *IEE Proc. Electric Power Appl.*, vol. 153, no. 6, pp. 898-904, 2006.

[6] Williamson S. and Smith S., "Pulsating torque and losses in multiphase induction machines," *IEEE Trans. Ind. Appl.*, vol. 39, no. 4, pp. 986-993, 2003.

[7] Abdel-Khalik A. S., Hamdy R. A., Massoud A. M., and Ahmed S., "Low-order space harmonic modeling of asymmetrical six-phase induction machines," *IEEE Access*, vol. 7, pp. 6866-6876, 2019.

[8] Che H. S., Abdel-Khalik A. S., Dordevic O., and Levi E., "Parameter estimation of asymmetrical six-phase induction machines using modified standard tests," *IEEE Trans. Ind. Electron.*, vol. 64, no. 8, pp. 6075-6085, 2017.

[9] Abdel-Khalik A. S., A. Massoud, and Ahmed S., "Standard three-phase stator frames for multiphase machines of prime-phase order: Optimal selection of Slot/Pole combination," *IEEE Access*, vol. 7, pp. 78239-78259, 2019.

[10] Abdel-Khalik A. S., Massoud A. M., and Ahmed S., "An improved torque density pseudo six-phase induction machine using a quadruple three-phase stator winding," *IEEE Trans. Ind. Electron.*, vol. 67, no. 3, pp. 1855-1866, 2019.

[11] Levi E., "Advances in converter control and innovative exploitation of additional degrees of freedom for multiphase machines," *IEEE Trans. Ind. Electron.*, vol. 63, no. 1, pp. 433-448, 2015.

[12] Rezazadeh G., Tahami F., Capolino G.-A., Vaschetto S., Nasiri-Gheidari Z., and Henao H., "Improvement of concentrated winding layouts for six-phase squirrel cage induction motors," *IEEE Trans. Energy Convers.*, vol. 35, no. 4, pp. 1727-1735, 2020.

[13] Tawfiq K. B., Ibrahim M. N., El-Kholy E., and Sergeant P., "Performance improvement of existing three phase synchronous reluctance machine: Stator upgrading to 5-Phase with combined star-pentagon winding," *IEEE Access*, vol. 8, pp. 143569-143583, 2020.

[14] Hadiouche D., Razik H., and Rezzoug A., "On the modeling and design of dual-stator windings to minimize circulating harmonic currents for VSI fed AC machines," *IEEE Trans. Ind. Appl.*, vol. 40, no. 2, pp. 506-515, 2004.

[15] Ariff E. A. R. E., Dordevic O., and Jones M., "A space vector PWM technique for a three-level symmetrical six-phase drive," *IEEE Trans. Ind. Electron.*, vol. 64, no. 11, pp. 8396-8405, 2017.

[16] Marouani K., Baghli L., Hadiouche D., Kheloui A., and Rezzoug A., "A new PWM strategy based on a 24-sector vector space decomposition for a six-phase VSI-fed dual stator induction motor," *IEEE Trans. Ind. Electron.*, vol. 55, no. 5, pp. 1910-1920, 2008.

[17] Liu Z., Zheng Z., Peng Z., Li Y., and Hao L., "A sawtooth carrier-based PWM for asymmetrical six-phase inverters with improved common-mode voltage performance," *IEEE Trans. Ind. Electron.*, vol. 33, no. 11, pp. 9444-9458, 2017.

[18] Abdel-Khalik A. S., Ahmed S., and Massoud A. M., "A nine-phase six-terminal concentrated single-layer winding layout for high-power medium-voltage induction machines," *IEEE Trans. Ind. Electron.*, vol. 64, no. 3, pp. 1796-1806, 2016.

[19] Abdel-Khalik A. S., Hamad M. S., Massoud A. M., and Ahmed S. J. I. T. o. I. E., "Postfault operation of a nine-phase six-terminal induction machine under single open-line fault," *IEEE Trans. Ind. Electron.*, vol. 65, no. 2, pp. 1084-1096, 2017.

[20] Kong W., Kang M., Li D., Qu R., Jiang D., and Gan C., "Investigation of spatial harmonic magnetic field coupling effect on torque ripple for multiphase induction motor under open fault condition," *IEEE Trans. Power Electron.*, vol. 33, no. 7, pp. 6060-6071, 2017.

[21] Munim W. N. W. A., Duran M. J., Che H. S., Bermudez M., Gonzalez-Prieto I., and Abd Rahim N., "A unified analysis of the fault tolerance capability in six-phase induction motor drives," *IEEE Trans. Power Electron.*, vol. 32, no. 10, pp. 7824-7836, 2016.

[22] Abdel-Khalik A. S., Ahmed S., and Massoud A. M., "Steady-state mathematical modeling of a five-phase induction machine with a combined star/pentagon stator winding connection," *IEEE Trans. Ind. Electron.*, vol. 63, no. 3, pp. 1331-1343, 2015.

[23] Paredes J., Prieto B., Satrustegui M., Elosegui I., and Gonzalez P., "Improving the performance of a 1-MW induction machine by optimally shifting from a three-phase to a six-phase machine design by rearranging the coil connections," *IEEE Trans. Ind. Electron.*, vol. 68, no. 2, pp. 1035-1045, 2020.

[24] Boldea I. and Nasar S., The induction machine handbook. . Boca Raton, FL: CRC Press, 2002.

[25] Abdel-Khalik A. S., Masoud M. I., Ahmed S., and Massoud A. M., "Effect of current harmonic injection on constant rotor volume multiphase induction machine stators: A comparative study," *IEEE Trans. Ind. Appl.*, vol. 48, no. 6, pp. 2002-2013, 2012.

[26] Xu H., Toliyat H. A., and Petersen L. J., "Rotor field oriented control of five-phase induction motor with the combined fundamental and third harmonic currents," in *Proc. APEC*, 2001, vol. 1, pp. 392-398: IEEE.

[27] Munoz A. R. and Lipo T. A., "Complex vector model of the squirrel-cage induction machine including instantaneous rotor bar currents," *IEEE Trans. Ind. Appl.*, vol. 35, no. 6, pp. 1332-1340, 1999.

[28] Dabour S. M., Abdel-Khalik A. S., Ahmed S., and Massoud A. M., "A new dual series-connected Nine-Switch Converter topology for a twelve-phase induction machine wind energy system," in *Proc. CPE-POWERENG*, 2017, pp. 139-144: IEEE.

[29] Rubino S., Bojoi R., Cavagnino A., and Vaschetto S., "Asymmetrical twelve-phase induction starter/generator for more electric engine in aircraft," in *Proc. ECCE*, 2016, pp. 1-8: IEEE.

[30] Che H. S., Duran M. J., Levi E., Jones M., Hew W.-P., and Rahim N. A., "Post-fault operation of an asymmetrical six-phase induction machine with single and two isolated neutral points," *IEEE Trans. Ind. Electron.*, vol. 29, no. 10, pp. 5406-5416, 2013.

[31] Metwly M. Y., Abdel-Majeed M. S., Abdel-Khalik A. S., Hamdy R. A., Hamad M. S., and Ahmed S., "A Review of Integrated On-Board EV Battery Chargers: Advanced Topologies, Recent Developments and Optimal Selection of FSCW Slot/Pole Combination," *IEEE Access*, vol. 8, pp. 85216-85242, 2020.

[32] Singh G., "Multi-phase induction machine drive research-A survey," *Electr. Power Syst. Res.*, vol. 61, no. 2, pp. 139-147, 2002.

[33] Abdel-Khalik A. S., Abdel-Majeed M. S., and Ahmed S., "Effect of winding configuration on six-phase induction machine parameters and performance," *IEEE Access*, vol. 8, pp. 223009-223020, 2020.

[34] Nelson R. and Krause P., "Induction machine analysis for arbitrary displacement between multiple winding sets," IEEE Transactions on Power Apparatus Systems, no. 3, pp. 841-848, 1974.

[35] Yepes A. G., Doval-Gandoy J., Baneira F., and Toliyat H. A., "Speed estimation based on rotor slot harmonics in multiphase induction machines under open-phase fault," *IEEE Trans. Power Electron.*, vol. 33, no. 9, pp. 7980-7993, 2017.

[36] Joksimović G., Mezzarobba M., Tessarolo A., and Levi E., "Optimal selection of rotor bar number in multiphase cage induction motors," *IEEE Access*, vol. 8, pp. 135558-135568, 2020.

[37] Abdel-Khalik A. S., Morsy A. S., Ahmed S., and Massoud A. M., "Effect of stator winding connection on performance of five-phase induction machines," *IEEE Trans. Ind. Electron.*, vol. 61, no. 1, pp. 3-19, 2013.

[38] Abdel-Khalik A. S., Ahmed S., Elserougi A. A., and Massoud A. M., "Effect of stator winding connection of five-phase induction machines on torque ripples under open line condition," *IEEE ASME Trans. Mechatron*, vol. 20, no. 2, pp. 580-593, 2014.

[39] Abdel-Khalik A. S., Elgenedy M. A., Ahmed S., and Massoud A. M., "An improved fault-tolerant five-phase induction machine using a combined star/pentagon single layer stator winding connection," *IEEE Trans. Ind. Electron.*, vol. 63, no. 1, pp. 618-628, 2015.

[40] Sadeghi S., Parsa L., and Toliyat H. A., "Extending speed range of five-phase PM machines by changing the stator windings connections," in *Proc. IEMDC*, 2011, pp. 1540-1545: IEEE.

[41] Mohammadpour A. and Parsa L., "Global fault-tolerant control technique for multiphase permanent-magnet machines," *IEEE Trans. Ind. Appl.*, vol. 51, no. 1, pp. 178-186, 2014.

[42] Abdel-Khalik A. S., Ahmed S., and Massoud A. M., "Low Space Harmonics Cancelation in Double-Layer Fractional Slot Winding Using Dual Multiphase Winding," *IEEE Trans. Magn.*, vol. 51, no. 5, pp. 1-10, 2015.

[43] Chen H., Li D., Qu R., Zhu Z., and Li J., "An improved analytical model for inductance calculation of interior permanent magnet machines," *IEEE Trans. Magn.*, vol. 50, no. 6, pp. 1-8, 2014.

[44] Abdel-Khalik A. S., Daoud M. I., Ahmed S., Elserougi A. A., and Massoud A. M., "Parameter identification of five-phase induction machines with single layer windings," *IEEE Trans. Ind. Electron.*, vol. 61, no. 10, pp. 5139-5154, 2014.

[45] Yepes A. G., Malvar J., Vidal A., Lopez O., and Doval-Gandoy J., "Current harmonics compensation based on multiresonant control in synchronous frames for symmetrical n-phase machines," *IEEE Trans. Ind. Electron.*, vol. 62, no. 5, pp. 2708-2720, 2014.

[46] Abdel-Khalik A. S., Ahmed S., Massoud A. M., and Elserougi A. A., "An improved performance direct-drive permanent magnet wind generator using a novel single-layer winding layout," *IEEE Trans. Magn.*, vol. 49, no. 9, pp. 5124-5134, 2013.

[47] Lei Y., Zhao Z., Wang S., Dorrell D. G., and Xu W., "Design and analysis of star-delta hybrid windings for high-voltage induction motors," *IEEE Trans. Power Electron.*, vol. 58, no. 9, pp. 3758-3767, 2010.

[48] Klingshirn E. A., "High phase order induction motors-part I-description and theoretical considerations," *IEEE Trans. Power Appar. Syst.*, no. 1, pp. 47-53, 1983.

[49] Abdel-Khalik A., Massoud A., and Ahmed S., "Torque density pseudo six-phase induction machine," ed: Google Patents, 2021.

[50] Abdel-Khalik A. S., Massoud A. M., and Ahmed S., "Nine-phase six-terminal induction machine modeling using vector space decomposition," *IEEE Trans. Ind. Electron.*, vol. 66, no. 2, pp. 988-1000, 2018.

[51] Abdel-Khalik A. S., Massoud A. M., and Ahmed S., "Application of standard three-phase stator frames in prime phase order multiphase machine construction," *IEEE Trans. Ind. Electron.*, vol. 66, no. 4, pp. 2506-2517, 2018.

[52] Bianchi N. and Dai Pre M., "Use of the star of slots in designing fractional-slot single-layer synchronous motors," *IEE Proc.-Electric Power Appl.*, vol. 153, no. 3, pp. 459-466, 2006.

[53] Rockhill A. and Lipo T., "A generalized transformation methodology for polyphase electric machines and networks," in *Proc. IEMDC*, 2015, pp. 27-34: IEEE.

[54] Reddy P. B., Huh K.-K., and El-Refaie A. M., "Generalized approach of stator shifting in interior permanent-magnet machines equipped with fractional-slot concentrated windings," *IEEE Trans. Ind. Electron.*, vol. 61, no. 9, pp. 5035-5046, 2014.

[55] Abdel-Khalik A. S., Gadoue S. M., Masoud M. I., and Wiliams B. W., "Optimum flux distribution with harmonic injection for a multiphase induction machine using genetic algorithms," *IEEE Trans. Energy Convers.*, vol. 26, no. 2, pp. 501-512, 2011.

[56] Mengoni M., Zarri L., Tani A., Parsa L.,Serra G. , and Casadei D., "High-torque-density control of multiphase induction motor drives operating over a wide speed range," *IEEE Trans. Ind. Electron.*, vol. 62, no. 2, pp. 814-825, 2014.

[57] Abdel-Khalik A. S., Masoud M. I., and Williams B. W., "Improved flux pattern with third harmonic injection for multiphase induction machines," *IEEE Trans. Power Electron.*, vol. 27, no. 3, pp. 1563-1578, 2011.

[58] Yepes A. G., Doval-Gandoy J., Baneira F., Perez-Estevez D., and Lopez O., "Current harmonic compensation for n-phase machines with asymmetrical winding arrangement and different neutral configurations," *IEEE Trans. Ind. Appl.*, vol. 53, no. 6, pp. 5426-5439, 2017.

Chapter 3

Virtual Vector Control of Six-Phase Induction Machines

Ignacio Gonzalez-Prieto[*]**, Juan Jose Aciego,**
Angel Gonzalez-Prieto and Mario J. Duran
Department of Electrical Engineering,
University of Málaga, Málaga, Spain

Abstract

Multiphase electric drives are considered an interesting alternative for high-power emerging applications with high-performance requirements, such as electric mobility or green energy generation. For instance, the post-fault capability of multiphase machines is particularly attractive when security is a critical need in the system. In addition, better current distribution and a lower torque ripple can also be achieved by selecting a multiphase solution. Nevertheless, a high-performance control technique is necessary to take advantage of these interesting features, providing at the same time an acceptable current quality. In this regard, model predictive control (MPC) strategies allow exploiting the additional freedom degrees of multiphase electric drives in a simple manner. Unfortunately, with conventional MPC schemes based on the use of a single control action per sampling period, the harmonic distortion may exceed the permissible limit. Consequently, this control family has often been discarded as a high-performance regulation technique. Fortunately for the MPC viability, multi-vector control actions, commonly termed as virtual voltage vectors, permit the harmonic content's minimisation with the application of several switching states per control cycle. This regulation solution has provided a satisfactory harmonic distortion, even outperforming the current quality indices of control strategies with explicit modulation stages. This chapter illustrates the role of the virtual voltage vectors in the control of multiphase induction motors. For that purpose, an asymmetrical six-phase induction machine fed by a dual three-phase voltage source converter is employed to test different multi-vector MPC approaches experimentally.

Keywords: induction motors, model predictive control strategies, virtual voltage vectors, voltage source converters

[*]Corresponding Author's Email: ignaciogp87@gmail.com.

1.   Introduction

The worldwide environmental situation is going through a critical moment with a significant over-demand of ecological resources and an excessive emission of greenhouse gasses. In fact, in the 26th UN Climate Change Conference of the Parties (COP26) in Glasgow on October 31 - November 13 2021, more restrictive protocols have been promoted to reduce these harmful gasses' emissions and optimise the use of ecological resources. The Earth Overshoot Day is a popular index to know our ecological demand since it illustrates when humanity's consumption of environmental resources and services in a given year exceeds what the Earth can regenerate in that same period. Unfortunately, Earth Overshoot Day has been reached earlier each decade. For instance, in 2021, it fell on July 29, i.e., 154 days before the end of the year, whereas in 1990, it was reached on October 15. In order to ensure the viability of our planet, an important number of researchers are trying to develop a more sustainable world. Focusing on the mobility, this activity consumes a third part of all final energy in the European Union and an important share of this energy is related to the use of fuel as a primary source. Consequently, transport is responsible for a significant percentage of greenhouse gas emissions in the European Union. Fortunately, an optimistic scenario appears with the new trend based on electric mobility. This alternative permits the development of zero-emission vehicles which can operate completely CO2-free in Tank-to-Wheel mode. This operating mode requires a charging network that is completely powered by renewable energies. In addition, electrical motors show higher performance than classical internal combustion engines. Therefore, the electrical propulsion systems provide better efficiency to the vehicle and, consequently, promote more sustainable use of the available energy.

Nowadays, induction motors (IM) are one of the most widely used rotating electrical machines due to their low cost, suitable reliability, reduced maintenance and simplicity. These electrical machines are based on the creation of a rotating Tesla's field, and consequently, the stator has been typically configured with a three-phase winding. However, a high number of phases can be employed to obtain diverse benefits [1, 2]. The use of induction electrical machines with more than three phases, namely multiphase IMs, usually provides an augmented fault-tolerant capability, a reduced per-phase current rating for the same voltage level, and the availability of additional operating modes [3, 4]. Multiphase IMs have been selected to carry out the energy conversion in the electric drive in a high number of works during the last decades [1, 5, 6, 7, 8, 9]. Although multiphase induction machines with a different number of phases can be found in the literature, the choice of a stator with several three-phase windings is one of the most accepted options in order to take advantage of the well-established three-phase technology [5, 6, 7, 8, 9]. In this regard, the asymmetrical six-phase IM has been considered as a popular case study, thanks to the reduced torque pulsations obtained when the machine is fed in a pulse-step mode [10]. However, regardless of the stator disposition [11], the implementation of a high-performance control technique is mandatory to obtain satisfactory performance.

Searching to maximise the current quality indices, field-oriented control (FOC) strategies using a modulation stage have been generally selected as the preferable control option in the field of electric drives [12]. The predominant role of FOC schemes was related to the knowledge of the reference voltage and the application of several switching states during

the control cycle in order to synthesise the reference value. Nevertheless, a new scenario appears if the control designer's goal is to include additional control restrictions in a simple manner. For that purpose, the finite-control-set model predictive control (FCS-MPC) has outperformed conventional linear controller capabilities [13, 14]. This FCS-MPC feature is particularly interesting in multiphase machines since there are some extra freedom degrees. However, conventional model predictive control strategies are characterised by the absence of explicit modulation stages, and as a consequence, a single control action is applied during the whole sampling period [15]. Consequently, important harmonic content can appear in the phase currents if the machine possesses a low value of the stator impedance. This limited capability of FCS-MPC strategies has been solved with the implementation of different multi-vector solutions where the fundamental objective is to apply several control actions per control cycle [15, 16, 17, 18, 19, 20, 21, 22, 23], to simultaneously satisfy the different requirements of each orthogonal subspace. The use of this approach was initially tested in direct torque control strategies (DTC) [24], where the use of a modulation stage is commonly omitted. Nevertheless, its implementation in FCS-MPC techniques is currently assumed as a must if a suitable current quality is required [16].

In the field of FCS-MPC for electric drives, a control action formed by several switching states is generally termed as a virtual voltage vector (VV). The use of these voltage vectors permits ensuring the flux/torque production with a low harmonic content [15, 16, 21, 22, 23]. Different sets of online [22] and offline [15, 16, 21, 23] estimated VVs had been explored during the last years to exploit the advantages of FCS-MPC providing at the same time a suitable current quality. With the latter requirement in mind, the selection of switching states with low production in the secondary plane is a crucial need to achieve an adequate reduction of the harmonic distortion [21, 16, 23]. In fact, recent publications have confirmed the goodness of large voltage vectors to generate VVs since this set of switching states is mapped onto the secondary subspace as small voltage vectors. On the other hand, the combination of one active VV with a null voltage vector allows the enhancement of the radial refinement in the plane related to the flux/torque production and the minimisation of the harmonic injection [23, 16]. Moreover, the implementation of an FCS-MPC based on an offline virtual voltage vector also implies a reduction of the computational burden because a reduced predictive machine model and cost-function can be employed [15, 16, 21, 23]. Although the previous information can be considered trivial in the light of the current state of the art, a tough research road has been trodden to establish this knowledge basis. This chapter describes the evolution of virtual voltage vector solutions for FCS-MPC strategies for asymmetrical six-phase induction machines.

2. Six-Phase Electric Drive Generalities

In modern variable-speed applications, such as electric vehicles or wind energy conversion systems, the electrical machines are usually fed by voltage source converters (VSC) to ensure the tracking of the reference speed with high efficiency. This section describes the fundamentals of a six-phase electric drive when an asymmetrical six-phase induction machine is fed by a dual three-phase two-level VSC (Figure 1). The considered multiphase drive can be employed in motor and generator mode without a lack of generality. In fact, Figures 2 and 3 show two different applications, a wind energy conversion system and

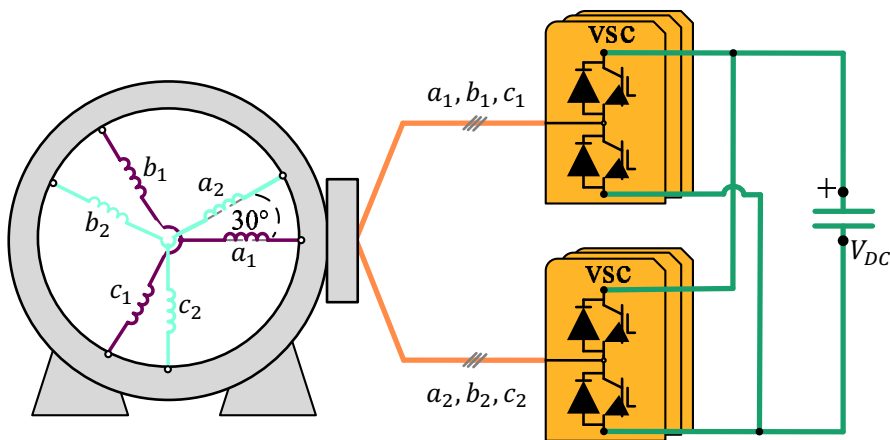electric vehicle, where the proposed multiphase system can be implemented.

Figure 1. Six-phase electric drive with an asymmetrical induction machine.
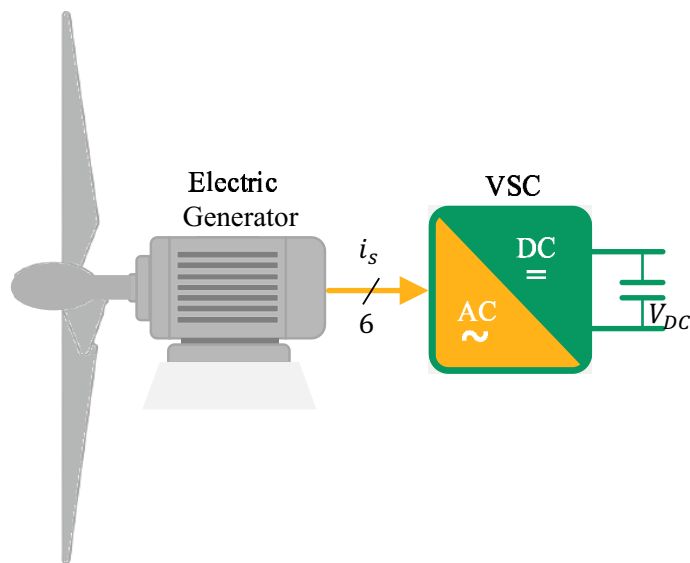

Figure 2. Six-phase wind energy conversion system.

Analysing the features of the proposed electric drive, the considered VSC provides 64 switching states to be employed as control actions. In the first stage of the MPC design, the control designer must use these single control actions to generate different sets of virtual voltage vectors. Each VSC leg is formed by two Insulated Gate Bipolar Transistors (IG-BTs), that operate in a complementary mode to avoid short circuit faults. Therefore, the
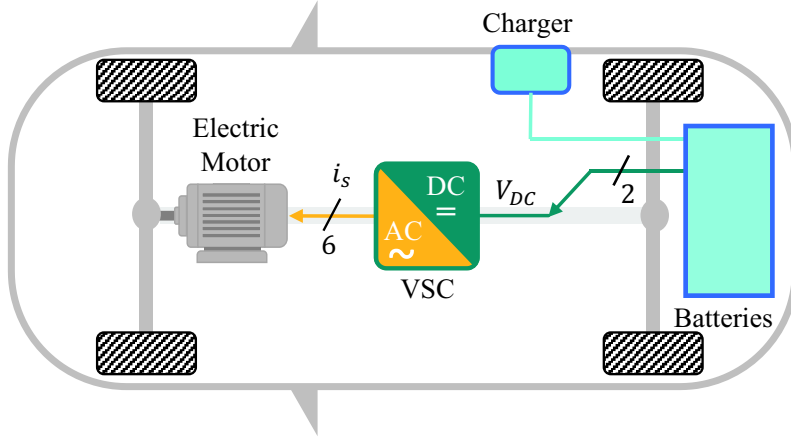
Figure 3. Six-phase electric vehicle.

performance of each VSC leg can be modelled using a binary variable S_{ij}, where $S_{ij}=1$ if the upper leg switch is ON and $S_{ij}=0$ when the opposite scenario occurs. The stator phase voltages can be estimated using the vector $[S]=[S_{a1}, S_{b1}, S_{c1}, S_{a2}, S_{b2}, S_{c2}]$ and the DC-link voltage V_{DC} as follows:

$$
\begin{bmatrix} v_{a1} \\ v_{b1} \\ v_{c1} \\ v_{a2} \\ v_{b2} \\ v_{c2} \end{bmatrix} = \frac{V_{DC}}{3} \begin{bmatrix} 2 & -1 & -1 & 0 & 0 & 0 \\ -1 & 2 & -1 & 0 & 0 & 0 \\ -1 & -1 & 2 & 0 & 0 & 0 \\ 0 & 0 & 0 & 2 & -1 & -1 \\ 0 & 0 & 0 & -1 & 2 & -1 \\ 0 & 0 & 0 & -1 & -1 & 2 \end{bmatrix} \begin{bmatrix} S_{a1} \\ S_{b1} \\ S_{c1} \\ S_{a2} \\ S_{b2} \\ S_{c2} \end{bmatrix}. \tag{1}
$$

Even though stator variables can be employed to model IMs, the use of a different reference frame is a common solution in the electric drive field to simplify the control of these electrical systems. In this regard, the vector space decomposition (VSD) is a well-known approach [25] that is typically applied to express phase variables in a new reference frame. For instance, phase variables can be transformed onto two-orthogonal subspaces using the amplitude invariant decoupling Clarke transformation matrix:

$$
[C] = \frac{1}{3} \begin{bmatrix} 1 & -\frac{1}{2} & -\frac{1}{2} & \frac{\sqrt{3}}{2} & -\frac{\sqrt{3}}{2} & 0 \\ 0 & \frac{\sqrt{3}}{2} & -\frac{\sqrt{3}}{2} & \frac{1}{2} & \frac{1}{2} & -1 \\ 1 & -\frac{1}{2} & -\frac{1}{2} & -\frac{\sqrt{3}}{2} & \frac{\sqrt{3}}{2} & 0 \\ 0 & -\frac{\sqrt{3}}{2} & \frac{\sqrt{3}}{2} & \frac{1}{2} & \frac{1}{2} & -1 \end{bmatrix}, \tag{2}
$$

$$
[v_\alpha, v_\beta, v_x, v_y]^T = [C] \cdot [v_{a1}, v_{b1}, v_{c1}, v_{a2}, v_{b2}, v_{c2}]^T, \tag{3}
$$

$$[i_\alpha, i_\beta, i_x, i_y]^T = [C] \cdot [i_{a1}, i_{b1}, i_{c1}, i_{a2}, i_{b2}, i_{c2}]^T, \tag{4}$$

where the α-β components are related to the flux/torque production and the x-y variables only produce stator copper losses in a distributed-winding machine with negligible spatial harmonics. In the Clarke transformation included in (2) the two zero-sequence components have been omitted, since the asymmetrical six-phase IM has been configured with two isolated neutral points and, consequently, these currents cannot flow.

After the application of the Clarke transformation matrix, the available voltage vectors can be mapped onto the aforementioned orthogonal subspaces. Figure 4 shows the voltage vector representation in the α-β and x-y planes. To identify each voltage vector, a decimal number equivalent to the binary number of the vector $[S]$ has been used. These voltage vectors are classified, according to their modulus in the main plane, as large (v^l), medium-large (v^{ml}), medium (v^m), small (v^s) and null (v^n) voltage vectors. In addition, these control actions have been classified using their contribution in both planes [16] with the ratio $R_{\alpha\beta xy}$:

$$R_{\alpha\beta xy} = \frac{|v_{\alpha\beta}|}{|v_{xy}|}, \tag{5}$$

where $|v_{\alpha\beta}|$ and $|v_{xy}|$ are the voltage vector modulus in the α-β and x-y planes, respectively. The control designer typically requires control actions with a suitable production in the main subspace (dependent on the flux/torque production) and a low contribution in the secondary subspace to minimise the harmonic injection. Table 1 shows the values of the ratio $R_{\alpha\beta xy}$ for the different sets of voltage vectors in the proposed topology.
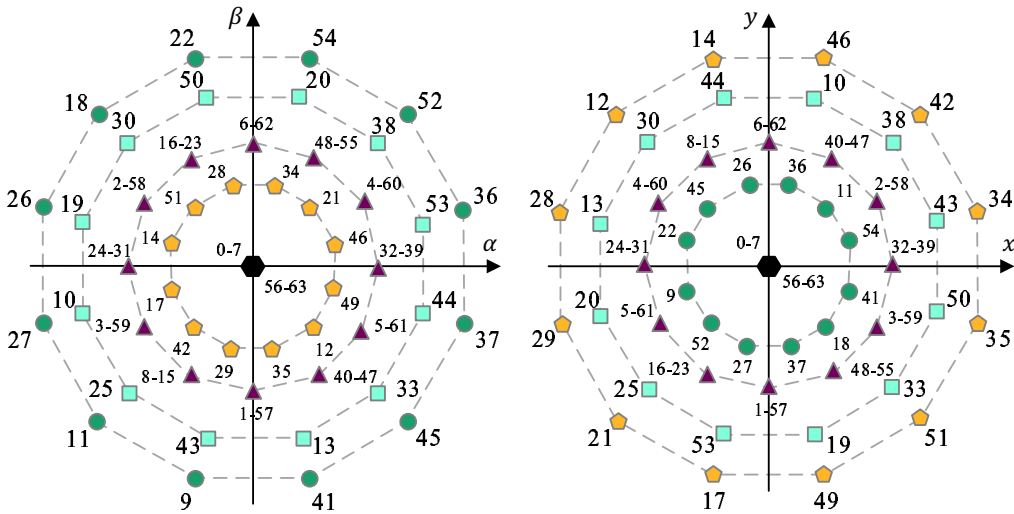
Figure 4. Available voltage vectors in the α-β and x-y subspaces in a six-phase system.

On the other hand, the asymmetrical six-phase IM performance can also be modelled using VSD variables. Applying this approach, the set of differential equations presents a clarified physical meaning. In other words, α-β equations are related to the flux/torque production whereas x-y components only generate stator copper losses. The following equa-

tions can be implemented to model the behaviour of an asymmetrical six-phase induction machine if VSD variables are employed:

$$v_{\alpha s} = (R_s + L_s \cdot \frac{d}{dt}) \cdot i_{\alpha s} + M \cdot \frac{di_{\alpha r}}{dt}, \tag{6}$$

$$v_{\beta s} = (R_s + L_s \cdot \frac{d}{dt}) \cdot i_{\beta s} + M \cdot \frac{di_{\beta r}}{dt}, \tag{7}$$

$$v_{xs} = (R_s + L_{ls} \cdot \frac{d}{dt}) \cdot i_{xs}, \tag{8}$$

$$v_{ys} = (R_s + L_{ls} \cdot \frac{d}{dt}) \cdot i_{ys}, \tag{9}$$

$$0 = (R_r + L_r \cdot \frac{d}{dt}) \cdot i_{\alpha r} + M \cdot \frac{di_{\alpha s}}{dt} + \omega_r \cdot L_r \cdot i_{\beta r} + \omega_r \cdot M \cdot i_{\beta s}, \tag{10}$$

$$0 = (R_r + L_r \cdot \frac{d}{dt}) \cdot i_{\beta r} + M \cdot \frac{di_{\beta s}}{dt} - \omega_r \cdot L_r \cdot i_{\alpha r} - \omega_r \cdot M \cdot i_{\alpha s}, \tag{11}$$

$$T_e = p \cdot M \cdot (i_{\beta r} \cdot i_{\alpha s} - i_{\alpha r} \cdot i_{\beta s}), \tag{12}$$

where p is the number of pole pairs, $L_s = L_{ls} + 3L_m$, $L_r = L_{lr} + 3L_m$, $M = 3L_m$ and ω_r is the rotor electrical speed ($\omega_r = p\,\omega_m$). Subscripts s and r denote stator and rotor variables, respectively. This set of equations is usually expressed in a discrete form in order to include the machine model into the MPC strategy.

For control purposes, the flux and torque components are typically decoupled using a rotating reference frame. This transformation can be carried out via Park transformation matrix:

$$[D] = \begin{bmatrix} \cos\theta_s & \sin\theta_s \\ -\sin\theta_s & \cos\theta_s \end{bmatrix}, \tag{13}$$

$$[i_{ds},\ i_{qs}]^T = [D] \cdot [i_{\alpha s},\ i_{\beta s}]^T, \tag{14}$$

where the flux generation is related to the d-current and the torque production is dependent on the q-current.

Table 1. Ratio $R_{\alpha\beta xy}$

Parameters	$\mathbf{v^l}$	$\mathbf{v^{ml}}$	$\mathbf{v^m}$	$\mathbf{v^s}$	$\mathbf{v^n}$
$\lvert \mathbf{v}_{\alpha\beta} \rvert \cdot \mathbf{100}$	64	47	33.3	17	0
$\lvert \mathbf{v}_{\mathbf{xy}} \rvert \cdot \mathbf{100}$	17	47	33.3	64	0
$\mathbf{R}_{\alpha\beta\mathbf{xy}}$	3.8	1	1	0.3	0

3. Virtual Voltage Vectors as Control Actions

Focusing on the MPC flexibility, the control designer possesses the capability to define the set of selectable switching states according to the employed electric drive or the specific control objectives. In this regard, virtual voltage vectors are multi-vector control actions where several switching states are applied during the sampling period to satisfy several orthogonal subspaces simultaneously. Different sets of virtual voltage vectors have been developed in the last years to increase the current quality indices of direct controllers, such as FCS-MPC strategies. In the design process of VVs, particular attention has been paid to the secondary subspace since the impedance of this subspace is generally much lower than in the α-β plane. This section describes the performance of four alternatives of VVs employed for the speed/current regulation of the topology described in Section 2 of this chapter.

3.1. Multi-Vector Approaches

As previously exposed, four different alternatives of multi-vector solutions for MPC schemes are described and tested in this work. At this point, the bases of these virtual voltage vector approaches are introduced.

- **VV-Vectors**:

The first appearance of a multi-vector solution for an FCS-MPC strategy was related to the design of control actions with a null average x-y voltage production. For that purpose, large and medium-large voltage vectors with the same direction in the main plane were selected because these switching states are mapped onto the secondary subspace with an opposite direction as shown in Figure 4. Taking advantage of this feature, a set of twelve different couples of active switching states was proposed as the first multi-vector solution for an FCS-MPC strategy in a multiphase electric drive [15]. Nevertheless, a specific duty cycle was necessary to obtain the desired null average x-y voltage injection during the sampling period. This timing estimation was also carried out in an offline process, using the x-y voltage production and taking into account the sampling period (T_s) constraint ($T_s = t_1 + t_2$). For the proposed six-phase electric drive and due to its voltage symmetry, the duty cycle of any large voltage vector was $t_1 = 0.73 \cdot T_s$, whereas for medium-large voltage vectors the application time was $t_2 = 0.27 \cdot T_s$. In this way, the virtual voltage vectors could be defined as follows:

$$[VV] = t_1 \cdot [v_{\alpha\beta xy}^l] + t_2 \cdot [v_{\alpha\beta xy}^{ml}], \tag{15}$$

where $v_{\alpha\beta xy}^l$ and $v_{\alpha\beta xy}^{ml}$ are the voltage projections of any large and medium-large voltage vector, respectively.

This VV approach provided twelve couples of active voltage vectors (see Table 2) with a null average x-y voltage production and, consequently, the harmonic content of the conventional FCS-MPC can be reduced. Unfortunately, it is not an optimal solution because medium-large voltage vectors also have a medium-large size in the x-y plane. Moreover, with the proposed VVs, the injection of active components cannot be regulated during the

control period according to the operating point. Focusing on the α-β plane, a limited refinement of the voltage output is achieved due to the reduced number of VVs and their static nature.

Table 2. Composition of VV-vectors

VV-vector	$\mathbf{v^l}$	$\mathbf{v^{ml}}$	VV-vector	$\mathbf{v^l}$	$\mathbf{v^{ml}}$
$\mathbf{VV_1}$	36	53	$\mathbf{VV_7}$	27	10
$\mathbf{VV_2}$	52	38	$\mathbf{VV_8}$	11	25
$\mathbf{VV_3}$	54	20	$\mathbf{VV_9}$	9	43
$\mathbf{VV_4}$	22	50	$\mathbf{VV_{10}}$	41	13
$\mathbf{VV_5}$	18	30	$\mathbf{VV_{11}}$	45	33
$\mathbf{VV_6}$	26	19	$\mathbf{VV_{12}}$	37	44

- **LVV-Vectors**:

This second multi-vector approach proposed twelve active couples of VVs formed by adjacent large voltage vectors [21]. In these couples of VVs, each large voltage vector was applied during the half of the sampling period ($t_1=t_2=0.5\cdot T_s$) to simultaneously ensure suitable utilisation of the DC-link voltage and a satisfactory voltage injection in the x-y plane. This solution was provided to mitigate the limited performance of medium-large voltage vectors in the x-y subspace for the considered topology. The application of two adjacent large voltage vectors allowed the application of active control actions with lower production in the secondary subspace, and consequently, a reduced current injection was expected. Nevertheless, according to the location of adjacent large voltage vectors in the secondary subspace, a null average x-y voltage cannot be achieved (see Figure 4). Therefore, the voltage vector contribution of these offline control actions can be estimated applying:

$$[LVV] = t_1 \cdot [v_{\alpha\beta xy}^{l1}] + t_2 \cdot [v_{\alpha\beta xy}^{l2}], \tag{16}$$

where $v_{\alpha\beta xy}^{l1}l$ and $v_{\alpha\beta xy}^{l2}$ are the voltage production of two adjacent large voltage vectors employed to create a LVV.

The application of this multi-vector approach provides to the control designer twelve static control actions (Table 3), where the contribution of the applied voltage vectors in the secondary subspace is lower than in the case of VVs. In addition, a higher average α-β voltage production is also achieved with this solution. Nevertheless, the radial refinement of the voltage output of these control actions is limited due to their static nature. This fact limits the minimisation of the secondary components and reduces the accuracy of the α-β response. On the other hand, a harmonic residual current can appear since the LVVs cannot achieve a null average x-y voltage production during the control period.

Table 3. Composition of LVV-vectors

LVV-vector	v^{l1}	v^{l2}	LVV-vector	v^{l1}	v^{l2}
LVV_1	37	36	LVV_7	26	27
LVV_2	36	52	LVV_8	27	11
LVV_3	52	54	LVV_9	11	9
LVV_4	54	22	LVV_{10}	9	41
LVV_5	22	18	LVV_{11}	41	45
LVV_6	18	26	LVV_{12}	45	37

- **LVVZ-Vectors**:

This multi-vector solution proposed a new set of control actions (Table 4) formed by couples of adjacent large voltage vectors and a null voltage vector with an adaptive application ratio [23]. The utilisation of the null voltage vector and a variable duty cycle allowed the adaptation of the active production in both planes according to the operating point. Therefore, this alternative avoided some of the most significant disadvantages of the LVV approach related to its static nature. From the point of view of the virtual voltage vector design, this solution can be defined as a hybrid strategy since the application time of the null voltage vector is estimated online. The average voltage output of these VVs can be modelled as follows:

$$[LV0] = t_a \cdot (\frac{1}{2} \cdot [v_{\alpha\beta xy}^{l1}] + \frac{1}{2} \cdot [v_{\alpha\beta xy}^{l2}]) + (1 - t_a) \cdot v_{\alpha\beta xy}^{n}, \tag{17}$$

where

$$t_a = \frac{i_q^*}{i_{qmax}}, \tag{18}$$

being $v_{\alpha\beta xy}^{n}$ the contribution of the null voltage vector in the different orthogonal subspaces, i_q^* the reference value of the q-current and i_{qmax} the rated value of this component.

Table 4. Composition of LVVZ-vectors

LVVZ-vector	v^{l1}	v^{l2}	v^{n}	LVVZ-vector	v^{l1}	v^{l2}	v^{n}
$LVVZ_1$	37	36	0	$LVVZ_7$	26	27	63
$LVVZ_2$	36	52	56	$LVVZ_8$	27	11	7
$LVVZ_3$	52	54	63	$LVVZ_9$	11	9	0
$LVVZ_4$	54	22	7	$LVVZ_{10}$	9	41	56
$LVVZ_5$	22	18	0	$LVVZ_{11}$	41	45	63
$LVVZ_6$	18	26	56	$LVVZ_{12}$	45	37	7

This virtual voltage vector solution shows a higher α-β refinement and a reduced active voltage production thanks to its capability to modify the duty cycles according to the operating conditions. However, a certain harmonic residual phase current can still appear for high-operating points. This situation is significantly adverse in high-operating points because, in this scenario, the application time of the null voltage vector is low.

- **MV4-Vectors**

This new generation of virtual voltage vectors was created to overcome the limitation of LVV with an adaptive application time, i.e., the non-cancellation of the average x-y voltage production. To satisfy this requirement, the minimum number of adjacent large voltage vectors is three, and for this reason, the proposed active control actions are formed by trios of adjacent large voltage vectors (see Table 5). Following the approach of [16], this set of switching states is combined with a null voltage vector. In this design solution, a null average x-y voltage production is obtained thanks to the use of these trios of adjacent switching states. The application of the null voltage vector allows the minimisation of the harmonic injection according to the operating point. The voltage production of this new generation of virtual voltage vectors can be characterised as follows:

$$[MV4] = t_a \cdot (t_1 \cdot [v_{\alpha\beta xy}^{l1}] + t_2 \cdot [v_{\alpha\beta xy}^{l2}] + t_3 \cdot [v_{\alpha\beta xy}^{l3}]) + (1 - t_a) \cdot v_{\alpha\beta xy}^{n}, \qquad (19)$$

where $t_1 = t_3 = 0.2679 \cdot T_s$ and $t_2 = 0.4642 \cdot T_s$ are the duty cycle of each large voltage vectors l_1, l_2 and l_3 (being l_2 located between l_1 and l_3). As in previous multi-vector approaches, the application time solution can be extended to any trio of large voltage vectors based on symmetry considerations.

This multi-vector solution permits a priori the minimisation of the voltage production in the secondary subspace. However, *what is the performance of the aforementioned multi-vector solutions if the x-y currents are analysed in-depth?*

Table 5. Composition of MV4-vectors

MV4-vector	v^{l1}	v^{l2}	v^{l3}	v^{n}	MV4-vector	v^{l1}	v^{l2}	v^{l3}	v^{n}
$MV4_1$	37	36	52	56	$MV4_7$	26	27	11	7
$MV4_2$	36	52	54	63	$MV4_8$	27	11	9	0
$MV4_3$	52	54	22	7	$MV4_9$	11	9	41	56
$MV4_4$	54	22	18	0	$MV4_{10}$	9	41	45	63
$MV4_5$	22	18	26	56	$MV4_{11}$	41	45	37	7
$MV4_6$	18	26	27	63	$MV4_{12}$	45	37	36	0

3.2. Harmonic Mitigation

The model of a basic RL circuit excited by the different multi-vector approaches can be employed in order to obtain the response of the previous question:

$$i_x = \frac{v_x}{R_s} + (i_{x0} - \frac{v_x}{R_s}) \cdot e^{-\frac{t}{\tau}}, \tag{20}$$

$$i_y = \frac{v_y}{R_s} + (i_{y0} - \frac{v_y}{R_s}) \cdot e^{-\frac{t}{\tau}}, \tag{21}$$

where $\tau = L_{ls}/R_s$ is the stator time constant (being R_s = 14.20 Ω and L_{ls} = 4.5 mH for the selected six-phase IM). This non-linear model provides a realistic insight on the current flowing along the machine windings. For this reason, some simulations have been carried out using (20) and (21) to obtain an illustrated view of the x-y performance for the considered virtual voltage vectors.

In the proposed simulation, a single control period has been assumed (being T_s= 100μs). In addition, the initial values of the currents, i_{x0} and i_{y0}, are set to zero. The first virtual voltage vector of each multi-vector solution has been selected to be applied in (20) and (21). For the case of the multi-vector alternatives, which allow the inclusion of the null voltage vector, the active application time has been set equal to half the sampling period (t_a= 0.5·T_s).

Figure 5 shows the behaviour of the x-y currents using (20) and (21) for the considered virtual voltage vectors. The use of the MV4 control action achieves the lower harmonic content due to the minimisation of the active voltage production and the generation of a null average x-y voltage during the sampling period. For the case of VV- and LVV-vectors (Figures 5(a) and Figure 5(b), respectively), the injection of the active components cannot be regulated according to the operating point, and consequently, the x-y currents are higher than in the case of LVVZ or MV4 vectors. Focusing on the role of large voltage vectors, the results added in Figure 5 confirm the goodness of using control actions based on these switching states due to their low x-y production.

On the other hand, the necessary number of changes in the VSC legs to generate the corresponding multi-vector control actions also needs to be analysed. In the field of electric drives, a desired feature is to provide suitable harmonic mitigation with a minimal cost, i.e., with a reduced switching frequency. From this point of view, *what is the cost of each virtual vector voltage solution?*

3.3. Switching Frequency

Taking symmetry considerations, the first control action of the considered multi-vector approaches can be analysed to know the number of switch changes to generate the virtual voltage vectors. In the case of VVs, the transition between large and medium-large voltage vectors implies the change of two VSC legs (Figure 6), whereas, for adjacent large voltage vectors, a single change is required (Figure 6). Consequently, from the perspective of the switching frequency, the cost of the LVV approach is lower than in the case of VVs. As expected, the combination of an LVV with a null voltage vector (LVVZ-vectors) entails more switch changes in the VSC legs. However, a pre-defined optimal null voltage vector can be employed for each LVVZ in order to minimise the switching frequency in the design
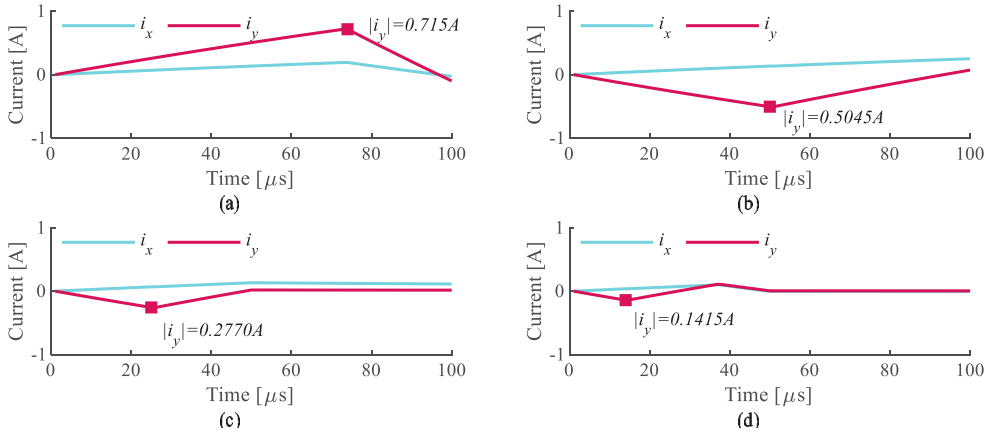
Figure 5. Simulation results of the x-y current evolution when (a) VV-vectors, (b) LVV-vectors, (c) LVVZ-vectors and (d) MV4-vectors are applied.

of the multi-vector control action. The same approach was also applied for MV4-vectors to reduce the number of changes in the VSC legs.

In conclusion, considering the switching frequency, the use of adjacent large voltage vectors can be considered as a suitable solution due to the reduced number of changes in the VSC legs. This fact can promote the design of control actions based on these switching states.

4.   Model Predictive Control Structure

The operating principle of MPC strategies for the current control of multiphase electric drives can be described in a simple manner. The available control actions are employed to predict the future currents in the electrical machine model. A two-step forward prediction process is usually applied to compensate for the time delay caused by the sampling and computational time. Then, after the two-stage predictive process, the future currents are evaluated in a cost-function to select the optimal voltage vector per control cycle. Therefore, to implement an MPC scheme, the control designer needs to develop a discrete machine model and a cost-function, where the available control actions are assessed as inputs (see Figure 7). This section details the alternatives to design the predictive machine model and the cost-function according to the employed control actions. Concerning the MPC structure of the proposed multi-vector variants, a single modification appears when the virtual voltage vectors require the online estimation of the active application time (t_a), as is illustrated in Figure 8.

4.1.   Predictive Machine Model

A discrete predictive machine model is generally employed to emulate the performance of the regulated multiphase machine. For that purpose, different discretisation techniques have been employed, such as Euler or Cayley-Hamilton, to develop a sample-data model of the
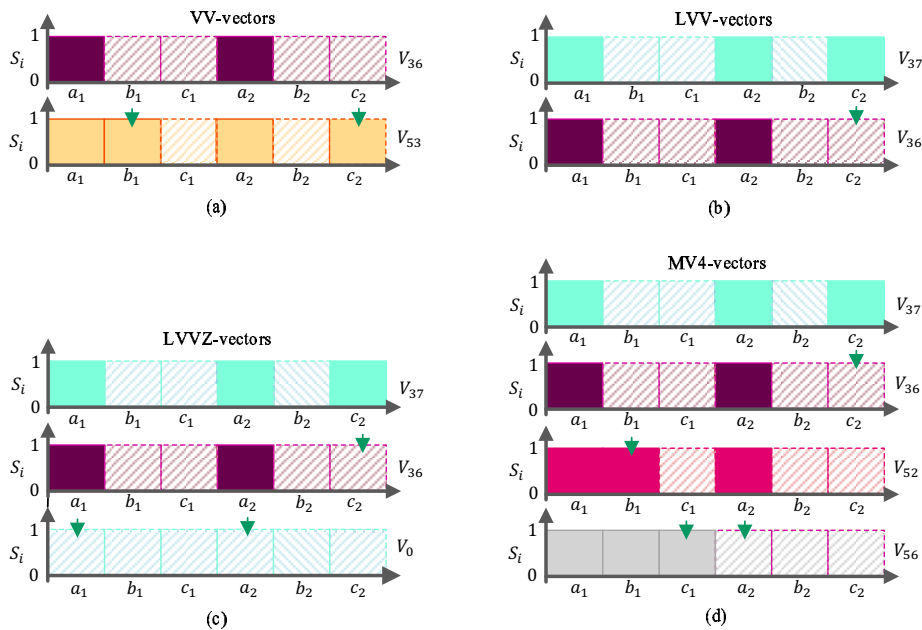
Figure 6. Transition in the VSC legs to create: (a) VV-vectors, (b) LVV-vectors, (c) LVVZ-vectors and (d) MV4-vectors.
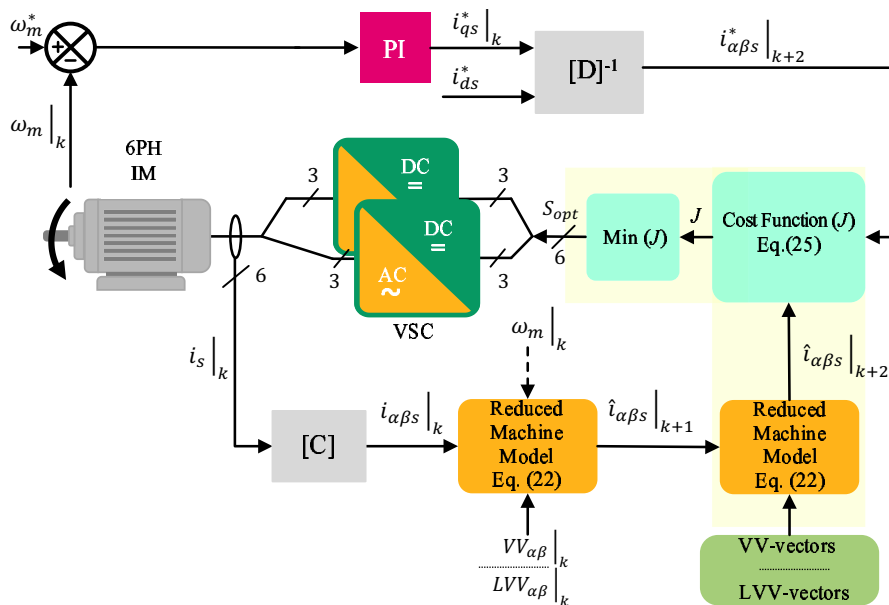

Figure 7. FCS-MPC structure when VV-vectors or LVV-vectors are applied.
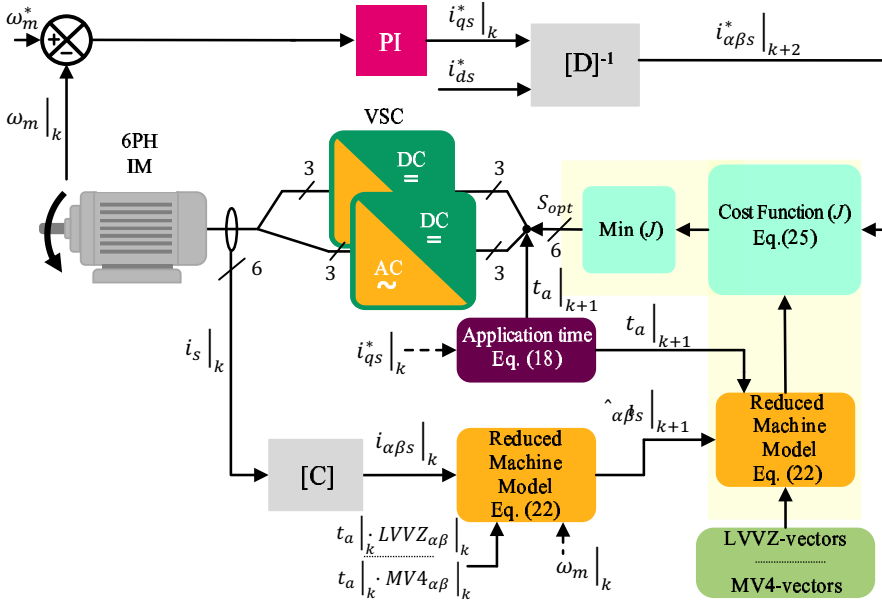
Figure 8. FCS-MPC structure when LVVZ-vectors or MV4-vectors are applied.

electric machine equations. The use of a reference frame based on the VSD approach is a popular solution to reproduce the behaviour of a multiphase machine. In the case of the considered control actions, the regulation of the x-y components is directly carried out by applying the proposed virtual voltage vectors. This fact permits the utilisation of a reduced machine model to predict the future stator α-β currents $(\hat{i}_{\alpha\beta s[k+1|k]})$ and rotor α-β fluxes $(\hat{\lambda}_{\alpha\beta r[k+1|k]})$, where the the secondary components can be omitted:

$$[\hat{X}_{\alpha\beta[k+1|k]}] = [X_{\alpha\beta[k]}] + T_s \cdot ([A] \cdot [X_{\alpha\beta[k]}] + [B] \cdot [U_{\alpha\beta[k]}]), \qquad (22)$$

where

$$[\hat{X}_{\alpha\beta[k+1|k]}] = [\hat{i}_{\alpha s[k+1|k]} \ \hat{i}_{\beta s[k+1|k]} \ \hat{\lambda}_{\alpha r[k+1|k]} \ \hat{\lambda}_{\beta r[k+1|k]}], \qquad (23)$$

$$[X_{\alpha\beta[k]}] = [i_{\alpha s[k]} \ i_{\beta s[k]} \ \lambda_{\alpha r[k]} \ \lambda_{\beta r[k]}], \qquad (24)$$

and the vector $[U_{\alpha\beta[k]}]$ is characterised by the average voltage production of the different multi-vector approaches modelled in the equations (15), (16), (18) and (19). On the other hand, matrices $[A]$ and $[B]$ are defined by the electric parameters of the electric induction machine.

4.2. Cost Function

The predicted and reference currents are typically employed in the cost function to select the most appropriate control action per control cycle. Nevertheless, taking advantage of the FCS-MPC flexibility, additional control constraints can be added in a simple manner [14]. For example, the reduction of the switching frequency has been considered in some works as an extra control requirement [14]. In the case of the proposed multi-vector alternatives, a

reduced cost function can be implemented since the secondary components can be regulated in open-loop mode using the designed control actions. Taking into account the previous assumption, the following cost function is implemented to ensure the suitable tracking of the reference currents ($i^*_{\alpha\beta s[k+2|k]}$):

$$J = (i^*_{\alpha s[k+2|k]} - \hat{i}_{\alpha s[k+2|k]})^2 + (i^*_{\beta s[k+2|k]} - \hat{i}_{\beta s[k+2|k]})^2. \tag{25}$$

The impact of each virtual voltage vector on the predicted currents needs to be evaluated in the proposed cost function in order to apply the optimum control action. Therefore, a cost function value is obtained for each multi-vector voltage, and then a minimisation process is carried out to select the most suitable sequence of switching states. Figure 9 and 10 illustrate the flowchart of the implemented two-stage prediction process and the minimisation algorithm.
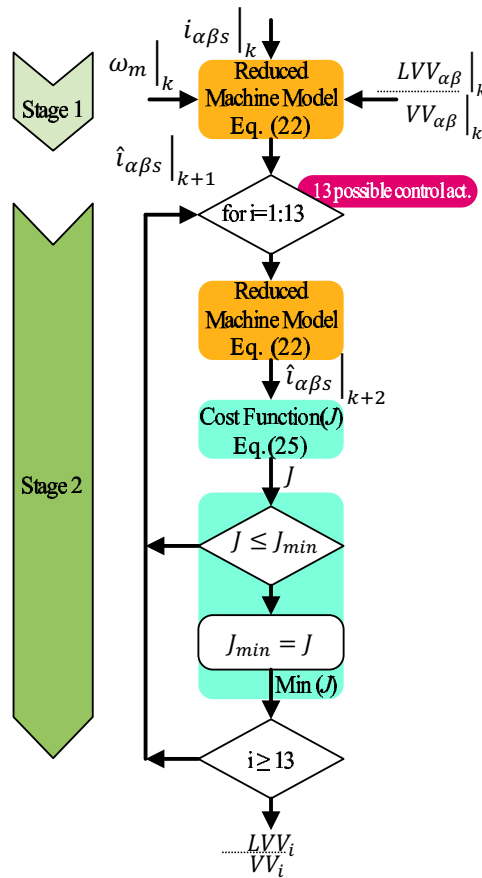
Figure 9. FCS-MPC flowchart when VV-vectors or LVV-vectors are applied.
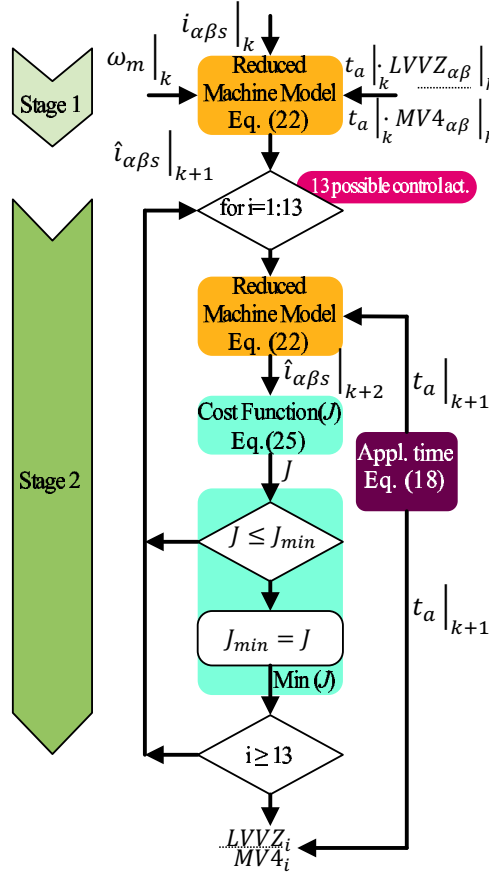
Figure 10. FCS-MPC flowchart when LVVZ-vectors or MV4-vectors are applied.

5. Comparative Experimental Results

5.1. Test Bench

The test bench of Figure 11 has been employed to explore the performance of the aforementioned multi-vector FCS-MPC alternatives when different operating conditions are emulated. The multiphase electric drive is formed by a six-phase squirrel-cage induction machine fed by a two-level dual three-phase voltage source converter (Semikron SKS22F). The VSC is fed by a single DC-link. The parameters of the machine, summarized in Table 6, have been obtained using the AC time domain and stand-still inverter supply test [26, 27].

A digital signal processor (DSP) executes the four predictive control strategies, concretely the model TMS320F28335 of Texas Instruments (TI). The employed DSP is programmed using a J-TAG connection and the TI property software (Code Composer). The speed and phase current values are measured by an encoder (GHN510296R) and four hall-effect sensors (LEM LAH 25-NP), respectively. Finally, the induction machine is loaded coupling to the shaft of a DC machine which acts as a generator. The armature circuit of this DC machine is connected to a set of variable passive loads that dissipates the power.
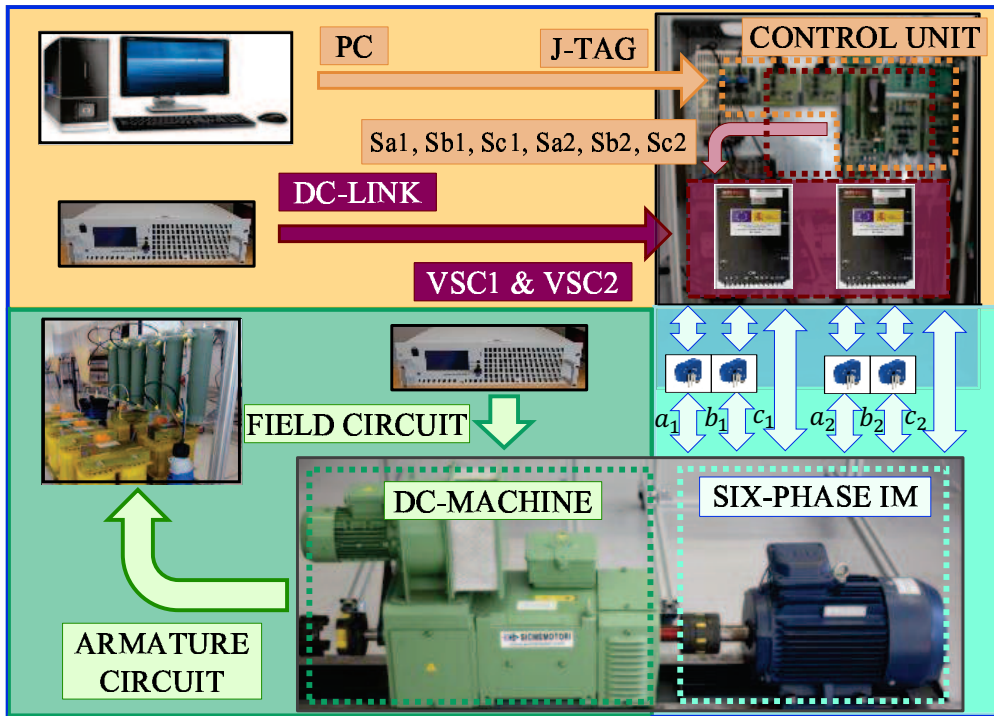
Figure 11. The employed test bench.

Table 6. Electric drive parameters

Parameter	Value
Power (kW)	1
I_{peak} (A)	4.5
$R_s(\Omega)$	14.195
$R_r(\Omega)$	3
L_m (mH)	370
L_{ls} (mH)	4.5
L_{lr} (mH)	55.12
V_{DC} (V)	300

Table 7. Quality indices Test 1

Operating Index	VV-MPC	LVV-MPC	LVVZ-MPC	MV4-MPC
THD(%)	25.7838	24.6909	10.1361	7.6164
Switching frequency (kHz)	4.2740	3.4031	4.9302	5.5198

Then the load torque is speed-dependent.

5.2. Results

Three different experimental tests have been carried out to confirm the capabilities of the proposed multi-vector strategies (VV-vectors, LVV-vectors, LVVZ-vectors and MV4-vectors) to be implemented in a FCS-MPC scheme. Tests 1 and 2 explore the steady-state performance of the four predictive strategies focusing on the signal quality and the switching frequency, whereas in Test 3, the dynamic response of these regulation techniques is assessed. The experimental results validate the analytical analysis and the simulated results included in Section 3.

- **Steady-State Performance in a Low-Speed Scenario**

In this first test, a low-speed situation is emulated, and for that purpose, the reference speed is set to 350 rpm. Concerning the tracking of the reference speed, the four multi-vector alternatives provide a suitable regulation with a reduced speed ripple (see Figure 12(a)). Attending to the currents related to the flux/torque production (Figure 12(b)), the control can be considered adequate without steady-state errors. However, two different scenarios can be identified according to the obtained current ripple in this subspace. As it can be observed in Figure 12(b) a higher ripple appears in the d-q currents when an active voltage injection is maintained during the whole control period, as in the case of VV-vectors and LVV-vectors. Analysing the secondary subspace, a similar result is obtained, i.e., the combination of adjacent large voltage vectors with a null voltage vector achieves a significant reduction of the harmonic content (see Figure 12(c)). As a result of the suitable regulation of both orthogonal planes, the phase currents are characterised by a sinusoidal waveform with a reduced harmonic distortion for the described LVVZ-vectors and MV4-vectors. Table 7 shows the total harmonic distortion of phase currents (THD) and the switching frequency for the analysed multi-vector solutions. Attending to the THD, the best response is obtained with the implementation of MV4-vectors with a value of 7.6164%. The lower switching frequency is obtained for the case of LVV-vectors because, as previously exposed, a single change in the VSC legs is necessary for the implementation of these virtual voltage vectors.

- **Steady State Performance in a High-Speed Scenario**

Test 2 explores a high-speed scenario where the reference speed is 700 rpm. Although a higher value of the reference speed is established in this test, the regulation of this variable is satisfactorily made by the four MPC schemes (Figure 13a). The tracking of the d-q
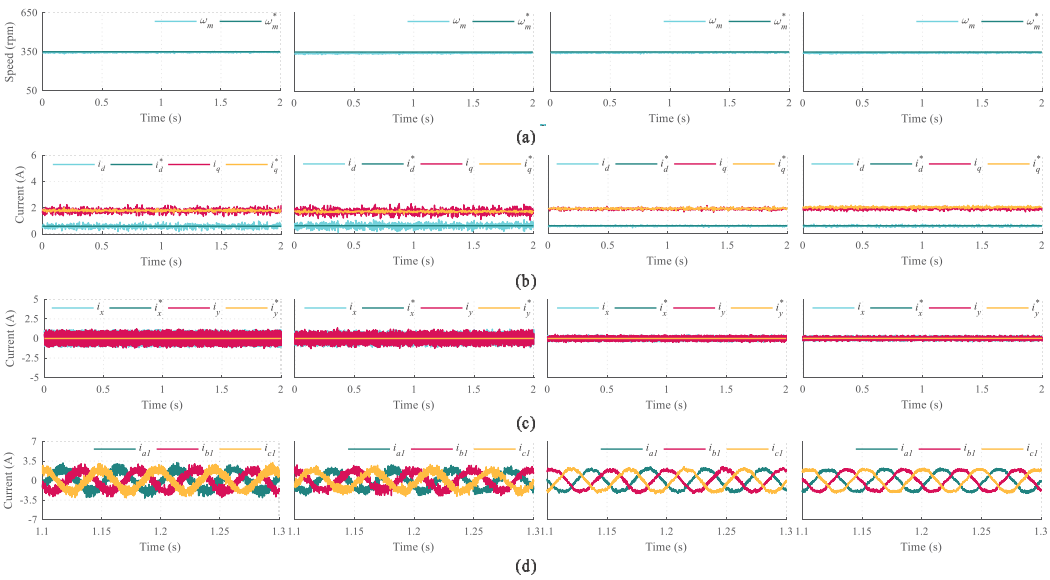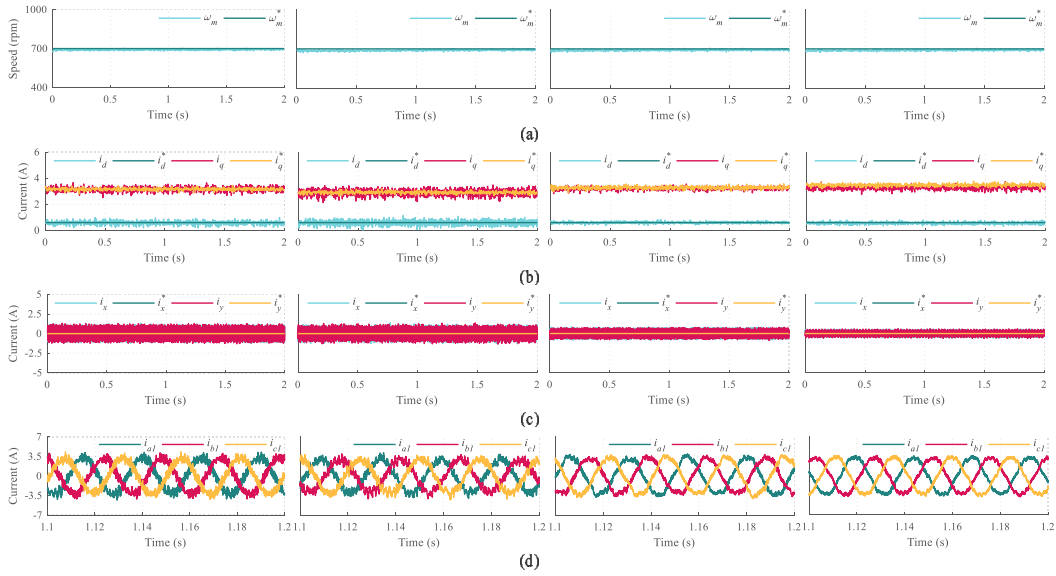
Figure 12. Steady-state performance at 300 rpm. From left to right: FCS-MPC based on VV-vectors, FCS-MPC based on LVV-vectors, FCS-MPC based on LVVZ-vectors and FCS-MPC based on MV4-vectors. From top to bottom: (a) motor speed, (b) d-q currents, (c) x-y currents and (d) set 1 of phase currents.

Table 8. Quality indices Test 2

Operating Index	VV-MPC	LVV-MPC	LVVZ-MPC	MV4-MPC
THD(%)	16.7825	17.2204	11.7944	7.3509
Switching frequency (kHz)	3.5979	2.8521	4.9592	5.6792

currents is suitable, but, as expected, the ripple is higher when VV-vectors or LVV-vectors are employed (see Figure 13b). The minimisation of the active component injection allows better regulation of the x-y currents, as shown in Figure 13c. Therefore, from the point of view of the harmonic content, MPC schemes based on an adaptive application ratio are the preferable choices thanks to their lower value of the total harmonic distortion 11.79% and 7.35%, respectively (Table 8). The minimum switching frequency is again minimised (2.8 kHz) when LVV-vectors are implemented as control actions. Therefore, this alternative can be selected if a reduced switching frequency is required.

- **Dynamic Response**

IMs are commonly employed in variable-speed applications. For this reason, the dynamic performance of the control mentioned above techniques needs to be tested. For that purpose, a speed ramp is emulated in Test 3 as shown in Figure 14. Regardless of the implemented multi-vector alternative, the regulation of the speed is satisfactorily carried out (see Figure 14a). As a consequence of the dynamic situation, the reference value of the q-current

Figure 13. Steady-state performance at 700 rpm. From left to right: FCS-MPC based on VV-vectors, FCS-MPC based on LVV-vectors, FCS-MPC based on LVVZ-vectors and FCS-MPC based on MV4-vectors. From top to bottom: (a) motor speed, (b) d-q currents, (c) x-y currents and (d) set 1 of phase currents.

is modified during the speed transient (14). In the case of secondary components, the injection of x-y currents is modified according to the operating point when the application time of active voltage vectors is estimated online. This advantage of the LVVZ-vectors and MV4-vectors cannot be exploited in the case of offline approaches and, as a consequence, the ripple of the x-y currents is not dependent on the operating scenario as it is illustrated in Figure 14c. The lower harmonic content in both planes permits the minimisation of the current ripple in the phase currents. This fact can be observed in Figures 14c and 14d when the MV4 approach is implemented.

Conclusion

The capability of several virtual voltage vectors alternatives to provide a suitable current quality, maintaining at the same time the inherent advantages of FCS-MPC strategies, has been tested in a six-phase IM. For that purpose, simulated and experimental results have been employed to illustrate the evolution of this popular control solution. From the harmonic mitigation point of view, a significant enhancement is achieved when a null voltage vector is employed and the active application time is online estimated (LVVZ-vectors and MV4-vectors). In this regard, a reduced harmonic distortion has been obtained when the MV4-vectors have been applied as active control actions. In fact, this control solution provides signal quality indices at the same level as conventional lineal controllers using an explicit modulation stage. Focusing on the switching frequency losses, a better response
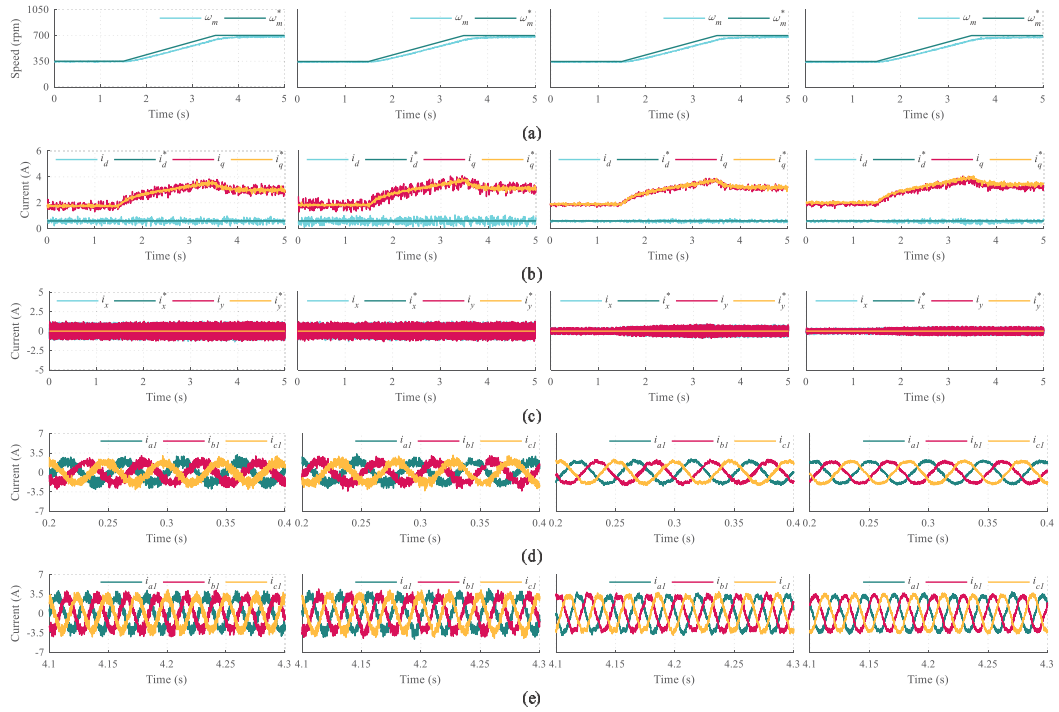
Figure 14. Dynamic response in a speed-ramp test. From left to right: FCS-MPC based on VV-vectors, FCS-MPC based on LVV-vectors, FCS-MPC based on LVVZ-vectors and FCS-MPC based on MV4-vectors. From top to bottom: (a) motor speed, (b) d-q currents, (c) x-y currents, (d) zoom 1 of set 1 of phase currents and (e) zoom 2 of set 1 of phase currents.

is obtained by selecting LVV-vectors since these virtual voltage vectors can be synthesised only with a single switch change in the VSC legs. Based on these results, multi-vector approaches are currently considered a satisfactory control solution in the field of multiphase electric drives.

References

[1] Levi E., Bojoi R., Profumo F., Toliyat H. A. and Williamson S., "Multiphase induction motor drives - A technology status review," *Electric Power Appl.*, vol. 1, no. 4, pp. 489-516, 2007.

[2] Singh G. K., "Multi-phase induction machine drive research -a survey," *Electr. Power Syst. Res.*, vol. 61, no. 2, pp. 139-147, 2002.

[3] Duran M.J., Levi E., and Barrero F., *"Multiphase electric drives: introduction,"*, Wiley Ency. Electr. and Electron. Engr, pp. 1-26, 2017.

[4] Levi E., "Advances in Converter Control and Innovative Exploitation of Additional Degrees of Freedom for Multiphase Machines," *IEEE Trans. Ind. Electron.*, vol. 63, no. 1, pp. 433-448, 2016.

[5] Bojoi R., Lazzari M., Profumo F. and Tenconi A., "Digital field-oriented control for dual three-phase induction motor drives," *IEEE Trans. Ind. Appl.*, vol. 39, no. 3, pp. 752-760, 2003.

[6] Bojoi R., Farina F., Lazzari M., Profumo F., Tenconi A., "Analysis of the asymmetrical operation of dual three-phase induction machines," *Proc. IEMDC*, vol. 1, pp. 429-435, 2003.

[7] Che H. S., Levi E., Jones M., Hew W. P. and Rahim N. A., "Current control methods for an asymmetrical six-phase induction motor drive," *IEEE Trans. Power Electron.*, vol. 29, no. 1, pp. 407-417, 2014.

[8] Tani A., Mengoni M., Zarri L., Serra G., and Casadei D., "Control of multiphase induction motors with an odd number of phases under open-circuit phase faults," *IEEE Trans. Power Electron.*, vol. 27, no. 2, pp. 565-577, 2012.

[9] Gonzalez-Prieto A., Gonzalez-Prieto I., Yepes A. G., Duran M. J. and Doval-Gandoy J., "Symmetrical Six-Phase Induction Machines: A Solution for Multiphase Direct Control Strategies," *Proc. ICIT*, 2021, pp. 1362-1367.

[10] Nelson R. H. and Krause P. C., "Induction Machine Analysis for Arbitrary Displacement Between Multiple Winding Sets," *IEEE Trans. Power Appar. Syst.*, vol. PAS-93, no. 3, pp. 841-848, 1974.

[11] Gonzalez-Prieto A., Gonzalez-Prieto I., Yepes A. G., Duran M. J. and Doval-Gandoy J., "On the Advantages of Symmetrical Over Asymmetrical Multiphase AC Drives with Even Phase Number Using Direct Controllers," *IEEE Trans. Ind. Electron.*, doi: 10.1109/TIE.2021.3104588.

[12] Lim C., Levi E., Jones M., Rahim N. A. and Hew W., "A comparative study of synchronous current control schemes based on FCS-MPC and PI-PWM for a two-motor three-phase drive," *IEEE Trans. Ind. Electron.*, vol. 61, no. 8, pp. 3867-3878, 2014.

[13] Perez-Estevez D. and Doval-Gandoy J., "A Model Predictive Current Controller With Improved Robustness Against Measurement Noise and Plant Model Variations", *IEEE Open J. Ind. Appl.*, vol. 2, pp. 131-142, 2021.

[14] Gonzalez-Prieto I., Zoric I., Duran M. J. and Levi E., "Constrained Model Predictive Control in Nine-Phase Induction Motor Drives," *IEEE Trans. Energy Conver.*, vol. 34, no. 4, pp. 1881-1889, 2019.

[15] Gonzalez-Prieto I., Duran M. J., Aciego J. J., Martin C. and Barrero F., "Model Predictive Control of Six-Phase Induction Motor Drives Using Virtual Voltage Vectors," *IEEE Trans. Ind. Electron.*, vol. 65, no. 1, pp. 27-37, 2018.

[16] Gonzalez-Prieto A., Gonzalez-Prieto I., Duran M. J., Aciego J. J. and Salas-Biedma P., "Current Harmonic Mitigation Using a Multi-Vector Solution for MPC in Six-Phase Electric Drives," *IEEE Access*, vol. 9, pp. 117761-117771, 2021.

[17] Luo Y. and Liu C., "Multi-Vectors based model predictive torque control for a six-phase PMSM motor with fixed switching frequency," *IEEE Trans. Energy Conver.*, vol. 34, no. 3, pp. 1369-1379, 2019.

[18] Yu B., Song W., Tang T., Wang S., and Bin P. Y., "A Finite Control Set model predictive current control scheme for five-phase PMSMs based on optimized duty ratio," in *Proc. APEC*, Anaheim, USA, 2019.

[19] Goncalves P. F. C., Cruz S. M. A., and Mendes A. M. S., "Fixed and variable amplitude virtual vectors for model predictive control of six-phase PMSMs with single neutral configuration," in *Proc. ICIT*, Melbourne, Australia, 2019.

[20] Goncalves P. F. C., Cruz S. M. A., and Mendes A. M. S., "Predictive current control based on variable amplitude virtual vectors for six-phase permanent magnet synchronous machines," in *Proc. ICIT*, Melbourne, Australia, 2019.

[21] Duran M. J., Ignacio Gonzalez-Prieto, Angel Gonzalez-Prieto, "Large virtual voltage vectors for direct controllers in six-phase electric drives," *Int. J. Electr. Power Energy Syst.*, vol. 125, 2021.

[22] Gonzalez-Prieto A., Gonzalez-Prieto I. and Duran M. J., "Smart voltage vectors for model predictive control of six-phase electric drives," *IEEE Trans. Ind. Electron.*, vol. 68, no. 10, pp. 9024-9035, Oct. 2021.

[23] Gonzalez-Prieto A., Gonzalez-Prieto I., Duran M. J., Carrillo-Rios J., Aciego J. J. and Salas-Biedma P., "Proportional Usage of Low-Level Actions in Model Predictive Control for Six-Phase Electric Drives," *Energies*, vol. 14, pp. 4358, 2021.

[24] Zheng L., Fletcher J. E., Williams B.W., and He X., "A novel direct torque control scheme for a sensorless five-phase induction motor drive," *IEEE Trans. Ind. Electron.*, vol. 58, no. 2, pp. 503-513, 2011.

[25] Zhao Y. and Lipo T. A., "Space vector PWM control of dual three-phase induction machine using vector space decomposition," *IEEE Trans. Ind. Appl.*, vol. 31, no. 5, pp. 1100-1109, 1995.

[26] Yepes A., Riveros J. A., Doval-Gandoy J., Barrero F., Lopez O., Bogado B., Jones M. and Levi E., "Parameter identification of multiphase induction machines with distributed windings-part 1: sinusoidal excitation methods," *IEEE Trans. Energy Conver.*, vol. 27, no. 4, pp. 1056-1066, 2012.

[27] Riveros J. A., Yepes A., Barrero F., Doval-Gandoy J., Bogado B., Lopez O., Jones M. and Levi E., "Parameter identification of multiphase induction machines with distributed windings-part 2: time-domain techniques," *IEEE Trans. Energy Conver.*, vol. 27, no. 4, pp. 1067-1077, 2012.

Chapter 4

Current Derating in Fault-Tolerant Multiphase Induction Motor Drives

Hang Seng Che[1,*]**, Mahdi Tousizadeh**[2]**,
Wan Noraishah Wan Abdul Munim**[3]
and Nasrudin Abd Rahim[1]
[1]UM Power Energy Dedicated Advanced Centre (UMPEDAC),
University of Malaya, Malaysia
[2]School of Engineering, University of Warwick,
United Kingdom
[3]School of Electrical Engineering, College of Engineering,
Universiti Teknologi MARA, Shah Alam, Malaysia

Abstract

In terms of reliability, multiphase drives are often considered to be superior to conventional three-phase drives due to their higher degrees of freedom. With the keen interest from both academia and industry, substantial progress has been observed in the development of fault-tolerant multiphase drives over the past two decades. When operating under open-circuit faults, the phase currents in a fault-tolerant multiphase machine will need to be increased above their pre-fault levels to maintain the same torque-speed performance. As a result, special care needs to be taken in understanding the post-fault current limits and control technique to ensure the safe operation of the machine. This chapter discusses the concept of current limits for a multiphase induction machine, based on a symmetrical six-phase machine, to demonstrate how the machine needs to be derated under different open phase faults. Furthermore, the impact of flux and torque current partitioning is discussed, where it is shown that the derating of current should be distributed to the flux and torque component correctly to maximize the post-fault performance of a multiphase drive.

Keywords: current control, fault-tolerant control, multiphase induction motor drives

---

*Corresponding Author's Email: hsche@um.edu.my.

1.   Introduction

Multiphase machines, i.e., machines with more than three phases, have been gaining popularity over the last two decades due to their inherent advantages over three-phase machines. One of the key merits of multiphase machines is undoubtedly their higher fault tolerance, where an N-phase machine driven by an N-leg inverter can continue to operate after the occurrence of open-circuit faults, as long as three or more phases remain intact. This is an important improvement over three-phase motor drive, where the occurrence of an open circuit fault (OCF) immediately reduces the machine into a single-phase machine, subsequently increasing the torque ripple and making it unable to self-start. Even though some fault-tolerant three-phase drives have been proposed, they generally require additional components and hardware reconfigurations. Hence, multiphase machines are still preferred in fault-tolerant critical applications.

It is noted that the OCFs can occur as either open switch fault (OSF) or open-phase fault (OPF). The former case refers to the condition where one or more switching devices (for e.g., MOSFET or IGBT) in a converter leg is open-circuited, due to reasons such as gating failure [1] or fault remedial control [2], such that the freewheeling diode(s) is still functional. On the other hand, OPF refers to the case where one or more phase connection(s) between the converter and machine is completely open-circuited, due to bad connection [3] or disconnection of the phase due to tripped circuit breakers or blown fuses [4]. While the two cases represent significantly different OPFs, it has been demonstrated in [1] that standard post-fault strategy based on OPF gives satisfactory performance even during open IGBT faults (if the two switches in the same leg are kept open but the freewheeling diodes are operational). Furthermore, an open IGBT fault can be converted into an OPF using additional protection devices, such as a relay, circuit breaker or fuse, which can help to reduce deterioration of the drive during post-fault operation [1]. Hence in this chapter, the OCF considered is referring to the OPF.

Even though multiphase machines can continue to operate after OCF, one or more stator phase windings will no longer be able to contribute to the control of the machine during post-fault operation. As a result, the currents in the remaining phases will have to be increased to compensate for the lost phase(s) to keep the torque-speed performance at their pre-fault levels. In addition, the post-fault machine may draw unequal current in the remaining phases since the machine is no longer a balance N-phase machine. All these can result in local hot spots in the machine, which can result in the subsequent failure of the machine. To avoid such catastrophic consequences, it is common to apply current derating on the multiphase machine during post-fault operations, where the torque-speed currents are reduced below their pre-fault levels to keep the remaining phase currents within the designed limits.

Depending on the number and position of the faulted phase(s), the derating factor for a fault-tolerant machine can differ. Interestingly, the phase currents depend on the induction machine's flux and torque currents. Hence, there can be multiple ways of derating the flux and torque currents while abiding by the same derating factor during post-fault operation. It is important to understand how the choice of derating flux and torque currents affects the attainable post-fault torque.

This book chapter discusses the concept of current derating in a fault-tolerant multi-

phase induction drive, using a symmetrical six-phase induction machine as an example. Initially, the current derating factors under different OCFs are discussed. Subsequently, the partitioning of this current derating between flux and torque currents is discussed, where it is shown that the actual post-fault torque of a fault-tolerant induction drive depends on the magnetizing inductance of the machine.

2.   Fault-Tolerant Six-Phase Induction Drive

2.1.   Vector Space Decomposition for Symmetrical Six-Phase Machine

Six-phase machines are most widely investigated among multiphase machines with different phase numbers. This is mainly because six-phase machines can be easily obtained by rewinding three-phase machines, making them more accessible to the research community. Furthermore, the modular three-phase structure in a six-phase machine allows the utilization of three-phase power electronics and equipment that are readily available in the market. Figure 1 shows the general winding configuration for a six-phase machine. The six stator windings can be considered as two three-phase windings, i.e., a_1, b_1 c_1 and a_2, b_2, c_2, spatially shifted by an angle γ. In the literature, the six-phase machine can be considered an asymmetrical six-phase (A6) or symmetrical six-phase machine (S6), depending on if γ is 30 or 60, respectively. It is worth noting that $\gamma=0$ is also possible, where the two three-phase windings appear to be directly "overlapped" with one another. Due to this, the six-phase machine with $\gamma=0$ is referred to as the "dual three-phase" (D3) machine.
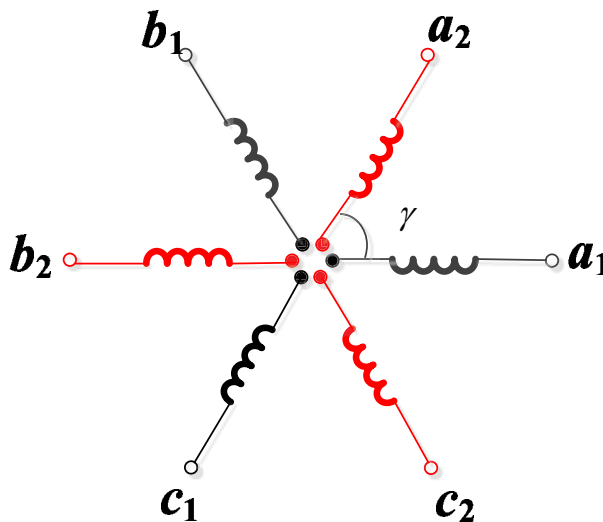
Figure 1. Spatial distribution between stator windings in a six-phase machine.

In addition, the six-phase machines can be further differentiated by the way in which the neutral points are configured. As shown in Figure 2, the stator windings can be configured with two isolated neutral (2N), one for each of the three-phase windings; alternatively, all
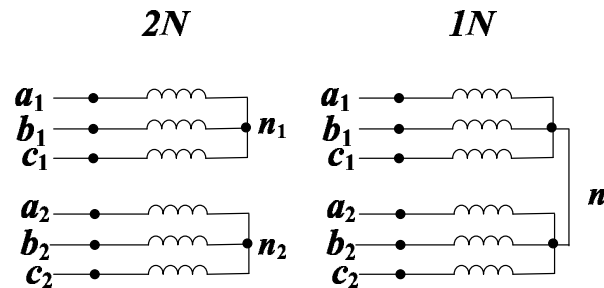
Figure 2. Winding configurations for (left) two isolated neutrals, 2N and (right) single isolated neutral point, 1N.
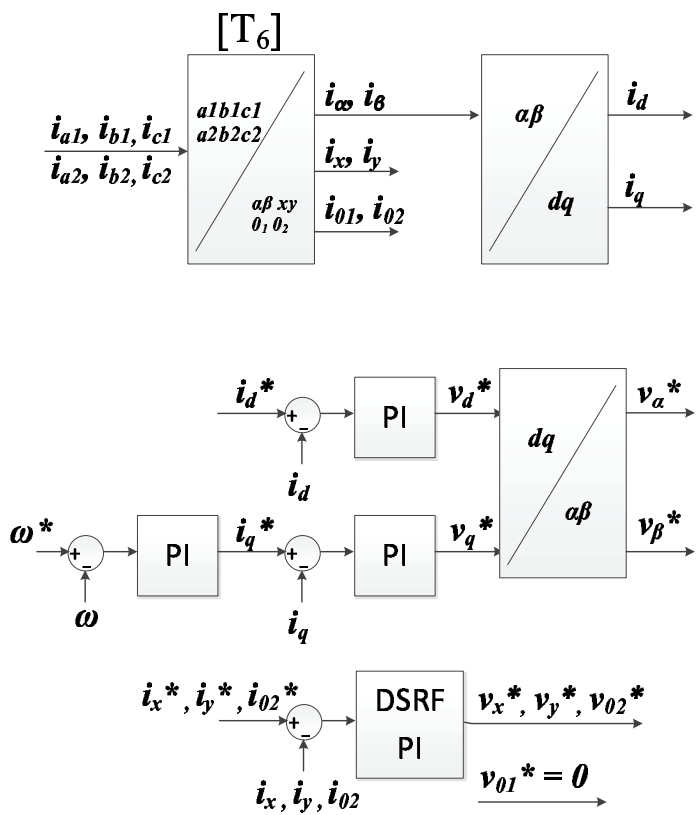
Figure 3. Field oriented control (FOC) of six-phase machine using DSRF-PI controllers.

six windings can be configured with a single isolated neutral (1N). The 2N configuration eliminates the zero sequence currents and simplifies the control of the six-phase machine. However, the 1N configuration gives higher DOF, which is better for fault-tolerant drives.

In this chapter, discussions will be based on a symmetrical six-phase induction machine

(S6), considering both single isolated neutral (abbreviated as S6-1N hereafter) and two isolated neutrals (abbreviated as S6-2N hereafter) configurations. The concept presented here can be easily extended to asymmetrical six-phase and dual three-phase machines, as well as multiphase machines with other phase numbers.

Vector space decomposition (VSD) is a widely accepted approach for modelling multiphase machines. Under the VSD method, an extended Clarke Transformation transforms the phase variables in multiphase machines into decoupled variables that can be mapped onto several decoupled planes or "vector spaces". For six-phase system, the transformation results in six decoupled components which are usually denoted as α, β, x, y, 0_1 and 0_2 components. The first two pairs of the components form two decoupled planes, i.e., the fundamental α-β plane and higher-order x-y plane; while the last two components, 0_1 and 0_2, represents the two zero sequence components in the transformed system.

Using this concept, the six-phase currents can be transformed into the corresponding current components in the decoupled vector spaces as:

$$\begin{bmatrix} i_\alpha & i_\beta & i_x & i_y & i_{01} & i_{02} \end{bmatrix}^T = [T_6] \begin{bmatrix} i_{a1} & i_{b1} & i_{c1} & i_{a2} & i_{b2} & i_{c2} \end{bmatrix}^T \tag{1}$$

$$[T_6] = \frac{1}{3} \begin{bmatrix} 1 & \cos(\frac{2}{3}\pi) & \cos(\frac{4}{3}\pi) & \cos(\gamma) & \cos(\frac{2}{3}\pi + \gamma) & \cos(\frac{4}{3}\pi + \gamma) \\ 0 & \sin(\frac{2}{3}\pi) & \sin(\frac{4}{3}\pi) & \sin(\gamma) & \sin(\frac{2}{3}\pi + \gamma) & \sin(\frac{4}{3}\pi + \gamma) \\ 1 & \cos(\frac{2}{3}\pi) & \cos(\frac{4}{3}\pi) & -\cos(\gamma) & -\cos(\frac{2}{3}\pi + \gamma) & -\cos(\frac{4}{3}\pi + \gamma) \\ 0 & -\sin(\frac{2}{3}\pi) & -\sin(\frac{4}{3}\pi) & \sin(\gamma) & \sin(\frac{2}{3}\pi + \gamma) & \sin(\frac{4}{3}\pi + \gamma) \\ \frac{1}{2} & \frac{1}{2} & \frac{1}{2} & \frac{1}{2} & \frac{1}{2} & \frac{1}{2} \\ \frac{1}{2} & \frac{1}{2} & \frac{1}{2} & -\frac{1}{2} & -\frac{1}{2} & -\frac{1}{2} \end{bmatrix} \tag{2}$$

It should be noted that here that (2) is "magnitude invariant" transformation with a coefficient of $\frac{1}{3}$, which is different from the "power invariant" transformation with a coefficient of $\frac{1}{\sqrt{3}}$.

Using the VSD approach, field-oriented control (FOC) of a six-phase machine can be achieved by extending the conventional FOC structure for a three-phase machine, as shown in Figure 3. Similar to conventional FOC, rotational transformation (based on rotor flux angle) is used to transform α-β currents into d-q currents, where d-axis current control the flux of the machine while q-axis current regulates the torque of the machine. Flux and torque control of the machine can be achieved using conventional Synchronous Reference Frame Proportional Integral (SRF-PI) controllers.

Unlike a three-phase machine, however, additional current controllers will be needed to control the x, y, 0_1 and 0_2 currents. One common practice is utilizing synchronous reference frame PI (DSRF-PI) controllers to control x, y, 0_1 and 0_2 currents. It should be noted that if a single isolated neutral configuration (1N) is utilized, 01 current will not flow and can hence be neglected from the control; if the S6 machine is configured with two isolated neutrals, both zero-sequence currents can be ignored.

During the healthy operation of a multiphase machine, only the α-β currents need to be controlled based on the flux and torque requirement, while the remaining x, y, 0_1 and 0_2 currents are controlled to be zero to reduce any additional losses in the machine.

2.2.   Post-Fault Operation under OPF

In healthy operation, the steady-state phase currents are balanced six-phase currents with equal amplitudes. Under this case, the α-β current are two sinusoidal currents with equal magnitude and frequency, which are phase-shifted by 90 degrees.

$$i_\alpha = I_{\alpha\beta}\cos(\omega t) i_\beta = I_{\alpha\beta}\sin(\omega t) \tag{3}$$

When OPFs occurs, the phase current of the faulted phase(s) will drop to zero and will no longer be controllable. This indicates that one or more degrees of freedom will be lost, and alteration to the machine control becomes necessary to ensure the machine can continue operating in post-fault mode. The loss of a degree of freedom will impose additional constraints on the x, y, 0_1, 0_2 currents such that they are no longer decoupled from the alpha-beta currents. Subsequently, new current references need to be derived for fault-tolerant six-phase machines, based on the following criteria: i) i_α and i_β should still be two sinusoidal currents phase-shifted by 90 degrees with equal frequency and magnitude. This is to ensure that balanced rotating MMF is still produced, such that the machine can operate with minimal torque ripple after the fault. ii) The references of x, y, 0_1, and 0_2 currents should consider the coupling due to the loss of a degree of freedom.

For the purpose of discussion here, it is assumed that an OPF occurs on phase-a1 of an S6-1N machine. Based on the $[T_6]$, the loss of a degree of freedom results in the following relation:

$$i_{a1} = i_\alpha + i_x + i_{02} = 0 \tag{4}$$

This implies that i_x and i_{02} can no longer be independently controlled to zero as was the case in healthy mode. It should be noted here that i_{01} has been eliminated from the equation since it will not flow under the S6-1N configuration. To allow a general discussion on the possible references for x, y, 0_2 currents, they can be expressed as a function of the alpha-beta currents and arbitrary coefficients $K_1\cdots K_6$, i.e.,

$$i_x = K_1 * i_\alpha + K_2 * i_\beta \tag{5}$$

$$i_y = K_3 * i_\alpha + K_4 * i_\beta \tag{6}$$

$$i_{02} = K_5 * i_\alpha + K_6 * i_\beta \tag{7}$$

Using the inverse [T6] transformation, the corresponding phase currents can be obtained as:

$$\begin{bmatrix} i_{a1} & i_{b1} & i_{c1} & i_{a2} & i_{b2} & i_{c2} \end{bmatrix}^T = [T_6]^{-1} \cdot \begin{bmatrix} i_\alpha & i_\beta & i_x & i_y & i_{01} & i_{02} \end{bmatrix}^T \tag{8}$$

It is easy to see that there exists infinite possibilities for $K_1\cdots K_6$ to be selected while satisfying the coupling constraints imposed by the OPF in (4). However, the choice of these coefficients will change the resultant phase currents which lead to an optimization problem: the value of $K_1\cdots K_6$ should be optimized depending on required optimization objectives.

There are two common optimization objectives here: to maximize the post-fault torque or to minimize the post-fault losses.

- Maximizing post-fault torque (MT)

    During post-fault operation, the faulted six-phase machine will have to deliver the required flux and torque with only five functioning phases. As a result, the currents in the remaining phases are expected to increase and the phase with the highest current will be the bottleneck that restricts the operation of the machine. In order to maximize the post-fault torques, $K_1 \cdots K_6$ should be selected such that the largest post-fault phase current is minimized, i.e.,

$$\textbf{Optimization objective for MT mode} = min(Max(i_k)) \qquad (9)$$

    where i_k is the phase current, with $k = \{a_1, \ldots, c_2\}$.

- Minimizing post-fault losses (ML)

    The total stator losses can be considered as the sum of the copper losses in the remaining phases:

$$P_{loss,cu} = (i_{b1}^2 + i_{c1}^2 + i_{a2}^2 + i_{b2}^2 + i_{c2}^2) \cdot R_s \qquad (10)$$

    Hence, to minimize the post-fault losses in the stator windings, the optimization objective for $K_1 \cdots K_6$ should be:

$$\textbf{Optimization objective for ML mode} = min((\sum i_k{}^2)) \qquad (11)$$

The optimization of $K_1 \cdots K_6$ based on objective functions (10) or (11) can be done using optimization tools available in MATLAB, excel, GAMS, etc. [7]. For the case of OPF in phase-a_1, the optimum values for the coefficients are:

Table 1. Optimized coefficients for S6-1N with 1 OPF

Mode	K_1	K_2	K_3	K_4	K_5	K_6
MT	-0.648	0	0	-0.368	-0.352	0
ML	-0.667	0	0	0	-0.333	0

Figure 4 shows the corresponding phase current for the healthy six-phase machine, as well as the post-fault phase currents under ML and MT modes. The figure shows that the phase currents in the remaining phases can increase beyond the rated phase current after OPF. For the case of a single OPF, the maximum phase currents are 1.453 and 1.296 times the rated values, respectively.

In order to achieve fault-tolerant control of a six-phase machine, modifications must be done on the current references in order to take in account the constraints imposed by the fault. Using the FOC structure shown in Figure3, fault-tolerant control of the S6 machine can be achieved by modifying the references for x, y, 0_1, 0_2 currents according to the coefficients $K_1 \ldots K_6$.
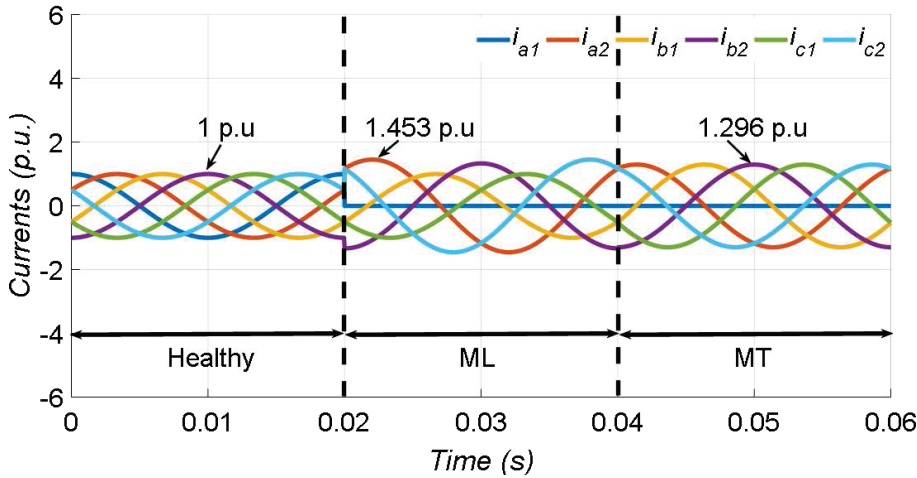
Figure 4. Phase currents for healthy and post-fault six-phase machine under ML and MT modes.

3.   Current Derating in Fault-Tolerant Drive

3.1.   Current Derating Factor

Even though the machine can operate with higher phase current after fault, prolonged operation in such condition is not advisable. This is because the higher phase current may violate the thermal design of the original machine and causes subsequent damage to the machine due to overheating of stator windings. To ensure the machine can operate safely after fault, the machine should be "derated" to reduce the phase currents to be equal or less than their rated values. For this purpose, a current "derating factor" was introduced [8], where the α-β currents are reduced by a factor δ, where

$$\delta = \frac{1}{max(i_k)} \tag{12}$$

Applying the derating factor will limit the maximum post-fault phase current to rated phase current, hence avoiding thermal hotspot that can further damage the faulted machine. However, since α-β currents are responsible for the flux and torque production in an induction machine, derating them will reduce the maximum achievable flux and torque performance of the machine.

Depending on the types of OPF and the mode of operation (MT or ML), the resultant derating factor for the faulted machine can be different. For a six-phase machine, the machine can tolerate up to 3 OPFs while operating in fault-tolerant mode. However, due to the symmetry of the phase winding arrangement, the types of OPF can be reduced down to 9 unique configurations as shown in Figure 5.

A summary of optimized coefficients for MT and ML as well as the corresponding derating factors for S6-1N machine under different OPFs are as shown in Table 2 and 3,
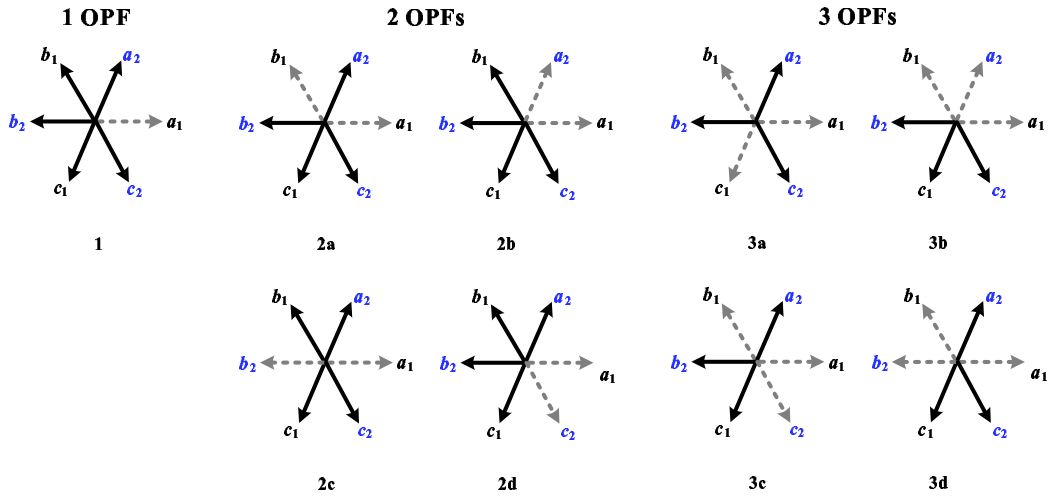
Figure 5. Possible open phase faults (OPF) for S6 machine.

respectively. As the names suggest, MT mode leads to a higher derating factor than ML mode, implying potentially higher attainable post-fault torque. It is interesting to note that for S6 machine, the MT and ML optimization resulted in the same coefficients and derating factors under 3 OPF scenarios.

Table 2. Optimized MT coefficients and Derating Factors for S6-1N under Different OPFs

OPF	K_1	K_2	K_3	K_4	K_5	K_6	δ
1	-0.648	0	0	-0.368	-0.352	0	0.771
2a	-0.750	0.433	-0.433	0.250	-0.250	0	0.433
2b	-1	0	-1.155	-1	0	0	0.500
2c	0	0	0	0	-1	0	0.577
2d	-1	0	1.155	-1	0	0	0.500
3a	-1	0	0	1	0	0	0.500
3b	0	1.732	-1.732	-2	-1	-1.732	0.167
3c	-1.5	0.866	0.866	-0.5	0.5	-0.866	0.289
3d	0	0	-1.732	1	-1	0	0.289

Using the same approach, the coefficients for a symmetrical six-phase machine with two-isolated neutrals, i.e., S6-2N, can also be derived. Compared to S6-1N, only 4 coefficients ($K_1 \ldots K_4$) need to be optimized since both 0_1 and 0_2 currents can be neglected in the 2N configuration. Furthermore, due to the lower degree of freedom, only 5 unique fault scenarios are applicable for S6-2N. Table 4 and 5 show the optimized coefficients for MT and ML modes of operation respectively for S6-2N machine. Compared to S6-1N, the

Table 3. Optimized ML coefficients and Derating Factors for S6-1N under Different OPFs

OPF	K_1	K_2	K_3	K_4	K_5	K_6	δ
1	-0.667	0	0	0	-0.333	0	0.688
2a	-0.833	0.289	-0.289	0.500	-0.167	-0.289	0.567
2b	-0.900	-0.173	-1.212	-0.900	0	0	0.475
2c	0	0	0	0	-1	0	0.577
2d	-0.900	0.173	1.212	-0.900	-0.100	-0.173	0.475
3a	-1	0	0	1	0	0	0.500
3b	0	1.732	-1.732	-2	-1	-1.732	0.167
3c	-1.5	0.866	0.866	-0.5	0.5	-0.866	0.289
3d	0	0	-1.732	1	-1	0	0.289

occurrence of an OPF in S6-2N will immediately give a derating factor of 0.5, i.e., the α-β currents will need to be derated by 50%. Due to this substantial derating under OPF, the S6-1N machine is usually preferred over S6-2N for the fault-tolerant drive.

Table 4. Optimized MT coefficients and Derating Factors for S6-2N under Different OPFs

OPF	K_1	K_2	K_3	K_4	δ
1	-1	0	0	-0.333	0.500
2a	-1	0	0	1	0.500
2b	-1	0	-1.155	-1	0.500
2d	-1	0	1.155	-1	0.500
3a	-1	0	0	1	0.500

4.   Current Derating Methods for Torque and Power Enhancement

Based on the vector space decomposition method, the phase current for an induction machine is a function of two components. Namely, the flux and torque currents, or i_d and i_q for the motor under rotor flux oriented control. Being aligned to the d-axis of the rotating frame, the rotor flux, ψ_r, is hence a function of i_d and magnetizing inductance L_m, i.e.,

$$\psi_r = L_m i_d \tag{13}$$

The output torque of the machine can be given as follows:

$$\tau = \frac{3}{2}\frac{P}{2}\frac{L_m^2 i_d i_q}{L_r} \tag{14}$$

Table 5. Optimized ML coefficients and Derating Factors for S6-2N under Different OPFs

OPF	K_1	K_2	K_3	K_4	δ
1	-1	0	0	0	0.500
2a	-1	0	0	1	0.500
2b	-1	0	-1.155	-1	0.500
2d	-1	0	1.155	-1	0.500
3a	-1	0	0	1	0.500

The torque equation can be simplified as a function of $d - q$ currents, and a parameter-dependent term κ_p:

$$\tau = \kappa_p i_d i_q \kappa_p = \frac{3}{2}\frac{P}{2}\frac{L_m^2}{L_r} \tag{15}$$

In a healthy machine, where x, y, 0_1 and 0_2 currents are zero, the vector sum of torque and flux current $|i_{dqs}|$ should be within the limit of rated phase current i_{k_rated} with the following relation,

$$|i_{dq}| = \sqrt{i_d^2 + i_q^2} \leq i_{k\_rated} \tag{16}$$

Various combinations of flux and torque currents allow the required torque to be generated. For the healthy drive with RFOC, the flux current is typically fixed to provide rated flux to the machine, while the remaining current space is allocated for the torque current. Under such circumstances, the rated torque is achievable with a rated phase current. However, if the machine is not operating at the rated torque, there are numerous ways to partition the stator current between the flux and torque components. Optimal selection of the flux-current has been a subject of various studies in the past, focusing on maximizing output torque [5], [6], [9] or minimizing machine losses [10], [11], restricted for healthy induction machines.

It is known that in fault-tolerant motor drive with the reduced number of active phases in post-fault mode, the flux and/or torque currents will need to be derated to ensure the thermal limits of the machine is not violated. As a result, i_{ds} and/or i_{qs} must be scaled-down with a specific derating factor δ corresponding to the current limit in post-fault. Hence, the equation (16) is no longer applicable and should be modified as

$$|\hat{i}_{dq}| = \delta|i_{dq}| \leq i_{k\_rated} \tag{17}$$

It should be highlighted that the (17) is a general expression where derating factor δ will vary depending on the motor's phase number, winding and neutral configurations, the number of faulted phase(s), relative positions of the faulted phase(s) as well as the choice of post-fault control.

The need for current derating causes the torque and power of the machine to be reduced accordingly, as discussed in [14], [15], [16], [17], [18]. Compared to permanent magnet

machines, the torque derating is especially severe in induction machines. For instance, [14], [18] reported that derating the phase current by a factor of 0.577 would reduce the torque to 1/3 of the rated torque for a fault-tolerant three-phase induction motor if the flux and torque currents are derated equally to 0.577 of rated values. However, this is usually not the case due to the saturation effect of magnetizing inductance.

Based on (17), there are multiple ways to derate d-q currents, so the available post-fault torque in a fault-tolerant IM drive depends on the derating method. There are two main approaches established for flux and torque currents derating in post-fault mode from the literature. The first approach is to maintain the flux current at rated value and only derate the torque current (this is referred to as Rated Flux Method, RFM, henceforth). Alternatively, both of the current components can be derated with the same factor (this is known as the Equal Derating Method, EDM, subsequently). The implication of each derating method is discussed here.

Table 6. Rated Parameters of 0.55 kW Symmetrical Six-Phase IM (S6)

Parameter	Value
Power	550W
Phase Voltage	240V
Phase Current	1.45A
Speed	1390 min-1
Frequency	50 Hz
Flux Current i_{d_rated}	1.155 A
Torque to Flux Current ratio ζ_{rated}	1.467

4.1.   Current Derating Methods

4.1.1.   Rated Flux Method (RFM)

The RFM is one of the most common approaches in fault-tolerant drives [19], [20] , where the flux current is kept at its rated value in post-fault, i.e.,

$$\delta_{d(RFM)} = 1 \quad \therefore \quad \hat{i}_{d(RFM)} = i_{d\_rated}. \tag{18}$$

By introducing the constant ζ_{rated}, which is defined as the ratio of rated i_q to rated i_d, i.e.,

$$\zeta_{rated} = \frac{i_{q\_rated}}{i_{d\_rated}} \tag{19}$$

Equation (16) can then be rewritten as:

$$\hat{i}_{q(RFM)} = \sqrt{\delta^2 i_{k\_rated}^2 - i_{d\_rated}^2} = \frac{\sqrt{\delta^2(1 + \zeta_{rated}^2) - 1}}{\zeta_{rated}} i_{q\_rated} \tag{20}$$

Based on (20) the derating factor imposed to the torque current component is found to be

$$\delta_{q(RFM)} = \frac{\sqrt{\delta^2(1 + \zeta_{rated}^2) - 1}}{\zeta_{rated}} \tag{21}$$

By substituting (18)-(20) into (14), the maximum post-fault torque in terms of rated torque under RFM will be

$$\hat{\tau}_{RFM} = \kappa_{p\_rated}.\hat{i}_{q(RFM)}.i_{d\_rated} = C_{RFM}.\tau_{rated} \tag{22}$$

where κ_{p_rated} specifies the rated value of κ_p as follows:

$$\kappa_{p\_rated} = \frac{n}{2}\frac{P}{2}\frac{L_{m\_rated}^2}{L_{r_{rated}}} \tag{23}$$

and C_{RFM}, the torque derating factor for RFM, is

$$C_{RFM} = \frac{\sqrt{\delta^2(1 + \zeta_{rated}^2) - 1}}{\zeta_{rated}} \tag{24}$$

4.1.2.   Equal Derating Method (EDM)

Another approach to reduce the post-fault current is to derate both i_d and i_q using the same derating factor imposed to the faulted drive [21], i.e.,

$$\delta_{d(EDM)} = \delta_{q(EDM)} = \delta \tag{25}$$

$$\hat{i}_{d(EDM)} = \delta.i_{d\_rated}\hat{i}_{q(EDM)} = \delta.i_{q\_rated} \tag{26}$$

By substitution of (25) and (26) into (14), the post-fault torque using EDM can be expressed as

$$\hat{\tau}_{EDM} = \kappa_{p\_EDM}.\delta^2.i_{d\_rated}.i_{q\_rated} = C_{EDM}.\tau_{rated} \tag{27}$$

where C_{EDM}, the torque derating factor for EDM, is

$$C_{EDM} = \frac{\kappa_{p\_EDM}}{\kappa_{p\_rated}}\delta^2. \tag{28}$$

From (28), it seems like the post-fault torque is reduced by a factor of δ^2 under the EDM method. However, this is only true if the magnetizing inductance is constant. However, in an actual induction machine, the magnetizing inductance increases with reduced flux current. As demonstrated in [21], this increase in L_m when reducing i_d will, to a certain extent, offset the reduction of torque. So, the term κ_p need to be recalculated for EDM as follows:

$$\kappa_{p\_EDM} = \frac{n}{2}\frac{P}{2}\frac{L_{m\_EDM}^2}{L_{r\_EDM}} \neq \kappa_{p\_rated} \tag{29}$$

4.1.3.   Comparison between RFM and EDM

By comparing the post-fault torque expressions in (22) and (27) for RFM and EDM, the following salient points can be made:

1. **RFM is simple but has limited application**

    One obvious advantage of RFM approach is its simplicity. According to 21, RFM is only applicable if the following relation is true:

    $$\zeta_{rated} > \sqrt{\frac{1}{\delta^2} - 1} \tag{30}$$

    Without loss of generality, for a particular derating factor, there is a minimum value for ζ_{rated}, below which operation in RFM is not feasible. It practically means the i_{d_rated} itself will overload the machine if (30) is not met, even without any i_q. For e.g., for $\delta = 0.577$, ζ_{rated} should be equal or higher than 1.414; for $\delta = 0.771$, ζ_{rated} should be equal or higher than 0.826, in order for RFM operation to be feasible.

    While not explicitly discussed in previous literature, this shortcoming can be a motivation to prefer EDM over RFM. Unlike RFM, the EDM can generally deliver a non-zero torque without overloading, regardless of machine type and size. This limitation will be discussed in the experimental results later.

2. **EDM allows higher post-fault torque current than RFM but not necessarily higher post-fault torque**

    From (20) and (26), it is clear that the maximum allowable post-fault torque current, $\hat{i}_q$, for RFM differs from that of EDM. Rearranging (20) and (26), their relation can be expressed as follows:

    $$\frac{\hat{i}_{q(RFM)}}{\hat{i}_{q(EDM)}} = \sqrt{\frac{(\delta\zeta_{rated})^2 + (\delta^2 - 1)}{(\delta\zeta_{rated})^2}} < 1 \tag{31}$$

    where derating factor is always less than unity $0 < \delta < 1$, $(\delta\zeta_{rted})^2$ is positive and $(\delta^2 - 1)$ is negative.

    From (31), the post-fault torque current is always higher in EDM compared to RFM. This is because the reduction of $\hat{i}_d$ in EDM provides additional room to accommodate relatively more $\hat{i}_q$. However, this does not guarantee higher post-fault torque in EDM.

3. **Dependency of the output torque on different coefficients for RFM and EDM**

    The derating factor, δ, is a typical coefficient that appears in both (24) and (28) that basically limits the achievable post-fault torque for RFM and EDM, respectively. While the effect of derating factor δ on the current limit is definite and independent of machine parameters, its impact on the maximum post-fault torque is not linear, both for RFM and EDM.

    For RFM, the achievable post-fault torque is a function of both δ and the rated current ratio, ζ_{rated}, as shown in (23). For EDM, however, the ratio of κ_{p_EDM} over

κ_{p_rated} is another key coefficient, other than δ, as stated in (28). If the rotor leakage inductance L_{lr} is relatively small, that is usually the case, the rotor self-inductance L_r and magnetising inductance L_m would be nearly equal ($L_r \approx L_m$) and therefore, (28) can be simplified and expressed in terms of magnetising inductance as follows.

$$C_{EDM} = \frac{L_{m\_EDM}^2}{L_{r\_EDM}} \cdot \frac{L_{r\_rated}}{L_{m\_rated}^2} \approx \frac{L_{m\_EDM}}{L_{m\_rated}}\delta^2 \tag{32}$$

Hence, the post-fault torque for polyphase machines under both RFM and EDM is a function of machine parameters (ζ_{rated} and L_{m_EDM}/L_{m_rated}) and derating factor. To further analyse and understand how one method compares to the other on different machines, it is necessary to utilise actual machines parameters.

4.2. Post-Fault Torque Characteristics

Based on (13)-(33), it is evident that the machine torque in healthy and post-fault operation can theoretically be obtained if the magnetising inductance and rated current ratio are known. By plotting the maximum feasible torque against different flux currents, the attainable torque under the RFM and EDM can be determined such that the suitable method can be selected. However, as will be shown subsequently, the characteristic of the magnetising inductance has a profound effect on the torque curve and will affect the conclusions to be made. To clearly illustrate this, two cases are considered here:

- Case A: Ideal magnetising inductance (constant L_m)

- Case B: Practical magnetising inductance (with saturation)

Figure 6 illustrates a typical magnetising inductance curve as a function of flux current i_d (normalised to the rated phase current of the machine) of an induction machine. While the magnetising inductance varies from machine to machine, the inductance generally reduces with increasing flux current i_d due to flux saturation. In this particular case, rated L_m is obtained under rated i_d, which is around 0.48 p.u. of the rated phase current.

Hence, when flux current i_d is reduced, the torque can decrease due to the reduction in i_d, but it can also increase due to the increase in L_m. The actual impact of flux current i_d derating on torque can be analysed by considering two cases: the case where magnetising inductance is considered to be ideal and constant regardless of i_d (Case A); and second case where a realistic magnetising inductance that changes with i_d is considered (Case B).

$$C_{EDM} = \frac{L_{m\_EDM}^2}{L_{r\_EDM}} \cdot \frac{L_{r\_rated}}{L_{m\_rated}^2} \approx \frac{L_{m\_EDM}}{L_{m\_rated}}\delta^2 \tag{33}$$

Hence, the post-fault torque for polyphase machines under both RFM and EDM is a function of machine parameters (ζ_{rated} and L_{m_EDM}/L_{m_rated}) and derating factor. To further analyse and understand how one method compares to the other on different machines, it is necessary to utilise actual machines parameters.
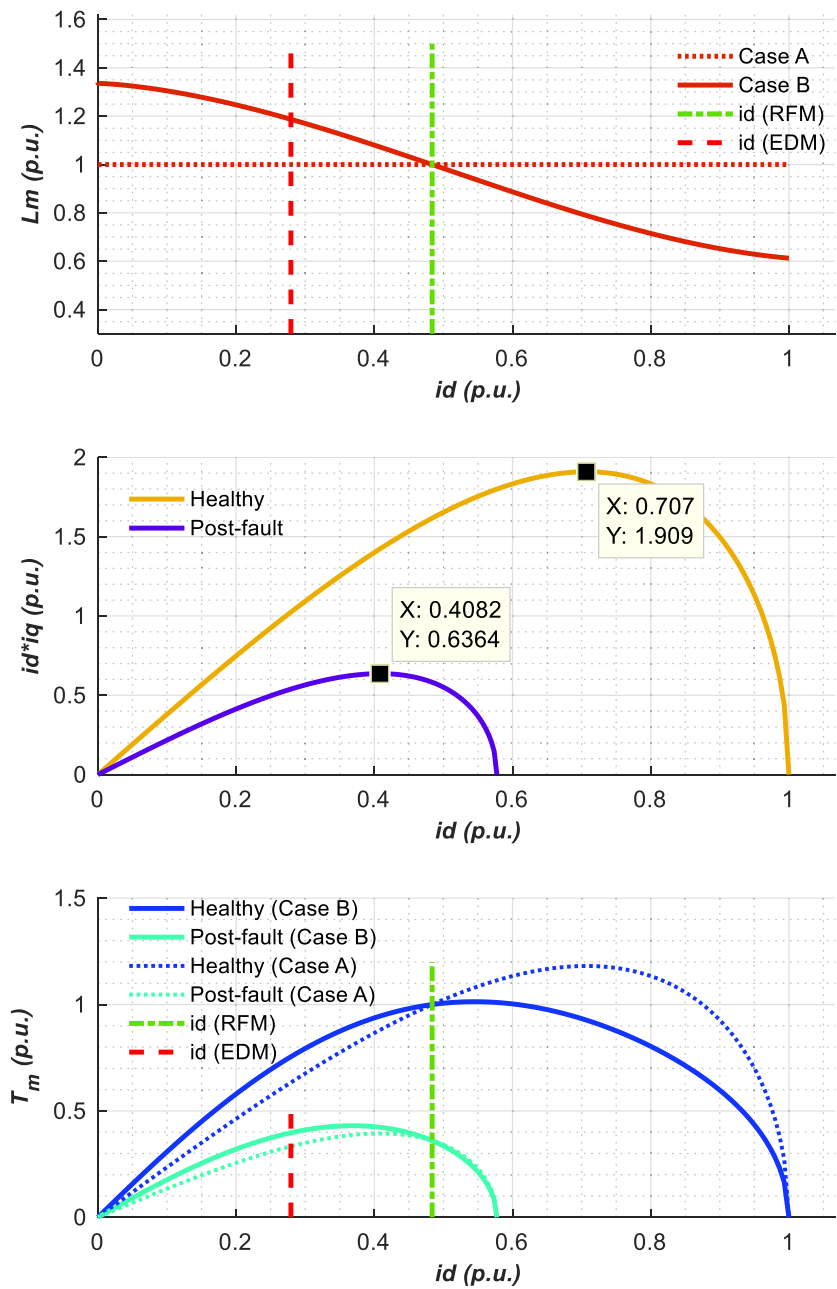
Figure 6. (top) Magnetizing inductance curves of Case A versus Case B, (middle) multiplication of flux and torque currents, and (bottom) healthy and post-fault torque curves for induction motor as a function of flux current i_d using ideal and practical magnetizing inductance curves.

4.2.1.   Torque Calculation for Case A (Ideal L_m)

Firstly, let's assumed that L_m is constant regardless of i_d, and has a rated value of 0.485 H as shown with a horizontal dotted line in the L_m section of Figure 6. As illustrated in the middle section of Figure 6, the normalized multiplication of flux and torque current, while maintaining the phase current at rated value, can be plotted as a function of the i_d for both healthy and post-fault scenarios, i.e., $\delta = 1.0$ and $\delta = 0.577$ respectively.

If L_m is assumed to be ideally constant, the i_d*i_q curve for the healthy machine will peak at $i_d = 0.707 p.u.$, as expected. The same conclusion can be drawn for the ideal torque curve, represented by blue dotted trace (Case A) in the torque section of Figure 6. This observation is in agreement with the theoretical discussion on maximum torque per ampere MTPA [6], which suggested that maximum torque is achievable where flux and torque current are equal $i_d = i_q$. However, having a high value of rated i_d of over 70% will result in a machine with a low power factor and efficiency. In practice, it is common for induction motors to have a lower rated i_d to maximize their efficiency, especially for variable torque applications. For the case of 1 kW motor, the rated i_d is measured to be $1.31 * \sqrt{2} = 1.85A$, as denoted in Figure 6 by vertical dash-dotted green lines ($i_{d\_rated} = 0.484$ p.u.).

For the derating factor of $\delta = 0.577$, the corresponding post-fault torque curve based on (1) and (3) are then calculated theoretically and shown by the dotted turquoise trace in the torque section of Figure 6. As L_m is assumed to be constant here, the factor κ_p in (15) will be a constant too. Subsequently, the torque curves for healthy and post-fault torque are simply scaled versions of the i_d*i_q curves in Figure 6, with the scaling factor being the derating factor (i.e., 1 and 0.577 respectively).

4.2.2.   Torque Calculation for Actual L_m

Due to the saturation effect of magnetizing inductance in an actual induction machine, the actual torque (Case B) will be higher than the ideal torque (Case A) for i_d lower than i_{d_rated}, and lower than the ideal torque for i_d above the i_{d_rated}. Hence, the actual torque curve of the machine (Case B) is found to be significantly different from the ideal case (Case A), which peaks at a relatively low i_d, well below the 0.707 p.u. value in the ideal case. Based on the sample machine with torque-i_d curves, as shown in Figure 6, the saturation effect of magnetizing induction will lead to approximately 7% higher achievable post-fault torque in EDM than RFM. This implies that if the characteristics of the magnetizing inductance can be predetermined, the following relation can be used to determine if RFM or EDM can provide higher post-fault torque in a fault tolerant induction motor drive:

$$\epsilon = (\frac{L_{m\_EDM}}{L_{m\_rated}}\delta^2) - (\frac{\sqrt{\delta^2(1 + \zeta_{rated}^2) - 1}}{\zeta_{rated}}) \tag{34}$$

such that $\epsilon < 0$ indicates that RFM is superior over EDM in terms of post-fault torque production and vice versa.

With the understanding of the effect of magnetizing inductance established, experimental tests are performed on S6 IM to demonstrate the validity of the discussion. In this case, the S6 IM is controlled using a fault-tolerant control scheme with SRF-PI controllers [7] while operating with 1 OPF. Figure 9 and Figure 10 show the results for single OPF with S6-1N, while Figure 11 and Figure 12 show the results for single OPF with S6-2N.
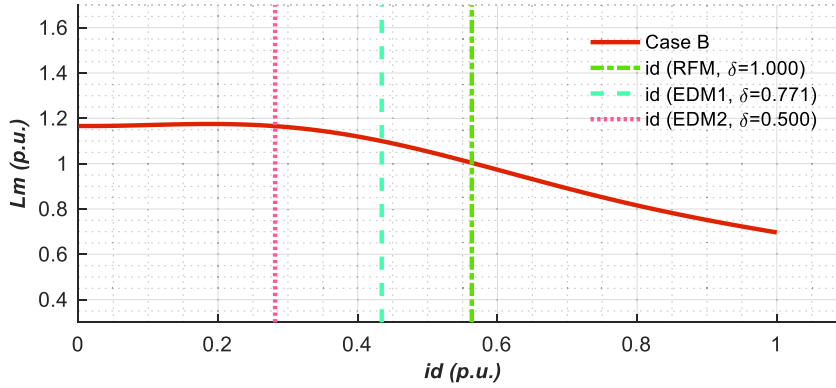
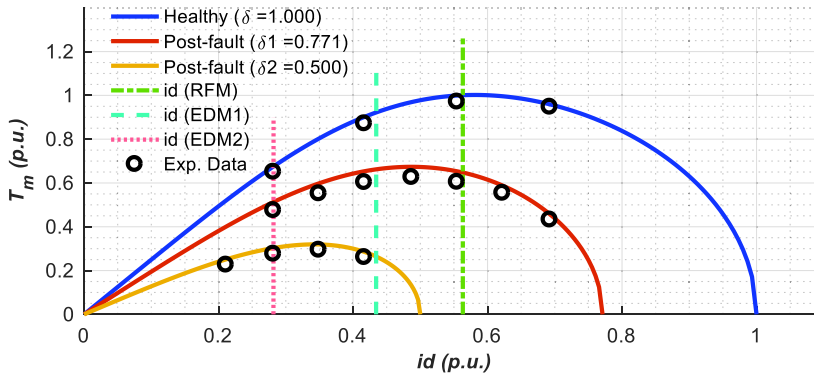Figure 7. The magnetizing inductance curve S6 IM.

Figure 8. The theoretical estimation and experimental results of output torque for S6 IM.

With a single neutral, the derating factor of $\delta_1 = 0.771$ is applied. As shown in Figure 10, both RDM and EDM give approximately the same torque performance for this particular machine. In terms of the voltages, the amplitude of $v_{\alpha\beta}$ is slightly lower in EDM compared to RFM due to the lower flux current in the former case. However, it can be observed that the amplitude of v_{xy0+} in Figure 10 remains fixed, regardless of the current derating method. This is because:

1) The amplitude of $x - y$ and 0_2 currents are purely functions of $\alpha - \beta$ currents, which are the same in both EDM and RFM as long as the maximum phase currents i_k are kept at rated values.

2) The $x - y$ and zero plane inductances are not affected by the magnetizing inductance.

Hence, the machine's x,y and 0_2 impedances remained relatively constant irrespective of the changes in flux current when switching from one flux derating method to another.

It should be highlighted here that the S6-2N machine operating under RFM ($\delta_1 =$
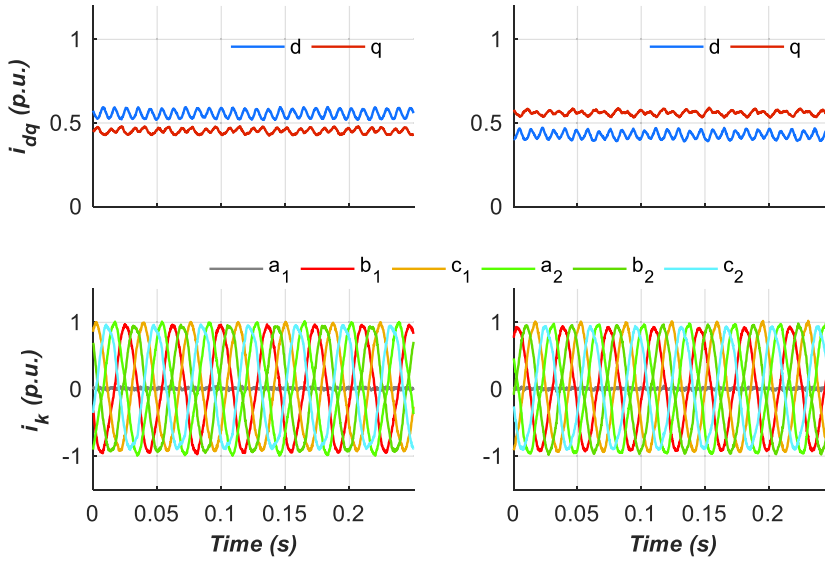
Figure 9. The current components under RFM with i_d=1.14A (left), and EDM with i_d=0.88A (right), experimented on S6 IM with 1OPF ($\delta1$=0.771), single neutral and rated phase current.
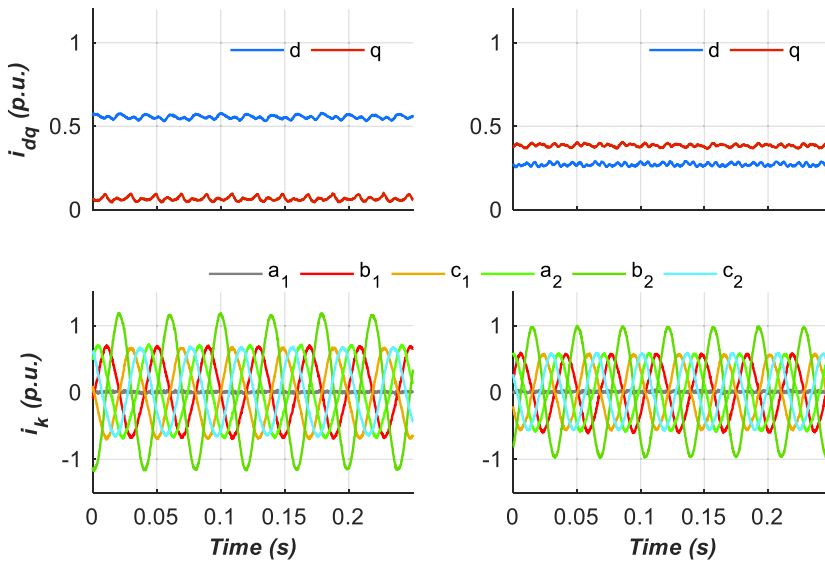
Figure 10. The current components under RFM with i_d=1.14A (left), and EDM with i_d=0.57A (right), experimented on S6 IM with 1OPF ($\delta2$=0.500), two isolated neutral and rated phase current.

Figure 11.   The $\alpha\beta$xy0+ components of voltage with output torque under RFM with i_d=1.14A (left), and EDM with i_d=0.88A (right), experimented on S6 IM with 1OPF ($\delta 1$=0.771), single neutral and rated phase current.

Figure 12.   The $\alpha\beta$xy0+ components of voltage with output torque under RFM with i_d=1.14A (left), and EDM with i_d=0.57A (right), experimented on S6 IM with 1OPF ($\delta 1$=0.500), two isolated neutral and rated phase current.

0.500) is unable to operate in the post-fault mode without violating the current limit since (30) does not hold true for this machine. As seen in Figure 12, approximately 20% of rated torque is achievable if the machine is allowed to be overloaded, with maximum phase current exceeding the rated value in Figure 11. On the other hand, the same machine is able to deliver 29% of rated torque if operated under EDM in post-fault operation. Furthermore, operating under EDM will allow the machine to operate above rated speed using the additional voltage margin available (due to the lower amplitude of $v_{\alpha\beta}$).

While for the case of the S6 machine here, EDM is preferred over RFM, this might not hold true for other induction machines. As demonstrated in [23], the choice between EDM and RFM depends heavily on the magnetizing curve of the machine. Understanding the machine characteristics will be instrumental in deciding the suitable flux derating method in a fault-tolerant induction drive. Furthermore, when designing a fault-tolerant induction motor, the proper design of the magnetizing inductance curve will also be important to ensure sufficient post-fault torque can be attained during fault-tolerant operation.

Conclusion

In this chapter, current derating in fault-tolerant multiphase induction motor drive is discussed. Firstly, the concept of vector space decomposition and its application on the control of the multiphase machine is presented, using a symmetrical six-phase induction machine (S6) as an example. Subsequently, the impact of current derating on the post-fault performance of the fault-tolerant drive is demonstrated. It is highlighted here that the achievable post-fault torque of a fault-tolerant induction motor drive depends on how the current derating factor is partitioned between the flux and torque current, as well as the machine's magnetizing induction characteristics. While experimental results are based on a 0.55kW symmetrical six-phase machine, the concept discussed here is valid for other types of multiphase induction machines.

References

[1] Guzman H., Barrero F., and Duran M.J., "IGBT-Gating Failure Effect on a Fault-Tolerant Induction Motor Drive," *IEEE Trans. Ind. Electron.*, vol. 62, no. 1, pp. 15-20, 2015.

[2] Ginart A., Kalgren P.W., Roemer M.J., Brown D.W., and Abbas M., "Transistor diagnostic strategies and extended operation under one-transistor trigger suppression in inverter power drives," *IEEE Trans. Power. Electron.*, vol. 25, no, 2, pp. 499-506, 2010.

[3] Tani A., Mengoni M., Zarri L., Serra G., and Casadei D., "Control of Multiphase Induction Motors With an Odd Number of Phases Under Open-Circuit Phase Faults," *IEEE Trans. Power. Electron.*, vol. 27, no. 2, pp. 565-577, 2012.

[4] Ryu H., Kim J., and Sul S., "Synchronous-Frame Current Control of Multiphase Synchronous Motor Under Asymmetric Fault Condition Due to Open Phases," *IEEE Trans. Ind. Appl.*, vol. 42, no. 4, pp. 1062-1070, 2016.

[5] Bozhko S., Dymko S., Kovbasa S., and Peresada S. M., "Maximum Torque-per-Amp Control for Traction IM Drives: Theory and Experimental Results," *IEEE Trans. Ind. Appl.*, vol. 53, no. 1, pp. 181-193, 2017.

[6] Wasynczuk O. et al., "A maximum torque per ampere control strategy for induction motor drives," *IEEE Trans. Energy Convers.*, vol. 13, no. 2, pp. 163-169, 1998.

[7] Munim W.N.W.A., Duran M.J., Seng Che H., Bermudez M., Gonzalez-Prieto I., Rahim N.A., "A Unified Analysis of the Fault Tolerance Capability in Six-phase Induction Motor Drives," *IEEE Trans. Power Electron.*, vol. 32, no. 10, pp. 7824-7836, 2017.

[8] Che H.S., Duran M.J., Levi E., Jones M., Hew W., Rahim N.A., "Post-fault Operation of an Asymmetrical Six-Phase Induction Machine With Single and Two Isolated Neutral Points," *IEEE Trans. Power Electron.*, vol. 29, no. 10, pp. 5406-5416, 2014.

[9] Bojoi R., Li Z., Odhano S. A., Griva G., and Tenconi A., "Unified direct-flux vector control of induction motor drives with maximum torque per ampere operation," in *Proc. ECCE*, pp. 3888-3895, 2013.

[10] Sung Woosuk, Shin Jincheol, and Jeong Yu-seok, "Energy-Efficient and Robust Control for High-Performance Induction Motor Drive With an Application in Electric Vehicles," *IEEE Trans. Veh. Technol.*, vol. 61, no. 8, pp. 3394-3405, 2012.

[11] Odhano S. A., Bojoi R., Boglietti A., Rosu S. G., and Griva G., "Maximum Efficiency per Torque Direct Flux Vector Control of Induction Motor Drives," *IEEE Trans. Ind. Appl.*, vol. 9994, no. c, pp. 4415-4424, 2015.

[12] Uddin M. N. and Nam S. W., "Development of a nonlinear and model-based online loss minimization control of an IM drive," *IEEE Trans. Energy Convers.*, vol. 23, no. 4, pp. 1015-1024, 2008.

[13] Uddin M. N. and Nam S. W., "New online loss-minimization-based control of an induction motor drive," *IEEE Trans. Power Electron.*, vol. 23, no. 2, pp. 926-933, 2008.

[14] Mirafzal B., "Survey of fault-tolerance techniques for three-phase voltage source inverters," *IEEE Trans. Ind. Electron.*, vol. 61, no. 10, pp. 5192-5202, 2014.

[15] Wang W., Cheng M., Zhang B., Zhu Y., and Ding S., "A fault-tolerant permanent-magnet traction module for subway applications," *IEEE Trans. Power Electron.*, vol. 29, no. 4, pp. 1646-1658, 2014.

[16] Zhang W., Xu D., Enjeti P. N., Li H., Hawke J. T., and Krishnamoorthy H. S., "Survey on fault-tolerant techniques for power electronic converters," *IEEE Trans. Power Electron.*, vol. 29, no. 12, pp. 6319-6331, 2014.

[17] de A. Ribeiro R. L., Jacobina C. B. B., da Silva E. R. C., and Lima A. M. N. M. N., "Fault-tolerant voltage-fed PWM inverter AC motor drive systems," *IEEE Trans. Ind. Electron.*, vol. 51, no. 2, pp. 439-446, 2004.

[18] Welchko B. A., Lipo T. A., Jahns T. M., and Schulz S. E., "Fault tolerant three-phase AC motor drive topologies; A comparison of features, cost, and limitations," in *Proc. IEMDC*, vol. 1, no. 4, pp. 539-546, 2004.

[19] Beltrao de Rossiter Correa M., Jacobina C. B., Cabral da Silva E. R., and Lima A. M. N., "An induction motor drive system with improved fault tolerance," *IEEE Trans. Ind. Appl.*, vol. 37, no. 3, pp. 873-879, 2001.

[20] Mendes A. M. S. and Marques Cardoso A. J., "Fault-tolerant operating strategies applied to three-phase induction-motor drives," *IEEE Trans. Ind. Electron.*, vol. 53, no. 6, pp. 1807-1817, 2006.

[21] Tousizadeh M., Che H. S., Selvaraj J., Rahim N. A., and Ooi B.-T., "Performance Comparison of Fault-Tolerant Three-Phase Induction Motor Drives Considering Current and Voltage Limits," *IEEE Trans. Ind. Electron.*, vol. 66, no. 4, pp. 2639-2648, 2019.

[22] Munim W. N. W. A., Tousizadeh M., and Che H. S., "Effects of zero-sequence transformations and min-max injection on fault-tolerant symmetrical six-phase drives with single isolated neutral," *J. Power Electron.*, vol. 19, no. 4, 2019.

[23] Tousizadeh M., Che H.S., Abdel-Khalik A.S., Munim W., Selvaraj J., and Abd Rahim N., "Effects of flux derating methods on torque production of fault-tolerant polyphase induction drives", *IET Electr. Power Appl.*, vol. 15, pp. 616-628, 2021.

Chapter 5

A Systematic Review of Fault Detection and Diagnosis Methods for Induction Motors

Narco Afonso Ravazzoli Maciejewski[1,*]**,**
Aline Elly Treml[2] **and Rogerio Andrade Flauzino**[1]
[1]Department of Electrical and Computer Engineering,
 University of Sao Paulo (USP), Brazil
[2]Centre of Engineering and Exact Sciences,
 Western Parana State University (UNIOESTE), Brazil

Abstract

Induction motors are the main elements for converting electrical energy into me-
chanics for the productive sector since their low cost and long durability include their
most attractive characteristics. Also, the need to reduce maintenance costs and the
implementation of predictive techniques, aiming to minimize setbacks generated by
unexpected disconnections of production lines, becomes essential and a great incen-
tive for the development of systems capable of identifying faults. Given this, this paper
implements a systematic search to identify papers and other scientific and technologi-
cal papers to reach state of the art and the technique of the theme of monitoring faults
in induction motors. With this, the primary methods used for this purpose were iden-
tified, and in this way, it is possible to suggest new lines of research on the subject of
detection and diagnosis of faults in induction motors.

Keywords: fault detection, fault diagnosis, predictive maintenance, condition monitoring,
bearing fault, stator fault, broken rotor bar fault, eccentricity fault

1.   Introduction

The growing need to search for more rational and economic processes concerning the effi-
cient use of electrical energy has resulted in detailed studies for the optimisation of man-
ufacturing techniques, which also aim at the adequate conservation of electrical energy.
Within this context, electric motors are essential equipment in most processes that involve

---

*Corresponding Author's Email: narcoafonso@gmail.com

the productive sectors, as they stand out as the main elements for converting electrical energy into mechanics. As a result, these electric machines have undergone improvements that meet the emerging needs of production processes due to their energy importance within the international scenario [1, 2].

A large part of the industrial applications that require converting electrical energy into mechanics uses rotating electrical machines, such as induction motors, as the low cost associated with long durability reflects their most attractive characteristics. In addition, the growing need of productive sectors facing preventive and predictive maintenance, aimed at reducing maintenance costs, minimising inconveniences generated by unplanned shutdowns of production lines, and even inhibiting the risk of work accidents, makes relevant and motivating the development of systems capable of identifying defects and incipient failures inherent to the machine [3].

Electric motors are exposed to various environmental conditions, operating under different loads, which, together with natural ageing, can cause failures inherent to the machines themselves or associated with severe conditions. In this context, monitoring to detect and diagnose defects in their early stages is of paramount importance to treat them properly, preventing failures and, consequently, reducing maintenance cost, parts inventory cost, and shutdown of the industrial sector in which the machines are contained [4].

Failures in electric motors can be, in general, of electrical characteristics, such as stator and rotor defects, and mechanical, such as eccentricity and mechanical component failures. In this way, the identification and application of techniques for predicting and preventing mechanical and electrical failures increase the availability and reliability of rotating electrical machines.

The methods and protocols used for protection are as old as the machines themselves. As for applications in induction motors, manufacturers initially had simple protections, such as overcurrent and overvoltage, to ensure safety and reliability in operation. However, as the functions of induction motors become increasingly complex, continuous monitoring becomes more and more necessary, as in applications in pumps, compressors, fans, and load handling. Given this, condition monitoring is essential to follow faults from the beginning, aiming to reduce the costs of tools and operators stopped and optimise maintenance functions and avoid financial losses.

Several faults can impair the required function of induction motors, the main ones being listed [5]:

- Faults in the stator resulting in the opening or short circuit of one or more phase windings of the stator;

- Abnormal connections of the stator windings;

- Broken rotor bar or cracked rotor terminals;

- Static and or dynamic air gap irregularities;

- Eccentricity causing problems to the stator core and the windings;

- The short winding of the rotor;

- Bearing and gearbox fault.

Of the faults presented, the hegemonic ones are those in the bearing, stator, rotor bars, and those related to eccentricity, which need more attention. These types of faults present several symptoms, with the prevailing voltages of unbalanced air opening and line currents, an increase in intermittent torque, a decrease in average torque, reduction of efficiency and excessive heating [5, 6].

Most of the techniques developed for fault detection and diagnosis in three-phase induction motors are currently applied to steady-state signals [7, 8, 9, 10]. However, it is interesting to clear up defects and evidence of occurrences still in the initial stage of operation or the transitory regime for some applications. These applications are based on intermittent machine start-up and also for initial commissioning tests after installation [11, 4].

Still, the interest in detecting and diagnosing transient defects is motivated by the excellent performance of the techniques in conditions where steady-state methods have poor performance, such as in the detection of broken bars in machines with low nominal slip, external bar breaks in double cage induction machine, bar breaks in machines with axial air ducts, asymmetries, and eccentricities of rotors in machines with continuous load oscillations [11, 12, 13, 14]. In these cases, failures are hardly detected in the steady-state of operation, as they are coupled to a fundamental component or noise, or they can lead to a false-positive diagnosis or type I error [11].

Otherwise, induction machines that occasionally operate in a restricted steady-state are gaining importance in the industrial environment. Relevant examples of such applications are wind power generation, electric vehicles, or motors driven by electronic converters that operate closed-loop controlled systems. Induction motors often experience continuous and random changes in load, speed, or power conditions in these applications. The application of conventional steady-state techniques such as Fast Fourier Transform, which calculates the discrete Fourier transform, leads to blurred spectra where the fault components scatter and become unidentifiable [15].

Most conventional steady-state detection and diagnostic methods identify distinct fault components in a current spectrum. Likewise, steady-state diagnostic methods are often based on intelligent systems, combining attribute selection and machine learning techniques to identify the evolution of fault components. Therefore, the attributes extracted from the signals constitute the fundamental step in the diagnosis of defects in the transient operating regime [11, 16]. As the detection and diagnosis of defects even in the transient operating regime are subject to several random factors, such as noise, the techniques used must be noise-robust, reducing the rate of errors and false alarms [17, 18].

To detect and diagnose faults in induction motors, many methods developed to date in the most diverse fields of science. Thus, this paper presents a systematic review of the literature to establish state of the art, allowing the knowledge of the papers and applications currently offer together with possible innovations on this theme.

This research is vast, as several combinations of techniques can be used to detect and monitor failures. As for the type of signal, electrical and mechanical are applied in time and/or frequency domains, and there are also different working regimes such as stationary and transient. Also, machine learning and attribute selection tools are often applied for this purpose. Given this, a combination of the various knowledge domains mentioned is relevant to composing this topic's state of the art.

2.   Types of Faults in Induction Motors

Its internal or external condition can influence the appearance of failures of an induction motor. The faults can be classified as mechanical, electrical, or environment-related failures according to their origin.

Thus, several fault detection techniques were developed to detect and diagnose fault-related signals. In this way, the following describes the faults that need more attention in the operation of rotating electrical machines.

2.1.   Bearing Faults

Usually, a rolling-element bearing consists of two concentric rings, which are a set of rollers or balls on the raceways between the inner and outer rings. Bearing failures can be classified as distributed or local [19]. Distributed faults include undulation, rough surface, oversized rolling elements, and misaligned runways. Localized faults include pits, chips, and cracks in the rolling surfaces. When a moving roller passes over the fault's surface, it generates a series of vibration impacts at that very moment. The period and amplitude of the effect is calculated by the position of the anomaly, speed, and dimension of the bearing. Mechanical vibrations are at each component's rotation rate and are produced by defective bearings. The characteristic frequencies associated with the raceways and the balls or rollers are determined by the speed of rotation and dimension of the machine's bearing and also determines the condition of the bearing using mechanical vibration analysis techniques [20].

2.2.   Stator Faults

Most of the induction motor's stator faults are subject to various stressful operating conditions, such as environmental, electrical, thermal, and mechanical. The most frequent and potentially disastrous faults are faults in the stator winding, namely open circuit, curve by curve, phase by phase, coil by coil and coil to earth. If a timely diagnosis is not made, it can cause terrible motor failure. The three main divisions of the stator failures are as follows [21, 22, 23]:

- **Housing:** includes vibration, circulating currents, earth faults and loss of refrigerants;

- **Lamination:** involves loosening the core and core hot spot;

- **Fault in the stator windings:** consists of the part of the final winding and part of the groove that includes movement of conductors, insulation wear.

2.3.   Broken Rotor Bar Faults

The appearance of breaks in the rotor bars is the result of a series of efforts that can be classified as thermal, caused by overload and thermal imbalances; magnetic, by electromagnetic forces and noises; vibration; environmental damage due to abrasion contamination of the rotor material; and, mechanically, due to bearing faults or due to the manufacturing process. In the face of such situations, the machine can continue operating. However, the presence of a broken bar, can cause electric arcs, originating in the middle of the fracture

of the broken or cracked bar, creating an overheating that will accelerate the development of the failure; new fractures, caused by mechanical efforts and high currents imposed on the adjacent bars; and, broken bar releases due to the action of centrifugal forces acting on the rotor, which can physically damage the other bars, the stator windings and also the magnetic circuit [24, 25, 26].

2.4.   Eccentricity Faults

The eccentricity of the air gap is the result of the uneven clearance between the rotor and the stator of the induction motor. Its two types are the static eccentricity of the airspace and the dynamic eccentricity of the air. Mixed eccentricity is a combination of static and dynamic eccentricity in the airspace, and the inclined eccentricity of the airspace is the axial non-uniformity of the airspace. The minimum length of the radial air space is fixed in the area for static eccentricity of the air space. At the same time, the center of the rotor and the center of rotation never coincide in the dynamic eccentricity. During the commissioning of the induction motor, incorrect positioning of the stator or rotor can result in static eccentricity. Dynamic eccentricity occurs due to bearing wear, shaft bending, or mechanical resonances at critical speeds [27, 28, 29].

3.   Systematic Review Methodology

The systematic review of the literature is a rigorous and replicable method to achieve relevant evidence for a specific research question [30]. This research method first appeared in areas related to health [30, 31]. However, there are currently conducts and uses in other areas. In engineering and exact sciences, several applications can be found in the most diverse lines of research, including systematic reviews that investigate other systematic reviews [31, 32].

Figure 1 summarizes the workflow of the systematic review steps. This process of searching, selecting, and analyzing the papers found was and carried out chronologically with possibilities of feedback at each new interaction of the phases. The first part consists of steps 1, 2, 3, and 4, which constitutes the protocol for applying the method, while the second part, composed of steps 5, 6, and 7, is the analysis of results, such as the literature analysis.

Under the methodological design of the systematic literature review, it was proposed, based on the objectives of this paper, a research question, Step 1, encompassing all aspects of mathematical and physical in detecting and diagnosing faults in induction motors.

The identification of the databases that outlined the searches, Step 2, was performed by bringing together the primary databases used in research in the area of engineering and exact sciences, represented by IEEExplore, Scopus, Web of Science, SciELO, Wiley, and CiteSeer. Step 3 was defined as the stage of determining the inclusion and exclusion criteria for further analysis and to form the meta-analysis of the related literature. The criteria for selecting articles were built on question modalities to narrow down the choice of papers of interest, and are shown below:
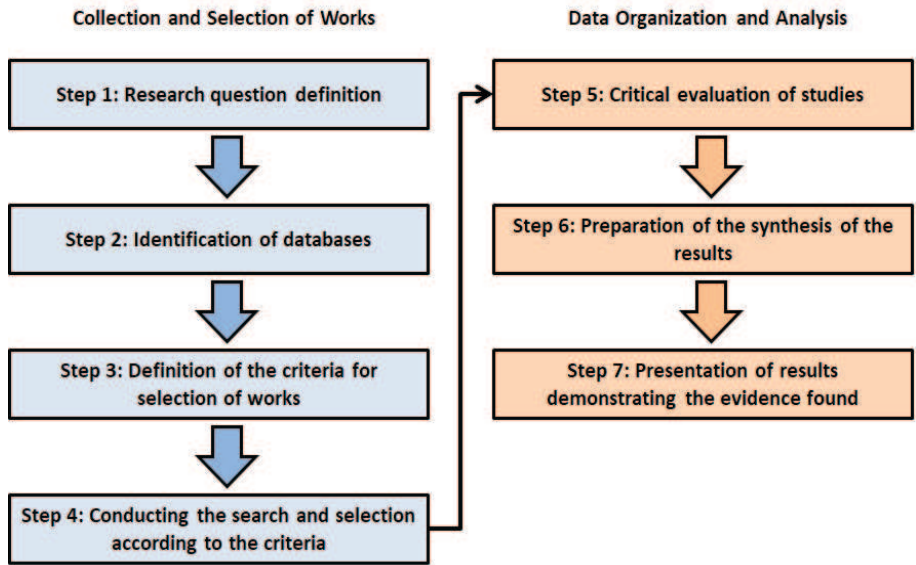
Figure 1. Steps of the systematic review used.

1. Is the paper related to the research question?

2. Is the paper related to the implementation of systems, applications or tools for analyzing and monitoring faults in induction motors?

3. Is the method used based on experiments, simulations or mathematical analyzes?

4. Is paper accessible institutionally?

5. Is the paper not repeated in the searched databases?

6. Is the paper written in Portuguese, Spanish, or English?

It is worth mentioning that these criteria are for the inclusion of papers for critical analysis, and, if any of these criteria are denied, the article must be excluded. Thus, finalizing the collection and selection of articles, Step 4, search and selection of articles began according to the criteria determined in Step 3. For this, keywords or similar words related to the theme for building a search string. With that, the words used in the search are presented in Table 1. It is worth mentioning that these words are related through logical operators for insertion in the literary bases.

After the construction of the string and the selection criteria, the search was initiated in each of the selected databases, and the attributes acquired from the search were inserted in an electronic spreadsheet. After the search period, in the first moment, the second part of the review is performed, that is, the selection and organization of the collected papers, which will be presented in the subsequent section.

Table 1. Structure of the types of keywords used in searches

Study object	Defects	Database
Asynchronous machine Induction motors	Bearing Stator Broken rotor bar Eccentricity Hybrid	Synthetic Experimental Hybrid
Signals	**Analysis regime**	**Analysis domain**
Electrical Mechanical Thermal Hybrid	Stationary Transient Hybrid	Time Frequency Time-frequency Hybrid

4.   Literature Meta-Analysis

The search period for the systematic review was between January 2013 and May 2020. With the application of the systematic literature search process, 3388 papers were identified, with this number reduced to 734 after the implementation of the inclusion criteria. Then, the title and summary of all the papers found were read to carry out the selection of papers. When the choice cannot be made without question, the reading of the complete paper was considered, until there were no doubts about the relevance of the paper. At the end of this process, 169 papers were obtained from which information was extracted to answer the research question.

In Figure 2, a bar graph is displayed containing the distribution, by year of paper, of the number of papers selected at the end of the systematic literature review. The figure shows that between the years 2013 and 2016, the average of published papers was 13, while in the following years to date, the standard has grown to approximately 29. This fact can be explained due to the consolidation of interest in the researched topic, mainly in the application of intelligent systems for fault detection in electrical machines.

The analysis of the 169 papers discovered in the systematic review allowed the implementation of the following meta-analysis, following Steps 5, 6, and 7 of the method.

As for the defects of the induction motors, 40.83% of the papers studied the bearing defects, 8.85% the defects in the stator, 20.71% the defects of the broken bar in the rotor, and 17.75% the defects of eccentricity. Some studies analyzed some defects together, being 11.83%, separating the defects, or not for the analysis hybrid.

An experimental database was used in 71 publications, of which 71.83% used data produced in institutions, universities or industries, and 28.17% investigated data kept in repositories. Of these studies, 7.69% of the selected papers built synthetic databases to evaluate prediction algorithms' performance. These databases were generated computationally to contain specific properties, such as the presence or absence of trend and or seasonality.

Regarding the type of acquired signals, 57.39% of the studies analyzed electrical sig-
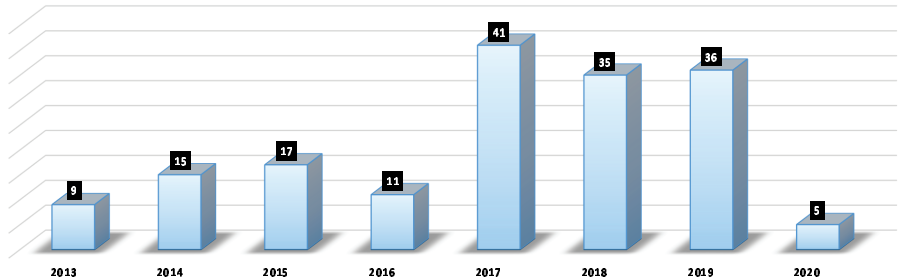
Figure 2. Distribution of the number of papers per year of publication.

nals, 29.59% mechanical signals, and 13.02% analyzed hybrid signals containing electrical and thermal or mechanical and thermal signals.

According to the analysis regime, studies that implemented the analysis methods in a stationary regime were 79.88%, a transient regime 2.96%, and a hybrid regime 17.16%. Moreover, regarding the analysis domain, 55.03% of the papers used methods in the time domain, 23.67% in the frequency domain, 8.88% in the time-frequency domain and only 21 papers applied hybrid domain. It is worth mentioning that in the frequency domain, 55.03% of the papers used the Motor Current Signature Analysis technique.

Until recently, the prevalent fault detection technique was the Motor Current Signature Analysis technique. References [33, 34] provide a helpful review of this technique based methods. In addition to the Fast Fourier Transform based techniques applied to the line current, broken bar faults, stator faults and dynamic eccentricity faults can also be detected using a higher-order spectrum. In particular, bispectrum and trispectrum, from a single radial vibration transducer measurement [35]. The study had been developed to detect and diagnose faults in inverter-fed and line-fed induction motors.

The papers that presented a selection of attributes were 66.27%, and 75.89% used the filter approach, 17.86% the wrapper approach, and only 6.25% the embedded approach. Of these papers, observing the attendance with which measures were used in publications, 24.85% of the studies adopted the Mean Absolute Error, 28.99% assessed the Root Mean Square Error, 30.18% verified the Mean Absolute Percent Error, 31.95% analyzed the Mean Symmetric Absolute Percent Error, 20.71% used the Mean Square Error, 12.42% addressed the Mean Absolute Error in Scale, 6.51% used the Correlation Coefficient, and 4.14% applied the relative absolute error as stopping criteria used in the evaluation of the subsets in the attribute selection process. The Theil U measurements, Prediction of Change in Direction, Root Mean Normal Square Error, and the Determination Coefficient appeared in 3.55% of the papers.

Besides applying attribute selection, many papers also use machine learning techniques for classification. Considering the attendance with which the methods appeared in papers, 47.93% of papers used Artificial Neural Networks, 37.27% built Integrated Autoregressive models of Moving Averages or Integrated autoregressive Seasonal Moving Averages, 13.02% used hybrid models, 21.89% applied Vector Support Machines, 11.83% performed variations of the k Nearest Neighbor algorithm, 8.88% used the Moving Aver-

age and Simple Exponential Smoothing methods, 4.14% addressed Bayesian techniques, and 4.14% used Holt-Winters models. Moreover, 65.68% of the selected papers applied some search techniques capable of choosing the model parameters in the best possible way. These techniques include training and test or holdout validation and cross-validation.

Processing techniques are related to the type of signal. Recently, a systematic review on detection and diagnosis methods for typical induction motor defects was published, to define the state of the art of this technology. According to the authors, the two main signals used for this purpose are electrical and mechanical, and 79.88% of applications are in steady-state [16]. Thus, techniques for processing mechanical vibration signals and electrical signals under steady-state conditions were analyzed.

During the execution of the meta-analysis, there were some works, out of a total of 169, which involved more popular assessments and methods and with more adequate results concerning the research theme. Because of this, these works are fundamental to compose state of the art on the subject of this research and provide a path for the proposal of a new method for monitoring and detecting defects in rotating electrical machines, based on intelligent systems.

Considering the results presented, the bearing defect showed a higher level of accuracy in detection and diagnosis, with an average percentage of 96.33% when using SVM techniques applied with statistical attributes such as kurtosis, the mean, and standard deviation in vibration cycles mechanics. Therefore, among the main typical defects of induction motors, the defect in rolling bearings is the one that presents the best physical representation of the defect. As for the stator defects, an accuracy of 87.22% was obtained. Failures of broken rotor bars, however, had an average accuracy of 92.56% for the works analyzed.

The paper of [36] highlighted that integrating elements of time in the learning process constitutes the most significant challenge in the use of Support Vector Machine to predict time series, as they are susceptible to errors when changes in distribution frequently occur throughout the series. To assist in this issue, the distribution of errors in the predictions obtained by the Support Vector Machine algorithm was investigated. Once the samples that produced the biggest errors were identified, their correlation with the changes that occurred in the distribution of the historical series was observed. The understanding of this behaviour motivated the authors to propose a time-dependent loss function, which makes it possible to include information about changes in the distribution of the series directly in the learning process. The experiments were conducted based on real data. The proposed method was compared with its alternative version, which adopts quadratic mean and six other prediction algorithms: Artificial Neural Networks, k Nearest Neighbor algorithm, Support Vector Machine, Robust Regression, and Integrated autoregressive Seasonal Moving Averages. The results, expressed by the Root Mean Square Error measure, suggested that the use of a time-dependent loss function can reduce the overall variance of errors and, therefore, lead to more accurate predictions.

Empirical evaluations that include statistical and machine learning algorithms were the subjects of 33 papers. Considering the results presented, the defect of rolling bearings showed a higher level of accuracy in the detection and diagnosis, with a percentage of 96.33% when using the Support Vector Machine techniques applied with statistical attributes, such as kurtosis, means and standard deviations in the mechanical vibration cycles. Therefore, among the main defects typical of induction motors it is the most easily verified

with monitoring. As for the stator faults, a maximum accuracy of 87.22% was obtained. The faults of broken rotor bars, however, showed a maximum accuracy of 92.56% for the analyzed works.

When commenting on hybrid faults, or faults occurring together, the methods of detecting and diagnosing faults still do not have enough accuracy to compare with the methods applied for only one fault. This is since there are many random factors involved and the difficulty of obtaining experimental data.

Even so, few studies presented methods capable of identifying joint defects, or hybrids, and when applied, the precision was low. This is explained by the fact that it is a challenge to monitor more than one defect simultaneously, but this is a common reality in induction motors, and one defect can lead to the appearance of others or become a fault. With the application of the method in this work, it was possible to verify the deficiency of current methods in detecting more than one defect at the same time. Even so, for state-of-the-art purposes, stator and broken bar defects, even though they have been frequently studied, need to be implemented by more reliable and agile methods to perform real-time monitoring, especially in analysis in the transient operating regime.

Conclusion

The induction motors are the most used elements for converting electrical energy into mechanics, presenting high applicability in the industrial sector due to the low cost and superior relative durability. Thus, fault detection and diagnosis in induction motors are of fundamental importance, as it increases the reliability of these elements. Given this, the development of methods to monitor faults is essential. Among the most common faults were those in the bearing faults, presenting the best detection accuracy. Thus, it is necessary to develop methods that accurately identify the fault of broken bars in the rotor, stator, and eccentricity.

Still, few studies presented methods capable of identifying faults together or hybrids, and when applied, the accuracy was low. This is explained by the fact that it is challenging to monitor one more fault at the same time, but that is an ordinary reality in induction motors, and one fault can lead to the appearance of others. With the application of the method of this paper, it was possible to verify the deficiency in the current techniques in detecting more than one fault simultaneously. Still, for state-of-the-art purposes, faults in the stator and broken bar, even if they have been studied a lot, need to be implemented more reliable and agile methods to carry out real-time monitoring.

References

[1] Puccini L.R., Giffoni M.G.P., Silva L.F., Utagawa C.Y., "Comparativo entre as bases de dados PubMed, SciELO e Google Acadêmico com o foco na temática Educação Médica", *Cadernos UniFOA*, vol. 10, no. 28, pp. 75-82, 2015.

[2] Romero-Trancoso R., et al., "FPGA-based online detection of multiple combined faults in induction motors through information entropy and fuzzy inference", *IEEE Trans. Ind. Electron.*, vol. 58, no. 11, pp. 5263-5270, 2011.

[3] Zhang X., Zhang T., Young A.A., Li X., "Applications and comparisons of four time series models in epidemiological surveillance data", *Plos One*, vol. 9, no. 2, pp. e88075, 2014.

[4] Bindu S., Thomas V., "Diagnoses of internal faults of three phase squirrel cage induction motor-a review", in *Proc. ICAECT*, 2014, pp. 48-54. IEEE.

[5] Vas P., Parameter Estimation, Condition Monitoring, and Diagnosis of Electrical Machines. Oxford, U.K.: Clarendon, 1993.

[6] Kliman G. B. and Stein J., "Induction motor fault detection via passive current monitoring", in *Proc. Int. Conf. Electrical Machines*, Cambridge, MA, Aug. 1990, pp. 13-17.

[7] Zamudio-Ramirez I., Antonino-Daviu J. A., Osornio-Rios R. A., de Jesus Romero-Troncoso R. and Razik H., "Detection of Winding Asymmetries in Wound-Rotor Induction Motors via Transient Analysis of the External Magnetic Field," *IEEE Trans. Ind. Electron.*, vol. 67, no. 6, pp. 5050-5059, 2020.

[8] Kang T. -J., Yang C., Park Y., Hyun D., Lee S. B. and Teska M., "Electrical Monitoring of Mechanical Defects in Induction Motor-Driven V-Belt-Pulley Speed Reduction Couplings," *IEEE Trans. Ind. Appl.*, vol. 54, no. 3, pp. 2255-2264, 2018.

[9] Diao L. -J., Sun D. -n., Dong K., Zhao L. -T. and Liu Z. -G., "Optimized Design of Discrete Traction Induction Motor Model at Low-Switching Frequency," *IEEE Trans. Power Electron.*, vol. 28, no. 10, pp. 4803-4810, 2013.

[10] Romero-Troncoso R. J. et al., "FPGA-Based Online Detection of Multiple Combined Faults in Induction Motors Through Information Entropy and Fuzzy Inference," *IEEE Trans. Ind. Electron.*, vol. 58, no. 11, pp. 5263-5270, 2011.

[11] Pons-Llinares J., Riera-Guasp M., Antonino-Daviu J.A., Habetler T.G., "Pursuing optimal electric machines transient diagnosis: The adaptive slope transform", *Mechanical Systems and Signal Processing*, vol. 80, pp. 553-569, 2016.

[12] Yang C., Kang T., Hyun D., Lee S. B., Antonino-Daviu J. A. and Pons-Llinares J., "Reliable Detection of Induction Motor Rotor Faults Under the Rotor Axial Air Duct Influence," *IEEE Trans. Ind. Appl.*, vol. 50, no. 4, pp. 2493-2502, 2014.

[13] Antonino-Daviu J. et al., "Detection of Broken Outer-Cage Bars for Double-Cage Induction Motors Under the Startup Transient," *IEEE Trans. Ind. Appl.*, vol. 48, no. 5, pp. 1539-1548, 2012.

[14] Pons-Llinares J., Antonino-Daviu J. A., Riera-Guasp M., Pineda-Sanchez M. and Climente-Alarcon V., "Induction Motor Diagnosis Based on a Transient Current Analytic Wavelet Transform via Frequency B-Splines," *IEEE Trans. Ind. Electron.*, vol. 58, no. 5, pp. 1530-1544, 2011.

[15] Henao H. et al., "Trends in Fault Diagnosis for Electrical Machines: A Review of Diagnostic Techniques," *IEEE Ind. Electron. Mag.*, vol. 8, no. 2, pp. 31-42, 2014.

[16] Maciejewski N.A.R., Treml A.E. and Flauzino R. A., "A Systematic Review of Fault Detection and Diagnosis Methods for Induction Motors," in *Proc. FORTEI-ICEE*, 2020, pp. 86-90.

[17] Rocha E. M., et al. "A fuzzy type-2 fault detection methodology to minimize false alarm rate in induction motor monitoring applications", *Appl. Soft Comput.*, vol. 93, pp. 106373, 2020.

[18] Abd-el-Malek M., Abdelsalam A.K., Hassan O.E., "Induction motor broken rotor bar fault location detection through envelope analysis of start-up current using Hilbert transform", *Mech. Syst. Signal Process.*, vol. 93, pp. 332-350, 2017.

[19] Bhowmik P.S., Pradhan S., and Prakash M., "Fault Diagnostic And Monitoring Methods Of Induction Motor: A Review", *Int. J. Appl. Control, Electr.and Electron. Eng.*, vol. 1, no. 1, p. 1-18, 2013.

[20] Chen S. and Lipo T. A., "Bearing currents and shaft voltages of an induction motor under hard-and soft-switching inverter excitation", *IEEE Trans. Ind. Appl.*, , vol. 34, no. 5, pp. 1042-1048, 1998.

[21] Duan F., Zivanovic R., "Diagnosis of Induction Motor Stator Faults by Parameter Estimation Technique Based on Direct Search on Sparse Grid", in *Proc. IET Int. Conf.*, 2012, pp. 127-127.

[22] Duan F., and Zivanovic R., "Induction Motor Stator Faults Diagnosis By Using Parameter Estimation Algorithms", in *Proc. SDEMPED*, 2013. pp. 274-280, IEEE.

[23] Jung J. -H., Lee J. -J. and Kwon B. -H., "Online Diagnosis of Induction Motors Using MCSA," *IEEE Trans. Ind. Electron.*, vol. 53, no. 6, pp. 1842-1852, 2006.

[24] Douglas H., Pillay P., and Ziarani A., "Detection Of Broken Rotor Bars In Induction Motors Using Wavelet Analysis", in *Proc. IEMDC*, 2003, pp. 923-928, IEEE.

[25] Ayhan B., Chow Mo-Yuen and Song Myung-Hyun, "Multiple signature processing-based fault detection schemes for broken rotor bar in induction motors," *IEEE Trans. Energy Conver.*, vol. 20, no. 2, pp. 336-343, 2005.

[26] Ayhan B., Chow M. -. and Song M. -., "Multiple Discriminant Analysis and Neural-Network-Based Monolith and Partition Fault-Detection Schemes for Broken Rotor Bar in Induction Motors," *IEEE Trans. Ind. Electron.*, vol. 53, no. 4, pp. 1298-1308, 2006.

[27] Cardoso A. J. M. and Saraiva E. S., "Computer-aided detection of airgap eccentricity in operating three-phase induction motors by Park's vector approach," *IEEE Trans. Ind. Appl.*, vol. 29, no. 5, pp. 897-901, 1993.

[28] Joksimovic G.M., "Dynamic Simulation Of Cage Induction Machine With Air Gap Eccentricity", *IEE Proc. - Elec. Power Appl.*, vol. 152, no. 4, pp. 803-811, 2005.

[29] Belmans R., Vandenput A. and Geysen W., "Influence of Torsional Vibrations on Lateral Oscillations of Induction Motor Rotors," *IEEE Power Eng. Review*, vol. PER-5, no. 7, pp. 49-50, 1985.

[30] Kitchenham B.A., Charters S., "Guidelines for Performing Systematic Literature Reviews in Software Engineering, Evidence-based Software Engineering", *Technical Report EBSE*, vol. 5, 2007.

[31] Kitchenham B., Pretorius R., Budgen D., Brereton O.P., Turner M., Niazi M., Linkman S., "Systematic literature reviews in software engineering a tertiary study", *Inf. Softw. Technol*, vol. 52, no 8, pp. 792-805, 2010.

[32] Kumar P., and Hati A.S., "Review on Machine Learning Algorithm Based Fault Detection in Induction Motors", *Arch. Comput. Methods Eng.*, vol. 28, no 3, pp. 1929-1940, 2021.

[33] El Hachemi Benbouzid M., "A review of induction motors signature analysis as a medium for faults detection," *IEEE Trans. Ind. Electron.*, vol. 47, no. 5, pp. 984-993, 2000.

[34] Benbouzid M. E. H. and Kliman G. B., "What stator current processing-based technique to use for induction motor rotor faults diagnosis?," *IEEE Trans. Energy Conver.*, vol. 18, no. 2, pp. 238-244, 2003.

[35] Arthur N. and Penman J., "Induction machine condition monitoring with higher order spectra," *IEEE Trans. Ind. Electron.*, vol. 47, no. 5, pp. 1031-1041, Oct. 2000

[36] Ristanoski G., Liu W., Bailey J., "A time-dependent enhanced support vector machine for time series regression", in *Proc. ICKDDM*, 2013, pp. 946-954.

About the Editor

JORGE RODAS was born in Asuncion, Paraguay, in 1984. He received his Engineer degree in electronic engineering from the Universidad Nacional de Asuncion (UNA), Paraguay, in 2009. He received his M.Sc. degrees from the Universidad de Vigo, Spain, in 2012 and from the Universidad de Sevilla, Spain, in 2013, and his joint-university Ph.D. degree between the Universidad Nacional de Asuncion and the Universidad de Sevilla in 2016. In 2021 he received his Master degree from the National Defence Council, Paraguay.

In 2011, he joined the Laboratory of Power and Control Systems (LSPyC), Faculty of Engineering, UNA, where he currently serves as a professor. He was visiting professor at the Ecole de Technologie Superieure (Montreal, Canada) and the Polytechnic University of Catalonia (Barcelona, Spain), in 2017 and 2022, respectively. He serves as an Associate Editor of Elsevier Alexandria Engineering Journal and Guest Editor in the IEEE Journal of Emerging and Selected Topics in Power Electronics, MDPI World Electric Vehicle Journal and frontiers in Energy Research. He served as Guest Editor of MDPI Energies. In 2020, Prof. Rodas received the Paraguayan National Science Award.

His research interests focus on applications of advanced control to real-world problems. Current research activities include applying finite control set model predictive control and nonlinear control to power electronic converters, renewable energy conversion systems, electric motor drives and robotic systems (especially drones).

Index

Power Electronic Converters and Induction Motor Drives

Jorge Rodas, PhD

E d i t o r

nova
science publishers